



INSTITUTE
OF
NAVAL ARCHITECTURE
AND
OCEAN ENGINEERING



Polish Maritime Research

No 4 (112) 2021
Vol. 28

ADDRESS OF PUBLISHER
& EDITOR'S OFFICE:

GDAŃSK UNIVERSITY
OF TECHNOLOGY

Institute
of Naval Architecture
and Ocean Engineering
G. Narutowicza 11/12
80-233 Gdańsk, POLAND

EDITORIAL STAFF:

Wiesław Tarełko
| Editor in Chief
Janusz Kozak
| Deputy Editors-in-Chief
Wojciech Litwin
| Deputy Editors-in-Chief

Price:
single issue: 25 PLN

Prices for abroad
single issue:
- in Europe EURO 15
- overseas USD 20

WEB:
pg.edu.pl/pmr

e-mail : pmr@pg.edu.pl

ISSN 1233-2585

CONTENS

- 4 Fengkun Li, Pengyao Yu, Qiang Wang, Guangzhao Li, Xiangcheng Wu,
*NUMERICAL ANALYSIS OF THE EFFECT OF FLEXIBILITY ON THE PROPULSIVE
PERFORMANCE OF A HEAVING HYDROFOIL UNDERGOING SINUSOIDAL AND
NON-SINUSOIDAL MOTIONS*
- 20 Huawu Zhang, Yihuai Hu, Jianhai He
WIND TUNNEL EXPERIMENT OF MULTI-MODE ARC SAIL DEVICE
- 30 Lech Rowinski, Maciej Kaczmarczyk
*EVALUATION OF EFFECTIVENESS OF WATERJET PROPULSOR FOR A SMALL
UNDERWATER VEHICLE*
- 42 Karol Niklas, Alicja Bera
*THE INFLUENCE OF SELECTED STRAIN-BASED FAILURE CRITERIA ON SHIP
STRUCTURE DAMAGE RESULTING FROM A COLLISION WITH AN OFFSHORE
WIND TURBINE MONOPILE*
- 53 Bogdan Rozmarynowski, Wojciech Jesien
*SPECTRAL RESPONSE OF STATIONARY JACK-UP PLATFORMS LOADED BY SEA
WAVES AND WIND USING PERTURBATION METHOD*
- 63 Mohammad Hossein Ghaemi
*PERFORMANCE AND EMISSION MODELLING AND SIMULATION OF MARINE
DIESEL ENGINES USING PUBLICLY AVAILABLE ENGINE DATA*
- 88 C.G. Rodriguez, M.I. Lamas, J.D. Rodriguez, A. Abbas
*ANALYSIS OF THE PRE-INJECTION SYSTEM OF A MARINE DIESEL ENGINE
THROUGH MULTIPLE-CRITERIA DECISION-MAKING AND ARTIFICIAL NEURAL
NETWORKS*
- 97 Patrycja Puzdrowska
*DIAGNOSTIC INFORMATION ANALYSIS OF QUICKLY CHANGING TEMPERATURE
OF EXHAUST GAS FROM MARINE DIESEL ENGINE PART I SINGLE FACTOR
ANALYSIS*
- 107 Yajing Li, Boyang Li, Fang Deng, Qianqian Yang, Baoshou Zhang
*RESEARCH ON THE APPLICATION OF COLD ENERGY OF LARGE-SCALE LNG-
POWERED CONTAINER SHIPS TO REFRIGERATED CONTAINERS*
- 122 Serhiy Serbin, Nikolay Washchilenko, Marek Dzida, Jerzy Kowalski
*PARAMETRIC ANALYSIS OF THE EFFICIENCY OF THE COMBINED GAS-STEAM
TURBINE UNIT OF A HYBRID CYCLE FOR THE FPSO VESSEL*
- 133 Xiaowen Li, Zhaoyi Zhu, Qinglin Chen, Yingqiang Cai, Miaoqiao Peng
*EXPERIMENTAL AND NUMERICAL STUDIES ON THE SHEAR STABILITY OF
SHIP'S THIN PLATES*

**ADDRESS OF PUBLISHER
& EDITOR'S OFFICE:**

**GDAŃSK UNIVERSITY
OF TECHNOLOGY**

**Institute
of Naval Architecture
and Ocean Engineering
G. Narutowicza 11/12
80-233 Gdańsk, POLAND**

- 142 Miroław Łącki**
*AN ADAPTIVE ISLAND MODEL OF POPULATION FOR NEUROEVOLUTIONARY
SHIP HANDLING*
- 151 Leszek Matuszewski, Piotr Bela**
NEW DESIGNS OF MAGNETIC FLUID SEALS FOR RECIPROCATING MOTION
- 160 Jerzy Kowalski, Wojciech Leńniewski, Daniel Piątek,
Dominika Cuper - Przybylska**
*ASSESSING THE POTENTIAL REPLACEMENT OF MINERAL OIL WITH
ENVIRONMENTALLY ACCEPTABLE LUBRICANTS IN A STERN TUBE BEARING:
AN EXPERIMENTAL ANALYSIS OF BEARING PERFORMANCE*
- 167 Ewa Piątkowska**
*INFLUENCE OF SOLID PARTICLE CONTAMINATION ON THE WEAR PROCESS
IN WATER LUBRICATED MARINE STRUT BEARINGS WITH NBR AND PTFE
BUSHES*
- 179 LETTER TO EDITOR**

Editorial

POLISH MARITIME RESEARCH is the scientific journal with a worldwide circulation. This journal is published quarterly (four times a year) by Gdansk University of Technology (GUT). On September, 1994, the first issue of POLISH MARITIME RESEARCH was published. The main objective of this journal is to present original research, innovative scientific ideas, and significant findings and application in the field of :

Naval Architecture, Ocean Engineering and Underwater Technology,

The scope of the journal covers selected issues related to all phases of product lifecycle and corresponding technologies for offshore floating and fixed structures and their components.

All researchers are invited to submit their original papers for peer review and publications related to methods of the design; production and manufacturing; maintenance and operational processes of such technical items as:

- all types of vessels and their equipment,
- fixed and floating offshore units and their components,
- autonomous underwater vehicle (AUV) and remotely operated vehicle (ROV).

We welcome submissions from these fields in the following technical topics:

- ship hydrodynamics: buoyancy and stability; ship resistance and propulsion, etc.,
 - structural integrity of ship and offshore unit structures: materials; welding; fatigue and fracture, etc.,
 - marine equipment: ship and offshore unit power plants: overboarding equipment; etc.
-

Scientific Board

Chairman : Prof. JERZY GIRTLEK - Gdańsk University of Technology, Poland

Vice-chairman : Prof. CARLOS GUEDES SOARES, Universidade de Lisboa, Lisbon, Portugal

Vice-chairman : Prof. MIROSŁAW L. WYSZYŃSKI - University of Birmingham, United Kingdom

Prof. POUL ANDERSEN Technical University of Denmark Kongens Lyngby Denmark	Prof. STOJCE DIMOV ILCEV Durban University of Technology Durban South Africa	Prof. JERZY MERKISZ Poznan University of Technology Poznan Poland
Prof. JIAHN-HORNG CHEN National Taiwan Ocean University Keelung Taiwan	Prof. YORDAN GARBATOV Universidade de Lisboa, Lisbon Portugal	Prof. VALERI NIEKRASOV Admiral Makarov National University of Shipbuilding Mikolaiv Ukraine
Prof. VINCENZO CRUPI University of Messina Messina Italy	Prof. STANISŁAW GUCMA Maritime University of Szczecin Szczecin Poland	Prof. SERHIY SERBIN Admiral Makarov National University of Shipbuilding Mikolaiv Ukraine
Prof. MAREK DZIDA Gdansk University of Technology Gdansk Poland	Prof. ANTONI ISKRA Poznan University of Technology Poznan Poland	Prof. JOZEF SZALA UTP University of Science and Technology Bydgoszcz Poland
Dr. KATRIEN ELOOT, Flanders Hydraulics Research, Antwerpen Belgium	Prof. JAN KICINSKI Institute of Fluid-Flow Machinery - Polish Academy of Sciences Gdansk Poland	Prof. HOANG ANH TUAN Ho Chi Minh City University of Technology (HUTECH) Ho Chi Minh Vietnam
Prof. ODD MAGNUS FALTINSEN Norwegian University of Science and Technology Trondheim Norway	Prof. ZBIGNIEW KORCZEWSKI Gdansk University of Technology Gdansk Poland	Prof. TADEUSZ SZELANGIEWICZ Maritime University of Szczecin Szczecin Poland
Prof. MASSIMO FIGARI University of Genova Genova Italy	Prof. JOZEF LISOWSKI Gdynia Maritime University Gdynia Poland	Prof. DRACOS VASSALOS University of Strathclyde Glasgow United Kingdom
Prof. HASSAN GHASSEMI Amirkabir University of Technology Tehran Iran	Prof. JERZY EDWARD MATUSIAK Aalto University Espoo Finland	

NUMERICAL ANALYSIS OF THE EFFECT OF FLEXIBILITY ON THE PROPULSIVE PERFORMANCE OF A HEAVING HYDROFOIL UNDERGOING SINUSOIDAL AND NON-SINUSOIDAL MOTIONS

Fengkun Li

Pengyao Yu*

Qiang Wang

Guangzhao Li

Xiangcheng Wu

College of Naval Architecture and Ocean Engineering, Dalian Maritime University, Dalian, China

* Corresponding author: yupengyao@dlnu.edu.cn (P. Yu)

ABSTRACT

Numerical simulations of fluid-structure interaction (FSI) on an elastic foil heaving with constant amplitude in freestream flow are carried out at a low Reynolds number of 20,000. The commercial software STAR-CCM+ is employed to solve the flow field and the large-scale passive deformation of the structure. The results show that introducing a certain degree of flexibility significantly improves the thrust and efficiency of the foil. For each Strouhal number St considered, an optimal flexibility exists for thrust; however, the propulsive efficiency keeps increasing with the increase in flexibility. The visualisation of the vorticity fields elucidates the improvement of the propulsive characteristics by flexibility. Furthermore, the mechanism of thrust generation is discussed by comparing the time-varying thrust coefficient and vortex structure in the wake for both rigid and elastic foils. Finally, in addition to sinusoidal motions, we also consider the effect of non-sinusoidal trajectories defined by flattening parameter S on the propulsive characteristics for both rigid and elastic foils. The non-sinusoidal trajectories defined by $S=2$ are associated with the maximum thrust, and the highest values of propulsive efficiency are obtained with $S=0.5$ among the cases considered in this work.

Keywords: Fluid-structure interaction; Flexible hydrofoil; Non-sinusoidal motions; Propulsive characteristics

INTRODUCTION

The fluid-structure interaction (FSI) phenomenon exists widely in nature and engineering systems [1-3] such as aerospace engineering, ocean engineering and biomedical engineering. These engineering fields always involve complex geometric shapes and large-scale active or passive flow-induced deformations. The nonlinear deformation of a structure is still challenging in FSI problems. Birds [4, 5], insects [6, 7] and aquatic animals [8] can gain efficient propulsion by flapping their flexible or elastic wings and fins. To simplify the model, in previous experiments or numerical simulations to analyse thrust generation and how to achieve efficient propulsion, the wings/fins have usually been considered as a rigid plate

or foil [7, 9, 10]. However, in fact, birds and aquatic animals will interact with the surrounding viscous fluid to generate large-scale deformations when they use their wings/fins to fly/swim. Inspired by this, the FSI problem in the propulsion of underwater bionic vehicles has been a hot topic in recent years [11]. Therefore, it is necessary to study the effect of flexibility on the thrust generation and effective propulsion of the foil.

In fact, many studies have reported the propulsion characteristics of rigid plates/foils immersed in free flow in the past few years. These plates/foils are set to undergo pitching, heaving and combined pitching and heaving motions in the fluid. Within a specific range of pitching and heaving frequency, the vortices on the surface of the plate/foil are shed and form a reverse von Kármán vortex street which is

a signature of thrust generation on the plate/foil [12-15]. In most of the literature, the dimensionless Strouhal number St is used to characterise the frequency of vortices shedding. Triantafyllou et al. [16] conducted experimental measurements on oscillating foils immersed in a uniform oncoming flow and found that the optimal propulsive efficiency was always attained within a narrow range of St ($0.2 \leq St \leq 0.4$). Eloy [17] reported similar conclusions to Triantafyllou et al. [16]. Pedro et al. [14] numerically investigated the influence of the Strouhal number and pitch angle on the efficiency of a foil undergoing the combined pitching and heaving motions. Similarly, Lewin and Haj-Hariri [18] numerically studied the power coefficient and fluid characteristics of a heaving foil at low Reynolds number. The effects of asymmetric non-sinusoidal trajectories were also discussed in this paper. The results showed that for a fixed St , the propulsive efficiency attained by the intermediate heaving frequency was always the largest, which was contrary to the conclusion of the ideal model of Wang et al. [19]. In addition to thrust force and efficiency, the wake patterns behind the rigid foil were also necessary for propulsion research [20]. Schnipper et al. [21] conducted an experimental study on a symmetrical pitching foil immersed in a vertically flowing soap film to reveal the transition mechanism of the wake by varying the oscillation frequency and amplitude of the flapping foil. Anderson et al. [22] compared the wake characteristics of pitching and heaving foils by a combination of experimental and numerical methods proposed in their study. The results showed that pitching and heaving foils had qualitatively similar wake maps spanned by the amplitude and flapping frequency. And the drag-thrust transition had a strong correlation with the changes in wake structure at low frequency and high amplitude.

Previously, we observed that the wings/fins of birds/fish are simply modelled as a rigid foil to discuss bionic propulsion. However, these wings/fins are flexible and it is necessary to discuss the effect of that flexibility on the propulsive characteristics and vortex structure of the foil [23-25]. Heathcote and Gursul [26] experimentally measured the thrust and efficiency of a heaving flexible teardrop/flat plate at Reynolds numbers of 9,000 to 27,000. The study reported that the maximum thrust and efficiency were obtained in the case of intermediate stiffness for all Reynolds numbers considered. For a fixed Reynolds number and Strouhal number, the vortex structures corresponding to the maximum thrust coefficient and maximum efficiency were analysed and compared. The stronger vortex structures behind the foil were associated with higher thrust, and weaker leading edge vortices were associated with higher efficiency according to the visualisation of the flow fluid. Soon after, Alben [27] analysed the thrust generation and vortex patterns of a pitching plate with a new formulation of motion at a small amplitude. Michelin and Smith [28] used the potential flow theory to investigate the effect of flexibility on the propulsive performance of a two-dimensional heaving wing in the inviscid limit. Recently, Zhang et al. [29] studied the effect of the mass ratio on the thrust generation of a two-dimensional elastic panel immersed in free flow. At low or intermediate mass ratios, the system resonance was beneficial for the improvement of the thrust

force and propulsive efficiency. However, for the cases of high mass ratio, the inertia of the panel was dominant. Thus, the system resonance was not conducive to thrust generation and significantly reduced the efficiency. Regarding the effect of spanwise flexibility, Heathcote et al. [30] performed a water tunnel experiment on the effect of spanwise flexibility on the propulsion characteristics of a rectangular heaving wing. The results showed that a certain degree of spanwise flexibility can improve the thrust and efficiency. The Strouhal number for which flexibility was beneficial for propulsive performance was consistent with that observed in aquatic animals and birds in nature, namely $0.2 \leq St \leq 0.4$.

Furthermore, most of the plates/foils mentioned in the previous literature experienced simple harmonic motions. Recently, it has also been observed that non-sinusoidal trajectories have a significant effect on the propulsion characteristics. The experiment by Read et al. [31] made a sinusoidal variation of the angle of attack by introducing higher harmonics in the heaving motion. The thrust coefficient was greatly improved at high Strouhal numbers. Xiao and Liao [32] numerically investigated the effect of the harmonic cosine angle of attack profile on the propulsive performance. The results showed that the degradation of thrust and efficiency could be greatly alleviated or removed at a high Strouhal number when the angle of attack was imposed as a cosine function. The stronger reverse von Kármán vortex street in the wake was considered to induce the improvement of the propulsive performance. A numerical study by Lu et al. [33] reported that non-sinusoidal trajectories affected the aerodynamics of the two-dimensional foil by affecting the instantaneous force coefficient and flow structure. The author reported that non-sinusoidal motions could also enhance the reverse von Kármán vortex street in the wake, which induced an increase in thrust force. More recently, Boudis et al. [34] proposed a new type of non-sinusoidal function to calculate the aerodynamics of an NACA0012 foil undergoing combined pitching and heaving motions at a Reynolds number of 11,000. The authors reported that non-sinusoidal motions greatly improved the thrust force; however, the propulsive efficiency attained with sinusoidal trajectories was always higher than that with non-sinusoidal motions.

While several previous researchers have reported the thrust generation, flow structure around the plate/foil and the effect of kinematic parameters, the effects of large-scale deformation due to the interaction with the fluid have rarely been reported. Recently, Manjunathan et al. [35] reported the thrust generation mechanism of an elastic flat plate which was set to experience sinusoidal motions. However, the effect of non-sinusoidal trajectories on the thrust generation is not discussed. And the hydrodynamic performance of the NACA airfoil is better than that of flat plates. Therefore, it is necessary to investigate the effect of non-sinusoidal trajectories on the thrust characteristics of the flexible NACA airfoil. The main aim of this present work is to investigate the effect of flexibility on the propulsive characteristics, vortex shedding and wake pattern behind the foil at a low Reynolds number of 20,000. We also explore the effect of non-sinusoidal trajectories on the

propulsive performance of an elastic foil. The rest of the paper is arranged as follows: First, we describe the problem of bionic propulsion and give the definition of related parameters in section 2. And we present the results and discuss the influence of flexibility on the propulsive performance in Section 3. Finally, we summarise the paper in Section 4.

COMPUTATIONAL APPROACH

PROBLEM DESCRIPTION

The fluid-structure interaction (FSI) of a two-dimensional elastic NACA0012 foil undergoing pure heaving motion is considered at low Reynolds numbers. The chord length c and dimensionless relative thickness are 0.1 m and 0.12 c , respectively. The heaving motion of the foil is governed by the following equation:

$$h_L(t) = h_0 c \cos(\omega t) \quad (1)$$

where h_0 denotes the dimensionless amplitude of the heaving motion, $\omega = 2\pi f$ denotes the angular frequency. f is the oscillation frequency of the flapping foil. It is observed that the leading edge of bird wings and fish fins has greater rigidity and produces hardly any flexible deformation [36]. Therefore, a new bionic deformation shape of the flexible foil is introduced in this paper. Only the trailing edge produces flow-induced deformation, as shown in Fig. 1. The distance between the leading edge and the deformation position of the trailing edge X_s is $1/3c$. The pitching motion is introduced by the flexibility of the foil, unlike most rigid foils undergoing combined heaving and pitching motion in the previous literature. The dimensionless bending stiffness parameter is expressed as the following equation:

$$\lambda = \frac{K}{\frac{1}{2}\rho_1 U_\infty^2 c^3} \quad (2)$$

In the present work, the relative dimensionless bending parameter λ^* is defined as the ratio of each foil to the most flexible foil. The details are shown in Table 1. The Reynolds numbers Re is expressed as follows:

$$Re = \frac{\rho_1 c U_\infty}{\mu} \quad (3)$$

where ρ_1 denotes the fluid density. μ denotes the dynamic viscosity of the fluid. U_∞ denotes the freestream velocity. The Reynolds number is fixed at 2×10^4 in this paper. In the works of Boudis et al. [34], the flattening parameter S was used to define the non-sinusoidal trajectories of the foil as follows:

$$h_L(t) = h_0 c \frac{S \cos(\omega t)}{\sqrt{S^2 \cos^2(\omega t) + \sin^2(\omega t)}} \quad (4)$$

where S denotes the flattening parameter. When $S = 1$, the trajectory is sinusoidal. Eq. (4) is used to achieve the non-sinusoidal trajectories of the flexible foil. Fig. 2 shows the

non-sinusoidal trajectories; when $S = 1$, the trajectory of the oscillating foil is harmonic. The Strouhal number is an important dimensionless parameter to characterise the kinematics in the study of the hydrofoil propulsion, defined as follows:

$$St = \frac{2h_0 c f}{U_\infty} \quad (5)$$

Tab. 1. Relative dimensionless bending stiffness of foils, $\lambda^* = \lambda/\lambda_0$

Young's Modulus, E (MPa)	Relative stiffness
0.05	1
0.1	2
0.3	6
0.5	10
0.75	15
1	20
2	40
4	80
rigid	∞

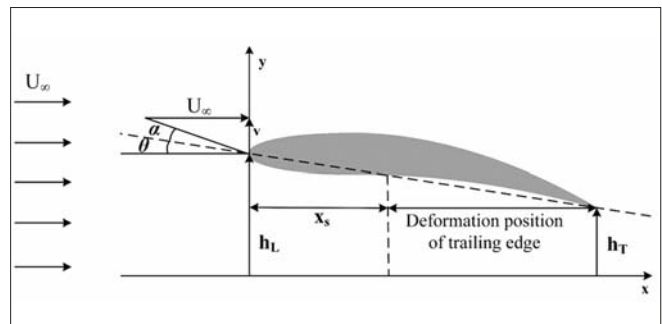


Fig. 1. Schematic of the flexible foil heaving periodically in the vertical direction

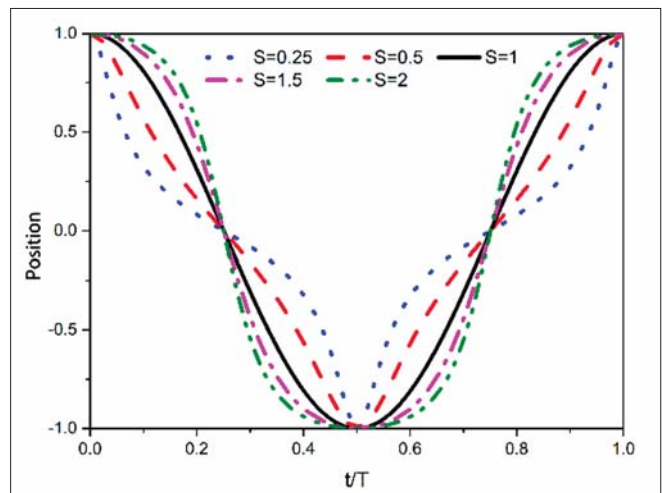


Fig. 2. Flapping trajectories according to different values of flattening parameter S

To evaluate the propulsive performance of the elastic foil, we define the following quantities. The time-varying thrust coefficient and the time-varying power-input requirement coefficient are calculated by the following equations:

$$C_T = \frac{F_x(t)}{0.5\rho_1 c U_\infty^2} \quad (6)$$

$$C_P = \frac{F_y(t) \cdot v(t)}{0.5\rho_1 c U_\infty^3} \quad (7)$$

where F_x is the instantaneous force of the foil in the thrust direction. The thrust coefficient C_T consists of two components, namely, the pressure component and shear component, expressed as $C_{T,P}$ and $C_{T,S}$. F_y is the instantaneous force of the foil in the lift direction. $v(t)$ is the velocity of the leading edge of the foil in the lift direction. The time-averaged coefficients of thrust and power are calculated from the average force per unit period and they can be expressed as follows:

$$C_{T,mean} = \frac{\frac{1}{T} \int_0^T F_x(t) dt}{0.5\rho_1 c U_\infty^2} \quad (8)$$

$$C_{P,mean} = \frac{\frac{1}{T} \int_0^T [F_y(t) \cdot v(t)] dt}{0.5\rho_1 c U_\infty^3} \quad (9)$$

Moreover, the propulsive efficiency can be defined as follows:

$$\eta = \frac{C_{T,mean}}{C_{P,mean}} \quad (10)$$

GOVERNING EQUATIONS

The flow around the two-dimensional elastic foil is assumed to be unsteady, viscous, and incompressible. It can be solved by calculating the Navier–Stokes equations as follows:

$$\nabla \cdot u_1 = 0 \quad (11)$$

$$\frac{\partial u_1}{\partial t} + (u_1 \cdot \nabla) u_1 = -\frac{1}{\rho_1} \nabla p + \nu \nabla^2 u_1 + F \quad (12)$$

where p is the pressure, F is the volume forces, u_1 is the fluid velocity, and ν is the viscosity.

The commercial computational fluid dynamic solver STAR-CCM+ is employed to solve the flow field. The Finite Volume Method is used to discretize the N-S equations. The SIMPLE (Semi-Implicit Method for Pressure-Linked Equations) algorithm is used to solve pressure-velocity coupling of the flow field. The pressure and momentum are discretised by a second-order implicit scheme. The turbulent model SST $k-\omega$ is used in all numerical simulations. The deformation of the flexible foil is governed by the structural momentum conservation equation, which can be expressed follows:

$$\nabla \times \sigma + \rho_2 (b - \ddot{d}) = 0 \quad (13)$$

where σ is the stress tensor, ρ_2 is the foil density, b is the body force, d is the displacement of the structure. The structure is considered as a linear constitutive material and can be expressed as follows:

$$\begin{aligned} \sigma &= 2\mu\epsilon + \lambda \text{tr}(\epsilon)I \\ \epsilon &= \frac{1}{2} ((\nabla \cdot d) + (\nabla \cdot d)^T) \end{aligned} \quad (14)$$

where σ is the stress tensor, ϵ is the strain tensor, I is the identity tensor, λ is Lamé's first parameter, μ is the shear modulus. The Finite Element Method is used to solve the large-scale deformation of the foil. Implicit coupling is employed. The fluid domain and structure domain exchange the geometric and force information at each time step. The pressure and shear force calculated are enforced as boundary conditions of the structure solver. The displacements of the structure are enforced as boundary conditions of the fluid solver. The interface of the fluid and structure needs to ensure that the velocity and displacement are continuous functions. The equations governing these boundary conditions are expressed as follows:

$$\sigma_s \cdot n = \sigma_f \cdot n, d_s = d_f \quad (15)$$

where subscript f denotes the fluid, subscript s denotes the structure.

BOUNDARY CONDITIONS AND GRID SENSITIVITY

Fig. 3 shows the computational domain and boundary conditions. The computational domain consists of two parts, a background zone and an overset zone. The background zone is a rectangle with $60c \times 40c$, and the overset zone is a circle with a radius of $1c$. A no-slip condition is imposed on the elastic foil surface, which means that the velocity of the fluid over the foil is zero. At the left, top and bottom boundaries, the boundary condition is set to the velocity inlet, which means that the pressure is zero gradient and the velocity is equal to freestream velocity $U_\infty = 0.2$ m/s. The right boundary is set to the pressure outlet. The mesh around the foil is refined to accurately simulate the fluid structure. To make the $y^+ \leq 1$, the height of the first layer grid is $10^{-5}c$. The overall situation of the grid is shown in Fig. 4.

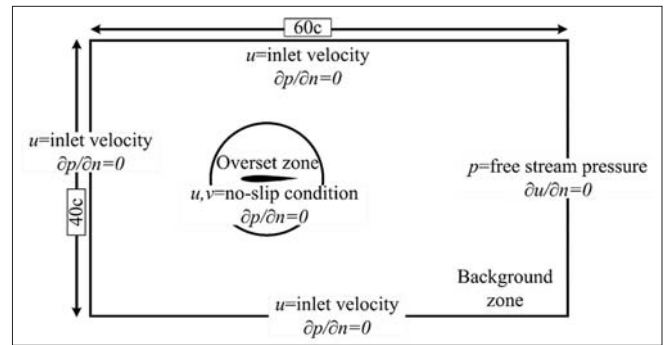


Fig. 3. Computational domain and boundary condition

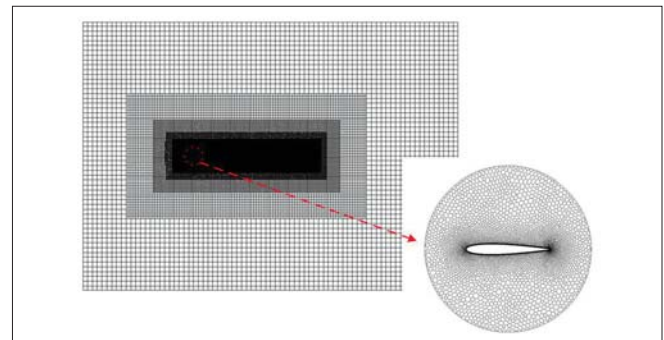


Fig. 4. The overall mesh situation and the overset domain mesh

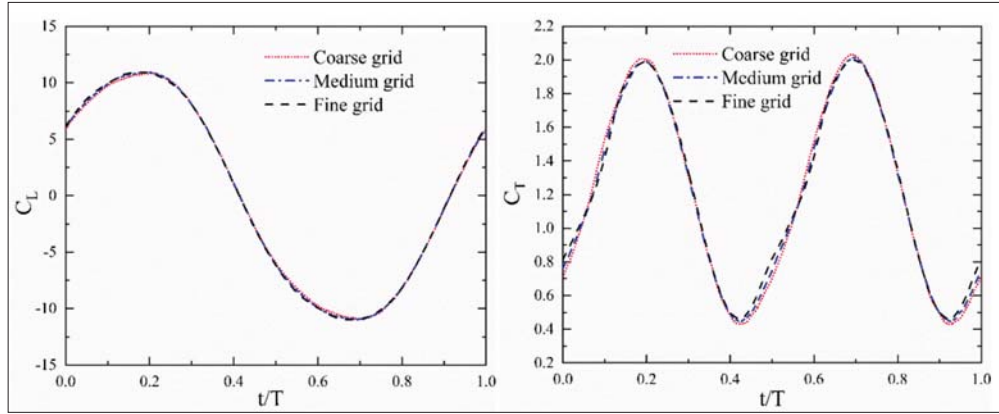


Fig. 5. Grid independence study: (a) the time-varying lift coefficient in one typical cycle; (b) the time-varying thrust coefficient in one typical cycle

Tab. 2. Characteristics of three mesh sizes for grid sensitivity

Grid name	Number of points on foil	Number of cells
Coarse grid	100	48574
Medium grid	200	86732
Fine grid	400	245194

CODE VALIDATION

To confirm the accuracy of the FSI solver in STAR-CCM+, we carried out two validations and the results were compared with the experimental data and numerical simulation data reported in the literature. The first validation is a heaving NACA0012 foil and the time-averaged thrust coefficient is calculated using the kinematic parameters $h_0 = 0.175$, $Re = 2 \times 10^4$, and the dimensionless reduced frequency k varying in the range of (2-8), ($k = 2\pi fc / U_\infty$). In Fig. 6, the results attained in the present work are compared with the experimental data of Heathcote et al. [30] and the numerical data of Young and Lai [37] dB. It can be seen that all the simulation results show similar trends and are in good agreement.

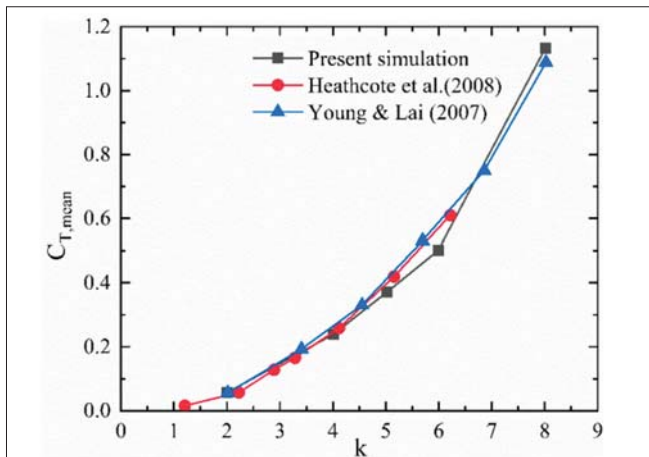


Fig. 6. Comparison of the time-average thrust coefficient with the previous literature

The second validation is the numerical simulation of a flow-induced passive deformation of a flexible plate connected behind the cylinder at low Reynolds numbers. The fluid-structure

interaction of a flexible plate added behind the cylinder proposed by Turek and Hron [38] has been a typical problem in the study of FSI in recent decades. The cylinder and the elastic plate are placed in a rectangular laminar field. The fluid flow through the cylinder and the unsteady vortex is shed, which stimulates the flexible plate to periodically oscillate. The computational configuration is shown in Fig. 7. The dimensionless length and thickness of the plate are $3.5D$ and $0.2D$, respectively. The structure to fluid density ratio, dimensionless Young's Modulus ($E/\rho f U_\infty^2$), Reynolds number and Poisson ratio are set to 10, 1400, 100, and 0.4, respectively. The no-slip boundary condition is imposed at the top and bottom of the computational domain. The left is set to the velocity inlet, and a parabolic velocity profile is set as follows:

$$v_1(0, y) = 1.5U \frac{y(H-y)}{\left(\frac{H}{2}\right)^2} \quad (16)$$

where U is the average inflow velocity and the maximum inflow velocity is $1.5U$. The left of the plate is fixed on the cylinder surface. The no-slip boundary condition is applied on the surface of the plate. To realise accurate simulations of the flow structure, the grid around the cylinder and plate is refined. The minimum grid size is set as $0.03D$ to ensure the grid converges. Fig. 8 shows the periodic vibration of the splitter plate with multiple bending modes caused by alternate shedding of vortices over the cylinder. The time-varying displacement of the reference point A (Fig. 7) in the y -direction when the plate achieves periodic self-sustaining oscillation is shown in Fig. 9. The result shows great agreement with the data reported by Turek and Hron [38]. The validations performed in this section confirmed that the FSI solver in STAR-CCM+ is able to simulate the deformation of the elastic hydrofoil.

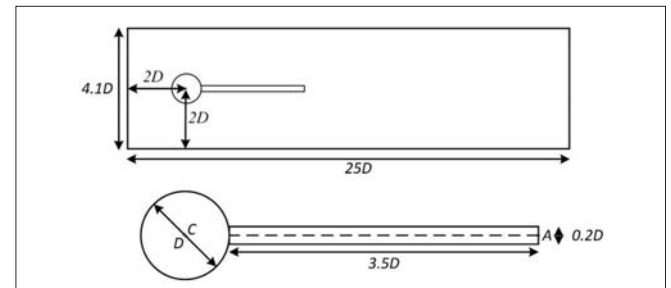


Fig. 7. Computational configuration

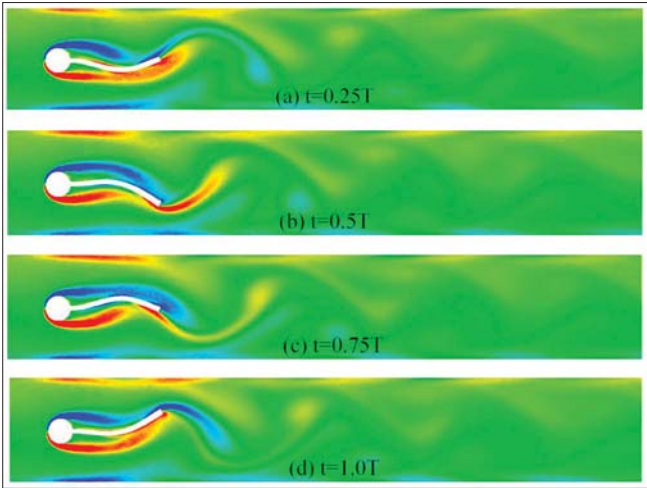


Fig. 8. Contours of the instantaneous spanwise vorticity during a vortex shedding period T

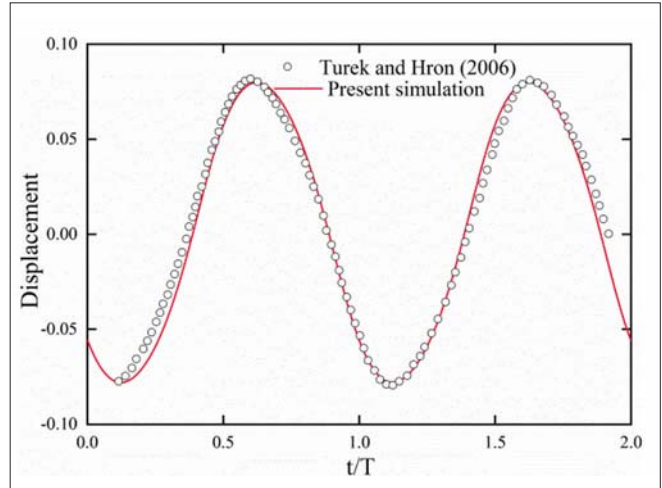


Fig. 9. Comparison of displacement of the reference point A in the y -direction

RESULTS AND DISCUSSION

EFFECT OF FLEXIBILITY ON THRUST AND EFFICIENCY

We study the effect of flexural rigidity on the propulsive performance of a flexible foil undergoing sinusoidal motion in this section. The Reynolds number Re , amplitude of the heaving motion h_0 , the structure to fluid density ratio and Poisson ratio are set to 2×10^4 , 0.3, 7.8 and 0.3, respectively. The Strouhal number St is varied in a narrow range from 0.2 to 0.4, consistent with the St of animals in nature (such as insects, birds, and

fish) observed in Taylor et al. [39]. Fig. 10 shows the overall propulsive performance as a function of the dimensionless relative bending stiffness, including the tip amplitude of the trailing edge (h_{Tip}), the time-averaged thrust coefficient ($C_{T,mean}$), the time-averaged power coefficient ($C_{P,mean}$) and the propulsive efficiency (η). As expected, the trends of h_{Tip} with λ^* are very similar within the range of St considered in this work and it decreases rapidly with the increase of bending stiffness of the foil at $\lambda^* \leq 10$. Then, it decreases steadily at $\lambda^* \geq 10$. h_{Tip} for higher St is larger than that for lower St over the whole range of bending stiffness. This is attributed to the increase in the reaction force exerted by the fluid on the foil, as the oscillation frequency of the foil increases.

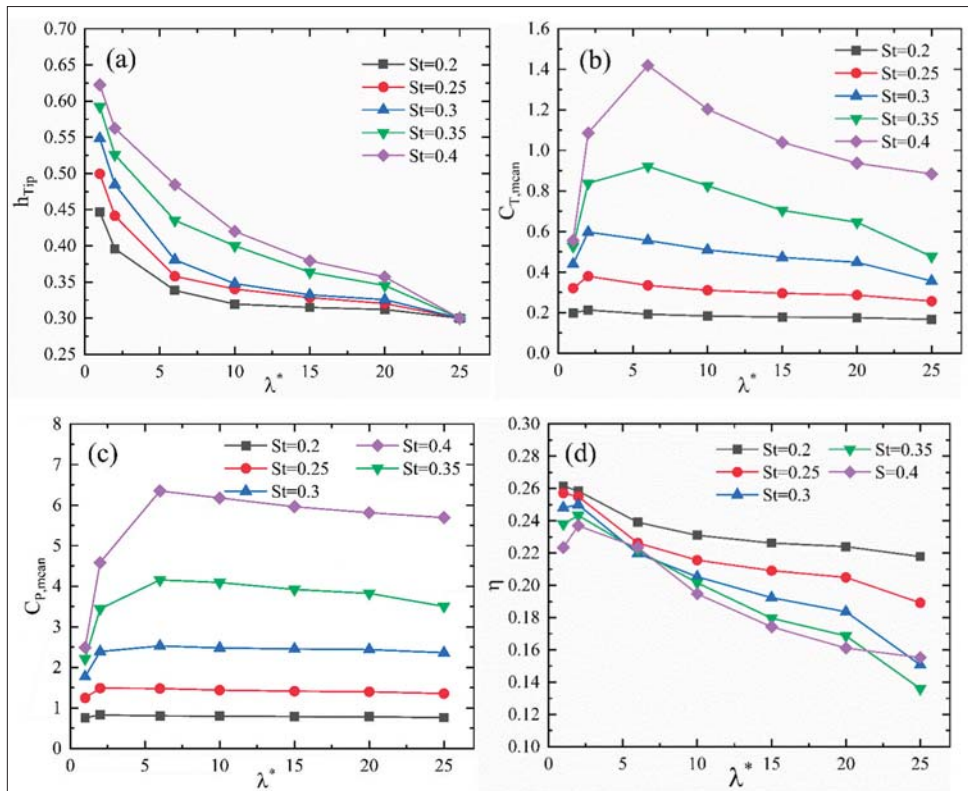


Fig. 10. Comparison of propulsive performance as a function of dimensionless relative bending stiffness: (a) tip amplitude of the trailing edge; (b) time-averaged thrust coefficient; (c) time-averaged power coefficient; (d) the propulsive efficiency

The variation trends of $C_{T,mean}$ and $C_{P,mean}$ with λ^* are plotted in Fig. 10(b) and Fig. 10(c). The trends are similar and show a peak in $C_{T,mean}$ and $C_{P,mean}$ for all St considered, which means that an optimal bending stiffness exists for thrust. The peak moves to a higher value of bending stiffness with the increase of the Strouhal number St. For St = 0.2, 0.25 and 0.3, $C_{T,mean}$ and $C_{P,mean}$ gradually increase until $\lambda^* = 2$ and start decreasing beyond it. $C_{T,mean}$ and $C_{P,mean}$ increase sharply until $\lambda^* = 6$ and start falling beyond it for St = 0.35 and 0.4. Fig. 11 shows the comparison of the averaged velocity profile in the wake of the rigid and elastic foils for St = 0.4. The three foils correspond to the rigid foil, the one that produces the largest thrust, and the most flexible foil. For the elastic foil of $\lambda^* = 6$, a higher positive additional x component of velocity is observed than in the most flexible foil ($\lambda^* = 1$). The magnitude of jet-like velocity is considered to be related to the generation of thrust, so a suitable flexibility can produce larger thrust than the most flexible foil ($\lambda^* = 1$). The far greater flexibility is found to be disadvantageous in terms of thrust generation. The Strouhal number St has a relatively large effect on the thrust improvement especially for high St. For St=0.4, the maximum $C_{T,mean}$ obtained by the flexible foil is around 1.42, almost 1.6 times larger than that by the rigid foil. However, it is 1.28 times that for St = 0.2. $C_{T,mean}$ obtained with high St is always higher than that obtained with low St and shows a monotonical increase with the increase of St. The maximum $C_{T,mean}$ obtained with St = 0.4 (at $\lambda^* = 6$) is around 6.6 times larger than that with St = 0.2 (at $\lambda^* = 2$). It can be predicted that a higher St may yield even higher thrust.

Fig. 10(d) shows the propulsive efficiency η as a function of bending stiffness λ^* . For St = 0.3, 0.35 and 0.4, η reaches the peak at $\lambda^* = 2$, then steadily decreases at $\lambda^* \geq 2$. For St = 0.2 and 0.25, there is no visible optimal value for η , and it decreases in the overall range of bending stiffness. It is assumed that introducing greater flexibility of the foil may produce higher efficiency. Unlike the thrust coefficient, a lower St seems to be more conducive to efficiency improvement.

The wake signature behind the foil has a significant effect on the propulsive performance. Fig. 12 shows the vorticity fields for three foils with different bending stiffness. The leading edge of the foil is moving downwards through the mean position at $t = 1/4T$. The rotational direction and position of the vortex in the wake have a decisive effect on the thrust generation of the foil. As shown in Fig. 12, the vortex pairs are arranged in

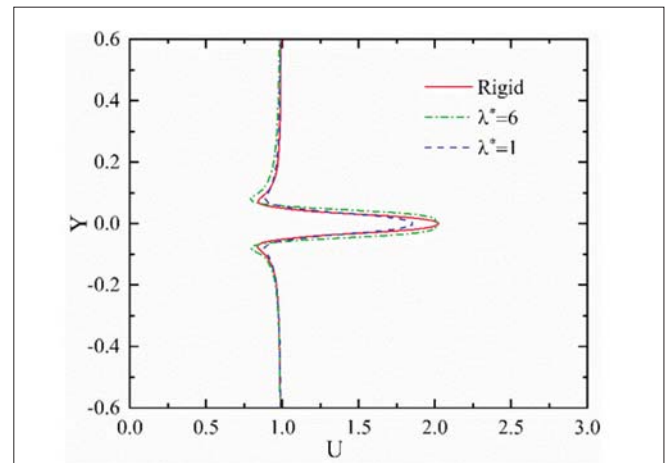


Fig. 11. Comparison between the profile of horizontal velocity U, with respect to vertical direction the elastic and rigid foils at (a) $t=T/8$, (b) $t=1T/4$, (c) $t=3T/8$

two rows, with the counterclockwise vorticity on the top and the clockwise vorticity on the bottom. The arrow indicates the direction of the flow velocity. Induced by the vortex in the wake, the flow direction is the same as the direction of freestream velocity. Therefore, the direction of the reaction force exerted by the fluid on the foil is opposite to that of freestream. The formation of a reverse von Kármán vortex street in the wake generates thrust on the foil. It is noted that the vortex pairs from the most flexible foil ($\lambda^* = 1$) are weaker and more compactly distributed in the x-direction than the other two foils. This vortex structure leads to a severe reduction in the thrust force of the most flexible foil. It is also seen that the deformation of the trailing edge of the elastic foil reduces the flow separation of the leading-edge vortex and makes it weaker. Minimising the strength of the leading-edge vortex is beneficial for achieving high efficiency [40, 41]. The flexibility of the foil can improve both the thrust and the efficiency, whereas the bending stiffness for maximising thrust and efficiency is not same. The foil maximising the efficiency seems to be more flexible than that maximising the thrust [Fig. 10(b) and Fig. 10(d)]. The vortex structure for the two foils oscillating in one typical period for St = 0.4 is shown in Fig. 13. Fig. 13(a)-(d) correspond to the stiffness ($\lambda^* = 6$) that produces the maximum thrust and Fig. 13(e)-(h) correspond to the stiffness ($\lambda^* = 2$) that produces the maximum efficiency. The vortices form on the leading edge of the foil and are swept into the trailing edge vortex system in

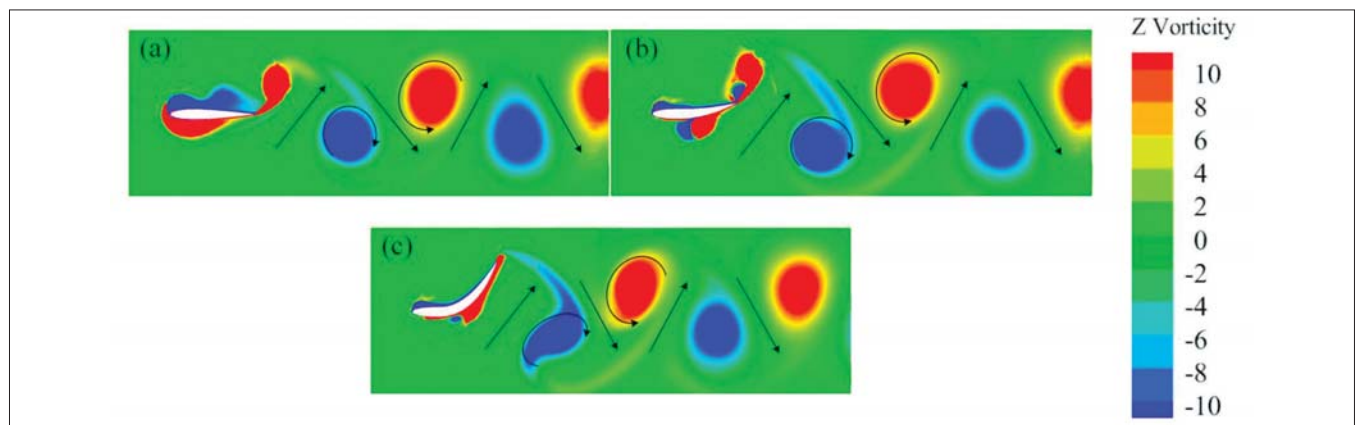


Fig. 12. Vorticity fields for three foils of different bending stiffness: (a) rigid foil; (b) $\lambda^*=6$; (c) $\lambda^*=1$

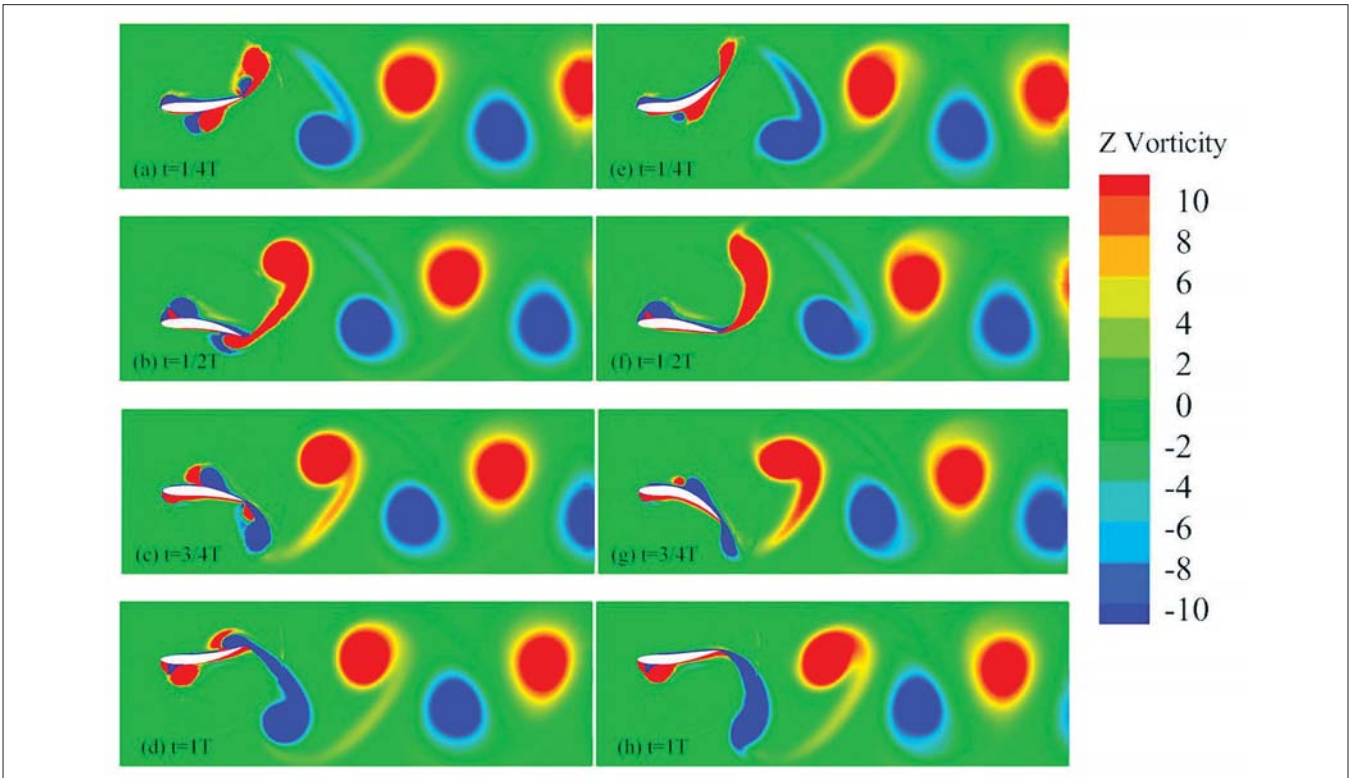


Fig. 13. Vorticity fields for two foils oscillating in one typical period for $St=0.4$: [(a)-(d)] $\lambda^*=6$ corresponding to maximum time-averaged thrust coefficient; [(e)-(h)] $\lambda^*=2$ corresponding to maximum efficiency

both cases. The vortices in the wake from the stiffer foil ($\lambda^* = 6$) are seen to be stronger, which induces high thrust. And the more flexible foil is better at making the leading edge vortices weaker, which is consistent with the higher efficiency.

ANALYSIS OF MECHANISM OF THRUST GENERATION

The mechanism of thrust generation is analysed for a rigid and an elastic foil by comparing the temporal variation of C_T , C_p and the wake structure in this section. The amplitude of heaving motion is $h_0 = 0.3$ for both cases. The Strouhal number and Reynolds number based on the chord length are 0.3 and 2×10^4 , respectively. The dimensionless relative bending stiffness is fixed at $\lambda^* = 6$ corresponding to the maximum thrust coefficient and efficiency for $St = 0.3$ (Fig. 10).

Rigid foil

Fig. 14(a) shows the time-varying displacement of the tip of the trailing edge h_T and instantaneous thrust coefficient C_T with two components of pressure and shear force for a rigid foil. The time-varying power coefficient for a rigid foil is plotted in Fig. 14(b). It is noted that the variation of h_T is sinusoidal and three peaks are observed in three typical cycles as expected, whereas six peaks are shown in the temporal variation of C_T . In other words, C_T attains its peaks twice in one oscillation cycle. C_T is minimum and negative at $t/T = 1.0$ when the foil is at the top position. Then, C_T increases sharply to the maximum value when the foil moves downwards to reach the position between the top and mean position at $t/T = 1.2$. At $t/T = 1.5$, the foil moves to the bottom position and C_T decreases from the maximum to the minimum value. When the foil returns

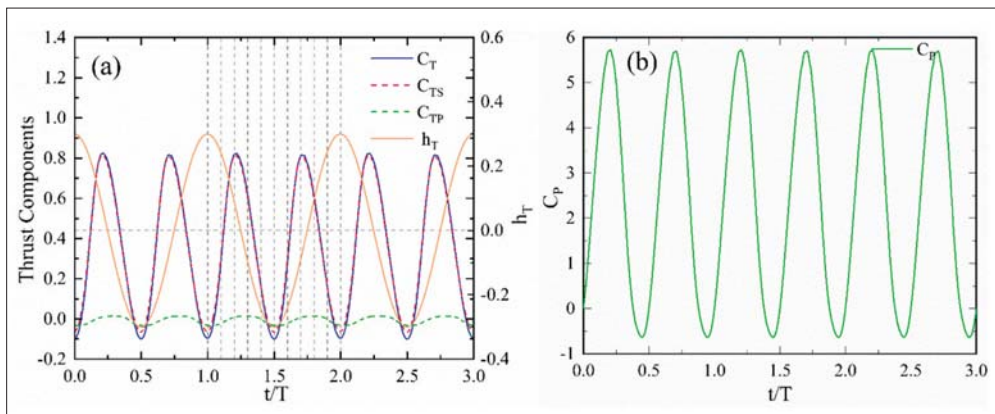


Fig. 14. (a) Temporal variation of thrust components and trailing edge displacement in three typical cycles for a rigid foil; (b) temporal variation of power coefficient for a rigid foil

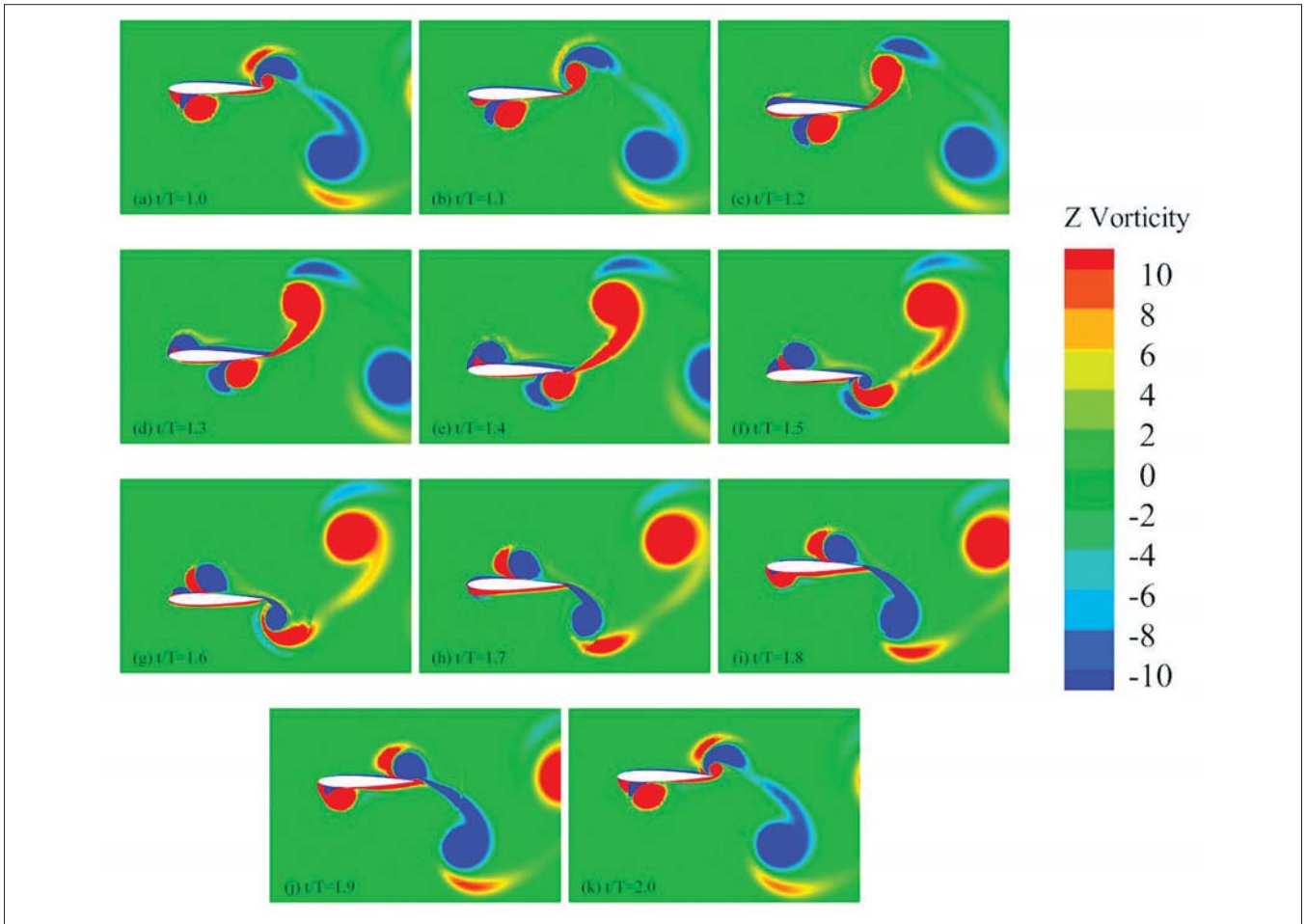


Fig. 15. Vorticity fields for a rigid foil in one typical cycle from $t/T=1.0$ to $t/T=2.0$

from the bottom position to the top position, C_T attains the maximum and minimum values successively at $t/T = 1.7$ and $t/T = 2.0$. It is noted that C_T always attains its minimum value when the foil is at both the top and bottom extremum position. When the foil moves from the extremum position to the mean position, C_T can attain the maximum value. The variation trend of the time-varying power coefficient (C_p) is similar to C_T . It attains two peaks in one typical cycle.

The trends of pressure component C_{Tp} and shear components C_{TS} of C_T are almost the same as for C_T . It is observed that the contribution of pressure to the thrust of the foil is much greater than shear force, which exerts drag on the foil. For $St = 0.3$, the time-averaged thrust coefficient $C_{T,mean}$ and the time-averaged power coefficient for the rigid foil are positive and are about 0.36 and 2.36, respectively. Therefore, the propulsive efficiency η calculated by Eq. (10) is around 0.15.

The vortex structure around a rigid foil at $St = 0.3$ in one cycle from $t/T = 1.0$ to $t/T = 2.0$ is shown in Fig. 15. It is observed that the vortices form on the leading edge of the foil and are shed from the trailing edge. At $t/T = 1.0$, on the lower surface of the foil, a pair of fully developed vortices start to move backwards along the foil surface and are shed from the trailing edge. At the same time, on the upper surface, another pair of vortices start to form and gradually develop with the downward movement of the foil until $t/T = 1.5$. At this time, the foil reaches

the bottom position and the vortices developed on the lower surface are completely shed, which leads to the time-varying thrust coefficient C_T being the minimum at $t/T = 1.5$. Then, the foil starts to move upwards. The vortices developed on the upper surface start to move backwards and are shed from the trailing edge. The shedding of the vortices minimises the thrust coefficient. The rotation direction of the shedding vortices is the opposite compared with the downwards movement of the foil. Another pair of vortices also develop on the lower surface, which will shed from the trailing edge in the next cycle of downward movement. It is also observed that although the vortices form and are shed in pairs, the strength of the pair of vortices is not equal. The clockwise vortex will eventually vanish in the wake when the foil moves downwards, while the counterclockwise vortex will vanish when the foil moves upwards.

Elastic foil

According to the analysis of the rigid foil, the time-varying displacement of the tip of the trailing edge h_T and time-varying thrust coefficient C_T with two components of pressure and shear force for an elastic foil in three typical cycles are shown in Fig. 16(a). The temporal variation of displacement of trailing edge h_T is sinusoidal, similar to the rigid foil. Due to the passive deformation of the elastic foil, the time at which h_T reaches

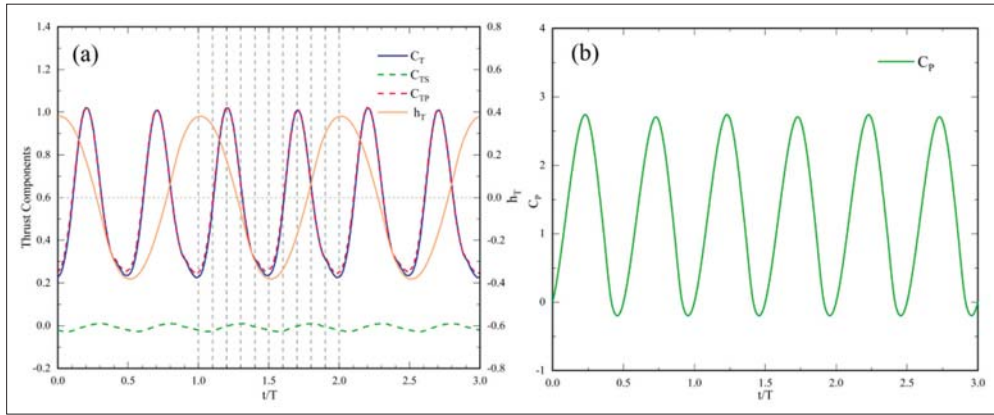


Fig. 16. (a) Temporal variation of thrust components and trailing edge displacement in three typical cycles for an elastic foil; (b) temporal variation of power coefficient for an elastic foil

its maximum value is slightly later than that of the rigid foil. The peak value of h_T is 0.38, which is 26.7% larger than that of the rigid foil. The temporal variation of C_T is sinusoidal. The variation frequency of C_T is twice as large as the oscillation frequency of the foil. It is noted that the deformation of the elastic foil has little effect on the shear force component of thrust; however, it greatly improves the positive pressure component. The time-averaged thrust coefficient $C_{T,mean}$ is significantly improved and is 0.56, 55.6% larger than the rigid foil. The time-averaged power coefficient $C_{P,mean}$ is 2.53, 7.2% larger than the rigid foil. The flexibility of the foil greatly

increases $C_{T,mean}$ while having little effect on $C_{P,mean}$. Based on this point, the propulsive efficiency η is notably improved. η for the elastic foil at $St = 0.3$ is around 0.22, 47.6% larger than the rigid foil.

In Fig. 17, the vortex shedding pattern for the elastic foil is similar to the rigid foil described previously in detail. The vortices form and develop on the leading edge of the foil and are then shed from the trailing edge. The reverse von Kármán vortex street is observed in the trailing edge vortex system behind the foil. The shedding of the vortices minimises the thrust when the foil moves to the top or bottom position.

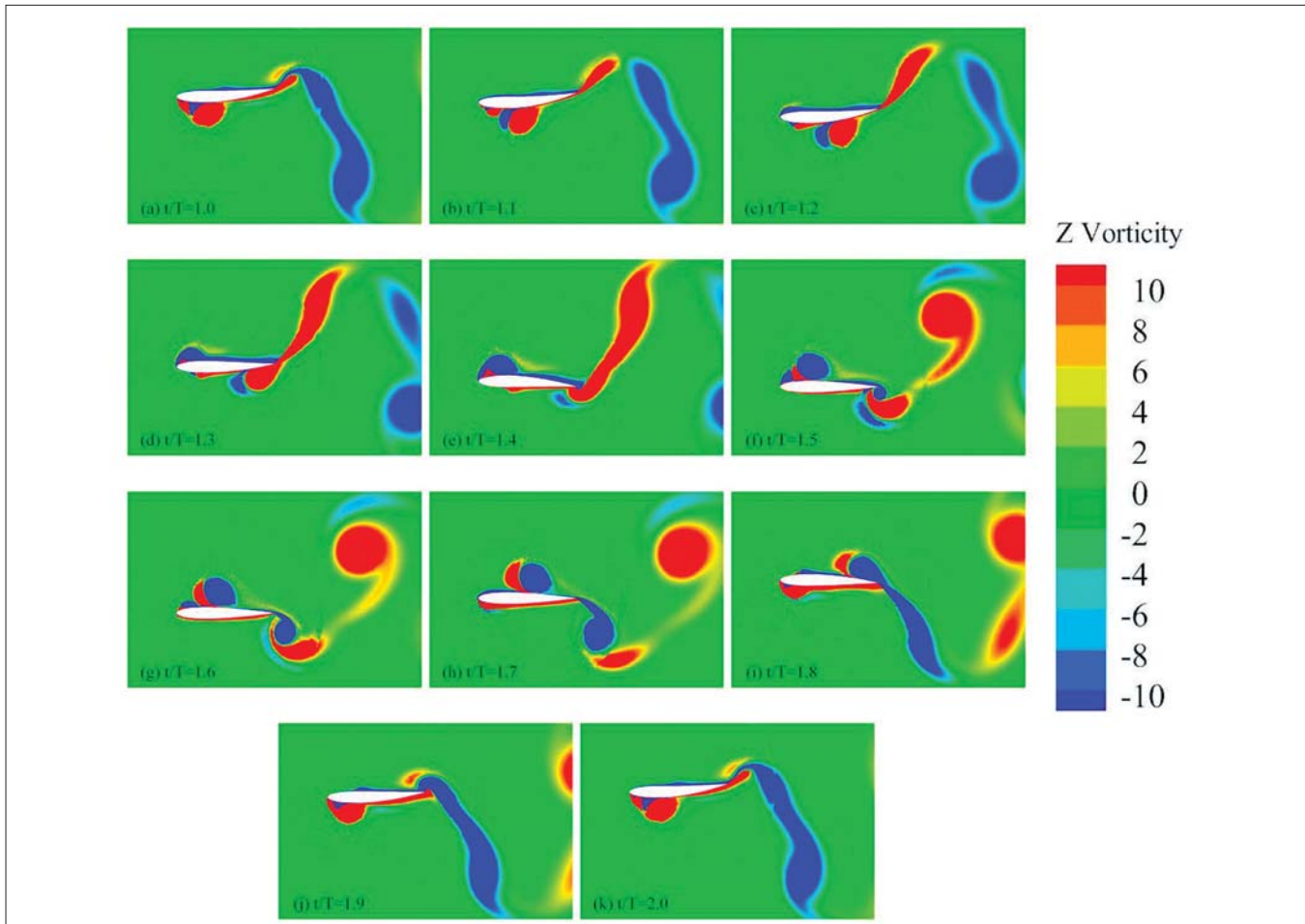


Fig. 17. Vorticity fields for an elastic foil in one typical cycle from $t/T=1.0$ to $t/T=2.0$

EFFECT OF NON-SINUSOIDAL TRAJECTORIES ON PROPULSIVE PERFORMANCE

In this section, we consider the effect of flexibility on the propulsive performance of an elastic foil undergoing two different non-sinusoidal trajectories defined by the flattening parameters S . The mathematical equation of the non-sinusoidal trajectories is based on the work of Boudis et al. [34]. The settings of the Reynolds number Re and amplitude of the heaving motion h_0 are the same as the previous sinusoidal motion, which are 2×10^4 and $0.3c$, respectively. The Strouhal number St is varied in a narrow range from 0.2 to 0.4.

Fig. 18(a)-(b) shows the time-averaged thrust coefficient $C_{T,mean}$ in one typical cycle as a function of bending stiffness λ^* for $S = 2$ and $S = 0.25$. The trends of $C_{T,mean}$ for the two non-sinusoidal trajectories are similar to sinusoidal motion. A peak value in the $C_{T,mean}$ curves for all St considered in this section is also observed. The peak values move to a larger λ^* with the increase of St in two cases. For $St = 0.2$ and 0.25 , $C_{T,mean}$ increases until $\lambda^* = 6$ and steadily decreases beyond $\lambda^* = 6$. For $St = 0.3$ and 0.35 , $C_{T,mean}$ increases rapidly at $\lambda^* \leq 10$ and decreases beyond it. $C_{T,mean}$ increases sharply until $\lambda^* = 15$ and starts decreasing at $\lambda^* \geq 15$. To clearly evaluate the effect of non-sinusoidal trajectories on $C_{T,mean}$, the maximum time-averaged thrust coefficient $MAX(C_{T,mean})$ for each St in three motions is plotted in Fig. 18(c). It is observed that $MAX(C_{T,mean})$ increases monotonically with the increase of St . The $MAX(C_{T,mean})$ obtained with non-sinusoidal trajectories is much larger than that with sinusoidal trajectories, especially for high St . At

$St = 0.4$, the values of $MAX(C_{T,mean})$ for $S = 2$ and 0.5 are 2.27 and 2.06, respectively, which are around 1.6 and 1.45 times larger than that for $S = 1$.

The time-averaged power coefficient $C_{P,mean}$ for $S = 2$ and $S = 0.5$ as a function of bending stiffness is plotted in Fig. 19(a)-(b). The variation trends of $C_{P,mean}$ are similar to $C_{T,mean}$ and show a peak value in the curves for two non-sinusoidal motions considered in this section. The peak value moves to high λ^* with the increase of St . For $S = 2$, for each St , the variation trends of $C_{P,mean}$ with λ^* are extremely steady at high bending stiffness and $C_{P,mean}$ increases sharply with the increase of λ^* at low stiffness. By contrast, for $S = 0.5$, $C_{P,mean}$ reduced rapidly at high λ^* . Fig. 19(c) shows the comparison of the maximum time-averaged power coefficient $MAX(C_{P,mean})$ attained by non-sinusoidal trajectories and sinusoidal trajectories. For each St , especially for high St , $MAX(C_{P,mean})$ for $S = 2$ is far greater than that for $S = 1$ and $S = 0.5$. For $St = 0.4$, the values for $MAX(C_{P,mean})$ for $S = 1$ and $S = 0.5$ are 6.35 and 8.33, respectively. For $S = 2$, the value is 14.8, which is 2.33 and 1.78 times larger than that for $S = 1$ and $S = 0.5$. An excessive power-input requirement seems to indicate low propulsive efficiency.

Fig. 20(a)-(b) shows the propulsive efficiency η attained by two non-sinusoidal trajectories as a function of bending stiffness for each St . The trends of propulsive efficiency η show monotonic variation; however, a local extremum is observed in the time-averaged thrust and power coefficient curves. η rapidly decreases with the increase of λ^* . The results show that introducing a certain degree of flexibility can greatly improve the propulsive efficiency η for all St considered. It is also noted

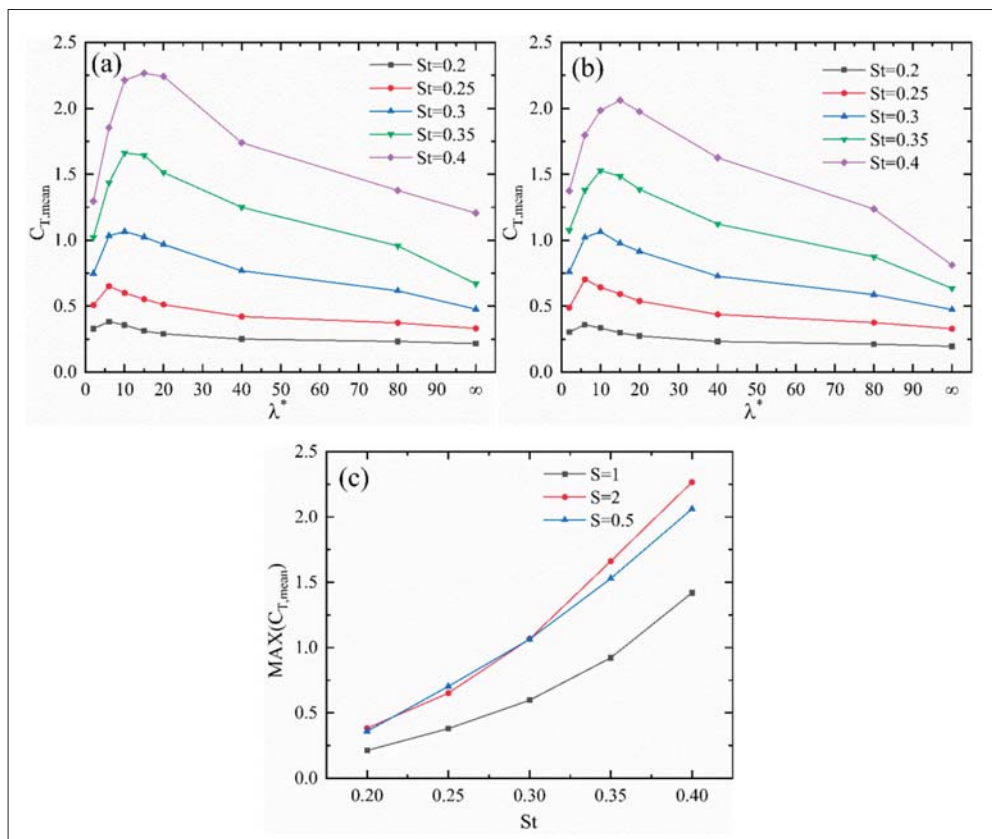


Fig. 18. Comparison of the time-averaged thrust coefficient as a function of bending stiffness: (a) $S=2$; (b) $S=0.5$. (c) Comparison of the maximum time-averaged thrust coefficient attained by non-sinusoidal trajectories and sinusoidal trajectory for each St

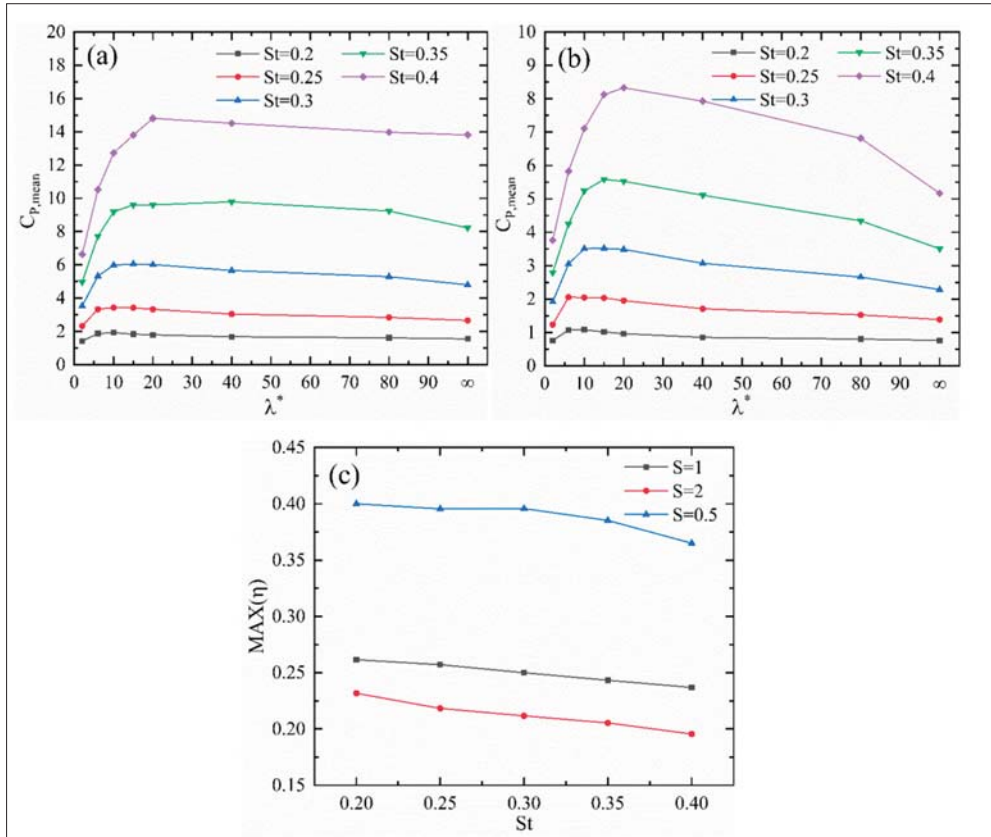


Fig. 19. Comparison of the time-averaged power coefficient as a function of bending stiffness: (a) $S=2$; (b) $S=0.5$. (c) Comparison of the maximum time-averaged power coefficient attained by non-sinusoidal trajectories and sinusoidal trajectory for each St

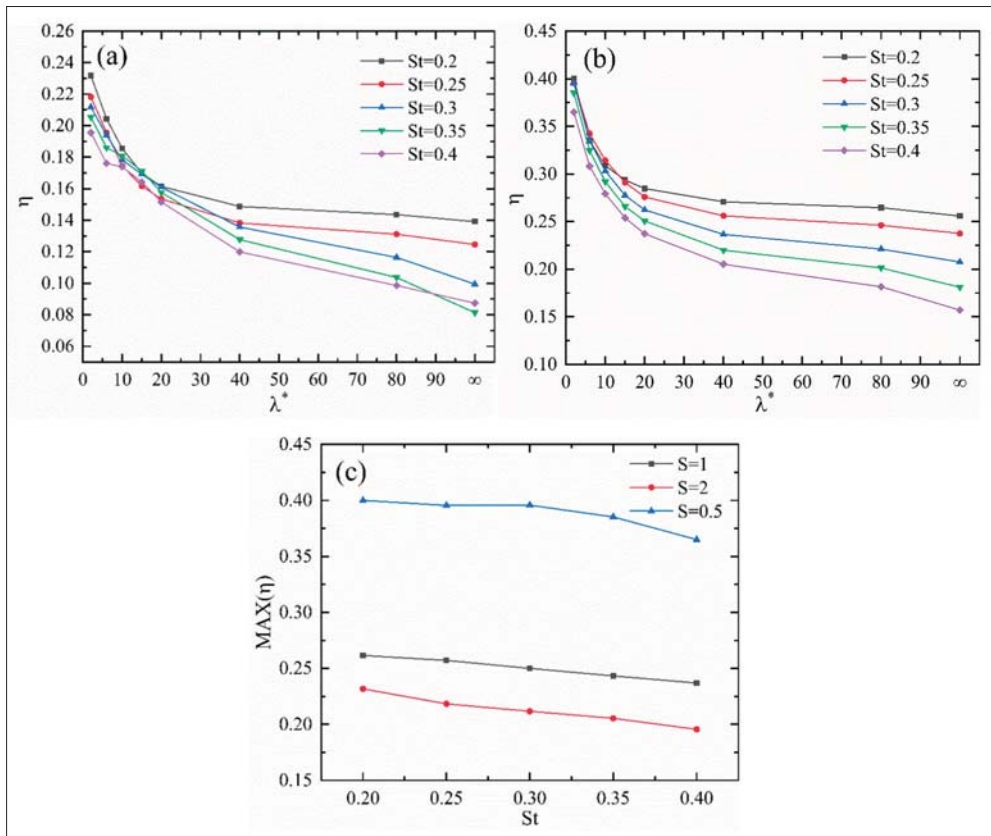


Fig. 20. Comparison of the propulsive efficiency as a function of bending stiffness: (a) $S=2$; (b) $S=0.5$. (c) Comparison of the maximum propulsive efficiency attained by non-sinusoidal trajectories and sinusoidal trajectory for each St

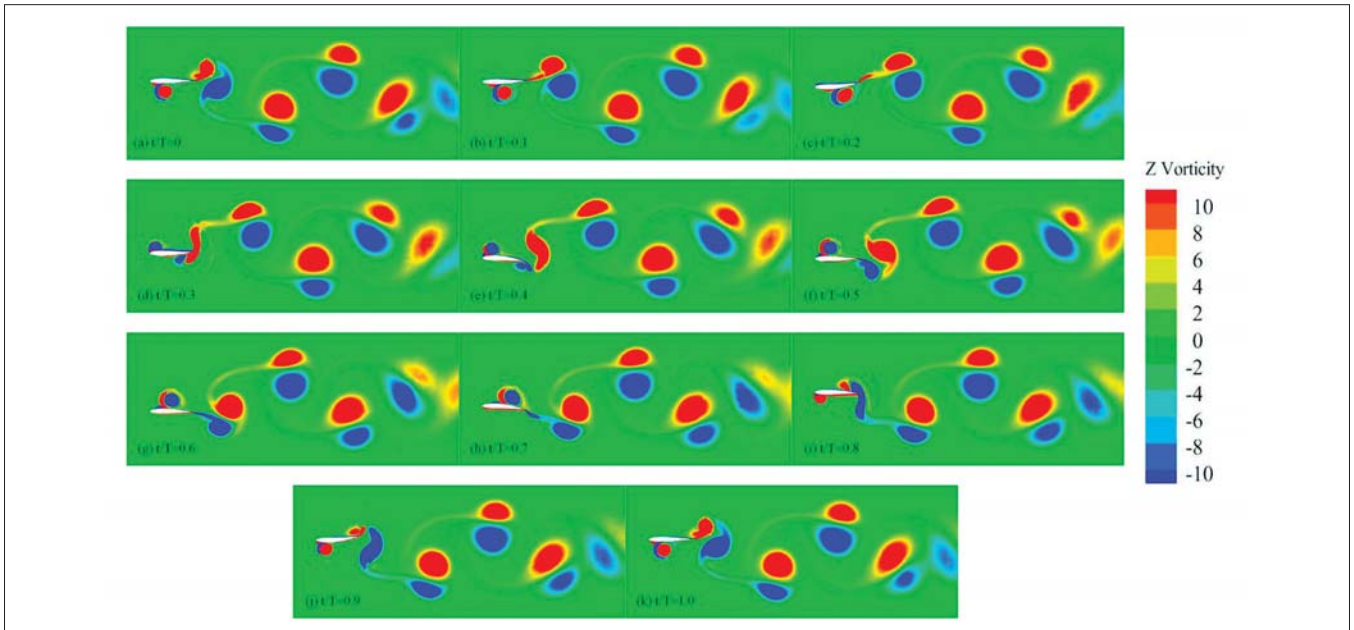


Fig. 21. Vorticity fields for $S=2$ in one typical cycle at $\lambda^*=15$

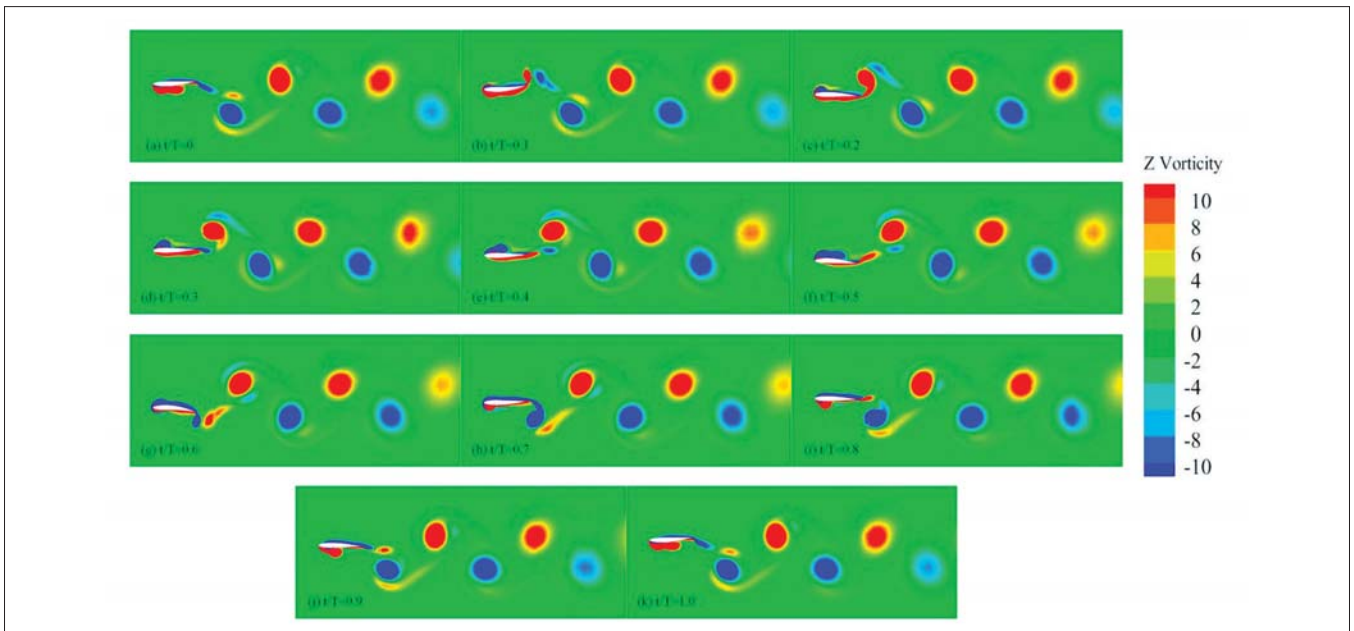


Fig. 22. Vorticity fields for $S=0.5$ in one typical cycle at $\lambda^*=15$

that low St is more beneficial to efficiency, similar to previous sinusoidal trajectories. Fig. 20(c) shows the comparison of the maximum propulsive efficiency attained by non-sinusoidal trajectories and sinusoidal trajectories for each St . It is observed that the maximum efficiency of the foil for each St decreases with the increase of St . However, the effect of St on the efficiency compared to the non-sinusoidal trajectories is limited. The maximum efficiency for each S appears at $St = 0.2$. The maximum efficiency obtained with $S = 0.5$ is much higher than that with $S = 1$ and $S = 2$. The maximum efficiency obtained with $S = 0.5$ at $St=0.2$ is 0.4, 1.53 times larger than that with $S = 1$. This is due to the substantial increase in thrust and the limited power input. For $S = 2$, the efficiency is lower than that with $S = 1$, hence the great power input.

To analyse the improvement of non-sinusoidal motions on the thrust and efficiency, we compare the vortex structure around the elastic foil in one typical cycle at $St = 0.3$ as shown in Fig. 21 and Fig. 22. The bending stiffness in the two cases is $\lambda^* = 15$, corresponding to the maximum thrust coefficient for non-sinusoidal trajectories. For $S = 2$, it is observed that two pairs of vortices in opposite rotating directions are shed from the trailing edge of the elastic foil in one cycle. While the foil is moving downwards from $t/T = 0$ to $t/T = 0.5$, two counterclockwise vortices are sequentially shed, while during the reverse movement from $t/T = 0.5$ to $t/T = 1.0$, two clockwise vortices are shed. This is different from the way of shedding vortices of sinusoidal trajectories, in which only one vortex is shed per half-cycle. It is also noted that the first shedding

vortex forms and develops on the leading edge, whereas the second shedding vortex is on the trailing edge. This will further increase the pressure differential between the upper and lower surfaces of the foil, thereby increasing the lift force compared to that of sinusoidal trajectories. The mode of two pairs of vortices shedding is associated with the case of the maximum thrust force. As shown in Fig. 22, for $S = 0.5$, the mode of shedding vortices is similar to $S = 2$. However, the second vortex is much weaker and vanishes rapidly without completely shedding. It is observed that the vortices have not fully developed on the surface of the foil. In the previous section, we pointed out that the leading edge vortex has a significant effect on the propulsive efficiency. This undeveloped leading edge vortex seems to greatly improve the efficiency of the foil for $S = 0.5$, which is consistent with the conclusion in Fig. 20(c).

CONCLUSIONS

The effect of flexibility on the propulsive performance of a heaving foil undergoing sinusoidal and non-sinusoidal motions at a low Reynolds number has been numerically investigated in this study. We employ the commercial software STAR-CCM+ to solve the flow field and large-scale passive deformation of the foil. Two validations have been performed and the accuracy of the solver in STAR-CCM+ has been verified by comparing results with the published data in the literature. We analyse the overall propulsive performance as a function of the dimensionless relative bending stiffness. Introducing a certain degree of flexibility can significantly improve the thrust and efficiency of the foil. A peak value is observed in the thrust coefficient, which means that an optimal bending stiffness exists for thrust. The velocity profile in the wake is used to illustrate the improvement. A higher positive additional x component of velocity is observed for the elastic foil. The higher magnitude of jet-like velocity will result in a higher thrust. For optimal stiffness, the maximum time-averaged thrust coefficient obtained with the elastic foil is almost 1.6 times larger than that with a rigid foil. For efficiency, there is no visible optimal value within the range of stiffness studied in this work. Introducing a greater degree of flexibility seems to be more beneficial for efficiency. From the analysis of the flow field and vortex structure in the wake, it can be concluded that the higher vortices intensity of the trailing edge is related to the case of high thrust, and the weaker leading edge vortices are associated with the case of high efficiency. A higher Strouhal number St is more beneficial for thrust generation and a lower St seems to be more conducive to efficiency improvement.

The thrust generation mechanism of rigid and elastic foils is analysed. The variations of h_T and C_T are similar for the rigid and elastic foils. C_T attains its peaks twice in one oscillation cycle in both cases. The maximum C_T of the elastic foil is much higher than that of the rigid foil. By analysing the vortex structure for both cases, it is noted that the vortices form and develop on the leading edge and then move backwards along the surface of the foil. Finally, a pair of counter-rotation

vortices are shed from the trailing edge of the foil to form the reverse von Kármán vortex street, which induces the generation of thrust.

Furthermore, the effect of non-sinusoidal trajectories on the propulsive performance of elastic foils is studied. The non-sinusoidal trajectories are realised by the flattening parameters S . The results show that the non-sinusoidal trajectories significantly affect the propulsive performance and vortex structure of the foil. For non-sinusoidal motions of $S = 2$, the time-averaged thrust coefficient is much higher than that obtained with sinusoidal motions. However, since the power input has also been greatly increased, the efficiency is lower than that obtained with sinusoidal motions. For non-sinusoidal motions of $S = 0.5$, the time-averaged thrust coefficient is also greatly improved and the power input is only slightly increased compared to the sinusoidal motions. The optimal propulsive efficiency of the elastic foil is obtained at $S = 0.5$. The impact of non-sinusoidal trajectories on thrust generation and efficiency is discussed in more detail by visualisation of the flow field. For $S = 2$, the shedding vortices show the new mode. Two pairs of counter-rotating vortices are shed in one cycle, which induces a stronger jet to improve the thrust. For $S = 0.5$, the surface of the foil shows the undeveloped vortices, which are associated with the high efficiency.

ACKNOWLEDGMENTS

This work was supported by the National Key Research and Development Program of China (Grant No. 2016YFC0301500); Natural Science Foundation of Liaoning Province in 2020 (Grant No. 2020-MS-125); State Key Laboratory of Ocean Engineering, Shanghai Jiao Tong University (Grant No. 1904).

REFERENCES

1. Y. Chen, J. Nan, and J. Wu, "Wake effect on a semi-active flapping foil based energy harvester by a rotating foil," *Computers & Fluids*, vol. 160, pp. 51–63, Jan. 2018.
2. S. Rashidi, M. Hayatdavoodi, and J. A. Esfahani, "Vortex shedding suppression and wake control: A review," *Ocean Engineering*, vol. 126, pp. 57–80, Nov. 2016.
3. E. Wang, Q. Xiao, Q. Zhu, and A. Incecik, "The effect of spacing on the vortex-induced vibrations of two tandem flexible cylinders," *Physics of Fluids*, vol. 29, no. 7, art. no. 077103, Jul. 2017.
4. F. T. Muijres, P. Henningsson, M. Stuijver, and A. Hedenstrom, "Aerodynamic flight performance in flap-gliding birds and bats," *Journal of Theoretical Biology*, vol. 306, pp. 120–128, Aug. 2012.
5. J. Zhang and X.-Y. Lu, "Aerodynamic performance due to forewing and hindwing interaction in gliding dragonfly flight," *Physical Review E*, vol. 80, no. 1, art. no. 017302, Jul. 2009.

6. Z. Cui, Z. Yang, L. Shen, and H. Z. Jiang, "Complex modal analysis of the movements of swimming fish propelled by body and/or caudal fin," *Wave Motion*, vol. 78, pp. 83–97, Apr. 2018.
7. W. Shyy et al., "Recent progress in flapping wing aerodynamics and aeroelasticity," *Progress in Aerospace Sciences*, vol. 46, no. 7, pp. 284–327, Oct. 2010.
8. M. S. Triantafyllou, G. S. Triantafyllou, and D. K. P. Yue, "Hydrodynamics of fishlike swimming," *Annual Review of Fluid Mechanics*, vol. 32, no. 1, pp. 33–53, 2000.
9. G. S. Triantafyllou, M. S. Triantafyllou, M. A. Grosenbaugh, "Optimal Thrust Development in Oscillating Foils with Application to Fish Propulsion," *Journal of Fluids and Structures*, vol. 7, no. 2, pp. 205–224, 1993.
10. J. A. Szantyr, R. Biernacki, P. Flaszynski, P. Dymarski, and M. Kraskowski, "An experimental and numerical study of the vortices generated by hydrofoils," *Polish Maritime Research*, vol. 16, no. 3, pp. 11–17, 2009.
11. E. J. Chae, D. T. Akcabay, A. Lelong, J. A. Astolfi, and Y. L. Young, "Numerical and experimental investigation of natural flow-induced vibrations of flexible hydrofoils," *Physics of Fluids*, vol. 28, no. 7, art. no. 075102, Jul. 2016.
12. J. M. Anderson, K. Streitlien, D. S. Barrett, and M. S. Triantafyllou, "Oscillating foils of high propulsive efficiency," *Journal of Fluid Mechanics*, vol. 360, pp. 41–72, Apr. 1998.
13. Koochesfahani and M. Manoochehr, "Vortical patterns in the wake of an oscillating airfoil," *AIAA Journal*, vol. 27, no. 9, pp. 1200–1205, 1989.
14. G. Pedro, A. Suleman, and N. Djilali, "A numerical study of the propulsive efficiency of a flapping hydrofoil," *International Journal for Numerical Methods in Fluids*, vol. 42, no. 5, pp. 493–526, Jun. 2003.
15. P. Flaszynski, J. A. Szantyr, and K. Tesch, "Numerical prediction of steady and unsteady tip vortex cavitation on hydrofoils," *Polish Maritime Research*, vol. 19, no. 3, pp. 3–15, 2012.
16. M. S. Triantafyllou, G. S. Triantafyllou, and R. J. Gopalkrishnan, "Wake mechanics for thrust generation in oscillating foils," *Physics of Fluids A: Fluid Dynamics*, vol. 3, no. 12, pp. 2835–2837, 1991.
17. C. Eloy, "Optimal Strouhal number for swimming animals," *Journal of Fluids and Structures*, vol. 30, no. 2, pp. 205–218, Apr. 2012.
18. G. C. Lewin and H. Haj-Hariri, "Modelling thrust generation of a two-dimensional heaving airfoil in a viscous flow," *Journal of Fluid Mechanics*, vol. 492, pp. 339–362, Oct. 2003.
19. Z. J. Wang, "Vortex shedding and frequency selection in flapping flight," *Journal of Fluid Mechanics*, vol. 410, pp. 323–341, May. 2000.
20. R. Godoy-Diana, J.-L. Aider, and J. E. Wesfreid, "Transitions in the wake of a flapping foil," *Physical Review E*, vol. 77, no. 1, art. no. 016308, Jan. 2008.
21. T. Schnipper, A. Andersen, and T. Bohr, "Vortex wakes of a flapping foil," *Journal of Fluid Mechanics*, vol. 633, pp. 411–423, Aug. 2009.
22. A. Andersen, T. Bohr, T. Schnipper, and J. H. Walther, "Wake structure and thrust generation of a flapping foil in two-dimensional flow," *Journal of Fluid Mechanics*, vol. 812, art. no. R4, Feb. 2017.
23. D. Weihs, "Hydromechanics of fish schooling," *Nature*, vol. 241, pp. 290–291, 1973.
24. J. Zhang, S. Childress, A. Libchaber, and M. Shelley, "Flexible filaments in a flowing soap film as a model for one-dimensional flags in a two-dimensional wind," *Nature*, vol. 408, no. 6814, pp. 835–839, Dec. 2000.
25. G. Xue et al., "Optimal design and numerical simulation on fish-like flexible hydrofoil propeller," *Polish Maritime Research*, vol. 23, no. 4, pp. 59–66, Dec. 2016.
26. S. Heathcote and I. Gursul, "Flexible flapping airfoil propulsion at low Reynolds numbers," *AIAA Journal*, vol. 45, no. 5, pp. 1066–1079, May 2007.
27. S. Alben, "Optimal flexibility of a flapping appendage in an inviscid fluid," *Journal of Fluid Mechanics*, vol. 614, pp. 355–380, Nov. 2008.
28. S. Michelin and S. G. L. Smith, "Resonance and propulsion performance of a heaving flexible wing," *Physics of Fluids*, vol. 21, no. 7, art. no. 071902, Jul. 2009.
29. Y. Zhang, C. Zhou, and H. Luo, "Effect of mass ratio on thrust production of an elastic panel pitching or heaving near resonance," *Journal of Fluids and Structures*, vol. 74, pp. 385–400, Oct. 2017.
30. S. Heathcote, Z. Wang, and I. Gursul, "Effect of spanwise flexibility on flapping wing propulsion," *Journal of Fluids and Structures*, vol. 24, no. 2, pp. 183–199, Feb. 2008.
31. D. A. Read, F. S. Hover, and M. S. Triantafyllou, "Forces on oscillating foils for propulsion and maneuvering," *Journal of Fluids and Structures*, vol. 17, no. 1, pp. 163–183, Jan. 2003.
32. Q. Xiao and W. Liao, "Numerical investigation of angle of

attack profile on propulsion performance of an oscillating foil,” *Computers and Fluids*, vol. 39, no. 8, pp. 1366–1380, Sep. 2010.

33. K. Lu, Y. H. Xie, and D. Zhang, “Numerical study of large amplitude, nonsinusoidal motion and camber effects on pitching airfoil propulsion,” *Journal of Fluids and Structures*, vol. 36, pp. 184–194, Jan. 2013.
34. A. Boudis, A. C. Bayeul-Laine, A. Benzaoui, H. Oualli, O. Guerri, and O. Coutier-Delgosha, “Numerical investigation of the effects of nonsinusoidal motion trajectory on the propulsion mechanisms of a flapping airfoil,” *Journal of Fluids Engineering*, vol. 141, no. 4, art. no. 041106, Apr. 2019.
35. S. A. Manjunathan and R. Bhardwaj, “Thrust generation by pitching and heaving of an elastic plate at low Reynolds number,” *Physics of Fluids*, vol. 32, no. 7, Jul. 2020.
36. R. J. Wootton, “Support and deformability in insect wings,” *Journal of Zoology*, vol. 193, no. 4, pp. 447–468, 1981.
37. J. Young and J. C. S. Lai, “Oscillation frequency and amplitude effects on the wake of a plunging airfoil,” *AIAA Journal*, vol. 42, no. 10, pp. 2042–2052, Oct. 2004.
38. S. Turek and J. Hron, *Proposal for Numerical Benchmarking of Fluid-Structure Interaction between an Elastic Object and Laminar Incompressible Flow* (Springer). Berlin: Springer, 2006.
39. G. K. Taylor, R. L. Nudds, and A. L. R. Thomas, “Flying and swimming animals cruise at a Strouhal number tuned for high power efficiency,” *Nature*, vol. 425, no. 6959, pp. 707–711, Oct. 2003.
40. K. Isogai, Y. Shinmoto, and Y. Watanabe, “Effects of dynamic stall on propulsive efficiency and thrust of flapping airfoil,” *AIAA Journal*, vol. 37, no. 10, pp. 1145–1151, Oct. 1999.
41. I. H. Tuncer and M. Kaya, “Optimization of flapping airfoils for maximum thrust and propulsive efficiency,” *AIAA Journal*, vol. 43, no. 11, pp. 2329–2336, Nov. 2005.

CONTACT WITH THE AUTHORS

Fengkun Li

e-mail: fengkun_li@dlnu.edu.cn

College of Naval Architecture and Ocean Engineering
Dalian Maritime University
No. 1 Linghai Road, 116026 Dalian
CHINA

Pengyao Yu

e-mail: yupengyao@dlnu.edu.cn

College of Naval Architecture and Ocean Engineering
Dalian Maritime University
No. 1 Linghai Road, 116026 Dalian
CHINA

Qiang Wang

e-mail: wangqiang5120@dlnu.edu.cn

College of Naval Architecture and Ocean Engineering
Dalian Maritime University
No. 1 Linghai Road, 116026 Dalian
CHINA

Guangzhao Li

e-mail: liguangzhao@dlnu.edu.cn

College of Naval Architecture and Ocean Engineering
Dalian Maritime University
No. 1 Linghai Road, 116026 Dalian
CHINA

Xiangcheng Wu

e-mail: lwuxiangcheng@dlnu.edu.cn

College of Naval Architecture and Ocean Engineering
Dalian Maritime University
No. 1 Linghai Road, 116026 Dalian
CHINA

WIND TUNNEL EXPERIMENT OF MULTI-MODE ARC SAIL DEVICE

Huawu Zhang*¹

Yihuai Hu¹

Jianhai He²

¹ Shanghai Maritime University, China

² Shanghai University of Engineering Science, China

* Corresponding author: zhanghw@shmtu.edu.cn (H. Zhang)

ABSTRACT

A ship's wind energy utilization device with multi-mode arc-shaped sails is designed, which have different working modes for sail-assisting or wind power generation according to the ship's navigation. The structural characteristics and working principles of this device are firstly described in this paper. Three sets of arc-shaped sails with different thickness (4.5 cm, 11.3 cm, 21.7 cm) were designed. Wind tunnel experiments were carried out in the respects of sail-assisting performance and wind-power generation to determine the best sail blade shape and to verify the energy-saving effect of this device. Experiments show that the sail with the smallest thickness (4.5 cm) has a better boosting effect than others, and the sail with the largest thickness (21.7 cm) has the best wind power generation performance. Considering the lateral force and the structural strength of the support, in the case of the comprehensive evaluation for the boosting and power generation performance, it is considered that the intermediate thickness (11.3 cm) is the best choice. The device has a good comprehensive energy utilization effect and has development and application value.

Keywords: marine engineering, multi-mode arc sail device, wind tunnel test, sail-assisted navigation, wind power generation

INTRODUCTION

Nowadays, shipping industries have become big energy consumers and the main source of air pollutants such as NO_x, SO_x, and particulate matter (PM). It was estimated that the overall amount of harmful gas emission from ships is three times that of on-shore enterprises and land transportation. Environmental protection regulations are becoming better and stricter. The Marine Environment Protection Committee (MEPC) of the International Maritime Organization (IMO) has issued a series of resolutions and mandatory requirements to control greenhouse gas (GHG) and harmful gas emissions from global ships [1, 2], which brings great pressure to shipping enterprises. Adjusting the energy structure, reducing energy consumption, reducing harmful gases and greenhouse gas emissions, and enhancing energy security has become the focus of international attention. How to take effective energy-saving measures has become one of the great concern issues of shipping enterprises.

Wind energy is a clean, safe, and renewable energy that is widely distributed and inexhaustible. The use of wind energy has no pollution to the environment, no ecologic damage, and has good environmental and ecological benefits. It is of great significance to the sustainable development for human society and shipping industries.

The main ways to harness wind energy onboard ships are sail-assisted navigation and wind power generation [3, 4]. Sails have a long history as the power source of ships. Sailing devices can only be used as sail aids when the ship is sailing. Some ships, such as yachts, fishing boats, and engineering ships do not have a long sail duration. They are often moored in berths or on the water for recreational or productive purposes and are unable to utilize wind energy. However, the ship's wind power generation devices are only used to generate electricity and cannot be used for sail-assistance.

Fu Yu [5] from Wuhan University of Technology designed a dual-purpose wind energy utilization device for sail-assisted navigation and wind power generation according to the route

characteristics of river-sea direct bulk carriers. He carried out simulation calculations and economic analysis on the device, but prototype tests and shipboard tests of the device were not available. The ship's wind energy utilization mode is single and cannot be flexibly adjusted according to the actual situation of the ship's navigation. This causes the ship to be inefficient in the utilization of wind energy during the whole operation cycle. It also lacks a simple and effective wind energy utilization device that can realize both wind-assisted navigation and wind power generation.

A multi-mode ship wind utilization device based on arc-shaped sails was proposed, which can adopt different modes under different conditions to combine the conversion of two working modes and improve the utilization efficiency of wind power. When the ship encounters favorable wind direction, the fuel consumption of the ship is reduced with the assistance by the wind. When the ship is docked or anchored, wind power generation can be carried out, which will greatly improve the comprehensive utilization efficiency of wind energy, especially suitable for engineering operation ships, fishing ships, and yachts with variable sailing conditions. To solve the optimal aerodynamic optimization design of the sail sheet, force, and power generation tests were conducted using a wind tunnel laboratory to verify the energy-saving performance of the device and provide a basis for the practical ship application of the multi-mode arc sail device.

MULTI-MODE SHIP WIND ENERGY UTILIZATION DEVICE

The overall structure of the device is shown in Fig. 1. It is supported by the main column, a beam, and a mast that carries two arc-shaped sail blades with the beam being connected to the main column. Three sets of electromagnets are symmetrically arranged on the main column, and the removable connecting rods are controlled to insert and withdraw the three fixed holes on the outer edge of the sail blade to form a blade locking mechanism. A disc generator is connected to the lower part of the column, which rotates and generates electricity. A stepper motor is mounted by its side on a movable tray. It can be separated from the main column when the wind power is generated and can be moved to the upright position when the sail assists the navigation and meshed with gears to change the sail angle according to different wind directions for providing maximum boosting force to the ship.

When the device is converted to the sail-assisted mode, the windward sides of both blades are in the same direction and locked, as shown in Fig. 1. The stepper motor is engaged with the main column through a conical snap ring to rotate the main column and adjust the sail angle for wind-assisted sailing. When the device needs to switch to power generation mode, moving the tray separates the gear of the stepper motor from the gear on the column. At the same time, one side of the sail blade rotates 180 degrees, reversing the sail on the other side. The position of the blade is shown in Fig. 13, forming a resistant-type wind turbine with power being generated by the disc motor connected to the column.

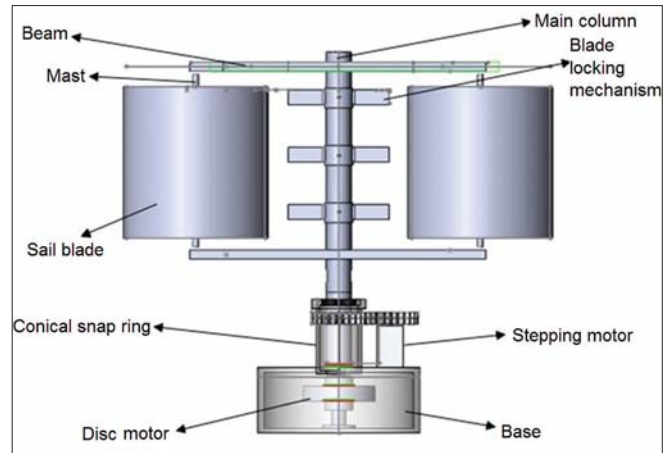


Fig. 1. Structure of multi-mode arc sail device

TEST EQUIPMENT AND TEST DEVICE MODEL

WIND TUNNEL

The wind tunnel used in the test is a closed-loop wind tunnel in the wind tunnel laboratory. The rated power is 132 kW and the frequency conversion motor drives the operation. The wind speed is controlled by a closed-loop. The test wind speed can be conveniently and accurately controlled continuously between 1–40 m/s. Airflow stability $\leq \pm 0.365\%$, airflow turbulence $\leq 0.275\%$, and airflow unevenness $\leq \pm 0.28\%$.

The test turntable is equipped in the test section of the wind tunnel. The rotation angle of the turntable is adjusted by a servo motor from -10° to 370° precisely and can be as accurate as 0.1° to change the deflection angle between the incoming flow and the sail model.

AERODYNAMIC MEASUREMENT SYSTEM

The six-component force measuring balance mounted on the turntable is used to measure the forces of the sail. The test wind speed is measured by a pitot tube and fed back to the control system to achieve wind speed via closed-loop control. The data of the six channels measured by the balance are collected by two sampling plates and output by the data processing computer. The forces and torques in three directions can be obtained directly.

The test model is connected to the measuring balance through the base. The test model and the measuring balance rotate with the turntable together to change the sail's different angles of attack. The force measurement in the test is based on the balance coordinate system. Since the balance is rotated by the turntable, the forces measured require a coordinate transformation. The zero position is the initial position, and the balance coordinate axis system is aligned with the wind tunnel coordinate axis system.

In this test, according to the mounting position of the model, the forces in the vertical direction can be ignored, and the F_x and F_z values in the horizontal plane of the balance can be recorded during the test. This force diagram is shown in Fig. 4.



Fig. 2. Installation's diagram of a multi-mode sailing device in the wind tunnel

TEST DEVICE

In this experiment, three groups of sail blades with different curvatures (thickness) were designed for comparison. In order to study the effect of different sail thicknesses (different camber ratios) on sail boosting and power generation, several sets of sails with different thicknesses were designed and corresponded to represent a certain range of camber ratios values. According to Z. Xiangming [6], the boosting characteristics of arc sails with different camber ratios in the range of 0.1–0.14 were studied. Their findings showed that the camber ratio of 0.14 has better aerodynamic performance. Combining the actual need of this study to consider both boosting and power generation modes, the two sail types with camber ratios in the range of 0.25 and one sail type exceeding the range of 0.25 camber ratios were designed as representatives for this study. From the perspective of refinement and optimization, more sails with different camber ratios need to be designed, but this study is mainly to give the combined effect of boosting and power generation on the new device as a whole, so an arc-shaped sail with the parameters shown in Table 1 was chosen. According to the increasing direction of sail thickness, they were numbered as No. 1, No. 2, and No. 3 in sequence. The installations of the test setup are shown in Fig. 2, with the specific dimensions are shown in Table 1 and Fig. 3.

WIND ASSIST TEST

The force test of the wind sail model is carried out in a uniform flow field. The zero position of the turntable corresponds to the zero position of the dynamometer and coincides with the wind tunnel coordinates. The model was mounted at the 0° angle of attack position. After the model was installed, data acquisition and zero calibration were performed in the windless state, then the fan was started. After the test wind speed was reached and stabilized, the data were measured and recorded. The turntable was rotated from the 0° angle of attack counterclockwise at 5° intervals to measure the forces at different angles of attack.

Tab. 1. Basic parameters of sail blades

NO.	Windward area(m ²)	Sails high(m)	Chord length(m)	Aspect ratio	Sail thickness(m)
1	0.638	0.5	0.46	1.087	0.045
2	0.638	0.5	0.46	1.087	0.113
3	0.638	0.5	0.46	1.087	0.217

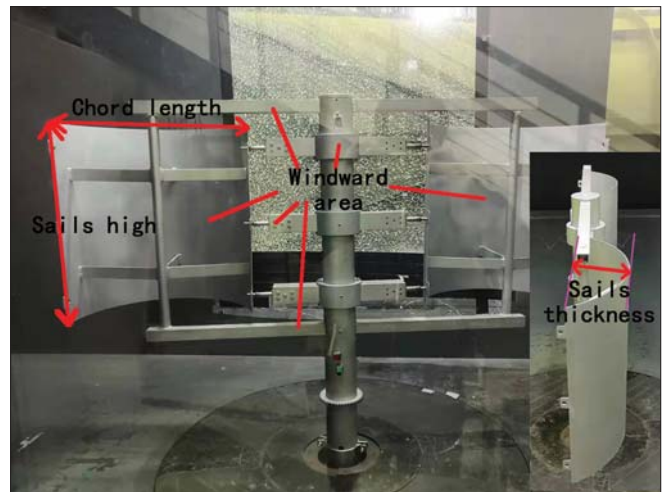


Fig. 3. Basic parameters identification of multi-mode sailing device

The aerodynamic force of the sail is decomposed into two components, the lift force F_L perpendicular to the incoming flow and the drag force F_d acting in line with the local wind direction, as shown in Fig. 4 [7, 8]. The wind direction angle θ is the angle between the wind speed vector and the sailplane direction, called the angle of attack of the sail. Since the wind direction does not change in the wind tunnel, the sail model can only rotate at different angles under the action of the turntable. The force of the sail model measured by the balance is based on the balance coordinates. The balance and the sail model follow the turntable together with the rotation angle θ . The measurement is performed on the balance. The lift force measured on the balance is F_z and the drag force is F_x . When calculating the aerodynamic force of the sail at different angles of attack, the drag force F_d parallel to the wind speed direction and the lift

force F_L perpendicular to the wind speed direction, need to be obtained by coordinate transformation, and then the lift force coefficient C_L and drag force coefficient C_d at different angles of attack are calculated according to the model and test parameters.

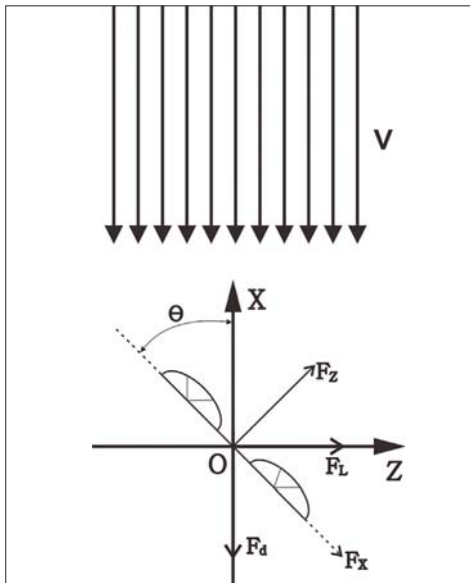


Fig. 4. The force diagram of multi-mode sail device

The lift force of the sail is [9, 10, 11]

$$F_L = F_Z \cos\theta + F_X \sin\theta \quad (1)$$

The drag force F_d is

$$F_d = F_X \cos\theta - F_Z \sin\theta \quad (2)$$

The lift force coefficient and drag force coefficient are expressed as

$$C_L = 2F_L / \rho V^2 S \quad (3)$$

$$C_d = 2F_d / \rho V^2 S \quad (4)$$

In Eq. (3) and Eq. (4), S is the windward area of the sail and ρ is the air density. According to the temperature and air pressure measured during the test, the air density is 1.26 kg/m^3 and V is the test wind speed.

During the test, when air flows through the test device, the device has an obstructive effect on the cross-section of the airflow channel. As the angle of attack changes, the cross-sectional area of the device changes in the direction of the airflow, and the obstruction changes accordingly. The walls of the wind tunnel restrict the airflow from expanding and spreading outward, allowing the airflow through the device to accelerate through the test device.

According to the law of continuity, the relationship between the test wind speed and the corrected wind speed can be derived.

$$\rho A_1 V_1 = \rho A V \quad (5)$$

When the wind speed is below Mach 0.3, the air density ρ can be regarded as incompressible fluid flow and the density

remains constant. A_1 is the cross-sectional area of the wind tunnel test section, located at the front of the test section, V_1 is the air velocity entering the test section, set by the experiment, A is the cross-sectional area of the airflow at the location of the test device, and V is the corrected velocity of the airflow when flowing through the device.

From the formula (5), we get:

$$V = A_1 V_1 / A \quad (6)$$

The forces on the sails for different angles of attack and thickness at test wind speeds of 5 m/s, 10 m/s, and 15 m/s are shown in Fig. 5, Fig. 6, and Fig. 7.

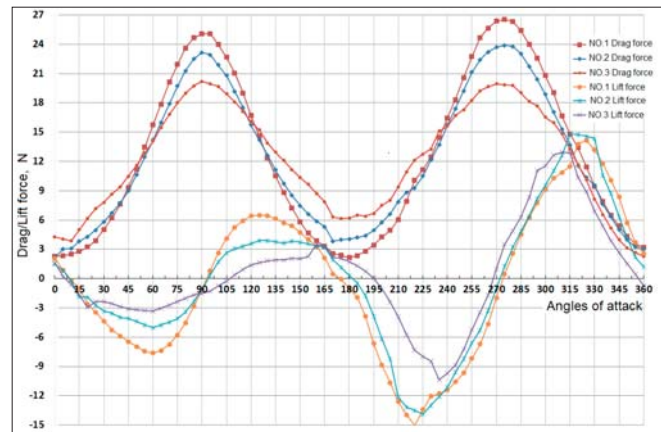


Fig. 5. Curves of sail lift forces and drag forces under different thickness at 5 m/s wind speed

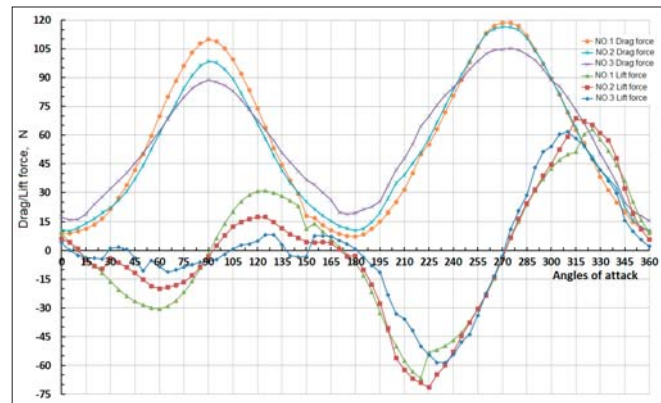


Fig. 6. Curves of sail lift forces and drag forces under different thickness at 10 m/s wind speed

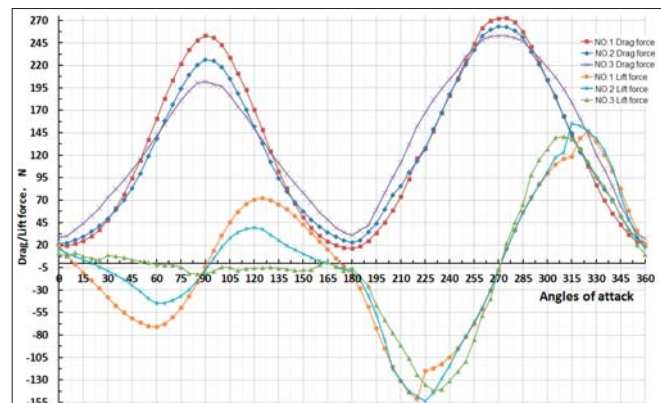


Fig. 7. Curves of sail lift forces and drag forces under different thickness at 15 m/s wind speed

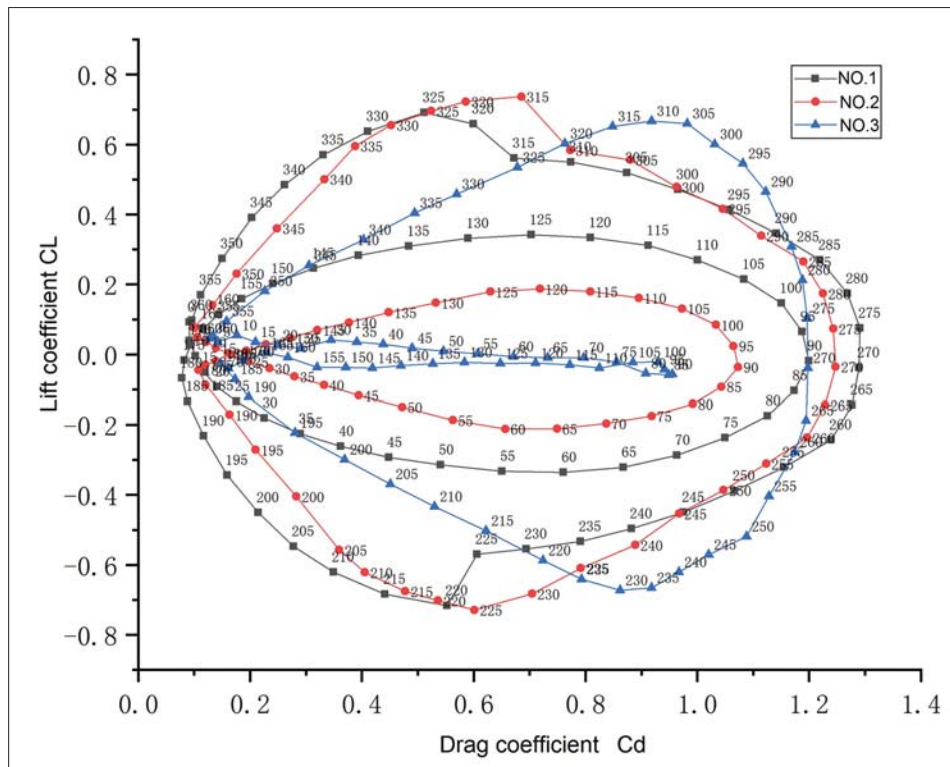


Fig. 8. Curves of lift coefficients and drag coefficients of sails with different thickness

The $C_L - C_d$ curves for the different thicknesses of the sail at the same wind speed are shown in Fig. 8.

From Figs. 5 to 7, it can be seen that the shapes of the corresponding lift-drag curves are approximately the same for different wind speeds, which indicates that the aerodynamic characteristics are not related to the wind speed, but the shape of the sail under the test conditions. During the rotation of the sail, when the concave and convex sides are perpendicular to the wind direction, the area exposed to the wind is the largest, and the drag force has two peaks. At this point, the lift force is almost zero. The angle between the device and the incoming flow is symmetrical, giving the same symmetrical flow field. The resistance curve is symmetrical to the incoming flow, showing the overall force symmetry. The lift force curves are symmetrical at 90° and 270° angles of attack, creating point symmetric curves of equal magnitude and opposite direction. The lift and drag coefficients for the three sails at different angles of attack are shown in Fig. 8. It should be noted that they have good symmetry in the upper and lower halves.

There are negative lift force values in Figs. 5 to 7, corresponding to the negative lift coefficient in Fig. 8. This is due to the measured values following the rotation of the balance, which is in the opposite direction of the fixed setup positive lift force. After the sail angle is greater than 180° , the upwind lift resistance of the concave surface is greater than that of the convex surface. When the angle of attack is between $210^\circ - 240^\circ$ and $300^\circ - 330^\circ$, when the angle between the concave surface and the airflow is between 30° and 60° , the device has the maximum lift force. At this time, the maximum lift force is near the 45° airflow angle. When the device is perpendicular to the direction of the airflow, the wind resistance of the concave surface is the largest.

SAILING AID AND ENERGY SAVING APPLICATION

A ship needs to maintain a certain heading (x -axis direction) when sailing. As shown in the wind axis coordinate system in Fig. 9, the ship's navigation is influenced by the apparent wind speed V_b , which is generated by the combination of the wind speed V_z and the sailing speed V_c . On the route, the wind direction and wind speed are constantly changing with time. The sail-assisted ship must operate the sail and change the windward angle of the sails so that the ship gets the maximum thrust in the forward direction [10]. That angle of attack that produces the most boosting force on the ship and has the least effect on the stability of the ship is an important factor in measuring the performance of the sail.

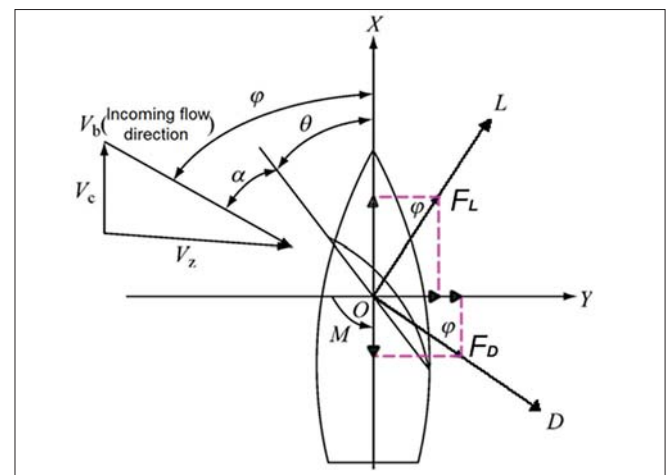


Fig. 9. The force analysis diagram of the sail on the ship

Fig. 9 shows the rectangular coordinate system O-LDZ [12], with the origin O at the center of the model bottom plate, the Z-axis vertically upright, the L-axis on the horizontal plane in the direction of lift, and the D-axis in the direction of drag. The aerodynamic force on the sail is decomposed into a drag force F_D along the incoming direction, a lift force F_L perpendicular to the incoming direction, and a torque M on the mast, with the reference point of the moment being the origin O.

According to the force analysis in Fig. 8, the boosting force produced by the sail on the boat is [13]:

$$T = F_L \sin\varphi - F_D \cos\varphi \quad (7)$$

The lateral force generated by the sail on the ship is:

$$H = F_L \cos\varphi - F_D \sin\varphi \quad (8)$$

Transformation of Eq. (7) yields:

$$T = \left(\frac{F_L}{\sqrt{F_L^2 + F_D^2}} \sin\varphi - \frac{F_D}{\sqrt{F_L^2 + F_D^2}} \cos\varphi \right) \sqrt{F_L^2 + F_D^2} \\ = A(\cos\beta \sin\varphi - \sin\beta \cos\varphi) = A \sin(\varphi - \beta) \quad (9)$$

Making the same transformation for Eq. (8), we get:

$$H = \left(\frac{F_L}{\sqrt{F_L^2 + F_D^2}} \cos\varphi + \frac{F_D}{\sqrt{F_L^2 + F_D^2}} \sin\varphi \right) \sqrt{F_L^2 + F_D^2} \\ = A(\cos\beta \cos\varphi + \sin\beta \sin\varphi) = A \cos(\varphi - \beta) \quad (10)$$

where $A = \sqrt{F_L^2 + F_D^2}$ called the modulus of lift force, and drag force being $\tan\beta = F_D/F_L$.

To make the maximum boosting force on the ship, there must be $\sin(\varphi - \beta) = 1$. At this time, the sail on the ship produces the maximum boosting force for A, the wind angle φ ranges from 0° – 180° , β for 0° – 90° , and $\varphi - \beta = 90^\circ$, so that there is maximum boosting force and minimum lateral force.

According to the formula of A, the lift and drag forces obtained by the three sets of sails at different angles of attack are calculated and then the maximum value of A is selected. Maximum boosting forces are shown in Table 2.

Tab. 2. Maximum boosting force Unit: N

Wind Speed	No.1	No.2	No.3
5 m/s	26.53	24	20.87
10 m/s	118.87	116.56	107.96
15 m/s	273.11	263.49	256.51

Fig. 10 shows the maximum boosting force curves of the three arc sails at different wind speeds.

It can be seen that when the thickness is minimum, the boosting force is maximum, and the larger the thickness, the smaller the maximum boosting force. The curves of No. 1 and No. 2 are closer, but there is not much difference in the values of the three.

The lift force and drag force data from wind tunnel tests of the device at different wind speeds were substituted into Eq. (7)

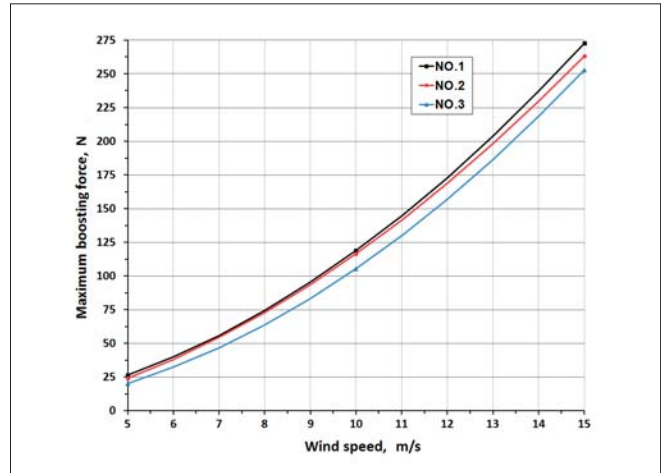


Fig. 10. Curves of maximum boosting force of sails under different wind speeds

and (8) using different wind angles φ between 0° to 180° , and different angles of attack in turn at the selected wind angles. To calculate the boosting force and lateral force of the ship, selecting the maximum boosting force obtained at all angles of attack at a fixed wind direction and the corresponding lateral force to form the maximum boosting force and lateral force curves of the three sets of sails is shown in Fig. 11.

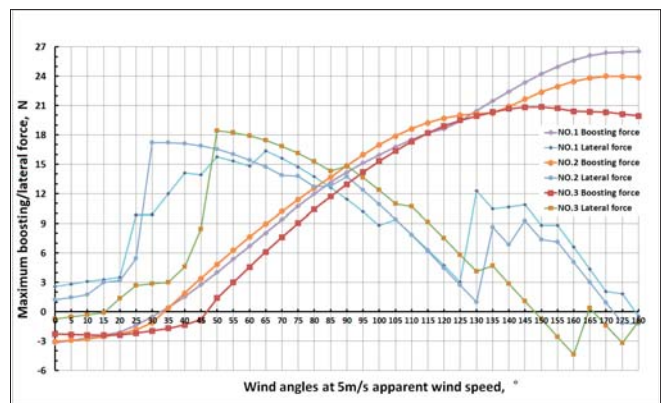


Fig. 11. Curves of maximum boosting force and corresponding lateral force of three sets of sails under different wind angles at 5 m/s apparent wind speed

Fig. 11 shows that for the sail with the largest thickness, the boosting force is negative when the wind angle is less than 50° , regardless of how the angle of attack is adjusted. For the other two sails, the boosting force is negative when the wind direction angle is less than 35° . As the wind direction angle increases, it is possible to obtain a gradually increasing boosting force by turning the sail angle of attack. When the wind angle is greater than 50° , the lateral force of the three sets of sails starts to decrease as the wind angle increases.

Fig. 11 shows that in the range of $35^\circ < \varphi < 125^\circ$, the boosting force of the three sets of sails increases with the increase of the wind direction angle, while the lateral force gradually decreases overall, with the smallest lateral force near 125° .

Generally, the speed of most ships is in the range of 10–30 knots, wind speed is in the range of 0–5 knots, and the sailing speed of ships is greater than wind speed in most cases. When the angle between wind speed and heading speed is small,

although the apparent wind speed obtained becomes larger, the angle between apparent wind speed and the heading is smaller, and it is difficult for the sail to produce an effective boost at a small angle. On the contrary, when the angle between wind speed and the heading speed is larger, it can make the angle between the apparent wind speed and course become larger and in the range of positive boost, but the apparent wind speed will become smaller and the boosting force to the boat will become smaller [14].

This device is suitable for ships sailing at low speeds around 10 knots. In most cases, the wind speed is not much different from the ship's speed, or the wind speed is greater than the ship's speed. Thus, the apparent wind speed can be kept at a large value and within the range of the positive boost angle in a wide range. According to Fig. 11, the apparent wind speed size and the angle formed by traversing the ship's speed, the possible wind speed angle change can be calculated. The apparent wind speed is in the range of less than 120° wind angle in most cases, in which the boosting force of sail No. 2 is greater than sail No. 1 and No. 3. When the wind speed is greater than the ship's speed, and the angle between the wind speed and the sailing speed is greater than 120°, then it is possible to enter the wind direction angle greater than 120°. At this time, the boosting force of sail No. 1 is greater than sails No. 2 and No. 3.

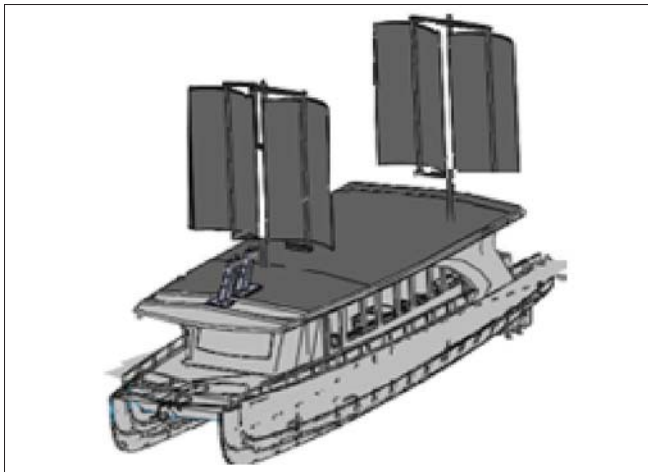


Fig. 12. Schematic diagram of installation of sailing yacht

The sail test results show that the sail blade with the smallest thickness has a better boosting effect in most working conditions. The wind speed is greater than the ship's speed when the apparent wind speed of the first sail is 5 m/s, with the wind direction angle of 120°, the boosting force is larger and the lateral force is smaller, and the maximum boosting force can reach 19.7 N. If two sets of sail devices are made according to the actual size with a similarity ratio of 10, considering the mutual influence of the sail arrays [15], the two devices can be staggered and installed on a yacht, as shown in Fig. 12. This can be applied only when the relative wind direction is exactly along the middle connecting direction, with the fore and aft sails of the device array being affected. According to the literature [15], the interference effect between the two sails becomes weaker when the distance between the two sails is

greater than 2 times the chord length and is not considered in this estimation. When the wind direction angle of sail No. 1 is 120° and the apparent wind speed is 5.0 m/s, it will generate a boosting force of 3940 N, which is 19.7 kW. A 20 m long, 4.5 m wide excursion boat with a design speed of 13 knots and a rated power of 194 kW [16], the sail can be boosted up to 10.15% of the rated power. With the sail booster, the relationship between the power P_r consumed by the ship, the propeller output power P_p , the main engine output power P_e , and the sail booster power P_s when the yacht maintains a constant speed can be expressed as:

$$P_r = P_p \eta_p + P_s \eta_s = P_e \eta_c \eta_p + P_s \eta_s \quad (11)$$

Where, η_p is the overall efficiency of the propeller, η_c is the comprehensive efficiency of the main engine drive system, η_s is the comprehensive efficiency of the sailing aid system [17].

From Eq. (11), it can be seen that P_r remains unchanged when sailing at a constant speed, the power applied to the hull by the sail is the reduced power of the main engine. The main engine of the ship can run at reduced power (i.e. reduce the throttle opening of the main engine and the fuel consumption of the main engine will be reduced). If the diesel engine propulsion power η_1 is of the rated power of the main engine, after using the sail, the power of the main engine drops to η_2 approximately, and the fuel-saving per hour is:

$$\Delta G = P_e g_1 \eta_1 - P_e g_2 \eta_2 \quad (12)$$

Where g_1 represents the fuel consumption of the main engine, and g_2 indicates the fuel consumption after the addition of sails.

In the R. Hongying [17], on an 80,000 ton bulk carrier with propulsion power of 8833 kW, it is calculated that when the sail device provides a 12% boosting force, the main engine fuel consumption rate g_1 is reduced from 168.47 g/(kW·h) to g_2 165.58 g/(kW·h). Calculated on 200 sailing days per year, the fuel-saving is 806 t, and the fuel-saving per hour is 168 kg. It can be seen that after the main engine is running at reduced power, fuel consumption can be greatly reduced when its load level is reduced, the operating condition of components improve, service life of the diesel engine is extended, maintenance interval is extended, and the maintenance cost is reduced, thereby saving operating costs and achieving the goal of energy-saving and emission reduction.

WIND POWER GENERATION TEST

One side of the sail blade of the multi-mode sail device is rotated 180° to become a drag type wind turbine, as in Fig. 13, due to the asymmetric shape of the blade in the windward direction, causing a difference in air resistance. When there is a concave surface subject to resistance, F_1 is greater than the convex surface subject to resistance F_2 . Therefore, the torque around the center axis is generated to rotate the wind wheel.

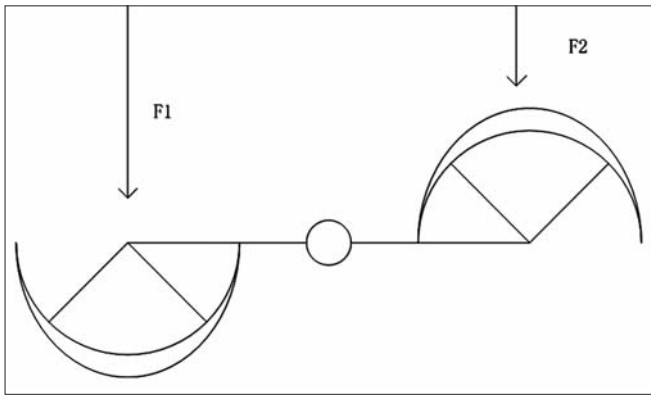


Fig. 13. Forces acting on sail blades in wind power generation mode

Wind tunnel tests were conducted in wind power generation mode to obtain the wind turbine speed and the output voltage of the disk motor at different wind speeds. Generally, in the wind power generation mode, the ship is in the suspended state. Compared to the wind boost mode, it lacks the self-navigation speed component when the apparent wind speed is relatively small. We selected the wind speeds of 4 m/s, 6 m/s, and 10 m/s for a wind power generation test. The disk generator used in the test has a rated speed of 36 r/min, a rated voltage of 13 V, and a rated power of 500 W. The test results are shown in Fig. 14 and Table 3.

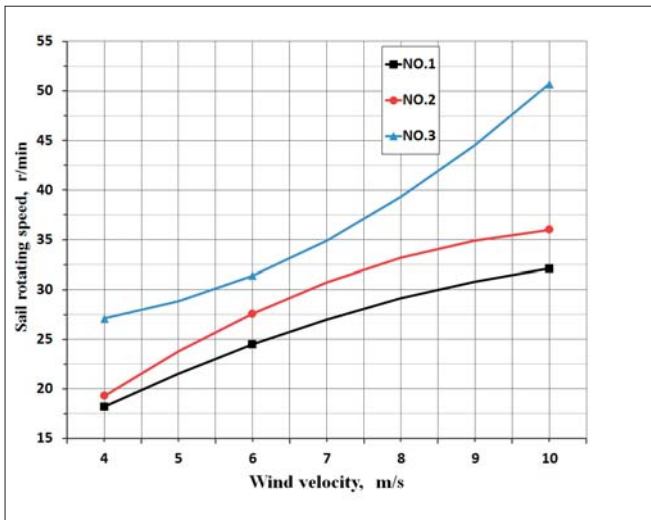


Fig. 14. Variation curve of wind turbine speed at different wind speeds

It can be seen in Fig. 14, that the slope of the speed curve of the No. 1 and No. 2 wind turbines gradually leans to be horizontal, indicating that the speed of the wind turbine will not increase indefinitely with the increase of wind speed. It shows that the operation state has been fully developed, and is not necessary to further increase the test wind speed, which

Tab. 3. Wind power test results

Wind Speed	RPM (r/min)			Output Voltage (V)		
	No. 1	No. 2	No. 3	No. 1	No. 2	No. 3
4 m/s	18.2	19.3	27.1	11.35	11.6	12.24
6 m/s	24.5	27.6	31.43	12.62	12.89	13.31
10 m/s	32.1	36	50.7	13.39	13.56	15.12

also shows the rationality of the test wind speed we selected. The smaller the arc, the smaller the difference in air resistance between the concave surface and the convex surface. As the wind speed increases, the wind turbine speed increases. The concave surface runs in the direction of the incoming wind speed, resulting in a decrease in the relative wind speed. The convex surface runs in the opposite direction to the incoming wind speed, the relative wind speed increases, and finally the wind turbine stabilizes at a certain speed. Due to the fact that No. 3 has the largest thickness, the concave-convex surface is still in the stage where the speed increases with the wind under the test wind speed.

According to the data obtained from the wind tunnel test, within a certain range, the higher the wind speed, the greater the wind turbine speed, the greater the generating voltage. At the same wind speed, the greater the thickness, the greater the wind turbine speed. Large arcs will produce relatively small resistance when the convex surface is upwind, while the concave surface will produce relatively large resistance when it is downwind, and the total torque will be large. In the test, due to the uneven force of the blades in the forward and backward winds, the periodic lateral wind force occurred within a fixed angle range, which caused the sail device to generate periodic unbalanced forces and moments, causing the base of the device to withstand lateral forces and overturning moments. In the case of insufficient stiffness, violent shaking will occur especially when passing through the speed resonance zone.

CONCLUSIONS

The wind turbine blade turning and locking mechanism can switch between different operation modes of the multi-mode windsurfing device. Wind tunnel tests show that sail blades with small thickness have better-boosting effects, but low power generation efficiency. Sail blades with large thickness have good power generation effects but have lower boost efficiency and will produce larger lateral forces and overturning moments. No. 1 and No. 2 boost forces are not much different, but both are better than No. 3. However, in terms of power generation, No. 2 and No. 3 are the best, and No. 3 produces a larger lateral and overturning force under the same support rigidity condition. The requirements for the support of the sail and the structural strength of the device base are relatively high because the device needs to maintain certain rigidity and the connection of the base must be checked for fatigue strength. In the case of comprehensive consideration of the two modes of power generation and boosting, considering both boosting and power generation, the No. 2 sail is the best choice.

The lateral force on the sail causes the ship to drift angle, and to maintain the course, the rudder must be steered to overcome the lateral force. Thus, the additional drag force caused by the rudder to balance the lateral force must be considered. In the power generation mode, the rotation of the device generates unbalanced lateral forces and moments. It is necessary to further check the structural strength of the ship, avoid the speed resonance zone, and study the effect of the rotation on the additional lateral forces of the ship and the course stability.

ACKNOWLEDGMENTS

The authors wish to thank the Science & Technology Commission of Shanghai Municipality and Shanghai Engineering Research Center of Ship Intelligent Maintenance and Energy Efficiency (Grant No. 20DZ2252300).

REFERENCES

1. T. C. Van, J. Ramirez, T. Rainey, Z. Ristovski, R. J. Brown, "Global impacts of recent IMO regulations on marine fuel oil refining processes and ship emissions", *Transportation Research Part D: Transport and Environment*, vol. 70, pp. 123–134, 2019. doi: 10.1016/j.trd.2019.04.001.
2. T. Chou, V. Kosmas, M. Acciaro, K. Renken, "A comeback of wind power in shipping: An economic and operational review on the wind-assisted ship propulsion technology", *Sustainability*, vol. 13, pp. 1880, 2021. doi: 10.3390/su13041880.
3. Y. Ling, X. Cai, "Exploitation and utilization of the wind power and its perspective in China", *Renewable and Sustainable Energy Reviews*, vol. 16, pp. 2111–2117, 2012. doi: 10.1016/j.rser.2012.01.039.
4. O. Ellabban, H. Abu-Rub, F. Blaabjerg, "Renewable energy resources: Current status, future prospects and their enabling technology", *Renewable and Sustainable Energy Reviews*, vol. 39, pp. 748–764, 2014. doi:10.1016/j.rser.2014.07.113.
5. F. Yu, X. Li, F. Fan, S. Qiang, "Feasibility analysis of dual-purpose wind energy device on river-sea bulk carrier", *China Ship Repair*, vol. 30, pp. 17–20, 2017. doi: 10.13352/j.issn.1001-8328.2017.03.006.
6. Z. Xiangming, H. Yihuai, W. Youcong, "Wind tunnel test on sails with different shape", *Journal of Shanghai Maritime University*, vol. 31, pp. 28–31, 2010.
7. F. Tillig, J. W. Ringsberg, "Design, operation and analysis of wind-assisted cargo ships", *Ocean Engineering*, vol. 211, pp. 107603, 2020. doi: 10.1016/j.oceaneng.2020.107603.
8. M. Pawłusik, R. Szłapczyński, A. Karczewski, "Optimising rig design for sailing yachts with evolutionary multi-objective algorithm", *Polish Maritime Research*, vol. 27, no. 4, 2020. doi: 10.2478/pomr-2020-0064.
9. D. Li, Y. Zhang, P. Li, J. Dai, G. Li, "Aerodynamic performance of a new double-flap wing sail", *Polish Maritime Research*, vol. 26, pp. 61–68, 2019. doi: 10.2478/pomr-2019-0067.
10. J. He, Y. Hu, J. J. Tang, S. Xue, "Research on sail aerodynamics performance and sail-assisted ship stability", *Journal of Wind Engineering and Industrial Aerodynamics*, vol. 146, pp. 81–89, 2015. doi: 10.1016/j.jweia.2015.08.005.
11. Y. Hu, X. Zeng, S. Li, "Research on the aerodynamic characteristics of ellipse wing sail". *Advanced Materials Research*, vol. 347–353, pp. 2249–2254, 2012. doi: 10.4028/www.scientific.net/AMR.347-353.2249.
12. Z. Xiangming, Z. Huawu, "Experimental study of the aerodynamics of sail in natural wind", *Polish Maritime Research*, vol. 25, pp. 17–22, 2018. doi: 10.2478/pomr-2018-0068.
13. D. E. Elger, M. Bentin, M. Vahs, "Comparison of different methods for predicting the drift angle and rudder resistance by wind propulsion systems on ships", *Ocean Engineering*, vol. 217, 108152, 2020. doi: 10.1016/j.oceaneng.2020.108152.
14. A. Babarit, G. Clodic, S. Delvoye, "Exploitation of the far-offshore wind energy resource by fleets of energy ships – Part 1: Energy ship design and performance", *Wind Energy Science*, vol. 5, pp. 839–853, 2020. doi: 10.5194/wes-5-839-2020.
15. Q. Li, Y. Nihei, T. Nakashima, Y. Ikeda, "A study on the performance of cascade hard sails and sail-equipped vessels", *Ocean Engineering*, vol. 98, pp. 23–31, 2015. doi: 10.1016/j.oceaneng.2015.02.005.
16. Yaguang Technology Group Co., "20m-FRP tour boat Performance" [Online]. (<http://en.ygkjgroup.com>). Accessed on July 5, 2021,
17. R. Hongying, H. Lianzhong, S. Peiting, L. Nan, "Comprehensive energy-saving and emission reduction potential of large sail-assisted ship", *Journal of Dalian Maritime University*, vol. 36, pp. 27–30, 2010. doi: 10.16411/j.cnki.issn1006-7736.2010.01.016.

CONTACT WITH THE AUTHORS

Huawu Zhang

e-mail: zhanghw@shmtu.edu.cn

Shanghai Maritime University
1550 Haigang Dadao, PuDong New Area
201306 Shanghai
CHINA

Yihuai Hu

e-mail: yhhu@shmtu.edu.cn

Shanghai Maritime University
1550 Haigang Dadao, PuDong New Area
201306 Shanghai
CHINA

EVALUATION OF EFFECTIVENESS OF WATERJET PROPULSOR FOR A SMALL UNDERWATER VEHICLE

Lech Rowinski*

Gdańsk University of Technology, Poland

Maciej Kaczmarczyk

* Corresponding author: rowinski@pg.edu.pl (L. Rowiński)

ABSTRACT

The goal of the project described is to replace the existing propulsion system of a small underwater vehicle with a solution less prone to mechanical damage and ensuring a lower risk of the entanglement of fibrous objects suspended in the body of water. Four typical marine screws are utilised in the current design of the vehicle. One possible solution of the problem is the application of waterjet propulsors located inside the body of the vehicle instead. The general condition of the application of the new solution was to secure at least the same motion control capabilities of the vehicle while the basic capability is its propulsion effectiveness at the required speed. Specific features of the considered waterjet propulsor, when compared with their application in surface vessel propulsion, are the lack of the head losses and the low significance of cavitation issues. One of the difficulties in the considered case is the small diameter of the propulsor in comparison to commercially available waterjet units, which have diameters between 0.1 [m] and 1.0 [m]. There is very little data regarding the design and performance of devices in the 0.02 to 0.05 [m] range. Methods utilised to forecast the performance of the new propulsion system are presented and results compared. These were semi-empirical calculations, numerical calculations and tests of real devices. The algorithm that is based on semi-empirical calculations is of particular interest while it offers possibility quick assessment of performance of a propulsor composed of several well defined components. The results indicate the feasibility of modification of the propulsion system for the considered vehicle if all the existing circumstances are taken into account.

Keywords: ship propulsion, hydromechanics, waterjet, underwater vehicle

OVERALL CHARACTERISTICS OF THE GLUPTAK UNDERWATER VEHICLE

Small underwater vehicles offer the ultimate in autonomous remote subsea survey capability. These free-swimming autonomous underwater vehicles are characterised by great manoeuvrability and high accuracy of stabilisation. Due to their small size, operational efficiency and transport properties, the advantages of autonomous underwater vehicles outweigh the advantages of manned underwater vehicles. Their propulsion system is an important element in energy conversion to generate a reaction sequence that consists of thrust momentum and pressure thrust. One of the possible solutions to ensure the appropriate values of these parameters

is the use of water jet propulsion system. Many different scientific and research centers are working on the solution of the effectiveness of this type of drive, the result of which can be found in many publications in this field, e.g. in [1], [2], [3] and [4].

In [1], an integrated magnetically slotless PM brushless machine having 2-segment Halbach array was proposed to employ in novel shaftless pump-jet propulsor the autonomous underwater vehicle. The optimal magnet ratio array was analytically determined and the electromagnetic performance of target machine is analysed by finite-element analysis. In order to exam the effectiveness of cooling system, a thermal and computational fluid dynamic coupled analysis was developed. The overall analysis results reveal that the

proposed magnetically slotless PM brushless machine achieves design requirements and capable for using in the units having shaftless pump-jet.

The performance parameters of waterjet propulsion, such as resistance, waterjet thrust, thrust deduction, and the physical quantity of the control volume, were solved by iteration and thy presented in [2]. Authors applied the proposed approach and the RANS CFD method to a waterjet propelled trimaran model. Although there were some differences between the two methods in terms of the local pressure distribution and thrust deduction, the relative error in the evaluation results for the waterjet propulsion performance was generally reasonable and acceptable. This indicates that the proposed method can be used at the early stages of ship design without partial information about the waterjet propulsion system, and especially in the absence of a physical model of the pump.

In [3] Authors present a numerical investigation into four different nozzles (cos, exponent, cylindrical and conical ones) for the water jet propulsion system of underwater vehicles. The effects of geometric parameters (length and wall roughness) and dynamic parameter (backpressure with constant pressure difference) of four different nozzles on the momentum thrust, average fluid velocity and vapour mass flow rate were analysed. The governing equations were solved through CFD software. The results showed that cos nozzle which produces more momentum thrust is the most appropriate, and the nozzle length L is proposed to set 36 mm. The effects of wall roughness were different on four nozzles, and the smooth inner wall was proposed for cos nozzles.

A special framework that allows you to determine the effectiveness of the water jet propulsion system is presented in [4]. This framework provided a basis for minimizing the waterjet propelled energy consumption through a proper force weighting.

The Gluptak underwater vehicle, as shown in the Fig. 1, was developed at Ship design department of Gdansk University of Technology [5], [6], [7]. It is a small, slow-moving, torpedo-like object. It is supplied with energy from an internal source (battery) and controlled remotely by means of an optical fibre. It is used to identify and destroy naval mines. The vehicle is able to flow at velocity of 3 [m/s] relative to the water. One of the limiting factors of the vehicle performance is the limited energy capacity of the internal battery pack and the power available for propulsion. Therefore, two basic parameters define the propulsion system. These are the available thrust and the widely understood overall efficiency. Additional factors are requirements regarding high manoeuvrability of the vehicle. In the horizontal plane, the vehicle is propelled by means of four screw propellers. The fifth propeller, built into the vehicle's hull, is used to control its vertical movement. It was placed at the centre of the vertical drag of the vehicle to ascend and descend at zero forward speed. The horizontal propellers are arranged in an X configuration as shown in the Fig. 3. Additionally, the axes of the propeller shafts are inclined 7 degrees relative to the longitudinal axis of the vehicle. Such an inclination angle is high enough to double the

turning moment generated by the propellers with reference to the vertical axis of the vehicle.



Fig. 1. Side view of the Gluptak vehicle. Length of the vehicle is 1.4 [m] and hull diameter is 0.25 [m]. Length of the stern, propulsion section is limited to 0.33 [m]

While the vehicle is moving forward, the left pair of propellers rotates anticlockwise and the right pair rotates clockwise. This solution helps to stabilise the vehicle and to reduce the rolling moment acting on the vehicle. This rolling moment is caused by torque of the propellers and changes of the speed of the motors due to inertia of the rotating components. To facilitate the manoeuvrability of the vehicle, the speed of each propeller is linearly controlled in the range of ± 3200 [rpm]. The highest sea current that allows for manoeuvring using turning moment is 0.5 [m/s]. The moment is generated by two pairs of horizontal propellers working in opposite directions. Above this velocity, the vehicle is only capable of moving forward, against the current. It can be inclined from the current line a few degrees in any direction by means of differentiating the speed of the propellers. In still, calm water, the Gluptak vehicle is able to manoeuvre quite well. However, reversing of the horizontal propellers is to be avoided due to the danger of mechanical destruction of the tether cable (the control fibre).

The screw propellers of the Gluptak vehicle are 0.1 [m] diameter, three-blade Wageningen B series propellers with a 0.3 surface coefficient and $P/D=0.635$. They are designed to operate with optimum performance (high thrust) in the forward direction. The propeller geometry was calculated using the typical procedure and corrected for real working conditions using experimental evaluation. The propeller's K_T , K_Q and η characteristics are presented in the Fig. 2.

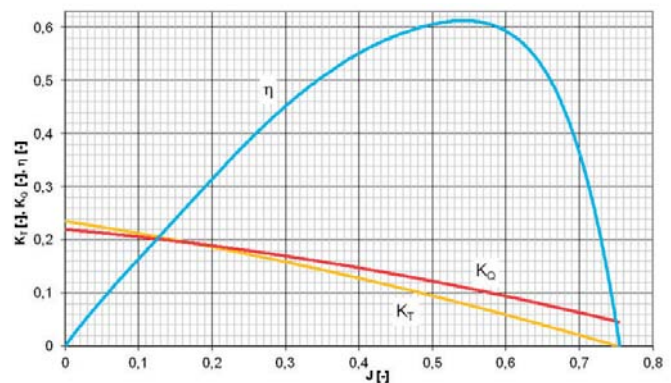


Fig. 2. The K_T and K_Q coefficient as well as η of the PG-100 propeller designed for a cruising speed of 3 [m/s] - three-blade Wageningen B series propellers have 0.3 surface coefficient and $P/D=0.635$

The propulsion system based on screw propellers proved to be effective in assumed conditions. However, the propellers are vulnerable to mechanical damage. They are in danger of sucking in quantities of different debris floating in the water (such as small stones, seaweed, ropes, tethers etc.). An example of such an incident is shown in the Fig. 3(a). The case presented indicates that comparatively thick (3 [mm] diameter) cable, reinforced with aramide fibre, can be easily sucked into the propeller and cause damage. The problem is obviously more serious in the case of the bare optical cable that is also utilised for vehicle control in the case of a combat mission. The optical fibre utilised for this purpose is only 0.25 [mm] thick and very fragile (made of glass). To reduce the risks and improve the handling capability, a grill guard was developed as the simplest solution to this problem. Its effectiveness has been proved during a series of experiments. The solution is not perfect but works to an acceptable extent. However, the introduction of the grill increases the drag force of the vehicle by approximately 35%. Such an increase of the drag is critically negative factor for the vehicle, which is supplied by an internal source of energy that offers limited power and capacity. Considering the grill guard to be a part of the propulsion system, the total efficiency of this system is approximately 40% and well below the 60% efficiency of the arrangement without the grill guard.

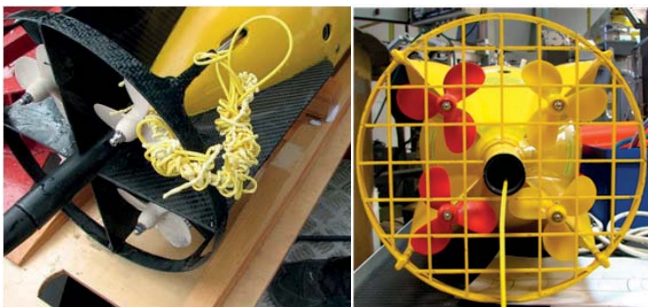


Fig. 3. Propeller of the Gluptak vehicle: a) the aramide reinforced tether cable entangled in one of the propellers of the Gluptak vehicle; b) arrangement of set of four screw propellers of the Gluptak vehicle, with the fibre protection grill guard (the directivity of the propellers is colour-coded to avoid mistakes during assembly)

DRAG FORCE OF THE GLUPTAK VEHICLE AND PROPULSOR DESIGN CONSTRAINTS

The external hull of the Gluptak vehicle is composed of the spherical bow, the cylindrical middle section and the conical stern section. The conical stern section contains propulsion components such as electric motors and propulsion shafts. Drag force curves of the Gluptak vehicle in different configurations that were investigated (measured) are shown in the Fig. 4. Differences between the bare hull and hulls with waterjet propulsors compared to the hull equipped with the grill guard are easily visible. To achieve a velocity of 3.0 [m/s], the vehicle body equipped with the grill guard requires 75 [N] of thrust. For the vehicle body without the grill and slightly deformed by the presence of waterjets, 50–56 [N]

of thrust force is required. An outsourced CFD analysis for the vehicle with water jet drives (WJ39G, which stands for off-the-shelf Graupner's water jet propulsion with 39 [mm] of rotor diameter) suggested nearly 41 [N] of the drag and it was underestimated by over 12%. Typically, for underwater vehicles such simulations lower the results in range of 20-30%.

The vehicle drag force is not the only constraint in the design of the propulsion suite of the Gluptak vehicle. Its geometrical configuration is limited by the available length of the stern section of the vehicle. The diameter of the flow tunnel of the propulsor and therefore the diameter of its rotor need to be kept at the minimum to ensure smooth flow around the stern. There are also issues that are not directly important problems for unidirectional propulsion. While the fins and the protection grill of the current configuration provide the vehicle with directional stability, this function needs to be ensured by a new arrangement. The manoeuvre properties and spatial orientation (location) of the water intakes must also be considered. However, investigations regarding these issues are not described in this paper.

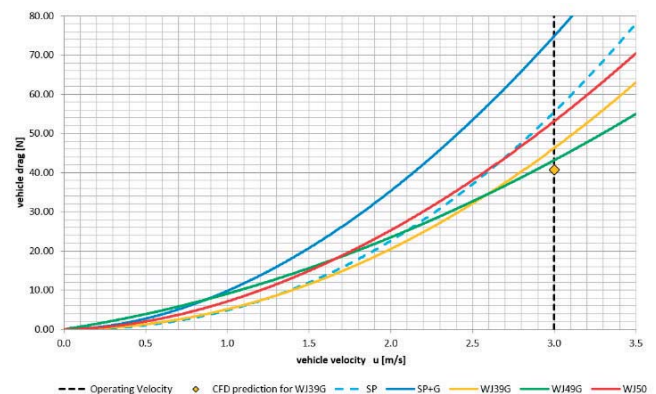


Fig. 4. Drag curves of the Gluptak vehicle in different configurations. SP – standard propellers, SP+G – standard propellers with protective grill, WJ39G – Graupner's water jet with 39 [mm] rotor diameter, WJ49G – Graupner's water jet with 49 [mm] rotor diameter, WJ50 – newly designed water jet with 50 [mm] rotor diameter

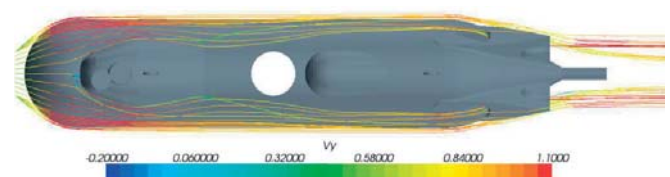


Fig. 5. Flow lines calculated for vehicle velocity of 3 [m/s] with pump rotors rotating (the colour scale: 1 - 3 [m/s])

As a result of the analyses the following requirements and constraints were defined for the single propulsor design four-unit propulsion system:

thrust at vehicle velocity of 3 [m/s]:	=>14 [N]
diameter of the flow tunnel:	as small as feasible
total length of the propulsor:	<= 0.33 [m]
radial extension of the case of the propulsor outside the vehicle body:	<= 0.05 [m]
power requirement (at motor shaft)	<=120 [W]

The goal of the study was to evaluate the required propulsion power and total efficiency of the propulsor that meet the defined restrictions. To compare the overall performance of waterjet propulsors with different pump rotor diameters, a semi-empirical procedure was utilised. Particular phenomena were investigated using programmes that implement CFD methods. Finally, real experiments were run to verify the calculations.

GENERAL ARRANGEMENT AND THEORETICAL PERFORMANCE OF THE WATERJET PROPULSOR

Among the available solutions for the Gluptak vehicle, a propulsion system composed of four waterjet propulsors seemed to be the most promising replacement for a screw propeller. However, low performance of the water jets was expected because of the vehicle's small dimensions and comparatively low speed. So, the proposal required detailed study regarding the geometry and operating parameters of the potential propulsor.

Description of the flow tunnel

The schematic outline of a waterjet propulsor is shown in the Fig. 6. It is composed of a flow tunnel and a pump rotor with a propulsion shaft. Characteristics of the flow tunnel are expressed with reference to points that are used to describe the waterjet. These are also measurement points and in accordance with the 23rd ITTC guidelines [8]. The flow tunnel elements are listed in Table 1 together with the semi-empirical formulas describing the flow losses due to the presence of these elements.

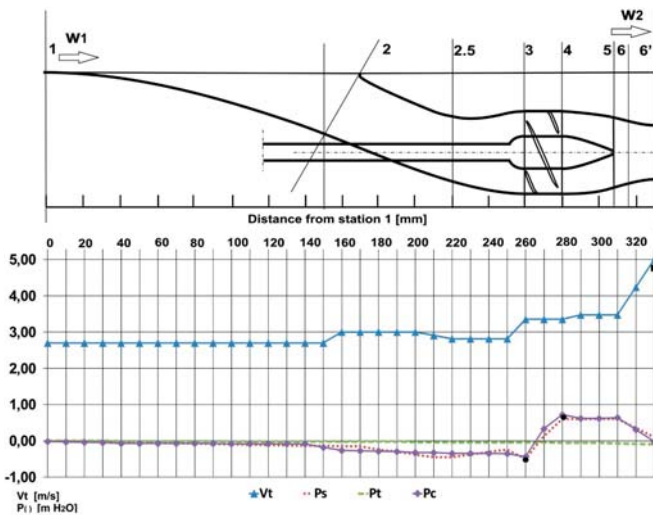


Fig. 6. The layout of the characteristic points (stations) and velocity symbols for station points of a waterjet propulsor following 23rd ITTC guidelines (top part) and results of study of flow inside the investigated 50 [mm] propulsor. V_t – flow velocity, P_s – total pressure calculated using CFD, P_t – pressure loss due to friction in the flow tunnel, and P_c – summary pressure estimated using semi-empirical models. Dots at 260 and 280 mm – pressures measured during experiment, square at 330 mm – measured output flow velocity

POWER AND EFFICIENCY OF A WATER JET PROPULSOR

Following Próchnicki [5], but without the assumption that the propulsor inflow velocity w_1 is equal to the vehicle velocity u , the thrust force is generated by the jet stream ejected out of the outlet nozzle at station 6. It is a product of the mass flow rate and the difference of absolute velocities at the inlet and outlet of the propulsor.

$$F_u = m \cdot (c_2 - c_1) \quad (1)$$

The absolute inlet velocity c_1 is:

$$c_1 = w_1 - u \quad (2)$$

whereas the absolute outlet velocity c_2 is equal to the difference between the relative outlet velocity and vessel velocity:

$$c_2 = w_2 - u \quad (3)$$

Therefore, considering Eq. (2) and substituting Eq. (1) into Eq. (3) results in the thrust force of the working jet propulsor:

$$F_u = m \cdot (w_2 - w_1) \quad (4)$$

The greatest thrust force is generated for zero forward speed, which means high jet thrust force at the vehicle start.

$$F_u|_{u=0} = m \cdot w_2 = F_u \max \quad (5)$$

The effective propulsion power is a product of the thrust force (equal to the vessel drag) and the vessel velocity:

$$N_u = F_u \cdot u = m \cdot (w_2 - w_1) \cdot u \quad (6)$$

The power of the outlet jet stream (carry-over loss) is described by the following equation:

$$N_{out} = m \cdot \frac{c_2^2}{2} = m \cdot \frac{(w_2 - u)^2}{2} \quad (7)$$

The pump power required to supply the propulsor is described by the power balance equation:

$$N_p \cdot \eta_p = N_u + N_{out} + N_{Loss} \quad (8)$$

So, calculation of the power required by the waterjet propulsor is easy to estimate if the tunnel losses and pump efficiency are known.

$$\eta_{WJ} = \frac{N_u \cdot \eta_p}{N_u + N_{out} + N_{Loss}} \quad (9)$$

The theoretical efficiency of a waterjet propulsor can be expressed by the formula below, which involves the velocity index μ :

$$\eta_{WJ}^0 = \frac{2 \cdot (1-\mu) \cdot \mu}{1-\mu^2 + 2 \cdot \frac{N_{l0}}{m \cdot w_2^2}} = \frac{2 \cdot (1-\mu) \cdot \mu}{1-\mu^2 \cdot \left(1 - 2 \cdot \frac{N_{l0}}{m \cdot u^2}\right)} \quad (10)$$

Where

$$\mu = \frac{u}{w_2} \quad (11)$$

is the non-dimensional velocity index.

A graphical representation of the relationships given by this formula is illustrated in the Fig. 7.

Considering the expression above, it can be seen that high efficiency is the result of the low carry-over loss, low tunnel loss, and high efficiency of the pump. It is apparent that, for the considered value of μ around 0.5, one can expect efficiency of between 50 and 60%, assuming moderate tunnel losses.

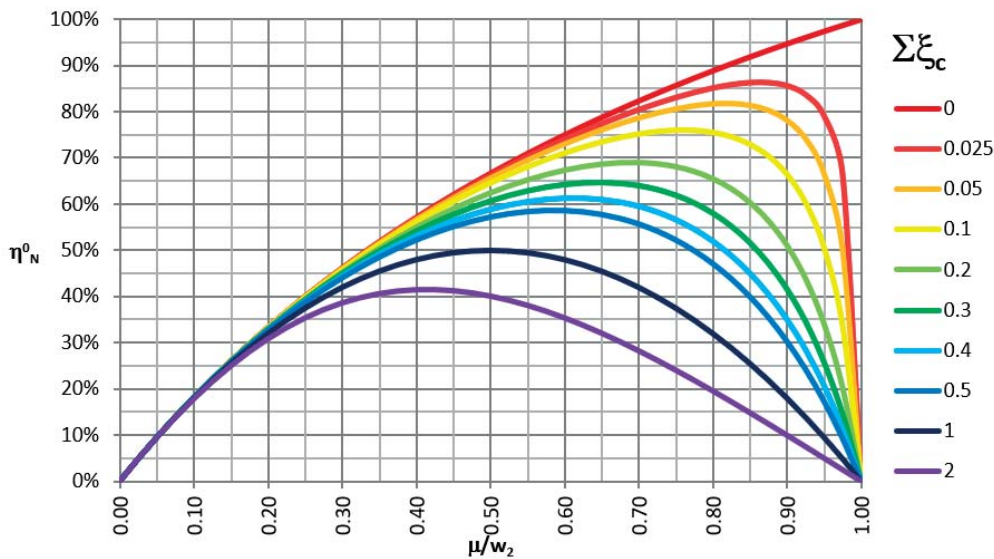


Fig. 7. Theoretical efficiency of waterjet propulsor

DESCRIPTION OF THE FLOW PARAMETERS USING BERNOULLI EQUATION

Following expression (9), the following values need to be estimated to calculate the efficiency of the waterjet propulsor:

- carry-over losses,
- flow losses inside the flow tunnel,
- efficiency of the pump.

The one-dimensional Bernoulli equation (12) was utilised to describe the flow parameters along the flow tunnel. It relates the velocities and pressures inside the flow tube if the usually used simplifying assumptions are valid:

$$\frac{\rho \cdot v^2}{2} + p = p_0 = \text{constant} \quad (12)$$

The graphical representation of the changes of the pressure and flow velocity along the flow tunnel, shown at the bottom

of the Fig. 6, is a good tool to study the influence of local features on the tunnel flow behaviour.

The station points indicated on this figure make it possible to divide the waterjet propulsor into sections (elements). Each of these elements affects the summary flow losses in the propulsor duct at a different rate and their estimation is crucial for the design process. The elements refer to particular parts of the geometry of the propulsor.

SEMI-EMPIRICAL MODELS DESCRIBING THE TUNNEL LOSSES

Semi-empirical models describing the tunnel losses were assumed to be the best tool to investigate the influence of various propulsor parameters on its performance. These models use expressions proposed by several researchers

who investigated particular phenomena in elements of flow duct. The performance of these tunnel elements is expressed by means of pressure (head) losses. Traditionally, pressure changes in the flow through pipes are expressed in [m] of water, which corresponds to the pressures generated by pumps expressed using the same units.

Particular expressions were selected for actual flow conditions, such as geometry ranges and the turbulence level expressed by the Reynolds number. They are listed in the Table 3, referenced to the

tunnel elements.

The general equation describing flow energy (head) losses is Weisbach's formula [9]:

$$h_{l(i)} = \xi_{(i)} \cdot \frac{v^2}{2 \cdot g} \quad (13)$$

The $\xi_{(i)}$ coefficient is the loss coefficient depending on the local geometry of the pipe element, such as the roughness, diameter reduction or expansion, pipe bend, protection grill etc.

Losses inside the flow tunnel were calculated separately for friction and local features. Therefore, the sum of flow losses expressed by the pressure drop in the fluid flowing through the tunnel is as follows:

$$h_l = \sum h_{fr} + \sum h_{ll} \quad (14)$$

As cavitation is not an issue for the considered application, there was no need to increase the pressure at the pump rotor space by means of increasing the rotor diameter relative to the flow pipe diameter. Therefore, for all calculations it was

assumed that the nominal diameter of the flow channel is equal to the diameter of the pump rotor. This also means that the nominal flow velocity inside the channel is equal to the velocity of the vehicle. The losses specific to the waterjet propulsor are commented upon below.

It was also assumed that the flow at the flow tunnel is fully developed and turbulent when the Reynolds number exceeds a value of 10^5 . According to the available data, such a flow friction coefficient depends mainly on the surface roughness of a duct, as indicated on the graph developed by Holbrook and White and approximated by Altsul [1] in the form of expression (15):

$$\lambda = 0.11 \cdot \left(\frac{68}{Re} + \frac{k}{d} \right)^{0.25} \quad (15)$$

where the k factor is surface roughness, assumed at 0.05 [mm] for all the considered cases. In practice, the roughness value cannot be scaled.

Velocity reduction between station 0 and station 1 – influence of the wake

The water that is ingested into the inlet of the waterjet tunnel partially originates from the hull's boundary layer. The mass-averaged velocity of the ingested water v_{in} is lower than the ship speed due to this boundary layer. The velocity deficit is expressed as the momentum wake fraction w and is defined as:

$$w = 1 - \frac{w_1}{u} \quad (16)$$

According to expression (4), the wake phenomenon increases the generated thrust but simultaneously, according to expression (6), increases the energy required to accelerate the water to the output velocity at station 6 to achieve the required thrust. Determination of the wake fraction is rather complex in the considered case, since the cross-sectional shape of the stream tube is not defined. Following Faltinsen, the

Tab. 1. The waterjet duct elements described using the station points

No.	Limiting stations	Element of the waterjet duct	Friction loss formula	Local loss formula
1	0 – 1a	Undisturbed flow far ahead of the vehicle	Not considered	Not considered
2	1a – 1	Area in front of the inlet influencing flow as turbulent boundary layer	reduction of average intake flow velocity	wake coefficient assumed $w = 1 - \frac{w_1}{u} = 0.05$
3	1	Local inlet loss due to start of the propulsor	–	wssumed at $\xi_{lin} = 0.05$
4	1 – 2	The inlet semi-open pipe, bend	$\xi_{fin} = (\lambda(l/d))/2$	$\xi_{fin} = \left[0.131 + 0.163 \cdot \left(\frac{d}{R_{in}} \right)^{3.5} \right] \cdot \frac{Y_{in}}{90}$
5	2	The pipe inlet	–	assumed at $\xi_{fp} = 0.2$
6	2 – 3	The pipe, the pipe bend	$\xi_{fpi} = \lambda(l/d)$	$\xi_{fpb} = \left[0.131 + 0.163 \cdot \left(\frac{d}{R_{pb}} \right)^{3.5} \right] \cdot \frac{Y_{pb}}{90}$
7	3 – 4	The diffuser	$\xi_{fd} = \frac{\lambda_t}{8 \sin\left(\frac{\delta_D}{2}\right)} \cdot \left[\left(\frac{A_{D2}}{A_{D1}} \right)^2 - 1 \right]$	$\xi_{id} = k_p \cdot \left(\frac{A_2}{A_1} - 1 \right)^2$ $k_p = 0.14,$
8	3 – 5	The pump pipe	$\xi_{pp} = \lambda(l/d)$	–
9	5	The inlet to the pump stator due to introduction of the stator blades	–	assumed $\xi_{is} = 0.1$
10	4 – 5	The pump stator	$\xi_{fs} = \frac{2 \cdot \lambda_t}{8 \sin\left(\frac{\delta_S}{2}\right)} \cdot \left[1 - \left(\frac{A_{S2}}{A_{S1}} \right)^2 \right]$	$\xi_{is} = 0.04 + \left(\frac{1}{\chi} - 1 \right)^2$ $\chi = 0.9$
11	5 – 6	The nozzle	$\xi_{fN} = \frac{2 \cdot \lambda_t}{8 \sin\left(\frac{\delta_N}{2}\right)} \cdot \left[1 - \left(\frac{A_{N2}}{A_{N1}} \right)^2 \right]$	$\xi_{iN} = 0.04 + \left(\frac{1}{\chi} - 1 \right)^2$ $\chi = 0.9$

wake fraction “may vary between 0 and 0.4 for a displacement vessel, depending on the hull form” [10].

The thickness of the turbulent boundary layer develops from the beginning of the vehicle body following changes of the value of the Reynolds number along the flow, where x is the distance from the beginning of the body.

$$Re_x = \frac{v \cdot x}{\nu} \quad (17)$$

For a flat plate, the flow is laminar up to $Re_c < 0.2 \cdot 10^6$ and completely turbulent above $Re_c > 3 \cdot 10^6$. However, because of the spherical nose, substantial turbulence may develop at the beginning of the spherical body. It is further amplified by several local obstructions present on the body of the vehicle.

Standard theory for a flat plate boundary layer, as described in several textbooks [10] [11], [12] can be used to get a first indication of the velocity distribution. It is convenient to use a power-law velocity profile for the thickness of the boundary layer [10]:

$$\delta = \frac{0.16 \cdot x}{(Re_x)^{1/7}} \quad (18)$$

According to expression (18), the thickness of the turbulent layer develops as shown in the Fig. 8. Fully developed turbulent flow is initiated just at the propulsor’s inlet, and its thickness is about 25 [mm]. This value corresponds well with data obtained from CFD simulations in the flow.

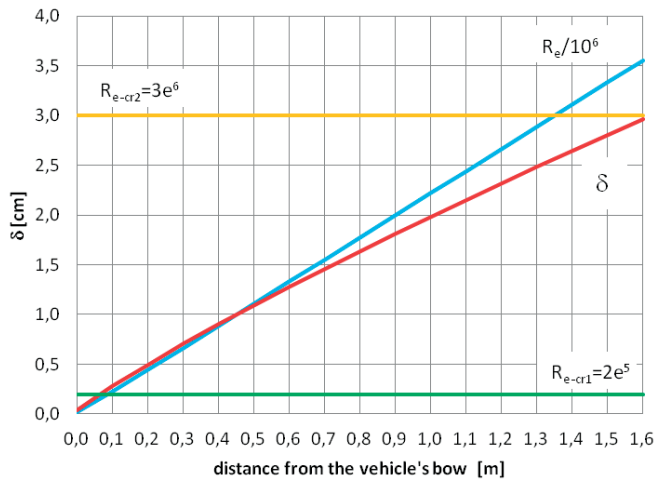


Fig. 8. Thickness of the boundary layer along a flat plate at water temperature of 15 [°C]

The CFD calculations, performed in parallel to this study, have indicated the average stream tube flow velocity as 2.7 [m/s] at station 1 of the propulsor, which corresponds to $w = 0.1$. However, the intermediate value of $w=0.05$ was adopted for the performance analyses because the assumed flow tube height is twice the thickness of the boundary layer. One needs to be aware of the substantial influence of the value of the wake friction coefficient on total propulsor performance. If $w = 0.1$ were assumed, the total water jet

efficiency estimated would rise by 5% for a 50 [mm] rotor diameter. Contrarily, for $w = 0.0$ the efficiency value would drop by 5%.

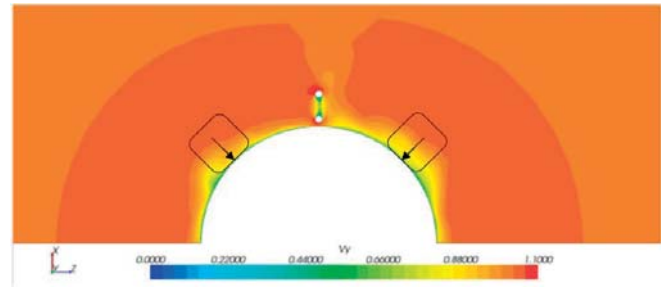


Fig. 9. Distribution of flow longitudinal relative velocities at the plane coincident with station 1 of waterjet propulsors. Reference velocity is 3 [m/s]. Flow intakes are indicated by arrows, stream tubes are indicated by rounded squares.

Tunnel inlet

Usually, the tunnel inlet of a water jet is a rectangular or oval opening in the vehicle hull. The 21st ITTC [13] recommends intake proportions at a ratio of 1.3:1.0 (length about 30% greater than width), but other research [8] indicates that changes within 20% in the proportions of the capture area deliver only about 1% difference in the estimated power (thrust). Moreover, van Terwisga [14] concluded that there was no significant effect on power (thrust) losses or gains between rectangular and elliptical intake shapes. He also found that variations of thrust are contained within 0.5% for the inlet proportions 1.3:1 and 1.5:1 (length: width). Also CFD analysis of the inlet with a trapezoidal shape suggests that there is no necessity to determine the inlet area precisely. Other researchers [6], [10], [15], indicate that this area is as important as the rest of the flow duct and cannot be neglected. It determines the character of the inflow to the next stage and has a substantial influence on drive efficiency. Therefore, it is recommended to analyse it precisely and perform further scrutiny of this area [8]. For the initial phase of investigation, the local loss coefficient of a constant value was assumed and it was later studied with the CFD method.

Tunnel bend at the inlet

The *Coandă effect* [16] is the tendency of a fluid flow to be attracted to a nearby surface. In practice, the *Coandă effect* changes the direction of the flow. If the surface curvature is smooth enough, it causes the fluid to stick to it. Fluid follows the surface until it ends sharply or the fluid stream is faced with some obstacle. In a case of the waterjet propulsor, the effect can be observed at the tunnel inlet where a part of the stream flowing around the vehicle’s body is redirected to the duct. The obvious advantage of this phenomenon is that, at least partially, it fills the inlet space with water. This in turn reduces the amount of water that needs to be sucked in and thus increases the overall performance of the propulsor.

Unfortunately, the precise determination of the water stream flowing into the tunnel is very difficult due to the nature of this natural phenomenon. Hence, the losses

estimations at this stage are only anticipations based on formulas related to a sudden change of flow direction or bend of a pipe.

THE PUMP AS ELEMENT OF THE WATERJET PROPULSOR

The pump efficiency of a waterjet propulsor is the second basic parameter, beside channel losses, that needs to be estimated to obtain its (WJ) overall efficiency. The pump rotor-stator part of the waterjet propulsor can be regarded as a standard pump section. The most popular types of pumps used in waterjet drives are axial, diagonal (mixed-flow), and helicoidal pumps (in outboard motors). There is limited information regarding the design of pumps of the considered parameters: rotor diameter $D < 0.050$ [m], head (output pressure) $H < 2$ [m] and volumetric output $q < 10$ [dm³/s] $\sim (Q < 20$ [m³/h]). In particular, there are no data regarding these parameters for axial pumps. So, general rules regarding assessment of the pump performance need to be applied in the case considered. An axial type pump was assumed for the propulsor. The choice was supported by general selection rules based on the pump kinematic speed index n_{SQ} , the value of which is defined by formula (11). It depends on the relation between Q , H and n , and it is closely related to the pump geometry. The speed index allows for comparison of pumps with identical dynamic characteristics but different geometry, and selection of the most appropriate type.

$$n_{SQ} = \frac{n \cdot Q^{1/2}}{H^{3/4}} \quad (19)$$

For the assumed parameters, its value is around 300 as most suitable for axial type pumps. Most sources present pump characteristics in the form of charts. There are some general data regarding performance and general rules regarding the selection of rotary pumps. The two graphs in the Fig. 10 show the efficiency of a wide range of pumps referenced to the pump velocity index. The diagram in the Fig. 10(a) suggests the application of an axial pump in the case considered. Axial pumps with a volumetric capacity of ~ 20 [m³/h] are considered very small and are rarely optimised to reach high efficiency. However, there is still a possibility to compare pumps of different sizes and hence obtain essential input data for semi-empirical calculations. According to both graphs in the Fig. 10, the pump efficiency for a pump with the assumed volumetric flow and a speed index of 300 has a value between 60% and 65%.

Some authors propose simple formulas that are supposed to determine the total performance of a pump, based on the model (reference) pump efficiency. Selected ones are listed in the Table 2, where the m index refers to the model pump. The d and d_m are pump rotor and the pump model rotor (reference) diameters respectively. These (21), (23), usually require some data regarding the speed of both pumps. In the case of a lack of information regarding the speed of the reference pump, the much simpler formula (22), developed by H.H. Anderson, can be used. For the purpose of this work, it was assumed that the reference pump had a 0.5 [m] rotor diameter and 90% efficiency at the operating point. These values are typical for large waterjet pumps [17]. Hence, for a rotor with 0.05 [m] diameter and using the *Anderson's* formula, the calculated efficiency is over 82%. It drops to just below 80% for a 30 [mm] diameter pump rotor. For further consideration, less optimistic efficiencies based on expression (23) and the data listed in the Table 2 were assumed.

According to these data, for a pump with a considered volumetric flow of ~ 20 [m³/h] (0.005 [m³/s]) and speed index of 300, the efficiency value would be estimated below 65%. To be on the safe side, the value of 60% was assumed for a rotor diameter of 50 [mm]. The efficiency values used for various investigated diameters are presented in the Table 3.

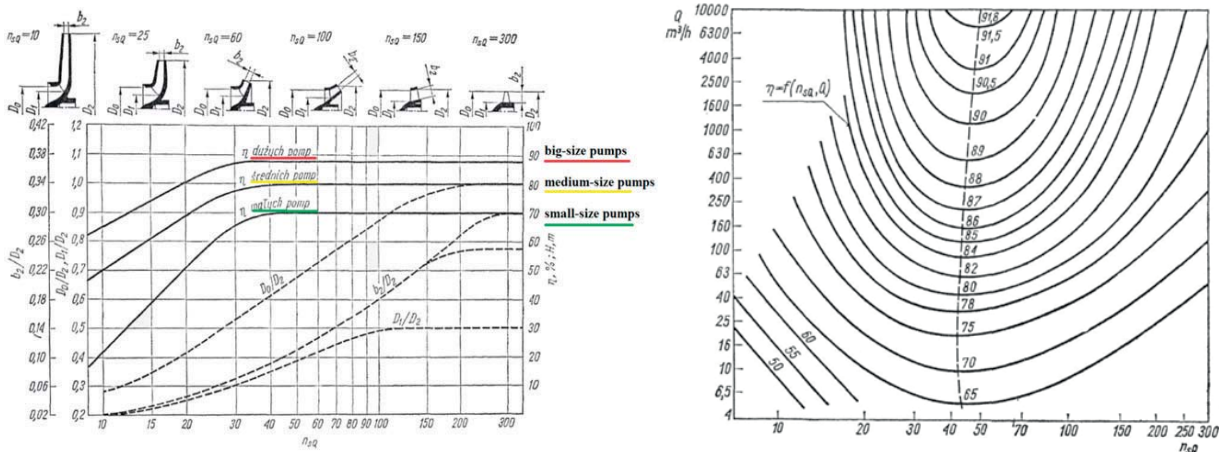


Fig. 10. General performance curves and selection rules of a rotary pump based on pump kinematic speed index by Neumaier and Gradewald in [12]

Tab. 2. Expected efficiencies of an axial pump for a low diameter waterjet propulsor

No.	Source of data	Formula	Efficiency
1	Gradewald [12]	Diagram in Fig. 10(a)	~ 60%
2	Neumaier [12]	Diagram in Fig. 10(b)	< 70%
3	Moody's formula [18]	$\eta = 1 - (1 - \eta_m) \cdot \left(\frac{d_m}{d}\right)^{0.45} \cdot \left(\frac{n_m}{n}\right)^{0.2}$ (21)	68% for d=0.05 m
4	Anderson [9], [19]	$\eta = 1 - (1 - \eta_m) \cdot \left(\frac{d_m}{d}\right)^{0.25}$ (22)	82% for d=0.05 m
5	Arnold & Nijhuis [17]	$\eta = 0.95 - \frac{0.05}{\sqrt[3]{Q}} - 0.125[\log(n_\omega)]^2$ (23)	65% for d=0.05m Q=0.006 m ³ /s n _ω = 3
6	Kim & Chun [2]	Experimental results for 64 mm rotor diameter 0.7% blade tip clearance 1.5 % blade tip clearance	61% 54%

Tab. 3. Efficiencies of axial pumps of small size waterjet propulsors depending on the rotor diameter assumed for semi-empirical calculations

No.	Parameter	Unit	Value				
1	Pump rotor diameter	[mm]	30	40	50	60	70
2	Estimated pump efficiency	[%]	50	57	60	62	64

EVALUATION OF BASIC PARAMETERS OF THE WATERJET PROPULSOR FOR ASSUMED OPERATIONAL CONDITIONS

Geometric limitations are important factors while considering the replacement for open screw propellers by means of waterjet propulsors. To preserve the propulsion and manoeuvring capabilities of the existing vehicle, it was assumed that the propulsion system needs to be arranged using the existing configuration. This assumption indicated a solution with the four units arranged in an X configuration. To minimise drag resistance, the waterjet propulsors were built into the stabilising fins to ensure undisturbed flow around the fins and external surfaces of the propulsors. The pump rotor diameter is to be possibly small for the same reason. The initial diameter of the pump rotor of the waterjet propulsor can be calculated using the following expression:

$$D_{opt} = 1.45 \sqrt[4]{\frac{F}{\rho n^2}} \quad (20)$$

It is further advised to adopt the diameter evaluated using this expression or the largest diameter allowed by the geometry of the vehicle. In the case considered, it was found (Fig. 11) that the rotor diameter is to be around 50 [mm] if a rotational speed near 5000 [rpm] is assumed.

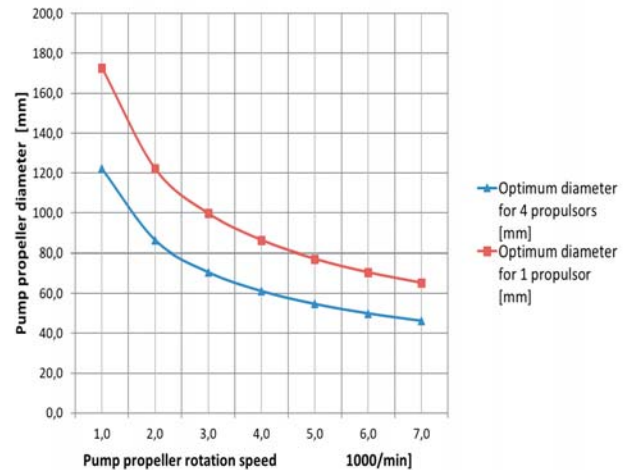


Fig. 11. Optimum pump rotor diameter calculated using expression (20) for the vehicle propelled by a single water jet propulsor with 56 [N] of thrust and or four water jet propulsors with 14 [N] of thrust

While the pump rotor diameter lower than 50 [mm] was found to be possibly appropriate in the considered application, a range of pump rotor diameters of 30, 40, 50, 60 and 70 [mm] was defined for further evaluation. Additional assumptions for comparison of the waterjet propulsors with the nominal diameters listed above were as follows:

1. The nominal flow velocity inside the pipe component of the propulsor is equal to the nominal velocity of the vehicle ($v_{pipe} = u = 3$ [m/s]);
2. The nominal diameter of a flow channel (pipe) between station 2 and station 2.5 was assumed to be equal to the nominal propeller diameter.

The following calculation algorithm was executed to find the rotor diameter that ensures the required thrust and highest possible efficiency:

1. The nozzle output flow velocity w_2 was set at a value that ensures the required thrust of 14 [N];

2. The fluid velocity at every tunnel component was calculated, using data regarding the geometry of this tunnel component;
3. The coefficient of losses for every component was calculated, split into friction $\xi_{f(i)}$ and local losses $\xi_{l(i)}$;
4. The pressure losses of all the components (friction and local) were summed along the tunnel, starting from station 1;
5. The pressure change due to change of water velocity at a point or a tunnel element was calculated;
6. All pressure changes including that resulting from the operating rotor were summed up along the tunnel, starting from station 1;
7. The power required to compensate the corresponding drop of pressure carry-over losses and ship propulsion was calculated;
8. The pump head was calculated for the propulsion power required.

Friction losses in a considered element of the tunnel were calculated for the end of this element. Local losses were introduced at the station where they occurred (input 1 at station 1, input 1 at station 2, and input to pump stator) or

for the end of a local feature (bend, diffuser, pump stator, confuser).

CALCULATION RESULTS

Excel spreadsheets were used for calculations using the semi-empirical algorithm. The resultant values for a water temperature of 15 [°C] are summarised in the Table 4. It contains the basic parameters of the flow parameters for characteristic points and elements of the flow tunnel. The calculated results describe averaged parameters of the flow in great detail and allow for study of the influence of a particular element of the geometry of the flow tunnel on the final performance of the propulsor. Fig. 6 shows these results for the 50 [mm] nominal rotor diameter in graphical form. The figure refers to the tunnel itself. For graphical presentation purposes, the values of friction losses between stations were linearly approximated. Local losses were introduced at the station of occurrence (pipe inlet loss, stator input loss) or linearly approximated between stations (bends, diffuser, confuser). Changes of flow velocities were introduced at the end of an element and linearly approximated between stations.

Tab. 4. Comparison of the relative parameters of waterjet propulsors with various pump rotor diameters for assumed thrust of 14 [N] and wake coefficient $w=0.05$

No.	Parameter	Symbol	Unit	Pump rotor diameter [mm]				
				30	40	50	60	70
1	Velocity of the vehicle	\mathbf{u}	m/s	3.00	3.00	3.00	3.00	3.00
2	Velocity at station no. 6	\mathbf{w}_2	m/s	9.45	6.56	5.23	4.50	4.06
3	Velocity index	$\mu=\mathbf{u}/\mathbf{w}_2$	-	0.32	0.46	0.57	0.67	0.74
4	Water jet thrust	F_u	N	14	14	14	14	14
5	Sum of coefficients of losses	$\Sigma\xi_c=\Sigma\xi_f+\Sigma\xi_l$	-	0.726	0.640	0.595	0.572	0.563
6	Pump output power required	N_p	W	95	78	72	71	75
7	Theoretical total waterjet efficiency	η_{wj0}	%	43	52	55	54	49
8	Estimated total waterjet tunnel efficiency	η	%	44	53	56	56	53
9	Estimated pump efficiency	η_p	%	55	57	59	60	61
10	Calculated pump speed index (kinematic)	Nsq	-	99	181	269	353	469
11	Estimated total propulsor efficiency	η_{prop}	%	22	30	34	35	34

Tab. 5. Energy (power) distribution in waterjet propulsors with pump rotors of different diameters

No.	Parameter	Symbol	Unit	Pump rotor diameter [mm]				
				30	40	50	60	70
1	Estimated motor output power required	N_m	W	191	138	124	121	124
2	Vehicle propulsion power	N_u	W	42	42	42	42	42
3	Relative propulsion power (= total water jet efficiency η_{prop})	ψ_u	%	22	30	34	35	34
4	Pump relative loss	Ψ_p	%	50	43	40	38	40
5	Carry-over relative loss	ψ_{co}	%	23	17	12	8	5
6	Sum of tunnel-related relative losses	Ψ_t	%	4	8	14	19	23
7	Tunnel friction relative losses	Ψ_f	%	2	3	4	5	5
8	Inlet (before pump) relative losses	ψ_{in}	%	1	3	6	9	12
9	Outlet (after pump: pump stator and confuser) relative losses	ψ_{out}	%	1	2	4	5	6

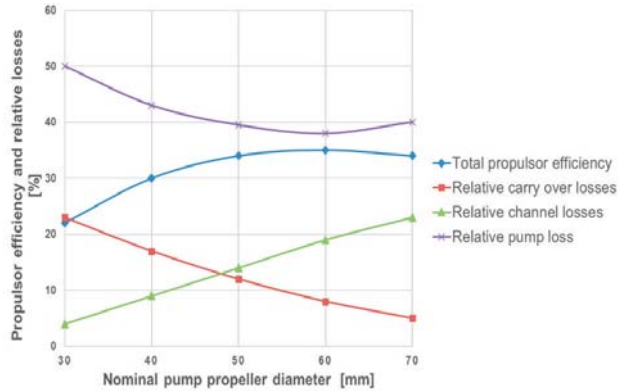


Fig. 12. Development of power distribution in small water jet propulsor depending on the pump propeller diameter (total propulsion efficiency = relative propulsion power).

CFD CALCULATIONS AND REAL EXPERIMENTS

For the selected nominal diameters of the propulsors (rotors), 3D geometrical models were prepared and studied using CFD flow calculations. The results of one of the simulations regarding a 50 [mm] nominal diameter are shown in the Fig. 6 in the form of the curve representing pressure changes in the flow duct.

As can be seen, there is good coincidence of the results of the semi-empirical and CFD calculations. The semi-empirical algorithm offers quite good modelling of the real performance of the whole waterjet propulsor that allows for rapid assessment of the principal geometric parameters. However, the numerical calculations offer the opportunity to study local phenomena of the flow in great detail. In fact, several detailed studies were performed to find the influence of the local geometries of the flow tunnel performance. Beginning from the inlet (station 1), the following issues were investigated:

1. Raising the inlet point above the hull surface to avoid intake of the turbulent layer.
2. Flash inlet geometry.
3. Curvature radius of the tunnel bent between station 1 and station 2.
4. Curvature radius of the tunnel bent between station 2 and station 3.
5. P/D ratio of pump rotor blades.
6. Geometry of the stator and stator blades between station 4 and station 5.
7. Geometry of the nozzle between stations 5 and 6.

The results of the CFD calculations of particular features as well as the results of tests of real propulsors will be presented in a separate publication.

SUMMARY

1. The results of the study confirm the usefulness of the semi-empirical method in the evaluation of the basic parameters of the waterjet pump rotor of unusual size.
2. The influence of the shape of the local cross-section area of the tunnel on the local flow parameters cannot be studied using the semi-empirical method.
3. Detailed design of local features requires the application of CFD methods, which proved to give realistic results.
4. A propulsor with a nominal diameter of 50 [mm] was selected for further investigations as offering the best compromise between its performance and low influence on the vehicle drag.
5. In practical terms, the study justifies the replacement of open screw propellers with water jets without a substantial penalty on the Gluptak vehicle's propulsion performance. This is true in spite of the much lower efficiency of the waterjet propulsor because of the possibility of removal of the fibre protection grill. The calculated motor output power of 124 [W] exceeds the assumed value of 120 [W] by just 3%.
6. Other issues regarding the underwater vehicle's performance such as its directional stability and the ability to manoeuvre require separate studies as well as solutions, and may influence the final propulsor configuration.

NOMENCLATURE

- ρ – water density [kg/m³]
- g – gravity acceleration [m/s²]
- u – ship speed [m/s]
- w – wake factor [-]
- w_1 – water velocity of inflow to flow channel [m/s]
- w_2 – outflow from confusor [m/s]
- μ – velocity index [-]
- $v_{(i)}$ – flow velocity, general [m/s]
- ν – fluid viscosity [m²/s]
- D – nominal diameter of propulsor (flow channel and pump rotor) [m]
- D_N – diameter of outlet nozzle [m]
- D_m – nominal diameter of reference (model) pump [m]
- $d_{(i)}$ – local diameter of the flow channel [m]
- $\delta_D, \delta_S, \delta_N$ – diffuser, stator and nozzle divergence angle [deg]
- F_u – thrust force [N]
- m – rate of water mass flow through propeller [kg/s]
- Q – volumetric output [dm³/s]
- P_r – pitch of pump rotor [m]
- k – surface roughness [mm]
- λ – pipe friction coefficient [-]
- $\zeta_{f(i)}, \zeta_{l(i)}$ – dimensionless coefficient of hydraulic losses due to friction and local channel geometry.
- H, p – pressure in flow duct [m H₂O]
- H_p – pump head (output pressure) [m H₂O]
- $h_{lo(i)}$ – local pressure or pressure loss [m H₂O]
- N_u – vehicle propulsion power [W]
- N_{co} – power to carry-over losses [W]

N_{lo} – power of losses [W]
 N_m – estimated motor output power required [W]
 η_{wj0} – theoretical total waterjet efficiency [%]
 η_p – pump efficiency [%]
 η_m – specific efficiency [%]
 $\psi_{(i)}$ – relative losses inside an element of the flow channel or due to local flow phenomenon [%]
 R_{in}, R_{pb} – radius of flow channel bent at intake and pipe [m]
 n – pump rotor rotation speed [1/s]
 n_{SQ} – pump velocity index (Q[m³/s], n [rpm], H[m])
 n_{ω} – pump velocity index (Q[m³/s], n [rad/s], H[m])

REFERENCES

1. Y. Shen *et al.*, ‘Design of Novel Shaftless Pump-Jet Propulsor for Multi-Purpose Long-Range and High-Speed Autonomous Underwater Vehicle’, *IEEE Trans. Magn.*, vol. 52, no. 7, 2016, doi: 10.1109/TMAG.2016.2522822.
2. L. Zhang, J. N. Zhang, Y. C. Shang, G. X. Dong, and W. M. Chen, ‘A Practical approach to the assessment of waterjet propulsion performance: The case of a waterjet-propelled trimaran’, *Polish Marit. Res.*, vol. 26, no. 4, 2020, doi: 10.2478/pomr-2019-0063.
3. L. Jian, L. Xiwen, Z. Zuti, L. Xiaohui, and Z. Yuquan, ‘Numerical investigation into effects on momentum thrust by nozzle’s geometric parameters in water jet propulsion system of autonomous underwater vehicles’, *Ocean Eng.*, vol. 123, 2016, doi: 10.1016/j.oceaneng.2016.07.041.
4. S. Wang, M. Fu, Y. Wang, and L. Zhao, ‘A Multi-Layered Potential Field Method for Water-Jet Propelled Unmanned Surface Vehicle Local Path Planning with Minimum Energy Consumption’, *Polish Marit. Res.*, vol. 26, no. 1, 2019, doi: 10.2478/pomr-2019-0015.
5. W. Próchnicki, *Analysis of the ship’s jet propulsion capabilities*. Gdansk: Politechnika Gdanska, 2001.
6. L. Rowinski, ‘Motion requirements of single mission mine counter submersible craft, Underwater Defence Technology Conference and Exhibition, Malmo, Sweden’, 2003.
7. L. Rowinski, ‘Articulated warhead mine disposal vehicle, Underwater Defence Technology Conference and Exhibition “UDT Europe 2008”, Glasgow, Great Britain’, 2008.
8. ‘The Specialist Committee on Validation of Waterjet Test Procedures’, in *Proceedings of the 24th ITTC*, 2005, p. Volume II.
9. F. M. White, ‘Fluid Mechanics seventh edition by Frank M. White’, *Power*, 2011.
10. F. O. M. Faltinsen, *Hydrodynamics of High-Speed Maritime Vehicles*. Cambridge University Press, 2005.
11. Tesch Krzysztof, *Fluid Mechanics*. Politechnika Gdanska, 2008.
12. H. T. Schlichting, *Boundary Layer Theory*. McGraw-Hill, 1979.
13. ‘Report of the Waterjets Group, Proceedings of the 21st International Towing Tank Conference, ITTC’96’, Trondheim, Norway, 1996.
14. T. J. C. Van Terwisga, ‘Waterjet-Hull interaction, Ph.D. Thesis’, 1996.
15. M. C. Kim and H. H. Chun, ‘Experimental Investigation into the performance of the Axial-Flow-Type Waterjet according to the Variation of Impeller Tip Clearance’, *Ocean Eng.*, vol. 34, no. 2, 2007, doi: 10.1016/j.oceaneng.2005.12.011.
16. C. Lubert, ‘On some recent applications of the coanda effect’, in *International Journal of Acoustics and Vibrations*, 2011, vol. 16, no. 3, doi: 10.20855/ijav.2011.16.3286.
17. J. Arnold; G.J. Nijhuis, *Selection design and operation of rotodynamic pumps. The Nijhuis Pampen*. 2005.
18. L. F. Moody, ‘The Propeller Type Turbine’, *Trans. Am. Soc. Civ. Eng.*, 1925.
19. H. H. Anderson, ‘Theory of Centrifugal Pumps’, in *Centrifugal Pumps*, 1993, pp. 36–43.

CONTACT WITH THE AUTHORS

Lech Rowinski
e-mail: rowinski@pg.edu.pl

Gdańsk University of Technology
 Narutowicza 11/12, 80-233 Gdansk,
POLAND

THE INFLUENCE OF SELECTED STRAIN-BASED FAILURE CRITERIA ON SHIP STRUCTURE DAMAGE RESULTING FROM A COLLISION WITH AN OFFSHORE WIND TURBINE MONOPILE

Karol Niklas*

Alicja Bera

Gdańsk University of Technology, Poland

* Corresponding author: karol.niklas@pg.edu.pl (K. Niklas)

ABSTRACT

Offshore wind farms are developing well all over the world, providing green energy from renewable sources. The evaluation of possible consequences of a collision involves Finite Element computer simulations. The goal of this paper was to analyse the influence of selected strain-based failure criteria on ship damage resulting from a collision with an offshore wind turbine monopile. The case of a collision between an offshore supply vessel and a monopile-type support structure was examined. The results imply that simulation assumptions, especially the failure criteria, are very important. It was found that, using the strain failure criteria according to the minimum values required by the design rules, can lead to an underestimation of the ship damage by as much as 6 times, for the length of the hull plate, and 9 times, for the area of the ship hull opening. Instead, the adjusted formula should be used, taking into account both the FE element size and the shell thickness. The influence of the non-linear representation of the stress-strain curve was also pointed out. Moreover, a significant influence of the selected steel grade on collision damages was found.

Keywords: Ship, collision, monopile, failure, crashworthiness

INTRODUCTION

The offshore production of energy from wind is developing dynamically (see Fig. 1 and Fig. 2). Large wind farm projects are underway on the Baltic Sea. Offshore wind farms are often located in the immediate vicinity of busy shipping routes and near coastlines with restricted areas. Key trends and statistics indicate dynamic development of the offshore wind energy sector [1-2]. This increases the risk of collisions between ships and wind farm support structures, which can lead to major damage to the environment and enormous financial losses. About 3,300 ships are involved in accidents each year. Collisions and groundings account for 43% of all accidents [3].

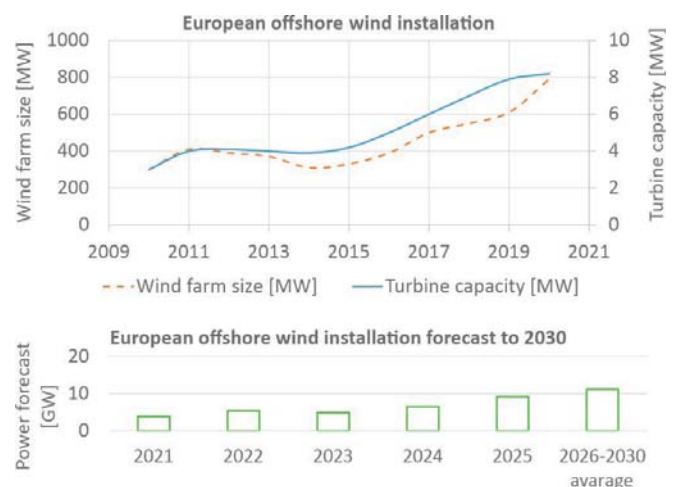


Fig. 1. European offshore wind farm installations (2010-2020) and the forecast until 2030 [2]



Fig. 2. Sample photograph of an offshore support vessel (OSV) operating at an offshore wind turbine (OWT) farm [1]

These issues are important and have been the subject of numerous scientific studies. Safety at sea is very important, therefore research has been carried out on various ocean engineering structures for different purposes and dynamics [4-12]. For example, an analysis of ship collisions with 3 types of support structures was published by [13]. The effects of the collisions on the support structures were analysed and the jacket was found to be the most robust structure type. The paper pointed out the strong influence of Finite Element (FE) computer simulation assumptions on the results. On the other hand, paper [14] presented the strength analysis of a large gravity type foundation, [15] presented strength analysis of a Tripile-type support structure and [16] showed the problems associated with the long-term use of structures at sea. However, by far the most common type of support structures used is the monopile (81% in Europe [17]), which is the subject of publications such as [18]. There are also hybrid solutions combining energy from floating wind towers and energy from sea waves [19-20]. Also, [21] and [22] studied the effect of different collision scenarios and model assumptions on the prediction of consequences of a collision between a ship and a support structure. Again, the tremendous influence of model assumptions on the results was highlighted.

Paper [23] dealt with the impact of collisions on potential damage to the turbine support column and blades. The most thorough analyses of the effect of model assumptions on collision outcome predictions to date was published in papers dealing with ship collisions and groundings, i.e. [24-28]. A benchmark study [26] of the impact of various modelling aspects has shown that the model of the material in question and the failure criteria are the two key assumptions in the computer simulation of collisions. The most commonly used are strain-based criteria, in which the range between the proposed values of failure strain for the normal-strength hull steel ranges from 0.1 to 0.7 [26], [29]. Such a wide range of values of the failure strain adopted by various authors may raise serious doubts about the reliability of the obtained results. A value of 0.2 is quite often used in ship collision

simulations [26], [30] and is often assumed to be equal to the minimum material requirements specified by the design rules [31]. At the same time, the value is much smaller than that obtained from experimental material tests in the case that, as the author explained, did not take into account the geometric stress concentrations present in the finite element mesh of relatively large size. The study by [32] used a failure strain value of 0.2 in ship collision simulations. In contrast, another author recommended a rupture strain value of 0.35 while performing a series of experimental validation studies [33]. In another study [34], the Yagi at all also refers to a failure rupture value of 0.2 without providing a reference. Yet another paper [35] pointed out the huge influence of the finite element size and the plate thickness by introducing a correction equation. For the formula, much higher values of failure strain, equal to 0.39 and 0.66 (depending on the size of the element), correctly reflected the conditions of the performed experiments – pressing the sphere model into a flat plate.

A comparison of collision simulation results for different failure criteria was published in [36]. Significant discrepancies were found in the results. The need to perform a mesh convergence study was indicated, since the size of the element used has a strong effect on the simulation results. At the same time, it was pointed out that the failure criteria took into account the mesh size and the shell thickness, predicted the collision damage with the highest accuracy.

A literature study indicated that various modelling assumptions are being used, which have a significant influence on the consequences of collisions between ships and offshore support structures. Different values of the most often used strain-based failure criteria are of great importance. Therefore, this paper analyses the influence of the selected strain-based failure criteria on the ship damage caused by a collision with a monopile support structure of an offshore wind turbine (OWT). The details of the material models and the damage criteria are described in Section 3.

GOAL AND SCOPE

The goal of this paper is to investigate the influence of the selected strain-based material failure criteria on the ship damage resulting from a collision with an offshore wind turbine monopile.

The scope of the work considers two selected failure criteria. The first criterion is the constant-value strain failure (referred to in the NORSOK standard [37] and recommended by DNV GL [38]) which is taken as the minimum required strain for the material. The second failure criterion analysed is the one proposed by [24], together with the uniform strain coefficient ε_g and the necking strain coefficient ε_e proposed by [39]. Both criteria were used in numerous research projects. For both criteria, two materials were investigated: normal steel grade S235 and high-strength steel grade S355. Both materials are commonly used in the shipbuilding industry. Moreover,

the article investigates the influence of the numerical representation of a stress-strain curve of ship damage.

Two cases were analysed. The first definition of the material curve was applied according to the DNV GL 2013 design rules [40], using the simplification by characteristic points. This approach has been used for over 30 years. The second definition of the material curve was applied according to the DNV GL 2019 design rules [31]. The new version uses a more detailed representation of the non-linear range of the stress-strain curve defined by Eq. (1). The presented study also aims to assess the potential influence of the material curve representation on the collision results. So far, there have been no guidelines on this. The research was performed by FEM non-linear collision simulations using LS-dyna v. 9.71 software. The critical case of the head-on collision was investigated for three initial ship velocities: $v = 2$ m/s, $v = 3$ m/s and $v = 4$ m/s. The vessel was represented by a deformable structure that impacted a rigid monopile-type support structure of an offshore wind turbine. The detailed numerical model and the simulation approach are described in the following section.

THE NUMERICAL MODEL USED FOR COLLISION SIMULATIONS

The computer simulations of collisions were made in accordance with the methodology defined by the NORSOK standard [37]. The ship's structure was modelled as deformable, while the tower was assumed to be rigid. Following the NORSOK standard, the collision simulation was performed as a 'strength design' with the ship intentionally forced to deform and dissipate the collision energy (Fig. 3).

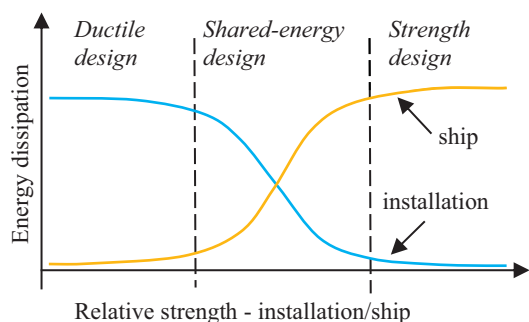


Fig. 3. Energy dissipation for strength, ductile and shared-energy design [37]

GEOMETRY, LOADS AND BOUNDARY CONDITIONS

The model of the ship and wind tower used in this study represented selected up-to-date industry-leading solutions. The geometry of the ship bow had a conical shaped hull with a bulbous bow, similar to that developed by the Havyard Company and often used in the Offshore Support Vessel (OSV). The ship length was LOA= 83.5 m, the beam was 17.5 m and the displacement was 6500 tons. The typical novel ship

structure was modelled to provide adequate representation. The thickness of the hull plating varied along the height of the vessel. It was 13 mm in the bottom section, 10 mm in the transition part and 8 mm in the upper section of the vessel. The FE model of the ship was built with the use of 2 types of elements: shells (plating, bulkheads, decks, framing) and beams (stiffeners flanges). The monopile tower represented a typical support structure of a 3 MW offshore wind turbine. It was a tube with a diameter of 4.3 m. The tower height was 115 m. The FE model of the tower was built with the use of shell elements.

The monopile was modelled as a non-deformable (rigid) part. The FE model of the ship and the monopile of the OWT is shown in Fig. 4 and Fig. 5. It also shows the mutual positions of the vessel and the column at the moment of impact. The impact point was at the D-Deck (see Fig. 4 and Fig. 5) and it was similar for all the analysed cases. The head-on collision scenario was analysed with the initial ship velocity in the x-axis direction. The ship having the displacement of 6500 tons struck the tower freely. The weight of the ship's structural components, not represented in the model directly, together with the added mass representing the surrounding water was assigned to the mass element at the point of the ship's centre of gravity (COG). This element was connected to the bow structure by massless rigid beam elements. The added mass was equal to 325 tons, referring to a 0.05 mass coefficient [41]. The value of friction coefficient of 0.2 was used, as in reference [42]. The OWT structure was clamped at the base.

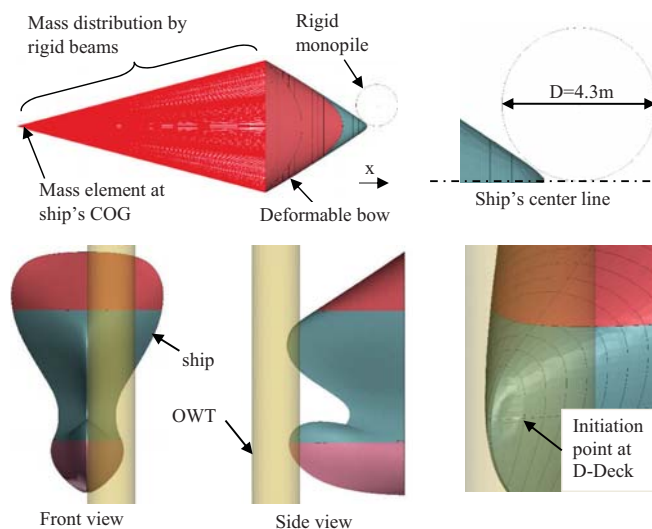


Fig. 4. The relative initial positions of the ship and the OWT monopile in the head-on collision simulation.

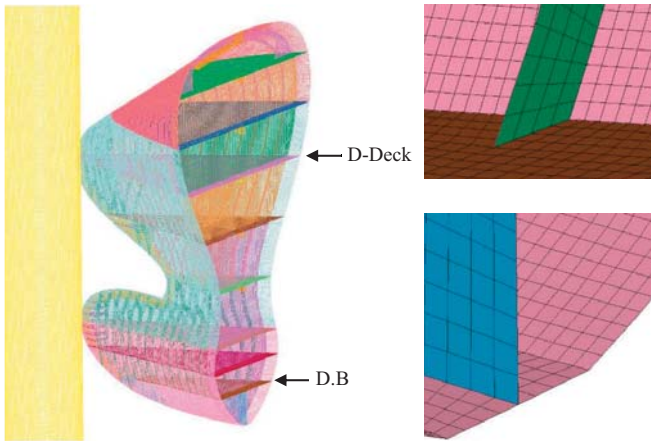


Fig. 5. The FE model of the ship's bow and the monopile (left); sample mesh details (right)

THE MATERIAL MODEL

Two grades of steel were considered for the collision simulations: normal-strength steel S235 and high-strength steel S355. The two materials were used to analyse the influence of the selected failure criterion on the collision damage, which will be described in the next paragraph. However, it is worth noting the definitions of the stress-strain curves given by DNV GL 2013 [40] and DNV GL 2019 [31]. The latter of the recommended practices defined the non-linear stress-strain relation using Eq. (1). In contrast, the previous definition was simplified by characteristic points and straight lines. It has been used in scientific research and industrial applications for a long time. In this paper, both of these definitions were investigated to identify the influence of the material stress-strain curve simplification on the results. The material data for both steel grades is summarised in Table 1 and plotted in Fig. 6. A steel density of 7850 kg/m³, a Young's modulus of 210 GPa and a Poisson's ratio of 0.3 were assumed. The deformable ship structure was modelled by material model *024-PIECEWISE_LINEAR_PLASTIC. The OWT monopile structure was modelled by the *020-RIGID material model.

$$\sigma = K \left(\varepsilon_p + \left(\frac{\sigma_{yeld2}}{K} \right)^{\frac{1}{n}} - \varepsilon_{p,y2} \right)^n \text{ for } \varepsilon_p > \varepsilon_{p,y2} \quad (1)$$

where:

σ – stress

K, n – Ramberg-Osgood parameters

$\varepsilon_p, \sigma_{yeld2}, \varepsilon_{p,y2}, \varepsilon_p$ – stress-strain curve parameters

Tab. 1 Material properties applied in collision simulations

Material	Minimum Yield point σ_y [MPa]	Minimum Ultimate Strength σ_{ult} [MPa]	K [MPa]	n [-]	Nonlinear range of stress-strain curve	Reference
S235	235	360			Simplified by characteristic points	DNVGL 2013 [40]
S355	355	470			Simplified by characteristic points	DNVGL 2013 [40]
S235	235		520	0.166	Equation 1	
S355	355		740	0.166	Equation 1	DNVGL 2019 [31]

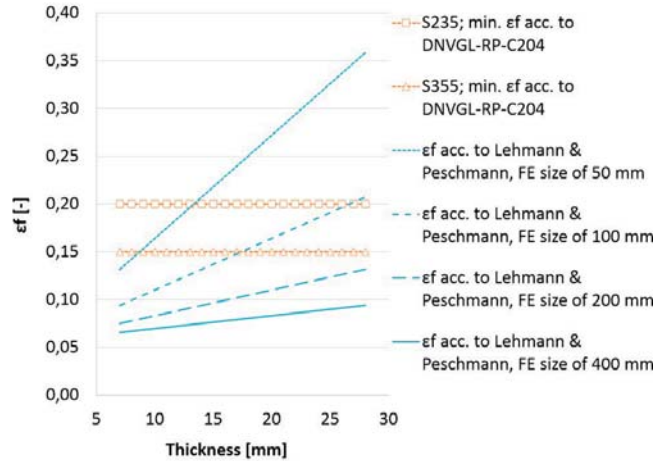


Fig. 6. Stress-strain curves representations – simplified acc. to DNVGL 2013 [40] and acc. to equation 1 and DNVGL 2019 [31].

The selected two strain-based failure criteria were considered in the analyses. The first criterion was according to the minimum required rupture strain value defined by the DNV GL design rules [38] and by the NORSOK standards [37]. The DNV GL rules require the minimum value of strain failure to be: 20% for the S235 and 15% for the S355 high tensile steel grades. These values were applied as modelling assumptions in many research publications [43-45].

The second criterion used in the research was introduced by [24] and is expressed as Eq. (2). This criterion includes the shell thickness, FE size, uniform strain coefficient $\varepsilon_g = 0.056$ and necking strain coefficient $\varepsilon_e = 0.54$, specified by Germanischer Lloyd [39].

$$\varepsilon_f(l_e) = \varepsilon_g + \varepsilon_e \left(\frac{t}{l_e} \right) \quad (2)$$

where:

ε_f – failure strain,

ε_g – uniform strain,

ε_e – necking strain,

t – plate thickness,

l_e – length of a single element.

Fig. 7 shows the dependence of failure strain ε_f on the FE mesh size and on the shell element thickness. For the adopted element size of 100 mm and for the plate thickness ranging from 7 to 15 mm, the calculated failure strain is in a range between $\varepsilon_f = 0.0938$ and $\varepsilon_f = 0.1370$. The failure strain, ε_f , according to the analysed criteria, is shown in Fig. 8.

THE FE MESH CONVERGENCE

The analysis of the finite element mesh convergence was performed for FE sizes 50, 100, 200 and 400 mm. The criterion used was the internal energy, which was analysed for different FE element sizes. It was found that the use of the 100 mm elements was the right choice as this size represented a compromise between the accuracy of the results obtained and the computational cost. A similar discretisation was used in [22] and [48]. The difference in the value of the maximum internal energy was 2% for the 50 mm and 100 mm element sizes. The difference between 100 mm and 200 mm was 8% and, for 100 mm and 400 mm, it was 21%.

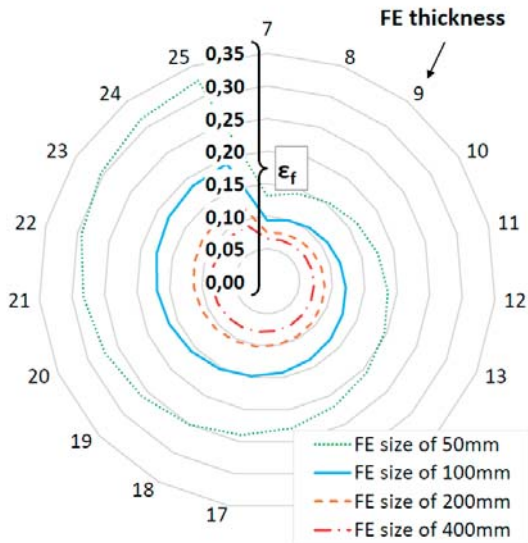


Fig. 7. Dependency of failure strain ϵ_f on the FE size and on the thickness, according to Lehmann and Peschmann [24].

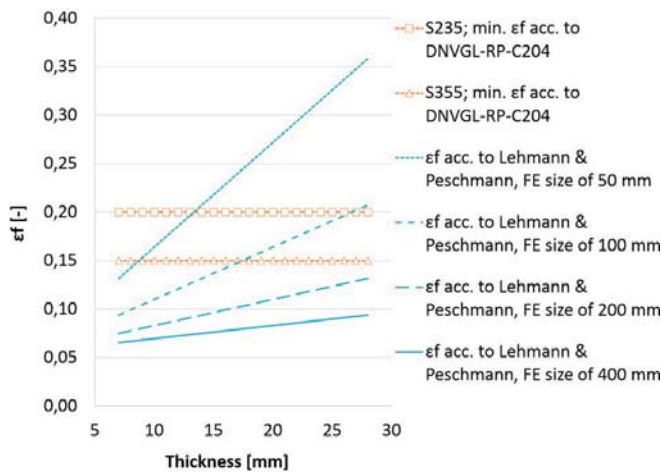


Fig. 8. Failure strain ϵ_f according to the DNVGL-RP-C204 [38] and Lehmann and Peschmann [24].

The strain rate dependency for steel was defined using the Cowper-Symonds model [46] according to Eq. (3). The material coefficients are $C=500 \text{ s}^{-1}$ ($p=4$) for steel S235 and $C=3200 \text{ s}^{-1}$ ($p=5$) for steel S355 [45-47].

$$\beta = 1 + \left(\frac{\dot{\epsilon}}{C}\right)^{\frac{1}{p}} \quad (3)$$

where:

$\dot{\epsilon}$ – strain rate,

C, p – material constraints.

RESULTS AND DISCUSSION

The results presented below refer to the computer simulations for three initial velocities of the ship: 2, 3 and 4 m/s. These speed increments increased the kinetic energy of the ship's collision with the support column of the offshore wind turbine and the energy was converted into internal energy, corresponding to the work applied to deform the ship's structure. The greater the initial collision energy, the greater the expected damage to the ship's structure. The simulations were also performed for two materials: normal-strength steel S235 and high-strength steel S355. The effect of the damage criteria was analysed for both material curves. The strongly non-linear nature of the simulations affects the calculated resultant damage to the ship. The influence of the two selected material failure criteria and the influence of the two representations of the material model curve were investigated. Typical physical quantities, such as the crushing force and the internal energy, were used for comparison purposes. The hull damage resulting from the collision was analysed using the length of the ship's hull rupture, L_r , and the area of the hull opening, A_o . The aforementioned simulation cases were solved and they delivered the following results, which will be discussed as groups, devoted to separate aspects.

THE INFLUENCE OF THE MATERIAL STRESS-STRAIN CURVE REPRESENTATION

The first group of results show the influence of the stress-strain curve representation on the collision results. The first curve used was a simplified representation, in accordance with the DNV GL 2013 design rules [40]. This approach was used for many years but has been changed, quite recently. The second representation of the material relation presents the most recent definition of the curve, according to the DNV GL 2019 design rules [31]. The curve was discretised with a strain step of 0.01. Such a definition aimed to ensure more accurate representation of the curve, especially in its non-linear range corresponding to plastic deformations. A strong influence of the material model representation by the stress-strain curve, according to DNV GL 2013 [40] and DNV GL 2019 [31], on the ship's damage was found (see Fig. 9). The

analysis was performed for the material failure criterion according to Lehmann and Peschmann [24]. The simplified curve representation, according to DNV GL 2013 [40], gave an overestimation of ship's damage, as measured by the area of the hull opening, A_o . Moreover, the results showed that this influence varied depending on the analysed initial ship velocities and steel grades. This can be explained by very high non-linearity of collision simulations. The highest divergence between the crushing forces and the resultant hull damage was found for the velocity of 4 m/s for both steel grades (S235 and S355). It is also noticeable that, even for comparable crushing forces, the resultant hull damage differed significantly (see the crushing force and the hull damage for steel S355 and for $v = 4$ m/s in Fig. 9).

and the Lehmann and Peschmann [24]. The influence of the failure criterion on the hull damage and internal energy, until the decoupling of the ship and the OWT, are shown in Fig. 10. In this analysis, the material stress-strain curve was modelled according to DNV GL 2019 [31]. The literature review presented in section 1 revealed significant differences in the values of failure strain used by various authors. The common value of the rupture strain, $\epsilon_f = 0.2$ for S235 and $\epsilon_f = 0.15$ for S355, was validated against the experimental results [38]. Other studies used different values, including the criterion in [24], which was recently implemented in [31]. The relationship includes the influence of the FE size and the shell thickness, to calculate the corrected value of the rupture strain. The comparison performed on these two

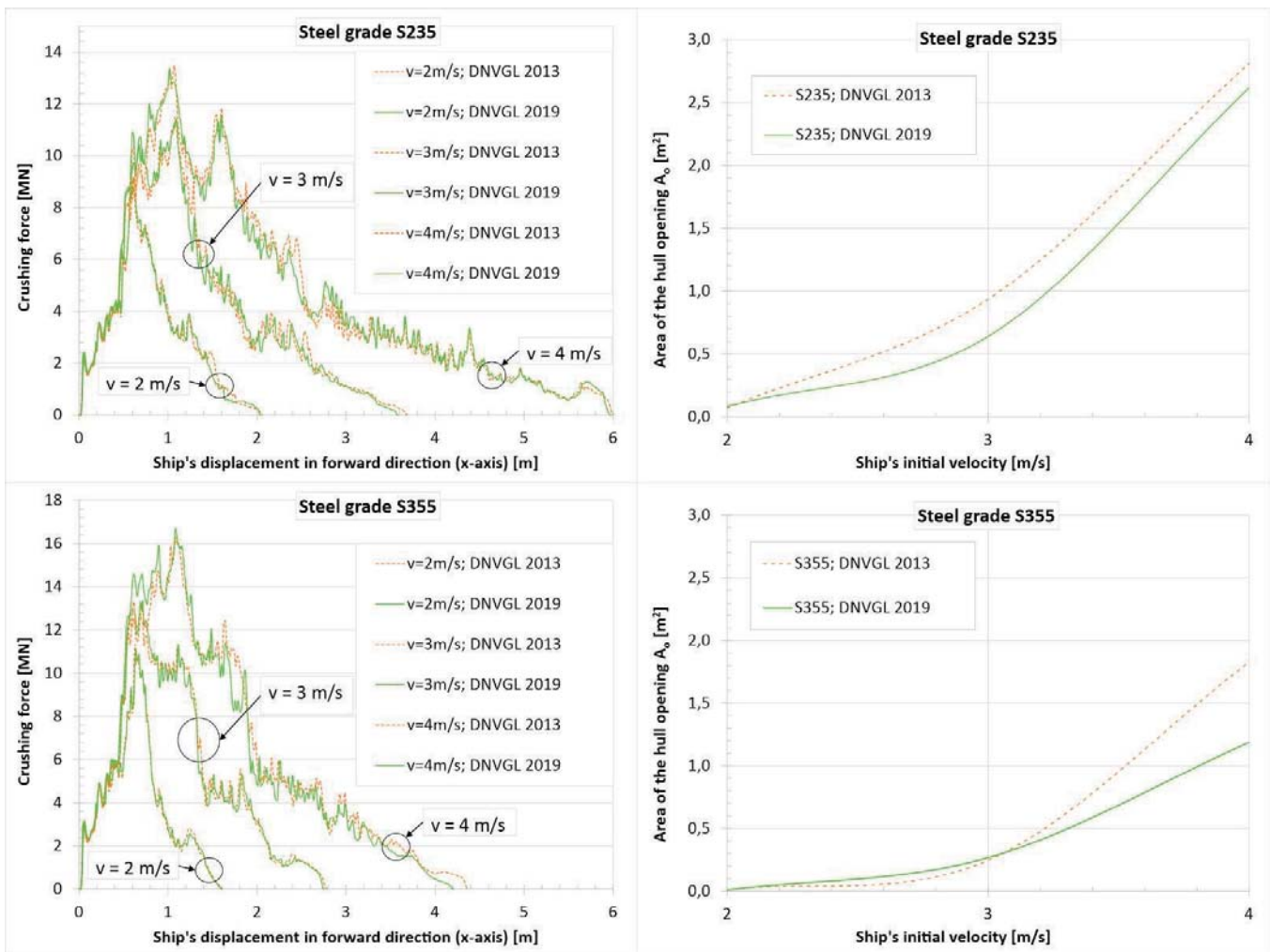


Fig. 9. The influence of the material stress-strain curve representation on the crushing force (left) and on the ship's hull damage (right).

THE INFLUENCE OF THE SELECTED STRAIN-BASED FAILURE CRITERIA

The following section presents the results of the collision simulations for the two material failure criteria, ϵ_f , as described in section 3.2, namely DNVGL-RP-C204 [38]

failure criteria showed a strong influence on the results. In the example of steel grade S235 and for the ship's initial velocity of 4 m/s, the calculated relative maximum crushing force differed by as much as 20%. As a result, the internal energies for both failure criteria were very different. Consequently, for different assumptions of the damage criterion, the resulting hull damage varied considerably. In the example with S235 steel grade and an initial ship's velocity of 4 m/s, the calculated hull shell rupture, L_r was equal to 1.38 m and 9.32 m for the

minimum required ε_f according to the DNVGL-RP-C204 [38] and Lehmann and Peschmann [24] failure criterion, respectively. The areas of hull opening, A_o , were 0.26 m² and 2.62 m², respectively. Thus, for S235 steel, the case using the $\varepsilon_f = 0.2$ criterion leads to a major underestimation of the hull damage. The influence was similar, but smaller, for S355 steel. For the initial ship's velocity of 4 m/s, the calculated hull shell rupture, L_r , was equal to 1.90 m and 4.56 m for the failure criteria [38] and [24], respectively. The area of the hull opening, A_o , was 0.43 m² and 1.19 m², respectively. As described above, the use of criterion DNV GL-RP-C204 [38] resulted in a significant underestimation of the ship's hull damage. Fig. 10 shows the internal energy plots for the analysed damage criteria and for the initial ship's velocities. The effect of the failure criteria analysed is more pronounced for the normal-strength steel S235 and, as expected, amplified with increasing impact energy. For all the analysed cases, the maximum internal energy was found in the Lehmann and Peschmann failure criterion [24]. However, for the

initial velocities of the ship at 3 m/s and 4 m/s, in the initial phase of impact for criterion DNV GL-RP-C204 [38], the value of internal energy was higher, which corresponded to larger plastic deformation of the ship's structure. It is worth noting that the slopes of the curves were slightly different and intersected each other, leading to significantly different damage resulting from the conversion of the ship's kinetic energy into plastic deformation.

For all analysed cases, the accelerations of a ship's centre of gravity (COG) for the S355 steel were higher compared to S235. For the Lehmann and Peschmann failure criterion [24] the average difference was 25%. For the criterion DNV GL-RP-C204 [38], it was 12%, on average. The resultant hull damage for the analysed simulation cases and initial ship speed of 4 m/s, are shown in Fig. 11. The hull damage presented perfectly illustrates the relations resulting from the influence of the analysed failure criteria and the method of the material curve representation.

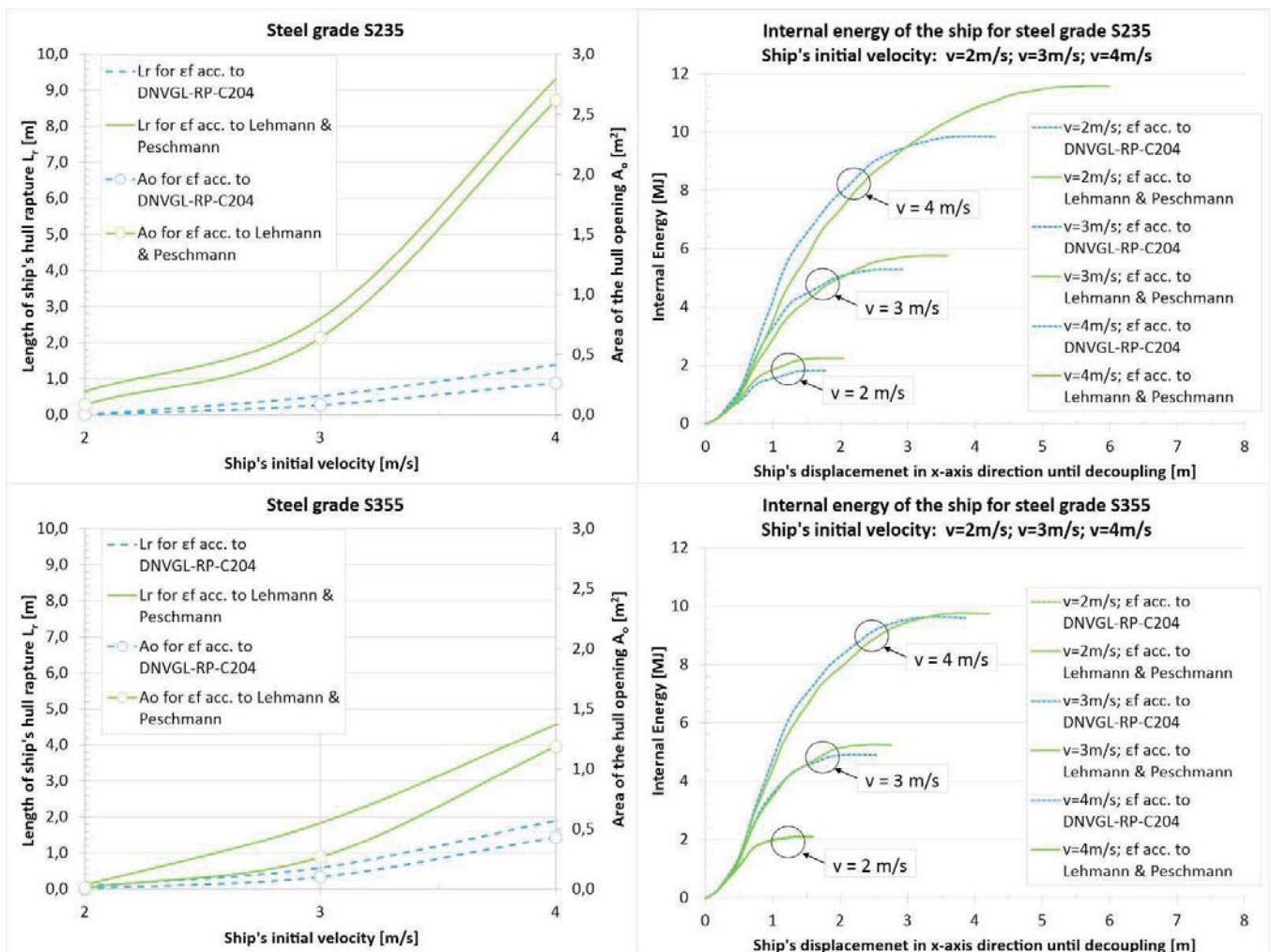


Fig. 10. The influence of the material failure criterion, ε_f , on the hull damage (left) and on the internal energy (right).

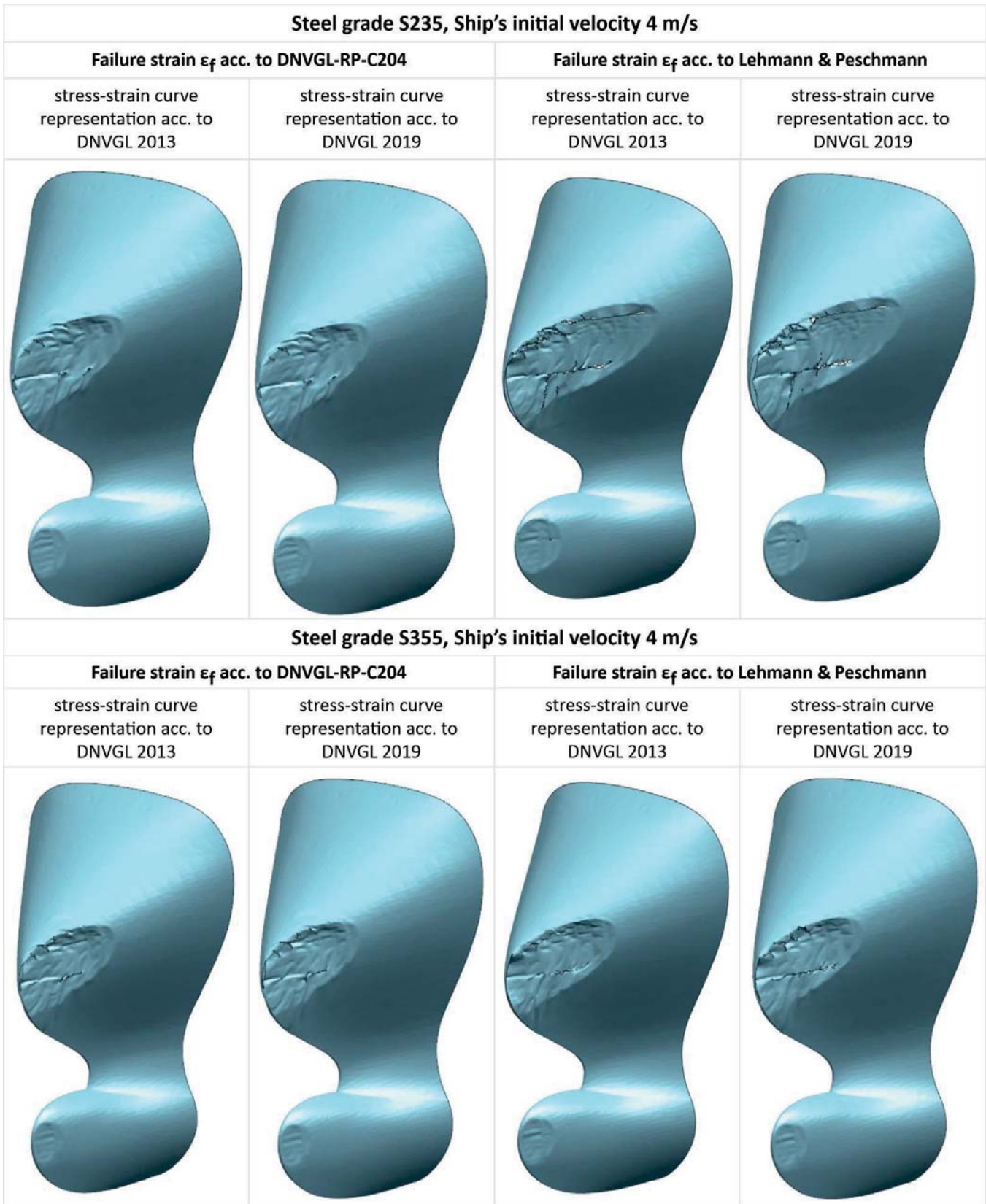


Fig. 11. The resultant hull damage for the analysed cases and the ship's initial velocity of 4 m/s.

CONCLUSIONS

The analysis of collision resistance of ships and offshore structures requires performing highly non-linear FE simulations. One of the main computational assumptions is the material model, including the failure criteria. So far, there are no straightforward design recommendations defining the proper approach to this. The literature review showed various modelling assumptions used by the authors. Thus, this article investigated the influence of the selected strain-based failure criteria and material modelling representations on the simulation results of ship collisions with OWT monopiles. The following conclusions were formulated:

- 1) The influence of the modelling of the material curve has a significant influence on the results. In highly non-linear simulations, like those of collisions, the simplification of the material stress-strain relation by straight lines plotted by characteristic points is too rough and can lead to inaccurate or erroneous results. The non-linear range of the material stress-strain relation needs to be represented by an adequate number of points. There is no specific guideline on how dense the representation should be. It was verified that, using the material modelling recommendation according to DNV GL 2013 [40] (which represents the material characteristics by 6 points (5 straight curves)), had a significant influence on the results. For steel S235, the values of the crushing force were up to 12% different from the results obtained from the simulations based on the accurately mapped material curve according to DNV GL 2019 [31]. Although the maximum value of the crushing force was determined correctly by the simplified material curve, the energy dissipation was changed. As a consequence, the resulting hull damage was significantly different for the analysed material modelling representations (DNV GL 2013 [40] and DNV GL 2019 [31]). In an example with an initial ship velocity of 4 m/s and steel S235, the hull plating opening, A_o , was 7% higher for the simplified curve representation [40]. For steel grade S355, the corresponding relative difference was as much as 54%. Using the simplified material curve leads to an overestimation of the resultant hull damage (on the 'safe side' from an engineering point of view). However, it does not necessarily have to be beneficial, from a design point of view, and can lead to oversized structural components, which has a negative influence on both the cost and weight.
- 2) The impact of the material's failure criterion is crucial. The performed comparison of the collision results obtained with the use of the two selected failure criteria showed the importance of this computational assumption. In the example with steel grade S235 and with an initial ship velocity of 4 m/s, the calculated relative maximum crushing force differed by as much as 20%. As a result, the internal energies were very different for each of the failure criteria. The resultant hull damage varied considerably for the failure criteria according to DNV GL-RP-C204 [38]. The first one lead to significantly lower hull damage. In the example with steel S235 and with the initial ship's velocity

of 4 m/s, the calculated hull damage was underestimated by up to 6 times for the length of the hull rupture and 9 times for the area of the hull opening. The observation was similar for steel grade S355, however, the impact on the results was relatively smaller. For steel grade S355 and the failure criterion, ε_p as the minimum required value, according to DNV GL-RP-C204 [38], there was an underestimation of the length of the hull rupture by 1.4 times and of the hull opening by 1.8 times. Thus, it can be concluded that performing collision simulations with an assumption of failure criteria equal to the minimum values defined by DNV GL-RP-C204 [38] can significantly underestimate the hull damage. The applied failure criterion should account for the effect of the FE element size and the material thickness, as in Lehmann and Peschmann [24]. The analysis of a collision may also consider using different failure criteria and comparing the results to those with a reasonable approach, resulting from risk assessment.

- 3) Although it was not the purpose of this paper, a significant influence of steel grade on the ship's hull failure was found. The relative reduction of the length of the S355 hull plating rupture was -31% and -51% for the ship's initial velocities of 3 m/s and 4m/s, respectively. Moreover, the relative reduction of the hull opening area was -58% and -55%. The influence of the steel grade selection on the hull damage is highly visible and will be investigated by the authors in detail in future research.

ACKNOWLEDGEMENTS

The research was supported by the Academic Computer Centre in Gdansk (CI TASK). All support is highly appreciated by the authors.

REFERENCES

1. L. Ramirez, D. Fraile, and G. Brindley, "Offshore wind in Europe: Key trends and statistics 2019," 2019.
2. L. Ramirez, D. Fraile, and G. Brindley, "Offshore wind in Europe: Key trends and statistics 2020," 2021.
3. EMSA, "Marine Casualties and Incidents PRELIMINARY ANNUAL OVERVIEW OF MARINE CASUALTIES AND INCIDENTS 2014-2020," no. April, 2021.
4. L. Junlai, X. Yonghe, W. Weiguo, and Z. Chi, "Analysis of the Dynamic Response of Offshore Floating Wind Power Platforms in Waves," *Polish Marit. Res.*, vol. 27, no. 4, pp. 17–25, 2020. doi: 10.2478/pomr-2020-0062
5. A. Karczewski and Ł. Piątek, "The influence of the cuboid float's parameters on the stability of a floating building," *Polish Marit. Res.*, vol. 27, no. 107, pp. 16–21, 2020. doi: 10.2478/pomr-2020-0042

6. K. Niklas and A. Karczewski, "Determination of seakeeping performance for a case study vessel by the strip theory method," *Polish Marit. Res.*, vol. 27, no. 108, pp. 4–16, 2020. doi: 10.2478/pomr-2020-0061
7. F. Wang and N. Chen, "Dynamic response analysis of drill pipe considering horizontal movement of platform during installation of subsea production tree," *Polish Marit. Res.*, vol. 27, no. 3, pp. 22–30, 2020. doi: 10.2478/pomr-2020-0043
8. J.T. Wu, J.H. Chen, C.Y. Hsin, and F.C. Chiu, "Dynamics of the FKT System with Different Mooring Lines," *Polish Marit. Res.*, vol. 26, no. 1, pp. 20–29, 2019. doi: 10.2478/pomr-2019-0003
9. E. Mieloszyk, M. Abramski, and A. Milewska, "CFGFRPT Piles with a Circular Cross-Section and their Application in Offshore Structures," *Polish Marit. Res.*, vol. 26, no. 3, pp. 128–137, 2019. doi: 10.2478/pomr-2019-0053
10. W. Litwin, W. Leśniewski, D. Piątek, and K. Niklas, "Experimental Research on the Energy Efficiency of a Parallel Hybrid Drive for an Inland Ship," *Energies*, vol. 12, no. 9, p. 1675, 2019.
11. V.S. Blintsov, K.S. Trunin, and W. Tarełko, "Determination of Additional Tension in Towed Streamer Cable Triggered by Collision with Underwater Moving Object," *Polish Marit. Res.*, vol. 27, no. 2, pp. 58–68, 2020. doi: 10.2478/pomr-2020-0027
12. K. Niklas and H. Pruszek, "Full scale CFD seakeeping simulations for case study ship redesigned from V-shaped bulbous bow to X-bow hull form," *Appl. Ocean Res.*, vol. 89, pp. 188–201, Aug. 2019.
13. F. Biehl, "Collision Safety Analysis of Offshore Wind Turbines," 4th LSDYNA Eur. Conf., pp. 27–34, 2005.
14. K. Niklas, "Strength analysis of a large-size supporting structure for an offshore wind turbine," *Polish Marit. Res.*, vol. 24, pp. 156–165, 2017. doi: 10.1515/pomr-2017-0034
15. P. Dymarski, "Design of Jack-Up Platform for 6 MW Wind Turbine: Parametric Analysis Based Dimensioning of Platform Legs," *Polish Marit. Res.*, vol. 26, no. 2, pp. 183–197, 2019. doi: 10.2478/pomr-2019-0038
16. B. Rozmarynowski, "Spectral Dynamic Analysis of A Stationary Jack-Up Platform," *Polish Marit. Res.*, vol. 26, no. 1, 2019. doi: 10.2478/pomr-2019-0005
17. WindEurope, "Offshore wind in Europe - Key trends and statistics 2020," *WindEurope*, vol. 3, no. 2, pp. 14–17, 2021.
18. N. Ren and J. Ou, "Dynamic numerical simulation for ship-OWT collision," *Proc. 2009 8th Int. Conf. Reliab. Maintainab. Safety, ICRMS 2009*, no. July, pp. 1003–1007, 2009.
19. E. Homayoun, H. Ghassemi, and H. Ghafari, "Power Performance of the Combined Monopile Wind Turbine and Floating Buoy with Heave-Type Wave Energy Converter," *Polish Marit. Res.*, vol. 26, no. 3, pp. 107–114, 2019. doi: 10.2478/pomr-2019-0051
20. J.R.A. Tomporowski, A. Al-Zubiedy, J. Flizikowski, W. Kruszelnicka, P. Bałdowska-Witos, "Analysis of the Project of innovative floating turbine," *Polish Marit. Res.*, vol. 26, no. 4, pp. 121–183, 2020. doi: 10.2478/pomr-2019-0074
21. A. Bela, L. Buldgen, P. Rigo, and H. Le Sourne, "Numerical crashworthiness analysis of an offshore wind turbine monopile impacted by a ship," *Anal. Des. Mar. Struct. - Proc. 5th Int. Conf. Mar. Struct. MARSTRUCT 2015*, no. 2013, pp. 661–669, 2015.
22. A. Bela, H. Le Sourne, L. Buldgen, and P. Rigo, "Ship collision analysis on offshore wind turbine monopile foundations," *Mar. Struct.*, vol. 51, pp. 220–241, 2017.
23. H. Jia, S. Qin, R. Wang, Y. Xue, D. Fu, and A. Wang, "Ship collision impact on the structural load of an offshore wind turbine," *Glob. Energy Interconnect.*, vol. 3, no. 1, pp. 43–50, 2020.
24. E. Lehmann and J. Peschmann, "Energy absorption by the steel structure of ships in the event of collisions," *Mar. Struct.*, vol. 15, no. 4–5, pp. 429–441, 2002.
25. K. Niklas and J. Kozak, "Experimental investigation of Steel-Concrete-Polymer composite barrier for the ship internal tank construction," *Ocean Eng.*, vol. 111, pp. 449–460, 2016.
26. Ringsberg, J., Amdahl, J., Chen, B., Cho, S.-R., Ehlers, S., Hu, Z., Kubiczek, J., Körgesaar, M., Liu, B., Marinatos, J., Niklas, K., Parunov, J., Quinton, B., Rudan, S., Samuelides, M., Soares, C., Tabri, K., Villavicencio, R., Yamada, Y., Yu, Z., & Zhang, S., "MARSTRUCT benchmark study on nonlinear FE simulation of an experiment of an indenter impact with a ship side-shell structure," *Mar. Struct.*, vol. 59, pp. 142–157, 2018.
27. A. AbuBakar and R.S. Dow, "The impact analysis characteristics of a ship's bow during collisions," *Eng. Fail. Anal.*, vol. 100, no. August 2018, pp. 492–511, 2019.
28. K. Niklas, "Numerical calculations of behaviour of ship double-bottom structure during grounding," *Polish Marit. Res.*, vol. 15, no. SUPPL. 1, 2008.

29. M.A.G. Calle and M. Alves, "A review-analysis on material failure modelling in ship collision," *Ocean Eng.*, vol. 106, pp. 20–38, 2015.
30. O. Kitamura, "FEM approach to the simulation of collision and grounding damage," *Mar. Struct.*, vol. 15, no. 4–5, pp. 403–428, 2002.
31. DNVGL, "DNV-RP-C208: Determination of Structural Capacity by Non-linear FE analysis Methods," 2019.
32. J.L. Martinez, J.C.R. Cyrino, and M.A. Vaz, "FPSO collision local damage and ultimate longitudinal bending strength analyses," *Lat. Am. J. Solids Struct.*, vol. 17, no. 2, pp. 1–19, 2020.
33. G. Wang, K. Arita, and D. Liu, "Behavior of a double hull in a variety of stranding or collision scenarios," *Mar. Struct.*, vol. 13, no. 3, pp. 147–187, 2000.
34. S. Yagi, H. Kumamoto, O. Muragishi, Y. Takaoka, and T. Shimoda, "A study on collision buffer characteristic of sharp entrance angle bow structure," *Mar. Struct.*, vol. 22, no. 1, pp. 12–23, 2009.
35. S. Ehlers, "The influence of the material relation on the accuracy of collision simulations," *Mar. Struct.*, vol. 23, no. 4, pp. 462–474, 2010.
36. S. Ehlers, J. Broekhuijsen, H.S. Alsos, F. Biehl, and K. Tabri, "Simulating the collision response of ship side structures: A failure criteria benchmark study," *Int. Shipbuild. Prog.*, vol. 55, no. 1–2, pp. 127–144, 2008.
37. Standards Norway, "NORSOK Standard - Design of steel structure N-004, Rev.3," 2013.
38. DNVGL, "DNVGL-RP-C204 - Design against Accidental Loads," 2017.
39. M. Scharrer, L. Zhang, and E.D. Egge, "Final report MTK0614, Collision calculations in naval design systems, Report Nr. ESS 2002.183," Hamburg, 2002.
40. DNVGL, "DNV-RP-C208: Determination of Structural Capacity by Non-linear FE analysis Methods," 2013.
41. S. Zhang, "The mechanics of ship collisions," Technical University of Denmark, 1999.
42. Verband Deutscher Ingenieure, "Systematic calculation of high duty bolted joints joints with one cylindrical bolt," Berlin, 2003.
43. O. Ozgur, "Numerical Assessment of FPSO Platform Behaviour in Ship Collision," *Trans. Marit. Sci.*, vol. 9, no. 2, 2020.
44. T. S. Bøe, "Analysis and Design of Stiffened Columns in Offshore Floating Platforms Subjected to Supply Vessel Impacts," Norwegian University of Science and Technology, 2018.
45. M.P. Mujeeb-Ahmed, S.T. Ince, and J.K. Paik, "Computational models for the structural crashworthiness analysis of a fixed-type offshore platform in collisions with an offshore supply vessel," *Thin-Walled Struct.*, vol. 154, no. June, p. 106868, 2020.
46. Livermore Software Technology, "LS-DYNA - KEYWORD USER'S MANUAL, VOLUME II Material Models," 2020.
47. Y.G. Ko, S.J. Kim, J.M. Sohn, and J.K. Paik, "A practical method to determine the dynamic fracture strain for the nonlinear finite element analysis of structural crashworthiness in ship–ship collisions," *Ships Offshore Struct.*, vol. 13, no. 4, 2018.
48. J. Travanca and H. Hao, "Energy dissipation in high-energy ship-offshore jacket platform collisions," *Mar. Struct.*, vol. 40, pp. 1–37, 2015.

CONTACT WITH THE AUTHORS

Karol Niklas

e-mail: karol.niklas@pg.edu.pl

Gdansk University of Technology,
Faculty of Mechanical Engineering and Ship Technology,
Narutowicza 11/12, 80-233 Gdansk,

POLAND

Alicja Bera

e-mail: alicja.bera@pg.edu.pl

Gdansk University of Technology,
Faculty of Mechanical Engineering and Ship Technology,
Narutowicza 11/12, 80-233 Gdansk,

POLAND

SPECTRAL RESPONSE OF STATIONARY JACK-UP PLATFORMS LOADED BY SEA WAVES AND WIND USING PERTURBATION METHOD

Bogdan Rozmarynowski¹

Wojciech Jesien²

¹ Gdańsk University of Technology, Poland

² Pratt & Whitney, Canada

* Corresponding author: bogrozma@pg.edu.pl (B. Rozmarynowski)

ABSTRACT

The paper addresses non-linear vibrations of offshore jack-up drilling platforms loaded by sea waves and wind in their stationary condition using the perturbation method. Non-linearity of dynamic equations of motion for fixed offshore platforms yields from two factors. The first is load excitation generating non-linear velocity coupling in a dynamic system. This coupling is inherent in the modified Morison equation, involving the excitation function in the form of the sum of the inertial and velocity forces of sea waves, taking into account relative wave-structure kinematics. Moreover, the wind acting on the exciting side causes similar effects. The second source is the subsoil-structure interaction problem, modelled by a system of springs and dashpots that yields stochastic non-linearity of the dynamic system. The matrix equations of structural motion in FEM terms are set up. The perturbation method is adopted to determine the mechanical response of the system, making it possible to determine response spectra of the first and the second approximations for displacements and internal forces of the platform. The paper is the continuation of research detailed in the paper [1]. It is assumed, that the fluctuation parts of the dynamic loading forces are in line with the direction of sea wave propagation. Sea current and lift forces effects are neglected in this study. A numerical example refers to structural data of the Baltic drilling platform in the stationary configuration, i.e. when three legs support the deck above the seawater level.

Keywords: Structural dynamics, Offshore structures, Loads, Fluid flexible structure interactions, Random variables, Stochastic processes, Spectral analysis, Perturbation method

INTRODUCTION

Complex conditions of the marine environment and the necessity of installing structures in increasingly deeper regions of the seas and oceans led to the spectacular development of various structural systems of offshore platforms. This development was linked with technological advances in ocean engineering, generated by the development of the oil industry, which triggered intensive development for new drilling sites, especially after the world oil crisis in 1970.

Depending on the application, different types of platforms can be built: for exploration, mining, or auxiliary platforms [2]. Taking into account the main factors that determine the

type of the installed platform, e.g. sea depth, subsoil type, seismic conditions, operation in the Arctic, the following types may be constructed: heavy reinforced concrete platforms, steel jackets, steel jack-up rigs, semi-submersible and spar structures or platforms moored through tethers (i.e. TLP - Tension Leg Platforms). Regardless of the platform type, computational analysis of platforms, necessary in their design [3], involves complex problems regarding the interaction of three media: water, structure, and subsoil. In each offshore platform case, the most important task is to determine wave and wind loads. With regard to environmental conditions, the loads produced by ship collision, ice floe pressure, sea current, and seismic activities should be estimated too [4].

The platforms fixed in the seabed involve a particular task to determine the subsoil parameters and adopt an appropriate failure model for fatigue analysis of structural joints [5]. All the issues described above affect the structural response, which is obtained in an approximated form due to the simplifying assumptions of physical phenomena. And, numerical methods make it possible to obtain approximate solutions for such formulated mathematical problems [6], [7], [8], [9], [10].

The work emphasises the use of the perturbation method to find a solution of non-linear dynamic equations of motion. The origins of the perturbation method or the small parameter method, are included in the works of Poincaré in the nineteenth century (see [11]). The perturbation method was first applied to deterministic systems [12] and later in the analysis of non-linear stochastic systems (see [13], [14], [15]).

The perturbation method is an asymptotic method whose solutions are power series. Convergence of this kind of expansion is usually slow, and in some cases the solution is divergent (see [16]). There are cases when an approximate solution limited to selected terms of the series is sufficient (see [13]). The perturbation method applied to the vibrations of a simplified platform model is addressed by Taylor [17], where the non-linearity of the system refers to damping, fluctuation effects in the modified Morison wave excitation formula. This paper does not cover the stochastic non-linearity caused by subsoil-structure interaction.

This study is the continuation of research presented in the paper [1], and it covers a dynamic analysis of a jack-up, movable type drilling platform (Fig. 1). The novel elements address the wind impact on the platform response. The work presents also a detailed formalism of the perturbation approach to the solution of non-linear platform dynamic systems.

The stationary work condition of a jack-up platform requires it to be attached to the seabed. The soil subsystem interacts with the structure through the foundation, therefore a subsoil-structure interaction problem is essential here, introducing non-linearity to the dynamic system. The study refers to the perturbation approach to the analysis of stochastically non-linear systems.

A simplified subsoil-structure interaction model is assumed as a system of springs and dashpots, representing the elastic and damping properties of the subsoil.

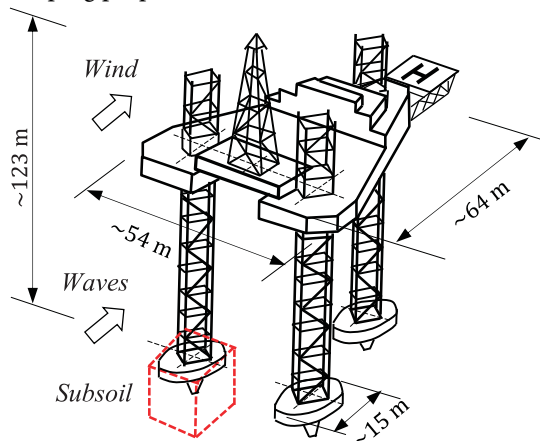


Fig. 1. General view of the platform

In the case of slender, elastic cylindrical members subjected to sea waves, the wave-structure interaction problem is inherently non-linear (see [18]). Waves produce kinematic variations of elastic members coupled with dynamic loads. The following relations hold: $H/D > 1$, $D/L < 0.2$, where H is the wave height, L is the wave length, and D is the cylinder diameter (potential theory is applied, with no diffractions effects).

The results of the proposed dynamic analysis contain the spectral densities of displacements and support reactions. Second-order response spectra are discussed. Detailed analysis of a damping part of the wave forces is provided. A numerical example of the jack-up platform shown in Fig. 1, formulated in real engineering categories, is presented. Numerical calculations were carried out with the help of the FEMAP software system version 10.1.1, the Excel environment, and the authors' computer programs written in Fortran.

DYNAMIC EQUATIONS OF MOTION

In the adopted analysis, it is possible to neglect or include the probabilistic parameters of the structure and its environment. Inertia, damping, and stiffness matrices may take a deterministic or probabilistic form. In such a system, the uncertainty of matrix terms generates excitation forces and subsoil layers. Dynamic equations of motion take a general form:

$$\begin{aligned} \mathbf{M}(\gamma)\ddot{\mathbf{q}}(\gamma, t) + \mathbf{C}(\gamma)\dot{\mathbf{q}}(\gamma, t) + \mathbf{K}(\gamma)\mathbf{q}(\gamma, t) = \\ = \mathbf{P}(t, \dot{\mathbf{q}}(\gamma, t), \ddot{\mathbf{q}}(\gamma, t)) \end{aligned} \quad (1)$$

where γ is an element from a set of elementary events Γ^1 . $\mathbf{M}(\gamma)$ represents the global inertia matrix, involving the structural mass and the mass of surrounding water (the latter called hydrodynamic, associated or added mass); $\mathbf{C}(\gamma)$ is the global damping matrix (deterministic or random) composed of three elastic continuous media: the structure, subsoil, and water; $\mathbf{K}(\gamma)$ is the global stiffness matrix involving subsoil and structural stiffness; $\mathbf{P}(t, \dot{\mathbf{q}}(\gamma, t), \ddot{\mathbf{q}}(\gamma, t))$ is the global vector of forces produced by sea waves and the wind acting on the platform. The latter time-variant vector with structural velocity vector $\dot{\mathbf{q}}(\gamma, t)$ and acceleration vector $\ddot{\mathbf{q}}(\gamma, t)$ affect the dynamic performance of the platform. Kinematic wave-structure coupling makes Eq. (1) non-linear. The orders of the listed matrices and vector are $n \times n$ and $n \times 1$, respectively, where n is the number of dynamic degrees of freedom.

While the equation coefficients and excitation function are uncertain, the dynamic system expressed by Eq. (1) is called stochastically non-linear (see [19], [20]).

It was found that a dynamic structure-subsoil-water system (Eq. (1)) involves a relation between the matrices $\mathbf{M}, \mathbf{C}, \mathbf{K}$ and the vibration frequency due to the hydrodynamic mass, damping and stiffness caused by the subsoil (see [21]). This relationship makes Eq. (1) more complex.

¹ This set contributes the component of probability space $(\Gamma, \mathcal{F}, \mathbb{P})$, where \mathcal{F} is a σ -algebra of subsets of Γ , \mathbb{P} is a probability measure defined on \mathcal{F} [16].

MASS MATRIX

The mass of the oscillating platform is concentrated at nodes of its discrete FEM model, thus the kinetic energy of the system involves translational degrees of freedom only. This simplification meets the expected accuracy of numerical computations, where the rotational inertia is negligible (e.g., the Timoshenko model in the structural dynamics of bars [22]).

The platform masses and the subsoil parameters are assumed independent of frequency. The mass of the added water is affected by the submerged element shape (see [5], [9], [10]). The work [21] indicates a relation between the added masses and the wave frequency. Due to small variations, it is routine in numerical computations of platform response that the added masses are constant throughout the wave excitation frequency range.

The total mass of the dynamic system follows the summation:

$$\mathbf{M} = \mathbf{M}_P + \mathbf{M}_S + \mathbf{M}_H, \quad (2)$$

where matrices \mathbf{M}_P , \mathbf{M}_S , \mathbf{M}_H are the global mass matrix of the structure, subsoil, and associated (hydrodynamic) water, respectively.

The terms of the matrix \mathbf{M}_S are based on [23]. Taking into account the additional subsoil mass matrix \mathbf{M}_s , the lumped soil is considered in the form of a cube (see Fig. 1), and its empirical coefficient depends on the oscillating mass (Table 1).

Table 1. Coefficients of co-oscillating subsoil masses

Degree of freedom of added mass	Added mass
Vertical	$1.50\rho_s R^3$
Horizontal	$0.28\rho_s R^3$
Rotational	$0.49\rho_s R^5$
Torsional	$0.70\rho_s R^5$

In Table 1 ρ_s is the soil density, R is the radius of the rigid disc resting on the subsoil (see Fig. 1).

The elements of the matrix \mathbf{M}_H are derived from the modified form of the Morison formula (see [1], [6], [21]). It should be emphasised that non-zero hydrodynamic masses occur only at nodes corresponding to structural elements immersed in water.

DAMPING MATRIX

The global damping matrix \mathbf{C} is the superposition of three matrices:

$$\mathbf{C} = \mathbf{C}_P + \mathbf{C}_S + \mathbf{C}_H \quad (3)$$

where the P , S , and H indices refer to structural damping, subsoil, and co-oscillating (hydrodynamic) water damping, respectively.

Structural damping, i.e., material damping produced by internal friction in the element material and damping in the joints between the structural elements, is approximated by the equivalent viscous damping according to the formula $\mathbf{C}_P = \alpha_M \mathbf{M}_P + \alpha_K \mathbf{K}_P$ (see [24]), and the coefficients α_M , α_K are defined by the so-called proportional damping (Rayleigh damping) of a “dry” structure. i.e., without a subsoil and surrounding water impact (see e.g. [23]).

Thus, the \mathbf{C}_P matrix is a linear combination of a kinetic energy measure (mass matrix) representing external damping and a potential energy measure (stiffness matrix) expressing the internal damping of a dynamic system.

Subsoil damping (the matrix \mathbf{C}_S in Eq. (3)) is reflected by a system of dashpots of frequency-variant parameters. These parameters are discussed in [1], [6], where the subsoil model is an elastic half-space. A weightless plate rests on an elastic subsoil and it is subjected to harmonic excitation. This pattern refers to radiation-type damping. The hysteretic (internal) damping of the subsoil is associated with its viscoelastic model (see [25]).

The damping part related to hydrodynamic damping \mathbf{C}_H occurs only in the nodes immersed in water. This issue is addressed in detail in [7], where the stochastic averaging method is used to solve non-linear platform vibrations.

STIFFNESS MATRIX

The system stiffness covers the structural stiffness (3D beam finite elements) and stiffness of the subsoil, represented by six springs along the DOFs (degrees of freedom) of the support nodes of the discrete platform model.

We assume the following superposition of the global stiffness matrix:

$$\mathbf{K} = \mathbf{K}_P + \mathbf{K}_S \quad (4)$$

where \mathbf{K}_P represents the global stiffness matrix of a platform made of 3D beam elements, and \mathbf{K}_S is a matrix representing contact between the platform structure and the subsoil.

While the structure–subsoil contact is modelled by a system of six springs and dashpots, the matrices \mathbf{K}_S and \mathbf{C}_S include six diagonal elements, referring to three translations and three rotations. In the probabilistic terms, the soil shear modulus G is represented by a Gaussian random variable, while Poisson’s ratio ν and mass density ρ_s are assumed to be deterministic. The mean values and variances of the stiffness and damping parameters are presented in [1], [6].

EXCITATION FORCES

The right-hand side of the equation of motion (1) specifies the marine environment of the offshore structures. Excitation forces are affected by the environment, i.e., waves, wind, and subsoil deformations (e.g., support settlement, seismic interactions, etc.).

The force vector in Eq. (1) includes components derived from a field of sea waves and wind. The random event identifier γ

is neglected here.

Let the total force vector be:

$$\mathbf{P}(t, \dot{\mathbf{q}}(t), \ddot{\mathbf{q}}(t)) = \mathbf{P}_F(t, \dot{\mathbf{q}}(t), \ddot{\mathbf{q}}(t)) + \mathbf{P}_W(t, \dot{\mathbf{q}}(t)) \quad (5)$$

where \mathbf{P}_F is a sea wave load vector at structural nodes in the immersed part, \mathbf{P}_W is a wind load vector at nodes above sea level.

The vectors \mathbf{P}_F and \mathbf{P}_W are time functions, with the structural velocity vector $\dot{\mathbf{q}}$ and the acceleration vector $\ddot{\mathbf{q}}$ (see Eq. (A.1) in Appendix).

In the probabilistic approach, the vectors \mathbf{P}_F and \mathbf{P}_W are the functions of random parameters, i.e., wave height, wave period, hydrodynamic coefficients, wind speed, sea current velocity, biological growth of elements immersed in seawater, etc. In papers [1], [6], it was assumed that wave and wind loads given a linear form are considered Gaussian, ergodic, stationary, and independent processes with zero means. Thus the linear sum of the processes expressed in formula (5) is also a stationary and ergodic Gaussian process.

SUBSOIL-STRUCTURE INTERACTION PROBLEM

The components of the dynamic equation of motion (1), based on the structure-subsoil interaction problem, are defined by the mass, damping, and stiffness matrices, i.e., \mathbf{M}_s , \mathbf{C}_s and \mathbf{K}_s (see Eqs. (2), (3), (4), and Table 1, respectively).

Three models are possible to analyse the structure-subsoil co-oscillating system:

1. Deterministic model 1 - constant parameters of stiffness and subsoil damping. This simplifying approach leads to a system of differential equations with constant coefficients. It is a numerical problem to apply equations uncoupled by modal reduction, while soil damping is high compared to structural damping, so the Rayleigh proportional damping may be irrelevant. In numerical terms, the modal transformation makes the mass and structural damping matrices diagonal, but the subsoil damping matrix does not follow; hence the equations are coupled. The work [23] shows that the subsoil damping matrix may be diagonalised if the least-squares method is applied to minimise the error function. This work assumes that the motion components associated with the rigid body structural vibrations are uncoupled.
2. Deterministic model 2 - variable parameters of stiffness and subsoil damping, the latter frequency variant. A system of differential equations with variable coefficients is solved. Relevant approximation functions are applied to the variable equation parameters (see [25]).
3. Random model - here the stiffness and subsoil damping parameters are random variables. The stiffness coefficients are Gaussian random variables while they

are with Gaussian distributed soil shear modulus G . Poisson's ratio and the mass density are deterministic. The damping factors are non-linear with regard to the shear modulus, so the mean values and variances of these parameters are achieved by an approximate solution - Taylor's series expansion. The mean values and variances of the subsoil stiffness and damping coefficients are presented in [1] and [6].

Deterministic models allow one to solve the contact problem in the time or frequency domains [19]. If the second deterministic model is applied, it is convenient to perform the analysis in a frequency domain. The stiffness terms associated with structural degrees of freedom decrease with increasing frequency, more for translational than rotational DOFs [23]. In the case of random models the solution may involve approximation methods, e.g., spectral analysis, a perturbation approach, averaging and simulation methods, etc.

PERTURBATION SOLUTION APPROACH

The dynamic equations of motion of the platform belong to a non-linear class of equations in both deterministic and probabilistic terms. The origin of non-linearity is the velocity component of force summation in a dynamic system and the coefficients of substitute springs and dashpots modelling the subsoil-structure interaction. These coefficients are frequency-variant, affected by the random subsoil shear modulus [6].

Different methods can be used to solve Eq. (1) (see [1], [7], [17]). In this study, the perturbation method is used.

The perturbation method is an asymptotic method, whose solutions are power series. Limiting an approximate solution to selected terms of a series makes a sufficient approximation in a variety of problems (see [11], [13]).

The fluctuations of random coefficients of the matrix in Eq. (1) are assumed to be small, and the perturbations of random magnitudes are limited to the first- or second-order approximations of the response series expansion (see [17]). The reference work regards the interaction of non-linear damping wave forces with a structural response, but neglects the soil-structure interaction problem.

Thus the matrix coefficients of Eq. (1) defined by the inertia, damping, and stiffness matrices are random variables as follows:

$$\begin{aligned} \mathbf{M} &= \mathbf{M}_0 + \varepsilon \mathbf{M}_1(\gamma), \\ \mathbf{C} &= \mathbf{C}_0 + \varepsilon \mathbf{C}_1(\gamma), \\ \mathbf{K} &= \mathbf{K}_0 + \varepsilon \mathbf{K}_1(\gamma) \end{aligned} \quad (6)$$

where index "0" is the mean coefficient, index "1" represents fluctuation, γ is an elementary event of an elementary space Γ , and ε is the small parameter, $\varepsilon \ll 1$.

The solution of Eq. (1) takes the perturbation expansion form:

$$\mathbf{q}(\gamma, t) = \mathbf{q}_0(\gamma, t) + \varepsilon \mathbf{q}_1(\gamma, t) + \varepsilon^2 \mathbf{q}_2(\gamma, t) + \dots \quad (7)$$

where terms up to ε^2 are retained, since the variable linear parts associated with the small parameter ε are not correlated with the excitation forces.

The operator of Eq. (1), $\mathbf{L} = \mathbf{L}(\gamma, t, \varepsilon)$, triggers:

$$\mathbf{L}\mathbf{q} = \mathbf{P}, \quad (8)$$

where $\mathbf{L} = \mathbf{L}(\gamma) = \mathbf{L}_0 + \varepsilon \mathbf{L}_1(\gamma) + \dots$, $\mathbf{q}(\gamma, t)$ s defined by Eq. (7), $\mathbf{P} = \mathbf{P}(\gamma, t) = \mathbf{P}_0(\gamma, t) + \varepsilon \mathbf{P}_1(\gamma, t) + \dots$ (see the Appendix and the load vector \mathbf{P}).

Expanding Eqs. (6) and (7) and comparing the corresponding terms, the set of equations takes the form:

$$\begin{aligned} \mathbf{L}_0 \mathbf{q}_0 &= \mathbf{Z}_0 \\ \mathbf{L}_0 \mathbf{q}_1 &= \mathbf{Z}_1 \\ \mathbf{L}_0 \mathbf{q}_2 &= \mathbf{Z}_2 \\ &\dots \end{aligned} \quad (9)$$

where .

$$\begin{aligned} \mathbf{L}_0 \mathbf{q}_0 &= \mathbf{M}_0 \ddot{\mathbf{q}}_0 + \mathbf{C}_0 \dot{\mathbf{q}}_0 + \mathbf{K}_0 \mathbf{q}_0, \\ \mathbf{Z}_0 &= \mathbf{P}_0, \mathbf{Z}_1 = \mathbf{P}_1 - \mathbf{L}_1 \mathbf{q}_0, \\ \mathbf{L}_1 \mathbf{q}_0 &= \mathbf{M}_1(\gamma) \ddot{\mathbf{q}}_0 + \mathbf{C}_1(\gamma) \dot{\mathbf{q}}_0 + \mathbf{K}_1(\gamma) \mathbf{q}_0, \\ \mathbf{Z}_2 &= -\mathbf{L}_1 \mathbf{q}_1 = -[\mathbf{M}_1(\gamma) \ddot{\mathbf{q}}_1 + \mathbf{C}_1(\gamma) \dot{\mathbf{q}}_1 + \mathbf{K}_1(\gamma) \mathbf{q}_1]. \end{aligned}$$

Formula (9) is a hierarchical set of linear equations of static equilibrium with deterministic coefficients and random excitations: \mathbf{Z}_0 , \mathbf{Z}_1 and \mathbf{Z}_2 . Regarding a vector \mathbf{Z}_1 , its approximation $\mathbf{Z}_1 \approx -\mathbf{L}_1 \mathbf{q}_0$ follows the linearisation method of Malhotra and Penzien [27] applied to the drag term of wave forces. Note that the excitation of the second equation is caused by the solution of the first equation, etc.

RESPONSE SPECTRA

The first Eq. (9) covers the stochastically linear problem in terms of the spectral density function $\mathbf{S}_{q_0 q_0}(\omega)$, while the second and third equations are related to higher-order spectra. Regarding the order ε^2 , the response spectral density is:

$$\begin{aligned} \mathbf{S}_{qq}(\omega) &= \mathbf{S}_{q_0 q_0}(\omega) + \varepsilon [\mathbf{S}_{q_0 q_1}(\omega) + \mathbf{S}_{q_1 q_0}(\omega)] \\ &+ \varepsilon^2 [\mathbf{S}_{q_1 q_1}(\omega) + \mathbf{S}_{q_0 q_2}(\omega) + \mathbf{S}_{q_2 q_0}(\omega)] \end{aligned} \quad (10)$$

where the indices $q_r q_s$, ($r, s = 0, 1, 2$) refer to the displacement components defined by Eq. (7).

The spectral density matrices in Eq. (10) associated with the small parameter ε equal zero (the autocorrelation function between vectors \mathbf{q}_0 and \mathbf{q}_1 is $\mathbf{R}_{q_0 q_1}(\tau) = 0$, thus $\mathbf{S}_{q_0 q_1}(\omega) = 0$). Two issues are vital here: zero-mean stochastic processes of the excitation process and cumulants of an order higher than two may be neglected for Gaussian approximation [17].

The following remarks are highlighted in the inquiry above:

1. Random variables $\mathbf{M}_1(\gamma)$, $\mathbf{C}_1(\gamma)$, $\mathbf{K}_1(\gamma)$ are small-valued and independent of $\mathbf{q}_0(\gamma, t)$. Thus the vector process \mathbf{Z}_1 is stationary in a broad sense and ergodic

in autocorrelation;

2. Fluctuating components of the matrices in Eq. (6) are defined by diagonal matrices:

$$\begin{aligned} \mathbf{M}_1(\gamma) &= \text{diag}[M_{S_i}(\gamma)], \mathbf{C}_1(\gamma) = \\ &\text{diag}[C_{S_i}(\gamma)], \mathbf{K}_1(\gamma) = \\ &\text{diag}[K_{S_i}(\gamma)] \end{aligned} \quad (11)$$

where $M_{S_i}(\gamma)$ is defined by soil masses (according to Table 1 including the mean values), while $C_{S_i}(\gamma)$ and $K_{S_i}(\gamma)$ are the random damping and stiffness of the soil addressed by Jesien [6] and [1];

3. The full correlation holds between the fluctuation components listed above;
4. Spectral density matrices $\mathbf{S}_{q_0 q_1}(\omega) = \mathbf{S}_{q_1 q_0}(\omega)$, $i = 1, 2$ show all zero terms (see [17]).

The presented argument leads to:

$$\mathbf{Z}_1 \approx -\mathbf{L}_1 \mathbf{q}_0 = [\mathbf{Z}_M + \mathbf{Z}_C + \mathbf{Z}_K] \quad (12)$$

where

$$\begin{aligned} \mathbf{Z}_M &= \mathbf{Z}_M(\gamma, t) = \mathbf{M}_1(\gamma, t) \ddot{\mathbf{q}}_0(\gamma, t), \\ \mathbf{Z}_C &= \mathbf{Z}_C(\gamma, t) = \mathbf{C}_1(\gamma, t) \dot{\mathbf{q}}_0(\gamma, t), \text{ and} \\ \mathbf{Z}_K &= \mathbf{Z}_K(\gamma, t) = \mathbf{K}_1(\gamma, t) \mathbf{q}_0(\gamma, t). \end{aligned}$$

The spectral density matrix of \mathbf{Z}_1 is:

$$\begin{aligned} \mathbf{S}_{Z_1 Z_1}(\omega) &= \mathbf{S}_{Z_M Z_M}(\omega) + \mathbf{S}_{Z_M Z_C}(\omega) + \mathbf{S}_{Z_M Z_K}(\omega) + \\ &\mathbf{S}_{Z_C Z_M}(\omega) + \mathbf{S}_{Z_C Z_C}(\omega) + \mathbf{S}_{Z_C Z_K}(\omega) + \\ &\mathbf{S}_{Z_K Z_M}(\omega) + \mathbf{S}_{Z_K Z_C}(\omega) + \mathbf{S}_{Z_K Z_K}(\omega) \end{aligned} \quad (13)$$

where:

$$\begin{aligned} \mathbf{S}_{Z_M Z_M}(\omega) &= \omega^4 \boldsymbol{\sigma}_M \mathbf{S}_{q_0 q_0}(\omega) \boldsymbol{\sigma}_M, \mathbf{S}_{Z_M Z_C}(\omega) = i\omega^3 \boldsymbol{\sigma}_M \mathbf{S}_{q_0 q_0}(\omega) \boldsymbol{\sigma}_C, \\ \mathbf{S}_{Z_M Z_K}(\omega) &= -\omega^2 \boldsymbol{\sigma}_M \mathbf{S}_{q_0 q_0}(\omega) \boldsymbol{\sigma}_K, \mathbf{S}_{Z_C Z_M}(\omega) = -i\omega^3 \boldsymbol{\sigma}_C \mathbf{S}_{q_0 q_0}(\omega) \boldsymbol{\sigma}_M, \\ \mathbf{S}_{Z_C Z_C}(\omega) &= -\omega^2 \boldsymbol{\sigma}_C \mathbf{S}_{q_0 q_0}(\omega) \boldsymbol{\sigma}_C, \mathbf{S}_{Z_C Z_K}(\omega) = i\omega \boldsymbol{\sigma}_C \mathbf{S}_{q_0 q_0}(\omega) \boldsymbol{\sigma}_K, \\ \mathbf{S}_{Z_K Z_M}(\omega) &= -\omega^2 \boldsymbol{\sigma}_K \mathbf{S}_{q_0 q_0}(\omega) \boldsymbol{\sigma}_M, \mathbf{S}_{Z_K Z_C}(\omega) = -i\omega \boldsymbol{\sigma}_K \mathbf{S}_{q_0 q_0}(\omega) \boldsymbol{\sigma}_C, \\ \mathbf{S}_{Z_K Z_K}(\omega) &= \boldsymbol{\sigma}_K \mathbf{S}_{q_0 q_0}(\omega) \boldsymbol{\sigma}_K \end{aligned}$$

and $\boldsymbol{\sigma}_M = \text{diag}(\sigma_{M_{ii}})$, $\boldsymbol{\sigma}_C = \text{diag}(\sigma_{C_{ii}})$, $\boldsymbol{\sigma}_K = \text{diag}(\sigma_{K_{ii}})$ are diagonal matrices, whose elements show standard deviations by Eq. (13).

The spectral density matrices of $q_0(\gamma, t)$ and $q_1(\gamma, t)$ take the form:

$$\mathbf{S}_{q_r q_r}(\omega) = \mathbf{H}_{q_r Z_r}(\omega) \mathbf{S}_{Z_r Z_r}(\omega) \mathbf{H}_{Z_r q_r}^*(\omega) \quad (14)$$

where $\mathbf{H}_{q_r Z_r}(\omega) = (\mathbf{K}_0 - \omega^2 \mathbf{M}_0 + i\omega \mathbf{C}_0)^{-1}$ is the complex transfer function matrix (see [1]), and $\mathbf{H}_{Z_r q_r}^*$ is its complex conjugate transpose, $r = 0, 1$.

Similarly to Eq. (14), the spectral density matrix in the reduced modal space $\mathbf{q} = \boldsymbol{\Phi}_h \mathbf{y}_h$, where $\boldsymbol{\Phi}_h$ is the matrix of eigenvectors of order $(n \times h)$, $h < n$, has the form:

$$\mathbf{S}_{y_r y_r}(\omega) = \widehat{\mathbf{H}}_{y_r Z_r}(\omega) \widehat{\mathbf{S}}_{Z_r Z_r}(\omega) \widehat{\mathbf{H}}_{Z_r y_r}^*(\omega) \quad (15)$$

where $\hat{H}_{y_r z_r} = [\Phi_h^T (K_0 - \omega^2 M_0 + i\omega C_0) \Phi_h]^{-1}$,
 $\hat{S}_{Z_r Z_r}(\omega) = \Phi_h^T S_{Z_r Z_r} \Phi_h$, $r = 0, 1$,

The spectral density matrix of the displacement vector $q(y, t)$ in Eq. (7) reads:

$$S_{qq}(\omega) = S_{q_0 q_0}(\omega) + \varepsilon^2 S_{q_1 q_1}(\omega) \quad (16)$$

Following Eq. (16), the response spectral density matrix $S_{qq}(\omega)$ is the sum of the two components. The first, i.e., the $S_{q_0 q_0}(\omega)$ matrix, is the first approximation, the second component, $S_{q_1 q_1}$, is the second approximation.

The response spectral density matrix of the internal forces of the j th beam element is:

$$S_{SS}^j(\omega) = K_P^j S_{qq}^j(\omega) (K_P^j)^T \quad (17)$$

where $S_{SS}^j(\omega)$ and $S_{qq}^j(\omega)$ denote the spectral density matrices of the internal forces and displacements for the element j respectively, and K_P^j is the stiffness matrix of the element j .

NUMERICAL EXAMPLE

A discrete 3D beam model of the platform is presented in Fig. 1. The axial, torsional, and bending stiffness parameters of the deck and columns of the platform are based on structural details shown in Fig. 2, 3, and 4.

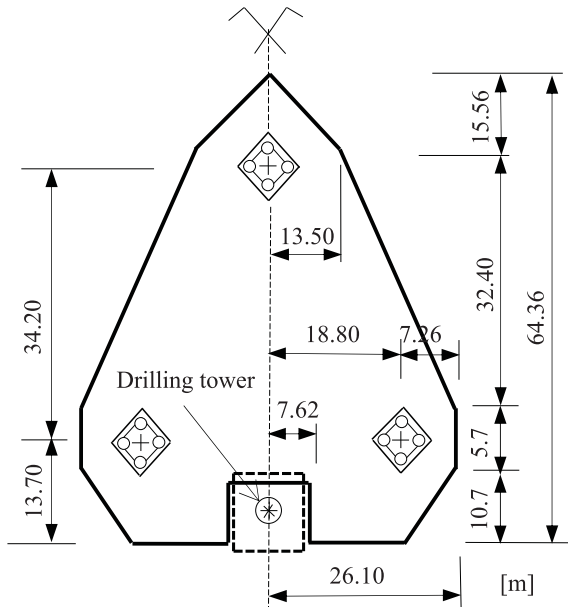


Fig. 2. Platform deck projection

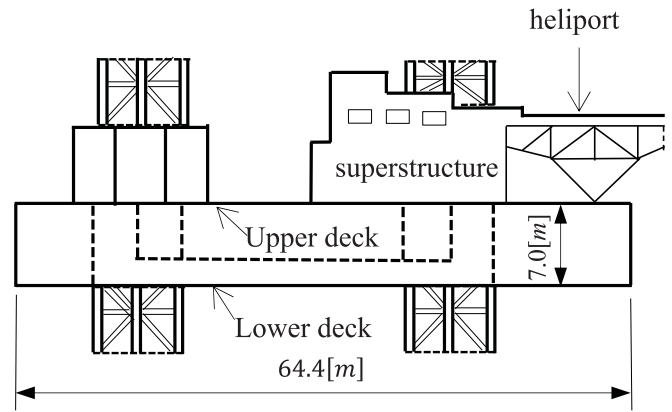


Fig. 3. Longitudinal cross-section of the platform

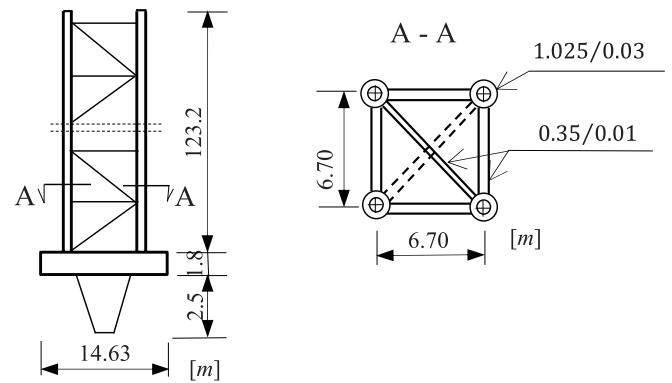


Fig. 4. Cross-sections of the platform leg

3D beam finite elements and the corresponding numbers of nodes are shown in Fig. 5 (see [1], [6]). The model specifies elastic supports and dashpots representing the stiffness and damping of the subsoil, respectively. This model involves 72 degrees of freedom. The axial, bending, and torsional stiffness parameters of the FEM beam model are (see [1]): $EA = \{8.40 \cdot 10^5; 0.79 \cdot 10^5\}$ [MN], $EJ = \{2.53 \cdot 10^6; 8.93 \cdot 10^5\}$ [MNm²], $GJ_s = \{1.94 \cdot 10^6; 6.86 \cdot 10^5\}$ [MNm²], the first part related to the deck, the second part referring to the legs of the structure. The total mass of the structure is $7710 \cdot 10^3$ [kg], regarding the deck and the legs.

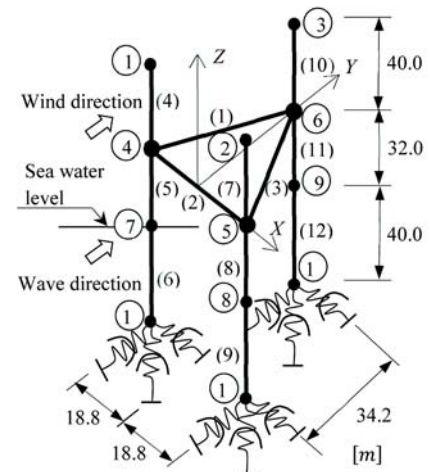


Fig. 5. Space FEM discrete model of the platform

The following data of the subsoil, wind and wave parameters are assumed:

- subsoil parameters: $E = 60[MPa]$, $\nu = 0.4$, $E(G) = 21.4[MPa]$, $\sigma_G = E(G)/2 = 10.7[MPa]$ (Young's modulus, mean value, and standard deviation of the shear modulus, respectively).
- wind parameters: $\bar{v}_{10} = 40[m/s]$, $K = 0.005$, $L = 1200[m]$, $a = b = c = 1$ (mean wind speed 10 m above the surface, surface drag coefficient, the length scale of turbulence, and empirical coefficients in Davenport's formula [28], representing the cross-spectral density of the longitudinal wind fluctuation velocity, respectively).
- wave parameters: $\bar{H} = 14m$, $\bar{T} = 10s$, $\bar{L} = 180m$, $C_M' = C_M'' = C_D = 1$ (mean height, period, and length for long-crested waves, empirical inertia, and drag coefficients of the Morison equation).

Fig. 6 presents the three lowest mode shapes of the free vibration problem.

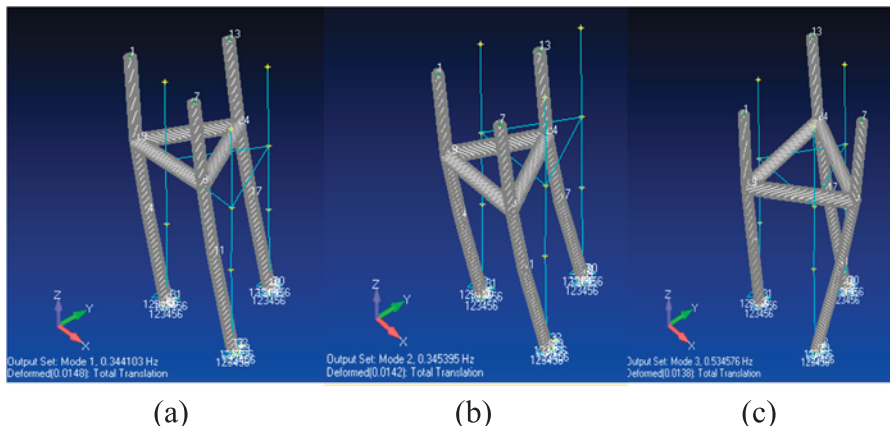


Fig. 6. The first three mode shapes of the platform: (a) $\omega_1 = 2.16 \text{ rad/s}$, (b) $\omega_2 = 2.17 \text{ rad/s}$, (c) $\omega_3 = 3.36 \text{ rad/s}$

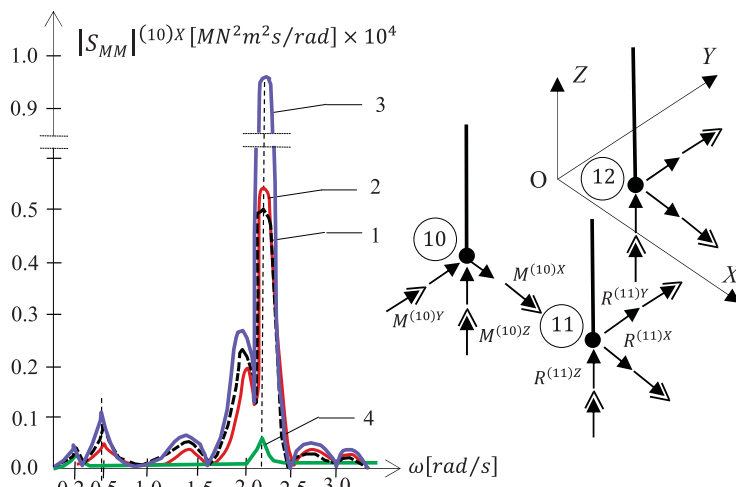


Fig. 7. Spectrum moduli of the responses of the FEM platform model loaded by waves and wind (the bending moment at the node 10 about OX-axis. 1: solution of a linear stochastic problem for waves and wind loads, 2: solution by stochastic averaging method [1], [7] (sea waves only), 3: perturbation solution of a non-linear stochastic problem, 4: solution of a stochastic linear problem for wind load only (see [6])

The cross-spectral density functions of the wave and wind loads are presented in [1].

Fig. 7 shows the bending moment power spectrum modules in the spring of the rotating support node (10), taking into account the solution of a linearised stochastic problem for wave and wind loads (curve 1), the stochastic averaging method regarding wave loads only (curve 2), the stochastic non-linear case with uncertain subsoil parameters (curve 3) and the solution regarding wind loads only (curve 4). The results were obtained for modal space reduction with $h = 7$ eigenvectors. In the spectrum waveform, the characteristic values are observable along the frequency axis ω , corresponding adequately to the frequency of the extreme wind spectrum ($\omega = 0.2 \text{ rad/s}$), the frequency of the extreme wave spectrum ($\omega = 0.5 \text{ rad/s}$) and the mean value of the first natural frequency ($\omega = 2.16 \text{ rad/s}$). Numerical integrations of these four response spectra variants lead to the following standard deviations of the bending moment at node 10: $\sigma_M = \{47.3; 44.5; 54.9; 20.9\}[MNm]$.

DISCUSSION

The perturbation method was used to study the non-linear vibration effects of the platform-wave-wind-subsoil interaction system. Two types of non-linear problems occur here. The first type stems from the modified Morison equation for wave loading (wave-structure interaction problem), the second one involves coefficients of the system of dynamic equations of motion containing components in the form of random variables (soil-structure interaction effects) defining the system as stochastically non-linear. The wave-structure interaction problem is included here by the added mass and hydrodynamic damping terms (see Eqs. (A.2) and (A.3)), and the fluctuating damping part of the wave force associated with a small parameter. Neglecting this part and assuming the stochastically linearised wind forces, the response spectra with the second-order terms of the jack-up structure considered in real engineering categories were presented.

1. Based on the numerical computations in this study and other published research, the following observations can be made: The response spectral density functions highlight two important features of structural behaviour. The first is that the variances are statistical parameters of the analysed processes. The second is that the distribution of the response spectra shows the dominant content in the frequency range associated with the structural natural frequencies (resonance zones).

2. A linearised structural response spectrum is a frequency function employing a linearised form of damping forces, which includes deterministic parameters of the subsoil. The introduction of random parameters converts the problem from a stochastically linear to a stochastically non-linear problem (the system equation operator is random).
3. Modal reduction of a dynamic system significantly simplifies the numerical computations, incorporating the lowest vibration forms (the presented example shows a 10% reduction of dynamic degrees of freedom). Due to the significant material damping, the subsoil introduces a disturbance in the modal formulation of the problem.
4. The subsoil–structure interaction effects represent non-linearity in the frequency range close to the first structural natural frequency. In the presented example the peak value of the bending moment spectrum at the first natural frequency is approximately twice the value of its linearised response. Beyond the resonance zones, the differences between linear and non-linear effects are negligible.
5. Zero values in the response spectra are caused by a sign change in the wave load on the platform legs, a problem that was noted and explained by Jesien [6].
6. The mean fluctuation peak of the wind velocity spectrum appears at the response spectrum due to wind load. The values of the peak are amplified at this frequency, but only in the resonance zones. Fig. 7 shows that the impact of the wind load on the response power spectrum is low (6% at the peak value of the resonance zone, as shown in variants 3 and 4).
7. The fluctuating part of the damping wave excitation force (i.e. the term P_{li} of Eq. (A.4) in the Appendix) in the structural response spectral analysis leads to higher-order convolution spectra of wave-particle kinematics (see [7], [17]). These response effects are insignificant for real sea states.
8. In offshore dynamic systems with small element diameters compared to the wave height, the main damping is produced by a wave velocity term of excitation forces. In RC platforms with significant dimensions of the submerged elements and significant mass, wave field disturbance (diffraction) occurs, and significant damping of the dynamic system is generated by the subsoil [5], [9].

CONCLUSION

The dynamic response of jack-up platforms subjected to wind and wave loads is more severe if the higher-order wave load components and uncertainty of subsoil parameters are included, and the problem is treated as a stochastically non-linear dynamic system. The linearisation of the platform dynamic system leads to underestimation of the system's dynamic response.

The inclusion of non-linear effects due to wave–structure and subsoil–structure interactions reveals substantial differences in the peaks of the response spectra in the resonance zone vs. the linearised form of the response spectra (with the non-linear effects being neglected).

These findings deserve future research, including the wave–structure kinematics interaction process.

REFERENCES

1. B. Rozmarynowski, “Spectral dynamic analysis of a stationary jack-up platform,” *Polish Marit. Res.*, vol. 26, no. 101, pp. 40–48, 2019, doi: 10.2478/pomr-2019-0005.
2. S. K. Chakrabarti, *Handbook of Offshore Engineering*, vol. I. Elsevier Ltd, 2005.
3. Y. Bai, *Marine Structural Design*. Elsevier Ltd, 2003.
4. S. E. Hirdaris et al., “Loads for use in the design of ships and offshore structures,” *Ocean Eng.*, vol. 78, pp. 131–174, 2014, doi: <https://doi.org/10.1016/j.oceaneng.2013.09.012>.
5. N. D. Barltrop and A. J. Adams, *Dynamics of Fixed Marine Structures*, 3rd ed. Butterworth-Heinemann Ltd, 1991.
6. W. Jesien, “Random vibration of the Baltic drilling platform subjected to wind loads and water waves,” *Earthq. Eng. Struct. Dyn.*, vol. 15, pp. 595–617, 1987, doi: 0098-8847/87/050595-23.
7. B. Rozmarynowski, “Averaged damping in random vibrations of the Baltic drilling platform,” *J. Sound Vib.*, vol. 139, no. 3, pp. 437–458, 1990, doi: [https://doi.org/10.1016/0022-460X\(90\)90675-P](https://doi.org/10.1016/0022-460X(90)90675-P).
8. G. Clauss, E. Lehmann, and C. Østergaard, *Offshore Structures: Conceptual Design and Hydromechanics*, vol. 1. Springer Berlin Heidelberg, 1992.
9. G. Clauss, E. Lehmann, and C. Ostergaard, *Offshore Structures Volume II Strength and Safety for Structural Design*. Springer Berlin Heidelberg, 1994.
10. J. F. Wilson, *Dynamics of offshore structures*. John Wiley & Sons, 1988.
11. M. H. Holmes, *Introduction to perturbation methods*. New York: Springer, 2013.
12. A. Nayfeh, *Perturbation methods*. New York: John Wiley & Sons, 1973.
13. S. H. Crandall, “Perturbation techniques for random vibration of non-linear systems,” *J. Acoust. Soc. Am.*, vol. 35, pp. 1700–1705, 1963, doi: <https://doi.org/10.1121/1.1918792>.

14. Y. K. Lin, Probabilistic theory of structural dynamics. New York: McGraw Hill, 1967.
15. M. Kaminski, The stochastic perturbation method for computational mechanics. Chichester: John Wiley & Sons, 2013.
16. K. Sobczyk, Stochastic differential equations for applications. Lyngby: Technical University of Denmark, 1985.
17. R. E. Taylor and A. Rajagopalan, "Dynamics of offshore structures, part I: perturbation analysis," J. Sound Vib., vol. 83, no. 3, pp. 401–416, 1982.
18. S. Massel, Ocean surface waves: their physics and prediction. Singapore: World Scientific, 1996.
19. G. Adomian, "Vibration in offshore structures: an analysis for the general non-linear stochastic case - part I," Math. Comput. Simul., vol. 29, no. 2, pp. 119–122, 1987, doi: [https://doi.org/10.1016/0378-4754\(87\)90102-9](https://doi.org/10.1016/0378-4754(87)90102-9).
20. G. Adomian, "Vibration in offshore structures — part II," Math. Comput. Simul., vol. 29, no. 5, pp. 351–356, 1987, doi: [https://doi.org/10.1016/0378-4754\(87\)90070-X](https://doi.org/10.1016/0378-4754(87)90070-X).
21. J. Penzien and S. Tseng, "Three-dimensional dynamic analysis of fixed offshore platforms," in Numerical Methods in Offshore Engineering, O. C. Zienkiewicz, R. W. Lewis, and K. G. Stagg, Eds. New York: John Wiley & Sons, 1979.
22. J. Thomas and B. Abbas, "Finite element model for dynamic analysis of Timoshenko beam," J. Sound Vib., vol. 41, no. 3, pp. 291–299, 1975, doi: [https://doi.org/10.1016/S0022-460X\(75\)80176-3](https://doi.org/10.1016/S0022-460X(75)80176-3).
23. R. W. Clough and J. Penzien, Dynamics of structures. McGraw Hill, 1993.
24. K. J. Bathe, Finite element procedures. Prentice Hall, 1996.
25. A. S. Veletsos and B. Verbic, "Basic response functions for elastic foundations," J. Eng. Mech., vol. 100, no. 2, pp. 1227–1248, 1974, doi: <https://doi.org/10.1061/JMCEA3.0001869>.
26. N. C. Tsai, "Modal damping for soil - structure interaction," J. Eng. Mech., vol. 100, no. 2, pp. 323–341, 1974.
27. A. K. Malhotra and J. Penzien, "Nondeterministic analysis of offshore structures," J. Eng. Mech., vol. 96, no. 6, pp. 985–1003, 1970.
28. A. G. Davenport, "The spectrum for horizontal gustiness near the ground in high wind," Q. J. R. Meteorol. Soc., vol. 87, pp. 194–211, 1961.

APPENDIX

The excitation force vector \mathbf{P}_i (Eq. (5)) at the i th submerged node of the platform is defined by the modified Morison formula (see [1], [6], [17], [21]):

$$\mathbf{P}_i = \mathbf{P}_{p_i} + \mathbf{P}_{a_i} + \mathbf{P}_{d_i} \quad (\text{A.1})$$

where $\mathbf{P}_{p_i} = C'_M \rho V_i \dot{\mathbf{v}}_{n_i}$, $\mathbf{P}_{a_i} = C''_M \rho V_i (\dot{\mathbf{v}}_{n_i} - \ddot{\mathbf{q}}_{n_i})$,

$$\begin{aligned} \mathbf{P}_{d_i} &= 1/2 C_D \rho A_i [(\mathbf{v}_{n_i} - \dot{\mathbf{q}}_{n_i}) |(\mathbf{v}_{n_i} - \dot{\mathbf{q}}_{n_i})|] \approx \\ &\approx K_{D_i} (\mathbf{v}_{n_i} |\mathbf{v}_{n_i}| - 2 |\mathbf{v}_{n_i}| \dot{\mathbf{q}}_{n_i}), \end{aligned}$$

ρ is the density of water, V_i , A_i are the volume and projected area associated with the i th node, $K_{D_i} = 1/2 C_D \rho A_i$, \mathbf{v}_{n_i} and $\dot{\mathbf{q}}_{n_i}$ are fluid particle velocity and structural velocity vectors at node i , "n" denotes normal to the cylinder axis, C'_M , C''_M , C_D are empirical coefficients affected by the cross-sectional shape, Reynolds and Keulegan-Carpenter numbers, and relative roughness (see [8], [9]).

Equation (A.1) takes the form:

$$\mathbf{P}_i = K_{M_i} \dot{\mathbf{v}}_{n_i} - K_{M_i}^a \ddot{\mathbf{q}}_{n_i} + K_{D_i} (\mathbf{v}_{n_i} |\mathbf{v}_{n_i}| - 2 |\mathbf{v}_{n_i}| \dot{\mathbf{q}}_{n_i}) \quad (\text{A.2})$$

where $K_{M_i} = C_M \rho V_i$, $C_M = (C'_M + C''_M)$, $K_{M_i}^a = C''_M \rho V_i$.

Assuming that the wave-particle kinematics is represented by a zero-mean stationary ergodic Gaussian stochastic process, the i th damping coefficient $2K_{D_i} |\mathbf{v}_{n_i}|$ takes the form [17]:

$$\begin{aligned} 2K_{D_i} |\mathbf{v}_{n_i}| \dot{\mathbf{q}}_{n_i} &= 2K_{D_i} E[|\mathbf{v}_{n_i}|] \dot{\mathbf{q}}_{n_i} + 2K_{D_i} \{|\mathbf{v}_{n_i}| - E[|\mathbf{v}_{n_i}|]\} \dot{\mathbf{q}}_{n_i} \\ &= K_{D_i} \sqrt{8/\pi} \sigma_{v_{n_i}} \dot{\mathbf{q}}_{n_i} + 2K_{D_i} \left[|\mathbf{v}_{n_i}| - \sqrt{2/\pi} \sigma_{v_{n_i}} \right] \dot{\mathbf{q}}_{n_i} \end{aligned} \quad (\text{A.3})$$

where $E[|\mathbf{v}_{n_i}|] = \sqrt{2/\pi} \sigma_{v_{n_i}}$ is the mean value of $|\mathbf{v}_{n_i}|$ and $\sigma_{v_{n_i}} \approx \sigma_{v_{n_i} - \dot{\mathbf{q}}_{n_i}}$ is the standard deviation of the water-particle velocity vector.

The second term of Eq. (A.2), i.e., $K_{M_i}^a \ddot{\mathbf{q}}_{n_i}$, is called the added mass term, while the first term of Eq. (A.3), i.e., $K_{D_i} \sqrt{8/\pi} \sigma_{v_{n_i}} \dot{\mathbf{q}}_{n_i}$, is the hydrodynamic damping term. These two terms are added to the corresponding structural mass (Eq. (3)) and damping matrices (Eq. (4)).

Considering the second term of Eq. (A.3) to be small (the fluctuating damping), the wave force \mathbf{P}_i reads:

$$\begin{aligned} \mathbf{P}_i &= K_{M_i} \dot{\mathbf{v}}_{n_i} + K_{D_i} \sqrt{8/\pi} \sigma_{v_{n_i}} \mathbf{v}_{n_i} - \varepsilon \left(2K_{D_i} \left[|\mathbf{v}_{n_i}| - \sqrt{2/\pi} \sigma_{v_{n_i}} \right] \dot{\mathbf{q}}_{n_i} \right) \\ &= \mathbf{P}_{0i} + \varepsilon \mathbf{P}_{1i} \end{aligned} \quad (\text{A.4})$$

where

$$\begin{aligned} \mathbf{P}_{0i} &= K_{M_i} \dot{\mathbf{v}}_{n_i} + K_{D_i} \sqrt{8/\pi} \sigma_{v_{n_i}} \mathbf{v}_{n_i}, \mathbf{P}_{1i} = \\ &= -2K_{D_i} \left[|\mathbf{v}_{n_i}| - \sqrt{2/\pi} \sigma_{v_{n_i}} \right] \dot{\mathbf{q}}_{n_i} \end{aligned}$$

The stochastically linearised wind force vector \mathbf{P}_j at the j th node above the sea water level takes the form (see [6]):

$$\mathbf{P}_j(t) = A \rho_A C_{DA} \left[1/2 |\bar{\mathbf{v}}_j| \bar{\mathbf{v}}_j + \left(|\bar{\mathbf{v}}_j| + \sqrt{1/2\pi} \sigma_{v'_m v'_m} \right) \mathbf{v}'_j \right] \quad (\text{A.5})$$

where A denotes the windward area of the platform, $\rho_A = 1.23 \text{ kg/m}^3$ is the air density, C_{DA} is the drag coefficient, $\bar{\mathbf{v}}_j$ and \mathbf{v}'_j are the mean value and the fluctuating part of the wind velocity vector, respectively, $\sigma_{v'_m v'_m}$ is the standard deviation of the fluctuating wind velocity for two points m and n on a vertical plane perpendicular to the mean wind velocity and $\sigma_{v'_m v'_m}^2 = \int_0^\infty S_{v'_m v'_m}(\omega) d\omega$, where $S_{v'_m v'_m}(\omega)$ is a single-sided Davenport spectrum [28].

CONTACT WITH THE AUTHOR

Bogdan Rozmarynowski
e-mail: bogrozma@pg.edu.pl

Gdańsk University of Technology
Narutowicza 11/12
80-233 Gdańsk
POLAND

PERFORMANCE AND EMISSION MODELLING AND SIMULATION OF MARINE DIESEL ENGINES USING PUBLICLY AVAILABLE ENGINE DATA

Mohammad Hossein Ghaemi*

Gdańsk University of Technology, Poland

* Corresponding author: ghaemi@pg.edu.pl (M.H. Ghaemi)

ABSTRACT

To analyse the behaviour of marine diesel engines in unsteady states for different purposes, for example to determine the fuel consumption or emissions level, to adjust the control strategy, to manage the maintenance, etc., a goal-based mathematical model that can be easily implemented for simulation is necessary. Such a model usually requires a wide range of operating data, measured on a test stand. This is a time-consuming process with high costs and the relevant data are not available publicly for a selected engine. The present paper delivers a rapid and relatively simple method for preparing a simulation model of a given marine diesel engine, based only on the widely available data in the project guides indicated for steady state conditions. After establishing the framework of the mathematical model, it describes how the parameters of the model can be adjusted for the simulation model and how the results can be verified as well. Conceptually, this is a trial and error method, but the presented case example makes clear how the parameters can be selected to reduce the number of trials and quickly determine the model parameters. The necessary descriptions are given through a case study, which is the MAN-B&W 8S65ME-C8 marine diesel engine. The engine is assumed to be connected to a constant pitch propeller. The presented mathematical model is a mean-value zero-dimensional type with seven state variables. The other variables of the engine are determined based on the state independent variables and the input value, which is the fuel rate. The paper can be used as a guideline to prepare a convenient mathematical model for simulation, with the minimum publicly available data.

Keywords: Marine diesel engine, Mathematical model, Mean-Value Model, Simulation of ship propulsion system

INTRODUCTION

DEFINITION OF THE PROBLEM

The modelling and simulation of marine diesel engines, their performance and unsteady state behaviour have been extensively taken into consideration during the last several decades. In recent years, more attention has been paid to determining the emissions induced by these engines, regarding their role in the production of air pollutants, mainly SO_x, CO_x, NO_x, soot and particulate matter (PM). NO_x and soot depend directly on the operational condition of a diesel engine, and the

rest firstly depend on the applied fuel and its components and then on the engine operational features. The parameters of the available mathematical models for simulation of diesel engines are mainly selected or adjusted using the data delivered by the engine manufacturers, which are usually measured on a test stand. In the detailed models the number, types and volume of the required data for adjusting the model parameters are high, and without enough measured data in the stand tests it is usually impossible to prepare a reliable simulation model for the given engine. On the other hand, the project guides delivered by the engine manufacturers usually do not include the data necessary for simulation of the performance of the diesel engine in transient conditions. This is a fundamental

problem for researchers, who are interested in simulating the behaviour of diesel engines in unsteady conditions. The results of such an investigation, in turn, are often required for better understanding of the interactions, for example, in the case of propeller-engine, hull-propeller-engine or hull-rudder-propeller-engine interactions, fuel consumption, combustion efficiency, emissions induced by the engine operation, control purposes, etc., see for example [1, 2, 3, 4, 5, 6].

LITERATURE REVIEW

There are many methods for the modelling of a ship propulsion system and particularly the transient behaviour of marine diesel engines, delivered in different studies. They vary from advanced models that calculate the details of internal processes such as the turbulence in receivers (manifolds) and cylinders, the effect of lubrication oil flow, changes in the chemical properties of exhaust gas components etc., to a simple single first-order system.

While the choice of the model to be used is usually based on the main goal of the modelling, nowadays, because of the availability of cheaper and accessible computational power, the major restriction on the complexity of the model to be simulated depends only on the availability of suitable data. In fact, the most time-consuming part is setting up the parameters of a simulation model, which usually consists of data collection, data analysis and filtering, and then the determination of various parameters of the model.

Excluding Artificial Intelligence (AI) and Neural Networks (ANN) identification methods, generally five groups of modelling methods can be found in the literature, while the majority of the delivered models are combinations of two or more methods. These methods and their historical background are described below and after that a short literature review on marine diesel engine modelling focusing on recent publications is delivered.

1. First-order and sometimes time-delayed model, e.g.:

$$G(s) = \frac{K \cdot e^{-T_0 s}}{1 + \tau s} = \frac{Q(s)}{H(s)} \quad (1)$$

where K is gain, T_0 is time delay, τ is a time constant, and Q and H represent the engine torque and fuel rate (or rack), respectively. In this case, the diesel engine has been considered as a black box and the internal events cannot be expressed using such a model. It is a linear model suitable, for example, in the case of ship positioning or manoeuvring models. The linearity of the model limits its application to a narrow range of operation. Gajek presented such a simple model of a diesel engine for use in the ship's dynamic model [7]. Andersen [8], Roszczyk et al. [9], Tittenbrun [10], Kowalski et al. [11] and Krutov [12] delivered some similar models, which they applied for engine transient response, ship electrical net analysis and control system studies.

2. Models based on identification methods. These are usually built according to statistical estimations. Although making a non-linear model using statistical

methods is theoretically possible, the author could not find any study applying such a model directly. Additionally, only a few linear statistical-based models have been reported. It is a unique method and a very large number of experimental data are required, therefore it is time-consuming and costly. Generally, a set of transfer functions are selected and their gains, parameters and coefficients are fitted to experimental test results. The model presented by Blanke and Andersen is an example of such a model [13]. Lam delivered a model that is performed using statistical-based methods for analysis of the diesel engine transient response [14].

3. Mean-value quasi-steady models make up the third group. The major limitation of the simple methods described above is the heavy reliance on a large fund of accurate engine data, and usually over a wide range of operation. When the goal is realistic modelling of unsteady phenomena, it can be achieved by assuming quasi-steady characteristics, where, at each instant, the characteristics are the same as in the related steady state. The engine set is divided into components, the engine as prime mover, inlet air and exhaust gas receivers, compressor and turbine, charge air cooler, etc. As a result, the approach of dividing the engine set into physical blocks is realised by representing each functional block by one or more equations or by employing look-up tables. However, the engine cylinders are still modelled as a black box and the inputs to the engine are fuel and air, while the output is exhaust gas. Therefore, only mean values of the engine variables can be calculated. The mean-value models reported by Ferenc et al. are adequate examples of such a method for medium-speed diesel engine application [15, 16, 17]. Smith [18], Taylor [19] and Ford [20] delivered some simplified and linearised mean-value models. Woodward and Lattore [21, 22], Hendricks et al. [23, 24, 25, 26], Jansen [27], Woud 28], Próchnicki [29, 30], also Próchnicki and Dzida [31] and lastly Kafar [32] presented transient simulation models of diesel engines and their application according to the mean-value method. Lan et al. presented a mean value quasi-steady model for analysis of the control system of a ship propulsion plant, but they concentrated on high- and medium-speed diesel engines [33].
4. Zero-dimensional instantaneous quasi-steady models are the fourth group of models. The difference between this model and the previous group is that here the internal events of engine cylinders are modelled in addition. These internal variables are mainly related to the mass and temperature of the working fluid during different engine operational processes. The most relevant examples of such an internal process are ignition and combustion. However, the variation of the gas state (for example, pressure and temperature), especially along the exhaust gas receiver (manifold) when a pulse turbocharger system is applied, has been ignored. In other words, the working fluid state at each treated component is instantaneously constant and the flow is homogeneous. In this regard, such a model is called

“zero-dimensional” or sometimes a “cycle model”. Olsen in 1958 reported on the development of a simulation model of a free piston engine [34]. Cook one year later published results generated by a cycle simulation model for a turbocharged diesel engine [35]. Whitehouse et al. in 1962 reported on a diesel engine cycle model, which considered in detail the full four-stroke cycle [36]. The single-cylinder model developed by Borman advanced the state-of-the-art considerably at the time of reporting in 1964 [37]. Six years later, Streit [38] extended the zero-dimensional model of Borman to accommodate a large two-stroke turbocharged diesel. In 1976 Marzouk improved the latter delivered version [40]. Later on Benson [41], Woschni [42, 43], Wiebe [44], and Watson [45, 46] published the results of a major development extending the 0-D concept to embrace transient simulation especially due to combustion and heat transfer aspects. Next, Banisoleiman et al. [47], Larmi [48] and Ghaemi [49] presented two advanced 0-D instantaneous quasi-steady models for modern long-stroke low- and medium-speed diesel engine transient response.

5. The last group of models is one-dimensional instantaneous quasi-steady. The available models of this group are very similar to the zero-dimensional quasi-steady models with one difference, which is variation of the working fluid state also in each individual component. In other words, the gas state can be illustrated not only as a function of time but also as a function of geometrical position, continuously, i.e., the system parameters and variables are not lumped but distributed. Benson in spent much time at the end of the 1950s using the graphical Method of Characteristics (MOC) to solve the 1-D unsteady flow equations for a two-stroke marine diesel exhaust system [50]. Later on Benson et al. [51, 52] developed this model. Blair et al. presented a complete engine model based on the MOC solution of the 1-D unsteady flow equations but concentrated on high-speed, high specific output two- and four-stroke applications [53, 54, 55, 56, 57]. Bazari in 1992 published a 1-D unsteady flow model for simulation of NOX and SOX emissions of a low-speed diesel engine [56]. In recent years, the attention of researchers has been mainly focused on the modelling of marine diesel engines for fuel consumption and emission reduction, better control of the performance of the engine or its components, increasing the energy efficiency of the ships, better description of the internal phenomena, particularly ignition and combustion processes, adequate matching of the engine and turbocharger, enhancing the simulation models for newly delivered solutions such as engines with alternative fuels, for instance LNG, biofuels, methanol or similar, dual-fuel systems, application of hybrid propulsion systems, etc. These new needs and questions have generated a

wide series of studies and publication of their results. A systematic review on the modelling of diesel engines for simulation and control can be found in [57].

Taking into account the possibilities that a mean-value model can bring to the research, which needs a model of the engine as part of a wider range model, recently more attention has been paid to this type of model; see, for example, Lee [58], Hendricks [59], Sengupta [60], Yacoub [61], Theotokatos [62], Guzzella [63], Yum [64], Scappin [65], Kharroubi [66], Baldi [67], Altosole et al. [68].

THE GOAL AND STRUCTURE

The main goal and new dimension of this paper is delivering a simple and practical method that can be rapidly applied for adjusting the parameters of a mean-value zero-dimensional model of a marine diesel engine without any need for access to the detailed, time-consuming and costly data that are taken from stand test results or have probably been recorded for a real installed engine on board a ship. This should enable researchers and engineers to identify the necessary parameters of the mathematical model and also verify the results based on the publicly available data in the project guides.

The structure of the paper is as follows: first, a general framework of a zero-order mean-values analytical model of a marine diesel engine is established and presented. Next, it is shown in a stepwise manner how to adjust the model parameters for a wide engine operational range, from 10% to 100% of MCR. Then, the parameter adjustment method is applied for a selected marine diesel engine, MAN-B&W 8S65ME-C8. Finally, the results of simulation are verified based on the available steady-state characteristics to check the accuracy of the adjusted parameters.

THE MEAN-VALUE MATHEMATICAL MODEL OF MARINE DIESEL ENGINE

The main components of a marine diesel engine are the turbocharger, charge air cooler, inlet air manifold or receiver, cylinders, fuel supply mechanism and exhaust gas receiver. This is shown in Fig. 1. Air is taken by the compressor of the turbocharger at point 0 at atmospheric pressure and temperature (p_{at} and T_{at}) and is compressed and delivered to a charge air cooler by passing point 1 to reduce the temperature, increase the density and enable the cylinders to be supplied with a larger amount of air. After passing point 2, the accumulated air in the inlet air manifold (or receiver), which can be integrated into the charge air cooler, has the mass and temperature indicated by m_{am} and T_{am} , respectively. The cylinders are charged by the compressed air and the fuel, where the latter can be identified by the mass fuel rate, \dot{m}_f , induced by the fuel rack, X_f . As a result, the engine torque M_e is delivered to the connecting shaft at the angular velocity of ω . After combustion, the exhaust gases pass point 4 and accumulate at the exhaust gas receiver. The mass and temperature of the exhaust gases in this receiver

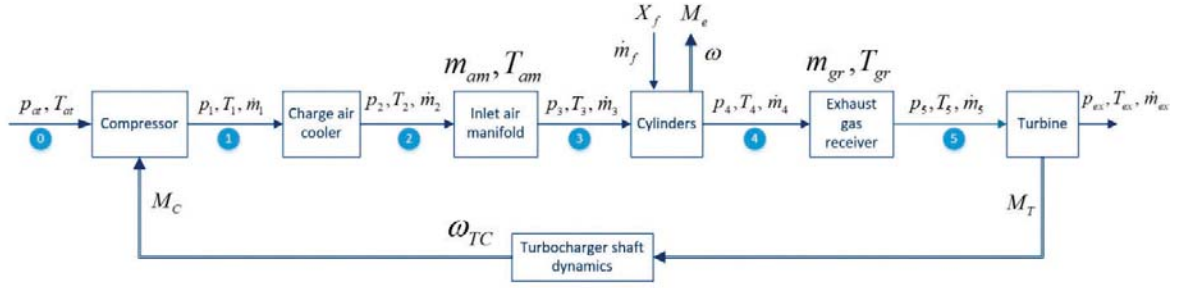


Fig. 1. Schematic illustration of a marine diesel engine's components and its variables at different points

are m_{gr} and T_{gr} , respectively. Next, the exhaust gases rotate the turbine of the turbocharger to generate the required power by the compressor. The turbine torque, M_T , and compressor torque, M_C , are equal at steady states, but during unsteady states the difference between them causes changes in the angular velocity of the turbocharger shaft, ω_{TC} , based on Newton's second law of angular motion. The pressures, temperatures and mass flow rate of air or exhaust gases at each point are indicated by p , T , and \dot{m} with a lower index that reflects the number of the considered point.

The following assumptions have been applied:

1. The losses in the flow rates due to leakages are negligible.
2. The pressure, temperature and specific volume at point 3 have the same respected values as in the intake air manifold.
3. The inlet air pressure and its mass flow rate are not changed between points 2 and 3, and the air cooler changes only the temperature of the air.
4. The pressures at points 4 and 5 are equal and are the same as the pressure of the exhaust gas receiver.
5. The temperature and specific volume of the exhaust gases through the turbine are not changed and are the same as the respected values for the exhaust gas receiver.
6. Both the air and exhaust gases are assumed to be semi-ideal gases.

These assumptions reduce the number of state variables, when the required accuracy of the simulation results can be satisfied with no significant deviation in comparison to the real case.

TURBINE

Mass flow rate of exhaust gases into the turbine

The mass flow rate of exhaust gases into the turbine can be modelled as an isentropic ideal gas flow through a converging-diverging nozzle with an equivalent cross-section area of A_T^* :

$$\dot{m}_5 = A_T^* \cdot \psi_T \cdot \sqrt{P_{gr} \cdot \rho_{gr}} \quad (2)$$

Hence ψ_T is the turbine flow function, which depends on the adiabatic exponent (heat capacity ratio), κ_T :

$$\psi_T(\pi_T) = \begin{cases} \left[\frac{2\kappa_T}{\kappa_T - 1} \left(\pi_T^{\frac{2}{\kappa_T}} - \pi_T^{\frac{\kappa_T + 1}{\kappa_T}} \right) \right]^{\frac{1}{2}} & ; \quad \pi_T \geq \pi_{Tcr.} \\ \left[\kappa_T \cdot \left(\frac{2}{\kappa_T + 1} \right)^{\frac{\kappa_T + 1}{\kappa_T - 1}} \right]^{\frac{1}{2}} & ; \quad \pi_T < \pi_{Tcr.} \end{cases} \quad (3)$$

where

$$\pi_{Tcr.} = \left(\frac{2}{\kappa_T + 1} \right)^{\frac{\kappa_T}{\kappa_T - 1}} \quad (4)$$

A_T^* is the equivalent cross-sectional area of the flow, which is a variable parameter and depends on the exit angle of the flow from the nozzle (here turbine) and the turbine pressure ratio, π_T :

$$\pi_T = \frac{p_{ex}}{p_{gr}} \quad (5)$$

where p_{ex} is the exhaust gases pressure after the turbine at the exit point and p_{gr} is the pressure of gases at the exhaust gas receiver.

Eq. (2) is suitable for an isentropic flow. For a real case there are two different possibilities to calculate the flow rate. The first one, based on [69], considers the cross-sectional area of the flow as a function of the geometrical value of this area, A_T , and a correcting coefficient, a_T , which depends on the pressure ratio of the turbine, π_T , and the velocity ratio, $\frac{u}{c_s}$, as follows:

$$A_T^* = a_T A_T \quad (6)$$

$$a_T = a_T \left(\pi_T, \frac{u}{c_s} \right) \quad (7)$$

$$u = r_{Tavg} \cdot \omega_{TC} \quad (8)$$

$$c_s = \left[\frac{2\kappa_T}{\kappa_T - 1} R_{gr} T_{gr} \left(1 - \pi_T^{\frac{\kappa_T - 1}{\kappa_T}} \right) \right]^{\frac{1}{2}} \quad (9)$$

In these relationships u stands for the turbine blade tip speed and c_s is the exhaust gases velocity under the isentropic condition and $r_{T\,avg}$ is the average radius of the turbine blades.

The second method, which is applicable in the absence of enough test results, considers A_T^* as a function of the same above-mentioned variables, which can be represented by the engine operating point, and then the equivalent cross-sectional area can be determined by using steady-state data for the given operating point.

Turbine energy balance

The power of the turbine is:

$$P_T = \dot{m}_5 \cdot (h_5 - h_{ex}) \quad (10)$$

where h stands for the enthalpy of the gases. Assuming the exhaust gases as semi-ideal gases, then this equation can be rewritten as follows:

$$P_T = \dot{m}_5 \cdot (c_{p5} \cdot T_5 - c_{pex} \cdot T_{ex}) \quad (11)$$

where c_p indicates the heat capacity at constant pressure. The isentropic temperature at the end of the expansion process after the turbine is:

$$T_{exs} = T_5 \cdot \pi_T^{\frac{\kappa_T - 1}{\kappa_T}} \quad (12)$$

By including the internal/adiabatic efficiency of the turbine for a real expansion process, this temperature in reality should be reduced as presented below:

$$T_{exs} = T_5 - \eta_T \cdot (T_5 - T_{exs}) \quad (13)$$

As a conclusion of the above equations, we get:

$$P_T = \dot{m}_5 \cdot \eta_T \cdot \frac{\kappa_T}{\kappa_T - 1} \cdot R_5 \cdot T_5 \cdot \left[1 - \pi_T^{\frac{\kappa_T - 1}{\kappa_T}} \right] \quad (14)$$

in which the gas constant and temperature at point 5 can be considered equal to the respected values for the exhaust gas receiver.

By excluding the heat exchange at the exhaust gas receiver, it is possible to assume that the temperature of the exhaust gases at point 5 and inside the exhaust gas receiver is the same. Therefore, the temperature of the exhaust gases at the outlet from the turbine is:

$$T_{ex} = T_{gr} - T_{gr} \eta_T \left[1 - \pi_t^{\frac{\kappa_t - 1}{\kappa_t}} \right] \quad (15)$$

In these calculations, it is assumed that a constant pressure exhaust gas receiver is applied, which today is a usual solution. For an impulse exhaust gas receiver, additionally a correction factor which has a higher value than one should be included, based on the experimental tests or using 3D CFD simulations.

Internal efficiency of the turbine

The static characteristic of the turbocharger is to be illustrated by the manufacturer. In this case, the turbocharger which consists of the compressor and turbine is considered as a unique element and its overall efficiency, η_{TC} , including the silencer pressure losses and the difference between the compressor and turbine mass flows, has been plotted against the pressure ratio of the compressor, π_C . This overall efficiency of the turbocharger, η_{TC} , can be approximated as a second-order polynomial function at steady states (see Fig. 2):

$$\eta_{TC} = \eta_T \cdot \eta_C = a_{TC} + b_{TC} \cdot \pi_C + c_{TC} \cdot \pi_C^2 \quad (16)$$

and then the turbine efficiency can be determined:

$$\eta_T = \frac{\eta_{TC}}{\eta_C \cdot \eta_{TM}} \quad (17)$$

where η_C is the compressor's adiabatic efficiency and can be specified based on the compressor map (which will be discussed later) and η_{TM} is the mechanical efficiency of the turbine.

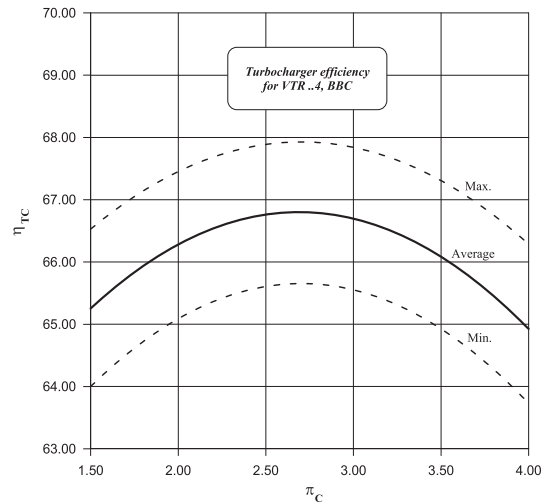


Fig. 2. Example of overall efficiency of the turbocharger [70]

Pressure ratio of the turbine

In order to specify π_T , it is necessary to express the exhaust gases pressure before and after the turbine, p_5 and p_{ex} . In many related references, p_{ex} has been considered equal to the ambient pressure, p_{at} and p_5 equal to the exhaust gas receiver pressure, p_{gr} . Although it is an alternative solution in the case of an absence of data, due to installation of the silencer and pressure drops in practice, there is a difference between these two sets of pressures

COMPRESSOR

Mass flow rate of air into the compressor

The mass flow rate of air through the compressor is a function of the angular velocity of the turbocharger shaft, ω_{TC} , the compressor pressure ratio, π_C , and the inlet air temperature:

$$\dot{m}_1 = \dot{m}_1(\omega_{TC}, \pi_C, T_0) \quad (18)$$

The most suitable way to determine the value of this function is by using the exact compressor map or similar scaled maps identified based on measurement or empirical relationships. The numerical modelling of the compressor map can be done using different approximation methods, supported by interpolation and extrapolation tools.

Ferenc, [15], has proposed the expression of the volumetric flow rate of the compressor, $\dot{v}_C(\omega_{TC}, \pi_C)$, by its approximation as a partial function as presented below

$$\dot{v}_C(\omega_{TC}) = \dot{v}_{C1}(\omega_{TC}) + \beta_{C1}(\omega_{TC}) \cdot [\beta_{C2}(\omega_{TC}) - \pi_C(\omega_{TC})]^{0.5} \quad (19)$$

hence

$$\dot{v}_{C1}(\omega_{TC}) = a_{C1} \cdot (\omega_{TC} - b_{C1}) \quad (20)$$

$$\beta_{C1}(\omega_{TC}) = a_{C2} \cdot (\omega_{TC} - b_{C2})^{-0.5} \quad (21)$$

$$\beta_{C2}(\omega_{TC}) = a_{C3} \cdot \omega_{TC}^{b_{C3}} + 1 \quad (22)$$

By the intersection of different values from the compressor map and considering three optional points of these characteristics, which have to satisfy Eq. (18), constant coefficients a_{C_i} and b_{C_i} can be determined. An example of a compressor map is presented in Fig. 3.

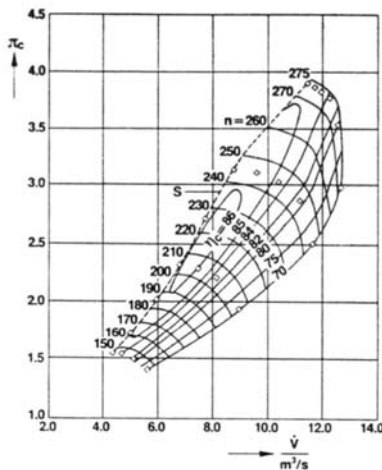


Fig. 3. Typical compressor characteristic (VTR ..4A) [70]

The compressor ratio pressure is known as the ratio of the total pressure to the ambient pressure:

$$\pi_c = (p_1/p_{at}) \quad (23)$$

when

$$p_1 = p_{am} - \Delta p_{blr} + \Delta p_{clr} + p_{dyn} \quad (24)$$

and where p_{am} is the air pressure in the scavenging air manifold/receiver, p_{at} is the ambient pressure, Δp_{blr} is the pressure increase due to the application of auxiliary blowers (if installed), p_{clr} is the pressure drop in the charge air cooler and p_{dyn} is the dynamic pressure at the compressor outlet.

The auxiliary blowers (usually one or two) operate in parallel and in series with the compressor and they are placed after the charge air cooler. p_{am} can be calculated from the mass balance and energy balance for the scavenging air manifold/receiver. For easy calculation and to prevent any iterative process, Δp_{blr} and p_{dyn} can be defined in a highly simplified form [48] as follows:

$$\Delta p_{blr} = p_{blr0} - a_{blr} (p_{am} - p_{at})^2 \quad (25)$$

and

$$p_{dyn} = a_{dyn} (p_{am} - p_{at}) \quad (26)$$

where a_{blr} and a_{dyn} are constants that should be expressed based on experimental tests or the characteristics of the auxiliary blowers and the compressor. Constant a_{blr} should be taken to give zero pressure rise at approximately 30–50% power. At higher power levels the auxiliary blowers do not operate. The constant a_{dyn} is taken to give a typical dynamic pressure at the compressor outlet.

Compressor energy balance

The power of the compressor is:

$$P_C = \dot{m}_1 \cdot (h_1 - h_0) \quad (27)$$

where h stands for the enthalpy of the inlet air. Assuming the air as a semi-ideal gas, then:

$$P_C = \dot{m}_1 \cdot (c_{p1} \cdot T_1 - c_{p0} \cdot T_0) \quad (28)$$

where the parameters of point 0 can be assumed to be the same as the atmospheric parameters. The isentropic temperature at the end of the compression process after the compressor is:

$$T_{1s} = T_{at} \cdot \pi_C^{\frac{\kappa_T - 1}{\kappa_T}} \quad (29)$$

By including the internal/adiabatic efficiency of the compressor for a real compression process, this temperature in reality should be higher:

$$T_1 = \frac{1}{\eta_C} T_{at} \cdot \pi_C^{\frac{\kappa_C - 1}{\kappa_C}} \quad (30)$$

As a conclusion of the above equations, we get:

$$P_C = \frac{1}{\eta_C} \cdot \dot{m}_1 \cdot \frac{\kappa_C}{\kappa_C - 1} \cdot R_{at} \cdot T_{at} \cdot \left[1 - \pi_C^{\left(\frac{\kappa_C - 1}{\kappa_C} \right)} \right] \quad (31)$$

The internal/adiabatic efficiency of the compressor is a function of the angular velocity of the turbocharger shaft, ω_{TC} , the compressor pressure ratio, π_C , and the inlet air temperature:

$$\eta_C = \eta_C(\omega_{TC}, \pi_C, T_0) \quad (32)$$

The adiabatic efficiency of the compressor, η_C , can be tabulated according to the exact or scaled compressor map (see Fig. 3). For values which are not mentioned in the prepared table, cubic interpolation is recommended. The total efficiency of the compressor, when in addition the mechanical losses are assumed to be independent from ω_{TC} and π_C and therefore constant, can be obtained by multiplying the adiabatic efficiency and this mechanical efficiency.

ANGULAR VELOCITY OF TURBOCHARGER SHAFT

When the power of the compressor and turbine are defined, the dynamic of the angular velocity of the turbocharger shaft can be specified:

$$J_{TC} \dot{\omega}_{tc} = M_T - M_C - M_{TCloss} \quad (33)$$

where J_{TC} is the mass moment of inertia of the turbocharger rotating parts and shaft, and M stands for the torque with lower indexes of T , C and TC_{loss} for the turbine, the compressor and the losses due to the heat dissipation and friction, respectively. The losses of the turbocharger, due to the high speed of the shaft, can be neglected or they may be adjusted based on the steady-state data by interpolation for different operating points.

CHARGE AIR COOLER

The reduction of the compressed air temperature at the inlet to the air manifold is achieved by a cooler. This is a function of the temperature of the available cooling medium and the effectiveness of the cooler, with the latter being expressed for an ideal gas as:

$$\begin{aligned} \varepsilon &= \frac{\text{actual heat transfer}}{\text{Maximum possible heat transfer}} \\ &= \frac{T_{in} - T_{out}}{T_{in} - T_w} \\ &= 1 - a_\varepsilon \cdot \dot{m}_1^2 \end{aligned} \quad (34)$$

where T_{in} and T_{out} are the air temperature before and after the cooler, respectively and T_w is the temperature of the water inflow through the cooler. The effectiveness, ε , is expressed as a function of the mass flow rate of the inlet air. As for the effectiveness, the pressure drop imposed by the cooler on the air flowing through it is expressed as a function of the mass flow rate of the inlet air, [48]:

$$\Delta p_{clr} = a_1^* \cdot \dot{m}_c^2 \frac{T_{in}}{p_{in}} \quad (35)$$

A linear relationship between the pressure drop in the cooler and the pressure of the scavenging air receiver can be considered:

$$\Delta p_{clr} = a_{clr} (p_1 - p_{at}) \quad (36)$$

Here, mass accumulation in the charge air cooler is not taken into account, when it is modelled through the scavenging air receiver/manifold.

Assuming that the cooling water temperature, T_w , is constant and the cooler efficiency, η_{clr} , is a function of the engine operating point (but constant at each point), the temperature of the compressed air after the cooler can be modelled as follows:

$$T_2 = T_1 - \eta_{clr} \cdot (T_1 - T_w) \quad (37)$$

MASS BALANCE EQUATION OF INLET AIR AND EXHAUST GASES RECEIVERS

The general equation of mass balance can be presented in the following simple form for each control volume:

$$\frac{dm}{dt} = \sum_{i=1}^n \dot{m}_i \quad (38)$$

Therefore, the continuity equations for the air mass flow rate through the intake air manifold/receiver (indicated by the lower index of am) and exhaust gases mass flow rate through the exhaust receiver (indicated by the lower index of gr) can be represented as follows, respectively:

$$V_{am} \cdot \dot{\rho}_{ia} = \dot{m}_1 - \dot{m}_3 \quad (39)$$

$$V_{gr} \cdot \dot{\rho}_{gr} = \dot{m}_4 - \dot{m}_5 \quad (40)$$

where V stands for the overall volume and ρ indicates the density.

ENERGY BALANCE EQUATION OF INLET AIR AND EXHAUST GASES RECEIVERS

The energy balance of the inlet air and exhaust gas receivers, as control volumes, expressed as the derivative of internal energy with respect to time, is as follows, [48]:

$$\frac{d(mu)}{dt} = \frac{dQ}{dt} - p \frac{dV}{dt} + \sum_{i=1}^n h_i \cdot \dot{m}_i \quad (41)$$

where m , u , p , V , Q and h are the mass, specific internal energy, pressure, volume, heat and specific enthalpy, respectively. The positive sign of the energy and mass transfer in this general equation and the further equations indicates the flow direction into the receivers.

The derivative of the internal energy is:

$$\frac{d(mu)}{dt} = m \frac{du}{dt} + u \frac{dm}{dt} \quad (42)$$

The derivative of the specific internal energy can be expressed through the temperature derivative of the fuel-to-air (or equivalence) ratio of the exhaust gas in the control volume. The internal energy is a function of the temperature and equivalence ratio:

$$\frac{du}{dt} = \frac{\partial u}{\partial T} \frac{dT}{dt} + \frac{\partial u}{\partial F} \frac{dF}{dt} \quad (43)$$

where the fuel-to-air ratio, f , is related to the equivalence ratio of exhaust gas, F , as

$$F = \frac{f}{f_{sto}} \quad (44)$$

and f_{sto} is the stoichiometric fuel-to-air ratio.

The partial derivative of internal energy with respect to temperature is the specific heat in constant volume, c_v . It can be expressed through the specific heat at constant pressure and gas constant:

$$\begin{aligned} \frac{\partial u}{\partial T} &= c_v \\ &= c_p - R \end{aligned} \quad (45)$$

hence c_p is the specific heat in constant pressure and R is the universal gas constant (8.4134 kJ/kmol K).

The partial derivative of internal energy with respect to the equivalence ratio of exhaust gas is:

$$\frac{\partial u}{\partial F} = u - u_{at} \quad (46)$$

The derivative of the equivalence ratio with respect to time can be expressed as:

$$\begin{cases} \frac{dF}{dt} = \frac{F1}{m} \left(\frac{F1}{f_{sto}} \frac{dm_{fb}}{dt} - F \frac{dm}{dt} \right) \\ F1 = 1 + F f_{sto} \end{cases} \quad (47)$$

By solving Eq. (44) with respect to the derivative of temperature and by using Eqs (42) and (43), the equation of the energy balance for a one-zero control volume can be expressed as:

$$\frac{dT}{dt} = \left[\frac{1}{m} \left(\sum \frac{dQ}{dt} + \sum h \frac{dm}{dt} - p \frac{dV}{dt} - u \frac{dm}{dt} \right) - \frac{\partial u}{\partial F} \frac{dF}{dt} \right] \frac{1}{\partial u / \partial T} \quad (48)$$

Considering that there is no change of the fuel-to-air ratio in the inlet air and exhaust gas receiver, $(dF/dt) = 0$, no change of the overall volume, $(dV/dt) = 0$, neglecting the heat exchange between the receivers' wall and the surround, $(dQ/dt) = 0$, and having that $h = c_p \cdot T$ $u = c_v \cdot T$, then the temperature time variation for each of these receivers can be rewritten as given below:

- For the intake air manifold/receiver:

$$\frac{dT_{am}}{dt} = \frac{1}{m_{am}} \left[\left(\frac{c_{p2}}{c_{vam}} \right) \cdot \dot{m}_2 \cdot T_2 - \left(\frac{c_{pam}}{c_{vam}} \right) \cdot \dot{m}_3 \cdot T_3 - T_{am} \cdot \dot{m}_{am} \right] \quad (49)$$

- For the exhaust gas receiver:

$$\frac{dT_{gr}}{dt} = \frac{1}{m_{gr}} \left[\left(\frac{c_{p4}}{c_{vgr}} \right) \cdot \dot{m}_4 \cdot T_4 - \left(\frac{c_{pgr}}{c_{vgr}} \right) \cdot \dot{m}_5 \cdot T_5 - T_{gr} \cdot \dot{m}_{gr} \right] \quad (50)$$

The mass flow rate at point 4, after the engine cylinders, i.e., \dot{m}_4 , should be determined as follows:

$$\dot{m}_4 = \dot{m}_3 + \dot{m}_f \quad (51)$$

where \dot{m}_f is the fuel mass flow rate into the engine cylinders. The pressure of the intake air and exhaust gases in these receivers can be determined as follows:

- For the intake air manifold/receiver:

$$p_{am} = \frac{m_{am} \cdot R_{am} \cdot T_{am}}{V_{am}} \quad (52)$$

- For the exhaust gas receiver:

$$p_{gr} = \frac{m_{gr} \cdot R_{gr} \cdot T_{gr}}{V_{gr}} \quad (53)$$

THE ENGINE CYLINDERS AND COMBUSTION PROCESS

For a mean-value model, it is assumed that all cylinders of the engine are shaping one block of the model. This means that instead of modelling each cylinder individually and then combining them to get the overall performance of the engine cylinders, the mean values of the variables of all the included cylinders are taken into account. The thermodynamic phases, i.e., closed cycle periods with and without combustion, exhaust or blow-down period, and valve overlap or scavenging period, as well as the inlet period, are not modelled separately. The heat exchange is considered and combustion efficiency is determined, but again as an overall process. In this case, the inputs to the cylinders are the charge air coming from the intake air manifold/receiver and the fuel mass flow rate. The outputs are the mass flow rate of the exhaust gases, engine torque, M_E , and engine shaft angular velocity, ω . Assuming that the power transmission from the cylinders to the engine shaft occurred immediately, without any time delay, then the dynamics of the engine shaft can be separately modelled by including all other moments of mass inertia related to other components of the engine and propeller shaft. Another important consideration is related to the influence of torsional vibrations of the crankshaft. These can be omitted here, because the time constant of the turbocharger and its components is much greater than the time constants determined for the dynamics of the crankshaft and engine shaft.

Mass flow rate through the engine

Similar to the model of the exhaust gases mass flow rate through the turbine of the turbocharger, here the mass flow rate of the medium through the engine can be modelled based on the flow function of a nozzle with an equivalent flow cross-sectional area. Therefore, the flow rate of the air and exhaust gases depends on the engine (cylinders) pressure ratio and it can be represented as follows:

$$\dot{m}_3 = A_{cyl}^* \cdot \psi_{cyl}(\pi_{cyl}) \cdot \sqrt{p_3 \cdot \rho_3} \quad (54)$$

where the flow function should be calculated as was mentioned in Eqs. (3) and (4) with the cylinders pressure ratio defined as follows:

$$\pi_{cyl} = \frac{p_{gr}}{p_{am}} \quad (55)$$

The equivalent cross-sectional area of the flow, A_{cyl}^* , can be assumed as a constant at a given operating point in steady states and derived from the experimental tests or calculated from the steady state characteristics delivered by the manufacturer. In unsteady states, its value can be interpolated for a quasi-steady approach. The values of the adiabatic exponent as a function of temperature, depending on the specific heats at constant pressure and constant volume for a given fuel-to-air ratio and temperature, can be determined as presented in Appendix A.

It should be noted that a part of the inlet air to the cylinders is used for blowing-down the cylinders and will not be part of the combustion process (Fig. 4).

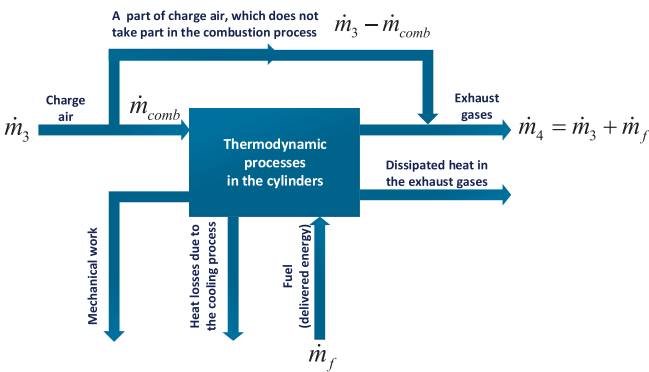


Fig. 4. Schematic diagram of mass flow and energy distribution in the engine cylinders

The fraction of air that takes part in the combustion process, \dot{m}_{comb} , can be determined by reduction of the theoretically calculated air consumed by the engine, \dot{m}_{comb_t} , using an efficiency index that applies the degree of filling the cylinders in reality in comparison to the theoretical value:

$$\dot{m}_{comb} = \eta_{cyl} \cdot \dot{m}_{comb_t} \quad (56)$$

where this efficiency, η_{cyl} , is the relation of the charge air supplied to the cylinders to the overall stroke volume of the cylinders. \dot{m}_{comb_t} can be determined as follows:

$$\dot{m}_{comb_t} = \frac{\omega}{2\pi} \cdot V_{cyl} \cdot \rho_3 \cdot Z \quad (57)$$

in which V_{cyl} is the stroke volume of one cylinder, measured from the bottom dead centre to the upper dead centre and Z is the number of cylinders. The density at point 3 can be considered as the air density in the intake air manifold/receiver, i.e.:

$$\rho_3 \approx \frac{R_{am} T_{am}}{p_{am}} \quad (58)$$

Based on [8], the filling efficiency is an inverse function of the blow-down coefficient, λ_b . This coefficient has been defined in national or international norms. For example [71] defines this efficiency as the ratio of the delivered mass of air to a cylinder within one working cycle to the trapped air mass in the cylinder:

$$\lambda_b \approx \frac{\dot{m}_3}{\dot{m}_{comb_t}} \quad (59)$$

hence:

$$\eta_{fill} = 1 - \exp(-k_b \cdot \lambda_b) \quad (60)$$

in which k_b is a constant that can be identified experimentally or determined based on the engine operational performance in steady states.

By considering the last five equations, \dot{m}_{comb} can be specified as follows:

$$\dot{m}_{comb} = \frac{\omega}{2\pi} \cdot Z \cdot V_{cyl} \cdot \frac{R_{am} T_{am}}{p_{am}} \cdot [1 - \exp(-k_b \cdot \lambda_b)] \quad (61)$$

where:

$$\lambda_b = \frac{2\pi \cdot \dot{m}_3 \cdot R_{am} \cdot T_{am}}{\omega \cdot Z \cdot V_{cyl}} \quad (62)$$

The indicated engine power

Taking into account the air mass flow rate that is to be used for the combustion process and having the fuel flow rate into the cylinders, then it is possible to calculate the indicated engine power:

$$P_E = \eta_E \cdot \dot{m}_f \cdot q_f \quad (63)$$

where P_E is the engine indicated power, η_E is the thermal efficiency of the engine, and q_f is the fuel low heat calorific value. In reality, the engine thermal efficiency is a function of different variables such as the inlet air flow rate, fuel flow rate, heat exchange of the cylinder walls, engine angular velocity, etc. However, it is common practice to consider it as a function of the engine's excess air coefficient, λ . This coefficient is defined as follows:

$$\lambda = \frac{\dot{m}_{comb}}{\lambda_t \cdot \dot{m}_f} \quad (64)$$

where λ_t is the required theoretical air excess coefficient calculated for stoichiometric chemical reaction of the combustion process.

To calculate the engine thermal efficiency in steady state, when the excessive air coefficient is known, the following approximation can be taken into account, [17]:

$$\eta_E(\bar{\omega}, \lambda) = \begin{cases} \eta_{EM}(\bar{\omega}) & ; \quad \lambda \geq \lambda_M \\ \eta_{EM}(\bar{\omega}) - \beta_E \cdot [\lambda_M(\bar{\omega}) - \lambda]^{\alpha_E} & ; \quad \lambda < \lambda_M \end{cases} \quad (65)$$

Hence:

$$\eta_{EM}(\bar{\omega}) = \begin{cases} a_{E1} \cdot \bar{\omega} + b_{E1} & ; \quad \bar{\omega} \leq \Omega \\ a_{E2} \cdot \bar{\omega} + b_{E2} & ; \quad \bar{\omega} > \Omega \end{cases} \quad (66)$$

$$\beta_E(\bar{\omega}) = \begin{cases} a_{E3} \cdot \bar{\omega} + b_{E3} & ; \quad \bar{\omega} \leq \Omega \\ a_{E4} \cdot \bar{\omega} + b_{E4} & ; \quad \bar{\omega} > \Omega \end{cases} \quad (67)$$

$$\lambda_M(\bar{\omega}) = \begin{cases} a_{E5} \cdot \bar{\omega} + b_{E5} & ; \quad \bar{\omega} \leq \Omega \\ a_{E6} \cdot \bar{\omega} + b_{E6} & ; \quad \bar{\omega} > \Omega \end{cases} \quad (68)$$

where α_E, a_{Ei}, b_{Ei} ($i = 1$ to 6) and Ω are constants, expressed by the experimental tests or determined based on the steady-state performances, and index M illustrates the optimal value of each parameter at the specified angular velocity ω . The symbol $\bar{\omega}$ indicates the non-dimensional value of the engine angular velocity in relation to its maximum value.

In steady state the temperature field of the combustion chamber walls is stabilised and can be presented as a function of the angular velocity of the engine and partial excessive air coefficient. However, when a rapid load changing happens, the temperature field of the combustion chamber walls does not vary in the same way as ω and λ change. Therefore, the engine's thermal efficiency calculated for the steady state does not coincide with the dynamic test results. As a conclusion, in transient conditions the engine's thermal efficiency differs from its value in the steady state. To overcome these difficulties, a highly simplified linear model can be applied as follows:

$$\Delta \eta_E = k_{\eta_E} \cdot \Delta \lambda \quad (69)$$

and the constant k_{η_E} can be determined for each operating point at steady state and then interpolated for unsteady states. Additionally, when the engine steady-state performances are given by the manufacturer, then for a given heat calorific value

of the fuel, and by knowing the engine power, the engine's thermal efficiency at each operating point can be calculated.

Combustion and the exhaust gases parameters

The energy balance equation of the cylinders can be represented as follows:

$$\dot{h}_{air} + \dot{q}_{comb} = \dot{q}_{loss} + P_E + \dot{h}_{ex_gas} \quad (70)$$

where \dot{h}_{air} is the rate of enthalpy of the charge air used for combustion, \dot{q}_{comb} is the rate of heat release during combustion, \dot{q}_{loss} is the rate of heat losses dissipated because of the cooling process, and \dot{h}_{ex_gas} is the rate of enthalpy of exhaust gases after combustion. The enthalpy of the supplied fuel is omitted here because its value in comparison to other elements of the equation is low and negligible. The elements of Eq. (70) can be determined as follows:

$$\dot{h}_{air_comb} = \dot{m}_{comb} \cdot c_{p_3} \cdot T_3 \quad (71)$$

$$\dot{h}_{ex_gas} = (\dot{m}_{comb} + \dot{m}_f) \cdot c_{p_4} \cdot T_{comb} \quad (72)$$

$$\dot{q}_{comb} = \dot{m}_f \cdot q_f \quad (73)$$

$$\dot{q}_{loss} = k_{loss} \cdot \dot{q}_{comb} \quad (74)$$

where T_{comb} is the temperature of that part of the exhaust gases which are produced during the combustion process. The last equation indicates that the rate of heat losses because of cooling is a part of the rate of heat released in the cylinders, and the coefficient of k_{loss} is constant for each operating point at the steady states. This coefficient can be measured indirectly or determined using the steady-state performance.

By substituting the last four equations in Eq. (71), the temperature of that part of the exhaust gases which are produced during the combustion process can be determined:

$$T_{comb} = \frac{q_f \cdot \dot{m}_f \cdot (1 - k_{loss}) - P_E}{(\dot{m}_{comb} + \dot{m}_f) \cdot c_{p_4}} + T_{am} \cdot \frac{\dot{m}_{comb}}{\dot{m}_{comb} + \dot{m}_f} \cdot \frac{c_{p_{am}}}{c_{p_4}} \quad (75)$$

where the thermodynamic parameters of point 3 are assumed to be the same as in the intake air manifold/receiver.

The temperature of the exhaust gases flowing to the exhaust gases receiver at point 4 is a result of mixing of the exhaust gases produced during the combustion process and the part of the charge air that did not participate in the combustion process (Fig. 5).

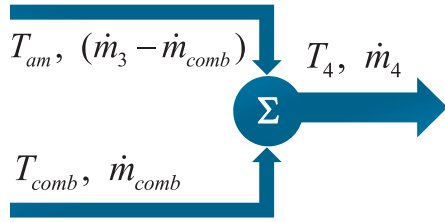


Fig. 5. The schematic diagram of the exhaust gases outflow parameters from the cylinders

The energy balance equation can then be written as follows:

$$T_4 \cdot \dot{m}_4 \cdot c_{p_4} = T_{am} \cdot (\dot{m}_3 - \dot{m}_{comb}) \cdot c_{p_{am}} + T_{comb} \cdot \dot{m}_{comb} \cdot c_{p_{comb}} \quad (76)$$

which in turn gives the following relationship for the temperature at point 4:

$$T_4 = T_{am} \cdot \frac{c_{p_3}}{c_{p_4}} \cdot \frac{\dot{m}_3 - \dot{m}_{comb}}{\dot{m}_4} + T_{comb} \cdot \frac{\dot{m}_{comb}}{\dot{m}_4} \cdot \frac{c_{p_{comb}}}{c_{p_4}} \quad (77)$$

where the heat capacity at constant pressure is to be considered the same for point 3 and the intake air manifold/receiver.

THE ANGULAR VELOCITY OF THE ENGINE SHAFT

The shafting system is modelled as a rigid body. The derivative of propeller shaft angular velocity is

$$(J_E + J_P + J_S) \cdot \dot{\omega} = M_E - (M_P + M_{loss}) \quad (78)$$

where ω is the angular velocity of the engine shaft, M indicates the torque, J stands for the mass moment of inertia, and lower indexes E , P , S and loss indicate the engine, propeller, power transmission shaft and its components, and mechanical losses, respectively.

Mechanical losses are caused by the engine reciprocating motion, rotation of the connected parts and engine-mounted and engine-driven auxiliaries. However, the main attempt in this case, at least for simulation of the dynamic behaviour of the diesel engine as a prime mover, is concentrated only on the engine, singularly. Potentially, the best method for evaluating the mechanical losses in the form of friction is to evaluate the indicated power output from an accurate cylinder pressure diagram and to subtract the measured brake power output. To do this carefully, it would be better to motor the engine, electrically. Mechanical losses can be presented in the form of either torque or mean effective pressure losses. It is recognised that the mechanical losses depend on the engine angular velocity (or mean piston speed) and the

peak cylinders pressure [72]. Although it affects the bearing loads, this effect is almost negligible. Therefore, the proposed mechanical losses in the form of the mean effective pressure can be presented as follows:

$$M_{loss} = a_l + b_l p_{peak}^{c_l} + d_l (\omega - \omega_{min})^{e_l} \quad (79)$$

where P_{peak} is the peak pressure of the cylinder, ω_{min} is the minimum required angular velocity of the engine for continuous running (minimum permissible velocity), and a_p , b_p , c_p , d_l and e_l are constants for losses calculation. If the second term of the above equation is not negligible, c_l can be considered equal to one [41]. e_l depends on the engine type and is between zero and one for a low-speed diesel engine and from one to two for a medium-speed diesel engine. Other constants should be verified based on the experimental data or steady-state performance for a given operating point. In the present study the effect of pressure is omitted, and M_{loss} is formulated as follows:

$$M_{loss} = a_l + d_l (\omega - \omega_{min}) \quad (80)$$

Hence, for modelling of the diesel engine, the problem of determining the propeller torque is not discussed here and for the sake of simplicity it is modelled as a second-order function of the engine shaft angular velocity:

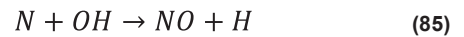
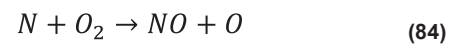
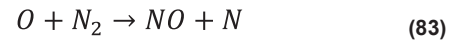
$$M_p = k_p \cdot \omega^2 \quad (81)$$

where k_p is a constant for a given operating point, which can be determined as follows:

$$k_p = \frac{N_E}{\omega^3} \quad (82)$$

NO_x EMISSION

The most important parameter affecting the generation of NO_x is the fuel-to-air equivalence ratio [73]. By considering the Zeldovich mechanism of NO_x generation:



and based on [73] the rate of formation of NO can be simplified as follows:

$$\frac{d[NO]}{dt} = \frac{6 \cdot 10^{16}}{\sqrt{T_b}} \exp\left(\frac{-69090}{T_{comb}}\right) [O_2]_e^{1/2} [N_2]_e$$

where [] denotes species concentrations in [mole/m³] and subscript stands for the equilibrium state and can be determined for a specific component of the intake air to the compressor. In the case of NO₂, it is shown that for the majority of marine diesel engines its approximate rate of

formation is usually around 10% of the rate of formation of NO [73].

THE OVERALL MODEL ALGORITHM

The considered state variables are:

1. Mass of air in the air inlet manifold/receiver, m_{am} ,
2. Temperature of air in the air inlet manifold/receiver, T_{am} ,
3. Mass of exhaust gases in the exhaust gases receiver, m_{gr} ,
4. Temperature of the exhaust gases in the exhaust gas receiver, T_{gr} ,
5. Angular velocity of the turbocharger shaft, ω_{TC} ,
6. Angular velocity of the power transmission shaft, ω ,
7. Rate of formation of NO (and NO₂)

After providing the initial values of the state variables and the mass flow rate of the fuel based on the selected operating steady point, the overall algorithm of the model for calculating the gradient of state variables is as follows:

1. Read the model parameters;
2. Determine or read the thermo-physical properties of the inlet air and the exhaust gases at different model points (see Appendix A);
3. Calculate the turbine variables:
 - i. Mass flow rate of the exhaust gases before the turbine, \dot{m}_5 , Eq. (2),
 - ii. The power of the turbine, P_T
4. Calculate the compressor variables:
 - i. The pressure after the compressor, p_1 , as well as the compressor pressure ratio,
 - ii. The volumetric flow rate and the compressor efficiency based on the similar compressor map,
 - iii. Read the correction factor of the compressor efficiency and calculate the scaled compressor efficiency, as well as the mass flow rate,
 - iv. The scaled compressor power.
5. Calculate the charge air cooler variables:
 - i. The temperature before the charge air cooler, T_1 ,
 - ii. The temperature after the charge air cooler, T_2 ,
6. Calculate the variables of the engine cylinders:
 - i. The mass flow rate of the air into the engine cylinders, \dot{m}_3 ,
 - ii. The mass flow rate of the exhaust gases after the engine cylinders, \dot{m}_4 ,
 - iii. The mass flow rate of that part of air that takes place in the combustion process, \dot{m}_{comb} ,
 - iv. The temperature of that part of the exhaust gases that are produced during the combustion process, T_{comb} ,
 - v. The temperature of the exhaust gases after the engine cylinders, T_4 ,
 - vi. The temperature of the exhaust gases after the turbine, T_{exit} ,
7. Calculate the propeller and engine torques.
8. Determine the gradients of state variables.

SETTING UP THE MODEL PARAMETERS

Generally, the model parameters should be set based on the experimental tests, empirical formulae or the available data delivered by the engine manufacturer. Here, mainly the latter is used. These are data that are publicly available. The assumption is that no additional protected or confidential data are required to set up the necessary parameters. The data should be taken from the engine project guides, turbocharger catalogues specified for the steady-state operational conditions. The widely available drawings of the engine and its components are necessary too.

The following part describes the procedure for determining or identifying the model parameters, step by step.

A. Preparing the initial data

1. Read the geometry of the engine, its cylinders, intake air manifold/receiver and exhaust gas receiver. These data should include at least the volume of the intake air manifold/receiver, the volume of the exhaust gases receiver, diameter of the cylinders, and the engine stroke. The number of cylinders should be given too. Calculate the overall volume of the cylinders:

$$V_{cyl} = \frac{\pi}{4} \cdot D_{cyl}^2 \cdot S_{cyl} \cdot Z_{cyl} \quad (86)$$

where D_{cyl} , S_{cyl} and Z_{cyl} stand for the diameter, stroke and number of cylinders, respectively.

2. Read the table of steady-state values of the engine variables at each operating point, which are given as a percent of the Service Maximum Continuous Rating. The variables should include at least the engine power, rate of rotation of the engine shaft, specific fuel consumption, exhaust gas amount and their temperature at the exit of the turbine.
3. Read the turbocharger parameters including at least the turbocharger efficiency and average radius of the compressor wheel. Additionally, having the compressor map may reduce the number of iterations in the further steps.
4. Specify the ambient conditions including pressure and temperature, and if possible the humidity.

B. Calculating the initial parameters

1. Having the efficiency of the turbocharger and the compressor map, calculate the turbine efficiency using Eq. (17). If the compressor map is not available, set the turbine efficiency between 0.85 and 0.95 respectively for SMCR between 10% and 100% and apply a linear regression. These values can be adjusted and improved for the applied turbocharger in the next trial and error step.
2. Assume the density of the exhaust gases receiver. The corresponding values for 10% of SMCR up to 100% can be linearly distributed from 1.25 kg/m³ to 1.30 kg/m³, respectively, for the first iteration. Again, they can be improved and correctly adjusted for the given engine in the next iterations.

3. Prepare a look-up table and read the values of the compressor efficiency, η_C , for different engine operating points at steady states. If the compressor map for the given engine is not available, select another but similar (as far as possible) compressor and then define a correction factor, CF , for the compressor efficiency:

$$\eta_C = CF \cdot \eta_{C_S} \quad (87)$$

where η_{C_S} stands for the similar compressor efficiency. At the beginning, the value of the correction factor can be set as equal for all operating points and it will then be modified in the further steps or iterations.

4. For the specified ambient conditions determine the parameters of the inlet air, i.e., the specific heats at constant pressure, $c_{p_{at}}$, and at the constant volume, $c_{v_{at}}$, adiabatic exponent, κ_{at} , and gas constant R_{at} ; see Appendix A.
 5. Select a charge air cooler and read the cooler efficiency. This can be considered as a constant value. For the specified ambient conditions set the temperature of the cooling water, T_w .
 6. For the applied fuel, read the low heat calorific value of the fuel, q_f .
- C. The iteration loop

For each operating point, i.e., %SMCR, which is hereafter indicated by OP , follow the procedure given below.

1. Having the temperature of the outflowing exhaust gases from the turbine, T_{ex} , (delivered by the engine manufacturer), use the following iteration method to calculate the temperature of the exhaust gases in the exhaust gases receiver:

- i. Inputs: T_{ex} , p_{at} , η_T , ρ_{gr} , \dot{m}_f and \dot{m}_{ex} ;
- ii. Calculate the fuel-to-air ratio, f :

$$f = \frac{\dot{m}_f}{\dot{m}_{ex} - \dot{m}_f} \quad (88)$$

- iii. Set $\Delta = 200$, (as an example, it should be a high enough value);
- iv. Set $T_{gl} = T_{ex} + \Delta$
- v. While $\delta > tol$ (for example: $tol = 0.01$)

- a. Calculate the adiabatic exponent, gas constant, pressure of the exhaust gases and turbine pressure ratio for temperature equal to T_{gl} and for the given fuel-to-air ratio (see Appendix A);
- b. Calculate the temperature of the outflowing exhaust gases considering $T_{gl} = T_5$:

$$T_{ex1} = T_{g1} - T_{g1} \cdot \eta_T \cdot \left(1 - \pi_T^{\frac{\kappa_{g1}-1}{\kappa_{g1}}} \right) \quad (89)$$

- c. Determine δ : $\delta = |T_{ex} - T_{ex1}|$
- d. Set $T_{gl} = (T_{gl} - \epsilon)$, where ϵ stands for the minimum temperature increment, e.g. 0.002;

End

- vi. Set: $T_{gr} = T_{gl}$.

2. Consider the temperature at point 5 equal to the temperature of the exhaust gases at the exhaust gas receiver: $T_5 = T_{gr}$.
3. Calculate the adiabatic exponent, gas constant, pressure of the exhaust gases at the exhaust gas receiver and the turbine pressure ratio for the temperature equal to T_5 and for the given fuel-to-air ratio at the specified OP (see Appendix A);
4. Calculate the mass flow rate through the turbine at point 5, \dot{m}_5 , Eqs. (2), (3) and (4);
5. Calculate the power delivered by the turbine, P_T , Eq. (14);
6. Calculate the mass of exhaust gases at the exhaust gases receiver:

$$\dot{m}_{gr} = \frac{p_{gr} \cdot V_{gr}}{R_{gr} \cdot T_5} \quad (90)$$

7. Set the pressure of the intake air manifold/receiver, p_{am} , considering that it should be higher than the pressure of the exhaust gases in the exhaust gas receiver by approximately 3% to 15% for the lowest and the highest operating point, respectively. This is an empirical result calculated for a set of selected large-stroke low-speed marine diesel engines. Here, a second order polynomial approximation is preferred, but a linear approximation should be enough too.
8. Calculate the compressor pressure ratio, π_C , Eqs. (23) to (26);
9. Having the real or similar compressor map, set and determine the compressor tip speed (the linear velocity of the compressor wheel tip) as a first- or second-order polynomial function of the OP , when the minimum value is considered for the lowest operating point;
10. Having the compressor tip speed, calculate the rate of revolution of the turbocharger shaft, ω_{TC} ;
11. Read the volumetric flow rate of the compressed air and the efficiency of the compressor from the applied or similar compressor map, \dot{v}_{C_S} ;
12. Using the volumetric flow rate of the real or similar compressor, calculate the mass flow rate of the compressed air, \dot{m}_{C_S} (see also Eq. (19)):

$$\dot{m}_{C_S} = \rho_{at} \cdot \dot{v}_{C_S} \quad (91)$$

13. Calculate the mass flow rate of the air after the compressor as follows:

$$\dot{m}_1 = \dot{m}_5 - \dot{m}_f \quad (92)$$

14. Determine the compressor efficiency by including the correction factor, see Eq. (87);
15. Calculate the initial power required by the compressor, Eq. (31);
16. Modify the correction factor as follows:

$$CF = \frac{\dot{m}_1}{\dot{m}_{C_S}} \quad (93)$$

17. Having the new correction factor, calculate the modified value of the mass flow rate of the air after the compressor by multiplying the value obtained from Eq. (91) to the correction factor;
18. Again calculate the power required by the compressor, Eq. (31), using the modified mass flow rate of the air after the compressor and consider this power as the compressor power for further calculations;
19. Calculate the temperature after the compressor, T_1 , using Eq. (30);
20. Having the temperature of the air after the compressor, it is now possible to estimate the temperature after the charge air cooler, T_2 , using Eq. (37). Additionally, for the sake of simplification and because of the relatively low temperature gradient in the inlet air manifold/receiver walls, the heat exchange can be neglected and the temperature of the inlet air to the engine cylinders, T_3 , can be assumed equal to T_2 , and then the thermodynamic parameters of the air at this temperature can be specified (Appendix A);
21. For further calculations, a simplification can be applied by considering the mass flow rate of the air after the charge air cooler, \dot{m}_2 , equal to the mass flow rate after the compressor (no losses). This mass flow rate can also be applied as the mass flow rate of the air into the engine cylinders, \dot{m}_3 . Additionally, the mass flow rate of the exhaust gases after the cylinders, \dot{m}_4 , should be equal to the mass flow rate of the inlet air into the engine cylinders added to the mass flow rate of the fuel, which is equal to the mass flow rate after the exhaust gas receiver into the turbine, \dot{m}_5 .
22. Again, by neglecting the heat exchange in the exhaust gas receiver walls, the temperature of the exhaust gases after the engine cylinders can be considered equal to the temperature of the exhaust gases after the exhaust gas receiver, i.e., $T_4 = T_5$;
23. Calculate the mass flow rate of the exhaust gases through the engine cylinders using Eq. (54) when applying Eq. (55), and the gas parameters are set for point 3 (before the engine cylinders);
24. Calculate the blow-down coefficient, λ_b , based on Eq. (62);
25. To be able to calculate k_b (the constant that should be specified for determining the combustion efficiency, see Eq. (60)), select an initial value for the filling efficiency, for instance 0.9 for all operating points. This value will be corrected for each operating point in the next loops. Then k_b is calculated as follows:
$$k_b = -\ln\left(\frac{1 - \eta_{fill}}{\lambda_b}\right) \quad (94)$$
26. Calculate the part of the air that takes part in the combustion process, \dot{m}_{comb} , using Eq. (61);
27. Calculate the engine power by applying Eq. (63);
28. To find k_{loss} , which is necessary for calculating the temperature of the part of the exhaust gases that is produced during the combustion process, T_{comb} , (see

Eq.(75)), apply the following loop for each operating point:

- i. Set: $k_{loss} = 0$; $\delta = 0$;
- ii. While $\delta \geq 0.001$ (note: 0.001 is a tolerance for accuracy of the temperature)
 - a. Calculate T_{comb} by using Eq. (75)
 - b. Calculate the thermodynamic properties of the exhaust gases at the temperature of T_{comb} and by considering the fuel-to-air ratio of the gases (Appendix A)
 - c. Calculate the nominal temperature of the exhaust gases after the engine cylinders at point 4, T_{40} , using Eq. (77);
 - d. Calculate $\delta = T_{40} - T_4$
 - e. Set $k_{loss} = k_{loss} + 1e-6$
- iii. End.

29. Determine the current mass of air in the air inlet manifold/receiver.

D. Checking process before the next loop

At the end of each iteration loop, it is necessary to check whether the calculated or adjusted parameters satisfy the basic equations in relation to each operating point at steady states. These basic equations and checking process are given below. The hierarchy of checking should be respected, e.g., it is necessary to satisfy Eq. (95) and then in the next loops satisfy Eq. (96), etc.

1.
$$P_C = P_T \quad (95)$$

If $P_C > P_T$, then the turbine efficiency, η_T , and/or exhaust gases density, ρ_{gt} , are candidates that should be increased and vice versa. The increment should be considered at a low level, for example $1e-7$, for each.

2.
$$\dot{m}_1 = \dot{m}_3 \quad (96)$$

If $\dot{m}_3 > \dot{m}_1$, then the correction factor for the compressor efficiency, CF , (see Eq. (87)) can be increased and vice versa. The increment again should be at a low level, e.g. $1e-6$.

3.
$$\begin{aligned} \dot{m}_4 &= \dot{m}_5 \\ &= \dot{m}_3 + \dot{m}_f \end{aligned} \quad (97)$$

Checking this equation, it is necessary to take into account also how the calculated exhaust gas temperature is matched to the given temperature by the manufacturers. This condition is affected by Eq. (75) and the coefficients included in this equation. The latter can be adjusted by fitting the filling efficiency to the adequate value.

4.
$$P_E = P_P \quad (98)$$

If $P_P \neq P_E$ then k_p in Eq. (82) should be adequately corrected.

CASE STUDY

The case selected for modelling and analysing is a MAN-B&W 8S65ME-C8.5 low-speed diesel engine. The Service Maximum Continuous Rating (SMCR) for the considered ship is set at 19433 kW @ 92.8 rpm.

The steady-state performance of the engine and necessary engine drawings can be taken from the Computerized Engine Application System (CEAS). The general features of the engine are given in Table 1. The engine performance at steady states at different operating points from 10% to 100% of SMCR is given in Table 2 and important variables are illustrated in Fig. 6.

Table 1. The general features of the selected engine (MAN-B&W 8S65ME-C8.5), [74, 75]

IMO Tier Regulation	Tier II
Catalogue	Official catalogue
Fuel Injection Concept	DI (Diesel)
Engine Category	ME
Turbocharger Efficiency	High
SFOC Optimized Load Range	High load
Fuel Sulphur Content	Low sulphur (0.5%)
Scrubber Installation	Installed
Total Brake Pressure of Exhaust System (Tier II Total Back Pressure [mbar])	30
SMCR Speed [rpm]	92.8
SMCR Power	9433 [kW]
Normal Cont. Rating (NCR)	100
Engine Cooling System	Fresh water
Custom Ambient Condition	ISO
Propeller Type	FPP
Hydraulic System Oil	Common
Hydraulic Power Supply	Mechanical
Turbocharger Lubrication	Common
Hydraulic Control System	Unified
Cylinder Lubrication	MAN B&W Alpha
Turbocharger	MAN B&W High Eff. TCA88
LCV for Fuel Oil [kJ/kg]	42707
Steam Pressure [bar]	7

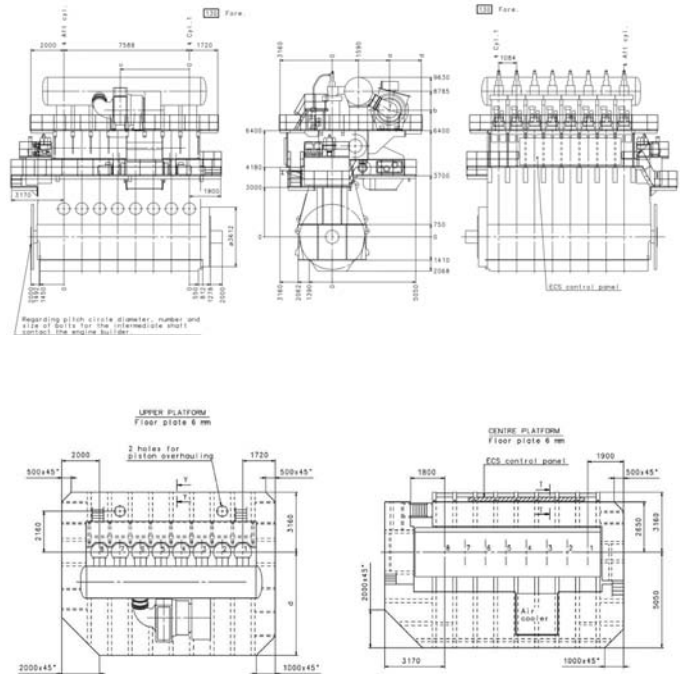


Fig. 7. Outline drawings of MAN B&W 8S65ME-C8.5-TII Engine, [74, 75]

Table 3. The necessary parameters of MAN-B&W 8S65ME-C8.5-TII engine for modelling, [74, 75]

Parameter	Unit	Value
Volume of the inlet air manifold	[m ³]	26.000
Volume of the exhaust gas receiver	[m ³]	20.313
Diameter of the cylinders	[m]	0.650
Stroke	[m]	2.730
Charge air cooler efficiency	[%]	88.68
Temperature of the inlet cooling water	[°C]	25

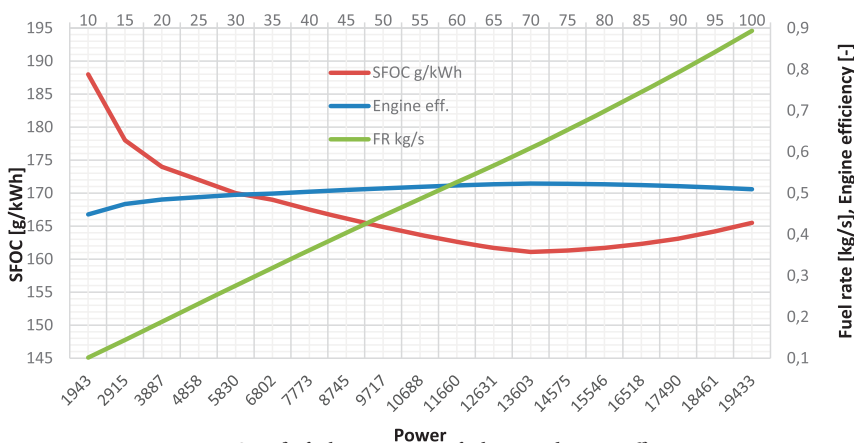


Fig. 6. Specific fuel consumption, fuel rate and engine efficiency

The geometry of the engine and its components is available from the Computerized Engine Application System (CEAS), as well as the Project Guide of the selected engine [74, 75]. Two selected drawings are shown in Fig. 7. Based on these drawings, all necessary geometric parameters of the engine can be specified. These parameters are given in Table 3.

The rate of operation, pressure ratio, efficiency, dimensions, weights, and other parameters of the MAN B&W High Eff. TCA88 turbocharger can be found in its publicly available manual and Project Guide [76]. Based on these data the average radius of the compressor wheel is 0.354 m. The compressor map with the related values is not available in the mentioned references and therefore a similar compressor, of which the map was presented in Fig. 3, is selected and then scaled for the applied turbocharger. Referring to Eqs. (19) to (22), the look-up table for the parameters \dot{v}_{C1} , β_{C1} and β_{C2} is given in Table 4

Table 2. MAN-B&W 8S65ME-C8.5 engine performance at steady states at different operating points (OP) of SMCR, [74, 75]

Load	Power	Speed	SFOC	FR	Engine eff.	Ex. gas temp.	Ex. gas amount
OP [%]	[kW]	[rpm]	[g/kWh]	[kg/s]	[-]	[°C]	[kg/s]
10	1943	43.1	188.0	0.101468	0.4485	165	9.9
15	2915	49.3	178.0	0.144131	0.4736	203	11.6
20	3887	54.3	174.0	0.187872	0.4845	219	13.9
25	4858	58.5	172.0	0.232104	0.4902	223	16.3
30	5830	62.1	170.0	0.275306	0.4959	217	19.3
35	6802	65.4	169.0	0.319316	0.4989	259	18.7
40	7773	68.4	167.5	0.36166	0.5033	251	21.2
45	8745	71.1	166.1	0.403485	0.5076	242	23.7
50	9717	73.7	164.9	0.445093	0.5113	234	26
55	10688	76.0	163.7	0.486007	0.5150	228	28.2
60	11660	78.3	162.6	0.526643	0.5185	224	30.4
65	12631	80.4	161.7	0.567342	0.5214	221	32.4
70	13603	82.4	161.1	0.608734	0.5233	220	34.4
75	14575	84.3	161.3	0.653041	0.5227	220	36.2
80	15546	86.1	161.7	0.698275	0.5214	221	38
85	16518	87.9	162.3	0.744687	0.5195	224	39.6
90	17490	89.6	163.1	0.792394	0.5169	228	41.2
95	18461	91.2	164.2	0.842027	0.5135	234	42.8
100	19433	92.8	165.5	0.893378	0.5094	241	44.3

Table 4. Parameters for identifying the selected compressor map

Compressor tip speed [m/s]	\dot{v}_{C1}	β_{C1}	β_{C2}
50	-5	25	1
100	-1.685006140	22.09147846	1.089617728
150	1.107917327	19.85276203	1.168744389
200	2.876162550	22.66164200	1.336188092
250	4.716031731	15.85172281	1.558461663
300	5.897304273	16.081286 0	1.870132421
350	9.25198641	9.443337977	2.267474338
400	11.78456552	6.429917587	2.809177986
425	13.16459085	4.743205422	3.156624514
450	13.89641087	5.975417504	3.518829733

To set the pressure of the intake air manifold/receiver for the first iteration, p_{am} , (Section “Setting Up the Model Parameters”, part C, Point 7) the following empirically obtained second-order polynomial is used:

$$p_{am}(OP) = (-0.00001 \cdot OP^2 + 0.0024 \cdot OP + 1) \cdot p_{gr} \quad (99)$$

To calculate the air pressure after the compressor, Eq. (24), it is necessary to adjust the pressure increase due to the application of auxiliary blowers (if installed), Δp_{blr} , pressure dropping in the charge air cooler, p_{clr} , and the dynamic pressure at the compressor outlet, p_{dyn} . Having in mind Eq. (26) and

(36), the following constants are applied, which are calculated empirically by selecting a series of the low-speed long-stroke supercharged diesel engines produced by MAN-B&W:

$a_{dyn} = 0.01$, $a_{clr} = 0.15425$ and $a_{clr} = 0$ (no blower is included in the system). The efficiency of the charge air cooler is calculated for different operating points at steady states and the average value is applied. This average value is 88.68%.

Next, by taking into account the selected compressor map, the compressor tip speed is determined as a second-order function of the operating point as follows (see Section “Setting Up the Model Parameters”, part C, Point 7):

$$u_{TC}(OP) = (0.027372 \cdot OP^2 + 6.942 \cdot OP + 20.334) \cdot p_{gr} \quad (100)$$

The filling efficiency is a function of the operating point. When no data is available, it can be considered as 0.9. However, it should be identified after adjusting k_b (see Eq. (60)) to assure that the determined temperature of the exhaust gases after the cylinders, T_d , satisfies its initiated value in respect to the steady-state data.

The data needed for calculating the NOx emissions are based on the values given in Table 5.

Table 5. Molar concentrations of elements and compounds in the atmospheric air

Gas		Average percentage share in the atmosphere [%]	Concentration [mol/cm ³]	Molar mass [g/mol]
Nitrogen	N ₂	78.084	3.48·10 ⁻⁵	28.02
Oxygen	O ₂	20.946	9.35·10 ⁻⁶	32
Argon	Ar	0.9340	4.17·10 ⁻⁷	40
Carbon dioxide	CO ₂	0.0360	1.6·10 ⁻⁸	44
Nitric oxide	NO	0.0003	1.34·10 ⁻¹⁰	30
Hydrogen	H ₂	0.0005	2.23·10 ⁻¹⁰	2

SIMULATION AND VALIDATION

The simulations are conducted for the range of 10% to 100% of SMCR, where the fuel flow rate firstly changed from the respected value for 100% of SMCR to a lower selected level decreased by 10% each time. Next, the fuel flow rate again increased from the given lower level to 100% of SMCR. The validation is checked regarding the consistency of the initial and final values, as well as the consistency of the values of variables at each operating point with the steady state data delivered by the engine manufacturer. Each of three simulation phases lasts 50 seconds. It should be noted that the simulation results presented here are for those parameters that were adjusted after the first iteration of the set-up process explained under “Setting Up the Model parameters”.

The selected variables are:

1. Fuel flow rate (input in respect to the operating point)
2. Flow rate of air after compressor
3. Flow rate of air into cylinders
4. Flow rate of air that takes part in combustion
5. Flow rate of exhaust gases after cylinders
6. Flow rate of exhaust gases into turbine
7. Temperature of air after compressor
8. Temperature of air into cylinders
9. Temperature of air that takes part in combustion
10. Temperature of exhaust gases into turbine
11. Temperature of exhaust gases after turbine
12. Pressure ratio of compressor
13. Pressure ratio of turbine
14. Tip speed of compressor wheel
15. Power of compressor
16. Power of turbine
17. Angular velocity of turbocharger shaft
18. Mass of air in intake air manifold
19. Temperature of air in intake air manifold
20. Pressure of air in intake air manifold
21. Mass of gases in exhaust gas receiver
22. Temperature of gases in exhaust gas receiver
23. Pressure of gases in exhaust gas receiver
24. Torque of propeller
25. Torque of engine
26. Power of engine
27. Angular velocity of engine shaft
28. Fuel-to-air ratio
29. Formation rate of nitric oxide

These variables have been illustrated in Figs. 8 to 14. The first figure shows the changing of the fuel flow rate as input and the other figures are the system responses. For the sake of clarity, the responses are presented only in the time interval between 40 seconds and 140 seconds. Similarly, for the turbocharger only 4 operating points were presented to keep the clarity of the figures. Moreover, as the rate of formation of nitric oxide rapidly changes in time, the figures are presented for shorter periods, when the fuel rate is changed at 50 seconds and 100 seconds.

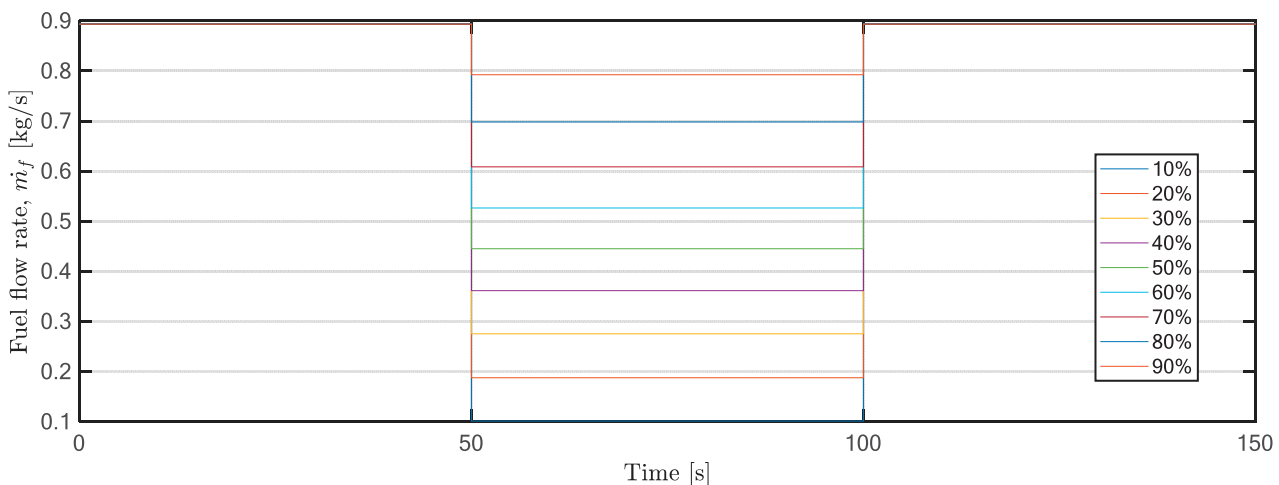


Fig. 8. Fuel flow rate as input

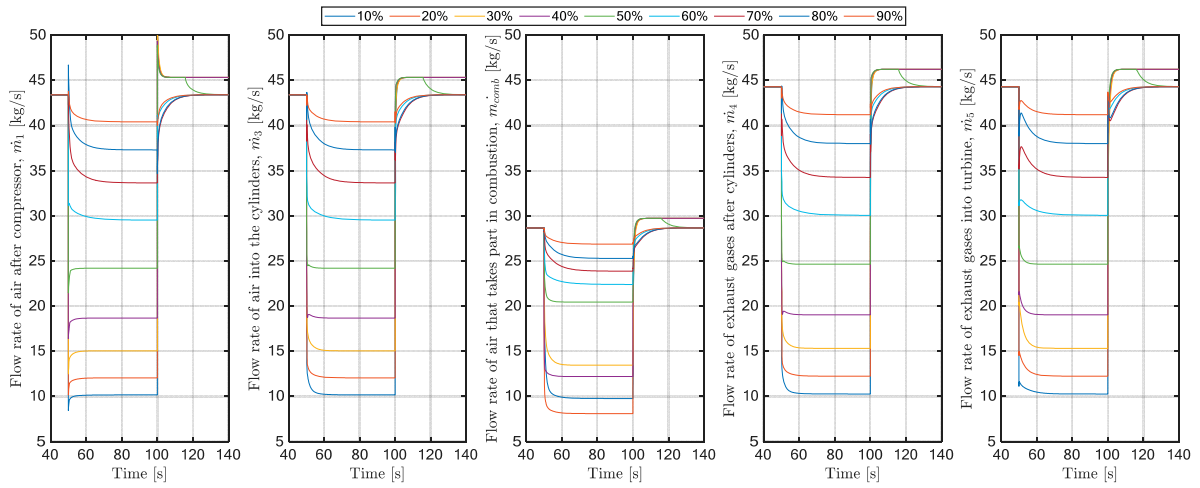


Fig. 9. Mass flow rates

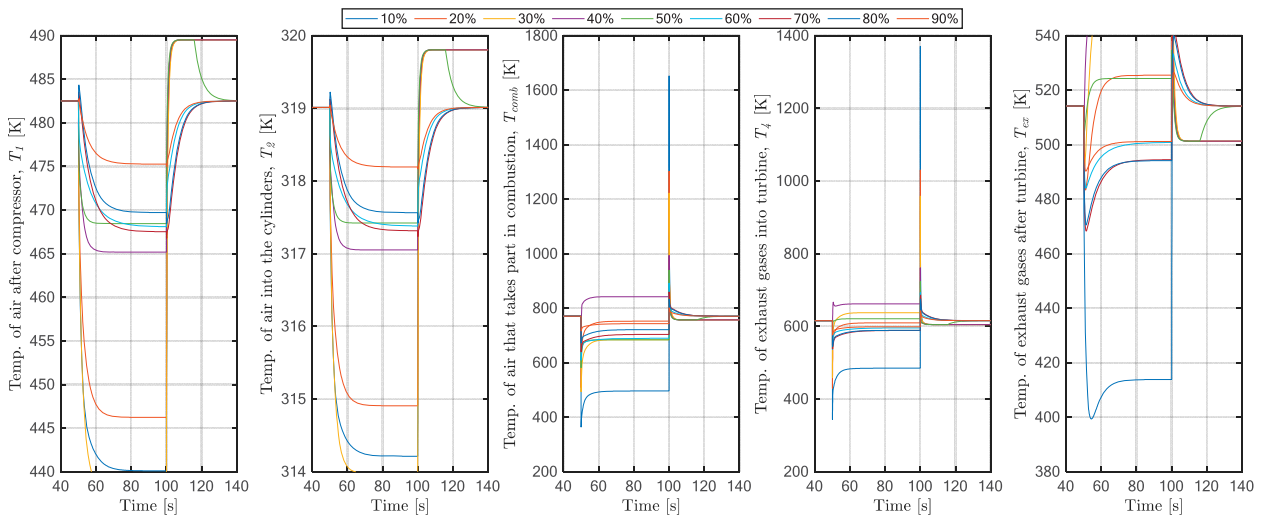


Fig. 10. Temperatures

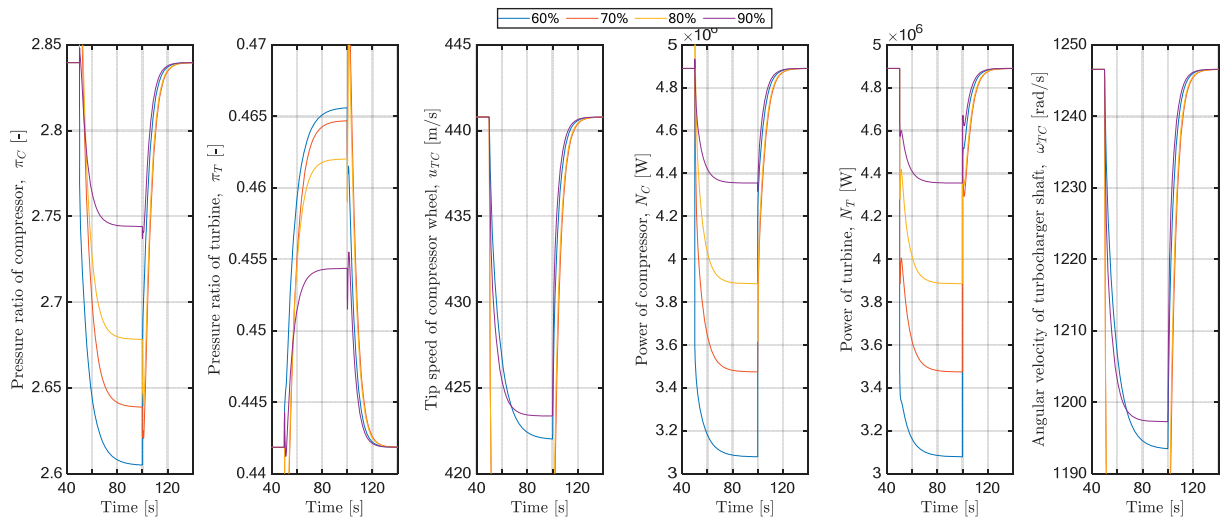


Fig. 11. Turbocharger variables for changing of fuel rate in respect of four operating points

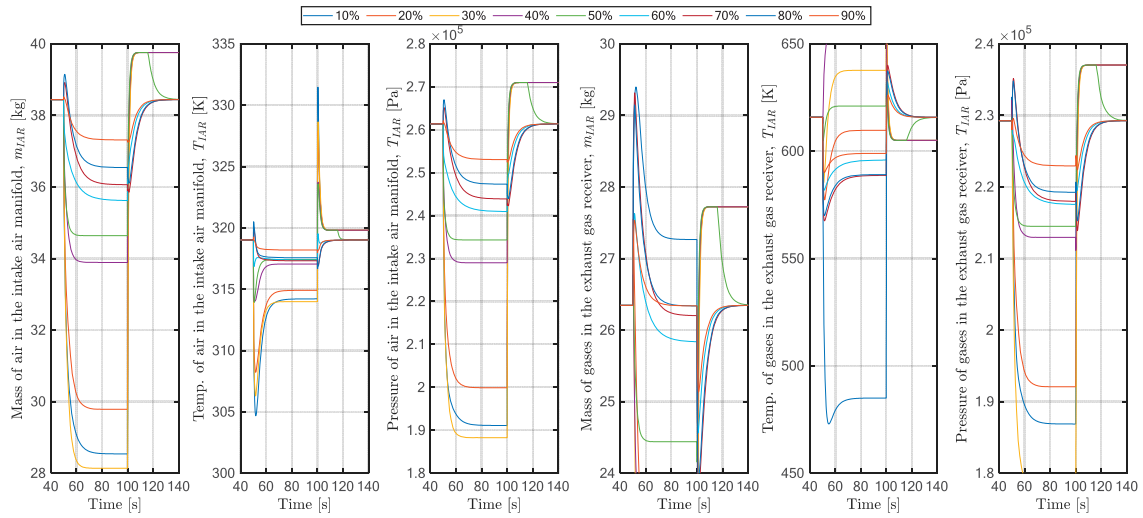


Fig. 12. Variables of inlet air manifold and exhaust gas receiver

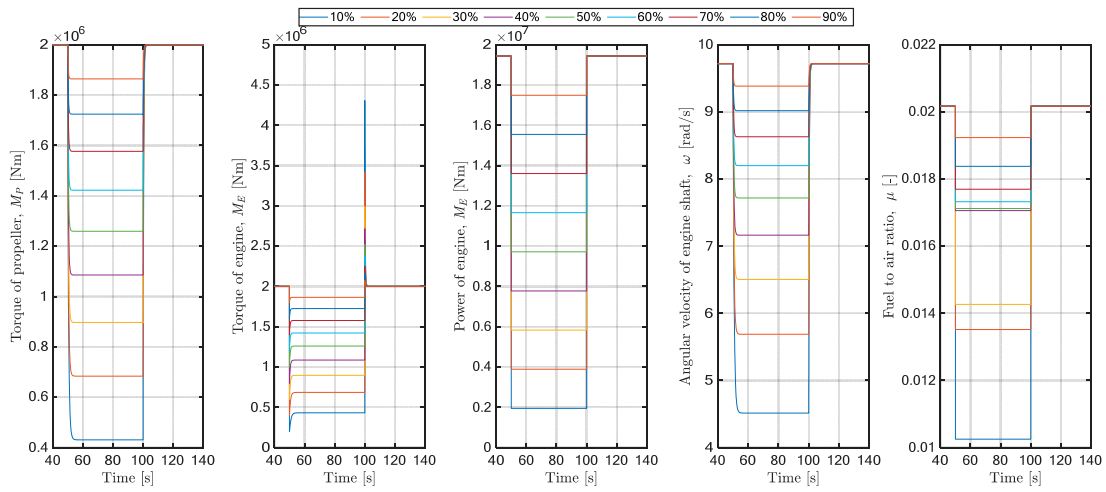


Fig. 13. General variables of engine and propeller

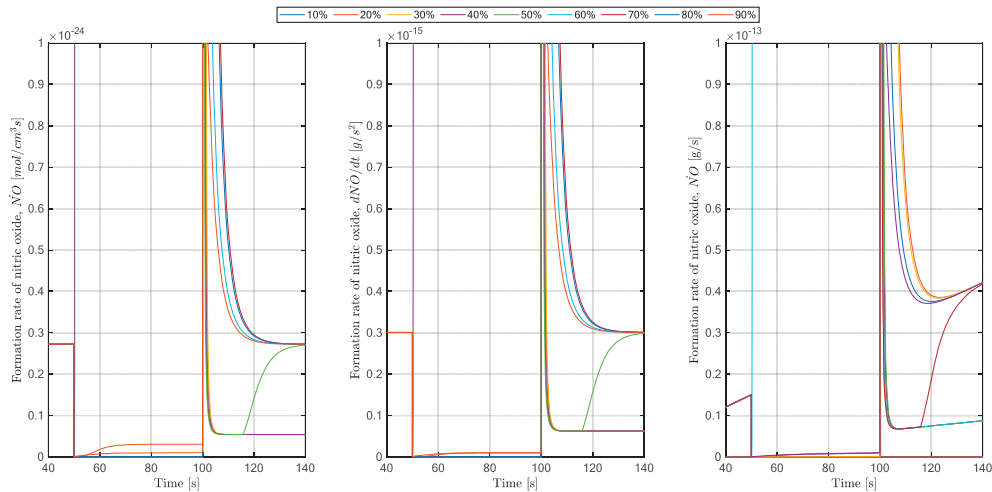


Fig. 14. Rate of formation and accumulated sum of emitted nitric oxide

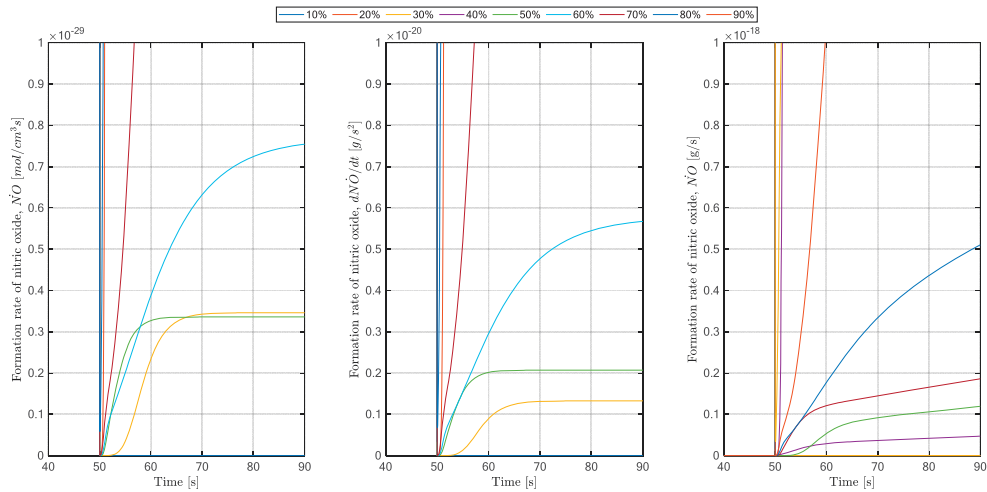


Fig. 14 (continued). Rate of formation and accumulated sum of emitted nitric oxide

To validate the result, the least accurate results, i.e. those are obtained after the 1st trial, are selected and presented, which are obtained using the adjusted system parameters after the first iteration. Based on these results, 7 variables among the 29 did not satisfy the first and the second conditions of consistency mentioned before, i.e., they do not return to the related values to 100% of SMCR at the end of simulation or their values at steady state are not equal to the respected values delivered in the engine project guide provided by the manufacturer. They are: temperature of exhaust gases after the turbine, and mass, temperature and pressure of the air in the inlet air manifold or the exhaust gases in the exhaust gases receiver. Of course, only a few variables are available from

the project guides, which can be compared to the simulation results. Three of them are shown in Fig. 15. The conditions are not satisfied only for a narrow range of operating points, between 40% and 60% of SMCR, except the temperature of exhaust gases after turbine (see Fig. 15). The values of the latter are consistent only for operating points above 50 (50% of SMCR). On the other hand, the relative error in all cases, except the temperature of exhaust gases after turbine, is not more than 4%. Therefore, it can be concluded that the applied method, even at the first iteration, gives acceptable results and the presented model and adjusted parameters are generally verified. Better results are achieved after 3rd trial but they are not presented here.

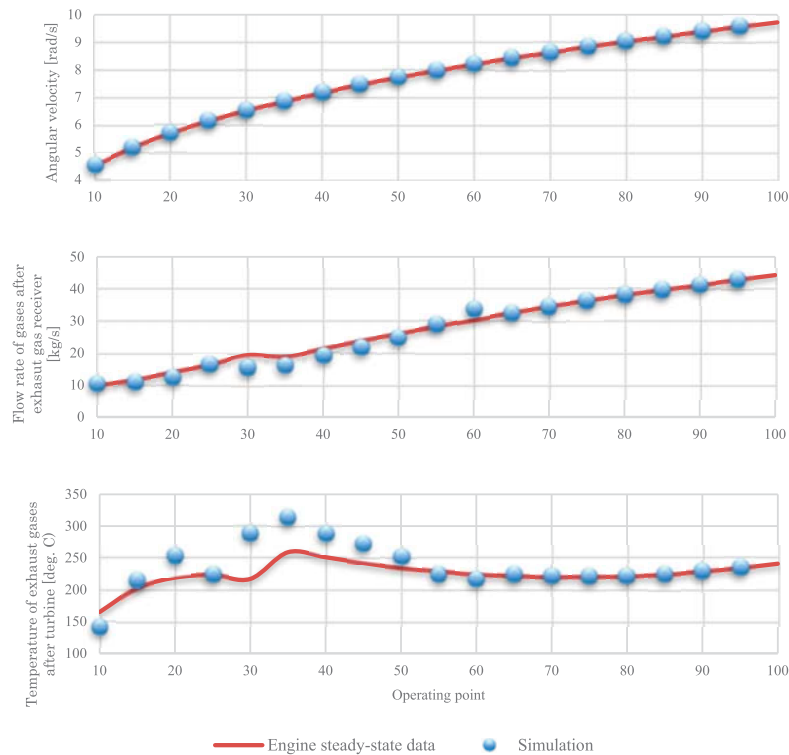


Fig. 15. Comparison of the engine steady-state data given by the manufacturer in the project guide with the simulation results

CONCLUSION

The development of a ship motion model as an overall system, with interacting subsystems such as the hull, propeller, engine and rudder, demands the use of a suitable mathematical model of the engine that is able to provide enough information not only about the torque and power but for internal events of marine diesel engines. These internal variables may have significant influences on the performance of ship propulsion systems. Different phenomena such as vibrations, emissions, structural failures and fatigue, ship control, etc. are also directly related to these variables. This requires an appropriate mathematical model of the engine. The mean-value quasi-steady zero-dimensional model seems to be the most suitable option for the mentioned investigations. However, given the lack of information to set up the parameters needed for the selected engine, it is impossible to easily imbed this type of model into the above-mentioned overall model. This paper is an answer to this need and presents how the model should be built, and its parameters can be determined using only publicly available data and without any experimental stand tests. The paper includes the fundamentals of the model, the algorithm of preparing the simulation model, and the procedure of determining the model parameters. A case study is selected and simulations are conducted. For 29 selected variables of the system the results of the simulation have been presented and then verified mainly against steady-state data. The method used for determining the system parameters is based on trial and error. However, it is shown that by using the presented method, even after the first iteration, the relative error is low. This conclusion legitimizes the use of the model and the method for further analyses, wherever rapid modelling of a marine diesel engine is needed.

REFERENCES

1. Wang F., Pulsation Signals Analysis of Turbocharger Turbine Blades Based on Optimal EEMD And TEO, Polish Maritime Research 3 (103) 2019 Vol. 26; pp. 78-86 10.2478/pomr-2019-0048.
2. Ghaemi M. H., Zeraatgar H., Analysis of Hull, Propeller and Engine Interactions in Regular Waves by a Combination of Experiment and Simulation, Journal of Marine Science and Technology, 26, pages 257–272, 2021.
3. Gu X., Jiang G., Guo Z., Ding S., Design and Experiment of Low-Pressure Gas Supply System for Dual Fuel Engine, Polish Maritime Research 2 (106) 2020 Vol. 27; pp. 76-84 10.2478/pomr-2020-0029.
4. Cepowski T., Regression Formulas for The Estimation of Engine Total Power for Tankers, Container Ships and Bulk Carriers on the Basis of Cargo Capacity and Design Speed, Polish Maritime Research, 1 (101) 2019 Vol. 26; pp. 82-94 10.2478/pomr-2019-0010
5. Yang Z., Tan Q., Geng P., Combustion and Emissions Investigation on Low-Speed Two-Stroke Marine Diesel Engine with Low Sulfur Diesel Fuel, Polish Maritime Research, 1 (101) 2019 Vol. 26; pp. 153-161 10.2478/pomr-2019-0017
6. Zeraatgar H., Ghaemi M. H., The Analysis of Overall Ship Fuel Consumption in Acceleration Manoeuvre using Hull-Propeller-Engine Interaction Principles and Governor Features, Polish Maritime Research 1 (101) 2019 Vol. 26; pp. 162-173 10.2478/pomr-2019-0018
7. Gajek J., Marine Propulsion System Simulator of a CPP (Symulator Okrętowego Układu Napędowego ze Śrubą Nastawną – in Polish), Budownictwo Okrętowe, March 1975.
8. Andersen T.E., On Dynamics of Large Ship Diesel Engine, PhD Thesis, Technical University of Denmark, 1974.
9. Roszczyk S., et al, Static and Dynamic Characteristics of Marine Generating Sets (Statyczne i Dynamiczne Własności Okrętowych Zespołów Prądotwórczych – in Polish), Wydawnictwo Morskie, Gdansk, 1976.
10. Tittenbrun S., Kowalski Z., Łastowski W. F., Characteristics of Rotational Speed Regulators of Ship Diesel Engines under the Light of Testing on Simulation Stands (Własności Regulatorów Prędkości Obrotowej Okrętowych Wysokoprężnych Silników Spalinowych w Świetle Badań na Stanowiskach Symulacyjnych – in Polish), Budownictwo Okrętowe, Dec. 1979.
11. Kowalski Z., Simulation Study of Ship Propulsion Subsystems (Badanie Symulacyjne Podsystemów Napędowych Statków – in Polish), Zeszyt Naukowe Politechniki Gdańskiej (Elektryka), No. 49, Poland, 1980.
12. Krutov V. I., Automatic Control of Internal Combustion Engines, Mir Publishers, Russia, 1987.
13. Blanke M., Andersen J. S., On Dynamics of Large Two Stroke Diesel Engines: New Results from Identification, Proceedings of 9th IFAC World Conference, Budapest, Hungary, 1984.
14. Lam W. C., Katagi T., Hashimoto T., Simulation of Transient Behaviour of Marine Medium Speed Diesel Engine, 3rd International Conf. of MCMC, Southampton, Sept. 1994.
15. Ferenc M., Numerical modeling of the Control Process of the Marine Diesel Engine with Consideration of Non-linearity (Modelowanie Numeryczne Procesu Regulacji Okrętowego Silnika Wysokoprężnego z uwzględnieniem nieliniowości – in Polish), Zeszyty Naukowe Politechniki Śląskiej, No. 567, 1978.

16. Ferenc M., Osuch W., Stokloska H., A simplified Mathematical Model of the Dynamics of a Medium Speed Diesel Engine (Uproszczony Model Matematyczny Dynamiki Średnioobrotowego Silnika Wysokoprężnego – in Polish), *Silniki Spalinowe* 4/89, Poland, 1989.
17. Ferenc M., Wideł S., Fiutkowski M., Principles for Selecting the Dynamic Characteristics of the Rotary Speed Controller for a Medium-Speed Diesel Engine Driving a Generator (Zasady Doboru Charakterystyki Dynamicznej Regulatora Prędkości Obrotowej Średnioobrotowego Silnika Wysokoprężnego Napędzającego Prądnicę, *Silniki Spalinowe – in Polish*), No. 3 '90. 1990.
18. Smith J. R., et al., Prediction of Dynamic Response of Marine System Incorporating Induction-Motor Propulsion Drives, *Proc. IEE*, Vol. 127, No. 5, Sept. 1980.
19. Taylor S. K., et al., The Predetermination of the Dynamic Response of Marine Systems Powered by Parallel Connected Gas Turbine and Diesel Generators, *CIMAC 1985*, paper D56, Oslo, 1985.
20. Ford M. P., A Simplified Turbocharged Diesel Engine Model, *Proceedings IMechE*, Vol. 201, paper D4, 1987.
21. Woodward J. B., Lattore R. G., Simulation of Diesel Engine Transient Behaviour in Marine Propulsion Analysis, Report MA-RD-940-83032, US Department of Transportation, Maritime Administration, 1983.
22. Woodward J. B., Lattore R. G., Modelling of Diesel Engine Transient Behaviour in Marine Propulsion Analysis, *SNAME Transactions*, Vol. 192, 1984.
23. Hendricks E., Chevalier A., Emerging Engine Control Technologies, Technical University of Denmark, 1985.
24. Hendricks E., Poulsen N. K., Minimum Energy Control of a Large Diesel Engine, *SAE Technical Paper Series* 861191, 1986.
25. Hendricks E., The Analysis of Mean Value Engine Models, *SAE Technical Paper Series* 890563, 1989.
26. Hendricks E., Mean Value Modelling of Large Turbocharged Two-Stroke Diesel Engines, *SAE Technical Paper Series* 890564, 1989.
27. Jansen J. P., et al., Mean Value Modelling of a Small Turbocharged Diesel Engine, *SAE Technical Paper Series* 910070, 1991.
28. Woud J. K., Boot P., Riet B. J., A Diesel Engine Model for the Dynamic Simulation of Propulsion Systems, *Schip en Werf de Zee*, Vol. 3, pp. 4-13, Jan. 1993.
29. Próchnicki W., Model Matematyczny Układu Turbozespół Dowodowający - Silnik Spalinowe Przeznaczone do Badań Zmiennych Warunków Ruchu Zespołu Napędowego Statku, *Praca Badawcza Nr. 86/93*, Wyd. O. i O., Politechnika Gdanska, Gdansk, 1993.
30. Próchnicki W., Modified System of Cooperation Between Turbocharger and Diesel Engine in Transient States, *1st International Symposium on Automatic Control of Ship Propulsion and Ocean Engineering Systems*, Gdansk, 1994.
31. Próchnicki W., Dzida M., Badania Wstępne Układu Turbozespół Doładowujący Silnik Spalinowy w Zmiennych Warunkach Ruchu Zespołu Napędowego Statku, *Praca badawcza No. 58/94*, W. O. i O., Politechnika Gdańska, Poland, 1993.
32. Kafar J., Mathematical Model of Dynamic Behaviour of a Diesel Engine in Propulsion System, *Polish Maritime Research*, No. 2/94, Poland, 1994.
33. Lan W. C., Katagi T., Hashimoto T., Quasi Steady State Simulation of Diesel Engine Transient Performance and Design of Mechatronic Governor, *Bulletin of MarEng Society of Japan*, Vol. 24, No. 1, Feb. 1996.
34. Olsen D. R., Simulation of a Free-Piston Engine with Digital Computer, *SAE Trans.*, Vol. 66, pp. 668-682, 1958.
35. Cook H. A., Analysis and Interpretation of Turbo-charged Diesel Engine Performance, *SAE Trans.*, Vol. 67, 1959.
36. Whitehouse N. D., et al., Methods of Predicting Some Aspects of Performance of a Diesel Engine Using a Digital Computer, *Proc. IMechE*, Vol. 176, No. 9, 1962.
37. Borman G. L., Mathematical Simulation of Internal Combustion Engine Processes, PhD Thesis, University of Wisconsin, 1964.
38. Streit E.E., Mathematical Simulation of Large Pulse-Turbocharged Two-Stroke Diesel Engine, PhD Thesis, University of Wisconsin, 1970.
39. Streit E.E., Mathematical Simulation of Large Pulse-Turbocharged Two-Stroke Diesel Engine, PhD Thesis, University of Wisconsin, 1970.
40. Marzouk M., Some Problems in Diesel Engine Research with Reference to Computer Control and Data Acquisition, *Proc. IMechE*, Vol. 190, No. 23/76, 1976.
41. Benson S., The Thermodynamics and Gas Dynamics of Internal Combustion Engine, Vol. I, Oxford, Clarendon Press, 1982.

42. Woschni G., Anisits F., Experimental Investigation and Mathematical Presentation of Rate of Heat Release in Diesel Engine Dependent upon Engine Operating Conditions, SAE Technical Paper Series 740086, 1974.
43. Woschni G., A Universally Applicable Equation for the Instantaneous Heat Transfer Coefficient in the Internal Combustion Engine, SAE Technical Paper Series 670931, 1967
44. Wiebe I., Halbempirische Formel für die Verbrennungsgeschwindigkeit, Velage de Akademik der Wissenschaften der VdSSR, Moscow, 1967.
45. Watson N., Marzouk M., A Non-Linear Digital Simulation of Turbocharged Diesel Engines under Transient Conditions, SAE Technical Paper Series 770123, 1977.
46. Watson N., Janota M. S., Turbocharging the Internal Combustion Engine, MacMillan Publish-ers Ltd., London, 1982.
47. Banisoleiman K., Bazari Z., Smith L. A., Mathieson N., Simulation of Diesel Engine Per-formance, Trans. IMarE, Vol. 105, pp. 117-135, 1993.
48. Larmi M. J., Transient Response Model of Low Speed Diesel Engine in Ice-Breaking Cargo Vessels, PhD Thesis, Helsinki University of Technology, Helsinki, 1993.
49. Ghaemi M. H.: Changing the Ship Propulsion System Performances Induced by Variation in Reaction Degree of Turbocharger Turbine, Journal of Polish CIMAC, Vol. 6., No.1 (2011), pages 55-70.
50. Benson R. S., Wave Action in the Exhaust System of a Supercharged Two-Stroke Engine Model, International Journal of Mechanical Science, Vol. 1, p. 253, 1959.
51. Benson R. S., et al., A Numerical Solution of Unsteady Flow Problems, International Journal of Mechanical Science, Vol. 6, pp. 117-144, 1964.
52. Benson R. S., Woods W. A., Woollat D., Unsteady Flow in Simple Branch Systems, Proc. IMechE, Vol. 178, Pt. 3I(iii), 1963/4.
53. Blair G. P., Arbuckle J. A., Unsteady Flow in the Induction System of a Reciprocating Internal Combustion Engine, SAE 700443, 1970.
54. Blair G. P., Goulburn J. R., The Pressure Time History in the Exhaust System of a High Speed Reciprocating Internal Combustion Engine, SAE 67077, 1967.
55. Blair G. P., McConnel H. J., Unsteady Gas Flow Through High Specific Output Four-Stroke Cycle Engines, SAE 740736, 1974.
56. Bazari Z., A DI Diesel Combustion and Emission Predictive Capability for Use in Cycle Simulation, SAE Technical Paper Series 920462, 1992.
57. Sujesh G., Ramesh S., Modeling and control of diesel engines: A systematic review, Alexandria Engineering Journal, Vol. 57, Issue 4, pp. 4033-4048, 2018, ISSN 1110-0168, <https://doi.org/10.1016/j.aej.2018.02.011> (<https://www.sciencedirect.com/science/article/pii/S1110016818301984>)
58. Lee B., Jung D., Kim Y. W., Physics-Based Control Oriented Mean Value Model for Diesel Combustion Process with EGR Sensitivity, Proceedings of the ASME Dynamic Systems and Control Conference, 2011, pp. 1-8.
59. Hendricks E., and Sorenson S., Mean Value SI Engine Model for Control Studies, American Control Conference, 1990, pp. 1882-1887.
60. Sengupta S., De S., Bhattacharyya A. K., Mukhopadhyay S., Deb A. K., Fault Detection of Air Intake Systems of SI Gasoline Engines using Mean Value and Within Cycle Models, 5th Annual IEEE Conference on Automation Science and Engineering, Bangalore, 2009, pp. 361-366.
61. Yacoub Y., Mean Value Modeling and Control of a Diesel Engine Using Neural Networks, Dr. of Mechanical Engineering Dissertation, West Virginia University, Morgantown, USA, 1999.
62. Theotokatos G. P., A Modeling Approach for the Overall Ship Propulsion Plant Simulation, 6th WSEAS International Conference on System Science and Simulation in Engineering, Venice, 2007, pp. 80-87.
63. Guzzella L., Onder C.H., Introduction to Modeling and Control of Internal Combustion Engine Systems, Springer, 2010.
64. Yum K. K., Modeling and Simulation of Transient Performance and Emission of Diesel Engine, NTNU - Trondheim 2012, pp. 64-68.
65. Scappin F., Stefansson S. H., Haglind F., Andreassen A., Larsen U., Validation of a zero-dimensional model for prediction of NOx and engine performance for electronically controlled marine two-stroke diesel engines, Applied Thermal Engineering, Volume 37, May 2012, Pages 344-352 2012.
66. Kharroubi K., Chen H., A Semi-Experimental Modeling Approach for a Large Two-Stroke Marine Diesel Engine Simulation, 27th CIMAC World Congress, Shanghai, China, May 13-16, 2013, Paper no. 105.
67. Baldi F., Theotokatos, G., Andersson K., Development of a combined mean value-zero dimensional model

and application for a large marine four-stroke diesel engine simulation, https://www.researchgate.net/publication/277338414_Development_of_a_combined_mean_value-zero_dimensional_model_and_application_for_a_large_marine_four-stroke_Diesel_engine_simulation

68. Altosole M., Campora U., Figari M., Laviola M., A Diesel Engine Modelling Approach for Ship Propulsion Real-Time Simulators, 2019, <https://www.mdpi.com/2077-1312/7/5/138/pdf>
69. Zimmer K., Aufladung von Verbrennungsmotoren, 1985, ISBN: 978-3-540-15902-5, <https://citations.springernature.com/book?doi=10.1007/978-3-662-05913-5>
70. Streuli A., Application of the BBC Power Turbine, BBC Brown Boveri, 1985.
71. Polish Norm PN-M-01521:1993, "Silniki spalinowe tłokowe – Terminologia".
72. Chen S. K., Flynn P., Development of a Compression Ignition Research Engine, SAE 650733, 1965.
73. Heywood J. B., Internal Combustion Engine Fundamentals, McGraw-Hill, 1988.
74. MAN-B&W Computerized Engine Application System (CEAS), <https://www.man-es.com/marine/products/planning-tools-and-downloads/ceas-engine-calculations>.
75. MAN B&W S65ME-C8.5-TII Project Guide Electronically Controlled Two-stroke Engines, online: https://www.academia.edu/35674638/MAN_B_and_W_S90ME_C8_TII_Project_Guide_Electronically_Controlled_Two_stroke_Engines
76. TCA Turbocharger, The Benchmark, online: https://turbocharger.man-es.com/docs/default-source/shopwaredocuments/tca-turbochargerf451d068cde04720bdc9b8e95b7c0f8e.pdf?sfvrsn=81b197c6_3, & Project Guide TCA Turbocharger, online: https://turbocharger.man-es.com/docs/default-source/shopwaredocuments/tca.pdf?sfvrsn=98c91c09_2.

APPENDIX A

AIR AND EXHAUST GAS PROPERTY RELATIONSHIPS

Tabulated data or algebraic expressions are required for the partial derivative of the internal energy u , with respect to the temperature and air-to-fuel ratio (and pressure, if dissociation is not to be neglected) and gas constant, R . Relationships

are required for air, combustion products and the mixture of the two. By derivative general algebraic expressions for combustion products in terms of the fuel-to-air ratio, the properties of mixtures of air or combustion products may be evaluated by using the appropriate overall value of the fuel-to-air ratio or equivalence ratio ($F=0$ for pure air).

A homogeneous mixture and equilibrium thermodynamic properties for the products of combustion are assumed. Rather than go through the full thermodynamics of combustion product calculations at each step, it is common to use algebraic expressions curve-fitted to the result of such calculations. Several algebraic expressions are available, of which one is as follows [41]:

$$u = K_1(T) - K_2(T) \quad [\text{kJ/kgK}] \quad (\text{A.1})$$

where

$$K_1(T) = 0.692T + 39.17 \times 10^{-6} T^2 + 52.9 \times 10^{-9} T^3 + -228.62 \times 10^{-13} T^4 + 277.58 \times 10^{-17} T^5 \quad (\text{A.2})$$

$$K_2(T) = 3049.39 - 5.7 \times 10^{-2} T - 9.5 \times 10^{-5} T^2 + + 21.53 \times 10^{-9} T^3 + 200.26 \times 10^{-14} T^4 \quad (\text{A.3})$$

and the gas constant is given by

$$R = 0.287 + 0.02F \quad [\text{kJ/kgK}] \quad (\text{A.4})$$

(per kg of original air).

The stoichiometric fuel-to-air ratio is 0.0676, hence the above expressions must be divided by $(1+0.0676F)$ if the value of u or R is required per unit mass of combustion products.

In Figs. A.1, A.2 and A.3, the specific heat at constant pressure, specific internal energy and specific enthalpy are plotted, respectively. Specific enthalpy was derived by integration of the specific heat. Specific enthalpy was set as zero at 298.15 K.

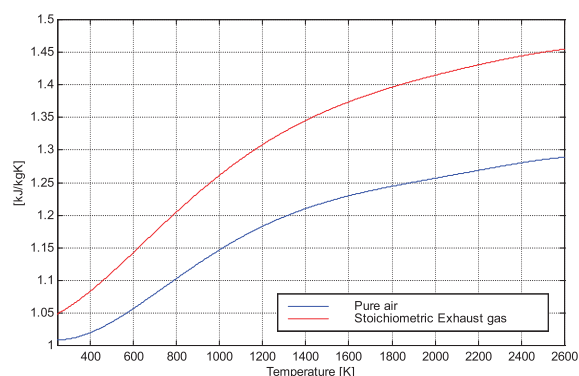


Fig. A.1. Heat capacity at constant pressure

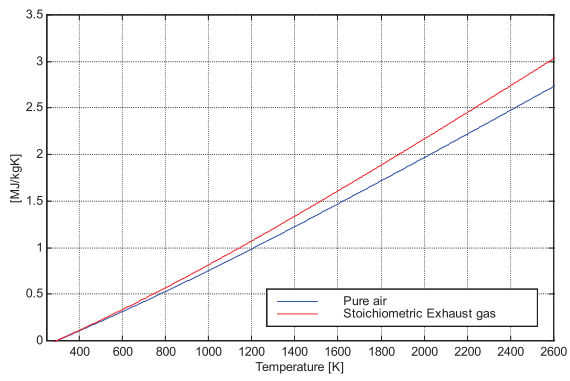


Fig. A.2. Specific enthalpy

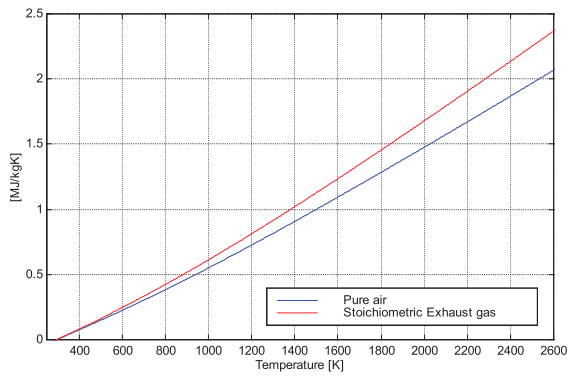


Fig. A.3. Specific internal energy

CONTACT WITH THE AUTHOR

Mohammad Hossein Ghaemi
e-mail: ghaemi@pg.edu.pl

Gdańsk University of Technology
 Narutowicza 11/12
 80-233 Gdańsk
POLAND

ANALYSIS OF THE PRE-INJECTION SYSTEM OF A MARINE DIESEL ENGINE THROUGH MULTIPLE-CRITERIA DECISION-MAKING AND ARTIFICIAL NEURAL NETWORKS

C.G. Rodriguez¹

M.I. Lamas^{*1}

J.D. Rodriguez¹

A. Abbas²

¹ University of Coruña, Spain

² Mississippi State University, USA

* Corresponding author: isabellamas@udc.es (M.I. Lamas)

ABSTRACT

The present work proposes several pre-injection patterns to reduce nitrogen oxides in the Wärtsilä 6L 46 marine engine. A numerical model was carried out to characterise the emissions and consumption of the engine. Several pre-injection quantities, durations, and starting instants were analysed. It was found that oxides of nitrogen can be noticeably reduced but at the expense of increasing consumption as well as other emissions such as carbon monoxide and hydrocarbons. According to this, a multiple-criteria decision-making (MCDM) model was established to select the most appropriate parameters. Besides, an artificial neural network (ANN) was developed to complement the results and analyse a huge quantity of alternatives. This hybrid MCDM-ANN methodology proposed in the present work constitutes a useful tool to design new marine engines.

Keywords: Marine engine, emissions, consumption, artificial neural networks, multi-criteria decision making, computational fluid dynamics

INTRODUCTION

The maritime industry is currently facing a crucial time regarding emission control, and engines have to deal with ever increasing legislative emission requirements. Special attention has been paid to NO_x emissions from marine engines mainly due to legislation imposed by the IMO (International Maritime Organization) through the MARPOL convention. The International Convention for the Prevention of Pollution from Ships (MARPOL) is the main international convention covering prevention of pollution of the marine environment by ships. It was adopted on 2nd November 1973 and has been updated through the years. Regarding air pollution, limits are established in annex VI "Prevention of air pollution from ships". Several works have been published to characterise NO_x emissions from marine engines [1-4], and both primary and

secondary NO_x reduction measures have been developed in recent years. Primary measures focus on reducing NO_x during the combustion phase, while secondary measures reduce NO_x in the exhaust gas through after-treatment devices. Both primary and secondary measures were summarised in recent reviews about emission reduction technologies for marine engines [5-7].

Engine experiments are usually expensive and time-consuming. In order to solve this issue, artificial neural networks (ANNs) have demonstrated the ability to reduce the experimentation cost and time. ANNs are computing systems inspired by the biological neural networks that constitute human brains. Such systems progressively improve their performance by a process called learning. They are able to learn complex non-linear and multivariable relationships between parameters and model nonlinear problems. The objective is to create a predictive model for the objects or

phenomena under investigation. ANNs have demonstrated great progress in recent years, and have been applied in many fields such as engineering, medical diagnosis, economics, etc. Regarding internal combustion engines, ANNs have been employed to predict different characteristics like performance, combustion, emissions, etc. in both compression-ignition and spark ignition engines [8]. Regarding compression-ignition engines, one can refer to the work of Kowalski [9], who characterised NO_x and fuel consumption from 15 and 16 inputs, respectively. Celik and Arcaklioglu [10] predicted the consumption, fuel-air equivalence ratio, and EGT, using as inputs the engine power, engine speed, and water temperature. Siami-Irdemoosa and Dindarloo [11] predicted the fuel consumption using the loading time, idle time to load, empty travel time, payload, idled empty time, and loaded travel time as inputs. Bietresato *et al.* [12] predicted the consumption and torque using the exhaust gas temperature and motor oil temperature as inputs. Goudarzi *et al.* [13] predicted the exhaust valve temperature using two temperatures at different points of the seat. Arcaklioglu and Çelikten [14] predicted the power, consumption and emissions using the injection pressure, throttle position, and speed as inputs. Nikzadfar and Shamekhi [15] used 10 engine inputs to predict consumption, torque, NO_x , and soot. Besides these works about diesel engines, other analysis can be found in the literature applied to compression-ignition engines using alternative fuels such as biodiesel [16-18], butanol [19], bioethanol [20], ethanol [21], different dual-fuel configurations [22-29], etc.

Primary measures that are commonly employed to reduce NO_x in engines involve multiple evaluation objectives which conflict with each other, *i.e.*, the improvement on one objective such as NO_x reduction sacrifices others such as emissions and/or consumption. Taking this into account, some researchers have developed multi-criteria decision-making (MCDM) models to complement ANN analyses. Prediction studies focused on ANN used together with MCDM can be found in some studies in the literature, applied to different aspects such as supplier selection for industries, failure estimations, machine selection, maintenance, etc. In these analyses, an MCDM is formulated, and ANNs are used to learn the relation among the criteria and alternatives and rank the alternatives. In engine engineering, hybrid MCDM-ANN methods can be found in the work of Tasdemir *et al.* [30], who analysed hydrocarbon emission, consumption, torque, and power using intake valve advancement and speed as inputs; Martínez-Morales *et al.* [31], who analysed NO_x emissions from the injection timing, torque, intake pressure, speed, ignition point, and throttle data; Etghani *et al.* [32], who developed a model to maximise the power and minimise the consumption and CO , CO_2 , NO_x and PM; Majumber *et al.* [33], who optimised the performance and emission parameters in a diesel engine using hydrogen in dual-fuel mode, etc.

The present work proposes a hybrid MCDM-ANN model to analyse the pre-injection pattern in the Wärtsilä 6L 46 marine engine. The data were obtained through a CFD (computational fluid dynamics) model previously validated with experimental

data. A pre-injection system was proposed to reduce NO_x emissions and the developed model was developed to analyse the most appropriate injection pattern. The effects of the pre-injection starting instant (S), quantity (Q), and duration (D) were studied.

METHODOLOGY

This section first describes the engine analysed and the corresponding CFD analysis employed to obtain the data samples necessary to train, learn and test the ANN. After that, the MCDM and ANN methodologies are addressed.

ENGINE ANALYSED AND CFD ANALYSIS

As indicated above, the present work analyses the commercial marine engine Wärtsilä 6L 46. This is a four-stroke engine with 6 in-line cylinders, and each cylinder has 2 inlet and 2 exhaust valves. The CFD analysis and validation with experimental results was developed in previous works [22-27]. The simulations were realised using the open software OpenFOAM. Turbulence was treated through the $k-\epsilon$ model. The fuel heat-up and evaporation was treated through the Dukowicz [34] model and the fuel droplet breakup through the Kelvin-Helmholtz and Rayleigh-Taylor [35] model. As a combustion model, Ra and Reitz's kinetic scheme [36], based on 131 reactions and 41 species, was employed. As the NO_x formation model, Yang *et al.*'s kinetic scheme [37], based on 43 reactions and 20 species, was employed. As the NO_x reduction model, Miller and Glarborg's kinetic scheme [38], based on 131 reactions and 24 species, was employed.

A comparison between the numerical and experimental results is illustrated in Figs. 1 and 2. Fig. 1 shows the emissions and SFC (specific fuel consumption) obtained numerically and experimentally at several loads, and Fig. 2 shows the in-cylinder pressure and heat release rate obtained numerically and experimentally at 100% load. As can be seen, both figures show a reasonable correspondence between the numerical and experimental results.

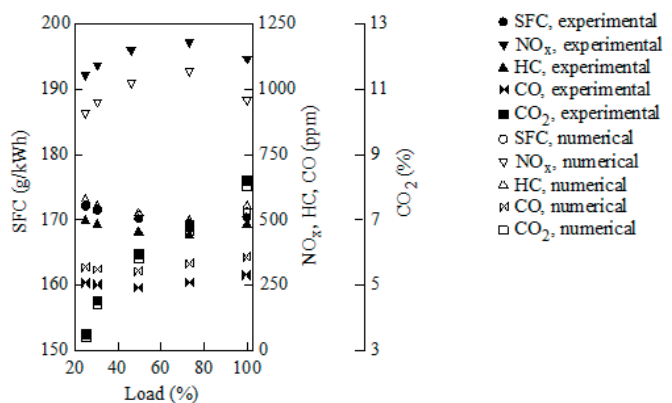


Fig. 1. SFC and emissions at different loads

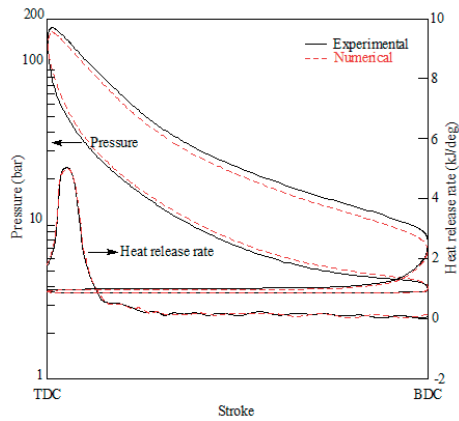


Fig. 2. In-cylinder pressure at 100% load

The data obtained through this CFD model were used as samples to train, validate and test the ANN. 180 cases were characterised through CFD using pre-injection quantities from 5 to 30%, starting instants from -23° to -18° CA ATDC (crank angle after top dead centre), and durations from 1 to 5° CA. All of these simulations were realised at 100% load and 500 rpm. Some of the results obtained for these 180 cases are illustrated in Figs. 3-6. These figures show the consumption, NO_x , CO and HC against the pre-injection quantity and starting angle using 1° injection duration, respectively. As can be seen in these figures, the NO_x emissions are reduced with increments of the pre-injection quantity and advances of the pre-injection starting instant. It is well known that NO_x is formed mainly due to the high temperatures reached during the combustion process. If these temperatures are reduced, the NO_x emissions are reduced too. Unfortunately, low combustion temperatures lead to lower power and thus higher consumption. Besides, lower combustion temperatures promote incomplete combustion, which is the main source of CO and HC emissions. According to these results, it can be seen that SFC, NO_x , CO and HC constitute conflicting criteria since none of the measures proposed in the present work are able to reduce all of them together.

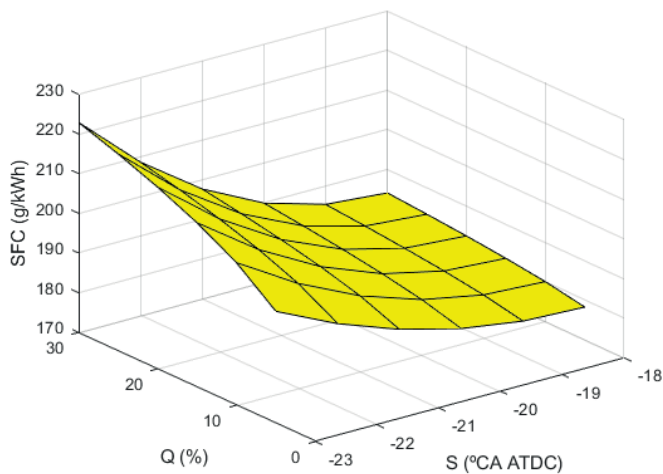


Fig. 3. Consumption against the pre-injection quantity and starting instant. 1° pre-injection duration

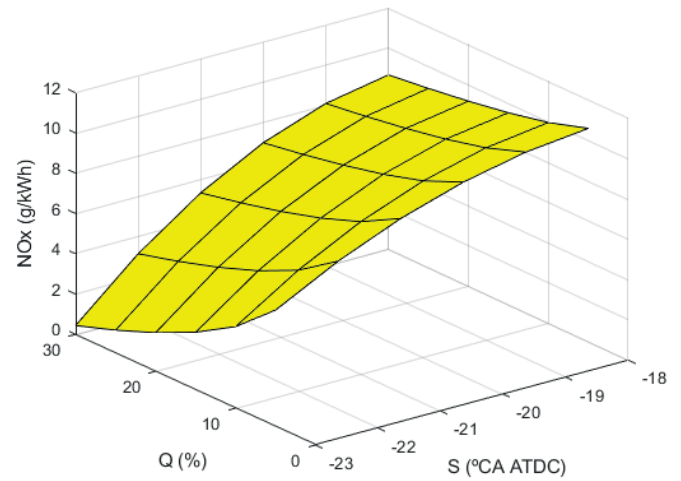


Fig. 4. NO_x emissions against the pre-injection quantity and starting instant. 1° pre-injection duration

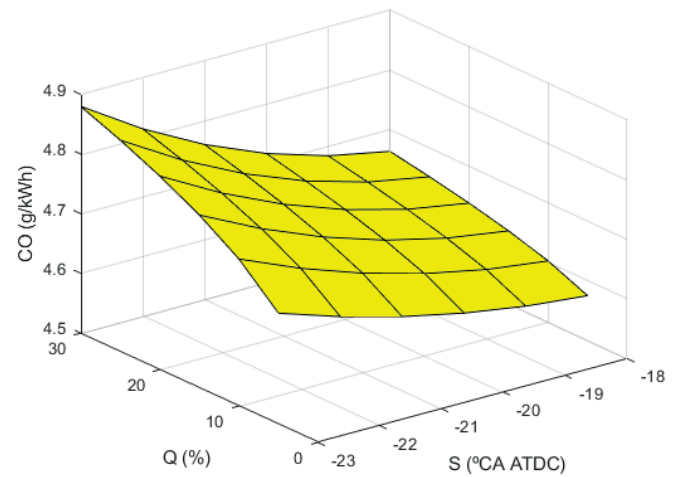


Fig. 5. CO emissions against the pre-injection quantity and starting instant. 1° pre-injection duration

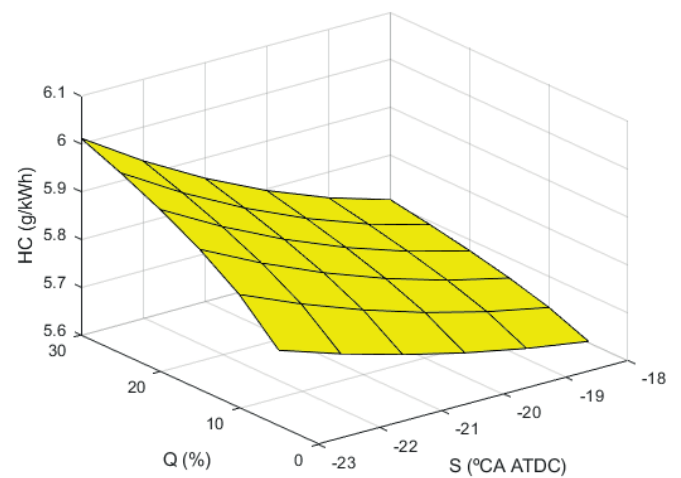


Fig. 6. HC emissions against the pre-injection quantity and starting instant. 1° pre-injection duration

MCDM ANALYSIS

Taking into account the 180 alternatives analysed through the CFD model and the four criteria considered (SFC, NO_x, CO, and HC), a 180 × 4 data matrix can be constituted with 180 rows and 4 columns. Each element X_{ij} indicates the performance of alternative i when it is evaluated in terms of the decision criterion j . This matrix is highlighted in red in Table 1. This table also shows the pre-injection starting instant, quantity, and duration corresponding to each alternative.

Tab. 1. Decision matrix

Case (i)	S (°CA ATDC)	C (%)	D (°CA)	Criterion (j)			
				$j = 1$	$j = 2$	$j = 3$	$j = 4$
				SFC (g/kWh)	NO _x (g/kWh)	CO (g/kWh)	HC (g/kWh)
1	-23	5	1	198.2	5.79	4.69	5.76
2	-23	5	2	196.3	6.25	4.71	5.78
.
.
.
180	-18	25	5	174.5	10.86	4.88	5.92

An important issue in MCDM methods consists in establishing the criteria weights, *i.e.*, the degree of importance of each criterion. Although several objective methods can be found in the literature, subjective methods are recommended since these are directly defined by experts in the field [8, 33]. In the present work, two main requirements were considered, consumption and emissions. An importance of 20% was provided for consumption and 80% for emissions. Regarding emissions, the importance of NO_x, CO and HC was also distributed equally, *i.e.*, 33.3% for each one. To summarise, these values on a per-unit basis are shown in Table 2. Logically, each column in Table 1 sums to 1 for the requirements. Regarding sub-requirements, the value of the part of the column corresponding to SFC is 1 and the part of the column corresponding to emissions sums to 1 too. The weight of each criterion is obtained by multiplying the weight of the requirement by the weight of the sub-requirement, leading to 0.5, 0.167, 0.167, and 0.167 for SFC, NO_x, CO, and HC, respectively. Logically, these weights also sum to 1. A sensitivity analysis of these criteria weights will be shown in the results section.

Tab. 2. Criteria weights, per unit basis

Requirement (α)	Sub-requirement (β)
SFC (0.5)	SFC (1)
Emissions (0.5)	NO _x (0.333)
	CO (0.333)
	HC (0.333)

Another important step consists in normalising the decision matrix. Normalisation is used to eliminate the units

of each criterion so that all the criteria become dimensionless and to set the ratings of different alternatives into the same range. Normalisation changes the different measurable values into comparable similar ones. Many normalisation techniques are available in the literature. In the present work, the so-called linear max-min normalisation technique was employed, according to which each normalised value, V_{ij} , is given by:

$$V_{ij} = 1 - \frac{X_{ij}}{X_{j,\max}} \quad (1)$$

The adequacy index was computed by the WSM (weighted sum method), according to which the adequacy index is given by Eq. (2). This procedure is also called SAW (simple additive weighting) and WLC (weighted linear combination). Taking into account the normalisation procedure applied, the most appropriate alternative is the one corresponding to the maximum AI.

$$AI_i = \sum_{j=1}^n w_j V_{ij} \quad (2)$$

where AI is the adequacy index, w_j the weight of the j -th criterion, and n the number of criteria.

ANN ANALYSIS

ANNs are structures that model human intuition by simulating the physical process upon which intuition is based, *i.e.*, the process of biological learning. In the present work the ANN was employed to obtain the adequacy index (AI) from three inputs: pre-injection starting instant, quantity, and duration. The software Matlab 2021b was used to develop the analysis. The structure of the ANN employed is shown in Fig. 7. As can be seen in this figure, the ANN has three parallel layers. The first layer, *i.e.*, the input layer, contains the three independent variables: S, Q, and D. The second layer is the hidden layer that contains the so-called hidden nodes, and the third layer is the output layer, containing the dependent variable/s. In this problem, a single variable, AI, was employed. Regarding the number of hidden layers, the general recommendation is to employ a single layer for most problems [39] [40], and multi-layered structures are only recommended for complex problems since too many hidden layers may cause memorising instead of generalising. The number of neurons in the hidden layer was established by comparing ANNs with a number of hidden neurons between 3 and 15. A low number of neurons may lead to inaccuracy and a high number to over-fitting. In this case, it was found that the ANN with 12 neurons provided the lowest error and thus this structure was selected.

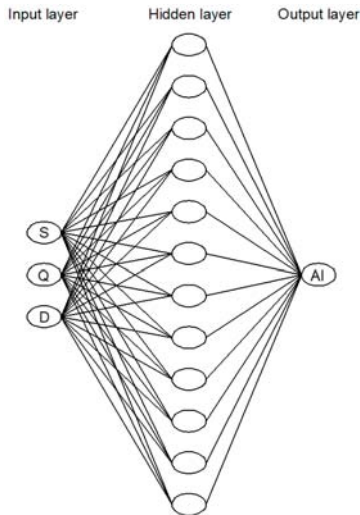


Fig. 7. ANN structure employed in the present work

As mentioned previously, 180 samples were employed and their data were obtained from CFD. 126 of these samples were used for learning, 27 for testing, and 27 for validation. Fig. 8 shows the regression results with respect to training, validation, testing, and all of them. This figure shows a satisfactory performance since $R = 0.99966$, very close to the optimum value of 1, indicating that the ANN provides an appropriate prediction accuracy.

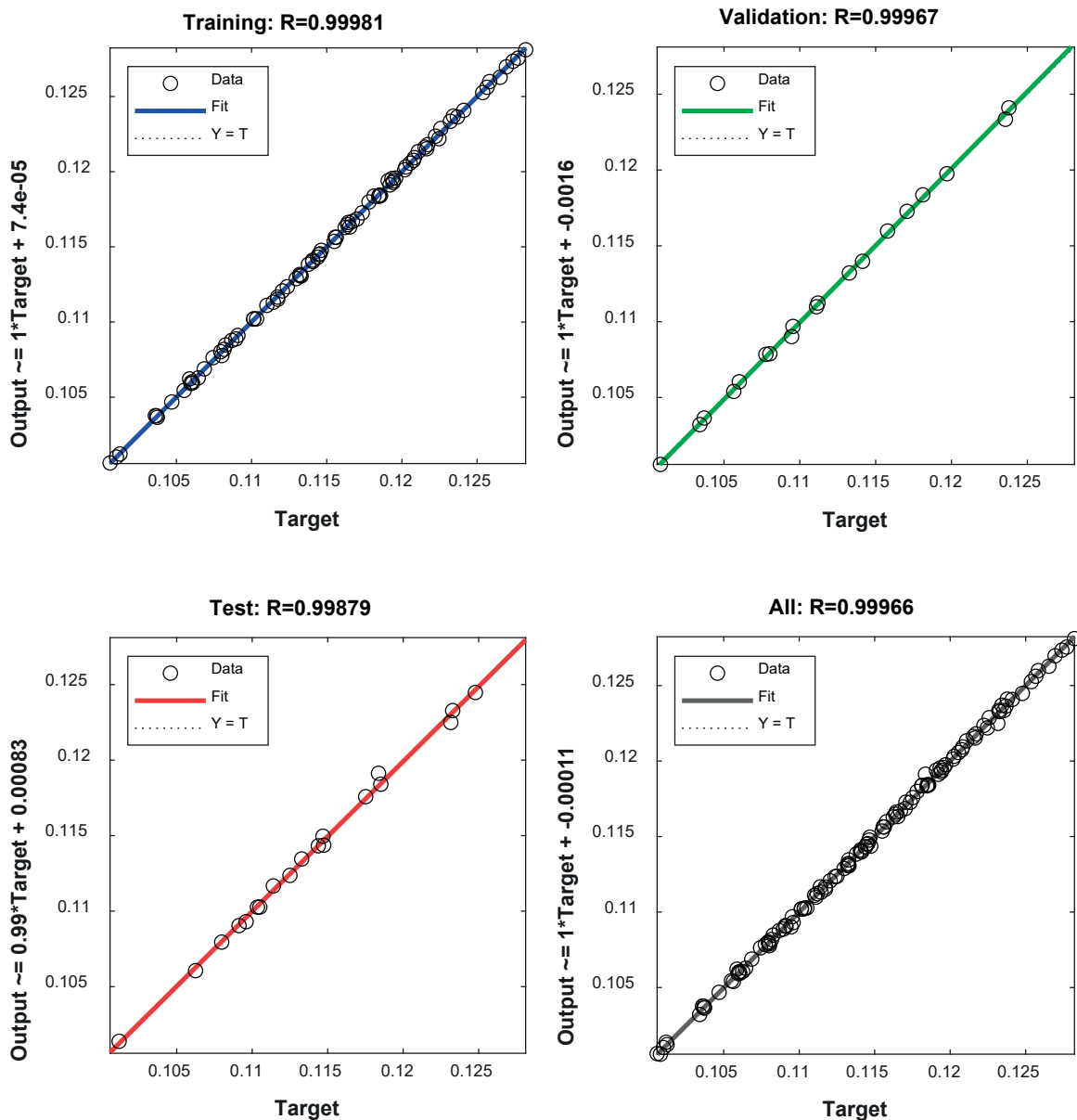


Fig. 8. Regression graphs of the ANN

RESULTS AND DISCUSSION

Fig. 9 shows the most appropriate option provided by the hybrid ANN-MCDM model, which corresponds to a -22.2° pre-injection starting instant, 25.4% quantity and 1° duration. This solution was obtained using the criteria weights shown in Table 2. It is useful to perform a sensitivity analysis of the criteria weights. According to this, Table 3 shows the most appropriate option under different weights of the consumption. In this analysis, the emissions were assigned equally with the remaining weight. As can be seen, as more importance is provided to the consumption, a lower pre-injection rate and more retarded starting instants are obtained since these effects reduce consumption. It is worth mentioning that some of the results obtained in Table 3 are not recommended in practical application despite the significant NO_x reductions obtained. A 30.5% pre-injection quantity is too high for an appropriate performance of the engine. Besides, a -23.1° starting instant is too early since the combustion must be produced after TDC. Regarding the injection duration, injections shorter than 1° were not analysed since some injectors are not able to provide these short injections.

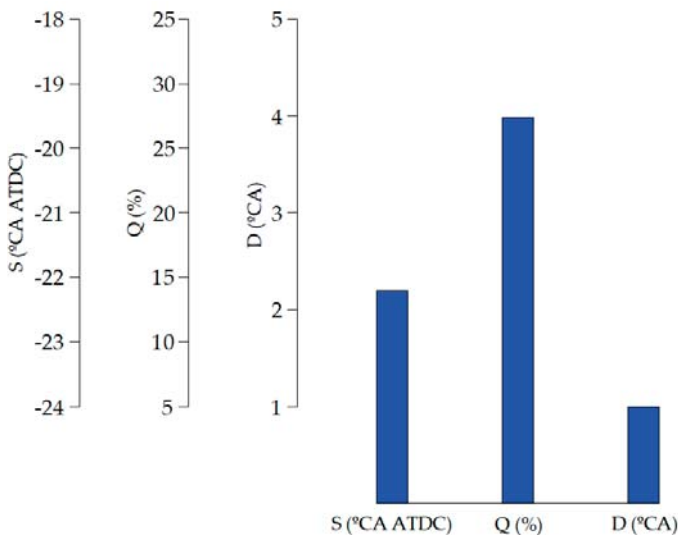


Fig. 9. Most appropriate option according to the MCDM model alone

Tab. 3. Most appropriate option under several criteria weights for the consumption according to the hybrid MCDM-ANN model

α_{SFC}	S (°)	Q (%)	D (°)
40	-23.1	28.3	1.5
45	-22.8	27.1	1.2
50	-22.2	25.4	1
55	-20.9	23.2	1
60	-18.5	19.8	1

CONCLUSIONS

This paper proposes a hybrid MCDM-ANN model to select the most suitable pre-injection pattern in the Wärtsila 6L 46 marine engine. The purpose is to reduce emissions and consumption as much as possible. The motivation comes from the ever stricter legislation, especially IMO MARPOL. The pre-injection quantity, starting instant, and duration were analysed. Since these measures have conflicting criteria on emissions and consumption, the hybrid MCDM-ANN developed in the present work model provides a tool to facilitate the selection for decision makers. The pre-injection quantity, starting instant, and duration were selected as input data for the ANN model, while the adequacy index was selected as the output data. The model is fast in application and allows the user to vary the input parameters in order to show their effects on the results.

This work provides useful information for marine engine designers. MCDM tools are becoming necessary to select between conflicting criteria, and ANN allows a huge quantity of alternatives to be analysed. Once the ANN is trained, it can be used for predicting solutions, in this case the adequacy index of each alternative. Manufacturers can find in the present study an assessment tool for designing their engines. The proposed model is applicable for a wide variety of multi-attribute decision-making problems and can be used for future ranking or selection. Future studies will focus on analysing more pollutant reduction measurements and other marine engines.

ACKNOWLEDGEMENTS

The authors would like to express their gratitude to Norplan Engineering S.L. and recommend the courses "CFD with OpenFOAM" and "C++ applied to OpenFOAM" available at www.technicalcourses.net.

REFERENCES

1. J. Kowalski and W. Tarelko, "NO_x emission from a two-stroke ship engine. Part 1: Modeling aspect," *Appl. Therm. Eng.*, vol. 29, no. 11–12, pp. 2153–2159, Aug. 2009, doi: 10.1016/j.applthermaleng.2008.06.032.
2. J. Kowalski and W. Tarelko, "NO_x emission from a two-stroke ship engine: Part 2 – Laboratory test," *Appl. Therm. Eng.*, vol. 29, no. 11–12, pp. 2160–2165, Aug. 2009, doi: 10.1016/j.applthermaleng.2008.06.031.
3. J. Girtler, "A method for evaluating the performance of a marine piston internal combustion engine used as the main engine on a ship during its voyage in different sailing conditions," *Polish Marit. Res.*, vol. 17, no. 4, Jan. 2010, doi: 10.2478/v10012-010-0033-0.

4. R. Zhao *et al.*, “A numerical and experimental study of marine hydrogen–natural gas–diesel tri-fuel engines,” *Polish Marit. Res.*, vol. 27, no. 4, pp. 80–90, Dec. 2020, doi: 10.2478/pomr-2020-0068.
5. X. Lu, P. Geng, and Y. Chen, “NO_x emission reduction technology for marine engine based on Tier-III: A review,” *J. Therm. Sci.*, vol. 29, no. 5, pp. 1242–1268, Oct. 2020, doi: 10.1007/s11630-020-1342-y.
6. S. Lion, I. Vlaskos, and R. Tacani, “A review of emissions reduction technologies for low and medium speed marine Diesel engines and their potential for waste heat recovery,” *Energy Convers. Manag.*, vol. 207, p. 112553, Mar. 2020, doi: 10.1016/j.enconman.2020.112553.
7. J. Deng, X. Wang, Z. Wei, L. Wang, C. Wang, and Z. Chen, “A review of NO_x and SO_x emission reduction technologies for marine diesel engines and the potential evaluation of liquefied natural gas fuelled vessels,” *Sci. Total Environ.*, vol. 766, p. 144319, Apr. 2021, doi: 10.1016/j.scitotenv.2020.144319.
8. A. N. Bhatt and N. Shrivastava, “Application of artificial neural network for internal combustion engines: A state of the art review,” *Arch. Comput. Methods Eng.*, May 2021, doi: 10.1007/s11831-021-09596-5.
9. J. Kowalski, “ANN based evaluation of the NO_x concentration in the exhaust gas of a marine two-stroke diesel engine,” *Polish Marit. Res.*, vol. 16, no. 2, Jan. 2009, doi: 10.2478/v10012-008-0023-7.
10. V. Çelik and E. Arcaklioğlu, “Performance maps of a diesel engine,” *Appl. Energy*, vol. 81, no. 3, pp. 247–259, Jul. 2005, doi: 10.1016/j.apenergy.2004.08.003.
11. E. Siami-Irdemoosa and S. R. Dindarloo, “Prediction of fuel consumption of mining dump trucks: A neural networks approach,” *Appl. Energy*, vol. 151, pp. 77–84, Aug. 2015, doi: 10.1016/j.apenergy.2015.04.064.
12. M. Bietresato, A. Calcante, and F. Mazzetto, “A neural network approach for indirectly estimating farm tractors engine performances,” *Fuel*, vol. 143, pp. 144–154, Mar. 2015, doi: 10.1016/j.fuel.2014.11.019.
13. K. Goudarzi, A. Moosaei, and M. Gharaati, “Applying artificial neural networks (ANN) to the estimation of thermal contact conductance in the exhaust valve of internal combustion engine,” *Appl. Therm. Eng.*, vol. 87, pp. 688–697, Aug. 2015, doi: 10.1016/j.applthermaleng.2015.05.060.
14. E. Arcaklioğlu and İ. Çelikten, “A diesel engine’s performance and exhaust emissions,” *Appl. Energy*, vol. 80, no. 1, pp. 11–22, Jan. 2005, doi: 10.1016/j.apenergy.2004.03.004.
15. K. Nikzadfar and A. H. Shamekhi, “Investigating the relative contribution of operational parameters on performance and emissions of a common-rail diesel engine using neural network,” *Fuel*, vol. 125, pp. 116–128, Jun. 2014, doi: 10.1016/j.fuel.2014.02.021.
16. K. Muralidharan and D. Vasudevan, “Applications of artificial neural networks in prediction of performance, emission and combustion characteristics of variable compression ratio engine fuelled with waste cooking oil biodiesel,” *J. Brazilian Soc. Mech. Sci. Eng.*, vol. 37, no. 3, pp. 915–928, May 2015, doi: 10.1007/s40430-014-0213-4.
17. S. Arumugam, G. Sriram, and P. R. S. Subramanian, “Application of artificial intelligence to predict the performance and exhaust emissions of diesel engine using rapeseed oil methyl ester,” *Procedia Eng.*, vol. 38, pp. 853–860, 2012, doi: 10.1016/j.proeng.2012.06.107.
18. A. Duran, M. Lapuerta, and J. Rodriguez-Fernandez, “Neural networks estimation of diesel particulate matter composition from transesterified waste oils blends,” *Fuel*, vol. 84, no. 16, pp. 2080–2085, Nov. 2005, doi: 10.1016/j.fuel.2005.04.029.
19. S. Gürgen, B. Ünver, and İ. Altın, “Prediction of cyclic variability in a diesel engine fueled with n-butanol and diesel fuel blends using artificial neural network,” *Renew. Energy*, vol. 117, pp. 538–544, Mar. 2018, doi: 10.1016/j.renene.2017.10.101.
20. H. Oğuz, I. Sarıtas, and H. E. Baydan, “Prediction of diesel engine performance using biofuels with artificial neural network,” *Expert Syst. Appl.*, vol. 37, no. 9, pp. 6579–6586, Sep. 2010, doi: 10.1016/j.eswa.2010.02.128.
21. P. Shanmugam, V. Sivakumar, A. Murugesan, and M. Ilangkumaran, “Performance and exhaust emissions of a diesel engine using hybrid fuel with an artificial neural network,” *Energy Sources, Part A Recover. Util. Environ. Eff.*, vol. 33, no. 15, pp. 1440–1450, May 2011, doi: 10.1080/15567036.2010.539085.
22. K. Çelebi, E. Uludamar, E. Tosun, Ş. Yıldızhan, K. Aydın, and M. Özcanlı, “Experimental and artificial neural network approach of noise and vibration characteristic of an unmodified diesel engine fuelled with conventional diesel, and biodiesel blends with natural gas addition,” *Fuel*, vol. 197, pp. 159–173, Jun. 2017, doi: 10.1016/j.fuel.2017.01.113.
23. N. Akkouche, K. Loubar, F. Nepveu, M. E. A. Kadi, and M. Tazerout, “Micro-combined heat and power using dual fuel engine and biogas from discontinuous anaerobic digestion,” *Energy Convers. Manag.*, vol. 205, p. 112407, Feb. 2020, doi: 10.1016/j.enconman.2019.112407.

24. S. Javed, R. U. Baig, and Y. V. V. S. Murthy, "Study on noise in a hydrogen dual-fuelled zinc-oxide nanoparticle blended biodiesel engine and the development of an artificial neural network model," *Energy*, vol. 160, pp. 774–782, Oct. 2018, doi: 10.1016/j.energy.2018.07.041.
25. S. Javed, Y. V. V. Satyanarayana Murthy, R. U. Baig, and D. Prasada Rao, "Development of ANN model for prediction of performance and emission characteristics of hydrogen dual fuelled diesel engine with *Jatropha Methyl Ester* biodiesel blends," *J. Nat. Gas Sci. Eng.*, vol. 26, pp. 549–557, Sep. 2015, doi: 10.1016/j.jngse.2015.06.041.
26. T. F. Yusaf, D. R. Buttsworth, K. H. Saleh, and B. F. Yousif, "CNG-diesel engine performance and exhaust emission analysis with the aid of artificial neural network," *Appl. Energy*, vol. 87, no. 5, pp. 1661–1669, May 2010, doi: 10.1016/j.apenergy.2009.10.009.
27. E. Uludamar *et al.*, "Evaluation of vibration characteristics of a hydroxyl (HHO) gas generator installed diesel engine fuelled with different diesel–biodiesel blends," *Int. J. Hydrogen Energy*, vol. 42, no. 36, pp. 23352–23360, Sep. 2017, doi: 10.1016/j.ijhydene.2017.01.192.
28. J. Syed, R. U. Baig, S. Algarni, Y. V. V. S. Murthy, M. Masood, and M. Inamurrahman, "Artificial neural network modeling of a hydrogen dual fuelled diesel engine characteristics: An experiment approach," *Int. J. Hydrogen Energy*, vol. 42, no. 21, pp. 14750–14774, May 2017, doi: 10.1016/j.ijhydene.2017.04.096.
29. H. Taghavifar, H. Taghavifar, A. Mardani, A. Mohebbi, S. Khalilarya, and S. Jafarmadar, "On the modeling of convective heat transfer coefficient of hydrogen fuelled diesel engine as affected by combustion parameters using a coupled numerical-artificial neural network approach," *Int. J. Hydrogen Energy*, vol. 40, no. 12, pp. 4370–4381, Apr. 2015, doi: 10.1016/j.ijhydene.2015.01.140.
30. S. Tasdemir, I. Saritas, M. Ciniviz, and N. Allahverdi, "Artificial neural network and fuzzy expert system comparison for prediction of performance and emission parameters on a gasoline engine," *Expert Syst. Appl.*, May 2011, doi: 10.1016/j.eswa.2011.04.198.
31. J. Martínez-Morales, H. Quej-Cosgaya, J. Lagunas-Jiménez, E. Palacios-Hernández, and J. Morales-Saldaña, "Design optimization of multilayer perceptron neural network by ant colony optimization applied to engine emissions data," *Sci. China Technol. Sci.*, vol. 62, no. 6, pp. 1055–1064, Jun. 2019, doi: 10.1007/s11431-017-9235-y.
32. M. M. Etghani, M. H. Shojaefard, A. Khalkhali, and M. Akbari, "A hybrid method of modified NSGA-II and TOPSIS to optimize performance and emissions of a diesel engine using biodiesel," *Appl. Therm. Eng.*, vol. 59, no. 1–2, pp. 309–315, Sep. 2013, doi: 10.1016/j.applthermaleng.2013.05.041.
33. M. Deb, P. Majumder, A. Majumder, S. Roy, and R. Banerjee, "Application of artificial intelligence (AI) in characterization of the performance–emission profile of a single cylinder CI engine operating with hydrogen in dual fuel mode: An ANN approach with fuzzy-logic based topology optimization," *Int. J. Hydrogen Energy*, vol. 41, no. 32, pp. 14330–14350, Aug. 2016, doi: 10.1016/j.ijhydene.2016.07.016.
34. J. K. Dukowicz, "A particle-fluid numerical model for liquid sprays," *J. Comput. Phys.*, vol. 35, no. 2, pp. 229–253, Apr. 1980, doi: 10.1016/0021-9991(80)90087-X.
35. L. M. Ricart, J. Xin, G. R. Bower, and R. D. Reitz, "In-cylinder measurement and modeling of liquid fuel spray penetration in a heavy-duty diesel engine," May 1997, doi: 10.4271/971591.
36. Y. Ra and R. D. Reitz, "A reduced chemical kinetic model for IC engine combustion simulations with primary reference fuels," *Combust. Flame*, vol. 155, no. 4, pp. 713–738, Dec. 2008, doi: 10.1016/j.combustflame.2008.05.002.
37. H. Yang, S. R. Krishnan, K. K. Srinivasan, K. C. Midkiff, "Modeling of NO_x emissions using a superextended Zeldovich mechanism," *ASME 2003 Internal Combustion Engine and Rail Transportation Divisions Fall Technical Conference*, 2003, doi: 10.1115/ICEF2003-0713.
38. J. A. Miller and P. Glarborg, "Modeling the formation of N₂O and NO₂ in the thermal DeNO_x process," *Springer Ser. Chem. Phys.*, vol. 61, pp. 318–333, 1996.
39. J. Sietsma and R. J. F. Dow, "Creating artificial neural networks that generalize," *Neural Networks*, vol. 4, no. 1, pp. 67–79, Jan. 1991, doi: 10.1016/0893-6080(91)90033-2.
40. D. Golmohammadi, "Neural network application for fuzzy multi-criteria decision making problems," *Int. J. Prod. Econ.*, vol. 131, no. 2, pp. 490–504, Jun. 2011, doi: 10.1016/j.ijpe.2011.01.015.

CONTACT WITH THE AUTHORS

M.I. Lamas

e-mail: isabellamas@udc.es

University of Coruna,
Mendizabal, 15403 Ferrol,
SPAIN

C.G. Rodriguez

e-mail: c.rodriguez.vidal@udc.es

University of Coruña,
Paseo Ronda, 15011 Coruña,
SPAIN

J.D. Rodriguez

e-mail: de.dios.rodriguez@udc.es

University of Coruña,
19 de Febreiro, 15405 Ferrol,
SPAIN

A. Abbas

e-mail: aa2642@mmsstate.edu

Missisipi State University,
Rood Hoad, 39762 Missisipi,
USA

DIAGNOSTIC INFORMATION ANALYSIS OF QUICKLY CHANGING TEMPERATURE OF EXHAUST GAS FROM MARINE DIESEL ENGINE PART I SINGLE FACTOR ANALYSIS

Patrycja Puzdrowska*

Gdańsk University of Technology, Poland

* Corresponding author: patpuzdr@pg.edu.pl (P. Puzdrowska)

ABSTRACT

In this paper, attention was paid to the problem of low controllability of marine medium- and high-speed engines during operation, which significantly limits the parametric diagnosis. The measurement of quickly changing temperature of engine exhaust gas was proposed, the courses of which can be a source of diagnostic information. The F statistic of the Fisher-Snedecor distribution was chosen as a statistical tool. Laboratory tests were carried out on the bench of a Farymann Diesel engine. The tests consisted of introducing the real changes in the constructional structure of the considered functional systems of the engine. Three changed parameters for the structure were reviewed: the active cross-sectional area of the inlet air channel, injector opening pressure and compression ratio. Based on the recorded plots of the quick-changing temperatures of the exhaust gases, three diagnostic measures were defined and subjected to statistical tests. The following data were averaged over one cycle for a 4-stroke piston engine operation, (1) the peak-to-peak value of the exhaust gas temperature, (2) the specific enthalpy of the exhaust gas, and (3) the rate of increase and decrease in the values for the quick-changing exhaust gas temperature.

In this paper will present results of the first stage of the elimination study: the one-factor statistical analysis (randomised complete plan). The next part will present the results of the second stage of studies: two-factor analysis (block randomised plan), where the significance of the effect of changing the values of the structure parameters on the diagnostic measures was analysed in the background of a variable engine load.

Keywords: marine diesel engine, exhaust gas temperature, diagnostic information, F-statistic of Fisher-Snedecor distribution

INTRODUCTION

The exhaust gas temperature is the basic diagnostic parameter for a marine diesel engine. This is the case for the one providing the main propulsion for the ship and the one that is an element of the power plant of the ship. The exhaust gas temperature is a parameter that characterises the quality of the fuel chemical energy transformation into mechanical energy as a result of complex physicochemical processes that occur in the combustion chamber of the engine. The exhaust gas temperature determines the efficiency of the thermodynamic processes taking place in the separated gas spaces in the thermo-fluid system of the engine during

transport of the working medium. Diagnostic information about the temperature of exhaust gases is strictly dependent on the place and precision of the measurement.

In this case, the object of the diagnostic tests is the construction elements that enclose the working spaces of a marine diesel engine (combustion chamber and channels of inlet air and exhaust gases) and also the injection equipment. Most marine diesel engines have strictly defined places for standard exhaust gas temperature measurement because of the requirements of classification societies [40, 41, 42, 43, 44]. For the main engines that compose the propulsion system of a ship, a measurement of the exhaust gas temperature after each cylinder is required as well as a calculation of its deviation

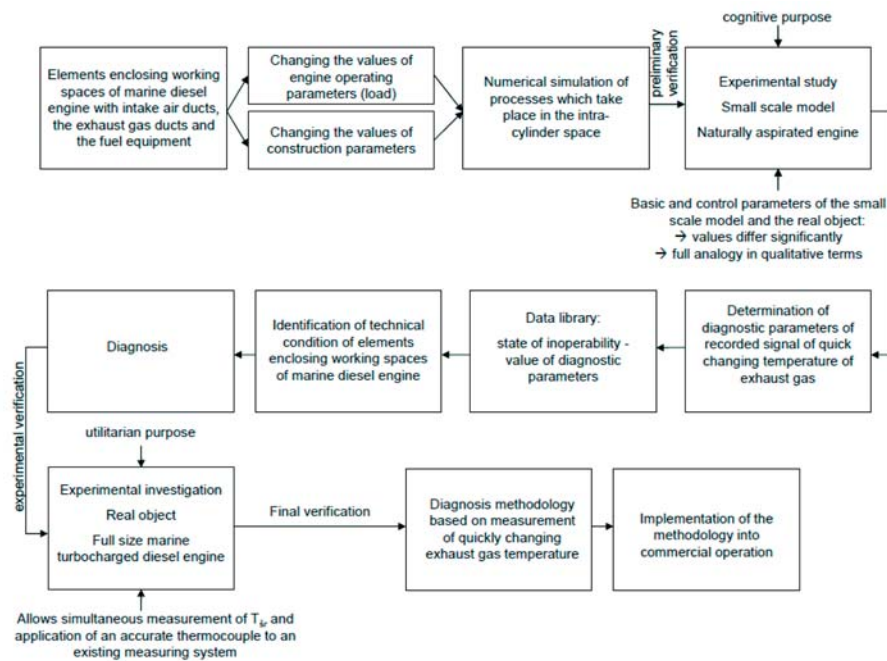


Fig. 1. Scheme for the study of the thermal-flow processes in the exhaust gas channel for the diagnostics of elements enclosing the working spaces of a marine diesel engine

from the average value for the whole engine (or cylinder block) [40]. In the case of marine diesel engines driving generators with a power output of more than 500 kW per cylinder, a measurement of the exhaust gas temperature after each cylinder is required [41]. When the engine is equipped with a pulse turbocharging system, the standard exhaust temperature measurement locations are before and after the turbocharger turbine [42]. For this purpose, traditional thermocouples with a large measurement inertia (time constants of the order of tenths of a second and more) are used and from which an average value for the periodically changing temperature of the exhaust gas flow is obtained [9]. The exhaust gas temperature measured at steady state conditions of the engine is usually recorded as a static value. When analysing the diagnostic information of this parameter in terms of depth and reliability of the diagnosis of the engine technical condition, it has been observed that dynamic measurements have a higher value. The observation of microdynamic processes (quick-changing processes) within a single working cycle of an engine in the steady state allows for a more detailed diagnosis. The average temperature recorded with standard thermocouples and its deviation by the permissible value set by the manufacturer does not provide as much information about the course of the combustion process, the technical condition of the fuel supply system, and the space enclosing the combustion chamber because of the quick-changing temperature and diagnostic parameters based on it. Therefore, it is possible to place a special thermocouple in the exhaust for a standard exhaust gas temperature measurement to obtain more diagnostic information, where the time constant is tens or even several milliseconds. At the same time, it must be possible to observe the average value of the exhaust gas temperature during engine operation. This requirement is not a major operational problem currently because of portable diagnostic systems [9, 34].

In the research carried out by the author of this paper, the thermodynamic processes that take place in the intra-cylinder spaces of a diesel engine were analysed, where the engine was treated as a generator with a quick-changing exhaust gas temperature. The experimental investigations were carried out on a single-cylinder naturally aspirated engine, which is a small-scale model of a real object, i.e., a full-size turbocharged marine engine. The observed basic and control parameters differed significantly (small scale effect); however, there was a significant qualitative analogy between the thermodynamic processes occurring in both engines (Fig. 1).

The problem of quick-changing gases temperatures is being dealt with by many research teams. Some of these were based, for example, on H. Pfriem's 1936 proposal to use two thermocouples of different diameters [1, 3, 4, 5, 6, 19, 20, 21, 28, 31]. The work of these authors extended the metrological knowledge related to the measurement of quick-changing temperatures of gases flowing at high velocities on the order of several tens of m/s, which occurs in the exhaust gas duct of a piston engine [9]. Moreover, docent S. Rutkowski made the first efforts in Poland to measure the quick-changing temperature of exhaust gases from a diesel engine for diagnostic purposes [29]. The main aim of the research was to determine the diagnostic relations between a decrease in the compression pressure of the factor in the cylinder and the dynamics of the changes in the observed temperature of the exhaust gases. Many authors work on the reconstruction of the exhaust gas temperature of a diesel engine in an analytical way that is based on an indicator diagram recorded during experimental tests [8, 22, 33, 35, 38]. These authors proposed methods for diagnosing marine engine workspaces, but none of them did it based on the direct measurement of the exhaust gas temperature. There are also research works available in the specialist literature, where the authors determined the exhaust gas temperature analytically with optoelectronic

measurements of the flame temperature in the combustion chamber of a laboratory engine; a linear dependence between its temperature and exhaust gas temperature was indicated [12]. A very important aspect of modern research in the field of marine engines is ecology. The analyses of the influence of various factors related to engine operation on the emission of exhaust gases are carried out. Application of alternative fuels or new structural solutions is aimed at minimizing the influence of exhaust gas components on the atmosphere [32, 37]. New measurement and numerical methods of obtained research results have also been proposed [10, 39].

The main research aims of author included the reconstruction of the quick-changing temperature of engine exhaust gases with mathematical modelling of the heat exchange in the thermocouple and the identification of known and recognizable defects in the marine diesel engine that have a direct or an indirect influence on the course of the combustion process. The utilitarian aim of the research was to develop a methodology for diagnostic tests of a marine engine in operating conditions based on measurements of the quick-changing temperature of exhaust gases.

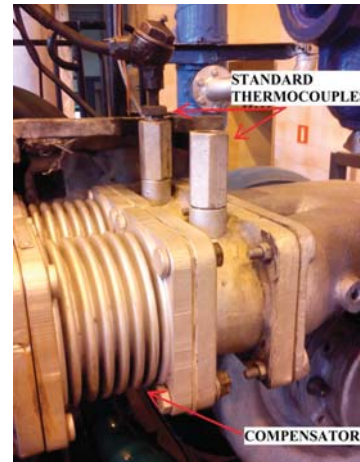
QUICK-CHANGING EXHAUST GAS TEMPERATURE AS A DIAGNOSTIC PARAMETER

During measurements of the quick-changing exhaust gas temperature, there are many problems that must be considered and partially or completely eliminated in order to obtain as much diagnostic information from this parameter as possible. These problems include primarily the inertia of the thermocouple, the dependence of the lifetime on the design and diameter of the thermocouple, the method of mounting the sensor and its heating [24, 25]. The most difficult from a metrological point of view is the selection of the place and mounting method for the thermocouple for the measurement of quick-changing temperatures of the exhaust gas when a ship engine working in real operating conditions (in a ship engine room) is considered. The best solution for this situation is to adapt a standard thermocouple for an engine measurement system (Fig. 2). The measurement of the quick-changing exhaust gas temperature at the standard measurement location seems to be the most advantageous solution, since the diagnostician does not interfere with the design of the engine working spaces. However, the following factors must be considered:

- delay of the signal in relation to the temperature signal recorded inside the cylinder and fluctuation of the recorded signals;
- resistance to flow in the exhaust gas channel, which depends on its constructional form and technical condition of the internal surface;
- wave phenomena taking place in the channel (interference and reflection of the pressure waves coming from the other cylinders cooperating with the channel supplying the turbocharger) [9]; and

- adiabatic compression of the gas column in front of the next pulses of exhaust gas leaving the engine cylinders [9].

a)



b)

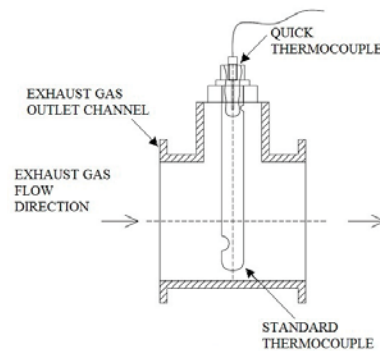


Fig. 2: (a) General view of exhaust gas ducts supplying a marine diesel engine turbocharger in a pulse system with a place for mounting standard thermocouples and (b) schematic diagram of adaptation of a standard thermocouple by mounting a thermocouple for high-speed measurements

Among many functional systems of marine diesel engines, the authors have pointed out the following as the most frequently damaged: the fuel supply system and working medium exchange system [9, 35]. Other types of damage are associated with the piston-crank system or bearings and disturbances in the combustion process, which may manifest themselves as a decrease in the compression ratio ϵ [3, 18, 36].

During diagnostic testing of an engine in a steady state of operation, the values of the control parameters, namely, the input and output, are recorded. For the purposes of diagnostic inference, those of the output parameters are selected because they react more strongly to changes in the values of the parameters of the construction structure than to changes in the values of the input parameters that force the implemented work process. In this way, a set of diagnostic parameters is obtained that is independent and complete. The basic condition for the selection of suitable diagnostic parameters is a much higher sensitivity of the output parameter with respect to the structure parameter than its sensitivity with respect to the input parameter. Comparing the sensitivities of multiple control parameters that are given in different units

of measurement forces the need to assume relative values of input, output and structure parameters for this purpose [8].

There are many methods of assessing the significance of the influence of changes in structure parameters on the analysed physical process and the values of the output (diagnostic) parameters. These include the concept known from classical mathematical analysis, which is the distance between functions, information entropy derived from qualitative information theory, and non-parametric and parametric statistical tests [9, 11, 13, 17, 30]. The diesel engine control parameter, i.e., the quick-changing exhaust gas temperature, can be a valuable source of diagnostic information provided that the condition assessment methodology based on this parameter is properly prepared [19]. To achieve this aim, it is important to select an appropriate measurement technique, tools for mathematical processing and methods of statistical and content-related analysis of the obtained results [14, 15].

F – STATISTICS AS A TOOL FOR IMPACT SIGNIFICANCE ANALYSIS

When assessing the influence of one input parameter of the engine (constructional structure) on one output parameter (quick-changing temperature of the exhaust gas), a program for a static and randomized complete experiment was developed that used the Fisher-Snedecor distribution for the analysis of the F statistic, since the conditions for the application of one-sided parametric tests were met [11, 23]. The null hypothesis, which is formulated in advance and verified with statistical tests, assumes that there is no influence of the input factor on the output factor. The influence of an input factor is considered significant when the calculated value of the applied statistic is equal to, or greater than, the critical value that is given in tables for the applied value of the significance level and number of degrees of freedom. In this study, it was assumed in advance that the results of the measurements of all control parameters can be modeled as random variables with a normal distribution, where the specified variance is a measure of the dispersion around the mean value. It was also assumed that the variances of the random variables are equal or close in value, and that the parametric tests for the variance had a one-sided critical area.

For the one-factor analysis (randomised complete plan), an assessment was made of the significance of the influence of the input factor, which was the structure parameter, over a specified range of variability according to the regulator characteristics on the determined diagnostic parameter (output factor).

The test (calculated) value of F statistic for the Fisher - Snedecor distribution was determined (in this case for specific enthalpy of exhaust gases as an output factor) based on the following relation:

$$F = \frac{\sum_{i=1}^p n_i \cdot (\bar{h}_i - \bar{h})^2 \cdot (n - p)}{[\sum_{i=1}^p \sum_{j=1}^q (h_{ij} - \bar{h})^2 - \sum_{i=1}^p n_i \cdot (\bar{h}_i - \bar{h})^2] \cdot (p - 1)} \quad (1)$$

where n_i is the number of specific enthalpy measurements at a given level, n is the total number of measurements, \bar{h}_i is the average specific enthalpy of the results of the measurements in the i -th row, \bar{h} is the average specific enthalpy of the results of all measurements, h_{ij} is the value of j -th specific enthalpy at level i , and p is the number of levels of variation of the input factor

As a complement to the statistical analysis, ΔF values, which are the difference between the value of the Fobl statistic calculated for the input factor under research and the critical value F_{kr} for the assumed values of the numerator and denominator degrees of freedom and the significance level. In the case of a single classification, the F statistic is calculated as the ratio of the variance of the input quantity to the variance characterizing the measurement imprecision. Thus, the larger the value of ΔF is, the greater the strength of the influence of the input factor on the output parameter under analysis.

STAGES OF ANALYSIS

To obtain the value of the Fobl statistic and the difference ΔF it was necessary to proceed according to the developed scheme [23]. The recorded signal in the first step was subjected to mathematical processing (removal of fluctuations from the measurement network by the method of sum of least squares). It was then determined the response of the thermocouple to the sinusoidal forced gas temperature; i.e., the phase shift and amplitude of temperature changes recorded by the thermocouple in relation to the forced, real gas temperature changes [24, 25]. Diagnostic measures were determined from the obtained real and interference-free quick-changing exhaust gas temperature. Due to the application of the randomised complete plan, irrelevant input quantities were extracted and eliminated from the test object function, and a substantive justification was performed. The final step was the implementation of the block randomised plan, and the statistical and substantive analysis will be presented as a continuation of this paper.

DIAGNOSTIC MEASURES

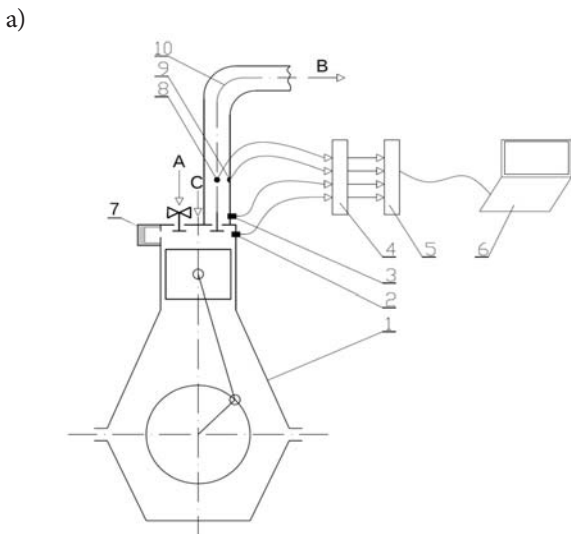
The results of the laboratory tests involved the exhaust gas temperature variation for a single engine operation cycle. Three different measurement signal standards were analysed, determined based on measurements and analysis of the quasi-periodic signal, i.e., the quick-changing temperature of exhaust gases in the exhaust duct of a marine diesel engine, which was determined from the signal subjected to earlier mathematical treatment [7, 16, 24, 28].

The average peak-to-peak value of the quick-changing temperature of exhaust gases ΔT_{sr} was determined as the difference between the maximum and minimum temperature values for particular engine operation cycles. The value of specific enthalpy of exhaust gas h_{sr} was determined by integrating the quick-changing temperature of the exhaust gas within the limits determined by the values of the angle

of rotation of the engine crankshaft for one cycle of work with a known value of the specific heat of the exhaust gas c_p , which was calculated from stoichiometric equations for their average temperature. The c_p value was determined based on fuel composition and over-air ratio measurements recorded for each operating condition of the marine diesel engine. The knowledge of the rate of increase and decrease in the exhaust gas temperature $\Delta T/\Delta \tau$ allowed the determination of the dynamics of the observed thermo-fluid process. Because the real signal after amplitude-phase correction was analysed is a sinusoidal waveform, the values of the rate of increase and decrease in exhaust temperature were the same. The exhaust gas temperature increase (decrease) rate was determined as a ratio of two differences: the difference between maximum and minimum values of exhaust gas temperature within one engine operation cycle in [K] and the difference between the time when the exhaust gas temperature within one engine operation cycle reached its maximum and minimum values [s]. The mentioned diagnostic measures are described in more detail in the publication [26].

EXPERIMENTAL RESEARCH ON A REAL OBJECT

The empirical research was carried out on a laboratory test stand comprising a single-cylinder, type D10 four-stroke Farymann Diesel marine diesel engine (Fig. 3) located in the Laboratory of Marine Power Plants Department, Faculty of Mechanical Engineering and Ship Technology, Gdansk University of Technology. The basic technical data of the engine are: nominal power of 6 kW, nominal speed of 1500 min⁻¹, nominal torque of 38 Nm, cylinder diameter of 90 mm, piston stroke of 120 mm, compression ratio of 22:1, and displacement of 765 cm³. Table 1 lists the measured control parameters and the measuring equipment used during the test.



b)

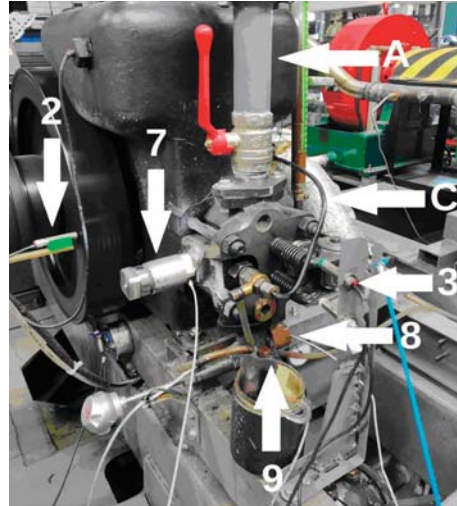


Fig. 3. (a) Schematic diagram and (b) view of the laboratory stand with locations of the measuring sensors: 1 is the Farymann Diesel engine type D10, 2 is the engine speed and TDC sensor, 3 is the exhaust valve opening sensor, 4 is the A/C converter, 5 is the recorder, 6 is the analysis program, 7 is the structural element enlarging the combustion chamber volume, 8 is the exhaust gas pressure sensor, 9 is the water cooled thermocouple, 10 is the exhaust gas outlet channel, A is the inlet air, B is the exhaust gas, and C is the supply fuel

Table 1: Control parameters recorded in the laboratory bench for the type D10 Farymann Diesel engine

Item	Parameter	Measuring device	unit	Measurement range
1	Exhaust gas temperature - T_{sp2}	Grounded type K thermocouple with the junction of external diameter of 0.5 mm, made from inconel	°C	0-1000
2	Exhaust gas pressure in the exhaust channel - P_{sp}	Optical pressure sensor - Optrand C12296	V	0-689475.73 Pa (0-100 psi), sensitivity 6.01·10 ⁻⁸ V/Pa (41.43 mV/psi)
3	Engine speed (angular position °C.A.) - n Top dead centre - TDC	Induction engine speed sensor and TDC sensor	min ⁻¹	0-3000
4	Load Current of the generator (armature) - I_{tw}	Electric current meter	A	0-15
5	Voltage at the armature terminals - U_{tw}	Voltmeter	V	0-250
6	Exhaust valve opening signal	Gap type opto-isolator with a comparator LM393	V mm	0-5 10 (gap)

A multifunctional DT-9805 measuring and recording module from the Data Translation company was used to record the control parameters. Matlab software was applied to record the registered data in the programming language. The measurements were carried out for 3 operating points according to the regulator characteristics due to the limited possibilities of the load control system and the control of the fuel dose feeding the tested engine. During the test, a constant rotational speed for the crankshaft was maintained in the range from 1442-1444 rpm for the following engine loads: $P_{obc1}=432W$, $P_{obc2}=768W$, and $P_{obc3}=1200W$. The sampling frequency was approximately 7000 Hz. The presented test results are the average of 90 consecutive measurements recorded under the same engine operating conditions determined by its load, crankshaft rotational speed and ambient parameters. During the tests, the engine was burning MGO marine fuel. The main objective of the empirical investigations was to establish the diagnostic value of the quick-changing temperature of the exhaust gas of a piston engine; therefore, it was necessary to determine its sensitivity to changes in the parameters of its constructional structure. Accordingly, the input variables were the structure parameters listed below.

Firstly, the active cross-sectional area of the inlet air channel A_{dol} changed its value relative to the reference state, which was understood as full opening of the control valve. This simulated the loss of permeability of the filter baffle. The value of the active cross-sectional area of the intake air duct flow was changed for 3 ranges (100% - 804 mm², 75% - 603 mm², and 50% - 401 mm²) [27]. The injector opening pressure p_{wtr} controlled by the spring relaxation in the injector was chosen as the second input parameter for the construction structure. In the tested engine, an injector with shims with a thickness δwtr equal to 1.3+1 mm was

installed, which resulted in a fuel injector opening pressure value of about 12 MPa (reference state value). During the test for condition 2, shims with a thickness of 1.3+0.5 mm were installed in the injector, which caused the injector opening pressure to decrease to 10 MPa, simulating the failure of the fuel injection system. In the third step, changes were made to the structure parameter of combustion chamber volume, which was reflected in the values of engine compression ratio ϵ . The reference value for the tested engine was $\epsilon_{REF}=\epsilon_1=22:1$, while the reduced value was $\epsilon_2=21:1$ due to the design limitations of the single cylinder engine, which was very sensitive to even the smallest changes in the values of the structure parameters. A decrease in the compression ratio was realised by the application of an additional structural element, increasing the volume of combustion chamber by $\Delta V_k=0,125 \cdot 10^{-5}$ m³. The original (reference) volume of the combustion chamber was $V_{k1}=3,787 \cdot 10^{-5}$ m³, and displacement volume was $V_s=79,5 \cdot 10^{-5}$ m³. Before starting the tests, a preliminary experiment was conducted to evaluate the effect of the engine load P on the quick-changing exhaust gas temperature (P was treated as an input parameter).

RESULTS

Mathematical and statistical analyses were used to calculate the values of the defined diagnostic measures (h_{sp} , ΔT_{sp} , $(\Delta T/\Delta \tau)_{sp}$) during one engine cycle. Values for the F_{obl} statistic were determined for the input parameters, which were the variable structure parameters (A_{dol} , p_{wtr} , ϵ). The following null hypotheses were posed to determine the value of the F_{obl} statistic H_{0i} :

Table 2. The value of the statistics F_{obl} and ($\Delta F=F_{obl}-F_{kr}$) for variable values of the analysed structure parameter: (a) active intake air flow area, (b) injector opening pressure, and (c) compression ratio

a)

Point according to the regulator characteristics	h_{sp} , kJ/kg	ΔT_{sp} , °C	$(\Delta T/\Delta \tau)_{sp}$, K/s
P_1 (432 W, 5.1 A, and 72 V)	157.10 (153.42)	30.44 (26.76)	30.42 (26.73)
P_2 (768 W, 6.8 A, and 96 V)	119.39 (115.70)	14.93 (11.24)	14.93 (11.25)
P_3 (1200 W, 8.5 A, and 120 V)	357.14 (353.45)	16.24 (12.55)	16.27 (12.59)

b)

Point according to the regulator characteristics	h_{sp} , kJ/kg	ΔT_{sp} , °C	$(\Delta T/\Delta \tau)_{sp}$, K/s
P_1 (432 W, 5.1 A, and 72 V)	0.81 (-5.18)	225.60 (219.61)	70.53 (64.55)
P_2 (768 W, 6.8 A, and 96 V)	5.72 (-0.27)	85.06 (79.08)	85.23 (79.24)
P_3 (1200 W, 8.5 A, and 120 V)	15.05 (9.06)	263.41 (257.43)	263.88 (257.89)

c)

Point according to the regulator characteristics	h_{sp} , kJ/kg	ΔT_{sp} , °C	$(\Delta T/\Delta \tau)_{sp}$, K/s
P_1 (432 W, 5.1 A, and 72 V)	52.34 (46.35)	70.22 (64.23)	70.32 (64.34)
P_2 (768 W, 6.8 A, and 96 V)	22.12 (16.13)	143.85 (137.86)	144.13 (138.14)
P_3 (1200 W, 8.5 A, and 120 V)	11.99 (6.00)	83.84 (77.85)	83.98 (77.99)

H_{01} : the value of the analysed structure parameter has no influence on the value of the specific enthalpy of the exhaust gas stream averaged over one engine operating cycle ($S_{H1}^2 = S_1^2$).

H_{02} : the value of the analysed structure parameter has no influence on the peak-to-peak value of the exhaust gas stream temperature within one engine operating cycle ($S_{H2}^2 = S_1^2$).

H_{03} : the value of the analysed structure parameter has no influence on the value of the rate of increase and decrease in the exhaust gas temperature within one engine operating cycle ($S_{H3}^2 = S_1^2$).

Based on the numerical data and the adopted significance level $\alpha=0.05$ and the assumption of the right-side critical area, the values of all three diagnostic measures were determined for the exhaust gas stream within one engine cycle for each measurement point (P_i), the variable structure parameter, and the number of degrees of freedom for the numerator and denominator f_1 and f_2 . Then, the critical value of the statistic $F_{kr}=F(\alpha; f_1; f_2)$ was read from the statistical tables [10] and the values of F_{obl} were determined, which are presented in Table 2. When the condition $F_{obl} > F_{kr}$ was met, the null hypothesis was rejected. In further diagnostic tests, it was assumed that in the considered range of variation of the engine load and for values of the structural parameter in analysed engine, it (the structural parameter) had a significant influence on the diagnostic measures determined within one working cycle of the marine piston engine (positive values of ΔF in Table 2 marked with blue colour).

To evaluate the significance of the influence of the structure parameters in the background of the variable load of the marine diesel engine, the characteristic curves presenting the diagnostic measures (h_{sr} , ΔT_{sr} , $\Delta T/\Delta \tau$) determined based on the variation of the quick-changing exhaust gas temperature as a function of the load of the tested engine were determined (Fig. 4). The measures of stratification of these characteristics are the analysed structure parameters (A_{dol} , p_{wtr} , ϵ).

Based on the results of the statistical analysis (Table 2) and the prepared variability characteristics of the determined diagnostic measures in the background of the engine load (Fig. 4), the following significant conclusions were drawn for the considered range of load variability and engine structure parameters.

1. Reducing the active area of the inlet air flow A_{dol} significantly affected all determined diagnostic measures (Tab. 2a). The strongest effect of this structure parameter occurred in the case of exhaust gas specific enthalpy (highest ΔF).
2. A reduced injector opening pressure p_{wtr} significantly improved the values of the peak-to-peak exhaust gas temperature and rate of increase (decrease) of the exhaust gas temperature for all analysed engine loads. However, the influence of this structure parameter on the exhaust gas specific enthalpy was significant only at the point of maximum engine load (Tab. 2b). The effect of injector opening pressure on the exhaust gas specific enthalpy, meanwhile, was much smaller ($\Delta F \approx 9$) than for the other two measures, where the value of ΔF was of the order of tens or even hundreds.
3. The effect of the reduced compression ratio ϵ was significant for all diagnostic measures determined and for the whole range of engine load variation considered (Tab. 2c).
4. For the specific enthalpy of exhaust gas h_{sr} , the reduced compression ratio increased the value of this diagnostic measure. On the other hand, other changes in the structure parameters (decrease in the active air flow area and decrease in fuel injection pressure) relative to the reference state resulted in a decrease in the value of this diagnostic measure (h_{sr}) (Fig. 4a).
5. In the case of the average peak-to-peak value and the rate of increase (decrease) of the exhaust gas temperature, all the introduced changes in the input parameters of

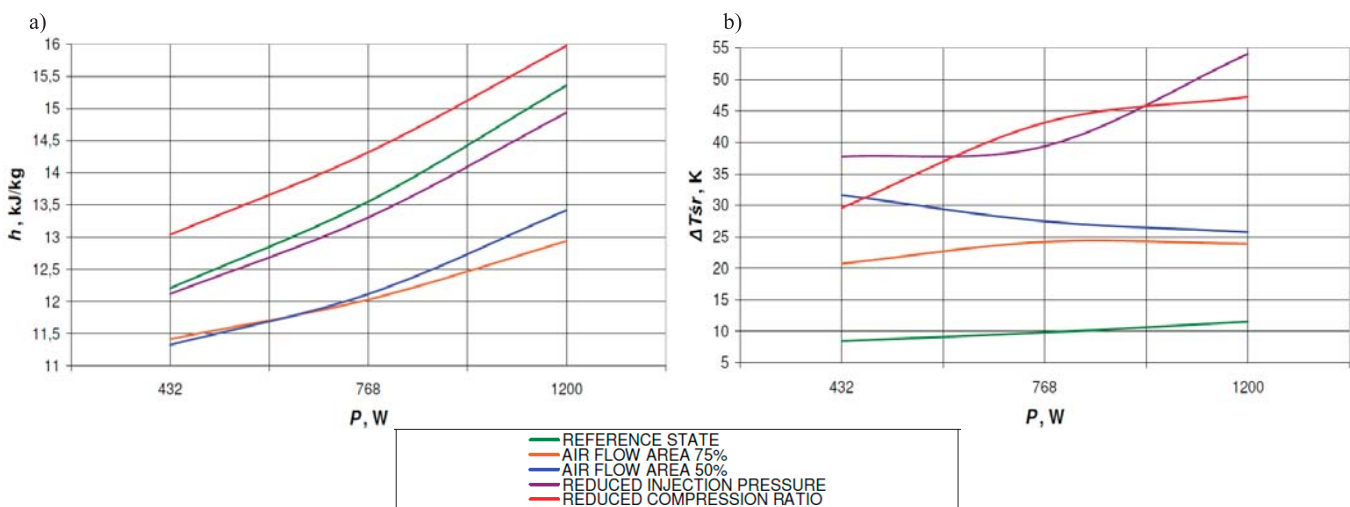


Fig. 4 Characteristics of variation of the determined diagnostic measures within one work cycle as a function of the load for the reference and partial operational states: (a) specific enthalpy of exhaust gas and (b) average value of peak-to-peak temperature of exhaust gas where the reference state is $A_{dol}=100\%$, $p_{wtr}=12$ MPa, $\epsilon=22:1$, the air intake is 75% and 50% relative to reference, the injector opening pressure was reduced to 10 MPa, and compression ratio was reduced to 21:1

the structure caused an increase in these diagnostic measures, which should be interpreted as an increase in the dynamics of the course of the quick-changing exhaust gas temperature (Fig. 4b).

FINAL REMARKS AND CONCLUSIONS

The quick-changing exhaust temperature in the outlet channel of the marine diesel engine can be a valuable source of diagnostic information about the condition of structural elements enclosing the combustion chamber, the fuel system and the inlet air channel. However, it is not always possible to measure these parameters in a combustion chamber primarily because of the low controllability of a serial engine. In such a case, a diagnostic alternative is the measurement of the temperature in the exhaust gas channel with an appropriate consideration of the phenomena occurring there that have an impact on the values of the determined diagnostic parameters. While measurements of the pressure in the exhaust gas duct are also not always possible, measurements of the static exhaust gas temperature are realised as a standard procedure. Therefore, by using a suitably "fast" thermocouple instead of a standard one during engine testing, much more detailed diagnostic information can be obtained. It is possible to develop a diagnosis methodology based on the quick-changing temperature.

In future work, a two-factor analysis is planned according to a randomised block plan. This will allow an evaluation of the influence of two input values. In the analysed case, this is the evaluation of the influence of structure parameters in the background of variable load. The final step of the statistical analysis of the measurement results obtained by using the complete and block randomised plans will be an assessment of the merit.

REFERENCES

PUBLICATIONS

1. Dahlström J., Experimental Investigations of Combustion Chamber Heat Transfer in a Light-Duty Diesel Engine. 2016. Lund University. Thesis for the degree of Doctor of Technology.
2. Debnath, B.K., Sahoo, N. and Saha, U. K., "Thermodynamic analysis of variable compression ratio diesel engine running with palm oil methyl ester", *Energy Conversion and Management*, vol. 65, pages 147-154. 2013. doi: 10.1016/j.enconman.2012.07.016
3. Fennell D. A., Exhaust gas fuel reforming for improved gasoline direct injection engine efficiency and emissions. 2014. University of Birmingham. Ph.D.
4. Fuente S.S., Reducing shipping carbon emissions under real operative conditions: a study of alternative marine waste heat recovery systems based on the organic rankine cycle. 2016. Ph.D.
5. Jaremkiewicz M. and Taler, J., 'Inverse determination of transient fluid temperature in pipelines' *Journal of Power Technologies*, 96(6). p. 385-389. 2016.
6. Jaremkiewicz M., *Odwrotne zagadnienia wymiany ciepła, występujące w pomiarach nieustalanej temperatury płynów. Rozprawa doktorska. Wydawnictwo Politechniki Krakowskiej*. 2011. ['Inverse heat transfer issues occurring in transient fluid temperature measurements'. PhD dissertation.]
7. Korczewski Z. and Puzdrowska P., 'Analytical method of determining dynamic properties of thermocouples used in measurements of quick – changing temperatures of exhaust gases in marine diesel engines' *Combustion Engines*, nr 162 (3), s. 300-306. 2015.
8. Korczewski Z. and Zacharewicz M., 'Alternative diagnostic method applied on marine diesel engines having limited monitoring susceptibility' *Transactions of the Institute of Measurement and Control*, 34 (8), p. 937-946. 2012. doi: 10.1177/0142331211426170
9. Korczewski, Z., *Diagnostyka eksploatacyjna okrętowych silników spalinowych – tłokowych i turbinowych. Wybrane zagadnienia. Wydawnictwo Politechniki Gdańskiej*. 2017. ['Operational diagnostics of marine internal combustion engines - piston and turbine engines. Selected issues']
10. Korczewski. 'Test Method for Determining the Chemical Emissions of a Marine Diesel Engine Exhaust in Operation', *Polish Maritime Research*, vol. 28, no. 3, 2021, doi: 10.2478/pomr-2021-0035.
11. Korzyński, M., *Metodyka eksperymentu. Planowanie, realizacja i statystyczne opracowanie wyników eksperymentów technologicznych. WNT*. 2017. ['Experimental methodology. Planning, execution and statistical processing of results of technological experiments']
12. Kowalczyk M., *Wybrane zagadnienia wymiany ciepła w silnikach wysokoprężnych - wymiana przez promieniowanie. Wydawnictwo Politechniki Poznańskiej*. 2000. ['Selected heat transfer issues in diesel engines - exchange by radiation']
13. Kudrewicz J., *Analiza funkcjonalna dla automatyków i elektroników. PWN*. 1976. ['Functional analysis for automation and electronics engineers']
14. Linschoten P., *Pressure and Temperature Measurements in*

- a Heavy-Duty Diesel Engine. 2018. Master of Science Thesis
15. Llamas X., Modeling and control of EGR on marine two-stroke diesel engines (Vol. 1904). 2018. Linköping University Electronic Press. DOI: 10.3384/diss.diva-144596
 16. Marszałkowski K. and Puzdrowska P., 'A laboratory stand for the analysis of dynamic properties of thermocouples' Journal of Polish CIMEEAC, vol. 10, nr 1 (2015), s. 111 – 120. 2015.
 17. Mazur M., Jakościowa teoria informacji. WNT. Warszawa. 1970. ['Qualitative information theory']
 18. Mijas, Ł. , Reiter, E. and Kukiełka, K., 'Wykorzystanie systemu ANSYS Workbench do analizy statycznej korbowodów' Autobusy: technika, eksploatacja, systemy transportowe. Instytut Naukowo-Wydawniczy 'SPATIUM' R. 14, nr 10 Str. 315-317. 2013. ['Using ANSYS Workbench for static analysis of connecting rods'. Buses: technology, operations, transportation systems.]
 19. Morey F. and Seers P., 'Comparison of cycle-by-cycle variation of measured exhaust - gas temperature and in - cylinder pressure measurements' Applied Thermal Engineering, nr 30, str. 487 - 491. 2010. DOI: 10.1016/j.applthermaleng.2009.10.011
 20. Olczyk A., 'Koncepcja pomiaru szybkozmiennej temperatury gazu z uwzględnieniem dynamicznej składowej temperatury' Pomiary Automatyka Kontrola, 53 Bis/9, s. 576-579. 2007. ['A concept for the measurement of rapidly varying gas temperature taking into account the dynamic temperature component' Measurements Automation Control]
 21. Pfriem H., 'Zur Messung veränderlicher Temperaturen von Gasen Und Flüssigkeiten' Gen. Ingen., vol. 7, no. 2, pp. 85-92. 1936. ['For measuring variable temperatures of gases and liquids']
 22. Polanowski S., 'Studium metod analizy wykresów indykatorowych w aspekcie diagnostyki silników okrętowych' Zeszyty Naukowe AMW, Nr 69 A. 2007. ['Study of Indicator Chart Analysis Methods in the Aspect of Marine Engine Diagnostics']
 23. Polański Z., Planowanie doświadczeń w technice. PWN. 1984. ['Planning experiments in technology']
 24. Puzdrowska P., 'Determining the time constant using two methods and defining the thermocouple response to sine excitation of gas temperature' Journal of Polish CIMEEAC – vol. 11, nr 1, s. 157 – 167. 2016.
 25. Puzdrowska P., 'Signal filtering method of the fast-varying diesel exhaust gas temperature' Combustion Engines, nr. 175(4), s.48-52. 2018. doi: 10.19206/CE-2018-407
 26. Puzdrowska, P., 'Application of the F-statistic of the Fisher-Snedecor distribution to analyze the significance of the effect of changes in the compression ratio of a diesel engine on the value of the specific enthalpy of the exhaust gas flow' Combustion Engines, 186, 80-88. 2021. doi: 10.19206/CE-141346
 27. Puzdrowska, P., 'Evaluation of the significance of the effect of the active cross-sectional area of the inlet air channel on the specific enthalpy of the exhaust gas of a diesel engine using statistics F of the Fisher-Snedecor distribution' Combustion Engines -Vol. 182, issue 3/2020, s.10-15. 2020. doi: 10.19206/CE-2020-302
 28. Roberts S. J., Stone R., et. al., 'Instantaneous Exhaust Temperature Measurement Using Thermocouple Compensation Techniques', SAE Technical Papers. 2004. doi: 10.4271/2004-01-1418
 29. Rutkowski S., Wykorzystanie dynamicznych pomiarów temperatur spalin wylotowych w diagnostyce okrętowych silników spalinowych, Kopia maszynopisu streszczenia artykułu z 1976 roku. 1976. ['The use of dynamic measurements of exhaust gas temperatures in the diagnosis of marine internal combustion engines', Typescript copy of an abstract of a 1976 paper]
 30. Shannon C. E., A mathematical theory of cryptography. A classified memorandum for Bell Telephone Labs. USA. 1945.
 31. Tagawa M. and Ohta Y., Two – 'Thermocouple Probe for Fluctuating Temperature Measurement in Combustion - Rational Estimation of Mean and Fluctuating Time Constants' Combustion and Flame, nr 109, str. 540-560. 1997. doi: 10.1016/S0010-2180(97)00044-8
 32. Wang and L. Yao, 'Effect of Engine Speeds and Dimethyl Ether on Methyl Decanoate HCCI Combustion and Emission Characteristics Based on Low-Speed Two-Stroke Diesel Engine', Polish Maritime Research, vol. 27, no. 2, 2020, doi: 10.2478/pomr-2020-0030.
 33. Wisłocki K., Studium wykorzystania badań optycznych do analizy procesów wtrysku i spalania w silnikach o zapłonie samoczynnym, Rozprawa habilitacyjna, Rozprawy nr 387, Wydawnictwo Politechniki Poznańskiej, 2004. ['A study of the use of optical testing for the analysis of injection and combustion processes in compression ignition engines', Habilitation dissertation.]
 34. Wiśniewski S., Termodynamika techniczna, WNT. 2005. ['Technical thermodynamics']
 35. Witkowski K., 'The Increase of Operational Safety of Ships

by Improving Diagnostic Methods for Marine Diesel Engine' Transnav the International Journal on Marine Navigation and Safety of Sea Transportation, vol. 11, no 2. 2017. doi: 10.12716/1001.11.02.15

36. Woś, P., Jaworski, A., Kuszewski, H., Lejda, K. and Ustrzycki, A., 'Technical and operating problems yielded from setting up the optimum value of geometric compression ratio in piston engines' Combustion Engines, Vol. 164, 1/2016, s. 3-14. 2016.
37. Yang, Q. Tan, and P. Geng, 'Combustion and Emissions Investigation on Low-Speed Two-Stroke Marine Diesel Engine with Low Sulfur Diesel Fuel', Polish Maritime Research, vol. 26, no. 1, 2019, doi: 10.2478/pomr-2019-0017.
38. Zacharewicz M., Metoda diagnozowania przestrzeni roboczych silnika okrętowego na podstawie parametrów gazodynamicznych w kanale zasilającym turbosprężarkę. Rozprawa doktorska. AMW. 2010. ['A method for diagnosing the working spaces of a marine engine on the basis of gasodynamic parameters in the turbocharger feed channel', PhD dissertation]
39. Zhao et al., 'A Numerical and Experimental Study of Marine Hydrogen-Natural Gas-Diesel Tri-Fuel Engines', Polish Maritime Research, vol. 27, no. 4, 2020, doi: 10.2478/pomr-2020-0068.

REGULATIONS, NORMS

1. International Association of Classification Societies, Requirements Concerning Machinery Installations. 'M35: Alarms, remote indications and safeguards for main reciprocating I.C. engines installed in unattended machinery spaces'. 2016.
2. International Association of Classification Societies, Requirements Concerning Machinery Installations. 'M36: Alarms and safeguards for auxiliary reciprocating I.C. engines driving generators in unattended machinery spaces'. 2016.
3. International Association of Classification Societies, Requirements Concerning Machinery Installations. 'M73: Turbochargers'. 2016
4. Polski Rejestr Statków, Przepisy. Publikacja nr 5/P. 'Wymagania dla turbosprężarek. Rozdział 2. Wymagana dokumentacja'. 2016['Requirements for turbochargers. Chapter 2 - Required documentation']
5. Polski Rejestr Statków, Przepisy. Publikacja nr 28/P. 'Próby silników spalinowych. Rozdział 1. Próba typu silników spalinowych. Rozdział 2. Próby zdawczo – odbiorcze silników spalinowych (szczególnie podrozdział 2.2.2)'. 2019. ['Internal combustion engine tests. Chapter 1: Type tests for internal combustion engines. Chapter 2: Acceptance tests of internal combustion engines (especially subchapter 2.2.2)']

CONTACT WITH THE AUTHOR

Patrycja Puzdrowska
e-mail: patpuzdr@pg.edu.pl

Gdańsk University of Technology
Narutowicza 11/12
80-233 Gdańsk
POLAND

RESEARCH ON THE APPLICATION OF COLD ENERGY OF LARGE-SCALE LNG-POWERED CONTAINER SHIPS TO REFRIGERATED CONTAINERS

Yajing Li¹

Boyang Li¹

Fang Deng¹

Qianqian Yang¹

Baoshou Zhang²

¹ College of Electromechanical Engineering, Qingdao University of Science and Technology, China

² School of Aerospace Engineering, Tsinghua University, China

* Corresponding author: qdlby@126.com (B. Li)

ABSTRACT

With the aim of considering the problem of excess fuel cold energy and excessive power consumption of refrigerated containers on large LNG-powered container ships, a new utilisation method using LNG-fuelled cold energy to cool refrigerated containers in cargo holds is proposed in this study, and the main structure of the cold storage in the method is modelled in three dimensions. Then, combined with the different conditions, 15 different combination schemes of high temperature cold storage and low temperature cold storage are designed to utilise the cold energy of LNG fuel, the exergy efficiency and cold energy utilisation rate calculation model of the system is established. The simulation tool 'Aspen HYSYS' is used to simulate and calculate the exergy efficiency and cold energy utilisation rate of the system under 15 combinations, verifying the feasibility of the scheme. According to the characteristics of such a ship's cross-seasonal navigation routes and the number of refrigerated containers loaded in different ports, the combination schemes of the number of low-temperature cold storage and high-temperature cold storage are selected. Thus, the average exergy efficiency and cold energy utilisation rate of the whole line is obtained, which proves that LNG-powered container ships could effectively utilise the cold energy of LNG. By calculating the total electric energy consumed by refrigerated containers on the whole sailing route, before and after the adoption of the LNG cold energy method, it is found that the adoption of this new method can promote the realisation of energy saving and emission reduction of ships.

Keywords: LNG-powered container ship, LNG cold energy utilization, Refrigerated container, Cold storage

INTRODUCTION

At present, many large ships mainly use reliable fuel oil as fuel and combustion produces a large amount of harmful gases, such as nitrogen oxides and sulphur oxides, causing serious atmospheric pollution [1-2]. In response to increasingly severe environmental problems [3], the IMO (International Maritime Organization) has put forward more and more stringent requirements on ship exhaust emissions [4-7]; this has prompted ship owners to urgently find cleaner, more environmentally friendly, alternative fuels [8-9].

In recent years, LNG (liquefied natural gas) has been used as a ship fuel because of its clean, efficient, and pollution-free

advantages [10, 11]. Rui Zhao et al. [12] proposed the use of hydrogen natural gas and diesel fuel engines on ships. Experiments and numerical simulations have verified that this type of engine has good combustion performance and can also reduce environmental pollution but, currently, dual-fuel diesel engines are mainly used, with LNG as the main fuel, which can also greatly reduce pollutant emissions. Such ships are called 'LNG powered ships'. With the increase in people's awareness of environmental protection, the number of LNG powered ships has gradually increased, especially in large container ships. Before the LNG fuel is sent to the main engine for combustion, it needs to be vapourised to the supply temperature and then used in the main engine of the ship.

During the process of vapourising the LNG fuel from -162°C to normal temperature ($20^{\circ}\text{C}\sim 40^{\circ}\text{C}$), each kilogram of LNG fuel can release $830\text{kJ} \sim 860\text{kJ}$ of cold energy [13, 14]. At present, when LNG is heated and vapourised, most of the cold energy is discarded with seawater and air and a large amount of cold energy cannot be used, resulting in a lot of wasted energy [15, 16]. It will also cause indirect pollution and harm to the surrounding seas due to the cold energy, therefore, industry needs to focus research on how to make full use of this part of the cold energy.

Currently, LNG cold energy can be used in seawater desalination, air separation, and Rankine cycle power generation, etc. [17-19].

Sang Hyun Lee et al. [20] proposed a new type of process that uses LNG cold energy for seawater desalination and can generate electricity, which can solve the energy-intensive problem of traditional seawater desalination, and optimise the economic analysis of this new process. Compared with traditional seawater desalination methods, this method has higher energy efficiency. Babu et al. [21] designed a hydrate desalination process that can use the cold energy produced by LNG vapourisation to improve the recovery rate of fresh water through an innovative hydrogenation process. Experiments show that the water recovery rate can reach 34.85%. Jing Sun et al. [22] proposed a method for seawater freezing and desalination using LNG cold energy for LNG receiving stations. It has been verified that this method has high heat transfer efficiency, but the ice production efficiency of the fluidised bed ice-maker is affected by the ability of particles to remove ice crystals. Therefore, the technology needs to continue to be optimised. Cao et al. designed and simulated the process of freezing desalination using LNG cold energy on a flake ice maker, established a kinetic model of the freezing section and performed numerical simulations. The results showed that a 1 kg equivalent of LNG cold energy can obtain approximately 2 kg ice melt water [23]. In the 1970s, Cravalho et al. proposed a zero-energy, theoretical system for recovering LNG cold energy to produce fresh water. The system included a heat engine, heat pump, LNG heat exchanger and two seawater heat exchangers. The maximum theoretical fresh water output of the system was about $6.7\text{ kg (water) kg (LNG)}^{-1}$ [24].

Using LNG cold energy in the air separation process can realise part of the cold energy recovery [25]. Yamanouchi, Nagasawa, and Wu all [26-28] proposed a process for cryogenic air separation using the cold energy released during the LNG vapourisation stage and verified the feasibility and rationality of the process, saving energy. LNG cold energy can also be used for the recovery of light hydrocarbons. Zhang used the cold energy in the LNG regasification process to recover light hydrocarbons and optimised the cold energy utilisation rate (CUR) and ethane recovery rate (ERR). Gu designed an LNG light hydrocarbon recovery process by adopting the method of partial condensation of natural gas and recycling the feed to improve the purity of light hydrocarbon products, such as ethane. Gao et al. used cold energy to improve the LNG light hydrocarbon recovery process. They made the demethanizer

work under high pressure (about 4.5 MPa), which can compress the thin natural gas product to pipeline pressure and reduce power consumption.

There have also been many studies on using LNG cold energy for Rankine cycle power generation. Koo studied a new solution for recovering LNG cold energy from LNG-powered ships, replacing the typical LNG fuel supply system with an organic Rankine cycle (ORC) system to recover the cold energy of LNG, which has more advantages than the traditional Rankine cycle. Big advantage. Six different ORC systems were proposed and optimised to verify the economic feasibility of the system [32-34]. Zhen Tian et al. proposed a parallel two-stage organic Rankine cycle (PTORC) system driven by an LNG fuel ship's waste heat. Through simulation and analysis, it is concluded that the PTORC system can effectively utilise the LNG cold energy and waste heat of dual-fuel ship engines [35]. Sun proposed a power generation system that uses the combination of waste heat from the main ship engine's flue gas and LNG low-temperature cold energy, and then analysed and simulated the system, using genetic algorithms to optimise the relevant parameters that affect the efficiency of the system. The exergy efficiency of the low-temperature Rankine cycle power generation system has been significantly improved [36]. Xu proposed a new type of power generation system that uses LNG cold energy for Rankine cycles, to reduce heat exchanger exergy loss, optimise the system, and improve the exergy efficiency of the system [37]. Liang et al. proposed a new LNG cold energy utilisation system that combines cold, heat and electricity. The system consists of a gas turbine, 4 Rankine cycles and a natural gas direct expander. The recovery and utilisation of the cold energy of LNG can improve the thermal efficiency and exergy efficiency of the system [38]. Fernández et al. proposed to capture BOG energy in LNG ships and produce high-energy and zero-emission hydrogen as a fuel for ships, using the cold energy of LNG fuel during the storage of hydrogen, thereby reducing the space occupied by hydrogen storage on the ship; the power consumed by the compressor when compressing hydrogen is calculated [39].

At present, the load of seawater desalination, air separation, air conditioning, etc. is relatively small, and only a small part of the cold energy is used, most of them being applied on land. Even if it is applied to ships, most of the cold energy released by LNG is still not used. In addition, the Rankine cycle power generation system is only widely used to drive steam turbines on LNG carriers. Because of its complex system structure, management requirements on ships are relatively high, and it is not widely used on other types of ships. Therefore, it is particularly important to find an efficient utilisation scheme of LNG cold energy that can be applied on ships.

With the widespread application of LNG fuel, large container ships took the lead in opening the prelude to LNG-powered ocean-going ships. This is not only because container ships have a high speed and consume a lot of fuel, but also because large container ships usually have a large number of refrigerated containers, which can reach more than 2,000, resulting in a large electrical load for refrigerated containers.

More importantly, LNG-powered container ships consume a lot of LNG fuel and release a lot of cold energy. Because the above-mentioned LNG cold energy utilisation has some shortcomings, there is a problem of excess LNG cold energy on such ships, and it happens that the refrigerated containers carried by the ships urgently need a large amount of cold energy. Therefore, it is proposed to use LNG cold energy for ship refrigerated containers. The specific method is to install an insulation layer in the cargo hold near the midship (a new type of cold storage). The goods that need to be refrigerated should be put into containers, which are placed in the new type of cold storage, using the refrigerant to transfer the LNG cold energy to the cold storage, and then the containers are cooled, to achieve the effect of refrigerated containers. Aspen HYSYS software was used to simulate the process, which proved the feasibility of the above plan.

STRUCTURAL MODEL OF THE COLD STORAGE

SELECTION OF THE PARENT SHIP

In order to realise the full and effective use of LNG cold energy on large container ships, this study is based on the world's largest container ship 'CMA CGM JACQUES SAADE' which is to be launched in 2020, as the parent ship. The ship can carry 23,000 standard containers (TEU), as shown in Fig. 1.



Fig. 1. 'CMA CGM JACQUES SAADE' LNG-powered container ship

The parent ship uses a CMD-WinGD 12*92DF dual-fuel low-speed diesel engine as the main engine of the ship. The main engine has a large power of 63,840 kW. Therefore, the LNG fuel consumption is high and releases more cold energy. In addition, the ship uses more electrical equipment and power consumption is large, with 6 generator sets; the specific parameters are shown in Table 1. The power of the refrigerated container is the average power of the refrigerated container obtained through experimental measurement during continuous operation.

Tab. 1. Related parameters of 'CMA CGM JACQUES SAADE'

Parameters	Value	Parameters	Value
Length overall (m)	399.9	Deadweight (ton)	216900
Breadth moulded (m)	61.3	Main engine power (kW)	63840
Depth (m)	33.5	Number of refrigerated containers (40 feet)	2200
Draft (m)	14.5	LNG fuel tank volume (m ³)	18600
Generator power (kW)	38404×4	Average power of refrigerator (40 feet) (kW)	4.8-5.8
	43202×2	Average speed (knot)	21.55

The parent ship selected in this study uses LNG as fuel and the specific composition of the LNG is shown in Table 2. When the container ship sails at 70% of the rated power of the main engine, through calculation, it can be concluded that the container ship can consume 6497 kg of LNG fuel per hour. The cold energy released per hour, during the LNG vapourisation process, can be calculated as 5.52×10^6 kJ, it can be seen that the container ship will release a large amount of cold energy during normal navigation.

Tab. 2. LNG composition

Component	Methane	Ethane	Propane	Iso-butane	N-butane	Nitrogen	Iso-pentane
Percentage	0.9390	0.0326	0.0069	0.0012	0.0015	0.0179	0.0009

OVERALL DESIGN SCHEME OF THE COLD ENERGY UTILISATION SYSTEM

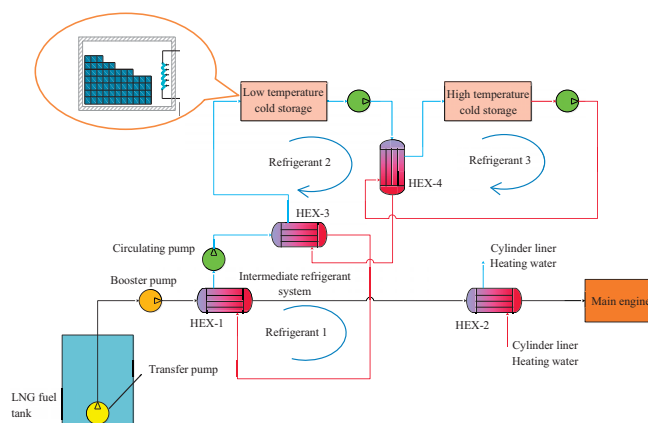


Fig. 2. LNG cold energy utilisation system

Because the temperature of LNG fuel is low, reaching -162°C , and the minimum design temperature of the cold storage is only -20°C , the heat exchange temperature difference is large and the selection of refrigerant is difficult. Excessive heat exchange temperature difference will cause a lot of waste of LNG cooling exergy. Therefore, when designing the system, an intermediate refrigerant system was added, as shown in Fig. 2, where the circulating refrigerant is refrigerant 1. The system is divided into an intermediate refrigerant system, a low temperature cold storage system, a high temperature cold

storage system, and the water heating system of the cylinder liner. The intermediate refrigerant system, low temperature cold storage system, and high temperature cold storage system adopt the cold energy cascade utilisation method. LNG first passes through the LNG heat exchanger HEX-1, transfers the cold energy to refrigerant 1 in the intermediate refrigerant system, and then uses the jacket water to heat and vapourise it through the LNG heat exchanger, HEX-2, and send it to the ship's main engine for combustion. Refrigerant 2 (in the low-temperature cold storage system) and refrigerant 1 (in the intermediate refrigerant system) exchange cold energy through HEX-3 and the high-temperature cold storage system exchanges cold energy through refrigerant 3 and refrigerant 2 in the low-temperature cold storage through HEX-4. Finally, by using the heat of the cylinder liner to heat the water, the remaining cold energy is consumed so that the LNG is completely vapourised to the intake temperature of the main engine of the ship.

DESIGN OF THE NEW COLD STORAGE MODEL

Refrigerated containers usually include low-temperature refrigerated containers and high-temperature refrigerated containers. Low-temperature refrigerated containers usually transport some low-temperature cargo, such as meat, fish and other foods. The temperature is usually -18°C to -20°C . High-temperature refrigerated containers usually transport fruit, vegetables and other cargo; the temperature is usually between 0°C and 5°C . Most of the refrigerated containers are equipped with refrigeration equipment and insulation layers, which not only increases the investment and construction cost of the ship, but also increases the power consumption caused by refrigeration of the refrigerated containers.

In order to meet the temperature requirements of low-temperature refrigerated containers and high-temperature refrigerated containers, low-temperature cold storage and high-temperature cold storage are divided. The cold storage is set in the cargo hold in the middle of the ship and the cargo hold is provided with an insulation layer. The reason for placing the cold storage in the middle of the hull is that the cargo hold has a more regular shape than the cargo hold on the bow and stern and can accommodate more containers. This method can not only put refrigerated containers in the cargo hold, it can also be put into ordinary containers but, more importantly, it allows an ordinary container store refrigerated or frozen goods like a refrigerated container. This not only improves the energy utilisation rate of the ship, but also reduces the increase in refrigeration caused by the refrigerated container during maritime transportation. The load on the ship's power grid can save ship operating costs. After calculation, each cold storage can accommodate 528 TEUs. The dimensions of the cold storage are shown in Table 3. Fig. 3 is a three-dimensional model of one of the cold storages.

Tab. 3. Relevant parameters of cold storage

Parameters	Length (m)	Width (m)	Height (m)
Value	12.60	54.67	31.69



Fig. 3. Model diagram of the new cold storage

SCHEME DESIGN

CALCULATION OF COOLING CAPACITY REQUIRED BY COLD STORAGE

In order to realise the utilisation rate of LNG cold energy on LNG-powered container ships, it is necessary to calculate the cooling load of the cold storage in the design scheme.

The specific calculation method for each cold storage is as follows. The total cold consumption is:

$$\dot{Q} = \dot{Q}_1 + \dot{Q}_2 + \dot{Q}_3 + \dot{Q}_4 \quad (1)$$

where \dot{Q}_1 is the heat flow rate between the cold storage and its surrounding environment (W); \dot{Q}_2 is the heat flow rate of the goods in the cold storage (W); \dot{Q}_3 is the heat flow rate generated when the cold storage is opened for ventilation (W); and \dot{Q}_4 is the equipment or operator heat flow rate (W).

Heat flow rate between cold storage and external environment \dot{Q}_1

The heat flow rate between the cold storage and external environment is calculated according to the following formula:

$$\dot{Q}_1 = KF\Delta T \quad (2)$$

where K is the heat transfer coefficient of the cold storage wall, $\text{W}/\text{m}^2\cdot\text{K}$; F is the heat transfer area of the cold storage, m^2 ; and ΔT is the temperature difference between the ambient temperature and the storage temperature, K. The temperature of the outer wall of the cold storage is 30°C in summer, 5°C in the winter, and 15°C in the spring and autumn.

Cargo heat flow rate of cold storage Q_{2L} , Q_{2H} ,

Low-temperature cold storage usually stores some low-temperature cargo, such as meat, fish and other foods. For the heat flow rate of low-temperature cold storage goods:

$$Q_{2L} = Q_{2aL} + Q_{2bL} + Q_{2cL} \quad (3)$$

In Eq. (3), Q_{2L} is the heat flow rate of the food, W; Q_{2bL} is the heat flow rate of the container box, W; and Q_{2cL} is the breathing heat of the food. For low-temperature storage, the breathing heat of the food is not considered, so =0W, then:

$$Q_{2L} = Q_{2aL} + Q_{2bL} \quad (4)$$

High-temperature cold storage usually stores some fruit, vegetables and other cargo. For the heat flow rate of high-temperature storage goods:

$$Q_{2H} = Q_{2aH} + Q_{2bH} + Q_{2cH} \quad (5)$$

where Q_{2aH} is the heat flow rate of the food, W; Q_{2bH} is the heat flow rate of the container box, W; and Q_{2cH} is the breathing heat of fruit and vegetables.

For the fruit and vegetables in the high-temperature cold storage, they will still breathe heat when they are stored in the cold storage. Therefore, when calculating the heat flow rate of the high-temperature cold storage goods, the breathing heat of the fruits and vegetables needs to be considered, then:

$$Q_{2H} = Q_{2aH} + Q_{2bH} + Q_{2cH} \quad (6)$$

The heat flow rate Q_3 generated when the cold storage door is opened for heat exchange

$$Q_3 = \frac{nV\rho_o(h_1 - h_2) * 10^3}{24 * 3600} \quad (7)$$

where V is the capacity of the cold storage, m^3 ; h_1 is the enthalpy of the air outside the storage, kJ/kg ; h_2 is the enthalpy of the air inside the cold storage, kJ/kg ; n is the number of air changes in the 24 h internal cold storage; and ρ_o is the internal cold storage air density, kg/m^3 .

Operating heat

$$Q_4 = Q_{4a} + Q_{4b} + Q_{4c} \quad (8)$$

Q_{4a} is the heat flow rate of the staff, W; Q_{4b} is the heat flow rate of the lighting equipment, W; Q_{4c} is the heat flow rate of the air cooler, W.

The cold storage is equipped with low-temperature cold storage and high-temperature cold storage. Usually the temperature of the low-temperature cold storage is $-18^\circ C$ to $-20^\circ C$ and the design temperature is $-20^\circ C$; the temperature of the high-temperature cold storage is usually $0^\circ C$ to $-5^\circ C$, and the design temperature is $3^\circ C$. The outside temperature in summer is $30^\circ C$, the summer temperature in winter is $5^\circ C$ and the outside temperature in spring and autumn is $15^\circ C$.

The heat flow rate of low-temperature cold storage and high-temperature cold storage in summer, winter, spring and autumn can be calculated. The specific values are shown in Table 4.

Tab. 4. Heat flow rate of high-temperature cold storage and low-temperature cold storage under different working conditions

Season	Load of low temperature cold storage (kW)	Load of high temperature cold storage (kW)
Summer	394.44	283.33
Winter	333.33	59.44
Spring and autumn	355.56	131.94

SPECIFIC SCHEME DESIGNS FOR DIFFERENT SAILING CONDITIONS

The ‘CMA CGM JACQUES SAADE’ serves Asian-European routes and the ship’s voyage cycle is as long as 84 days, as shown in Table 5. Because of the long routes and the different latitudes of the ports it passes, the temperature along the route differs, and the same voyage will have different seasons. In addition, there are multiple ports of call in the voyage; in different port of call, the number of containers and types of goods are different, and the number of low temperature and high temperature cold storage is also different. Taking the above factors into consideration, combined with the cold storage’s demand for cold energy and the total cold released by the system, Table 6 lists different combination schemes of low-temperature cold storage and high-temperature cold storage in different seasons.

Tab. 5. Sailing schedule for a certain voyage

Port	Arrival time	Departure time	Port	Arrival time	Departure time
Ningbo	March 3	March 7	Rotterdam	April 15	April 17
Yan Tian	March 9	March 10	Marsaxlokk	April 22	April 23
Singapore	March 17	March 18	Suez Canal	April 26	April 27
Suez Canal	March 29	March 30	Port Klang	May 6	May 8
Le Havre	April 5	April 7	Xin Gang	May 18	May 20
Dunkirk	April 8	April 9	Busan	May 22	May 24
Hamburg	April 12	April 14	Ningbo	May 25	May 26

Tab. 6. Combination scheme of the number of low temperature cold storage and high temperature cold storage

Conditions	Summer					Winter					Spring and autumn				
Scheme	S ₁	S ₂	S ₃	S ₄	S ₅	S ₆	S ₇	S ₈	S ₉	S ₁₀	S ₁₁	S ₁₂	S ₁₃	S ₁₄	S ₁₅
Number of high temperature cold storage	1	1	2	1	2	3	3	2	2	3	2	2	3	2	3
Number of low temperature cold storage	2	3	1	1	0	4	2	3	2	0	3	2	1	1	0

SYSTEM SIMULATION

In order to verify the feasibility of the above 15 combination schemes, this study used Aspen HYSYS to carry out simulation calculations.

SELECTION OF REFRIGERANT

In order to ensure that the cold storage system can exchange heat normally and achieve a good heat transfer effect, a suitable refrigerant needs to be selected before the simulation, which can be selected according to the target temperature of different modules. Table 7 shows the target temperature range of different modules.

Tab. 7. Temperature range corresponding to different modules

Cold energy utilisation system	System temperature (°C)	The temperature range of the refrigerant (°C)
Intermediate refrigerant system	-40°C to -60°C	<-60°C
Low temperature cold storage system	Cold storage temperature -20°C to -18°C	≤-40°C
High temperature cold storage system	Cold storage temperature 0°C to -5°C	<-10°C

The selection of refrigerant must comply with the criteria for refrigerant selection. Whether the refrigerant is properly selected will affect the refrigeration effect and system performance of the cold storage. The cold storage system requires more cold energy. The selected refrigerant should have a large specific heat capacity, to carry the large amount of cold energy that will be generated if the refrigerant temperature change is too large, resulting in icing phenomenon. Because it is used for cold storage circulation, the refrigerant should not have a risk of burning or exploding, and its toxicity should be low because the refrigerant is used for cold storage circulation. The size of cold storage is large and the amount of refrigerant required is also large. Low-cost, easy-to-obtain, and quick-to-supply refrigerants should be selected, therefore, priority should be given to ethylene glycol aqueous solution, which is a more commonly used refrigerant. For high-temperature cold storage, the design temperature is 3°C, and the freezing point of the refrigerant is required to be <-10°C. 30% ethylene glycol aqueous solution is preferred and the freezing point of the glycol aqueous solution

is -15°C, which meets the temperature requirements of high-temperature cold storage. For low-temperature cold storage, the design temperature is -20°C, the minimum freezing point of the refrigerant is required to be ≤-40°C, and the freezing point of 50% ethylene glycol aqueous solution is -40°C, which meets the temperature requirements for low-temperature cold storage. Therefore, the refrigerant in the low-temperature cold storage and the high-temperature cold storage are 30% and 50% ethylene glycol aqueous solution, respectively.

Low-temperature cold storage requires a lot of cold energy. The intermediate refrigerant should carry enough cold energy to ensure the normal operation of the system. Therefore, the intermediate refrigerant needs to undergo phase change, and the refrigerant undergoing phase change has a larger latent heat of phase change and a better heat transfer effect. Fig. 4 shows the condensation pressure curves of different refrigerants at different condensation temperatures.

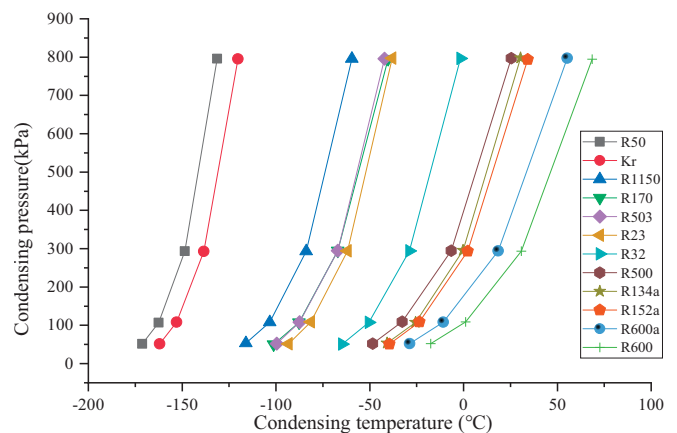


Fig. 4. Correspondence graph of condensation temperature and condensation pressure of different refrigerants

The intermediate refrigerant needs to undergo a phase change within the required temperature range of -40°C to -60°C. It can be seen from Fig. 4 that the refrigerants that meet the conditions are R23, R503, and R170. The main component of R23 is trifluoromethane, which is easily soluble in water, flammable and explosive, and has a high pressure. The safety level of the pipeline needs to be relatively high, and this refrigerant will release highly toxic fumes when heated and decomposed, so it is not suitable for cold storage systems. The main component of R170 is ethane, which is a hydrocarbon-carrying refrigerant and is more environmentally friendly. It often replaces R13 and R503 as a refrigerant, so R170 can be used as the intermediate refrigerant. The refrigerant is

a substance that easily evaporates. In the actual application process, in order to avoid this problem as much as possible, the sealing performance of the pipeline should be improved. The refrigerant may cause corrosion to the pipeline, so the pipeline material should be selected with corrosion resistance in mind.

DETERMINATION OF SIMULATION PARAMETERS

Assuming that the power unit of the ‘CMA CGM JACQUES SAADE’ LNG-powered container ship is operating at 70% load, it is calculated that, under this working condition, the LNG intake flow rate of the main engine is 6497 kg/h. Aspen HYSYS software was used for calculating the simulations of LNG and the physical property method of the refrigerant was Peng-Robinson. The physical property method of the jacket water was NBS Steam. The pump efficiency is 75% and the minimum heat exchange temperature difference of the heat exchanger was set at 8°C. 50% ethylene glycol aqueous solution was used as the low-temperature storage refrigerant, 30% ethylene glycol aqueous solution was used as the high-temperature cold storage refrigerant, and R170 was used as the intermediate refrigerant. In this simulation, it was assumed that the process is static and stable.

In order to avoid temperature crossing in the LNG heat exchanger, and to ensure that each cold energy utilisation system can meet the refrigeration requirements, the heat outlet temperature of the HEX-3 heat exchanger should be lower than the design temperature of the low-temperature cold storage (-20°C). It should not be lower than the inlet temperature of the cold flow (-30°C). In the same way, the hot flow outlet temperature of the HEX-4 heat exchanger

should be 3°C lower than the design temperature of the high-temperature cold storage, and should not be lower than the cold flow inlet temperature (-5°C). According to the condensation pressure corresponding to the condensation temperature of the refrigerant in Fig. 4, the pressure of stream A-3 was set to 500 kPa. Taking Scheme 1 as an example, the main parameter settings in the system are shown in Table 8.

Tab. 8. Main parameter settings in the system

Stream name	Medium	P (kPa)	T (°C)	Flow (kg/h)
LNG-1	-	200	-163	6497
LNG-2	-	1600	-	-
NG-4	-	-	40	-
A-1	R170	-	-40	-
A-2	R170	-	-60	-
A-3	R170	500	-	-
B-1	Cylinder liner heating water	-	80	-
B-2	Cylinder liner heating water	-	68	-
C-2	50% ethylene glycol solution	-	-30	-
C-5	50% ethylene glycol solution	-	-20	-
D-2	30% ethylene glycol solution	-	-5	-
D-6	30% ethylene glycol solution	-	3	-
D-9	30% ethylene glycol solution	-	3	-

The parameter settings of other combination schemes are the same as the key node parameter settings of Scheme 1, and will not be repeated here. Taking Scheme 1 as an example, Fig. 5 is a diagram of the simulated system.

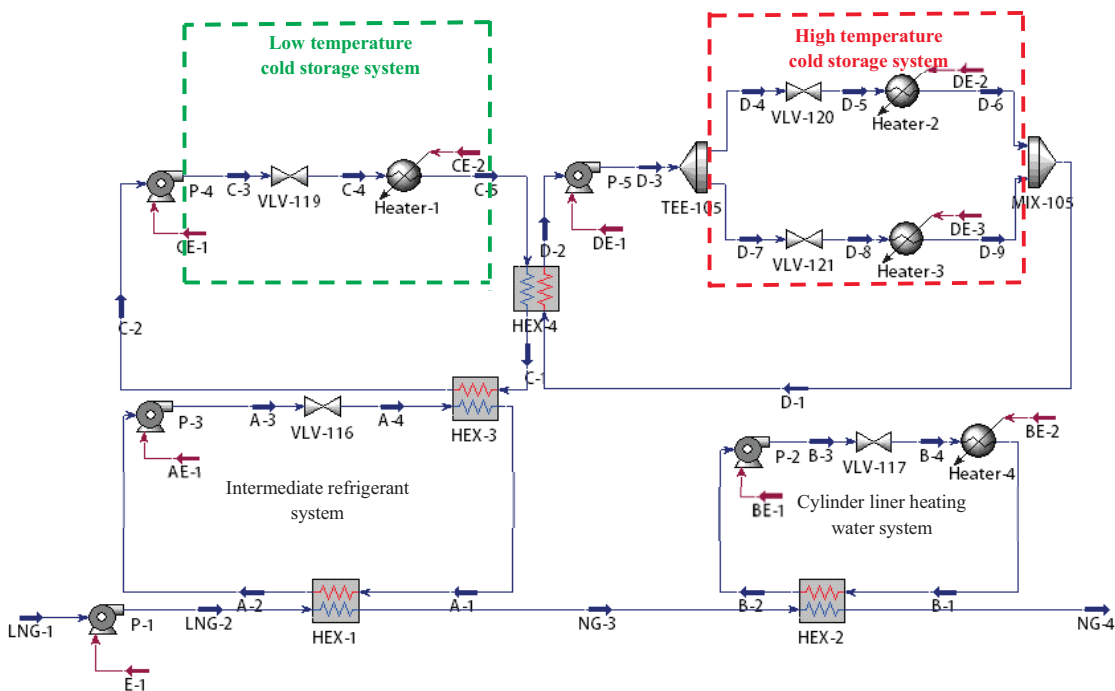


Fig. 5. LNG cold energy utilisation simulation system diagram

ANALYSIS OF SIMULATION RESULTS

Through the simulation, it can be seen that the 15 combination schemes of low and high temperature cold storage can all run normally in the Aspen HYSYS simulation.

(1) Exergy efficiency calculation model

Using Aspen HYSYS to simulate the system, the main parameters of each node of the system can be obtained, including temperature, pressure and flow, entropy, enthalpy, etc. Among these, the flow of the intermediate refrigerant in the cold storage system can be calculated by the known heat load. The flow rate of the jacket heating water in the jacket water heating system can also be calculated. Taking scheme 1 as an example, the important node parameters are shown in Table 9.

The exergy of logistics generally includes physical exergy and chemical exergy. In the process of cold energy utilisation, LNG mainly involves changes in physical form, mainly physical exergy changes. The cold energy utilisation system proposed in this paper is a stable flow system. For a stable flow system, according to the first law of thermodynamics:

$$\delta Q = dH + \frac{1}{2}mdc^2 + mgdz + \delta W_A \quad (9)$$

From the second law of thermodynamics,

$$\delta Q = T_0 ds \quad (10)$$

Therefore,

$$T_0 ds = dH + \frac{1}{2}mdc^2 + mgdz + \delta W_A \quad (11)$$

$$\delta W_A = -dH + T_0 ds - \frac{1}{2}mdc^2 - mgdz \quad (12)$$

Therefore, in the environmental state, from a given import state integral to an export state integral, the exergy of stable logistics is:

$$E_{xmass} = W_A = H - H_0 - T_0(S - S_0) + \frac{1}{2}mdc^2 + mgdz \quad (13)$$

Since the kinetic and potential energy of the logistics in the cold energy utilisation system have small changes and can be ignored, the calculation formula for the exergy of the stable flow system logistics is:

$$E_{xmass} = W_A = H - H_0 - T_0(S - S_0) \quad (14)$$

Therefore,

$$E_{xmass} = m[(h - h_0) - T_0(s - s_0)] \quad (15)$$

In the formula: m is the mass flow of each stream and h and s are the enthalpy and entropy of each flow, respectively.

The power consumption of the working fluid pump is:

$$W_p = \frac{m(h'_0 - h'_i)}{\eta_p} \quad (16)$$

In the formula: η_p is the isentropic efficiency of the pump; h'_i is the enthalpy value of the pump inlet flow; and h'_0 is the enthalpy value of the pump outlet flow.

Tab. 9. The main simulation results parameters of scheme 1

Stream name	Flow (kg/h)	T (°C)	P (kPa)	s (kJ/kgK)	h (kJ/kg)
LNG-1	6497	-163	200	4.461	-5240
NG-4	6497	40	1560	9.604	-4336
B-1	47180	80	120	1.075	-15590
B-2	47180	68	100	0.930	-15640
B-3	47180	68.03	300	0.931	-15640
B-4	47180	68.03	280	0.931	-15640
A-1	7278	-40	460	6.384	-2934
A-2	7278	-60	440	4.200	-3411
C-1	51300	-5.863	240	-15.390	-9932
C-2	51300	-30	220	-15.890	-9400
C-5	51300	-20	260	-15.660	-9372
D-1	80790	3	260	-2.028	-10830
D-2	80790	-5	240	-24.580	-10850

In this study, the exergy efficiency is used as an indicator to evaluate the energy utilisation of the system, because the exergy efficiency can reflect the ability of the system to perform external work. The system uses LNG cold energy to refrigerate the ship's cold storage, which can save the power consumption of the refrigerated container refrigeration unit. This reduces the load of the ship's power grid, so it can be considered that the system is doing external work. In addition, the system uses LNG cold energy to refrigerate the ship's cold storage, which belongs to heat exchange and refrigeration. Therefore, the utilisation rate of LNG cold energy can also be used as another indicator to evaluate the energy utilisation of the system.

The exergy efficiency ε is the ratio of the effective income exergy to the consumption exergy. In this study, effective exergy E_{CS} is the exergy input from the working medium of cold storage to the environment of low temperature cold storage and high temperature cold storage. If the pump power consumption (W_p), the LNG cold exergy consumed ($E_{LNG} - E_{NG-4}$) and the exergy of the jacket water (E_p) are used as the

consumption exergy, then the exergy efficiency calculation model of the system is:

$$\varepsilon = \frac{E_{CS}}{\mathcal{W}_p + E_{LNG-1} - E_{NG-4} + E_F} \quad (17)$$

The values obtained through Aspen HYSYS can be put into equations Eq. (15) and (16), respectively, to work out the exergy of flows of each part and the power consumption of the pump. Then, the corresponding calculated values can be put into Eq. (17) and the exergy efficiency of the system under various schemes can be obtained.

(2) Calculation model of the cold energy utilisation rate

The utilisation rate of cold energy can be used to measure the utilisation of cold energy by the system. The utilisation rate of cold energy η is the ratio of the effective utilisation of cold energy to the total cold energy released by the system. The cold energy utilisation in this study is the cold energy consumed by low-temperature cold storage and high-temperature cold storage, Q_{CS} , and the total cold energy is the cold energy, Q_{LNG} , released by the vapourisation of LNG. The calculation model of the cold energy utilisation rate of the system is:

$$\eta = \frac{Q_{CS}}{Q_{LNG}} \quad (18)$$

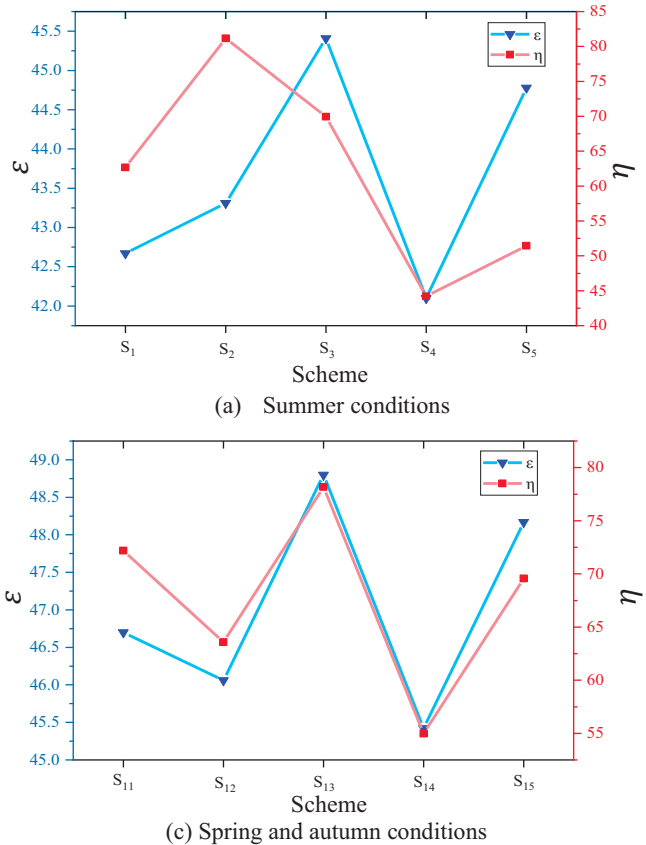


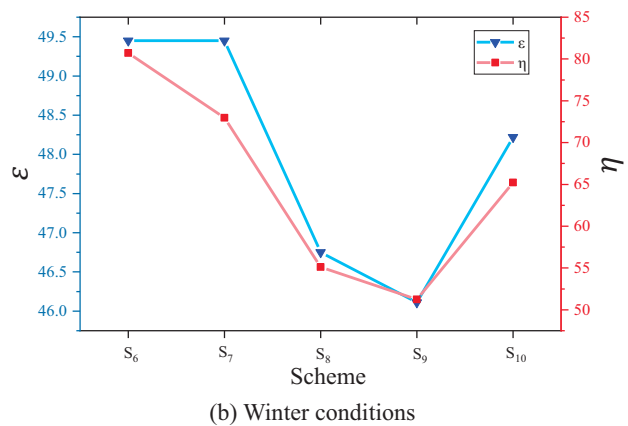
Fig. 6. The exergy efficiency of the system and the cold energy utilisation rate of the system under different combination schemes

According to the different combination schemes of low-temperature cold storage and high-temperature cold storage, under different working conditions, the total cooling capacity required by the cold storage can be calculated under different combination schemes. Bringing the calculated value into Eq. (18) can find the cold energy utilisation rate of different combination schemes under different working conditions.

(3) Summary of results

According to the different schemes listed in Table 6, the exergy efficiency and cold energy utilisation rate of different schemes can be calculated for different seasons. The calculated results are shown in Fig. 6.

From Fig. 6(a), it can be seen that, in summer conditions, the system of scheme 3 (2 low-temperature cold storage and 1 high-temperature cold storage) has the highest exergy efficiency, which can reach 45.41%. The corresponding cold energy utilisation rate is 69.93%. Scheme 2 (1 low-temperature cold storage, 3 high-temperature cold storage) has the highest cold energy utilisation rate, which can reach 81.16%, and the corresponding system's exergy efficiency is 43.31%. From Fig. 6(b), it can be seen that, in winter conditions, scheme 6 (3 low-temperature cold storages, 4 high-temperature cold storages) and scheme 7 (3 low-temperature cold storages, 2 high-temperature cold storages) have the highest exergy efficiency, which can reach 49.45%, and the cold energy utilisation rate of scheme 6 is the highest, at 80.72%. It can be seen from Fig. 6(c) that, in the spring and autumn conditions, the exergy efficiency of the system of scheme 13 (3 low temperature storage and 1 high temperature storage) is the highest, which can reach 48.80%, and the cold energy utilisation rate is also the highest at this time (78.17%).



ANALYSIS OF ACTUAL ROUTE APPLICATION

EXERGY EFFICIENCY AND COLD ENERGY UTILISATION RATE

Tab. 10. Different departure times at the starting port

T	T ₁	T ₂	T ₃	T ₄	T ₅	T ₆	T ₇	T ₈
Departure time	March 3	April 28	June 2	July 28	September 2	October 28	December 2	January 27

Based on the characteristics of cross-seasonal navigation of LNG-powered container ships, different combination schemes of low-temperature cold storage and high-temperature cold storage are proposed for different seasons. Aspen HYSYS software is used to simulate and calculate the different combination schemes of the system. According to the simulation results, the exergy efficiency and cold energy utilisation rate of the system under different combination schemes can be obtained. In order to explore the utilisation

of LNG cold energy during actual navigation of this type of ship, the different departure times at the starting port are listed. They are marked as T₁-T₈ and the specific departure times are shown in Table 10.

When a ship sails between two adjacent ports on the route, it is affected by the type and quantity of local cargo, the different number of containers, and the changing number of low-temperature cold storage and high-temperature cold storage required. According to actual research, the number of refrigerated containers between two adjacent ports can be obtained. According to Table 6, the combination of high-temperature cold storage and low-temperature cold storage between two adjacent ports can be selected, as shown in Table 11. For the convenience of presentation, Ningbo (A), Yantian (B), Singapore (C), Suez Canal (D), Le Havre (E), Dunkirk (F), Hamburg (G), Rotterdam (H), Marsaschloch (I), Suez Canal (J), Port Klang (K), Tianjin Xingang (L), and Busan (M) call ports are recorded as A-M, respectively. Among them, in the table, n represents the number of containers, unit 10³; n_L represents the number of low-temperature cold storage, unit: piece; n_H represents the number of high-temperature cold storage, unit: piece; and S represents the combination scheme adopted.

Tab. 11. Schemes of low-temperature cold storage and high-temperature cold storage under different conditions

Port	T									Port	T									
	T ₁	T ₂	T ₃	T ₄	T ₅	T ₆	T ₇	T ₈	T ₁		T ₂	T ₃	T ₄	T ₅	T ₆	T ₇	T ₈			
A-B	n	1.1	1	1	1	1	1	1	1	G-H	n _H	2	1	2	2	2	2	2	2	
	n _L	2	2	2	2	1	2	2	2		S	S ₉	S ₁₃	S ₁₂	S ₁₂	S ₁₂	S ₉	S ₉	S ₉	
	n _H	3	1	1	1	3	2	2	2		H-I	n	0.85	0.80	0.95	0.85	0.95	0.85	0.85	0.85
	S	S ₁₁	S ₃	S ₃	S ₃	S ₂	S ₁₂	S ₁₂	S ₁₂			n _L	3	2	3	3	2	2	2	3
B-C	n	1.3	1.3	1.3	1.3	1.3	1.3	1.3	1.3	I-J	n _H	0	1	0	1	2	2	2	1	
	n _L	1	1	1	1	1	1	1	1		S	S ₁₀	S ₁₄	S ₁₅	S ₁₃	S ₁₂	S ₁₂	S ₉	S ₁₃	
	n _H	3	2	2	3	3	3	3	3		J-K	n	0.70	0.68	0.80	0.70	0.80	0.70	0.70	0.70
	S	S ₂	S ₁	S ₁	S ₂			n _L	2	2	1	2	2	2	3	2				
C-D	n	1.5	1.5	1.5	1.5	1.5	1.5	1.5	1.5	K-L	n	0.70	0.68	0.80	0.70	0.80	0.70	0.70	0.70	
	n _L	1	1	1	1	1	1	1	1		n _H	1	1	0	1	1	1	0	1	
	n _H	3	3	3	3	3	3	3	3		S	S ₃	S ₃	S ₁	S ₁₄	S ₃	S ₁₄	S ₁₀	S ₃	
	S	S ₂		n	0.70	0.68	0.80	0.70	0.80	0.70	0.70	0.70								
D-E	n	1.5	1.5	1.5	1.5	1.5	1.5	1.5	1.5	L-M	n _L	2	2	1	2	2	2	3	2	
	n _L	1	1	1	1	1	2	2	2		n _H	1	1	2	1	1	1	0	1	
	n _H	3	3	3	3	3	3	3	3		S	S ₃	S ₃	S ₁	S ₃	S ₃	S ₁₄	S ₁₅	S ₃	
	S	S ₂	S ₁₁	S ₁₁	S ₁₁		n	0.45	0.55	0.55	0.50	0.60	0.50	0.50	0.50					
E-F	n	1.40	1.40	1.35	1.40	1.40	1.40	1.40	1.40	M-A	n _L	1	2	2	1	2	2	1	1	
	n _L	2	2	2	2	2	2	3	2		n _H	1	0	1	1	1	1	1	1	
	n _H	3	3	3	3	3	3	4	3		S	S ₄	S ₅	S ₃	S ₄	S ₁₄	S ₁₄	S ₄	S ₄	
	S	S ₁₁	S ₁₁	S ₁₁	S ₁₁	S ₁₁	S ₁₁	S ₆	S ₁₁		n	0.38	0.38	0.45	0.40	0.45	0.40	0.40	0.40	
F-G	n	1.30	1.30	1.28	1.30	1.30	1.30	1.30	1.30	M-A	n _L	2	1	1	2	3	3	2	2	
	n _L	3	2	3	2	2	3	3	3		n _H	1	1	0	1	0	0	1	1	
	n _H	2	2	1	3	3	2	2	2		S	S ₃	S ₄	S ₅	S ₁₄	S ₁₀	S ₁₀	S ₁₄	S ₁₄	
	S	S ₇	S ₁₂	S ₁₃	S ₁₁	S ₁₁	S ₇	S ₇	S ₇		n	320	300	350	300	380	300	300	300	
G-H	n	1.00	1.08	1.10	1.00	1.10	1.00	1.00	1.00	M-A	n _L	2	2	1	2	1	3	2	3	
	n _L	2	3	2	2	2	2	2	2		n _H	0	0	1	1	1	0	1	0	
											S	S ₁₄	S ₁₀	S ₁₄	S ₁₅	S ₁₄	S ₁₀	S ₁₄	S ₁₅	

According to the research above, the parent ship may need to complete the switch between the low-temperature cold storage and the high-temperature cold storage in a certain port due to the change in the combination schemes of low-temperature cold storage and high-temperature cold storage. In actual applications, it is relatively easy to complete this process by valve control, as shown in Fig. 7. If it is assumed that cold storage 1 is a low-temperature cold storage at the beginning and cold storage 2 is a high-temperature cold storage, valves 1, 4, 3, and 6 are opened, and valves 2, 5 are closed, then the high-temperature cold storage needs to be turned into a low-temperature cold storage. Valves 1, 2, 4 and 5 are opened and valves 3 and 6 are closed so that the transition from a high-temperature cold storage to a low-temperature cold storage can be completed. The transition from a low-temperature cold storage to a high-temperature cold storage can also be completed in the same way. In the actual application process, when switching between high-temperature cold storage and low-temperature cold storage, refrigerants of different concentrations may be mixed, but because the amount of refrigerant is relatively small, this will not have much impact on the normal operation of the system. In addition, the sealing performance of the pipeline should be strengthened to prevent the leakage of the refrigerant.

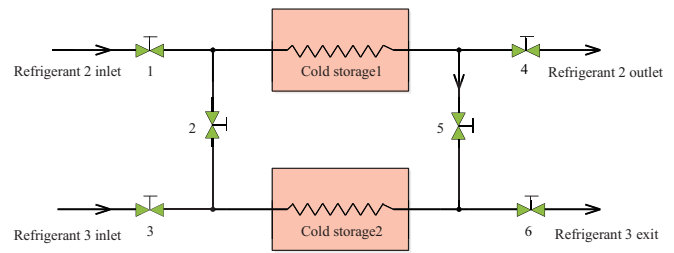


Fig. 7. System diagram of low-temperature cold storage and high-temperature cold storage switching

According to the combination schemes of low-temperature cold storage and high-temperature cold storage selected between two adjacent ports at different departure times of the starting port listed in Table 11. The exergy efficiency and cold energy utilisation rate of the system between two adjacent ports on the entire route are summarised in Fig. 8 and Fig. 9.

It can be seen from Fig. 9 and Fig. 10 that the exergy efficiency and cold energy utilisation rate of the system between adjacent ports change dynamically. The number of refrigerated containers in different ports and the number of low-temperature cold storage and high-temperature cold storage are different. Therefore, the combination schemes of low-temperature cold storage and high-temperature cold storage used between two adjacent ports is also different.

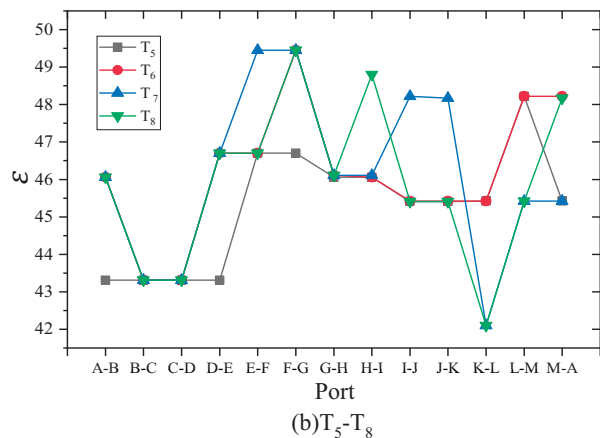
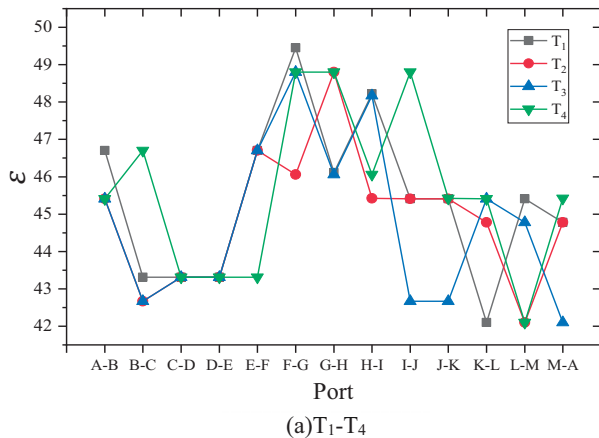


Fig. 8. Exergy efficiency of the system at different departure times from the starting port

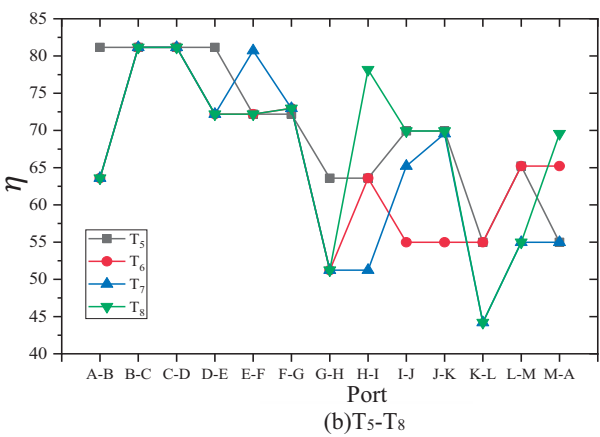
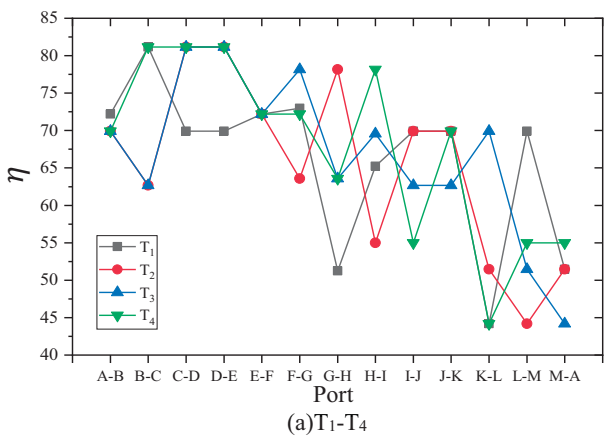


Fig. 9. Cold energy utilisation rate of the system at different departure times from the starting port

As a result, the system's exergy efficiency and cold energy utilisation rate change dynamically along the entire route.

In order to better evaluate the utilisation of cold energy by the system during the entire voyage, according to the system's exergy efficiency and cold energy utilisation rate between two adjacent ports on the route, the average exergy efficiency and average cold energy utilisation rate of the system along the entire route are calculated. The results are shown in Fig. 10.

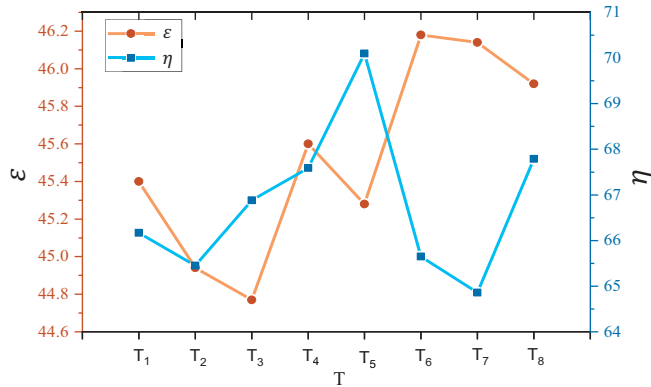


Fig. 10. The average exergy efficiency and average cold energy utilisation rate of the system along the entire route

Fig. 10 shows that the highest average exergy efficiency and average cold energy utilisation rate of the system along the entire route are 46.18% and 70.10%, respectively; the lowest average exergy efficiency and average cold energy utilisation rate of the system are 44.77% and 64.86%, respectively. It can be seen that if an LNG-powered container ship adopts the LNG cold energy utilisation system proposed in this study, then it can effectively utilise LNG cold energy.

ECONOMIC ANALYSIS

The LNG cold energy utilisation method proposed in this study will reduce part of the electrical energy of the ship's power grid that is consumed by refrigerated container refrigeration, but when the ship calls at a port or the LNG cold energy is not enough to ensure the refrigeration of all the refrigerated containers in the cold storage, it is necessary to consume the electric energy of the ship's power grid and use refrigeration equipment to refrigerate a single refrigerated container. According to actual investigations, the average power of a 40-foot refrigerated container during continuous refrigeration operation is between 4.8 kW and 5.8 kW. In this study, the electric energy consumed by the refrigerated containers before and after the cold storage refrigeration was calculated by using the LNG cold energy during the entire voyage period, corresponding to the different departure times at the starting port. The calculated results are denoted as E_1 and E_2 , respectively. The calculated results are shown in Fig. 11. The amount of fuel saved q can be calculated from the saved electric energy $E_1 - E_2$ and, thus, the reduced carbon emissions Mc can be calculated from the saved amount of fuel. The calculated results are shown in Fig. 12.

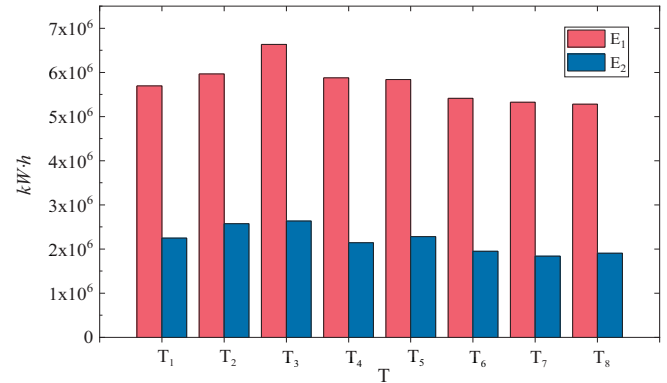


Fig. 11. Comparison of cold storage power consumption at different departure times from the starting port

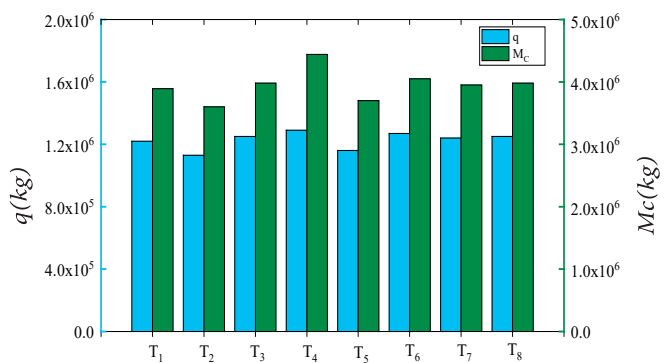


Fig. 12. Fuel saving and carbon emission reduction at different departure times from the port of origin

It can be seen from Fig. 11 and 12 that the electric energy consumption of refrigeration equipment is significantly reduced after the use of LNG cold energy to refrigerate the cold storage. Along the entire route, the maximum electric energy can be reduced by 7.14×10^6 kW·h, which is equivalent to saving 1.29×10^6 kg of fuel, reducing 4.44×10^6 kg of carbon emissions and improving the energy utilisation rate of the whole ship. This accords with the general trend of energy saving and emission reduction and has good value in its practical application.

CONCLUSIONS

In order to solve the problems of excessive LNG cold energy and large power consumption of refrigerated containers on LNG-powered container ships, this study proposed a new utilisation method that uses LNG cold energy to cool refrigerated containers in the cargo hold of ships. According to the actual operating conditions of the ship and the characteristics of the route, different combination schemes of the number of low-temperature cold storage and high-temperature cold storage units are designed. Exergy efficiency and cold energy utilisation rates of different combination schemes were calculated by Aspen HYSYS software and the economic efficiency of the cold energy utilisation system of

LNG fuel along the whole route was evaluated and analysed; the conclusions were as follows:

1. This research proposes a new utilisation method for using the cold energy of LNG-powered container ships for refrigerated containers. On this basis, a new type of cold storage using LNG cold energy was designed and the low-temperature cold storage and high-temperature cold storage models were further established. The main structure of the new cold storage was modelled in three dimensions and finally realised the cascade utilisation of LNG fuel cold energy, which can effectively solve the problem of excess cold fuel energy on LNG-powered ships, improve the energy utilisation rate and improve the economy of the ships. It has a very good practical significance to realise the energy saving and emission reduction of ships.

2. This study designed the number of low-temperature cold storage and high-temperature cold storage units under different seasonal conditions, according to the heat load of the cold storage of the parent ship in different seasons, combined with the total cold released by the ship during navigation. 15 different low-temperature cold storage and high-temperature cold storage combinations were investigated as optimal schemes.

3. Aspen HYSYS software was used to establish a new LNG-powered ship's cold energy utilisation process and set the parameters of key nodes in it to obtain the parameters of each node. The calculation model of the system's exergy efficiency and cold energy utilisation rate under different combination schemes was established and the exergy efficiency and cold energy utilisation rate of the new utilisation method was calculated. It can be concluded that the highest exergy efficiency of the system in the 15 combination schemes reached 49.45%, and the highest cold energy utilisation rate reached 81.16%, which provides theoretical support for evaluating the exergy efficiency and cold energy utilisation rate of the system along the entire route.

4. In order to get close to the actual sailing situation of the ship, this research is based on the characteristics of the ship's cross-seasonal navigation, regarding the different departure times at the starting ports and the number of refrigerated containers between two adjacent ports (the combination schemes of the number of low-temperature cold storage and high-temperature cold storage was selected for it). The average exergy efficiency and cold energy utilisation rate of the system along the entire route were summarised. It was found that the average exergy efficiency and average cold energy utilisation rate of the system were at their lowest at 44.77% and 64.86%, respectively, which proved that this type of ship can effectively utilise LNG cold energy.

5. This study calculates the total electrical energy consumed by refrigerated containers along the entire route before and after using the LNG cold energy utilisation method. It was found that, after adopting the new cold energy utilisation method, the power consumption for refrigerated container refrigeration was significantly reduced, and the power consumption could be reduced by 7.14×10^6 kW·h, which was equivalent to saving 1.29×10^6 kg of fuel and 4.44×10^6 kg of

carbon emissions. It can be seen that the LNG cold energy utilisation method proposed in this study has a promoting effect on the green development of ships.

ACKNOWLEDGEMENTS

The project was funded by Natural Science Foundation of Shandong Province of China (ZR2021ME156), Tsinghua University Shuimu Scholar Program (2020SM027) and China Postdoctoral Science Foundation (BX20200187, 2021M691718).

REFERENCES

1. X. Gu, G. Jiang, Z. Guo, and S. Ding, 'Design and Experiment of Low-Pressure Gas Supply System for Dual Fuel Engine', *Polish Marit. Res.*, vol. 27, no. 2, 2020, doi: 10.2478/pomr-2020-0029.
2. O. Cherednichenko, S. Serbin, and M. Dzida, 'Application of Thermo-chemical Technologies for Conversion of Associated Gas in Diesel-Gas Turbine Installations for Oil and Gas Floating Units', *Polish Marit. Res.*, vol. 26, no. 3, 2019, doi: 10.2478/pomr-2019-0059.
3. S. Serbin, B. Diasamidze, and M. Dzida, 'Investigations of the working process in a dual-fuel low-emission combustion chamber for an fpso gas turbine engine', *Polish Marit. Res.*, vol. 27, no. 3, 2020, doi: 10.2478/pomr-2020-0050.
4. T.C. Van, J. Ramirez, T. Rainey, et al. 'Global impacts of recent IMO regulations on marine fuel oil refining processes and ship emissions', *Transportation Research Part D*, vol. 70, 2019, doi: 10.1016/j.trd.2019.04.001.
5. L.P Perera, and B. Mo, 'Emission Control Based Energy Efficiency Measures in Ship Operations', *Applied Ocean Research*, vol. 60, 2016, doi: 10.1016/j.apor.2016.08.006.
6. H.P. Nguyen, A.T. Hoang, S. Nizetic, et al. 'The electric propulsion system as a green solution for management strategy of CO₂ emission in ocean shipping: A comprehensive review', *International Transactions on Electrical Energy Systems*, 2020, doi: 10.1002/2050-7038.12580.
7. N.R. Sharma, D. Dimitrios, A.I. Ler, et al. 'LNG a clean fuel the underlying potential to improve thermal efficiency', *Journal of Marine Engineering & Technology*, 2020, doi: 10.1080/20464177.2020.1827491.
8. I. Mallidis, S. Despoudi, R. Dekker, et al. 'The impact of sulphur limit fuel regulations on maritime supply chain network design', *Annals of Operations Research*, vol. 294, no. 8, 2018, doi: 10.1007/s10479-018-2999-4.

9. L.B. Reinhardt, D. Pisinger, M.M. Sigurd, et al. 'Speed optimizations for liner networks with business constraint', *European Journal of Operational Research*, vol. 285, no. 3, 2020, doi: 10.1016/j.ejor.2020.02.043.
10. Eun, Soo, and Jeong, 'Optimization of power generating thermoelectric modules utilizing LNG cold energy', *Cryogenics*, vol. 88, 2017, doi: 10.1016/j.cryogenics.2017.10.005.
11. O. Schinas, and M. Butler, 'Feasibility and commercial considerations of LNG-fueled ships', *Ocean Engineering*, vol. 122, 2016, doi: 10.1016/j.oceaneng.2016.04.031.
12. R. Zhao et al., 'A Numerical and Experimental Study of Marine Hydrogen-Natural Gas-Diesel Tri-Fuel Engines', *Polish Marit. Res.*, vol. 27, no. 4, 2020, doi: 10.2478/pomr-2020-0068.
13. M. Badami, J.C. Bruno, A. Coronas, and G. Fambri, 'Analysis of different combined cycles and working fluids for LNG exergy recovery during regasification', *Energy*, vol. 159, 2018, doi: 10.1016/j.energy.2018.06.10.
14. B.B. Kanbur, L. Xiang, S. Dubey, F.H. Choo, and F. Duan, 'Cold utilisation systems of LNG: a review', *Renewable and Sustainable Energy Reviews*, vol. 79, 2017, doi: 10.1016/j.rser.2017.05.161.
15. J. Dong, S. Huang, S. Li, Y. Yao, Y. Jiang, 'LNG cold energy used in cold storage refrigeration performance simulation research', *Journal of Harbin Institute of Technology*, vol. 49, no. 2, 2017.
16. T. Banaszkiwicz, 'The Possible Coupling of LNG Regasification Process with the TSA Method of Oxygen Separation from Atmospheric Air', *Entropy*, vol. 23, no. 3, 2021, doi: 10.3390/e23030350.
17. W. Lin, M. Huang, H. He, et al., 'A transcritical CO₂ Rankine Cycle with LNG cold energy utilisation and liquefaction of CO₂ in gas turbine exhaust', *Journal of Energy Resources Technology*, vol. 131, no. 4, 2009, doi: 10.1115/1.4000176.
18. T. Jin, J.J. Hu, G.B. Chen, and K. Tang, 'Novel air separation unit cooled by liquefied natural gas cold energy and its performance analysis', *Journal of Zhejiang University*, vol. 41, no. 5, 2007.
19. E. Baldasso, M.E. Mondejar, S. Mazzoni, et al., 'Potential of liquefied natural gas cold energy recovery on board ships', *Journal of Cleaner Production*, vol. 271, 2020, doi: 10.1016/j.jclepro.2020.122519.
20. H.L. Sang, and K. Park, 'Conceptual design and economic analysis of a novel cogeneration desalination process using LNG based on clathrate hydrate', *Desalination*, vol. 498, 2021, doi: 10.1016/j.desal.2020.114703.
21. P. Babu, A. Nambiar, R.C. Zheng, et al., 'Hydrate-based desalination (HyDesal) process employing a novel prototype design', *Chemical Engineering Science*, vol. 218, 2020, doi: 10.1016/j.ces.2020.115563.
22. J. Sun, K. Han, C. Xie, et al., 'Liquid-solid fluidized bed seawater ice desalination based on LNG cold energy'. *Modern Chemical Industry*, vol. 40, no. 7, 2020, doi: 10.16606/j.cnki.issn0253-4320.2020.07.042.
23. I.M. Mujtaba, W. Cao, and C. Beggs, 'Theoretical approach of freeze seawater desalination on flake ice maker utilizing LNG cold energy', *Desalination*, vol. 355, 2015, doi: 10.1016/j.desal.2014.09.034.
24. E.G. Cravalho, J.J. McGrath, and W.M. Toscano, 'Thermodynamic analysis of the regasification of LNG for the desalination of sea water', *Cryogenics*, vol. 17, no. 3, 1977, doi: 10.1016/0011-2275(77)90272-7.
25. T. He, R. Zheng, J. Zheng, Y. Ju, et al., 'LNG cold energy utilisation: prospects and challenges', *Energy*, vol. 170, 2019, doi: 10.1016/j.energy.2018.12.170.
26. N. Yamanouchi, and H. Nagasawa, 'Using LNG cold for air separation', *Chemical Engineering Progress*, vol. 75, no. 7, 1979.
27. Y. Wu, Y. Xiang, L. Cai, et al., 'Optimization of a novel cryogenic air separation process based on cold energy recovery of LNG with exergoeconomic analysis', *Journal of Cleaner Production*, vol. 275, 2020, doi: 10.1016/j.jclepro.2020.123027.
28. M. Mehrpooya, B. Golestani, and S. Mousavian, 'Novel cryogenic argon recovery from the air separation unit integrated with LNG regasification and CO₂ transcritical power cycle', *Sustainable Energy Technologies and Assessments*, vol. 40, no. 3, 2020, doi: 10.1016/j.seta.2020.100767.
29. R. Zhang, C. Wu, W. Song, et al., 'Energy integration of LNG light hydrocarbon recovery and air separation: Process design and technic-economic analysis', *Energy*, vol. 207, 2020, doi: 10.1016/j.energy.2020.118328.
30. Z. Gu, 'The simulation and operation optimization of the C₂+ recovery process from LNG', *Petrochemical Industry Application*, vol. 37, no. 4, 2018.
31. T. Gao, W. Lin, and A. Gu, 'Improved processes of light hydrocarbon separation from LNG with its cryogenic energy utilised', *Energy Conversion & Management*, vol. 52, no. 6, 2011, doi: 10.1016/j.enconman.2010.12.040.

32. T. Yamamoto, T. Furuhashi, N. Arai, and K. Mori, 'Design and testing of the Organic Rankine Cycle', *Energy*, vol. 26, no. 3, 2001.
33. N.B. Desai and S. Bandyopadhyay, 'Process integration of organic Rankine cycle', *Energy*, vol. 34, no. 10, 2009, doi: 10.1016/j.energy.2009.04.037.
34. J. Koo, S.R. Oh, Y.U. Choi, et al., 'Optimization of an Organic Rankine Cycle System for an LNG-Powered Ship', *Energies*, doi: 10.3390/en12101933.
35. Z. Tian, W. Zeng, B. Gu, et al., 'Energy, exergy, and economic (3E) analysis of an organic Rankine cycle using zeotropic mixtures based on marine engine waste heat and LNG cold energy', *Energy Conversion and Management*, vol. 228, 2020, doi: 10.1016/j.enconman.2020.113657.
36. X. Sun, S. Yao, J. Xu, et al., 'Design and Optimization of a Full-Generation System for Marine LNG Cold Energy Cascade Utilisation', *Journal of Thermal Science*, vol. 29, no. 3, 2020, doi: 10.1007/s11630-019-1161-1.
37. L. Xu, and G. Lin, 'LNG-FSRU new LNG cold energy power generation optimization plan', *Natural gas chemical industry (C1 chemistry and chemical engineering)*, vol. 45, no. 5, 2020.
38. L. Zhao, J. Zhang, X. Wang, et al., 'Dynamic exergy analysis of a novel LNG cold energy utilisation system combined with cold, heat and power', *Energy*, vol. 212, 2020, doi: 10.1016/j.energy.2020.118649.
39. I.A. Fernández, M.R. Gómez, J.R. Gómez, and L.M. López-González, 'Generation of H₂ on Board Lng Vessels for Consumption in the Propulsion System', *Polish Marit. Res.*, vol. 27, no. 1, 2020, doi: 10.2478/pomr-2020-0009.

CONTACT WITH THE AUTHORS

Boyang Li

e-mail: qdllby@126.com

College of Electromechanical Engineering,
Qingdao University of Science and Technology,
Qingdao, 266061 Qingdao,
CHINA

Yajing Li

e-mail: sdliyajing@126.com

CHINA
College of Electromechanical Engineering,
Qingdao University of Science and Technology,
Qingdao, 266061 Qingdao,
CHINA

Fang Deng

e-mail: dengfhelen@163.com

College of Electromechanical Engineering,
Qingdao University of Science and Technology,
Qingdao, 266061 Qingdao,
CHINA

Qianqian Yang

e-mail: sdqdyqq@126.com

College of Electromechanical Engineering,
Qingdao University of Science and Technology,
Qingdao, 266061 Qingdao,
CHINA

Baoshou Zhang

e-mail: sxsdzbs@126.com

School of Aerospace Engineering,
Tsinghua University,
Beijing, 100084 Beijing,
CHINA

PARAMETRIC ANALYSIS OF THE EFFICIENCY OF THE COMBINED GAS-STEAM TURBINE UNIT OF A HYBRID CYCLE FOR THE FPSO VESSEL

Serhiy Serbin*¹

Nikolay Washchilenko¹

Marek Dzida²

Jerzy Kowalski²

¹ Admiral Makarov National University of Shipbuilding, Ukraine

² Gdańsk University of Technology, Poland

* Corresponding author: serbin1958@gmail.com (S. Serbin)

ABSTRACT

A thermal diagram of the combined gas-steam turbine unit of a hybrid cycle, which is an energy complex consisting of a base gas turbine engine with a steam turbine heat recovery circuit and a steam-injected gas turbine operating with overexpansion, is proposed. A mathematical model of a power plant has been developed, taking into consideration the features of thermodynamic processes of simple, binary, and steam-injected gas-steam cycles. Thermodynamic investigations and optimization of the parameters of a combined installation of a hybrid cycle for the generation of electrical energy have been carried out. Three-dimensional calculations of the combustion chamber of a steam-injected gas turbine were carried out, which confirmed the low emissions of the main toxic components.

Keywords: Combined-cycle, Gas turbine, Steam turbine, Power plant

SYMBOLS AND ABBREVIATIONS

C	Molar concentration, mol/m ³	v	Velocity, m/s
C_N	Specific fuel consumption, kg/(kW·h)	X	Mass fraction; relative steam flow rate
c_p	Average mass heat capacity, kJ/(kg·K)	x	Dryness factor
D	Diffusion coefficient, m ² /s	Y	Mass concentration, kg/m ³
d	Relative steam content	α	Air excess coefficient; discharge coefficient
E	Activation energy, J/mol	β	Coefficient of leakage
G	Mass flow rate, kg/s	ε	Turbulent dissipation rate, m ² /s ³
g	Relative capacity	η	Efficiency
H_U	Lower calorific value of the fuel	π_c	Total pressure ratio of the compressor
h	Enthalpy, kJ/kg	ρ	Mass density, kg/m ³
k	Circulation ratio; isentropic index; turbulent kinetic energy, m ² /s ²	ν	Total pressure recovery coefficient
L_0	Stoichiometric amount of air, kg/kg	C	Compressor
M	Molecular weight, kg/mol	CC	Combustion chamber
N	Power, kW	CDT	Compressor drive turbine
N_c	Specific power, kJ/kg	$CGSTU$	Combined gas-steam turbine unit
P	Pressure, Pa	GSC	Gas-steam condenser
R	Gas constant, kJ/(kmol·K); rate of component's formation, mol/(m ³ ·s)	GT	Generator turbine
T	Temperature, K	$FPSO$	Floating Production, Storage, and Offloading vessel
		GTA	Gas turbine aggregate
		GTE	Gas turbine engine
		HPC	High-pressure compressor

HPT	High-pressure turbine
HRC	Heat recovery circuit
HRS	Heat-recovery steam generator
LPC	Low-pressure compressor
LPT	Low-pressure turbine

SIGT	Steam-injected gas turbine
SIGTA	Steam-injected gas turbine aggregate
SC	Steam condenser
ST	Steam turbine

INTRODUCTION

Combined gas-steam turbine plants are increasingly used for the generation of electrical energy [1]. A large number of thermal circuits have been developed that allow the heat of exhaust gases from gas turbine engines (GTE) of a simple cycle in a heat recovery circuit (HRC) to be utilized for generating steam of various parameters [2-4]. Superheated steam is usually supplied to a steam turbine (ST) to generate additional power and implement a binary steam-gas cycle, or is injected into the combustion chamber (CC) of the so-called steam-injected gas turbine (SIGT) to implement a steam-injected cycle [5-6]. In the turbines of the SIGT, the expansion of the gas-steam mixture is carried out with an additional (in comparison with the GTE of a simple thermal scheme) generation of mechanical energy. To trap the moisture contained in the gas-steam mixture, it is possible to use the so-called gas-steam condenser operating at atmospheric pressure, where a large amount of water introduced into the cycle condenses, and dehydrated combustion products are released into the atmosphere. With the help of the feed pump, the water is again directed to the heat-recovery steam generator (HRS). The thermal circuit that implements such a steam-injected cycle with moisture trapping is called "Aquarius" [7]. Implementation of the SIGT cycle with steam injection into the combustion chamber makes it possible to increase the efficiency of the cycle by 22.5-30.7%, and the specific power by 49-73% in comparison with the GTE of a simple scheme [8].

Note that the combined gas-steam turbine plants are most in demand for thermal power stations, where the power capacities are very significant. Currently, the capabilities of such installations are expanding and are promising for marine applications, especially for Floating Production, Storage, and Offloading (FPSO) vessels. Power plants for the FPSO vessels are characterized by high values of the generated power, because they are designed to generate electricity for the needs of oil production, storage, and unloading of oil as well as to supply energy to various auxiliary equipment for processing crude oil and associated gas [9-10].

Many FPSO vessels are equipped with gas turbines and combined power plants. Examples are the vessels Global Producer III, Armada Olombendo, Dhirubhai-1, Pioneiro de Libra, Cidade de Itajaí, Triton, Cidade de Maricá, and others [9, 11, 12]. The total capacity of power plants is largely determined by the purpose of the vessel and varies from 30 to 150 MW, and the energy consumption is extremely irregular and is determined by the characteristics of the oil field, the production platform, and the completeness of the equipment used. In most cases, it is envisaged to use from 2 to 4 gas turbine engines, often operating at partial loads.

This investigation examines the thermal diagram of a power plant that combines the advantages of a gas turbine aggregate (GTA) with a heat recovery circuit (GTA with HRC) with the advantages of a steam-injected gas turbine aggregate (SIGTA) operating with overexpansion.

1. THERMAL DIAGRAM OF THE INSTALLATION

A thermal diagram of the combined gas-steam turbine unit of a hybrid cycle (CGSTU) created based on a serial gas turbine engine, which also includes a steam-injected gas turbine operating with overexpansion and a steam turbine heat recovery circuit for a serial gas turbine engine, is proposed. The GTA with HRC is designed based on the UGT25000 gas turbine engine serially produced by Zorya-Mashproekt, with a capacity of 26,700 kW and efficiency of 36.3% at ISO conditions [13]. The diagram of the proposed hybrid cycle power plant is shown in Fig. 1.

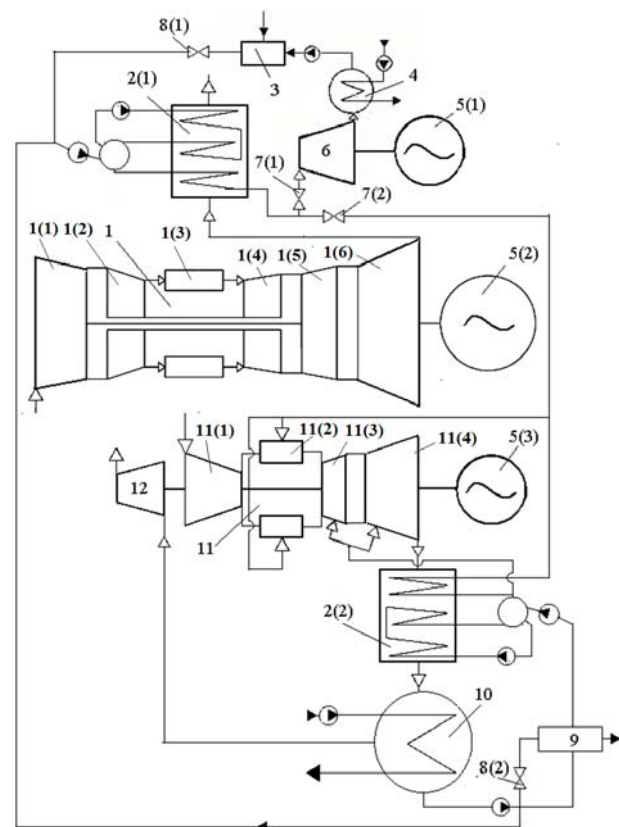


Fig. 1. Thermal diagram of the combined gas-steam turbine unit of a hybrid cycle: 1 - GTE UGT25000; 1(1) - LPC; 1(2) - HPC; 1(3) - CC; 1(4) - HPT; 1(5) - LPT; 1(6) - GT; 2(1), 2(2) - HRS; 3 - boiler water tank; 4 - steam condenser; 5(1), 5(2), 5(3) - electric generators; 6 - ST; 7(1), 7(2) - steam valves; 8(1), 8(2) - water valves; 9 - water treatment unit; 10 - gas-steam condenser; 11 - SIGT; 11(1) - C; 11(2) - CC; 11(3) - CDT; 11(4) - GT; 12 - exhauster.

The thermal diagram includes (a) a serial GTE UGT25000 '1' operating on an electric generator '5(2)', (b) a steam turbine HRC consisting of a heat recovery steam generator '2(1)' and a steam turbine '6' with the appropriate equipment, which is loaded on the electric generator '5(1)', as well as (c) a SIGTA, which includes the SIGT '11', HRSG '2(2)', as well as a gas-steam condenser '10'. The GTE '1' is developed according to the kinematic scheme with a two-spool compressor: '1(1)' - LPC and '1(2)' - HPC and involves a combustion chamber '1(3)' and three turbines: '1(4)' - HPT, '1(5)' - LPT, '1(6)' - GT. The SIGT '11' consists of a single-spool compressor '11(1)', a combustion chamber with power steam injection '11(2)', a compressor drive turbine '11(3)' and a generator turbine '11(4)'. The SIGT operates with overexpansion, which is provided by the exhauster '12', and transfers power to the electric generator '5(3)'.

The exhaust gases after the base GTE UGT25000 enter the HRC '2(1)', which generates superheated steam. The steam supply to the ST '6' and the combustion chamber of the SIGT is regulated depending on the position of the valves '7(1)' and '7(2)'. When the valve '7(1)' is open and the valve '7(2)' is closed, the CGSTU operates as a gas turbine aggregate with the single pressure steam-water HRC, and the rest of the equipment may not be used. When the valve '7(2)' is open, one part of the steam from the HRSG '2(1)' (up to 50% of its steam capacity) is injected into the CC of the SIGT '11', and the other part of the steam continues to flow to the ST '6' of the HRC of the basic gas turbine engine '1'.

The HRSG '2(2)', which is located at the exit from SIGT '11', generates superheated steam at the same pressure as the HRSG '2(1)'. Both superheated steam, which is injected to the mixing zone of the combustion chamber's flame tubes, and dry saturated steam, which is fed to the cooling of the CTD '11(3)' and GT '11(4)' nozzle and rotor blades, and also the casing of the SIGT '11', are generated.

The waste gas-steam mixture after the SIGT '11' passes through the HRSG '2(2)' and enters the gas-steam condenser '10', in which most of the steam injected into the CC, as well as steam from the cooling system of the high-temperature turbine part of the engine, is condensed into the water and, using a pump, enters the water treatment unit '9'.

After the gas-steam condenser '10', the combustion products containing the residual amount of steam enter the exhauster '12', in which they are compressed to atmospheric pressure and discharged into the atmosphere. From the water treatment unit '9', using feed pumps, water flows back to the HRSG '2(1)' and '2(2)' separators.

A thermodynamic investigation and optimization of the cycle parameters for the considered scheme of the combined CGSTU of a hybrid cycle for a thermal power station were carried out for the case of using GTE UGT25000 as a base one. The results of the efficiency of the thermal scheme were obtained taking into consideration the international standards ISO 9001-2008 (without taking into account the total pressure loss at the inlet and outlet of the engine and an ambient temperature of 288 K). In the investigation, the values of total pressure losses along the CGSTU path, the

efficiency of the turbine and compressor stages, and other similar parameters were taken under the manufacturer's recommendations [14].

It is assumed that the basic GTE will be used without changes in design and parameters. In addition to the basic gas turbine engine, a steam turbine HRC with the single pressure HRSG and optimal steam parameters, the SIGT, the HRSG '2(2)', the exhauster, and the gas-steam condenser were designed. In the proposed article, the parameters of the SIGT with HRC and overexpansion are investigated in the most detail. Note that, in this case, a significant part of the steam generated by the HRSG of the base GTE is additionally supplied to the SIGT.

2. MATHEMATICAL MODEL OF PROCESSES IN THE COMBINED GAS-STEAM TURBINE UNIT OF A HYBRID CYCLE

The developed mathematical model of the combined gas-steam turbine unit of a hybrid cycle for a thermal power station consists of several modules.

Module one is a mathematical model of a basic GTE loaded on an electric generator, which is verified according to the data of the manufacturer under ISO conditions, which are open access. This, using the method of balancing the object's thermodynamic parameters, makes it possible to obtain reliable values of some key functional parameters of the mathematical model that determine the level of technology of the produced turbomachines, as well as to estimate the values of the coefficients and parameters that are absent in the advertising materials of the manufacturer but are necessary for further calculations.

Module two recalculates the main parameters of the basic gas turbine engine for the conditions of its operation as part of a thermal circuit with a gas outlet pipe and a connected heat recovery steam generator HRSG '2(1)'. The coefficients of the influence of total pressure losses of the above-mentioned devices located in the exhaust duct of the gas turbine engine, obtained in the previous stage by the method of two-sided variation, are used to define the efficiency of the gas turbine engine η_g , the effective power of the gas turbine engine N_{eGTE} , and the temperature of the engine exhaust gases T_4 .

Module three is a mathematical model of a steam turbine heat recovery circuit consisting of the HRSG '2(1)', a steam turbine loaded on an electric generator, a steam condenser (SC), and pumps serving the HRC equipment. It is assumed that the ST is designed to operate with the full amount of steam that the HRSG '2(1)' is capable of generating at the full power mode of the base GTE.

The steam pressure in the separator of the HRSG '2(1)' is determined by the formula

$$P_{HRSG} = \frac{P_{out} \cdot \pi_{cSIGT} \cdot v_{cc}}{v_{s3} \cdot v_{ss1} \cdot v_{id}} \quad (1)$$

where P_{out} is the outside air pressure, π_{cSIGT} is the total pressure ratio of the SIGT compressor, v_{cc} , v_{s3} , v_{ss1} , v_{id} are the

total pressure recovery coefficients for the SIGT's combustion chamber, the steam line from the HRSG '2(1)' to the CC, the HRSG '2(1)' steam superheater, and the steam injection device, respectively.

The superheating temperature in the '2(1)' is taken according to the coupled steam parameters [10]

$$T_{ss1} = F(P_{HRSG}, \eta_{st}, x_{min}, P_Z) \quad (2)$$

where P_Z is the steam pressure in the SC, η_{st} is the internal efficiency of the ST, and x_{min} is the permissible rate of the steam dryness fraction after the last stage of the ST.

The relative steam capacity of the HRSG '2(1)' for superheated steam

$$g_{ss} = \frac{\beta_{l1} \cdot \beta_{go1} \cdot c_{pg4} \cdot (T_4 - T_{eb1})}{(h_{ss1} - h_{ws}) + k_c \cdot (h_{ws} - h_{w2e})} \quad (3)$$

where β_{l1} is the coefficient of leakage of the HRSG '2(1)', β_{go1} is the discharge coefficient of the base GTE's gas outlet device, k_c is the circulation ratio of the HRSG '2(1)' pump, c_{pg4} is the average mass heat capacity of the gas in the superheating and evaporating banks of the HRSG '2(1)', h_{ss1} is the enthalpy of superheated steam at the outlet of the HRSG '2(1)', h_{ws} , h_{w2e} are the enthalpy of water at the pressure saturation line in the separator and at the outlet of the economizer bank of the HRSG '2(1)', respectively, and T_{eb1} is the temperature behind the evaporating bank.

This module also determines the power of the steam turbine, the energy consumption for the operation of the auxiliary equipment of the HRC, the power and efficiency of a thermal power station in the configuration of a combined GTA with a steam HRC.

Module four is a mathematical model of a steam-injected gas turbine aggregate, consisting of a SIGT operating with overexpansion and loaded onto a separate electric generator, a heat recovery steam generator HRSG '2(2)' and a gas-steam condenser (GSC). Superheated steam is supplied to the SIGT's CC both from its own HRSG '2(2)' and from the HRSG '2(1)' in the fraction X of its total steam capacity.

The relative amount of steam from the HRSG '2(1)' injected into the CC, which is necessary to achieve the specified temperature at the turbine inlet and the specified air excess coefficient α in this CC, is determined by the formula

$$g_{ss1} = \frac{\frac{1}{\alpha \cdot L_0} A - B}{(h_{3s} - h_{ss}) / \alpha_{cc}} - g_{ss2} \frac{(h_{3s} - h_{ss2})}{(h_{3s} - h_{ss})} \quad (4)$$

where

$$A = H_U \cdot \eta_{cc} - [c_{p_{scp}}|_{293}^{T_3} \cdot (L_0 + 1) - c_{pa}|_{293}^{T_3} \cdot L_0] \cdot (T_3 - 293),$$

$$B = c_{pa}|_{293}^{T_3} \cdot (T_3 - 293) - c_{pa}|_{293}^{T_2} \cdot (T_2 - 293).$$

In formula (4) T_2 is the air temperature behind the SIGT's compressor, T_3 is the temperature of the gas-steam mixture before the SIGT's compressor turbine, h_{ss} is the enthalpy of superheated steam at the outlet from the HRSG '2(1)', h_{ss2} is the enthalpy of superheated steam at the outlet from the HRSG '2(2)', h_{3s} is the enthalpy of superheated steam in the gas-steam mixture at the outlet of the SIGT's CC, g_{ss2} is the relative steam capacity of the HRSG '2(2)' for superheated steam, H_U is the lower calorific value of the fuel, L_0 is the stoichiometric amount of air, α is the given value of the air excess coefficient of the SIGT's CC, α_{cc} is discharge coefficient of the CC, η_{cc} is the coefficient of combustion completeness in the CC, $c_{p_{scp}}$ is the average mass heat capacity of stoichiometric combustion products, and c_{pa} is the average mass heat capacity of air.

The relative steam capacity of the HRSG '2(1)' for superheated steam

$$A = H_U \cdot \eta_{cc} - [c_{p_{scp}}|_{293}^{T_3} \cdot (L_0 + 1) - c_{pa}|_{293}^{T_3} \cdot L_0] \cdot (T_3 - 293), \quad (5)$$

$$B = c_{pa}|_{293}^{T_3} \cdot (T_3 - 293) - c_{pa}|_{293}^{T_2} \cdot (T_2 - 293).$$

where β_{go2} is the discharge coefficient of the SIGT's gas outlet device, β_{l2} is the coefficient of leakage of the HRSG '2(2)', Σg_{scoi} is the total relative flow rate of dry saturated steam used to cool the SIGT's turbine stages, $c_{p_{gs4}}$ is the average mass heat capacity of the gas-steam mixture in the superheating and evaporating banks of the HRSG '2(2)', h_{ss2} is the enthalpy of superheated steam at the HRSG '2(2)' outlet, h_{11} is the enthalpy of dry saturated steam at the HRSG '2(2)' outlet, h_{ws2} is the enthalpy of water at the pressure saturation line in the separator of the HRSG '2(2)', T_{dgs} is the temperature of the gas-steam mixture at the outlet from the SIGT, and T_{eb2} is the temperature of the gas-steam mixture behind the evaporating bank of the HRSG '2(2)'.

The absolute value of the air flow rate through the SIGT's compressor is found by the formula

$$G_{c_{SIGT}} = G_{c1} \cdot \frac{g_{ss} \cdot X}{g_{ss1}} \quad (6)$$

where G_{c1} is the air flow rate through the compressor of the base GTE.

The amount of water lost in the SIGT cycle with exhaust gases after the GSC is determined by the formula

$$G_{weg} = \frac{d_{GSC} \cdot (G_{c_{SIGT}} \cdot \beta_{go2} - G_{w\Sigma})}{(1 - d_{GSC})} \quad (7)$$

where $G_{w\Sigma}$ is the total amount of water vapor in the gas-steam flow before the GSC.

In formula (7), the value of the relative steam content in the flow behind the GSC,

$$d_{GSC} = \frac{R_g}{R_s \cdot \left(\frac{P_{out}}{v_{go} \cdot \pi_{ex} \cdot P_{s2}} - 1 \right) + R_g} \quad (8)$$

where P_{s2} is the partial steam pressure in the mixture behind the GSC, R_g and R_s are the gas constants for combustion products and steam, respectively, π_{ex} is the exhauster compression ratio, and ν_{go} is the total pressure recovery coefficient for the exhaust SIGT's path after the exhauster.

The exhauster drive power

$$N_{ex} = (G_{cSIGT} \cdot \beta_{go_2} - G_{w\Sigma} + G_{weg}) \cdot c_{p_{ex}} \cdot \frac{T_8 \cdot (\pi_{ex}^{k_{ex}-1} - 1)}{\eta_{ex}} \quad (9)$$

where T_8 is the temperature of the gas-steam mixture at the outlet of the GSC, $c_{p_{ex}}$ is the average mass heat capacity of the gas-steam mixture in the exhauster, k_{ex} is the isentropic index for the pressure increasing process in the exhauster, η_{ex} is the internal adiabatic efficiency of the exhauster, and $G_{w\Sigma}$ is the total amount of water vapor in the gas-steam flow before the GSC.

The SIGT's compressor drive power

$$N_{cSIGT} = G_{cSIGT} \cdot c_{pc} \cdot \frac{T_{ou} \cdot (\pi_{cSIGT}^{k_c-1} - 1)}{\eta_{cSIGT}} \quad (10)$$

where c_{pc} is the average mass heat capacity of air in the SIGT's compressor, k_c is the isentropic index for the pressure increasing process in the SIGT's compressor, and η_{cSIGT} is the internal adiabatic efficiency of the SIGT's compressor.

The effective power of the SIGT

$$N_{eSIGT} = G_{cSIGT} \cdot N_{sp_t} \cdot \eta_t - N_{cSIGT} - N_{ex} \quad (11)$$

where N_{sp} is the specific power of the SIGT's turbine part, and η_t is the mechanical efficiency of the SIGT's turbine part.

The total electrical power of the power plant

$$N_{elCGSTU} = N_{eSIGT} \cdot \eta_{eg_3} + N_{eGTE} \cdot \eta_{eg_2} + N_{eST} \cdot \eta_{eg_1} \quad (12)$$

where N_{eGTE} is the effective power of the base GTE, N_{eST} is the effective steam turbine power, η_{eg1} , η_{eg2} , η_{eg3} are the efficiency of the listed electric generators.

The specific fuel consumption at the CGSTU's power plant

$$C_{Ne} = \frac{G_{fh} + G_{fh_2}}{N_{eGTE} + N_{eST} + N_{eSIGT}} \quad (13)$$

where G_{fh} and G_{fh_2} are the hourly fuel consumption of the base GTE and the SIGT, respectively.

The efficiency of the CGSTU's power plant

$$\eta_{eCGSTU} = \frac{3600}{C_{Ne} \cdot H_U} \quad (14)$$

3. OPTIMIZATION OF THE PARAMETERS OF THE COMBINED GAS-STEAM TURBINE UNIT OF A HYBRID CYCLE

Figure 2 shows the dependences of the efficiency of the combined CGSTU of a hybrid cycle on the total compressor pressure ratio $\pi_{c\Sigma}$ in the SIGT and the exhauster compression ratio π_{ex} . The results were obtained for the case of injection of the entire amount of steam generated by the HRSG located behind the base GTE into the SIGT at the temperature of the gas-steam mixture at the turbine inlet $T_3 = 1500$ K and the air excess coefficient in the combustion chamber $\alpha_0 = 1.5$.

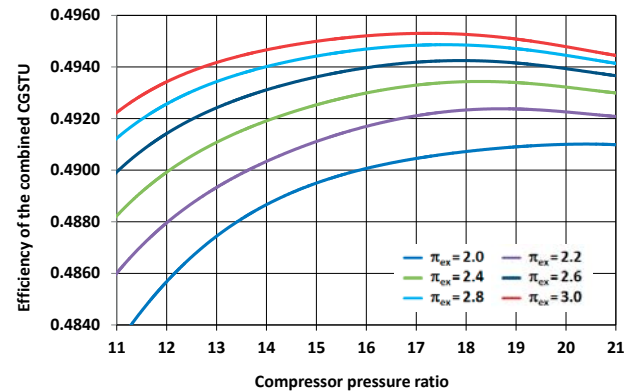


Fig. 2. Dependences of the efficiency of the combined CGSTU of a hybrid cycle for a thermal power station on the compressor and exhauster pressure ratios.

Analysis of the data shows the possibility of achieving the efficiency of the combined CGSTU at the level of 49.1–49.5% with the optimal compressor pressure ratio of 16–20 in the SIGT and varying the exhauster pressure ratio in the range from 2.0 to 3.0.

Figure 3 shows the dependences of the electric power of the combined CGSTU of a hybrid cycle on the compressor pressure ratio in the SIGT and the exhauster pressure ratio for the same initial conditions.

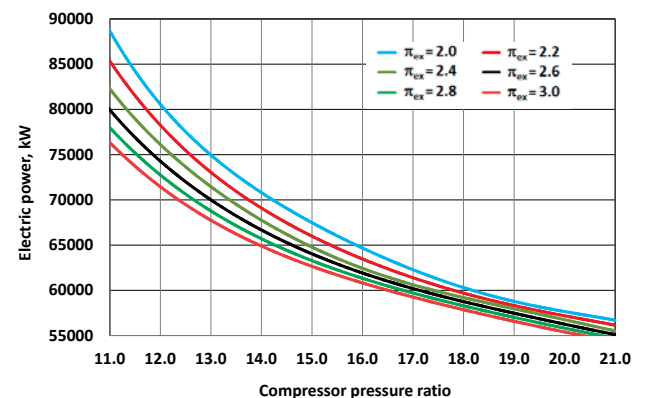


Fig. 3. Dependences of the electric power of the combined CGSTU of a hybrid cycle on the compressor and exhauster pressure ratios.

The analysis shows the possibility of achieving the electric power of the power plant at the level of 55–65 MW with the optimal compressor pressure ratio of 16–20 in the SIGT and a change in the exhauster pressure ratio in the range from 2.0 to 3.0.

The investigation of the influence of the air excess coefficient α_0 in the SIGT combustion chamber on the efficiency indicators of the CGSTU (Fig. 4) shows that with an increase in the value of this parameter from 1.5 to 2.0, the efficiency of the installation increases from 49.4 to 50.6%, and the optimal SIGT compressor pressure ratio $\pi_{c\Sigma}$ decreases from 17.5 to 11.5. The results presented were obtained at the temperature of the gas-steam mixture at the turbine inlet $T_3 = 1500$ K and the exhauster pressure ratio $\pi_{ex} = 2.6$.

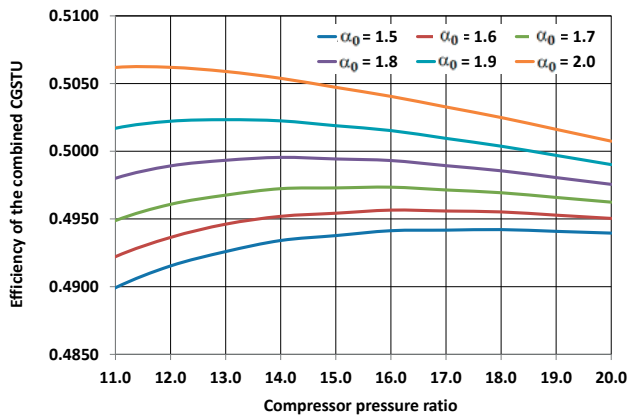


Fig. 4. Dependences of the efficiency of the CGSTU of a hybrid cycle on the compressor pressure ratio and the air excess coefficient in the SIGT.

The graphs of the dependences of the electric power of the combined CGSTU of a hybrid cycle on the SIGT compressor pressure ratio $\pi_{c\Sigma}$ and the air excess coefficient α_0 in the combustion chamber for the same initial conditions are shown in Fig. 5.

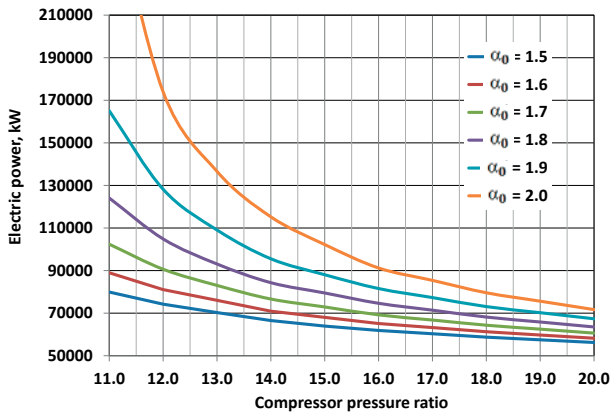


Fig. 5. Dependences of the electric power of the combined CGSTU of a hybrid cycle on the SIGT compressor pressure ratio and the air excess coefficient in the combustion chamber.

The analysis of the dependencies shows the possibility of achieving the electric power of the power plant at the level of 60–210 MW at the values of the optimal SIGT compressor ratios from 17.5 to 11.5, respectively.

The combined CGSTU of a hybrid cycle for a thermal power station is supposed to be used in the power range of 50–80 MW. In this regard, the possibility of the partial supply of steam generated by the HRSG behind the UGT25000 gas turbine

engine to the SIGT combustion chamber with constant electric generator power, driven from the steam turbine of the base GTE HRC, is considered. For the subsequent analysis, let us introduce the parameter of the partial steam supply X , which is the ratio of the mass flow rate of steam, which is injected into the SIGT combustion chamber, to the total steam flow rate generated by the HRC of the base gas turbine engine.

Figure 6 shows the dependences of the efficiency of the combined CGSTU of a hybrid cycle on the SIGT compressor pressure ratio and the amount of steam injected into the SIGT combustion chamber from the HRSG located behind the base engine, and Fig. 7 shows the dependences of the electric power of a thermal power station on the same parameters. The results were obtained for the temperature of the gas-steam mixture at the SIGT turbine inlet $T_3 = 1500$ K, the air excess coefficient in the combustion chamber $\alpha_0 = 1.8$, and the exhauster pressure ratio $\pi_{ex} = 2.6$.

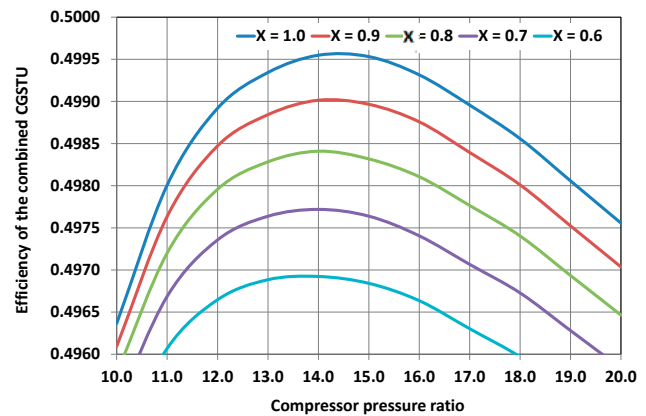


Fig. 6. Dependences of the efficiency of the combined CGSTU of a hybrid cycle on the SIGT compressor pressure ratio and the parameter of the partial steam supply.

Analysis of the graphical dependencies shows a decrease in the efficiency of the CGSTU by 0.11–0.16% and a decrease in the power of the power plant by 6.3–7.2% for every 10% decrease in the mass quantity of injected steam in the considered range of its flow rates. Thus, for example, by injecting 60% of steam from its total amount, it is possible to reduce the power of the installation from 84.3 to 64.3 MW (Fig. 7).

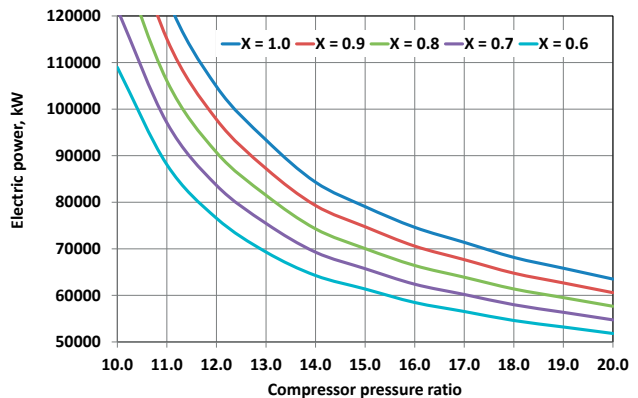


Fig. 7. Dependences of the electric power of the CGSTU on the SIGT compressor pressure ratio and the parameter of the partial steam supply.

Note that a decrease in the amount of steam supplied to the SIGT combustion chamber has a very weak effect on the value of the optimal SIGT compressor pressure ratio. Thus, the optimal SIGT compressor pressure ratio varies from 14.5 to 14.0 with a decrease in the steam supply by 60%.

To substantiate the choice of the temperature of the gas-steam mixture at the SIGT turbine inlet, the influence of this parameter (in the range of 1500-1560 K) on the efficiency indicators of the investigated CGSTU is considered. As follows from the graphical dependencies in Fig. 8, with an increase in the value of this parameter, the CGSTU efficiency increases from 49.7 to 51.15%, and the optimum compressor pressure ratio $\pi_{c\zeta}$ is reduced from 14.2 to 9.5. The above results were obtained with the air excess coefficient in the SIGT combustion chamber $\alpha_0 = 1.8$, the exhauster pressure ratio $\pi_{ex} = 2.6$, and with injection to the combustion chamber of 60% of the steam generated by the HRSG behind the base engine.

The influence of the temperature of the gas-steam mixture at the SIGT turbine inlet in the range of 1500-1560 K on the electric power of the combined CGSTU of a hybrid cycle can be estimated from the data in Fig. 9 obtained for the same initial conditions. An increase in the power of the power plant of 4-7% is observed for each increase in the temperature T_3 by 10 degrees.

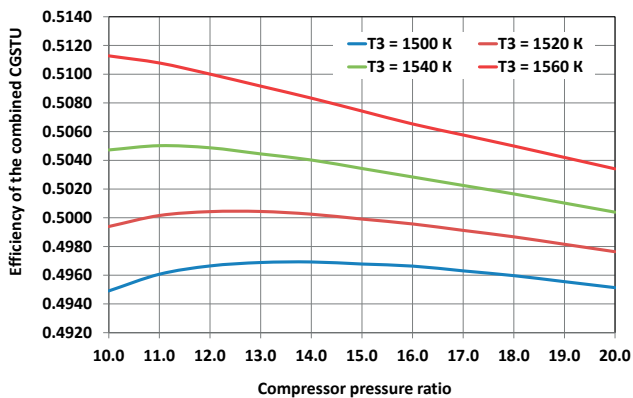


Fig. 8. Dependences of the efficiency of the combined CGSTU of a hybrid cycle on the SIGT compressor pressure ratio and the temperature of the gas-steam mixture at the turbine inlet.

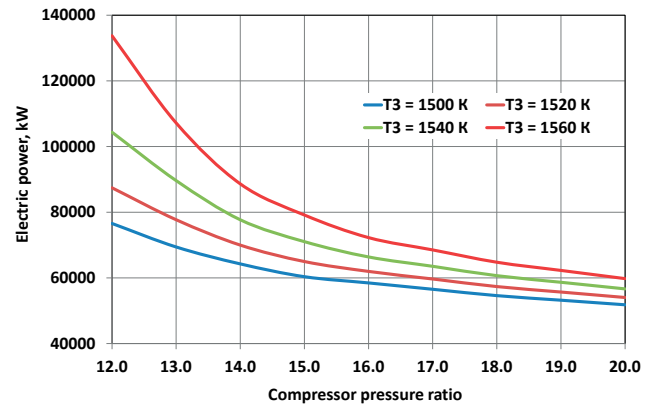


Fig. 9. Dependence of the electric power of the combined CGSTU of a hybrid cycle on the SIGT compressor pressure ratio and the temperature of the gas-steam mixture at the turbine inlet.

The analysis of the capabilities of the combined CGSTU of a hybrid cycle when using the UGT25000 gas turbine engine as the base engine makes it possible to recommend the optimal (taking into consideration the accepted technical limitations) combinations of heat recovery circuits design parameters. These parameters (Table 1) are the pressure P_{HRSG} and temperature of the superheated steam T_{ss} , the parameter of the partial steam supply X into the SIGT combustion chamber, as well as the parameters of the steam-injected gas turbine and the exhauster, depending on the estimated electric capacity $N_{elCGSTU}$ of the power plant. The effective power of the steam-injected gas turbine N_{eSIGT} and steam turbine N_{eST} the air flow rate G_{cSIGT} through the SIGT, and the efficiency of the installation η_e depending on the optimized parameters, are given in Table 1.

Figure 10 shows the dependences of the specific fuel consumption during the operation of the basic GTE, the basic GTE together with a steam turbine, and during the operation of the combined gas-steam turbine unit with a hybrid cycle for an 80 MW thermal power station, depending on the load. Calculations show that power up to 14 MW is provided by the operation of only the basic GTE UGT25000 (simple thermodynamic cycle). To achieve a power of 14-33 MW, it is sufficient to operate a gas turbine engine and a steam turbine, providing a specific fuel consumption of 0.156 kg/(kW·h) at a load of 33 MW (binary steam-gas cycle). Higher powers of 33-80 MW are covered by the joint work of the entire energy complex of the CGSTU, including a steam-injected gas turbine. In this case, the specific fuel consumption is reduced to 0.146 kg/(kW·h) at a load of 80 MW.

Tab. 1. Parameters of the CGSTU of a hybrid cycle.

$N_{elCGSTU}$, MW	N_{eSIGT} , MW	N_{eST} , MW	G_{cSIGT} , kg/s	η_e , %	$\pi_{c\zeta}$	T_3 , K	α_0	π_{ex}	P_{HRSG} , MPa	T_{ss} , K	X
50	20.42	4.80	18.00	49.60	14.5	1500	1.66	2.8	1.56	715	0.40
60	31.45	3.99	30.48	49.91	14.0	1510	1.72	2.6	1.51	710	0.50
70	41.58	3.98	43.18	50.43	13.85	1528	1.78	2.6	1.49	706	0.50
80	51.76	3.97	55.67	50.72	13.35	1536	1.80	2.6	1.44	704	0.50
90	62.54	3.96	69.32	50.88	12.85	1537	1.82	2.6	1.385	699	0.50
100	72.44	3.95	82.26	50.97	12.5	1535	1.84	2.6	1.35	696	0.50

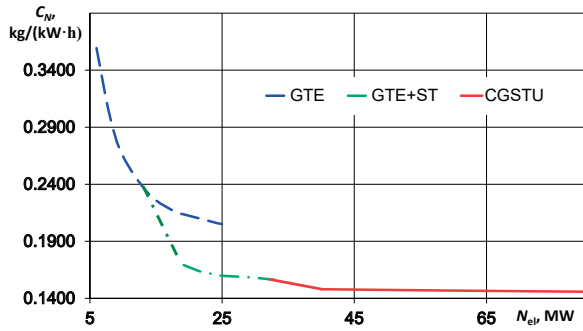


Fig. 10. Dependences of specific fuel consumption on the CGSTU power.

4. ECOLOGICAL CHARACTERISTICS OF THE COMBUSTION CHAMBER OF A STEAM-INJECTED GAS TURBINE

One of the important issues that determine the applicability of heat engines for work in a thermal power station is their environmental performance. As mentioned above, the injection of ecological steam into the primary zone of the combustion chamber is an effective method for reducing nitrogen oxide emissions. To analyze the emission characteristics of a 51.76 MW steam-injected gas turbine as part of an energy system with a total electric power of 80 MW (Table 1), the corresponding three-dimensional calculations of the working process of the gas turbine combustion chamber with the injection of ecological and power steam were carried out.

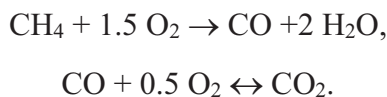
The modeling of physical and chemical processes in the combustion chamber of a steam-injected gas turbine is based on solutions of the differential equations of mass, impulse, and energy conservation for the multi-component, turbulent, chemically reacting system [15-17].

The source of chemical species m due to reaction R_m is computed as the sum of the reaction sources over the k reactions

$$R_m = \sum_k R_{mk}, \quad (15)$$

where R_{mk} is the rate of formation (destruction) of species m during reaction k .

Combustion in the gaseous phase is modeled as simple two-step chemical reactions:



The reaction rate is calculated considering the Arrhenius, Magnussen, and Hjertager models [18]:

$$R_{mk} = v_{mk} M_m T^{\beta_k} A_k \prod_j [C_j]^{v_{jk}^l} \exp(-E_k/RT), \quad R_{mk} = A \rho \frac{\varepsilon}{k} \frac{X_m}{v_{mk}} \quad (16)$$

where v_{mk} is the stoichiometric coefficient, M_m is the molecular weight of species m , β_k is the temperature exponent, A_k is the pre-exponential factor, C_j is the molar concentration of each species j , v_{jk}^l is the concentration exponent, E_k is the activation energy, R is the gas constant, A is the empirical constant; ρ is the mass density, k is the turbulent kinetic energy, ε is the turbulent dissipation rate, and X_m is the mass fraction of chemical species m .

The reaction rate is taken to be the smaller of these two expressions. This chemistry-turbulence approach is used because there are regions within the steam-injected combustion chamber where the turbulent mixing rate is faster than the chemical kinetics.

To predict the emission of nitrogen oxide NO, the mass transfer equation, which includes convection, diffusion, and formation/decomposition of NO, is used [19]:

$$\nabla \cdot (\rho \vec{v} Y_{\text{NO}}) = \nabla \cdot (\rho D \nabla Y_{\text{NO}}) + S_{\text{NO}} \quad (17)$$

where Y_{NO} is the NO mass concentration, D is the diffusion coefficient, \vec{v} is the velocity vector, and S_{NO} is the source term depending on the NO_x formation mechanism.

Note that such a model was previously used to predict the characteristics of the combustion chamber of a 16 MW steam-injected gas turbine. Calculated and experimental distributions of the emission of toxic components (nitrogen oxides and carbon monoxide), as well as temperatures, confirmed the adequacy of the mathematical model [15, 16].

The combustion chamber of the "Aquarius" type gas turbine engine was chosen for investigation (Fig. 11). In this combustion chamber, the injection of the ecological and power steam is realized. The combustion chamber has a cannular design with twenty flame tubes. The main feature of its design is the injection of ecological steam into the primary combustion zone and power steam into the mixing zone, which allows the specific engine power to be increased and enhances the ecological parameters.

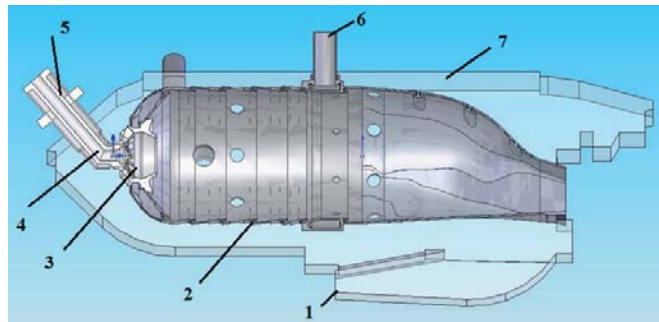


Fig. 11. The scheme of the investigated combustion chamber: 1 – air after compressor; 2 – flame tube; 3 – swirler; 4 – nozzle; 5 – ecological steam injection; 6 – power steam injection; 7 – casing.

In the calculations, the amount of ecological steam injected into the primary zone was 30% of the total amount of steam supplied to the combustion chamber.

Figure 12 shows the contours of the temperature and mass fractions of CH_4 , CO , and H_2O inside the combustion chamber. It can be seen that active fuel burnout begins not near the nozzle, but at some distance from the fuel injection sections. This is due to some overcooling of the primary chamber's zone due to the injection of ecological steam and an increase in the velocity of the fuel-air-steam mixture in it. Despite this, the fuel burnout is practically completed

before the cross-section of the injection of radial air jets into the flame tube. These radial jets transform the burning fuel flame in a certain way and intensify the mixing of the components. Directly behind the vane swirler, a system of recirculation flows is formed, which stabilizes the position of the flame front and, despite the cooling effect of the ecological steam, ensures the ignition of fresh portions of fuel. Note that in several operation modes, especially with an increase in the flow rate of ecological steam, it may be necessary to use additional stabilizers, for example, plasma igniters and intensifiers [20, 21].

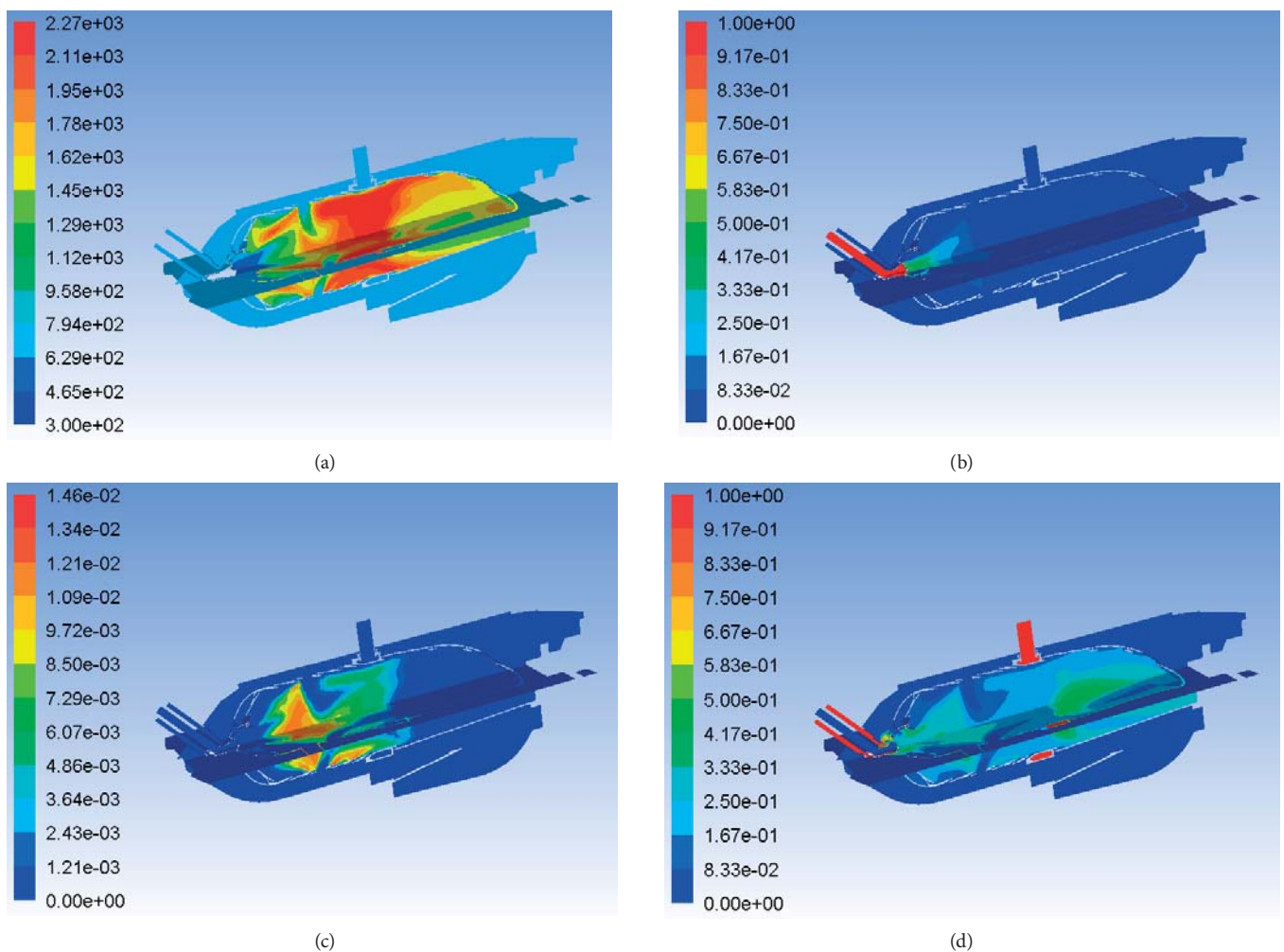
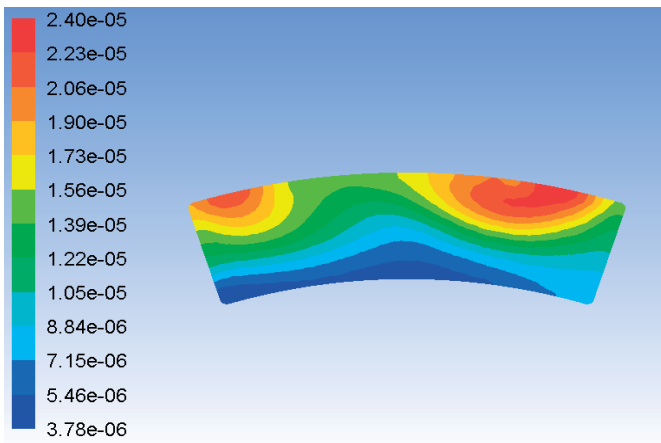


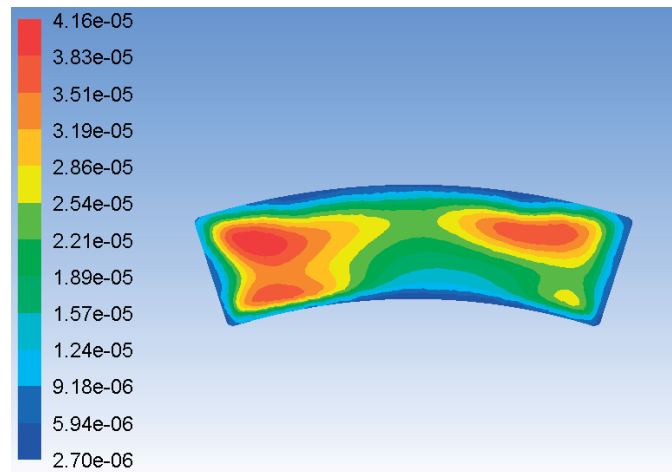
Fig. 12. Contours of temperature, K (a), and mass fractions of CH_4 (b), CO (c), H_2O (d) inside the combustion chamber.

Figure 13 shows the contours of the mole fractions of the main pollutants: nitrogen oxide and carbon monoxide in the outlet section of the flame tube. The uneven distribution of these components over the outlet section is visible, which is explained by the rather high uneven distribution of the power steam in the dilution zone of the combustion chamber. This requires further optimization of the power steam feeding design.

Despite the somewhat prolonged process of carbon monoxide burnout, its calculated emission at the combustion chamber outlet is 22.4 ppm. At the same time, the calculated emission of nitrogen oxide NO is equal to 12.3 ppm, which satisfies the modern requirements for gas turbine engines.



(a)



(b)

Fig. 13. Contours of mole fractions of NO (a) and CO (b) at the combustion chamber outlet.

CONCLUSIONS

The thermal diagram of the combined gas-steam turbine unit of a hybrid thermodynamic cycle for a thermal power station, developed based on a serial gas turbine engine, is considered. The thermal diagram also includes a steam-injected gas turbine operating with overexpansion and a steam turbine heat recovery circuit for a serial gas turbine engine. Analysis of the calculation results revealed the following.

1. The possibility of creating a combined gas-steam turbine unit based on a serial gas turbine engine with a capacity of 26,700 kW and efficiency of 36.3% for a thermal power station with capacity up to 100 MW and efficiency of 49.6-51% using a hybrid thermodynamic cycle is shown.

2. The design optimal parameters of the steam-injected gas turbine have been substantiated and, for a thermal power station capacity range from 50 to 100 MW, should have a capacity from 20.4 to 72.4 MW, respectively.

3. It is proposed for the temperature level of the working fluid behind the combustion chamber of 1500-1400 K to accept the total compressor pressure ratio of 12.5-14.5 in the steam-injected gas turbine at the exhauster compression ratio of 2.6-2.8.

4. The rational values of the air excess coefficient in the range of 1.66-1.84 for the combustion chamber of the steam-injected gas turbine were determined when injecting 40-50% of steam, which is generated by the heat recovery circuit of the base gas turbine engine.

5. The three-dimensional calculations of the working process in the combustion chamber of a 51.76 MW steam-injected gas turbine confirmed the feasibility of dividing the injected steam into ecological and energy steam. The first determines the required emission characteristics of the combustion chamber, and the second leads to an increase in the specific power of the gas-steam turbine plant.

REFERENCES

1. Kehlhofer R. Combined-cycle gas and steam turbine power plants. Penn Well Publishing Co. 1997;388.
2. Carcasci C., Pacifici B., Winchler L., Cosi L., Ferraro R. Thermoeconomic Analysis of a One-Pressure Level Heat Recovery Steam Generator Considering Real Steam Turbine Cost. *Energy Procedia* 2015; 82:591-598.
3. Nirbito W., Arif Budiyanto M., Muliadi R. Performance Analysis of Combined Cycle with Air Breathing Derivative Gas Turbine, Heat Recovery Steam Generator, and Steam Turbine as LNG Tanker Main Engine Propulsion System. *J. Mar. Sci. Eng.* 2020; 8(726):1-15.
4. Matveev I.B., Serbin S.I., Washchilenko V.N. Plasma-assisted treatment of sewage sludge. *IEEE Trans. Plasma Sci.* 2016; 44(12):3023-3027.
5. Cheng D.Y., Nelson, A.L.C. The chronological development of the Cheng cycle steam injected gas turbine during the past 25 years. *Proceeding of ASME Turbo Expo 2002*, Amsterdam, GT-2002-30119. 2002;1-8.
6. Bondin Y.N., Krivutsa V.A., Movchan S.N., Romanov V.I., Kolomeev V.N., Shevtsov A.P. Operation experience of a gas turbine unit GPU-16K with steam injection. *Gas Turbine Technologies* 2004; 5:18-20 (in Russian).
7. Movchan S.N., Romanov V.V., Chobenko V.N., Shevtsov A.P. Contact Steam-and-Gas Turbine Units of the "AQUARIUS" Type: The Present Status and Future Prospects. *Conference: ASME Turbo Expo 2009: Power for Land, Sea, and Air.* 2009;1-7.

8. Romanovsky G.F., Washchilenko N.V., Serbin S.I. Theoretical bases of designing ship gas turbine units. Ukrainian State Maritime Technical University. 2003 (in Ukrainian).
9. Offshore Magazine. Leadon FPSO delivered on time, complete, within budget. 2002. <https://www.offshore-mag.com/production/article/16759844/leadon-fps0-delivered-on-time-complete-within-budget>.
10. Cherednichenko O., Serbin S., Dzida M. Application of thermo-chemical technologies for conversion of associated gas in diesel-gas turbine installations for oil and gas floating units. *Polish Maritime Research* 2019; 3(103):181-187.
11. Ocyan. FPSO Cidade de Itajaí. 2017. https://api.ocyant.com/sites/default/files/2018-09/cidade_do_itajai_0.pdf.
12. Offshore Technology. Triton Oil Field, North Sea Central. 2018. <https://www.offshore-technology.com/projects/triton/>.
13. Gas Turbine Engine UGT25000, <https://zmturbines.com/en/serial-production/engines/ugt-25000/>.
14. Gas Turbine World. 2004-05 GTW Handbook, Pequot Publishing Inc., 2006.
15. Serbin S.I., Kozlovskiy A.V., Burunsuz K.S. Investigations of non-stationary processes in low emissive gas turbine combustor with plasma assistance. *IEEE Trans. Plasma Sci.* 2016; 44(12):2960-2964.
16. Matveev I.B., Serbin S.I., Vilkul V.V., Goncharova N.A. Synthesis Gas Afterburner Based on an Injector Type Plasma-Assisted Combustion System. *IEEE Trans. Plasma Sci.* 2015; 43(12):3974-3978.
17. Matveev I., Serbin S., Mostipanen A. Numerical optimization of the "Tornado" combustor aerodynamic parameters. *Collection of Technical Papers. 45th AIAA Aerospace Sciences Meeting*, Reno, Nevada, AIAA 2007-391. 2007; 7:4744-4755.
18. Magnussen B.F., Hjertager B.H. On mathematical models of turbulent combustion with special emphasis on soot formation and combustion. *16th Int. Symp. on Combustion*. The Combustion Institute. 1976; 16(1):719-729.
19. Launder B.E., Spalding D.B. *Lectures in Mathematical Models of Turbulence*. London: Academic Press; 1972.
20. Serbin S.I., Matveev I.B. Theoretical and experimental investigations of the plasma-assisted combustion and reformation system. *IEEE Trans. Plasma Sci.* 2010; 38(12):3306-3312.
21. Serbin S.I., Matveev I.B., Goncharova N.A. Plasma assisted reforming of natural gas for GTL. Part I. *IEEE Trans. Plasma Sci.* 2014; 42(12):3896-3900.

CONTACT WITH THE AUTHORS

Serhiy Serbin

serbin1958@gmail.com

Admiral Makarov National University of Shipbuilding,
Geroes of Ukraine, 54025 Mikolayiv,

UKRAINE

Nikolay Washchilenko

e-mail: nnuy5te@gmail.com

Admiral Makarov National University of Shipbuilding,
Geroes of Ukraine, 54025 Mikolayiv,

UKRAINE

Marek Dzida

e-mail: dzida@pg.edu.pl

Gdańsk University of Technology,
Gabriela Narutowicza Street, 80-233 Gdańsk,

POLAND

Jerzy Kowalski

e-mail: jerzy.kowalski@pg.edu.pl

Gdańsk University of Technology,
Gabriela Narutowicza Street, 80-233 Gdańsk,

POLAND

EXPERIMENTAL AND NUMERICAL STUDIES ON THE SHEAR STABILITY OF SHIP'S THIN PLATES

Xiaowen Li
Zhaoyi Zhu*
Qinglin Chen
Yingqiang Cai
Miaojiao Peng

School of Marine Engineering, Jimei University, China
Fujian Provincial Key Laboratory for Naval Architecture and Ocean Engineering, China

* Corresponding author: 1988zhuzhaoyi@163.com (Z. Zhu)

ABSTRACT

The stability of thin plate plays an important role in the design and strength check of ship structure. In order to study the shear stability of ship's thin plates, in-plane shear buckling tests were carried out using a picture frame fixture and a 3D full-field strain measurement system. The critical buckling load, full-field displacement/strain information, and load-displacement curve were obtained. The finite element model with the frame fixture was established based on ABAQUS, with the eigenvalue buckling analysis and nonlinear buckling analysis being carried out to obtain the mechanical response information of the buckling and post-buckling of the ship's thin plate. The effectiveness and accuracy of the numerical simulation method are verified by comparing the numerical simulation with the experimental results. On this basis, the critical buckling load obtained by shear test, numerical simulation, and theoretical calculation is analyzed, and the function of the frame shear fixture and its influence on the critical buckling load are defined. The research in this paper provides a useful reference for the testing and simulation of in-plane shear stability of ship's thin plates.

Keywords: shear stability, ship's thin plate, full-field strain measurement, buckling, nonlinear

INTRODUCTION

The stability of the plate has always played an important role in the design and strength check of the ship's structure. A large number of marine accidents show that the damage of ship structure is usually not caused by insufficient strength, but due to the loss of stability. When the overall longitudinal bending or torsion of the hull occurs, the hull plate may be subjected to axial compression load or shear load. When the axial compressive stress or shear stress reaches a certain value, the hull plate will be unstable [1-2].

The stability of thin-walled structures has always been a focus of scholars at home and abroad [3-456]. Previous studies

have focused on buckling and post-buckling of the stiffened plates. In literature [7], the trigonometric function was used to simulate rotational restraining rigidity of stiffener, and Ritz method was used to establish an analytical model for the local skin buckling problem of riveted stiffened panels under uniaxial compression. In literature [8], a rectangular plate model with inclined stiffener was used to simulate the pure shear stress state of the wedge-shaped webs, and its elastic buckling was numerically analyzed. In literature [9], eigenvalue buckling analysis and nonlinear buckling analysis were performed for marine composite stiffened plates based on a numerical method and finite element calculation. X. Shi (2005) used the commercial finite element software,

NASTRAN, to analyze the stability of composite panels[10]. Based on mechanical experiments and numerical simulation, Y. Peng, et al.(2020) studied the buckling and post-buckling behavior of the al-li alloy stiffened panel under shear load[11].

In the study of plate stability, Roberts and Azizian (1984) used the finite element method to analyze the elastic buckling of a square plate with holes under in-plane loads. In literature [12], the ABAQUS software was used to analyze the ultimate strength of the hull panel model under axial pressure. In literature [13], the elastic buckling and post-buckling behaviors of unstiffened panels under complex stress states were analyzed and compared with the empirical formula and American Bureau of Shipping specification. L. Sun (2014) applied near field dynamics to the analysis of the stability of metal plates under axial compression[14]. In literature [15], the Galerkin method was used to solve the elastoplastic buckling problem of rectangular plates under shear stress. In literature [16], the buckling problem of anisotropic rectangular plate under shear stress was solved by differential quadrature method. In literature [17], the differential equation of transverse displacement function in shear buckling of rectangular plate was established, and the determinant of coefficient matrix of homogeneous linear algebraic equation was simplified by using the point distribution method and antisymmetric characteristics of buckling deformation, and the analytical solution of critical buckling load of rectangular plate was obtained. Pham (2017) studied the shear buckling of a plate with holes by using the finite strip method and proposed an approximate formula for the shear buckling coefficient of a square plate with central circular holes and square holes[18].

Local rectangular thin plates under shear stress are widely used in engineering structures such as ships and buildings and buckling instability of local plates has become one of the main forms of engineering structural failure. In the past, there had been many studies dedicated to tensile, compressive, and bending load conditions. It is difficult to test the buckling instability of local rectangular plates under shear stress. The Galerkin method, differential quadrature method, analytical method, and finite element method were mainly used to solve the problem. The analytical solutions need programming operations. Finite element simulation [19-20] can avoid complicated programming for buckling analysis, but the calculation accuracy is limited to the design accuracy of the model and boundary conditions. Additionally, these methods need to be supported by mechanical experiments.

Therefore, this paper focuses on the buckling characteristics of a ship's thin plates under in-plane shear loading by means of mechanical experiments and numerical simulation. A picture frame fixture was designed and manufactured, and a diagonal tensile method was used to conduct the shear test on square thin plates. In the numerical simulation, eigenvalue analysis method and nonlinear analysis method were used to study the buckling behavior of ship's thin plates. The effectiveness of the numerical method was expected to be verified through

the comparative analysis of mechanical experiments and numerical simulation. Meanwhile, the effect of the frame fixture and its influence on the critical buckling load were studied. The experiment and numerical simulation method will provide an effective reference for the study of in-plane shear stability of ship's thin plates.

SHEAR TEST

The ship's side plate is the main component of hull structure to resist shear load and must meet the requirements of shear stability. Generally, the boundary of the hull plate is supported by strong structures (such as hull longitudinal, bulkhead, etc.). When the supporting unit on the opposite side of the hull plate is relatively displaced, the hull plate will be subjected to shear load. Because the stiffness of the boundary support element is much larger than that of the plate, even if the plate element loses stability, the deformation of the support element on the opposite side along the edge of the plate is very small. It can be considered that the four sides of the plate are subjected to uniform shear force. Based on this working mode, the restraint condition of the support element on the thin plate should be fully considered in the shear stability test. The structural form and load condition of the side plate element in this paper are shown in Fig.1.

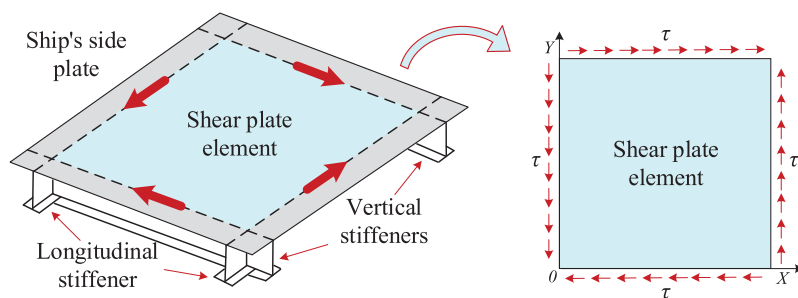


Fig. 1. Schematic of shearing condition of ship's thin plate

TEST PLATE

The thin plate is one of the most common structural plate elements in the ship structure. The shear test plate is designed as shown in Fig. 2. Among them, the square with a side length of 310 mm is the shear area, and there are loading areas with a width of 40 mm around the shear area. There are multiple holes in the loading area to ensure uniform force. The thickness of the test plate is 1 mm, the material is ordinary marine steel, the elastic modulus is 210 GPa, and the Poisson's ratio is 0.3. The stress-strain relationship of the test material was measured by tensile test, as shown in Fig. 3.

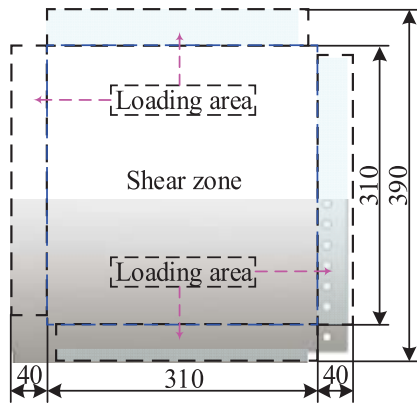
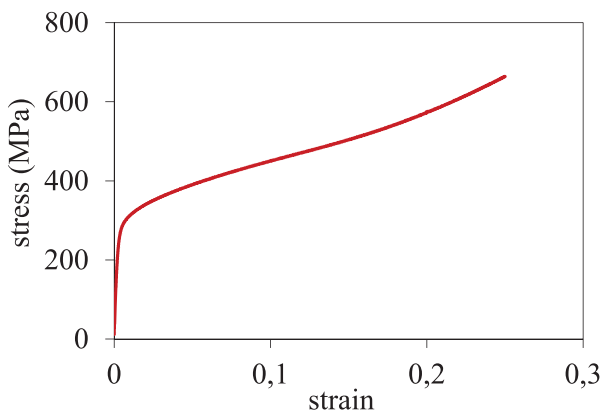


Fig. 2. Schematic of the test plate and its dimensions (all dimensions are in mm)



(a) Tensile test system



(b) Tensile test results

Fig. 3. True stress-strain curve from tensile test

INSTRUMENTATION/EQUIPMENT DETAILS AND TEST PROCEDURE

The shear buckling test of the thin plate is a difficult structural test, which requires a reasonable fixture to transfer the shear load to the test plate. In this paper, a picture frame fixture using a diagonal tensile method was adopted as shown in Fig. 4. The four sides of the test plate are bolted to four pairs of shear plates, and the shear plates are hinged together at the top. When the testing machine is loaded, the tensile force P , provided by the testing machine, is decomposed into T_{xy} along

the direction of the shear plate. The test piece is tensioned in the vertical diagonal (Π) direction and compressed in the horizontal diagonal (I) direction, so that the test piece is subjected to the shear load. For the study of the buckling performance of the thin plate under shear load, the four sides of the plate are required to be simply supported and torsion limited, and the shear load is uniformly applied to the boundary of the plate. This is an ideal state of shear testing.

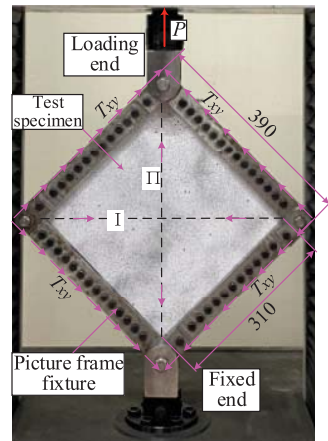


Fig. 4. Test setup of specimen and frame fixture

As shown in Fig. 5, the shear test was carried out on a WDW100-100C electronic universal test machine, with a maximum load of 100 kN and a continuous loading rate of 5 mm/min. In order to accurately measure the deformation of the plate surface, the XTDIC-CONST 3D full-field strain measurement and analysis system was applied to the test process. The surface of the test plate was sprayed with primer and speckle in advance, so that the change of displacement field and strain field on the surface of the test plate could be measured in real time. As shown in Fig. 5, the digital image correlation (DIC) measuring equipment is arranged at a specific position directly in front of the test plate.

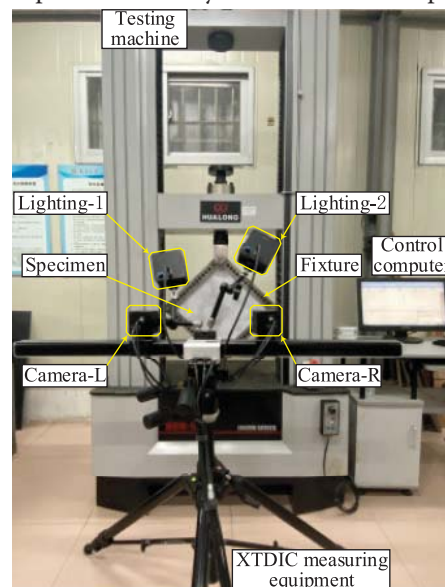


Fig. 5. Shear buckling test of the ship's thin plate

NUMERICAL SIMULATION

BUCKLING ANALYSIS METHOD

Eigenvalue Buckling

Linear buckling is also called eigenvalue buckling analysis. The buckling loads and buckling modes of the structure can be obtained by calculating the eigenvalues of the singular stiffness matrix. The corresponding buckling load can be determined by the following linear generalized eigenvalue equation [10,21]:

$$([K_0] + \lambda[K_\sigma])\{U\} = 0 \quad (1)$$

Where, $[K_0]$ is the linear stiffness matrix of the structure, $[K_\sigma]$ is the geometric stiffness matrix of the structure, λ is the load scaling factor, and $\{U\}$ is the lateral displacement vector. It can be seen from Equation (1) that the linear stability problem of the structure is the eigenvalue problem, and the corresponding critical load and instability mode can be obtained by solving the eigenvalue and eigenvector.

Nonlinear Buckling

The nonlinear buckling theory is to establish the equilibrium equation on the structure configuration which changes constantly during the loading process. For the imperfect plate with initial geometric defects or the laminate with tension-bending coupling effect, that is, under in-plane loading, the transverse displacement will appear from the beginning of loading and become a nonlinear bending problem. The governing equation is as follows:

$$K_T \Delta U = \Delta P \quad (2)$$

Where, K_T , is the tangent stiffness matrix of the structure at a certain increment step, ΔP is the current external load increment of the structure, and ΔU is the current displacement increment of the structure. The above formula can also be written as follows:

$$([K_L] + [K_\sigma] + [K_{NL}])\Delta U = \Delta P \quad (3)$$

Where, K_L is the linear stiffness matrix, which is independent of node displacement. K_{NL} , is the initial displacement matrix, which represents the influence of element position change on element stiffness matrix.

According to nonlinear buckling theory, there can be several extreme points in the equilibrium path of a structure under load, and such extreme points are called nonlinear

buckling points. The buckling load of the structure is usually determined by the first extreme point. In the nonlinear analysis, the stability problem and strength problem of the structure are related to each other and can be studied from the change law of the whole process of load-displacement curve.

FINITE ELEMENT MODEL

In order to effectively simulate the test conditions, the finite element model as shown in Fig. 6 was established based on ABAQUS. The plane continuous shell element S4R was used in test plate and fixtures. The S4R is a 4-node first order reduction integral element, which uses linear interpolation methods, allows finite film strain and large rotation angle, considers the influence of shear deformation, and is suitable for geometrical and material nonlinear analysis. The constraint conditions between the four groups of shear plates and the loading area of the test plate were set as tie binding constraints to simulate bolted connection. The hinge connection units were used to simulate the effect of the hinge connection between the shear plate shaft hole and the pin.

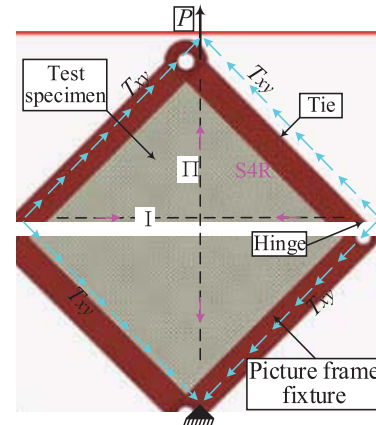


Fig. 6. Finite element model

RESULTS AND DISCUSSIONS

LOAD-DISPLACEMENT CURVES

Fig. 7 indicates the load (P)-displacement (D) curve of the ship's thin plate, where D represents the displacement difference between the upper and lower diagonal points of the plate. As can be seen from the graph, the trend and results of the experiment and simulation are consistent. By comparing and analyzing the test and simulation results, it is found that as the load increases, there are obvious linear segments in the test and simulation curves, and the linear segment of the simulation curve has a longer duration and a greater slope. When the load increases to point A ($P \approx 15.04$ kN), the structure produces buckling instability, the slope of load-displacement curve changes suddenly, and the structure stiffness begins to decrease. As the load

continues to increase, the load-displacement curve remains approximately linear until the load increases to point B ($P \approx 26.02$ kN), at which time the maximum stress in the plate exceeds the yield limit of the material, and the structure begins to exhibit plastic deformation. With the increase of the plastic deformation area, the linear relationship of the load-displacement curve disappeared. When the load increases to point C ($P \approx 35.68$ kN), the slope of the curve changes greatly, and the structure stiffness decreases. After that, the slope of the curve changed relatively gently. Only when the load increases to point D ($P \approx 62.30$ kN), a small abrupt change occurs, and the structure stiffness decreases again. Based on the simulation curve, the key moments of the four slope sudden changes of A, B, C, and D can be extracted. In order to further verify the validity of the finite element results, the test results of the above four key moments under the same load are analyzed emphatically.

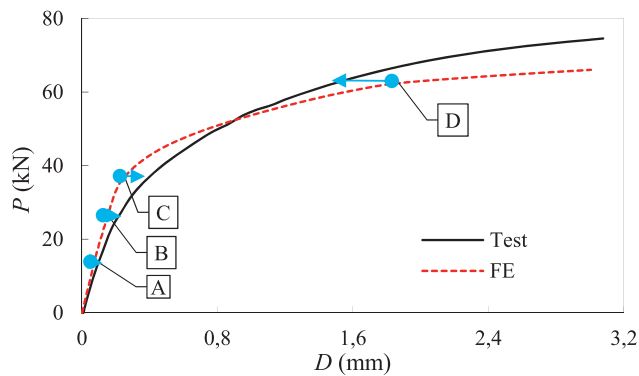


Fig. 7. Force versus displacement of the test sample

FULL-FIELD DISPLACEMENT AT CRITICAL MOMENTS

Based on the DIC full-field strain measurement system, full-field displacement information at the four key moments of A, B, C, and D during the shear test were extracted and compared with the numerical simulation results, as shown in Fig. 8. It is found that the displacement distribution of finite element simulation and experimental measurement results are basically the same. The normal displacements of the horizontal and vertical diagonals extracted from the experiment and simulation are shown in Fig. 8. The numerical simulation results of the four key moments A, B, C, and D are basically consistent with the experimental values, and the curve change trend is consistent. On the vertical diagonal, there is a half wave symmetric along the horizontal diagonal of the plate, and the displacement of the center point of the wave is the largest and gradually decreases towards both ends. There are three half waves on the horizontal diagonal, the waveform is symmetrical along the vertical diagonal, there is a large wave at the center point, and there are two wavelets symmetrically on both sides. The amplitude of the three waves increases as the load increases. The results shown

in Fig. 9 are consistent with the displacement field shown in Fig. 7. Therefore, the validity and accuracy of the numerical simulation method are further verified.

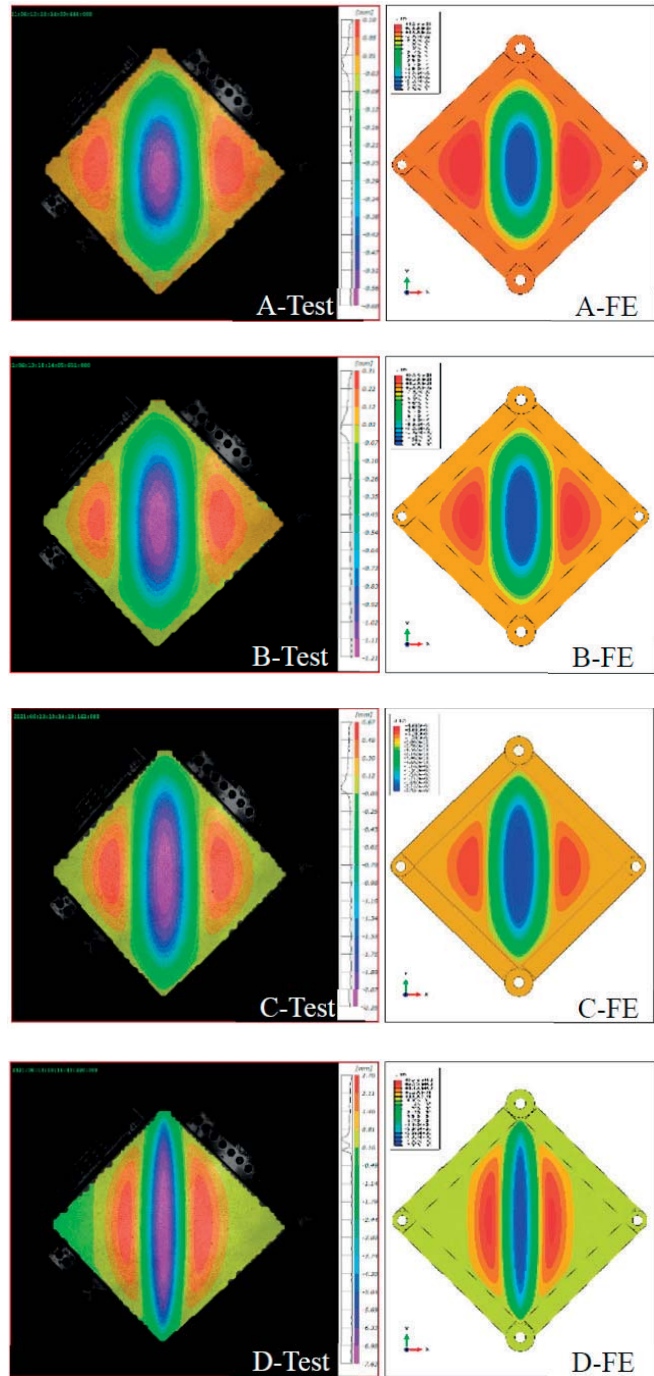
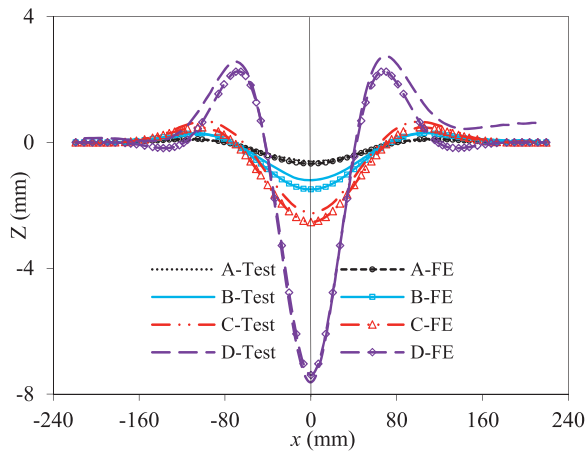
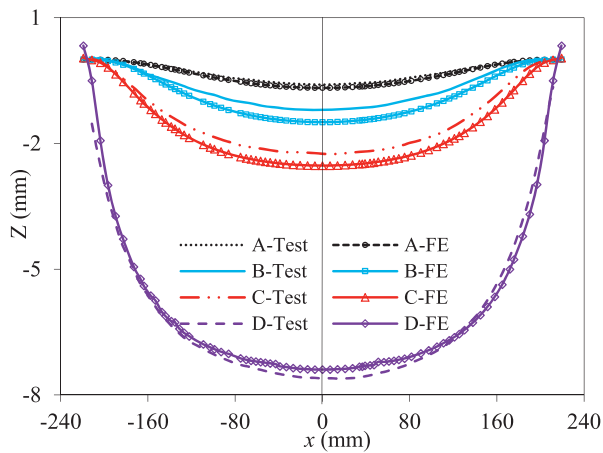


Fig. 8. Full-field stress distributions of moment A, B, C, and D



(a) Horizontal diagonal



(b) Vertical diagonal

Fig. 9. Distribution of diagonal normal displacement

CRITICAL BUCKLING LOAD

Usually, the load at the first abrupt slope of the load-displacement curve is taken as the buckling instability load (P_{cr}) of the structure. The buckling time of the test plate can also be observed and judged by the strain bifurcation method, that is, the load at the bifurcation point of the strain-load curve is used as the critical buckling load of the structure. In order to obtain a more accurate buckling instability load, the 10 key points, shown in Fig. 10, are designed on the front and back sides of the plate. The vertical and horizontal diagonal lines of the plate are divided into eight equal parts. Considering the symmetry of the test plate, the equal points in the upper left quarter region are taken, and the corresponding strain-load curve was extracted. The points 0, 3, 4, 5, and 9 are located on the front of the plate, while the points 0', 3', 4', 5' and 9' are on the back of the plate.

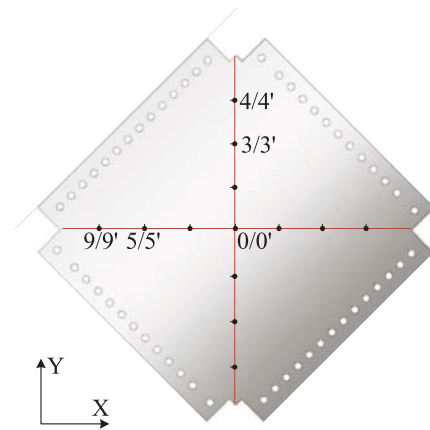
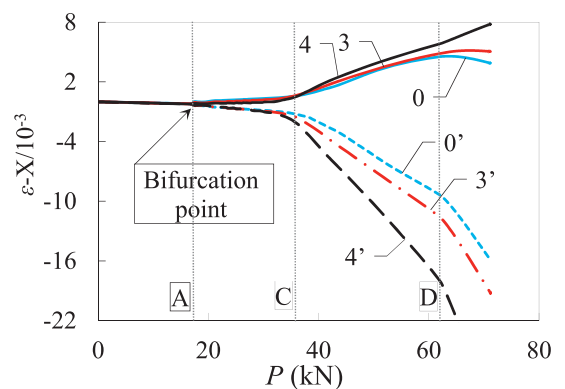
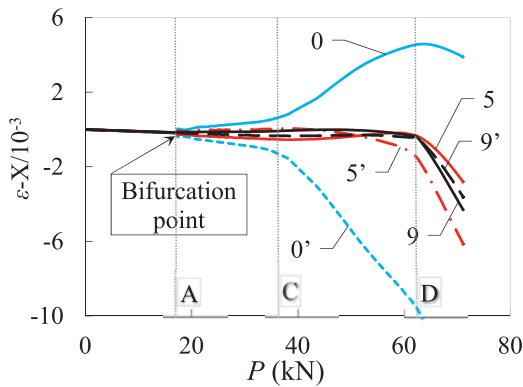


Fig. 10. The key points of the test plate

Fig. 11 shows the strain-load curves of the 10 key points. By comparing Fig. 11a and 11b, it is found that the positions of strain bifurcation of the key points on the vertical diagonal and horizontal diagonal are the same, and the corresponding loads are both 15.04 kN, which is the critical buckling load of the plate. The strain in the X direction along the vertical diagonal is much larger than that along the horizontal diagonal. On the vertical diagonal, the closer to the center of the plate, the smaller the strain value is. On the horizontal diagonal, the strain in the X direction is small and changes very little, but the closer to the center of the plate, the greater the strain value. The strain-load curve was partitioned based on time A, C, and D as shown in Fig. 7. At line A, the critical buckling load was consistent with the bifurcation point. At line C, the sudden change of the strain-load curve on the vertical diagonal is larger, which is consistent with the sudden change of the slope of the load-displacement curve at point C as shown in Fig. 7. At line D, the change of the strain-load curve on the horizontal diagonal is large, which is consistent with the sudden slope of the load-displacement curve at point D as shown in Fig. 7. Fig. 12 illustrates the full-field strain distribution corresponding to time C and D. The comparison shows that the finite element simulation is basically consistent with the test measurement results, which, once again, proves the effectiveness and accuracy of the numerical simulation.



(a) The key point of 0/0', 3/3', 4/4'



(b) The key point of 0/0', 5/5', 9/9'

Fig. 11. Strain-load curves

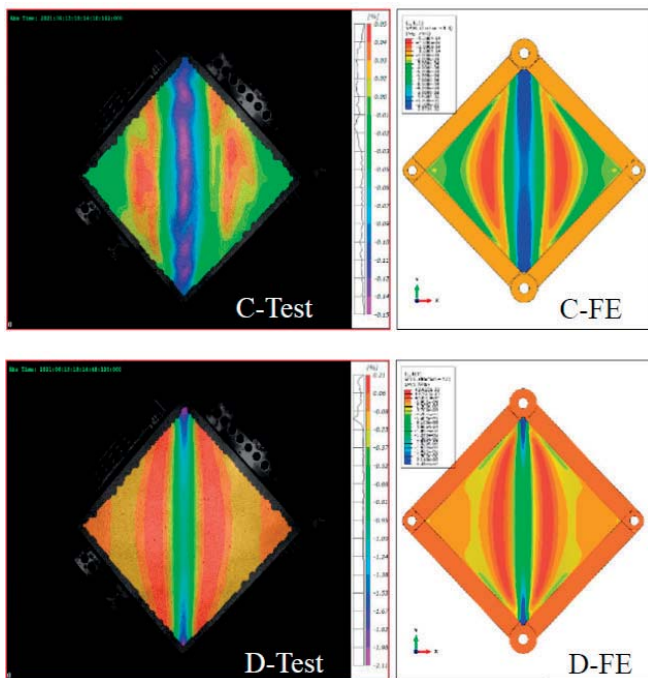


Fig. 12. Full-field strain distributions

The critical buckling loads of the thin plate obtained by different methods are summarized as shown in Table 1. Compared with the test results, it can be seen that the critical buckling load obtained by the eigenvalue analysis method is higher than the test one, with the error being 7.25%. The buckling load calculated by the eigenvalue method is higher, partly because the nonlinearity of the structure and the defects of the structure are not considered. The nonlinear analysis method makes up for the deficiency of eigenvalue buckling analysis to a certain extent. Although the obtained buckling load is also higher than the experimental result, the error is relatively small, only 2.80%. For the shear condition of rectangular thin plate, the critical buckling load can be calculated by the theoretical formula [22]. The theoretical value is smaller than the experimental result, and the corresponding error is large, about 11.35%. The reason being that the theoretical formula is for the ideal shear condition with uniform shear force on the four sides, and the experiment

and simulation are not a real pure shear mode due to the existence of frame fixture. For this reason, it is necessary to consider the influence of the picture frame fixture on the experiment and simulation.

Table 1. Comparison of critical buckling loads

Method	Critical Buckling Load (kN)	Error %
Shear test (P_T)	14.63	-
Finite element - eigenvalue analysis (P_{FE-L})	15.69	7.25
Finite element - Nonlinear analysis (P_{FE})	15.04	2.80
Theoretical calculation (P_{theory})	12.97	11.35

INFLUENCE OF THE PICTURE FRAME FIXTURE

In the study of the shear stability of thin plates, we usually think of obtaining the buckling and post-buckling performance of the plates when it is subjected to pure shear load. However, in the actual test, an auxiliary fixture must be used. The fixture will also deform during the stress process. Therefore, when the plate buckles, the load measured by the testing machine is not the true buckling load of the plate. The fixture is related. That is to say, in the shear test process, the picture frame fixture not only transmits the load, but also participates in the deformation of the structure, and shares part of the load, so the load recorded by the testing machine includes both the load that causes the plate to buckle, and the load that causes the deformation of the fixture. Therefore, the critical buckling load of the plate after using the fixture is greater than that under pure shear condition.

To this end, the influence factor λ of picture frame fixture is proposed to characterize the influence of the fixture on the critical buckling load of the thin plate, and the relationship between numerical simulation and theoretical calculation or finite element simulation without fixture is established by λ . Suppose the following relationships exist:

$$\lambda = (P_{FE} - P_{theory}) / P_{FE} \quad (4)$$

In the formula, PFE represents the critical buckling load obtained by the nonlinear finite element analysis method, and Ptheory represents the critical buckling load obtained by theoretical calculation. As shown in Fig. 13, the critical buckling loads of the plates with different thicknesses under the same working conditions are calculated. Comparing the simulation results with the theoretical values, it is found that the trend of the two is consistent, and there is a linear relationship between the critical buckling load and the cube of the plate thickness. It can be seen that the influence of the picture frame fixture on different thickness plates has a certain universality under the same working condition. However, by analyzing the curve between λ and plate thickness (see

Fig. 14), it is found that λ is not a constant value, it increases with the increase of the plate thickness. When the plate thickness is small, λ is also small, indicating that the fixture has small influence on the critical buckling load. With the increase of plate thickness, the influence of the fixture on the critical buckling load increases, but when the plate thickness increases to a certain extent, the influence of the fixture on the critical buckling load gradually becomes gentle.

Based on the power index fitting method in MATLAB, the fitting formula of the influence factor λ of the picture frame fixture is obtained as follows:

$$\lambda = 0.05008 t^{0.9282} + 0.1619 \quad (5)$$

Where, t is plate thickness. Therefore, the influence of the frame fixture on the critical buckling load of the thin plate under different plate thicknesses can be obtained.

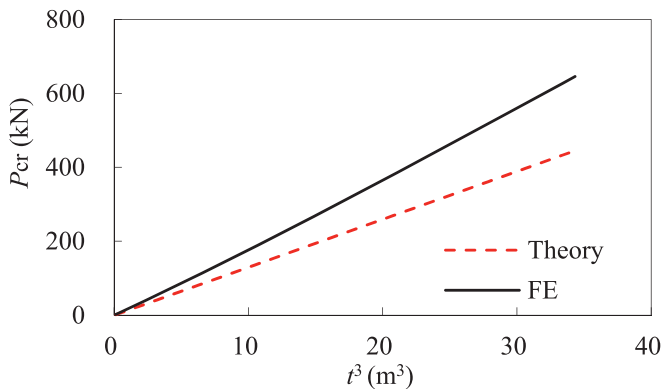


Fig. 13. The relationship between P_{cr} and t_3

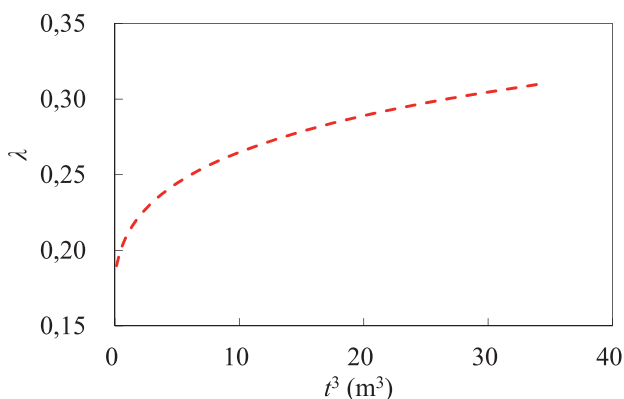


Fig. 14. The relationship between λ and t_3

CONCLUSIONS

Based on mechanical experiment and numerical simulation, the in-plane shear stability of ship's thin plates was investigated, the buckling and post-buckling behavior, and the influence of the picture frame fixture on the shear instability of the rectangular thin plate were explored. The

mechanical response characteristics of load-displacement curves, load-strain curves, critical buckling loads, full-field deformation, and influence factor of the picture frame fixture were obtained. By comparing the numerical simulation with the mechanical tests, the following conclusions are drawn:

Based on ABAQUS, eigenvalue buckling analysis and nonlinear buckling analysis were carried out on the finite element model with the picture frame fixture. The critical buckling load, full-field displacement, and strain obtained by simulation are in good agreement with the results of full-field strain measurement system of DIC, which proves the effectiveness and accuracy of the numerical simulation method.

By comparing and analyzing the critical buckling load obtained by the three methods of shear test, numerical simulation, and theoretical calculation, it is concluded that the critical buckling load obtained by eigenvalue analysis method is higher than the test result, because the nonlinear and structural defects of the structure are not considered. The nonlinear buckling analysis method makes up for the shortcomings of linear buckling analysis, so the critical buckling load obtained is the closest to the test result. The error between the theoretical calculation result and the test value is the largest, because the theoretical formula is for the ideal shear condition with uniform shear force on the four sides, while the experimental and simulation results both consider the influence of the picture frame fixture.

The stress field provided by the picture frame fixture is quite different from that of pure shear. After the picture frame fixture is adopted, the buckling load of the structure will be greater than the buckling load of the thin plate under the ideal shear condition. Considering that the stability of thin plate is sensitive to boundary condition, the influence of the picture frame fixture must be considered in the numerical simulation of the in-plane shear stability test to ensure the validity of simulation result. In this paper, the influence factor λ of the picture frame fixture is defined to represent the influence of this fixture on the critical buckling load of the thin plate, and the relationship between numerical simulation and theoretical calculation or finite element simulation without fixture is established through λ .

ACKNOWLEDGEMENT

This work was financed by the National Natural Science Foundation of China (Grant No. 51909103) and the Natural Science Foundation of Fujian Province (Grant No. 2021J01841).

REFERENCES

1. W. Zhao, Z. Xie, X. Wang, X. Li, J. Hao, 'Buckling behavior of stiffened composite panels with variable thickness skin under compression', *Mechanics of Advanced Materials and Structures*, 2019. pp. 1–9, doi: 10.1080/15376494.2018.1495795.

2. Y. Chen, C. Yu, H. Gui, 'Research development of buckling and ultimate strength of hull plate and stiffened panel', *Chinese Journal of Ship Research*, 2017. pp. 54–62.
3. Q. Zhu, F. Wang, X. Wang, 'A correction method of load-end shortening curves for longitudinal multi-span beam column buckling', *Shipbuilding of China*, 2014. pp. 46–53.
4. O. Ozguc, 'Assessment of buckling behaviour on an fpso deck panel', *Polish Maritime Research*, 2020, doi: 10.2478/pomr-2020-0046.
5. P. Bielski, L. Samson, O. Wysocki, J. Czyzewicz, 'Simple computational methods in predicting limit load of high-strength cold-formed sections due to local buckling: A case study', *Polish Maritime Research*, 2018. pp. 73–82, doi: <https://doi.org/10.2478/pomr-2019-0064>.
6. O. Ozgur, 'Estimation of buckling response of the deck panel in axial compression', *Polish Maritime Research*, 2018. pp. 98–105, <https://doi.org/10.2478/pomr-2018-0136>.
7. J. Chen, B. Kong, P. Chen, J. Yang, X. Gan, 'Local buckling analysis method of elastically restrained riveted stiffened panels under uniaxial compression', *Journal of Nanjing University of Aeronautics & Astronautics*, 2020. pp. 989–996, doi: 10.16356/j.1005-2615.2020.06.019.
8. Y. Jin, G. Tong, 'Elastic shear buckling of web plates in tapered I-girders', *Engineering Mechanics*, 2009. pp. 1–9.
9. X. Li, Z. Zhu, Y. Li, Z. Hu, 'Research on buckling and post buckling behavior of composite stiffened panel for ships', *Shipbuilding of China*, 2020. pp. 186–194.
10. X. Shi, 'Nonlinear buckling analysis of plates and shells with finite element method', Nanjing: Nanjing University of Aeronautics and Astronautics, 2005.
11. Y. Peng, Y. Ma, Y. Zhao, L. Zhu, 'Study on shear buckling performance of Al-Li Alloy Stiffened panel', *Acta Aeronautica et Astronautica Sinica*, 2020. pp. 408–417.
12. L. Feng, J. He, H. Shi, Q. Zhang, D. Li, 'Influence factors and sensitivity analysis of numerical calculation of hull panel ultimate strength', *Ship Science and Technology*, 2017. pp. 48–53.
13. J. Xia, E. Qi, 'Ultimate strength analysis of unstiffened plates under complex stress', *Proceedings of the 20th Anniversary Academic Conference in Commemoration of Ship Mechanics*, Zhoushan, Zhejiang, China, 2017, pp. 419–430.
14. L. Sun., 'Stability analysis method study of metallic plates based on peridynamics', Shanghai: Shanghai Jiao Tong University, 2014.
15. S. Renu, L. Roshan, 'Buckling and vibration of non-homogeneous orthotropic rectangular plates with variable thickness using DQM', *Advances in Intelligent Systems and Computing*, 2014. pp. 295–304. doi: 10.1007/978-81-322-1602-5_33.
16. E. Jaberzadeh, M. Azhari, 'Elastic and inelastic local buckling of rectangular plates subjected to shear force using the Galerkin method', *Applied Mathematical Modelling*, 2009. pp. 1874–1885. doi: <https://doi.org/10.1016/j.apm.2008.03.020>.
17. D. Yang, Y. Huang, G. Li, 'Shear buckling analysis of anisotropic rectangular plates', *Chinese Journal of Applied Mechanics*, 2012. pp. 221–224.
18. C. H. Pham, 'Shear buckling of plates and thin-walled channel sections with holes', *Journal of Constructional Steel Research*, 2017. pp. 800–811. doi: <https://doi.org/10.1016/j.jcsr.2016.10.013>.
19. Y. Cui, F. Tu, Z. Xu, 'In-plane stress analysis of thin sheet with irregular shape', *Machinery Design and Manufacture*, 2012. pp. 218–220. doi: 10.19356/j.cnki.1001-3997.2012.08.081.
20. W. Fu, F. Yan, H. Wang, A. Lai, 'The buckling numerical analysis of rectangular plates under shear force', *Machinery Design and Manufacture*, 2015. pp. 20–22, 26. doi: 10.19356/j.cnki.1001-3997.2015.08.006.
21. N. Z. Chen, C. G. Soares, 'Buckling analysis of stiffened composite panels', *III European Conference on Computational Mechanics*. Springer Netherlands, 2006.
22. X. Liu, 'Ship structure and strength', Harbin: Harbin Engineering University Press, 2010.

CONTACT WITH THE AUTHORS

Zhaoyi Zhu

e-mail: 1988zhuzhaoyi@163.com

School of Marine Engineering, Jimei University
Fujian, Xiamen, Jimei District

Fujian Provincial Key Laboratory for Naval Architecture
and Ocean Engineering
CHINA

AN ADAPTIVE ISLAND MODEL OF POPULATION FOR NEUROEVOLUTIONARY SHIP HANDLING

Mirosław Łącki*

Gdynia Maritime University, Poland

* Corresponding author: m.lacki@wn.umg.edu.pl (M. Łącki)

ABSTRACT

This study presents a method for the dynamic value assignment of evolutionary parameters to accelerate, automate and generalise the neuroevolutionary method of ship handling for different navigational tasks and in different environmental conditions. The island model of population is used in the modified neuroevolutionary method to achieve this goal. Three different navigational situations are considered in the simulation, namely, passing through restricted waters, crossing with another vessel and overtaking in the open sea. The results of the simulation examples show that the island model performs better than a single non-divided population and may accelerate some complex and dynamic navigational tasks. This adaptive island-based neuroevolutionary system used for the COLREG manoeuvres and for the finding safe ship's route to a given destination in restricted waters increases the accuracy and flexibility of the simulation process. The time statistics show that the time of simulation of island NEAT was shortened by 6.8% to 27.1% in comparison to modified NEAT method.

Keywords: artificial neural networks, evolutionary algorithms, neuroevolution, ship movement control, ship manoeuvring

INTRODUCTION

The safety of maritime transport is a key factor in the manoeuvres of seagoing vessels. Due to human errors, a lack of information, bad weather or high vessel traffic, there is still a high risk of ship collision, potentially resulting in a threat to life, cargo and the environment. There are various tools, procedures and manoeuvring decision support systems that have evolved over time and are still being adapted to new conditions, for example, to support unmanned ships (Maritime Autonomous Surface Ships).

Intelligent adaptive computer decision support systems with evolutionary algorithms (EAs) are also used in this field to accelerate decision processes and to reduce the impact of human errors. Determining the parameters of evolutionary

processes is often the most important factor in tuning the efficiency of the EA for a certain task. The automation of this process allows the solution to be found more rapidly without the redundant designer influence and is strictly related to another problem in heuristic search methods, like EAs, which is premature convergence. The problematic result of premature convergence may be getting stuck in a local extremum [1]. Thus, in an evolutionary system, it is important to maintain the diversity of the population during the entire search for the global optimum [2].

The motivation for this work is the desire to find a new approach to solve navigational tasks that would provide improved results in comparison to the standard single-population approach. In order to achieve this goal, an island model of population, composed of islands of equal sizes,

performing independently of each other, with adaptive dynamic evolutionary parameters, is proposed. The island model approach is often described in the literature to be more effective than the tasks evaluated on a single population [3] we consider popular evolution schemes of panmictic (steady-state). This has inspired the author to use it in a neuroevolutionary ship handling system to automate its adjustment for different navigational situations.

This study is organised as follows. The related works are briefly presented, followed by a description of the simulation models of the vessels. The results of the simulation are then presented and the conclusions are gathered in the final section.

RELATED WORKS

The neuroevolutionary method is a combination of three main techniques, namely, artificial neural networks (ANNs), EAs and reinforcement learning (RL). All these techniques are well known and have been used in different combinations in many fields of research. The main focus of this research is the usage of neuroevolution in ship manoeuvrings and control, but it can be used in other tasks as well.

In related works, researchers have investigated the feasibility of various types of neural network methods, including for the performance and emission characteristics of diesel engines fuelled with biodiesel-based fuels [4]. ANN techniques have also been widely applied for navigational tasks, for example, ship fuel consumption prediction with back-propagation networks [5], predicting both fuel consumption and travel time [6], vessel position and trajectory prediction with generalised regression neural networks [7], classifying inland water vessels with the GoogLeNet Network Toolbox [8], data-driven models of ANNs for the time series prediction of ship motion [9], a radial basis function ANN in ship dynamic positioning system [10] and the training of marine control engineering professionals [11].

EAs with the island model of population were used in [12], where the island-based population was transformed into a multi-agent system capable of learning and adapting the inter-island links based on the experience obtained during the evolutionary process. Another usage of EAs with islands was described in [13], where each island modified a fragment of the chromosome that encoded a possible solution of the multi-objective optimisation problem. The important factors of the island model are the number of islands and island population size, as described in [14], where a single run of the largest population possible with multiple small population independent runs of benchmark tests was carried out. The main result suggested that a single large run reaches the solution faster than the small runs. A comparison of multi-population and single-population EAs was made for path planning in maritime collision avoidance [15]. In this case, the multi-population approach improved the results of the path planning task.

An interesting novel approach to the island models of an EA was described in [16], where the island had different sizes and was managed by a differential evolution algorithm.

In evolutionary multi-objective optimisation, it is possible to find a set of Pareto-optimal solutions. Such an approach may be applied to multiple real-life navigational problems, including the weather routing of transoceanic vessels [17].

RL, as described in [18], is one of the basic machine learning paradigms, in which an autonomous agent is able to take actions in an environment in order to maximise its cumulative reward value. Due to the exploration versus exploitation trade-off, RL requires feasible exploration policies, especially in online continuous state problems. The deep RL variant of this method has been applied in various complex tasks, like the automation of security solutions in network systems [19] it is important to investigate the behavior of the attacker after successful exploitation (post-exploitation, where the analysis of the behaviour of the attacker after successful exploitation was performed with the Advantage Actor Critic algorithm compared to the standard RL algorithms.

RL has many advantages in heuristic searches and has been successfully applied in the dynamic motion control of vehicles [20]. RL performs well in combination with ANNs treated as agents taking actions according to RL policy [21].

MATERIALS AND METHODS

For the purpose of this study, two methods of neuroevolution have been implemented and tested, namely, the modified adaptive NeuroEvolution of Augmenting Topologies (NEAT) (mNEAT) and the new modified island-based NEAT (iNEAT) algorithms. Both algorithms, designed and developed by the author, come from the NEAT method introduced by Stanley and Risto [22]. The standard NEAT method starts with a population of small ANNs and allows its topology to augment in an evolutionary process to a feasible size, capable of finishing the given task properly.

The direct encoding method has been used to create a functional structure of the ANN in NEAT from two genomes containing information on the topology and network connections (Fig. 1). Each value in both genomes (except for the number of inputs and outputs) may be altered in the mutation process.

The simulation was carried out with a computer application created by the author of this work. The computations were performed on a PC with an AMD Ryzen 5 2600 processor and 16 GB of RAM. The simulation was divided into stages for each task consecutively. In each stage, there were the time calculations of reaching the fitness value threshold by the population.

The training process of the NEAT method consists of three main steps, namely, the evaluation of vessel movements, selection and reproduction. The evaluation of each individual was processed during the whole simulation after some important events took place, as for example:

- Moving the vessel out of the area or on forbidden sector, i.e., the safety domain of an encountered vessel;
- Making rapid and/or frequently changing manoeuvres, i.e., frequent alterations in rpm, leading to improper

movement parameters for the ship, i.e., linear and/or angular velocity becomes too low or too high;

- Moving the vessel away from the goal;
- Reaching the goal.

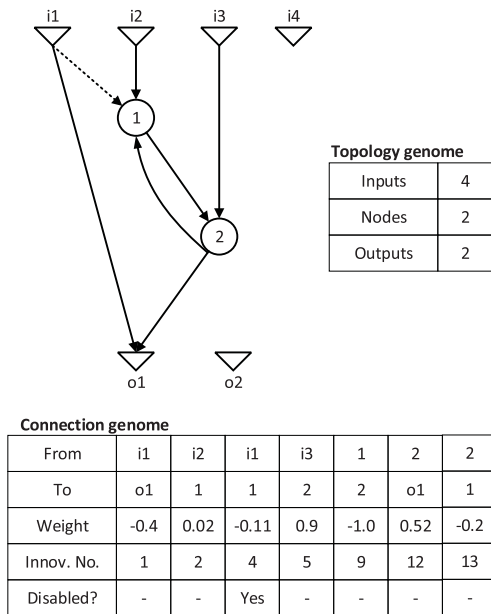


Fig. 1. An example of direct encoding in the NEAT method. The topology (phenotype) of the ANN is created from connection genomes (genotype)

All these events must be arbitrarily rated, resulting in a reward to an evaluated individual, thus valuating its fitness. The fitness value is important in the evolutionary stage of the algorithm because it affects the chance of reproduction and survival of the individual selected to the next generation.

The evolutionary process of the system consists of three main steps:

- Selection of the best individual (or individuals) of each island;
- Reproduction (with cross-over and mutation sub-processes);
- Replacement (offspring replaces worst individuals on each island).

NEAT modifies the topology of the ANNs using an EA. This approach allows a population of individuals to be obtained that are well suited for the task. In the mNEAT and iNEAT algorithms, there is a small probability of removing a node or connection, thus allowing the individuals to shrink and remove unnecessary genes from genome due to dynamically changing environment. It is also a method to avoid slowing of the learning progress of excessively large phenotypes if some rapid changes occur in the navigational task.

INPUT AND OUTPUT SIGNALS

The number and type of network input and output signals must be determined during the system design phase. A properly designed set of signals included in the model is crucial for the system performance and should provide the most accurate representation of the real navigational situation.

The following input signals were considered and implemented in the system with three degrees of freedom of movement of the vessel:

- Course over ground;
- Angular velocity;
- Speed over ground;
- Position of vessel;
- Distance and angle to goal, obstacles and encountered vessel;
- Visibility of goal, obstacles and other vessels;
- Propeller rpm (actual and suggested by ANN);
- Rudders' deflection (actual and suggested).

In the designed system, some other signals from the environment may be considered, if included in the ship model, i.e., wind, sea current, waves, cargo, trim and roll.

There are two output signals of the ANNs that generate control values for the vessel:

- Revolutions of main propeller (in rpm);
- Rudders' deflection.

Some input and all output signals are normalised as real values within the range $\langle 0.0; 1.0 \rangle$. Some input signals are of the Boolean type (e.g., is the goal visible? Is the goal on course? Is an obstacle on course?).

Each node in the network is a neuron that computes its output value from $\langle 0.0; 1.0 \rangle$ as a result of the normalised sum of its input values. The computation is performed using the sigmoid function described with Eq. (1):

$$o_j = \frac{1}{1 + e^{-(S_j \beta + \theta_j)}} \quad (1)$$

where o_j is the output of a neuron, S_j is the sum of the input values x_{nj} adjusted with weights w_{nj} , β is the slope coefficient and θ_j is the bias.

SIMULATION MODELS

The results of the simulation, shown below, are obtained for the VLCC crude oil tanker *Esso Norway II* with a single propeller and rudder and for the container ship *Cape Norman* (shown in Fig. 2). The main parameters of the simulated vessels are given in Table 1. The simulation models consist of three degrees of freedom of movement of the vessel. The main equation (Eq. (2)) of the ships' relative motion was formulated by Fossen [23]:

$$Mv + C(v_r)v_r + D(v_r)v_r + g(\eta) = \tau_p + \tau_{cs} + \tau'_e \quad (2)$$

where M is the mass matrix, C is the centripetal and Coriolis coefficients, D is the damping matrix, v_r is the velocity vector, $g(\eta)$ is the restoring forces vector and τ represents the forces affecting the vessel from the propeller (p), control surfaces (cs) and environmental disturbances (e).



Fig. 2. (a) VLCC oil tanker Esso Norway II (1969–1985). Source: <http://www.aukevisser.nl>.

(b) Container ship Cape Norman. Source: <https://www.marinetraffic.com/en/photos/of/ships/shipid:881996>

Tab. 1. Main parameters of the oil tanker Esso Norway II and the container ship Cape Norman

Parameter	Esso Norway II	Cape Norman
Overall length	323.8 m	175 m
Length between perpendiculars	304.8 m	170 m
Beam	47.3 m	26.5 m
Max. draft	18.46 m	14.2 m
Deadweight tonnage/capacity	193048 t	1504 TEU
Max. revolutions of propeller	80 rpm	480 rpm
Max. simulation rudder deflection	$\pm 20^\circ$	$\pm 30^\circ$

In this simulation, it was assumed that the Esso Norway II encounters a second vessel of similar size moving forward on a steady course. The maximum rudder deflection was limited to $\pm 20^\circ$ and $\pm 30^\circ$ regarding the simulation model accuracy. The safety domain was established as a simplified rectangle shape three lengths ahead of the bow, one length behind the stern (Fig. 3) and five lengths in total. The width of this domain is two lengths of the vessel. The domain surface area for the vessel is $\sim 150000 \text{ m}^2$.

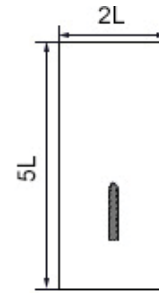


Fig. 3. Simplified safety domain of encountered vessel

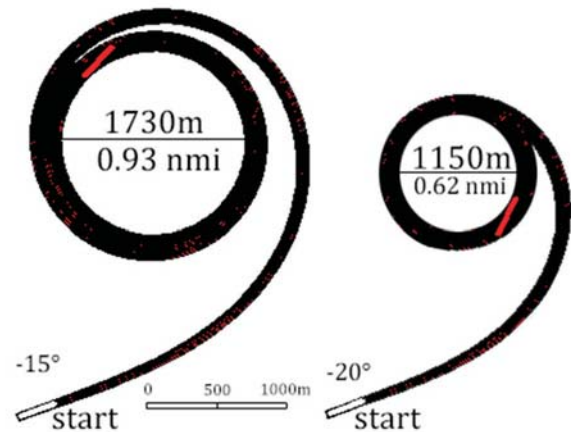


Fig. 4. Simulation results of Esso Norway II turning circle for two rudder deflections

It is noteworthy that the manoeuvrability characteristics of the VLCC oil tanker are very restricted due to its size and tonnage. Its turning circle diameter is $\sim 1150 \text{ m}$ (~ 0.62 nautical miles) for a maximum rudder deflection of -20° (see Fig. 4) and with full speed ahead (80 rpm).

PSEUDOCODE OF NEUROEVOLUTIONARY ISLAND APPROACH (INEAT)

The following list of instructions shows the main steps of the iNEAT algorithm:

1. Generate population p_0 with k individuals $i[1..k]$;
2. Give each individual i its initial basic structure consisting of $0..n$ nodes and c connections ($c > 0$);
3. Place each individual randomly in one of g groups (islands);
4. Start simulation and evaluation;
5. Evolve population regarding selection policy and mutation rates in each island separately;
6. Copy best individuals from each island to separate island g_0 ;
7. Cross over individuals from g_0 with random individual from each island and replace the worst individual on the island with the offspring;
8. If the overall fitness value is not obtained: go to 4, else end simulation.

Each island has different and dynamically valued evolutionary parameters. At the beginning, the mutation rate is greater and its value is gradually lowered according

to the overall fitness value of the population. If the fitness becomes lower because of rapid environmental changes, then the mutation parameters increase its value proportionally to these changes.

The islands operate autonomously and they periodically exchange the best individuals among each other during the process of evolution. Such a migration of individuals is carried out regarding the archipelago topology and the defined migration policy. The details of the migration specify the frequency of migration, the quantity of migrants and the method in which migrants are introduced into the target population.

During the simulation, the program runs until the population reaches a certain level of average fitness, calculated with Eq. (3), or its operation is terminated at the user's request. The threshold value of the average fitness of the whole population depends largely on the complexity of a given task:

$$f = \frac{t}{c + t + o + r} \quad (3)$$

where f is the overall fitness value of the population, t is the number of individuals that reached the goal, c is the number of individuals that crashed, o is the number of individuals that left the area and r is the number of individuals that were turning in a circle. The range of the values of f is [0.0, 1.0].

The fitness value threshold for overtaking and crossing situations was set at 0.3. This threshold was different for the third task. In passing through restricted waters, the probability of crashing with an obstacle was greater; thus, the overall performance of the population was lower than in the open sea. This was the reason for setting the fitness value threshold to 0.2 in this task.

RESULTS

This section contains three subsections describing each navigational task. Passing through restricted waters is for the container ship *Cape Norman*, with the assumption that the ship is far away from the bank and other ships. Overtaking and crossing manoeuvres are for the oil tanker *Esso Norway II* according to the Convention on the International Regulations for Preventing Collisions at Sea (COLREGs), published by the International Maritime Organisation in 1972. The mathematical formulations necessary to implement the COLREGs can be described and solved by the algebra of vectors [24] and then manoeuvres can be performed with the proposed EA methods (mNEAT and iNEAT), as compared below.

OVERTAKING

The overtaking manoeuvre is described by Rule 13 in the COLREGs. In the example below, our vessel is heading north

with a speed of 5 m/s (9,7 kn) and encounters another vessel located straight ahead at point A (Fig. 6) heading north at 3 m/s (5,8 kn). In this case, an overtaking manoeuvre has to be taken.

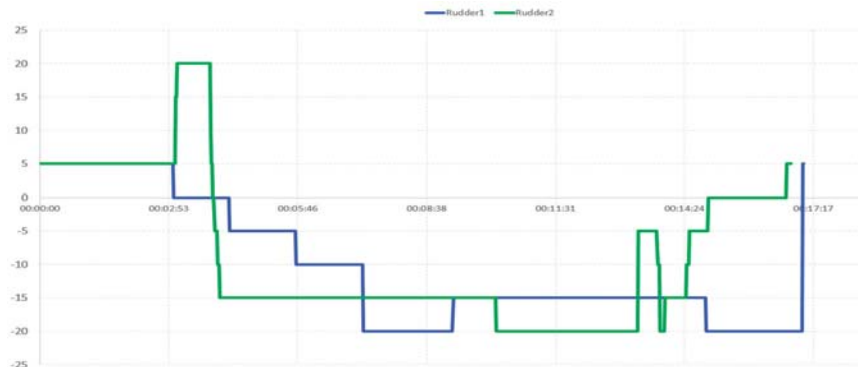


Fig. 5. Rudder angle comparison during overtaking manoeuvre: rudder1 (blue) – mNEAT; rudder2 (green) – iNEAT

As shown in Fig. 5, where the rudder angles of the best individuals are compared, there are some differences between the two results. At the beginning, both neural network outputs generate an angle of 5° (5° to port). In the classic mNeat method, there is a gradual change in the rudder angle from 5° to -20°, while the iNEAT change is radical from +20° to -15° and then to -20°, resulting in a longer and wider turning manoeuvre. In this scenario, the mNEAT results are more stable and with better course over ground than iNEAT.

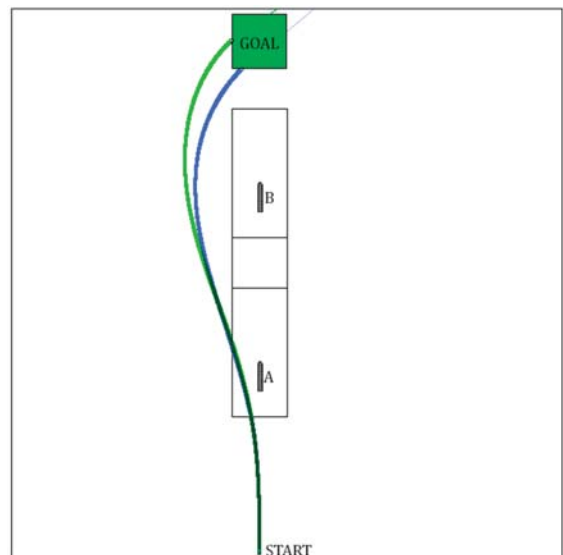


Fig. 6. Registered paths of vessels midship in overtaking situation: blue path – mNEAT; green path – iNEAT. Encountered vessel moves from A to B during whole manoeuvre

The result of this simulation requires further adjustments. The vessels from both solutions reach the goal with course

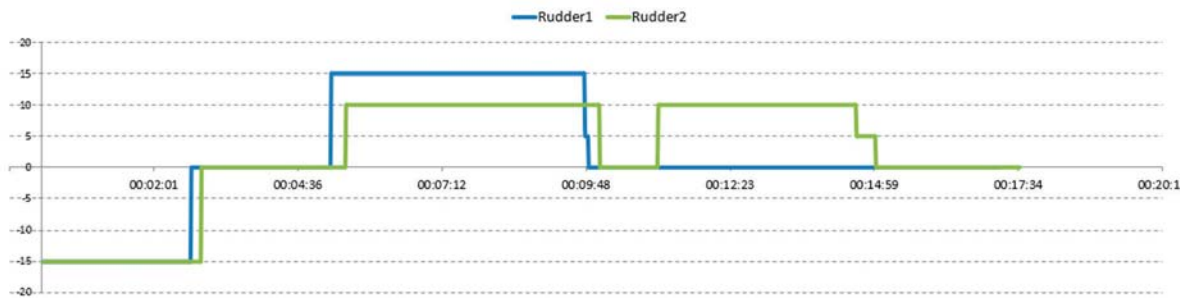


Fig. 7. Rudder angle comparison during crossing situation: rudder1 (blue) – mNEAT; rudder2 (green) – iNEAT

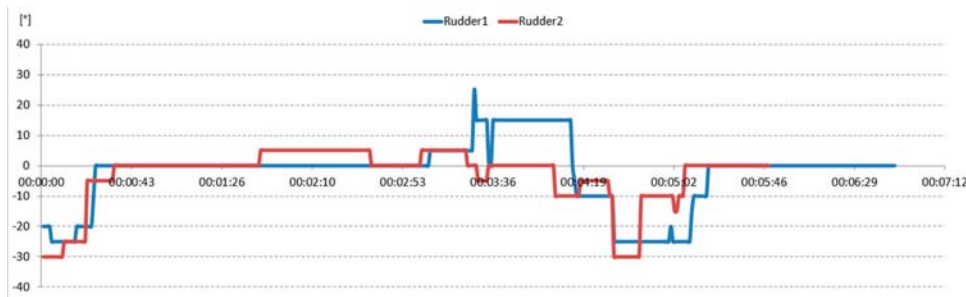


Fig. 9. Rudder angle comparison during passing through restricted waters: rudder1 (blue) – mNEAT; rudder2 (red) – iNEAT

over ground far from 0° (38° for mNEAT and 54° for iNEAT). Perhaps a stronger negative reinforcement value shall be inflicted to individuals with a high COG (Course Over Ground) value at the destination.

CROSSING SITUATION

The crossing situation is described by Rule 15 in the COLREGs. In this scenario, the Esso Norway II is a give-way vessel, forced to take proper manoeuvres to avoid collision with another vessel on its starboard.

Both results (Fig. 7) of the suggested rudder deflection are acceptable and the final choice of the solution may be determined by the impact of the penalties for the maximum rudder deflection or the rewards for the straight ahead course (0°).

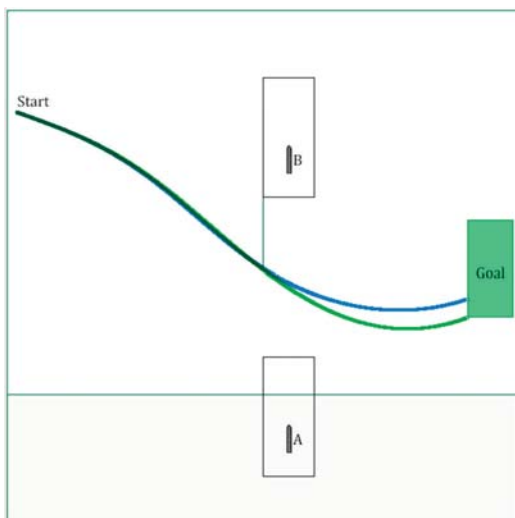


Fig. 8. Two paths of the vessel during crossing manoeuvres: blue path – mNEAT; green path – iNEAT. Encountered vessel is moving steadily from A to B

The final trajectories do not differ much (see Fig. 8). The mNEAT route seems to be flatter with a better final COG. In this task, there was a quantitatively stable group of vessels that had chosen a relatively safe circulation manoeuvre, instead of the risk of going towards the forbidden domain of the encountered vessel or area boundaries. This group was too weak to dominate the population but also too strong to be completely eliminated from the population during selection and reproduction.

PASSING THROUGH RESTRICTED WATERS

The simulation model of the Cape Norman was assigned to this task. One of the hardest manoeuvres was the narrow turn on starboard near the destination zone (see Fig. 11).

The results clearly show that iNEAT (red) is better than mNEAT (blue) in terms of the number of manoeuvres (rudder deflection values and alterations, Fig. 9), propeller suggested revolutions (Fig. 10) and the trajectory shape (Fig. 11).

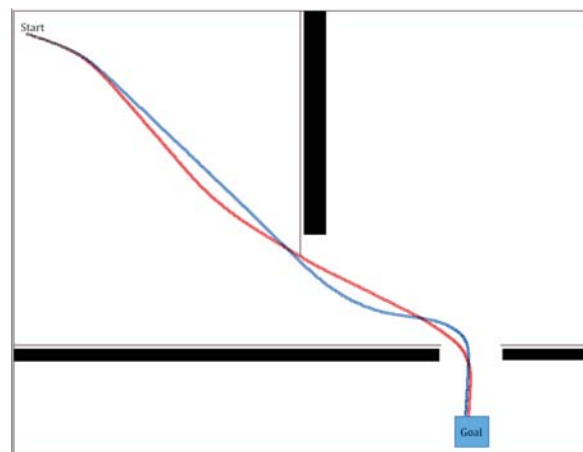


Fig. 11. Path of the midships of the vessel comparison during passing through restricted waters: blue path – mNEAT; red path – iNEAT

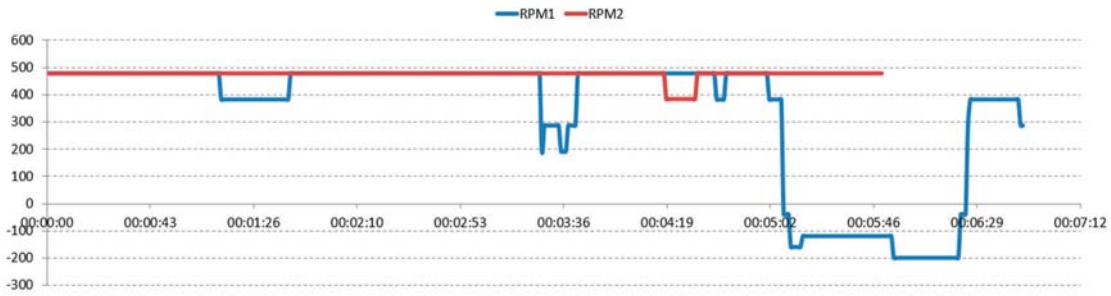


Fig. 10. Propeller revolution comparison during passing through restricted waters: RPM1 (blue) – mNEAT; RPM2 (red) – iNEAT

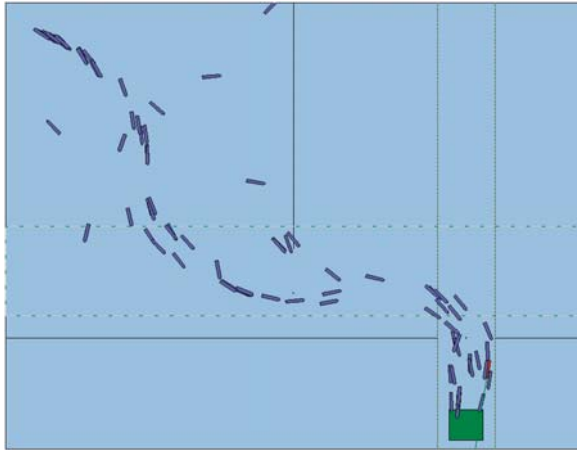


Fig. 12. Example of an ongoing simulation

An example of the evolutionary learning process during the simulation is presented in Fig. 12. As shown, a situation occurs where the population has already learned how to reach the goal and most of the individuals follow the best helmsman (marked as red). The tuning process now begins with a stricter selection threshold. Some of the vessels explore new solutions,

which eventually may be better rewarded than actions taken by the current best helmsman. A comparison of the time statistics for all navigational tasks for the first simulation run is presented in Fig. 13 and Table 2.

Tab. 2. Time statistics for simulated navigational tasks

Manoeuvres	Average time of acquiring fitness value threshold, 20 runs		Improvement rate	Median absolute deviation	
	mNEAT	iNEAT		mNEAT	iNEAT
Overtaking	0:05:10	0:04:25	14.4%	0:00:50	0:01:34
Crossing	0:07:58	0:07:25	6.8%	0:01:05	0:00:50
Restricted waters	0:13:02	0:09:30	27.1%	0:01:55	0:01:22

The time statistics show that the iNEAT approach is faster, particularly for the passage through restricted waters (Fig. 13(c)), despite the fact that it requires additional time for island management operations. The example in Fig. 13(d)

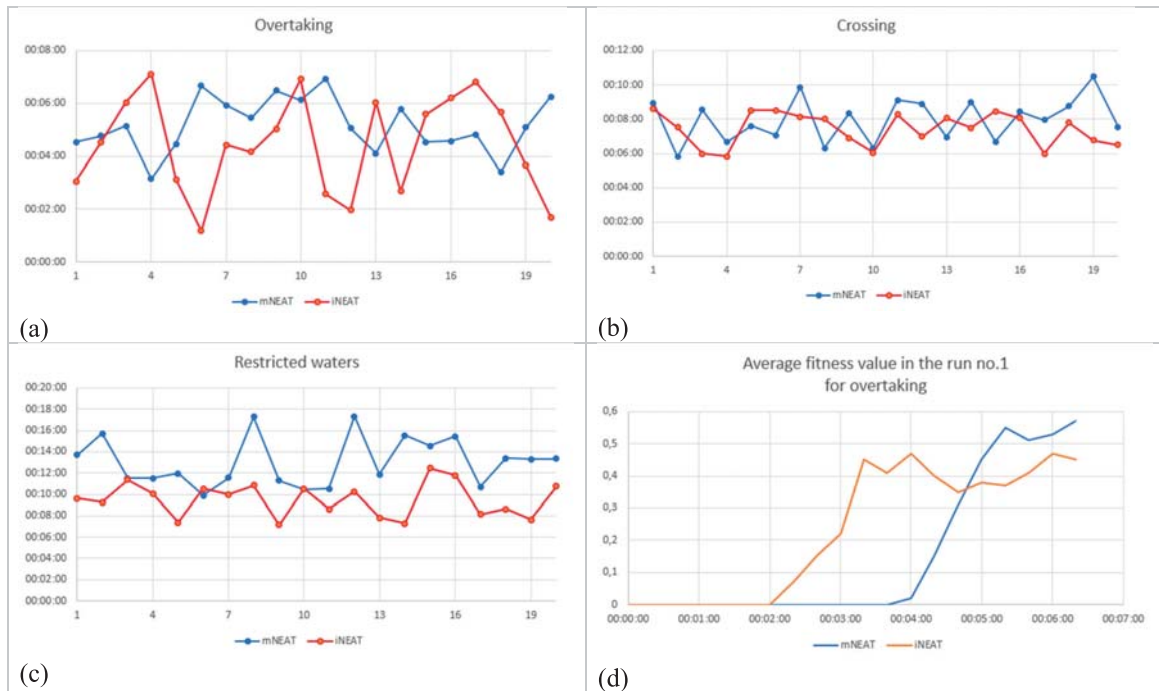


Fig. 13. Time of fitness value threshold acquisition in 20 runs for overtaking (a), crossing (b) and passage through restricted waters (c). An example fitness value acquisition process for the first run in overtaking (d). The threshold value for this task is 0.3.

shows that mNEAT is able to achieve higher average fitness values of ~0.55 for mNEAT and ~0.45 for iNEAT at the sixth minute of the simulation. This is due to the fact that the evolutionary parameters in iNEAT take a wider range of values, resulting in wider search space exploration and a potentially higher percentage of failures for some individuals.

CONCLUSIONS

The proposed new iNEAT method increases the accuracy and flexibility of the simulation process. This system allows for the simulation of the complex behaviour of the ship in a dynamic environment in a much larger space of states than is possible in classical reinforcement learning algorithms [18].

The simulation results show that the island separated population in an evolutionary ANN may slightly accelerate some complex and dynamic navigational tasks. The time statistics show that the time of simulation of island NEAT was shortened by 6.8% to 27.1% in comparison to modified NEAT method.

The proposed system has several important advantages that positively affect the efficiency of maritime transport. These are, among others:

- Possibility of usage on manned and unmanned vessels, which may lead to better automation of processes in the sea navigation;
- Providing additional data useful for decision makers during manoeuvres;
- Reduction of ship operating costs, human errors and detrimental impact of maritime transport on the environment.

All these benefits are strictly dependent on the size and dimensions of the search space, the number of signals analysed, the size of the ANN population and the encoding methods of the signals considered in the simulated environment. The population divided into islands with different evolutionary parameters allows the individuals to spread over a wider search space, resulting in a better chance of finding an optimal or sub-optimal solution. The diverse genetic pool is also much more flexible in dynamic environments. The drawback of this solution is the lower average fitness value of the population and additional procedures required for island management.

Due to the dynamic parametrisation of the island separated population, it is possible, in some cases, to find the correct solutions that allow us to reduce the number of manoeuvres, like rudder deflections or rpm alterations, resulting in lower fuel consumption.

The island model requires the topology of the migration and the migration policy to be established, which are tasks that require additional time and preparations. There are some proposals for the future research directions in ship handling neuroevolutionary methods, such as:

- Implementation of multi-size island model without migration;

- Introduction of environmental disturbances from influence of wind, current and waves on the moving vessel;
- Combining island model with indirect encoding neuroevolutionary methods;
- Evaluation of different population sizes on the algorithm's efficiency.

DATA AVAILABILITY

The simulation data used to support the findings of this study are available from the author upon request.

CONFLICTS OF INTEREST

The author declares that he has no conflicts of interest.

FOUNDING STATEMENT

This research was funded by the statutory activities of Gdynia Maritime University, grant number WN/2021/PI/2.

REFERENCES

1. D. Whitley, S. Rana, and R. Heckendorn, "The Island Model Genetic Algorithm: On Separability, Population Size and Convergence," *Journal of Computing and Information Technology*, vol. 7, 1998.
2. H. M. Pandey, A. Chaudhary, and D. Mehrotra, "A comparative review of approaches to prevent premature convergence in GA," *Applied Soft Computing*, vol. 24, pp. 1047–1077, 2014, doi: <https://doi.org/10.1016/j.asoc.2014.08.025>.
3. E. Alba and J. M. Troya, "An analysis of synchronous and asynchronous parallel distributed genetic algorithms with structured and panmictic Islands," in *Parallel and Distributed Processing*, Berlin, Heidelberg, 1999, pp. 248–256.
4. A. Hoang et al., "A review on application of artificial neural network (ANN) for performance and emission characteristics of diesel engine fueled with biodiesel-based fuels," *Sustainable Energy Technologies and Assessments*, Jun. 2021, doi: [10.1016/j.seta.2021.101416](https://doi.org/10.1016/j.seta.2021.101416).
5. S. L. Boungh Yew and K. K. Kee, "Artificial Neural Network Back-Propagation Based Decision Support System for Ship Fuel Consumption Prediction," 2018. doi: [10.1049/cp.2018.1306](https://doi.org/10.1049/cp.2018.1306).
6. W. Tarełko and K. Rudzki, "Applying artificial neural networks for modelling ship speed and fuel consumption," *Neural Computing & Applications*, vol. 32, pp. 17379–17395, 2020. doi: [10.1007/s00521-020-05111-2](https://doi.org/10.1007/s00521-020-05111-2)

7. J. Liu, G. Shi, and K. Zhu, "Vessel Trajectory Prediction Model Based on AIS Sensor Data and Adaptive Chaos Differential Evolution Support Vector Regression (ACDE-SVR)," *Applied Sciences*, vol. 9, p. 2983, 2019, doi: 10.3390/app9152983.
8. K. Bobkowska and I. Bodus-Olkowska Izabela, "Potential and Use of the Googlenet Ann for the Purposes of Inland Water Ships Classification," *Polish Maritime Research*, vol. 27, pp. 170–178, 2020. doi: 10.2478/pomr-2020-0077
9. G. Li, B. Kawan, H. Wang, and H. Zhang, "Neural-network-based modelling and analysis for time series prediction of ship motion," *Ship Technology Research*, vol. 64, 2017, doi: 10.1080/09377255.2017.1309786.
10. T. Niksa-Rynkiewicz and A. Witkowska, "Analysis of impact of ship model parameters on changes of control quality index in ship dynamic positioning system," *Polish Maritime Research*, vol. 26, no. 1(101), pp. 6–14, 2019. doi: 10.2478/pomr-2019-0001
11. J. Lisowski, "Computational Intelligence in Marine Control Engineering Education," *Polish Maritime Research*, vol. 28, no. 1, pp. 163–172, 2021, doi: doi:10.2478/pomr-2021-0015.
12. R. Lopes, R. Pedrosa Silva, F. Campelo, and F. Guimarães, "A Multi-agent Approach to the Adaptation of Migration Topology in Island Model Evolutionary Algorithms," in *Proceedings - Brazilian Symposium on Neural Networks, SBRN, 2012*, pp. 160–165. doi: 10.1109/SBRN.2012.36.
13. P. García-Sánchez, J. Ortega, J. González, P. A. Castillo, and J. J. Merelo, "Distributed multi-objective evolutionary optimization using island-based selective operator application," *Applied Soft Computing*, vol. 85, p. 105757, 2019, doi: <https://doi.org/10.1016/j.asoc.2019.105757>.
14. E. Cantú-Paz and D. E. Goldberg, "Are Multiple Runs of Genetic Algorithms Better than One?," in *Genetic and Evolutionary Computation — GECCO 2003*, Berlin, Heidelberg, 2003, pp. 801–812.
15. R. Śmierzchalski, Ł. Kuczkowski, P. Kolendo, and B. Jaworski, "Distributed Evolutionary Algorithm for Path Planning in Navigation Situation," *TransNav, the International Journal on Marine Navigation and Safety of Sea Transportation*, vol. 7, pp. 293–300, 2013, doi: 10.12716/1001.07.02.17.
16. A. Skakovski and P. Jędrzejowicz, "An island-based differential evolution algorithm with the multi-size populations," *Expert Systems with Applications*, vol. 126, pp. 308–320, 2019, doi: <https://doi.org/10.1016/j.eswa.2019.02.027>.
17. J. Szlupczyńska and R. Szlupczyński, "Preference-based evolutionary multi-objective optimization in ship weather routing," *Applied Soft Computing*, vol. 84, p. 105742, 2019, doi: <https://doi.org/10.1016/j.asoc.2019.105742>.
18. L. P. Kaelbling, M. L. Littman, and A. W. Moore, "Reinforcement Learning: A Survey," *Journal of Artificial Intelligence Research*, vol. cs.AI/9605, pp. 237–285, 1996, doi: 10.1613/jair.301.
19. R. Maeda and M. Mimura, "Automating post-exploitation with deep reinforcement learning," *Computers & Security*, vol. 100, p. 102108, 2021, doi: <https://doi.org/10.1016/j.cose.2020.102108>.
20. R. De Nardi, J. Togelius, O. E. Holland, and S. M. Lucas, "Evolution of Neural Networks for Helicopter Control: Why Modularity Matters," *Evolutionary Computation, 2006. CEC 2006. IEEE Congress on*, pp. 1799–1806, 2006, doi: citeulike-article-id:4142097.
21. N. T. Siebel and G. Sommer, "Evolutionary reinforcement learning of artificial neural networks," *International Journal of Hybrid Intelligent Systems - Hybridization of Intelligent Systems*, vol. 4, pp. 171–183, 2007.
22. K. O. Stanley and M. Risto, "Efficient Reinforcement Learning Through Evolving Neural Network Topologies," presented at the *Proceedings of the Genetic and Evolutionary Computation Conference, 2002*.
23. T. I. Fossen, *Guidance and control of ocean vehicles*. Chichester, UK: Wiley, 1994.
24. R. Zaccone, M. Martelli, and M. Figari, "A COLREG-Compliant Ship Collision Avoidance Algorithm," *Jun. 2019*, pp. 2530–2535. doi: 10.23919/ECC.2019.8796207.

CONTACT WITH THE AUTHOR

Mirosław Łacki

e-mail: m.lacki@wn.umg.edu.pl

Gdynia Maritime University
Morska 81/87
81-225 Gdynia
POLAND

NEW DESIGNS OF MAGNETIC FLUID SEALS FOR RECIPROCATING MOTION

Leszek Matuszewski*

Piotr Bela

Gdańsk University of Technology, Poland

* Corresponding author: leszekma@pg.edu.pl

ABSTRACT

The operating conditions of magnetic fluid seals during reciprocating motion are so different from those observed in rotating motion that the use of their conventional structures for reciprocating motion seals yields no good results. The analysis of the sealing mechanism of magnetic fluid seals in reciprocating motion shows that the operation of these seals is affected by the carry-over phenomenon and magnetic fluid film deformation in the sealing gap, which depends on the velocity of the reciprocating motion. The reduced amount of magnetic fluid in the sealing gap caused by the reciprocating motion of the shaft is the main reason for seal failures.

The paper presents a short characterisation of magnetic fluid sealing technology, the principle of sealing, the operation of the magnetic fluid and the seal failure mechanism in linear motion of the shaft. Moreover, some new structural designs of hybrid seals, being combinations of typical hydraulic seals with magnetic fluid seals for reciprocating motion, and some examples of magnetic fluid sealing structures for hydraulic cylinders and piston compressors which have practical application values are presented.

Keywords: magnetic fluid seal, reciprocating motion, critical pressure, sealing mechanism, failure reason of the seal, new seal designs

INTRODUCTION

At present, magnetic fluid sealing is the most important industrial application of magnetic fluid technology developed mainly in the last two decades. Magnetic fluids (ferrofluids) consist of the colloidal suspension of submicron size magnetic particles (e.g. Fe_3O_4 – magnetite) in various fluids used as carrier liquids. In the simplest form, a magnetic fluid seal consists of a pair of magnetically permeable pole pieces separated by an axially polarised permanent magnet and the ferrofluid. The flux lines formed in the closed magnetic circuit concentrate the ferrofluid in radial sealing gaps between the shaft and the pole pieces, thus producing a seal with virtually immeasurable leakage, low viscous drag and no contact wear.

Magnetic fluid seals offer high reliability and cost-effective solutions to many difficult sealing problems in modern machinery and processing equipment, especially in rotating motion in high vacuum and low-pressure gas applications.

These seals can also be used for reciprocating motion with low linear velocity e.g. in vacuum linear feedthroughs, hydraulic cylinders and reciprocating compressors [1, 2, 5].

Conventional ferrofluid rotary shaft apparatus are not satisfactory when the shaft must perform linear motion, since the ferrofluid gets displaced along the shaft during linear motion of the shaft resulting in the ultimate failure of the seal.

In order to overcome these disadvantages and improve the seal life, a newly designed sealing structure are used, that prevent the deformation of the magnetic fluid film and reduce the loss of magnetic fluid in the sealing gap.

ANALYSIS OF THE SEALING MECHANISM IN RECIPROCATING MOTION

The operating conditions of magnetic fluid seals during reciprocating motion are so different from those with rotating motion, that the use of their conventional structures for

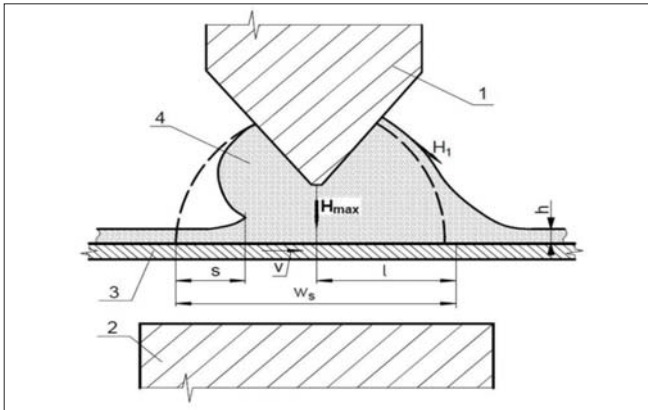


Fig. 1. Study of the carry-over phenomenon and magnetic fluid seal deformation: 1, 2 – rod-like pole pieces, 3 – disk, 4 – magnetic fluid

reciprocating motion seals yield no good results. Analysis of sealing mechanism of the magnetic fluid seal in reciprocating motion shows that the operation of these seals is affected by the carry-over and the magnetic fluid deformation in the sealing gap, which depends on the velocity of reciprocating motion. The reduction of magnetic fluid quantity in the sealing gap, caused by the reciprocating motion of the shaft is main reason of the seal failure.

One of the basic parameters of magnetic fluid seal is critical pressure. It is the maximum operating pressure of the magnetic fluid seal. In the case increase of the pressure in the seal above the critical pressure, the continuity of the fluid sealing ring is disrupted.

The study of magnetic fluid carry-over [3, 4] is made using an experimental model with the rod-like pole pieces 1 and 2 (Fig. 1). The peripheral part of disk 3 coming into the gap between the pole pieces moves at a speed v during its motion. Magnetic fluid 4 fills the sealing gap between pole piece 1 and disk 3.

The experimental apparatus made it possible to model the operation of a one-tooth magnetic fluid seal in linear shaft motion without pressure difference. The magnetic forces operating along the length l of the magnetic fluid seal affect the formation of the film carried away. The results have shown that the thickness h of the magnetic fluid film carried away by

the shaft increases with the increasing speed v and dynamic viscosity η , which can lead to magnetic fluid seal failure. The increase of the magnetic field gradient decreases h by several times, but it does not eliminate the carry-over completely.

The seal deformation changes the magnetic field intensity H values on its free surfaces which leads to the dependence of the critical pressure drop $\Delta p_{CR,1}$ upon the shaft motion direction. Fig. 2a shows the magnetic fluid position and Fig. 2b – the magnetic field intensity distribution H under magnetic fluid seal stage in the reciprocating motion. With allowance for the above stated assumption and with the stationary shaft:

$$\Delta p_{CR,1} = \mu_0 M_s (H_1 - H_2) \quad (1)$$

where:

- μ_0 – vacuum magnetic permeability,
- M_s – saturation magnetization of magnetic fluid,
- H_1 – magnetic field intensity in the point A at stationary shaft,
- H_2 – magnetic field intensity in the point D at stationary shaft

When the shaft moves one way with the external pressure difference or opposing it, the critical pressure drop $\Delta p_{CR,1}$ will accordingly be:

$$\Delta p_{CR,1} \rightrightarrows = \mu_0 M_s (H_B - H_2), \quad (2a)$$

$$\Delta p_{CR,1} \leftarrow = \mu_0 M_s (H_1 - H_C), \quad (2a)$$

where:

- H_B – magnetic field intensity in point B at stationary shaft.
- H_C – magnetic field intensity in point C at stationary shaft.

The sign with arrows \rightrightarrows means movement in line with the pressure gradient and in opposite direction.

Due to distribution under the stage the decrease of $\Delta p_{CR,1} \rightrightarrows$ will be more substantial than $\Delta p_{CR,1} \leftarrow$. The comparison of values of $\Delta p_{CR,1}$ calculated according to (2a) and (2b) with the results of experimental study of magnetic fluid seal of conventional type shows that at the pressure

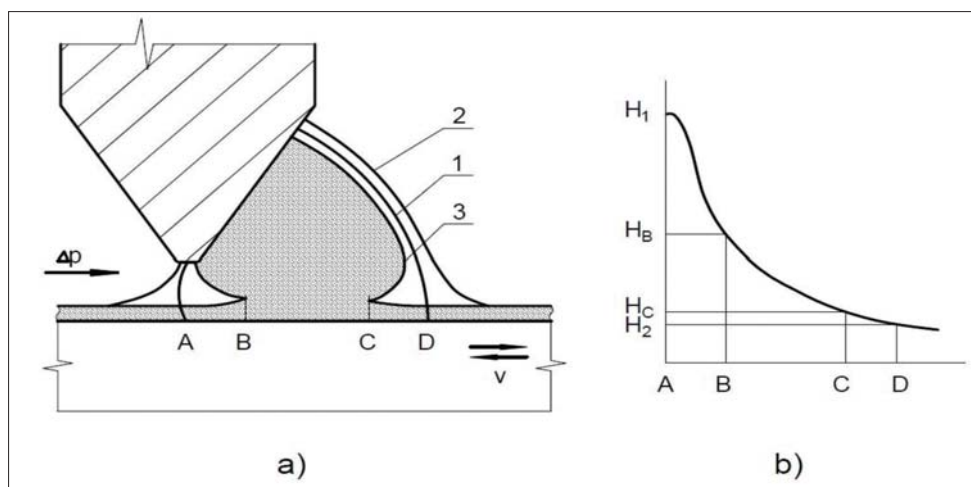


Fig. 2. Magnetic fluid position (a) and magnetic field intensity distribution H (b) under the magnetic fluid seal stage: 1 – stationary shaft, 2 – shaft moving in the direction of pressure gradient Δp , 3 – shaft moving in the direction opposite to pressure gradient Δp

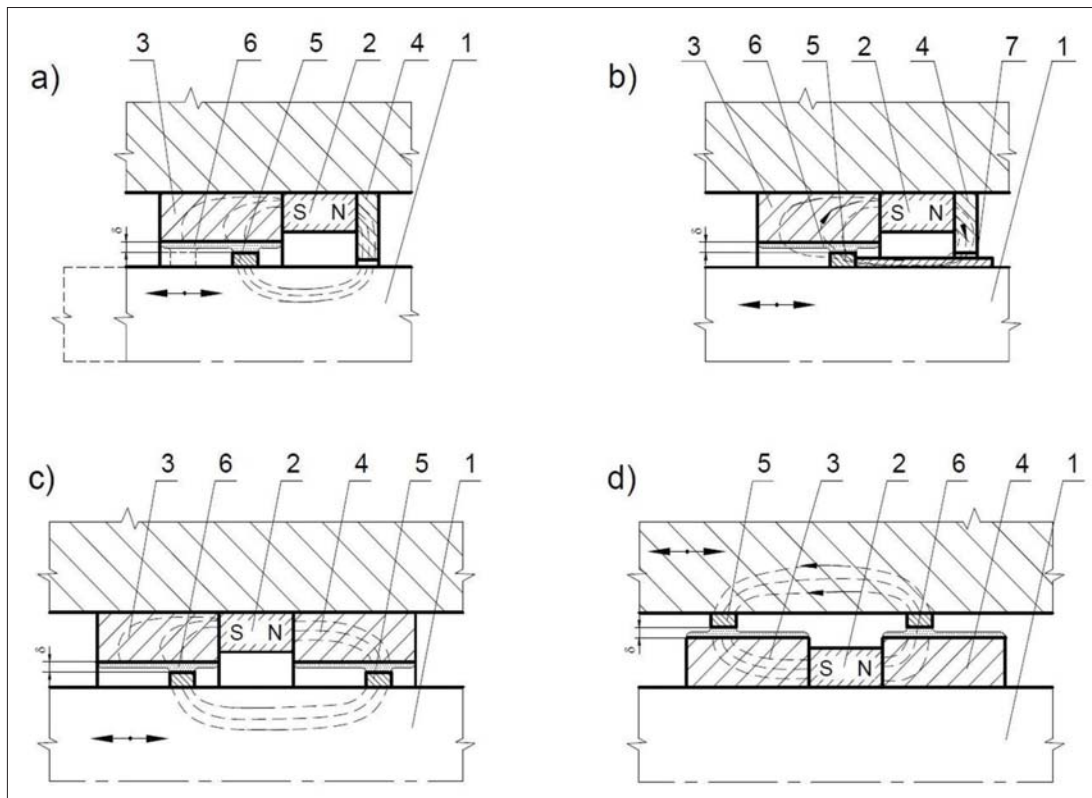


Fig. 3. Basic configurations of magnetic fluid seal for linear motion. From a to d – variants of seal design 1 – piston rod, 2 – axially polarised permanent magnet, 3, 4 – pole pieces, 5 – annular ring, 6 – magnetic fluid (ferrofluid), 7 – magnetically permeable sleeve

difference $\Delta p < \Delta p_{CR,1} \Rightarrow$ good hermetic sealing is ensured; at $\Delta p_{CR,1} \Rightarrow \Delta p < \Delta p_{CR,1} \Leftarrow$ temporary micro punctures affect the tightness; and $\Delta p \geq \Delta p_{CR,1} \Leftarrow$ causes complete seal failure. Thus, the seal deformation is the principal cause of the decrease of tightness and the critical pressure differences of magnetic fluid seal in reciprocating motion of the shaft.

BASIC CONFIGURATIONS OF MAGNETIC FLUID SEAL FOR LINEAR MOTION

Fig. 3 shows a basic configuration of the magnetic fluid seal that is particularly useful as a hermetic seal of a shaft arranged relatively for linear reciprocating motion [6]. In the seal configuration shown in Fig. 3a, the axially polarised annular permanent magnet 2 is fixed within a bore of the housing. Pole pieces 3, 4 are press-fitted within the housing at both sides of the magnet. Pole piece 3 has a cylindrical inner face that is coaxial with and spaced from shaft 1. The inner face of this pole has an axial length equal to or greater than the stroke of the reciprocating movement of the shaft. The axial and radial dimensions of pole piece 4 are such that it closely faces the shaft 1 in a spaced relationship to form part of the magnetic flux circuit, generated by magnet 2. An annular ring 5 made of magnetically permeable material is hermetically press-fitted around shaft 1. As shown, the axial length of ring 5 is smaller than that of pole piece 3. The radial diameters of the outer face of ring 5 and the inner face of pole piece 3 are selected in such a way that a small radial gap δ is formed between them. The magnetic flux generated by magnet 2 forms a closed magnetic circuit, as schematically

shown by the dotted lines. The magnetic fluid 6 is magnetically retained in the gap δ to provide a hermetic seal between pole piece 3 and ring 5. As shaft 1 performs a linear motion together with ring 5, the inner portion of the magnetic fluid 6 follows the linear movement of the ring. Since the axial length of pole piece 3 is equal to or greater than the stroke of linear movement of shaft 1, the inner portion of the magnetic fluid 6 is constantly in contact with the ferrofluid film, and a hermetic seal is established during the linear motion. Fig. 3b shows the seal configuration designed for use with a magnetically non-permeable shaft. In this case, the sleeve 7 made of magnetically permeable material is fitted over shaft 1, and adheres to ring 5. Thus, the magnetic flux circuit is completed to magnetically retain the magnetic fluid 6 in the gap δ . The seal configuration shown in Fig. 3c is designed to perform a hermetic seal in two stages. In this case, two pole pieces have an axial length equal to or larger than the linear stroke of shaft 1, and a second ring 5 is press-fitted over the shaft to form the second gap δ in which the magnetic fluid 6 is retained. The seal configuration shown in Fig. 3d is designed to be used together with a magnetically permeable housing. An axially polarised annular magnet 2 is fitted over shaft 1 and sandwiched between magnetically permeable pole pieces 3, 4, which are hermetically press-fitted over the shaft. The annular rings 5 are hermetically press-fitted within a bore of the housing situated opposite pole pieces 3, 4. The magnetic fluid 6 is retained in the gaps δ , to provide a pair of hermetic seals between the shaft and the housing. This seal apparatus may be advantageously employed in places where the housing undergoes linear reciprocating movement.

SOME NEW DESIGNS OF COMBINED FLUID SEALS FOR RECIPROCATING MOTION REVIEW

Below are presented some new designs of hybrid seals of elements for reciprocating motion, being combinations of typical hydraulic seals with magnetic fluid seals. Fig. 4 shows a hybrid seal for large-size elements of reciprocating and rotating motion [7]. A characteristic structural feature of this seal is that two sealing units, separated by an axially polarised annual permanent magnet 4, are mounted in the gland chamber of housing 2. Each unit consists of the support sleeve 3 with single asymmetric pole pieces 5 and non-magnetic spacers 7 alternately fixed in cylindrical bore chambers 3b of support sleeves 3. Moreover, non-magnetic spacers 7 and soft sealing rings 8 of rectangular cross-section, made of braided packing rope, for instance, are mounted on both ends of each sealing package. The sealing projection in each single asymmetric pole piece 5 is determined by the conical surface of its inner opening. In each sealing package, single asymmetric pole pieces 5 are directed with their sealing surfaces toward the annual permanent magnet 4. An additional single soft sealing ring 8 of rectangular cross-section is mounted between the inner side surfaces of flanges 3a of support sleeves 3, the cylindrical surface of the annular permanent magnet 4, and the piston rod 1. The gland chamber is closed from both sides of housing 2 by pressure glands 10, in which plain bearing bushings 11 adhering to the surface of piston rod 1 are mounted. The magnetic fluid 6 is retained in the annular sealing gaps δ created between the sealing projections of single asymmetric pole pieces 5 and the surface of piston rod 1. Closed magnetic circuits $\Phi_1, \Phi_2, \Phi_3, \Phi_4$ are created by annular permanent magnet 4, support sleeves 3, single asymmetric pole pieces 5, magnetic fluid 6, and piston rod 1.

Fig. 5 shows another hybrid seal for large-size elements of reciprocating and rotating motion [8]. In the central part of this seal, in housing 2, the sealing unit consisting of two asymmetric multi-edge pole pieces 4 separated by axially polarised annular permanent magnet 3 is mounted. Other sealing sub-assemblies are mounted on both ends of this seal, each sub-assembly consisting of at least three symmetric multi-edge pole pieces 7 separated by axially polarised annular permanent magnets 5, 6 mounted in cylindrical bore chambers

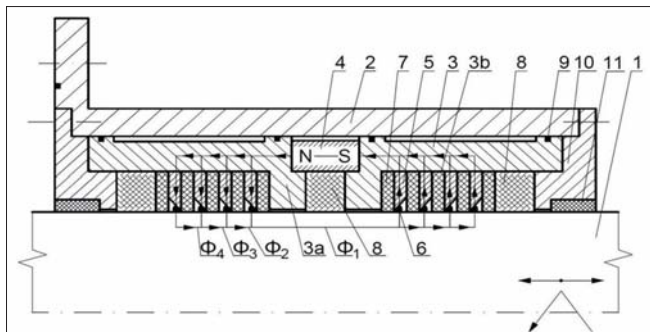


Fig. 4. Hybrid seal for large-size elements of reciprocating and rotating motion:
1 - piston rod or shaft, 2 - housing, 3 - support sleeve, 3a - flange, 3b - bore chamber, 4 - annular permanent magnet, 5 - single pole piece, 6 - magnetic fluid, 7 - non-magnetic spacer, 8 - soft sealing ring, 9 - "O"-ring seal, 10 - pressure gland, 11 - plain bearing bushing, δ - sealing gap, $\Phi_1 - \Phi_4$ - closed magnetic circuits

in pole pieces 7. Permanent magnets 5, 6 adhere with poles N to the side surfaces of the central symmetric multi-edge pole piece 7. Moreover, elastic pressure rings 9 of circular cross-section, made of elastomeric material, and pressure glands 10 made of low friction material and adhering to the surface of piston rod 1 are mounted in the annular chambers created between the side surfaces of symmetric multi-edge pole pieces 7 and the inner cylindrical surfaces of permanent magnets 5, 6. An additional soft sealing ring 11 is placed between the inner side surfaces of asymmetric multi-edge pole pieces 4, the inner cylindrical surface of permanent magnet 3, and the piston rod 1. Moreover, non-magnetic spacers 13 are placed on both ends of the sealing sub-assemblies, as well as between symmetric multi-edge pole pieces 7 and asymmetric multi-edge pole pieces 4. The magnetic fluid 8 is retained in the annular sealing gaps δ created between sealing projections situated on the inner cylindrical surfaces of symmetric multi-edge pole pieces 7 and asymmetric multi-edge pole pieces 4, and the surface of piston rod 1. Closed magnetic circuits Φ_1, Φ_2 are created by symmetric multi-edge pole pieces 7, permanent magnets 5, 6, magnetic fluid 8, and piston rod 1, while the closed magnetic circuit Φ_3 is created by permanent magnet 3, asymmetric multi-edge pole pieces 4, magnetic fluid 8, and piston rod 1.

Fig. 6 shows another patent pending (P-438268) design of hybrid seal for large-diameter elements of rotating or reciprocating motion [9]. In this design, two multi-edge pole pieces 3 having the form of flange bushes with sealing projections formed on the inner cylindrical surfaces of their flanges 3a are mounted in the gland chamber of housing 2. The pole pieces are separated by axially polarised annular permanent magnet 4. Moreover, two sealing packages, each consisting of soft sealing ring 9 of rectangular cross-section and at least two radially polarised permanent magnets 5, 6 separated by non-magnetic spacers 7, are mounted in bore chambers 3b of multi-edge pole pieces 3 situated at the side of piston rod 1. The adjacent permanent magnets 5, 6 have an alternating sequence of poles N and S with respect to piston rod 1, while the gland chamber is closed on both sides of housing 2 with pressure glands 11, in which porous sliding bearings 12 adhering to piston rod 1 are mounted. An additional soft sealing ring 9 of rectangular cross-section,

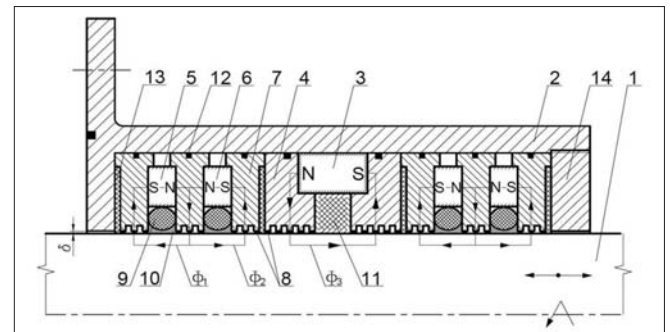


Fig. 5. Hybrid seal for large-size elements at rotating or reciprocating motion:
1 - shaft or piston rod, 2 - housing, 3, 5, 6 - axially polarised annular permanent magnets, 4 - multi-edge asymmetric pole piece, 7 - multi-edge symmetric pole piece, 8 - magnetic fluid, 9 - elastic pressure ring of circular section, 10 - sliding bushing, 11 - soft sealing ring, 12 - "O"-ring seal, 13 - non-magnetic spacer, 14 - nut, δ - sealing gap, Φ_1, Φ_2, Φ_3 - closed magnetic circuits

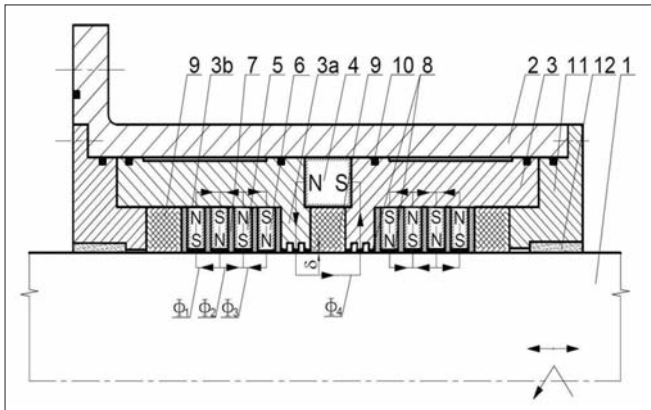


Fig. 6. Hybrid seal for large-diameter elements of rotating or reciprocating motion: 1 - shaft or piston rod, 2 - housing, 3 - multi-edge pole piece, 3a - flange, 3b - bore chamber, 4 - axially polarised permanent magnet, 5, 6 - radially polarised permanent magnets, 7 - non-magnetic spacer, 8 - magnetic fluid, 9 - soft sealing ring, 10 - "O"-ring seal, 11 - pressure gland, 12 - porous sliding bearing, δ - sealing gap, Φ_1, Φ_2, Φ_3 - closed magnetic circuits

made of braided packing rope for instance, is mounted between the inner facing surfaces of flanges 3a of multi-edge pole pieces 3, the inner cylindrical surface of axially polarised annular permanent magnet 4, and piston rod 1. The magnetic fluid 8 is retained in annular sealing gaps δ created between the sealing projections of multi-edge pole pieces 3 and the surface of piston rod 1, and between the inner cylindrical surfaces of the radially polarised permanent magnets 5, 6 mounted in bore chambers 3b of multi-edge pole pieces 3 and piston rod 1. The closed magnetic circuits Φ_1, Φ_2 , and Φ_3 are created by piston rod 1, radially polarised permanent magnets 5, 6, and magnetic fluid 8, while the closed magnetic circuit Φ_4 is created by axially polarised permanent magnet 4, multi-edge pole pieces 3, magnetic fluid 8, and piston rod 1.

Fig. 7 presents the patent pending (P-437268) combined design of a hybrid seal for large-diameter elements of rotating or reciprocating motion [10]. This design is composed of multi-edge pole pieces, an axially polarised annular permanent magnet, magnetic fluid, soft sealing rings, coil springs, back-up and pressure rings, pressure glands, and porous sliding bearings. The characteristic feature of this design is that two multi-edge pole pieces 3, having the form of flange bushes with sealing projections 3c formed on the inner cylindrical surfaces of their flanges 3a, are mounted in the gland chamber of housing 2 and separated by the annular permanent magnet 4. Moreover, soft sealing rings 6 and sub-assemblies consisting of pressure rings 9, coil springs 8, and back-up rings 7 are mounted in bore chambers 3b of pole pieces 3 situated at the side of piston rod 1. These sub-assemblies are pressed from outside by pressure glands 10 with mounted porous sliding bearings 11 adhering to the surface of piston rod 1. An additional soft sealing ring 6, made of braided packing rope for instance, is placed in the chamber created between the inner facing surfaces of flanges 3a of multi-edge pole pieces 3, the permanent magnet 4, and the piston rod 1. The magnetic fluid 5 is retained in annular sealing gaps δ created between sealing projections 3c of multi-edge pole pieces 3 and the surface of piston rod 1. The closed magnetic circuit Φ is created by piston rod 1, multi-edge pole pieces 3, annular permanent magnet 4, and magnetic fluid 5.

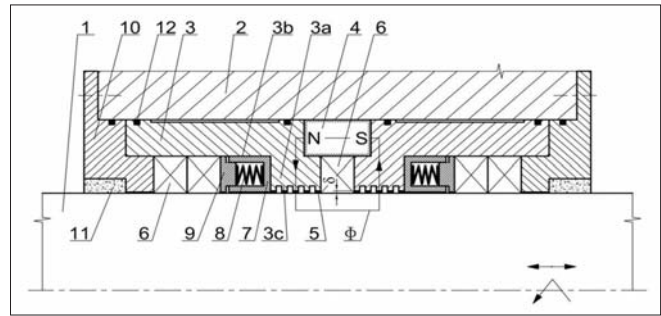


Fig. 7. Hybrid seal for large-size elements at rotating or reciprocating motion: 1 - shaft or piston rod, 2 - housing, 3 - multi-edge pole piece, 3a - flange, 3b - bore chamber, 3c - sealing projection, 4 - annular permanent magnet, 5 - magnetic fluid, 6 - soft sealing ring, 7 - back-up ring, 8 - coil spring, 9 - pressure ring, 10 - pressure gland, 11 - porous sliding bearing, 12 - "O"-ring seal, δ - sealing gap, Φ - closed magnetic circuit

Fig. 8 shows the patented (PL234946) solution of a hybrid seal for elements of rotating or reciprocating motion [11]. In this seal, two multi-edge pole pieces 3 having the form of flange bushes with sealing projections made on the cylindrical surfaces of their flanges 3a are mounted in the gland chamber of housing 2 and separated by axially polarised annular permanent magnet 4. Moreover, two sealing packages, each consisting of soft sealing ring 7 of rectangular cross-section and permanent magnet 5 of "C"-shaped cross-section are placed in bore chambers 3b of multi-edge pole pieces 3 situated at the side of piston rod 1. The arms of permanent magnet 5 directed towards the surface of piston rod 1 are the poles N and S. An elastic sealing ring 8 of circular cross-section is placed, together with back-up rings 9, at the inner side of permanent magnet 5, between poles N and S. The gland chamber is closed on both sides of housing 2 by pressure glands 12 with mounted porous sliding bearings 13 adhering to the surface of piston rod 1. Moreover, a single soft sealing ring 7 of rectangular cross-section, made of braided packing rope for instance, is placed between the inner facing surfaces of flanges 3a of multi-edge pole pieces 3, the cylindrical surface of axially polarised permanent magnet 4 and piston rod 1. The magnetic fluid 6 is retained in annular sealing gaps δ created between the sealing projections of multi-edge pole pieces 3 and the

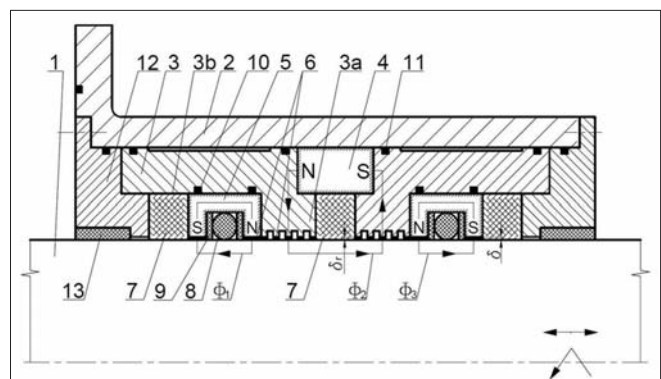


Fig. 8. Hybrid seal for elements of reciprocating or rotating motion: 1 - piston rod or shaft, 2 - housing, 3 - multi-edge pole piece, 3a - flange, 3b - bore chamber, 4 - axially polarised annular permanent magnet, 5 - permanent magnet of "C"-shaped cross-section, 6 - magnetic fluid, 7 - soft sealing ring, 8 - elastic sealing ring of circular cross-section, 9 - back-up ring, 10, 11 - "O"-ring seals, 12 - pressure gland, 13 - porous sliding bearing, δ - sealing gap, Φ_1, Φ_2, Φ_3 - closed magnetic circuits

surface of piston rod 1, and between the cylindrical surfaces of the arms composing the poles N and S of permanent magnets 5 of “C”-shaped cross-section and the surface of piston rod 1. Closed magnetic circuits Φ_1 and Φ_3 are created by permanent magnets 5 of “C”-shaped cross-section, piston rod 1, and magnetic fluid 6, while the closed magnetic circuit Φ_2 is created by multi-edge pole pieces 3, axially polarised annular permanent magnet 4, piston rod 1, and magnetic fluid 6.

APPLICATION EXAMPLES OF MAGNETIC FLUID RECIPROCATING SEALING

Fig. 9 shows two variants of combined types of the magneto-fluid reciprocating sealing structure for hydraulic cylinders. Fig. 9a shows a patented (Int.CL.F16J15/43 no 109505985) reciprocating sealing device with magnetic fluid for the hydraulic cylinder [12], which comprises a cylinder shell 2, multi-edge pole pieces 3, axially polarised permanent magnet rings 4, non-magnetic conductive rings 5, magnetic fluid 6 and distance magnetic isolation rings 7. According to the principle of operation of the reciprocating sealing device with magnetic fluid for the hydraulic cylinder, the magnetic source is provided by multiple permanent magnets, while the non-magnetic conductive rings are arranged in the space formed by pole pieces 3, permanent magnets 4 and piston rod 1 in the enclosing mode. The non-magnetic conductive rings 5 are provided with pole teeth; therefore, the problem of the pressure resistance of the existing single-magnetic-source magnetic fluid sealing device and the existing multi-magnetic-source magnetic fluid sealing device is solved, along with the problem of the magnetic fluid utilisation rate of an existing magnetic fluid sealing device. Fig. 9b shows a combined magnetic fluid reciprocating sealing structure (Patent CN, In.CL. F16J15/43, no 108869751) [13], which has a plurality of annular multi-edge pole pieces 3 axially arranged at intervals inside the space between the outer surface of piston rod 1 and the inner surface of cylinder shell 2. The inner cylindrical surface of each pole piece is provided with pole teeth. The axially magnetised permanent magnet rings 4 are clamped between every two neighboring pole pieces 3, which are opposite in magnetic polarity. The sealing gaps δ created between the pole teeth and the outer surface of piston rod 1 are filled with magnetic fluid 7. An annular accommodating space is formed between the inner spherical surface of each axially magnetised permanent magnet ring 4 and the outer surface of piston rod 1. This space is closed with double acting seals in which sliding rings 6, made of low friction material, are energised by elastomeric “O”-rings 5. In this case the “O”-rings 5 preload the sliding rings 6 in the thin flexible middle section. In both seal designs closed magnetic circuits Φ are created by multi-edge pole pieces 3, permanent magnets 4, magnetic fluid 5 and piston rod 1. The combined magnetic fluid reciprocating sealing structure created by adding double-acting seals into the traditional magnetic fluid sealing design can further enhance the sealing and press-resistant performance and eliminate the loss of magnetic fluid.

Fig. 10 shows the magnetic fluid sealing structure for reciprocating motion used in hydraulic cylinders [14]. The

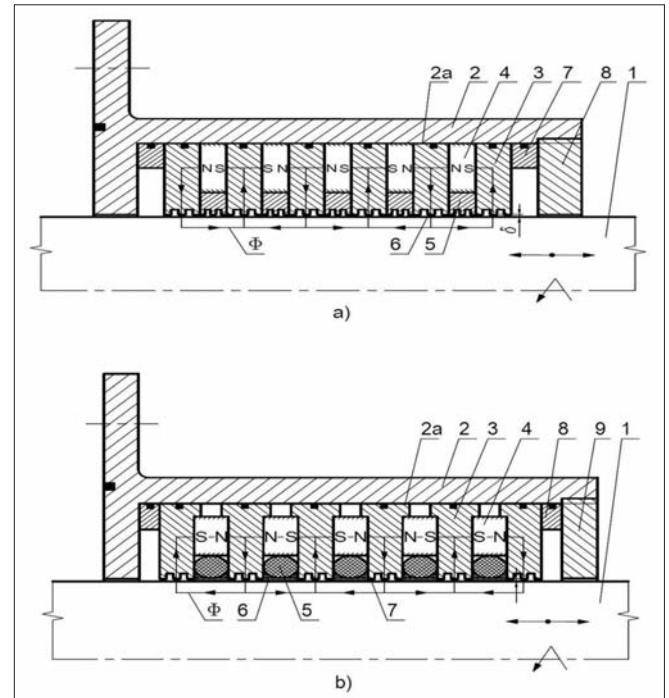


Fig. 9. Combined types of magneto-fluid reciprocating sealing structure for hydraulic cylinder a), b) design variants: a) 1 - piston rod, 2 - cylinder shell, 2a - bore chamber, 3 - multi-edge pole piece, 4 - axially polarised permanent magnet ring, 5 - non-magnetic conductive ring, 6 - magnetic fluid, 7 - distance magnetic isolation ring, 8 - nut, δ - sealing gap, Φ - closed magnetic circuit b) 1 - piston rod, 2 - cylinder shell, 2a - bore chamber, 3 - multi-edge pole piece, 4 - axially polarised permanent magnet ring, 5 - elastomeric “O”-ring, 6 - sliding ring, 7 - magnetic fluid, 8 - distance ring, 9 - nut, δ - sealing gap, Φ - closed magnetic circuit

magnetic fluid sealing structure comprises the cylinder shell 2, the reciprocating piston rod 1 arranged in the inner cavity of the shell, multi-edge pole pieces 3, 4 and axially polarised permanent magnets 5, 6. The multi-edge pole pieces 3, 4 are arranged on the two sides of each permanent magnet 5, 6. At least one groove is formed around the inner circle face of each pole piece 3, 4 and a Y-shaped sealing ring 8 is arranged in each groove. Pole teeth are arranged on the inner circle faces of the pole pieces 3, 4. The sealing gaps δ exist between the pole teeth and the outer surface of the reciprocating piston rod 1. The magnetic fluid 7 is injected into gap positions. Two closed magnetic circuits Φ_1 , Φ_2 are created by multi-edge pole

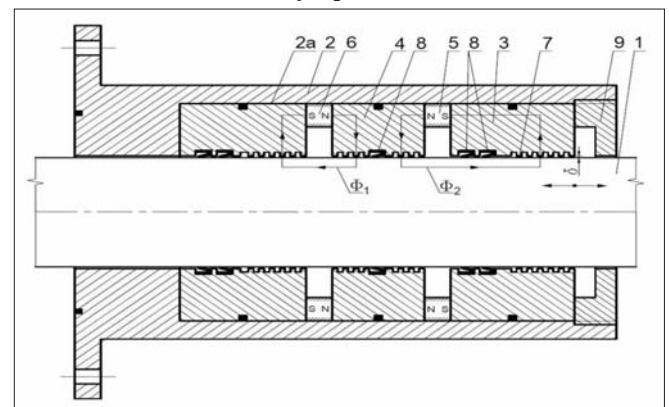


Fig. 10. Magnetic fluid sealing structure for reciprocating motion: 1 - piston rod, 2 - cylinder shell, 2a - bore chamber, 3, 4 - multi-edge pole pieces, 5, 6 - axially polarised permanent magnets, 7 - magnetic fluid, 8 - “Y”-shaped sealing rings, 9 - nut, δ - sealing gap, Φ_1 , Φ_2 - closed magnetic circuits

pieces 3, 4, permanent magnets 5, 6, magnetic fluid 7 and piston rod 1. Through the combined use of the magnetic fluid and the Y-shaped sealing rings, a sealing structure that gives excellent pressure resisting and high sealing performance is formed. Accordingly, due to the fact that the magnetic fluid seal has a dustproof function, the pollution from outside impurities to the Y-shaped sealing rings is reduced, the purity of the sealed medium is improved, and the service interval of the sealing ring is prolonged to the maximum degree, thus meeting the requirements for zero leakage and long service life of hydraulic cylinders.

Fig. 11 shows the reciprocating shaft's sealing apparatus, which combines a ferrofluid seal with hydraulic sealing rings [15]. The sealing device comprises the cylinder shell 2, piston rod 1, axially polarised annular permanent magnet 3, multi-edge pole pieces 4, magnetic fluid 5, two fixed bases 6, Y-seal rings 7 and double acting seal rings 8. The pole pieces 4 separated by permanent magnet 3 are mounted in an inner cavity of the cylinder shell 2. The fixed bases 6, with Y-seal rings 7 and double acting seal rings 8 installed in their grooves, are placed on both ends of the sealing chamber.

These parts are pressed tightly by the end cover 12 connected with the cylinder shell 2 by bolts. The magnetic fluid 5 is injected into the sealing gaps δ before assembling. The closed magnetic circuit Φ is created by permanent magnet 3, multi-edge pole pieces 4, magnetic fluid 5 and piston rod 1. The sealing apparatus, being the combination of a magnetic fluid seal and traditional hydraulic sealing rings, solves the problem of leakage in the reciprocating type of compressors.

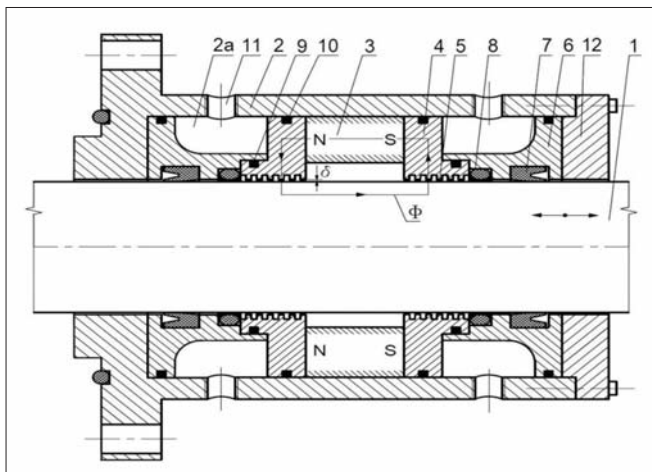


Fig. 11. Reciprocating shafts sealing apparatus combining magnetic fluid seal with double seal-ring and Y- seal-ring: 1 - piston rod, 2 - cylinder shell, 2a - cooling chamber, 3 - axially polarised annular permanent magnet, 4 - multi-edge pole piece, 5 - magnetic fluid, 6 - fixed base, 7 - Y-shaped seal-ring, 8 - double acting seal ring, 9, 10 - "O"-ring seals, 11 - water intake, 12 - cover, δ - sealing gap, Φ - closed magnetic circuit

Fig. 12 shows a combined design seal of the double-acting piston in the hydraulic cylinder with magnetic fluid seals [16]. The sealing set consists of two "U"-shaped sealing rings 4 with back-up rings 5, two axially polarised permanent magnets 6, two non-magnetically permeable sleeves 9, fixed in piston 3 and two multi-edge pole pieces 8 located on each side of piston 3. Two closed magnetic circuits Φ_1 , Φ_2 are created by piston 3, permanent magnets 6, multi-edge pole pieces 8, magnetic

fluid 7 and cylinder shell 2. The magnetic fluid 7 is retained by magnetic forces in small sealing gaps δ between tooth-like projections of piston 3, the multi-edge pole pieces 8 and the inner cylindrical surface of cylinder shell 2, thus providing proper lubrication of the piston and increasing the cylinder tightness.

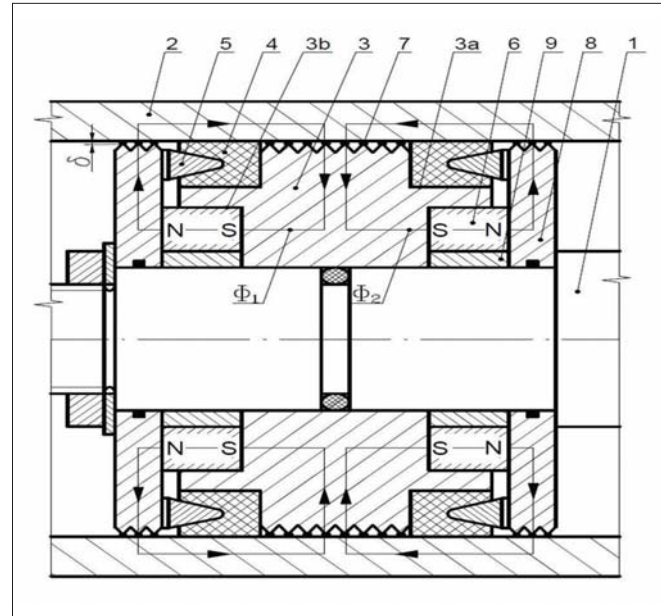


Fig. 12. Combined seal of the double-acting piston in hydraulic cylinder: 1 - piston rod, 2 - cylinder shell, 3 - piston, 3a,3b - recesses, 4 - "U"-shaped sealing ring, 5 - back-up ring, 6 - axially polarised permanent magnet, 7 - magnetic fluid, 8 - multi-edge pole piece, 9 - non-magnetically permeable sleeve, δ - sealing gap, Φ_1 , Φ_2 - closed magnetic circuits

Fig. 13 presents the variable-tooth and variable-gap type magnetic fluid reciprocating sealing structure for hydraulic cylinders [17]. A number of annular multi-edge pole pieces 6-12 are arranged at intervals in the axial direction in the space between the outer surface of a piston rod 2 and the inner wall of cylinder shell 1. The pole teeth are arranged on the inner circumferential face of each pole piece, while the axial magnetising type permanent magnet 13 is clamped between each pair of the adjacent pole pieces. The polarities of the magnetic poles of each pair of the adjacent axial magnetising type permanent magnets 13 are opposite. The sealing gaps δ created between the pole teeth and the outer surface of piston rod 2 are filled with magnetic fluid 14. The sizes of the sealing gaps δ between the pole teeth and the outer surface of piston rod 2 decrease sequentially in the direction from the high-pressure to the low-pressure side, and the sizes of the sealing gaps δ between all the pole teeth on the same pole piece and the outer surface of piston rod 2 are equal. Closed magnetic circuits Φ are created by pole pieces 6-12, annular permanent magnets 13, magnetic fluid 14 and piston rod 2. According to the principle of operation of the variable-tooth and variable-gap type magnetic fluid reciprocating sealing structure for the hydraulic cylinder, the condition that the pressure endurance capability is gradually enhanced, and the magnetic fluid leakage resistance is gradually increased is obtained through the structure change, and then the effect of further improving the sealing pressure resistance is achieved.

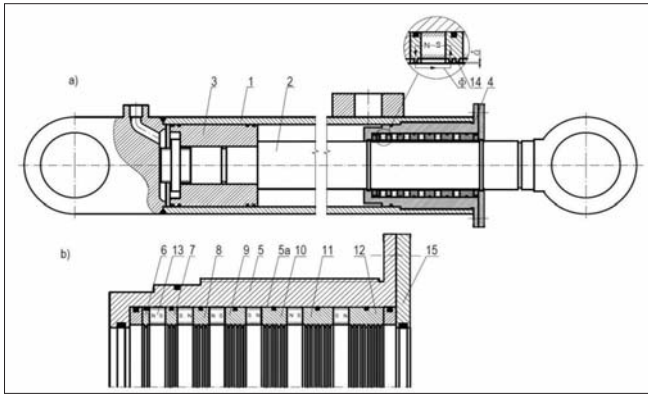


Fig. 13. Variable-tooth and variable-gap type magnetic fluid reciprocating sealing structure for hydraulic cylinder: a) hydraulic cylinder with magnetic fluid sealing structure, b) magnetic fluid sealing structure 1 - cylinder shell, 2 - piston rod, 3 - piston, 4 - head, 5 - flanged bushing, 5a - sealing chamber, 6-12 - multi-edge pole pieces, 13 - axially polarised annular permanent magnet, 14 - magnetic fluid, 15 - cover, δ - sealing gap, Φ - closed magnetic circuit

CONCLUDING REMARKS

The article provides an overview of new seal solutions pointing a ship's main and auxiliary equipment installed on ships. Although the article focuses on the reciprocating movement to point out its characteristic features, in practice this movement is often accompanied with rotating movement. Ship machinery, in general, includes various machines such as the main engine, propulsion engines, electrical generators, etc., various systems such as electrical, piping, refrigeration and air conditioning, firefighting and protection systems, as well as the deck machinery and cargo handling equipment, bow thrusters and stabilisers, instrumentation and control, safety equipment, and other auxiliary machinery and equipment [12, 13, 18]. The auxiliary machinery may operate to support the main propulsion engines, heat exchangers and air compressors, for instance, or to support ship maneuvering and cargo handling – propellers and shafting, steering gear and deck cranes, or to support ship services such as ballast water distribution and sewage systems.

Following shipbuilding area the designers specify the seal types from the point of view of the longest maintenance interval. Service costs in maritime industry are extremely high in comparison with regular factories. Nowadays, ship crews are reduced to a few persons that cannot provide servicing, and the ship operation must rely on the highest durability of machines. Reciprocating shafts can be found in drive and steering systems of critical ship machinery, such as pitch control, various engines including the main one, thrusters, rudder systems, stabilisers, etc. The limited article space here did not allow a detailed presentation of the selected solutions. Moreover, some of them are patent pending. However, the solutions presented in the article provide an opportunity for the readers to decide where and when to use a particular sealing kit.

Although that overview presents general purpose applications of fluid seals the author see their realisation in ship industry particularly sensible. The analysis of the sealing mechanism of magnetic fluid seals in reciprocating motion shows that the operation of these seals is affected by the carry-over phenomenon and magnetic fluid deformation in the

sealing gap, which depends on the speed v of the reciprocating motion. This deformation and the reduction of the amount of magnetic fluid in the sealing gap caused by the reciprocating motion of the piston is the main reason for failures of magnetic fluid seals.

In order to prolong the lifetime of seal operation, newly designed structures are used that prevent the deformation of the magnetic fluid film and reduce the loss of magnetic fluid in the sealing gap. These new structure designs of hybrid seals, being a combination of typical hydraulic seals with magnetic fluid seals for reciprocating motion, have practical application especially in hydraulic cylinders and piston compressors.

REFERENCES

1. Berkovsky B.M., Medvedev V.F., Krakov M.S.: Magnetic Fluids- Engineering Applications, Oxford University Press, Oxford,1993.
2. Magnetic Fluids in Machine Design, Ed. By Orlov D.V.,Podgorkov V.V.,Publisher "Mashinostrojenie", Moscow,1993.
3. Evsin S.I., Sokolov N.A., Stradomsky Y.I,Charkovsky V.B.: Development of magnetic fluid reciprocating motion seals, Journal of Magnetism and Magnetic Materials, vol.85, 1990.
4. Evsin S.I.,Stradomsky Y.I.,Charkovsky V.B.: Classical magnetic liquid seal under conditions of reciprocating motion of a rod, Magneto hydrodynamics, vol. 22,no 3, 1986.
5. Ochoński W.: Magnetic fluid seals for reciprocating motion, Proc. of the 15th Int. Colloquium Tribology, Stuttgart/Ostfildern, January 2006.
6. Patent USA, Int.CL.F16J15/40, no 5165701, Magnetic fluid seal apparatus.
7. Patent PL, Int.CL.F16J15/53, no 187576, Multi-stage magnetic fluid shaft seal (in polish).
8. Patent application P-435694, Hybrid seal for large-size elements with rotating or reciprocating motion (in polish).
9. Patent application P-438268, Hybrid seal for large-size elements with reciprocating motion and rotating motion (in polish).
10. Patent application P-437268, Hybrid seal for elements with reciprocating motion or rotating motion (in polish).
11. Patent PL,Int.CL.F16J15/53, no 234946, Hybrid seal for large-size elements with rotating or reciprocating motion (in polish).

12. Patent CN, Int.CL. F16J15/43, no 109505985, Reciprocating sealing device for hydraulic cylinder magnetic fluid.
13. Patent CN, In.CL. F16J15/43, no 108869751, Combined type magnetofluid reciprocating sealing structure.
14. Patent CN, Int.CL. F16J15/43, no 107893854, Magnetic fluid sealing structure for reciprocating motion.
15. Patent application USA, Int.CL. F16J15/43, no 2011/0215533, Reciprocating shafts sealing apparatus combined a ferrofluid seal with a C-slip-ring and a YX-seal-ring.
16. Patent SU, Int.CL. F16J15/40, no 1537940, Hydraulic cylinder piston packing.
17. Patent CN, Int.CL. F16J15/43, no 108775304, Variable-tooth and variable-gap type magnetic fluid reciprocating sealing structure for hydraulic cylinder.
18. The Maritime Engineering Reference Book – A Guide to Ship Design, Construction and Operation, 2008, Pages 344, 346-482, Chapter 6 – Marine engines and auxiliary machinery. doi: <https://doi.org/10.1016/B978-0-7506-8987-8.00006-8>.

CONTACT WITH THE AUTHORS

Leszek Matuszewski

e-mail: leszekma@pg.edu.pl

Piotr Bela

e-mail: piotr.bela@pg.edu.pl

Gdańsk University of Technology
Narutowicza 11/12
80-233 Gdańsk
POLAND

ASSESSING THE POTENTIAL REPLACEMENT OF MINERAL OIL WITH ENVIRONMENTALLY ACCEPTABLE LUBRICANTS IN A STERN TUBE BEARING: AN EXPERIMENTAL ANALYSIS OF BEARING PERFORMANCE

Jerzy Kowalski*¹

Wojciech Leśniewski¹

Daniel Piątek¹

Dominika Cuper - Przybylska²

¹ Gdańsk University of Technology, Poland

² Gdynia Maritime University, Poland

* Corresponding author: jerzy.kowalski@pg.edu.pl (J. Kowalski)

ABSTRACT

This study compares the performance of a plain bearing, with a similar structure to a tail shaft stern bearing, lubricated with either mineral oil or an environmentally acceptable lubricant (EAL). The main characteristic of the bearing is its length/diameter ratio of <1. Measurements are carried out with the bearing operating under loads from 0.5 to 1 MPa and seven speeds ranging from 1 to 11 rev/s. The bearing lubricated with either mineral oil with a viscosity grade of 100 or an environmentally acceptable lubricant (EAL) with a viscosity grade of 100 or 150 is investigated according to the ISO standard. Bearing wear is simulated by increasing the clearance circle by 0.1 mm. According to the results obtained, the use of an EAL in place of mineral oil does not cause significant changes in the bearing performance, regardless of the value of the clearance radius. The pressure distribution in the oil film, bearing load carrying capacity, eccentricity and friction coefficient have similar values for the entire load and speed ranges considered, and the discrepancies in the results are within the range of the measurement errors. Only an increase in EAL viscosity causes significant changes in bearing performance and these changes comply with the general theory of lubrication.

Keywords: environmentally acceptable lubricants (EALs), mineral oil, stern tube bearing, bearing wear, marine bearing

INTRODUCTION

A tail shaft scabbard bearing is an integral part of the propulsion system of a ship. The standard structure of this tribological node is a hydrodynamically lubricated transverse plain bearing. In this case, mineral oil in a circulating system acts as the lubricant. Such a system allows for control of the flow, temperature and cleanliness of the oil, which translates to durability, reliability and high energy efficiency of the bearing. In contrast, oil circulation is isolated from the marine environment by a sealing system, which, despite its complex structure, is not perfect. According to [1], ~2.6 litres per day of lubricating oil leak into marine environments from the tail shaft scabbard of an average ship. The accumulation at sea of

oil from shipboard tubes causes significant environmental degradation.

For this reason, lubricants are sought that meet the requirements set for oils intended for lubricating plain bearings and are simultaneously environmentally friendly. One of the first legal standardisations in this area was presented by the United States, which, as early as 2013, introduced a new class of lubricating oils, referred to as environmentally acceptable lubricants (EALs) [2]. Generally, EALs are defined as biodegradable, non-bioaccumulative and minimally harmful to aquatic environments. The simplest solution is to use water as a lubricant [3][6], which is undoubtedly an environmentally inert substance and a common lubricant in historical guava bearings. However, its low viscosity contributes to a relatively low bearing capacity.

In recent years, virtually all major lubricant manufacturers have introduced EALs into their range of lubricating oils. For the most part, these are oils produced on the basis of hydrocarbons of biological origin with various structures [7], although, according to the manufacturers' declarations, some substances are water based. Commercially available EALs have physical parameters similar to the parameters of mineral oil. Despite this, shipowners continue to use mineral oil for fear of, among other things, EALs becoming old and possibly losing the required bearing capacity of stern bearings and intensifying bearing pan wear as a consequence. This phenomenon is clearly visible in the engine lubrication oils [8]

The presented condition constitutes the primary motivation for the undertaken research, which seeks to compare the operation of a plain bearing, with a structure similar to that of a stern bearing of a ship, lubricated with either mineral oil or an EAL. Although the issue of EAL aging was presented in a multi-faceted manner in [9], an analysis of the literature on the subject confirms that there are relatively few studies that address this issue. The performance parameters for mineral oil and EALs with relatively high viscosity under elastohydrodynamic lubrication conditions have been investigated [10], while in [11], the rheological properties of EALs were addressed. A comparison of mineral oil and EAL performance was presented in [12]; however, this was for a relatively narrow bearing with a structure not used in tail shaft scabbards and a limited range of load conditions. A broader range of studies on water-lubricated stern bearings can be found, as this structure solution is increasingly used in the shipbuilding industry. For example, problems of structure and the performance of water-lubricated bearings have been presented [13] and [14], while [15] and [16] considered the influence of stern tube bearing deformations on the lubrication parameters. For this reason, this study compares a wide range of performance criteria of a stern bearing under varying load conditions and degrees of wear and lubricated with mineral oil and two types of EALs.

LABORATORY TESTS

Measurements were made on the test stand demonstrated in Fig. 1 and the pan structure in Fig. 2. A shaft with a diameter of 100 mm was supported by two roller bearings and driven by an electric motor. The structure of the stand allowed the shaft speed to be adjusted and measured. A 200 mm wide alloy bearing pan casing was mounted on the shaft, complete with a seal and lubricating oil inlet and outlet ports. The casing could accommodate 16 sensors for measuring the high-speed hydrodynamic pressure and four shaft position sensors relative to the pan. The pan casing was supported from below by an independently powered hydraulic cushion, which allowed the plain bearing to be loaded. By using a cushion, it was also possible to measure friction in the bearing. Table 1 shows the parameters of the tested lubricants. Measurements were made using a DV-1 rotational viscometer and a DMA35N petrol densitometer.



Fig.1. Laboratory stand

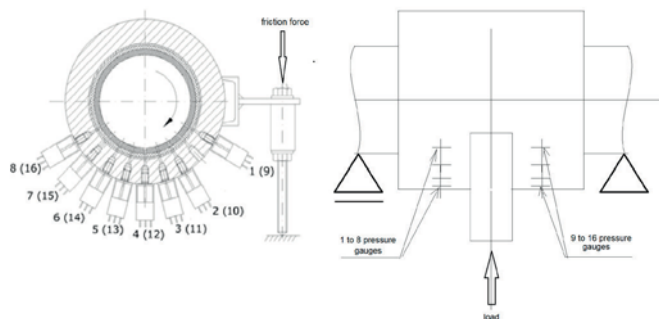


Fig.2. Laboratory stand scheme

Tab. 1. Parameters of mineral oil and EALs

Lubricant	Viscosity@25 °C [mPa s]	Viscosity@40 °C [mPa s]	Density@40 °C [kg/m ³]	Viscosity index*
Mineral oil	222.38	93.52	873.8	97.4
EAL 1	176.70	94.29	910.3	98.5
EAL 2	290.53	145.25	914.7	98.6

*Viscosity@100 °C is extrapolated

The bearing parameters were measured in six stages each with three observations whilst maintaining the oil temperature in the bearing constant at 40±0.5 °C. A white bearing alloy pan with a length/diameter ratio of two was used. This value is close to the aft bearing structure of the tail shaft. Each stage measured the operating parameters of the plain bearing lubricated with the tested oil for three average pressures of 0.50, 0.75 and 1.00 MPa and seven rotational speeds of 11, 9, 7, 5, 3, 2 and 1 rev/s. The hydrodynamic pressure in the bearing lubrication wedge was measured at 16 measurement points, as shown in Fig. 2. The position of the shaft relative to the pan at both ends of the pan, the oil temperature before, after and inside the pan, the shaft speed, the bearing friction torque and the force loading of the bearing were also determined. The parameters of the measuring sensors are presented in Table 2. The load and speed ranges are given in Table 3.

Tab. 2. Parameters of measurement gauges

Gauge	Method	Accuracy	Range
Pressure	Piezoelectric	0.3%	0–6 MPa
Rotational speed	Tachometric	±2.5 rpm	0–6000 rpm
Temperature	K-type	±0.5 °C	0–100 °C
Shaft centre position	Proximity probe	±1%	0–10 mm
Friction force	Tensometric	±0.25%	0–100 N

Tab. 3. Measurement stages

Stage*	Lubricant	Diameter clearance [mm]
1	Mineral oil	0.34
2	EAL 1	0.34
3	EAL 2	0.34
4	Mineral oil	0.44
5	EAL 1	0.44
6	EAL 2	0.44

*Each stage consists of three average pressures of 0.50, 0.75 and 1.00 MPa and seven rotational speeds of 11, 9, 7, 5, 3, 2 and 1 rev/s. Three observations for each stage are considered.

In order to test the influence of bearing wear on the bearing performance, measurements were also carried out for a reduced shaft diameter (larger clearance circle) of 0.1 mm.

RESULTS AND DISCUSSION

This study compares the performance of a stern bearing of a ship lubricated using mineral oil and EALs. A mineral oil with a viscosity grade of 100, according to the ISO standard (kinematic viscosity in mm²/s at 40 °C), was adopted as the base oil. In order to select a representative EAL, some viscosity and density tests were conducted for commercially available EALs. Figure 3 presents the measurement results. According to the presented results, it can be seen that EALs of the same viscosity grade have a higher density compared to mineral oil. In Table 1, it can also be observed that the EALs relative to mineral oil show a reduced viscosity change together with the temperature change. This phenomenon is confirmed by the viscosity index values.

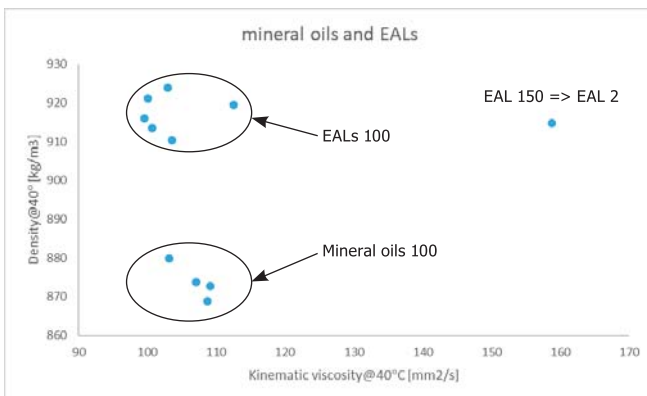


Fig.3. Parameters of mineral oils and EALs

The essential parameter of the stern bearing from the perspective of the energy balance of the ship is its friction loss. Obviously, the friction coefficient in a bearing lowers the viscosity of the lubricating oil. Unfortunately, the reduction in oil viscosity also contributes to a substantial reduction in the load-bearing capacity. Figure 4 presents the influence of bearing speed on the friction coefficient. An increase in the bearing speed increases the friction coefficient for both the mineral oil and EALs, as expected. The Hersey–Stribeck relation illustrates the characteristics of these changes. It is noteworthy that replacing the mineral oil with an EAL does not cause significant changes in the friction factor, assuming that the viscosity of both oils is similar. A slight increase in the friction coefficient is observed for EAL 1 compared to the mineral oil at a load of 0.75 MPa, but this change does not exceed the measurement error. Only the use of the EAL with a higher viscosity grade results in a significant increase in the friction coefficient. It is also interesting that an increase in bearing load causes a significant decrease in the friction coefficient.

When the measurements were conducted, the oil film pressure was also recorded using 16 pressure sensors, arranged as presented in Fig. 1. The pressure distribution in the oil film in the two bearing cross sections was obtained on this basis. As expected, the highest pressure was observed at the location of the sensors numbered 5 and 13. These are sensors with a banding angle of 105° counting in the direction of rotation of the bearing. Example measurement results for a load equal to 1 MPa and a speed of 11 rev/s are shown in Fig. 5(a). The horizontal axis shows the angle position of the sensors. The maximum pressures for all considered bearing speeds and loads are presented in Figs. 5(b)-(d).

According to the results presented, an increase in rotational speed causes a decrease in the maximum pressure in the oil film. The classic theory of hydrodynamic lubrication presents an increase in the relative velocity of the lubricated surfaces with a decrease in the Sommerfeld number, which translates to a reduction of the eccentricity of the bearing (*e*). In contrast, the bearing eccentricity is in the basic equation of pressure in the third exponent in the denominator. Despite the increase in sliding speed (and rotational speed), the pressure in the bearing decreases. The results presented in Fig. 5 also show that the maximum oil film pressure increases with increasing load. Using EALs instead of mineral oil with the same viscosity does not cause quantitative or qualitative changes in the maximum pressure. Only the use of EALs of higher viscosity causes a noticeable reduction in the maximum oil film pressure, but only at relatively low bearing speeds. This result is consistent with the classic theory of lubrication. An increase in oil viscosity results in a decrease in the Sommerfeld number and bearing eccentricity.

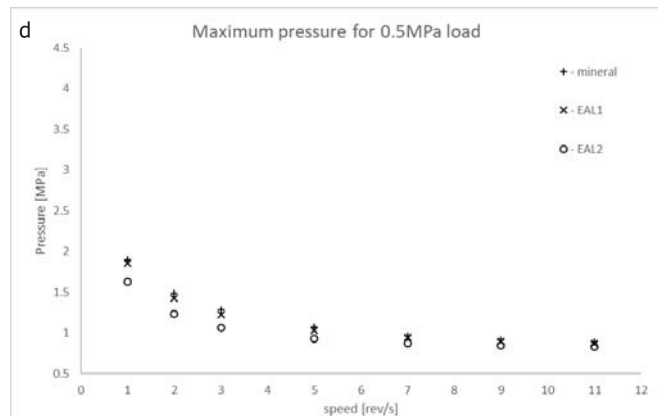
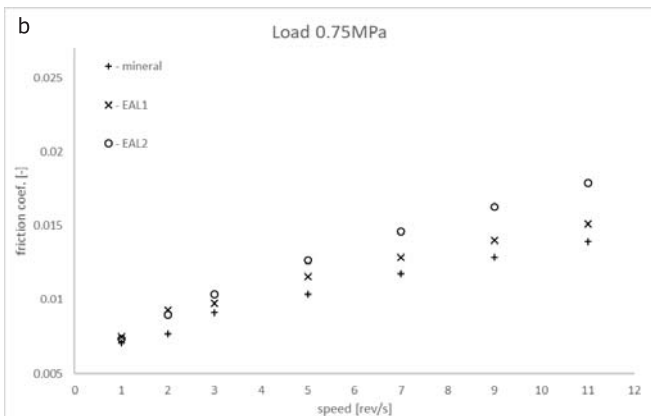
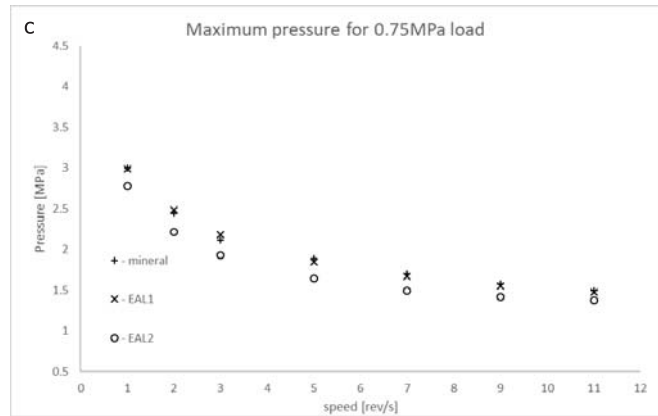
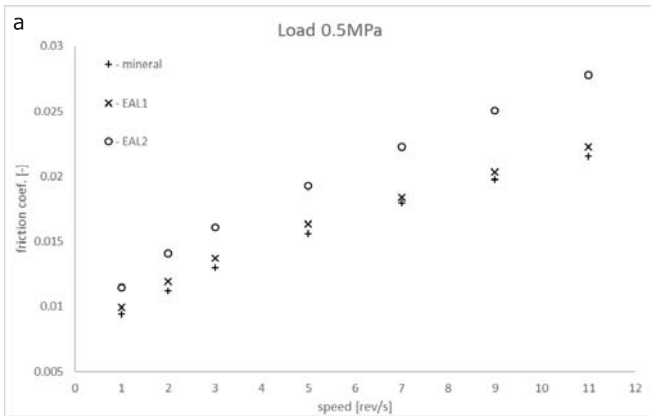
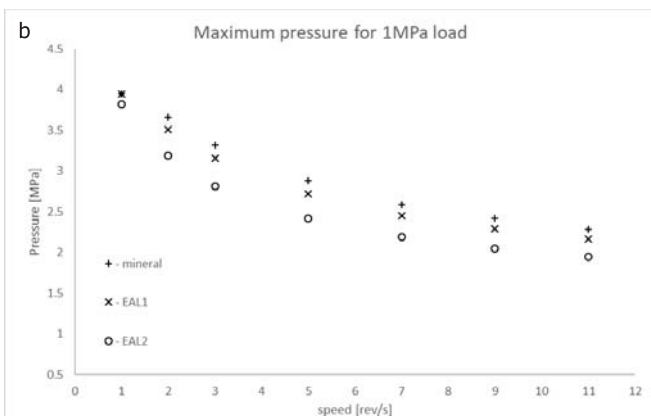
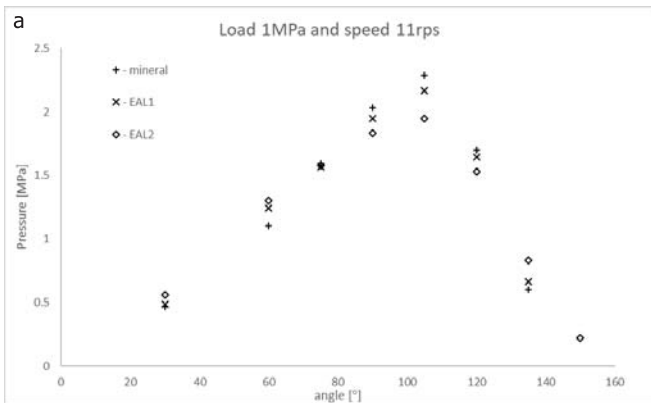


Fig.4 – Friction coefficients for mineral oil and EALs

Fig.5. Pressures in the oil film; a – example of pressure values for 1MPa and 1 rev/s, b-d – maximum pressure for different bearing loads and speeds



The instantaneous position of the shaft in the bearing was also recorded during the measurements. According to the obtained results, the position of the shaft oscillates during bearing operation with a frequency proportional to its rotational speed. This phenomenon is neglected in the classic theory of lubrication. The instantaneous variable position of the shaft is reduced to eccentricity, with a constant value representing the average value of the position of the shaft axis relative to the pan axis. Figure 6 presents the eccentricity for the considered bearing speeds and loads. The results show that a rotational speed of 5 rev/s causes a decrease in eccentricity and thus an increase in oil film thickness. A further increase in the rotational speed does not change the eccentricity value of the bearing. An increase in eccentricity with increasing load was also observed. The analysis also showed that, according to Fig. 6, the use of an EAL with a viscosity close to that of mineral oil does not affect the shaft positions in the bearing and an increase in viscosity reduces the eccentricity and increases the oil film thickness.

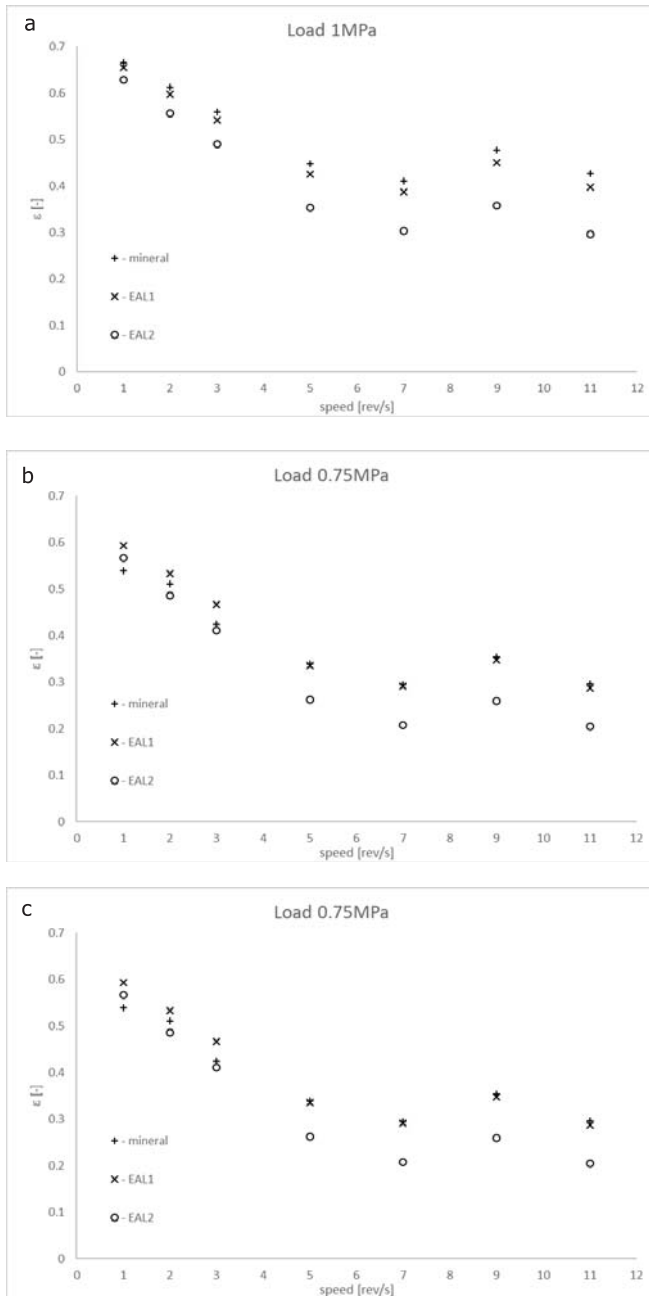


Fig. 6. Eccentricity for different bearing loads and speeds

In order to verify the performance of the bearing lubricated with an EAL after its wear, the performance of the bearing with increased clearance radius was measured. As previously mentioned, wear was simulated by reducing the shaft diameter by 0.1 mm. Figure 7 presents the wear effect on the friction coefficient. An increase of 0.1 mm in diameter clearance does not cause significant changes in friction. However, changes in the friction coefficient not exceeding 0.002 can be observed for low loads and speeds. Despite slight changes in the friction coefficient, an increase in clearance radius changes the pressure distribution in the oil film. Figure 8(a) shows an example of the pressure measurement results for EAL 1 with a load of 1 MPa and a speed of 11 rev/s. An increase

in clearance radius increases the maximum hydrodynamic pressure and decreases the pressure in the extreme areas of the oil film. This means that although the load remains constant, the maximum unit pressures increase with increasing bearing wear. The use of EAL instead of mineral oil does not cause any changes to the pressure distribution in the bearing even after it has worn out. It can be observed in Figs. 8(b)-(d) that the increase in maximum pressure is more pronounced at high loads and low speeds. The observed maximum pressure difference when increasing the diameter clearance by 0.1 mm reaches 0.7 MPa regardless of the oil used.

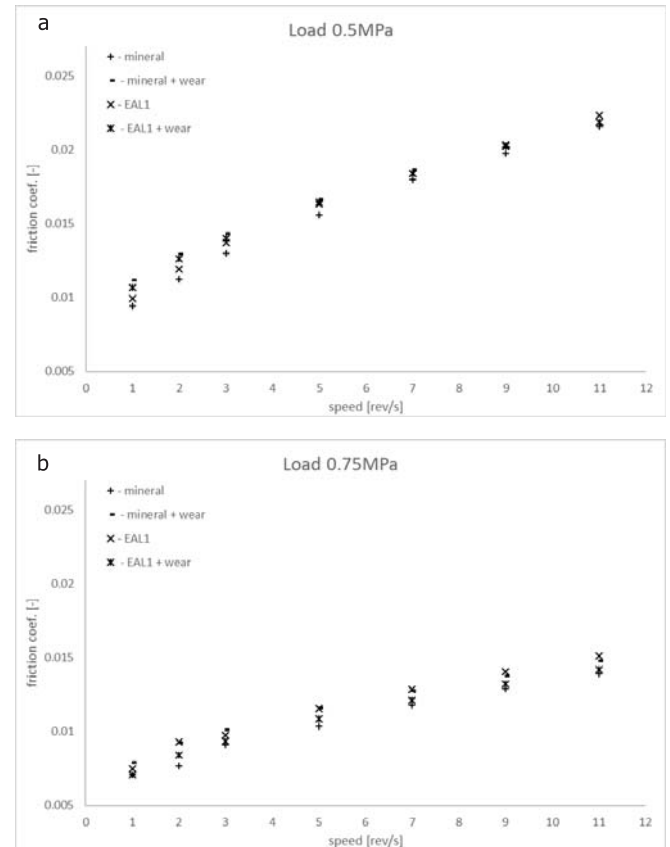
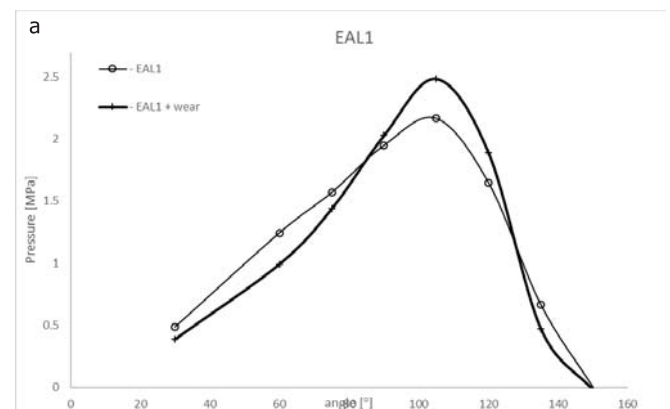


Fig. 7. Friction coefficient for different diameter clearances of bearing



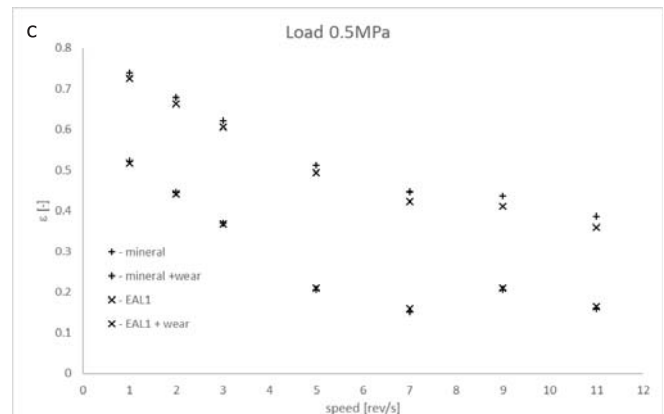
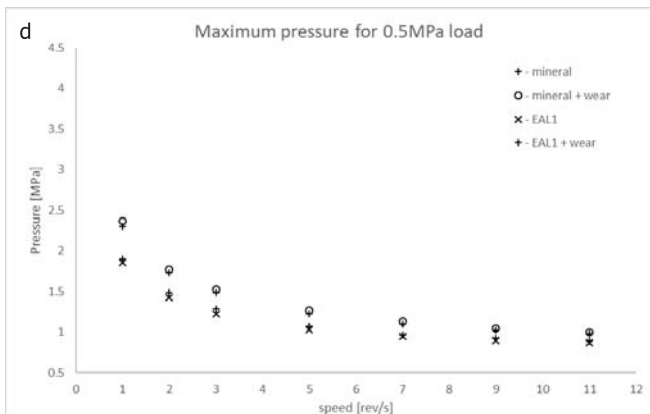
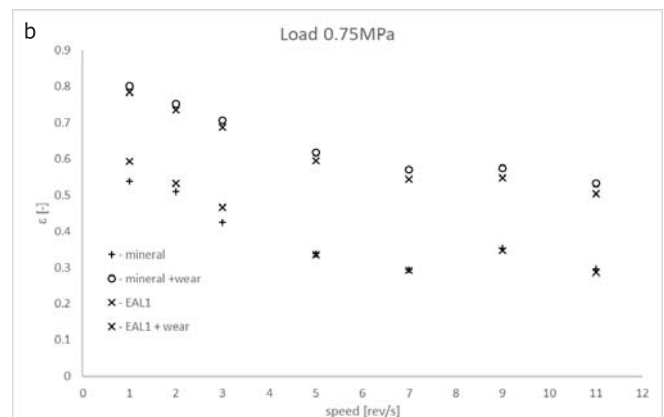
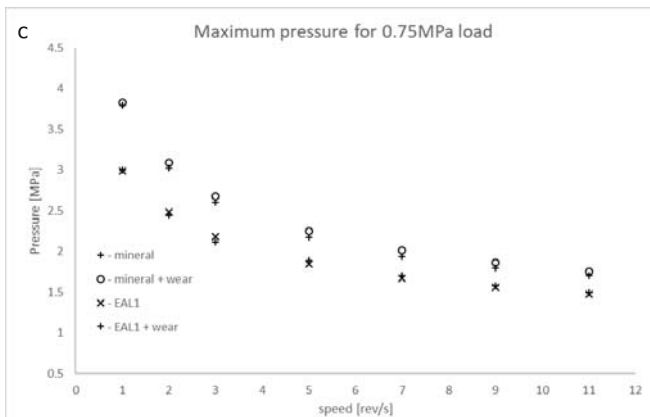
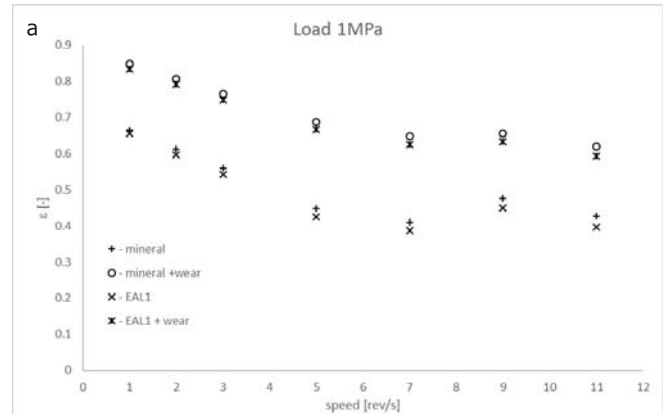
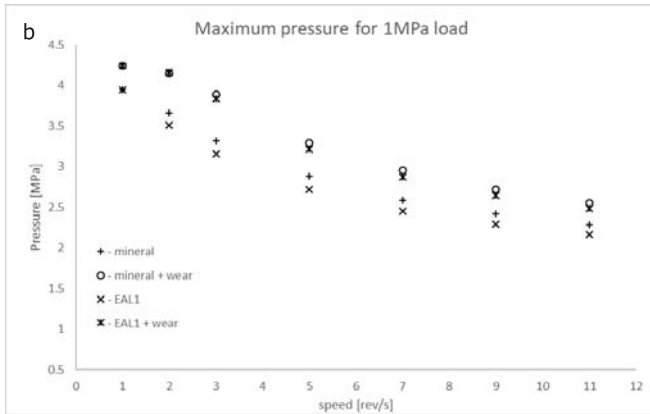


Fig. 8. Pressures in the oil film for different diameter clearances of bearing; a – example of pressure values for EAL1, b-d - maximum pressure for different bearing loads and speeds

Fig. 9. Eccentricity for different diameter clearances of bearing

Figure 9 presents the influence of bearing wear on its eccentricity. According to the results presented, the eccentricity value increases with increasing wear, with the differences increasing with decreasing load and not depending on speed. Changing mineral oil to EAL of the same viscosity grade does not affect the eccentricity of the bearing even after it has worn out.

CONCLUSIONS

This study compared the performance of a plain bearing with a length/diameter ratio of two lubricated with mineral oil or an EAL. The oil film pressure distribution, friction coefficient and instantaneous shaft axis position were measured. According to the results presented, the following general conclusions can be drawn:

- Changing mineral oil to an EAL of the same viscosity grade in the stern tube bearing does not affect its performance. Both the friction force and pressure distribution in the oil film and the average position of the shaft axis in relation

to the pan axis do not differ by values greater than the measurement error of the measuring system. This means that the oil composition does not have a significant influence on the bearing operation, so an EAL of the same viscosity can replace mineral oil without the need to make any structural changes to the bearing. The influence of the EAL on the wear and aging of seals and the aging phenomenon of the EAL itself was not addressed in this article.

- The bearing operating parameters do not change during operation with increased clearance radius resulting, e.g., from wear.
- The conclusions presented are valid for the replacement of mineral oil by an EAL with not only a similar viscosity but also a similar viscosity index. This condition does not have to be fulfilled when the bearing operates in a small temperature range.

REFERENCES

1. J. Lundberg, 'Undocumented oil leakages: A study about stern tube seals and leakages', Dissertation, 2021.
2. Kelly, C. A., et al. 'Underwater emissions from a two-stroke outboard engine: a comparison between an EAL and an equivalent mineral lubricant', *Materials & Design* 26.7, 609–617, 2005.
3. W. Litwin and A. Olszewski, 'Assessment of possible application of waterlubricated sintered brass slide bearing for marine propeller shaft', *Polish Marit. Res.*, 19,1, 54–61, 2012.
4. M. Wodtke and W. Litwin, 'Water-lubricated stern tube bearing - experimental and theoretical investigations of thermal effects', *Tribology International*, 153, 106608, 2021.
5. W. Litwin and C Dymarski, 'Experimental research on water-lubricated marine stern tube bearings in conditions of improper lubrication and cooling causing rapid bush wear', *Tribology International*, 95, 449–455, 2016.
6. Z. Guo, Ch. Yuan, A. Liu and S. Jiang, 'Study on tribological properties of novel biomimetic material for water-lubricated stern tube bearing', *Wear*, 376–377, 911–919, 2017.
7. J. C. J. Bart, E. Gucciardi and S. Cavallaro, 'Renewable feedstocks for lubricant production', *Biolubricants*, 121–248, 2013.
8. A. Młynarczak, K. Rudzki, 'Optimisation of the topping-up process of lubricating oil in medium-speed marine engines', *Polish Marit. Res.*, 28, 2, 78–84, 2021.
9. F. J. Owuna, 'Stability of vegetable based oils used in the formulation of ecofriendly lubricants – a review', *Egypt. J. Pet.*, 29, 251–256, 2020.
10. R. Bayat and A. Lehtovaara, 'EHL/mixed transition of fully formulated environmentally acceptable gear oils', *Tribol. Int.*, 146, 106158, 2020.
11. Borrás, F. Xavier, Matthijn B. De Rooij and Dik J. Schipper, 'Rheological and wetting properties of environmentally acceptable lubricants (EALs) for application in stern tube seals', *Lubricants* 6.4, 100, 2018.
12. Yano, Akihiko, et al. 'Study on the load carrying capacity of sliding bearing lubricated by synthetic ester oils', *Tribology Online* 10.5, 377–389, 2015.
13. W. Litwin, 'Water-lubricated bearings of ship propeller shafts - Problems, experimental tests and theoretical investigations', *Polish Marit. Res.*, 16, 4, 41–49, 2009.
14. W. Litwin, 'Influence of main design parameters of ship propeller shaft water-lubricated bearings on their properties', *Polish Marit. Res.*, 17, 4, 39–45, 2010.
15. G. N. Rossopoulos, Ch. I. Papadopoulos and Ch. Leontopoulos, 'Tribological comparison of an optimum single and double slope design of the stern tube bearing, case study for a marine vessel', *Tribology International*, 150, 106343, 2020.
16. T. He, D. Zou, X. Lu, Y. Guo, Z. Wang and W. Li, 'Mixed-lubrication analysis of marine stern tube bearing considering bending deformation of stern shaft and cavitation', *Tribology International*, 73, 108–116, 2014.

CONTACT WITH THE AUTHORS

Jerzy Kowalski

e-mail: jerzy.kowalski@pg.edu.pl

Gdańsk University of Technology,
Narutowicza 11/12, 80-233 Gdańsk,
POLAND

INFLUENCE OF SOLID PARTICLE CONTAMINATION ON THE WEAR PROCESS IN WATER LUBRICATED MARINE STRUT BEARINGS WITH NBR AND PTFE BUSHES

Ewa Piątkowska*

Gdańsk University of Technology, Poland

* Corresponding author: ewapiatk@pg.edu.pl (E. Piątkowska)

ABSTRACT

This paper reports on a study of the influence of solid particle contamination on the wear process in water-lubricated slide bearings (steel-acrylonitrile-butadiene rubber (NBR) and steel-polytetrafluoroethylene (PTFE)). To compare the wear of the shaft journal and bushes (NBR and PTFE) when lubricated with fresh water and contaminated water, an experiment was carried out to identify key factors that influence the state of wear of slide bearing. The amount of wear was checked by means of geometric structure measurements on the journals, namely, roughness profile measurements using both a contact profilometer and an optical microscope. The obtained results enabled correlations between the material comprising the sliding sleeve, roughness of the journals and contamination inside the water-lubricated slide bearings.

Keywords: water lubrication, solid particles contaminations, wear, strut bearings, plain bearings (NBR and PTFE)

INTRODUCTION

To ensure acceptable and fault-free operation of a vessel and its propulsion system, it is necessary to constantly monitor the diagnostics of all the components. Water-lubricated slide bearings are elements highly prone to failure, especially when it comes to seawater-lubricated slide bearings in the shaft line of propellers in vessels. Their premature wear is one of the root causes of repairs to ships, which then leads to downtime and an increase in operational costs. Given these circumstances, the selection of the correct type of slide

bearing and an investigation of the impact of lubricants (e.g., contaminated water) on the wear process is crucial.

Special consideration should be given to the working conditions of the propeller shaft strut bearings (Fig.1). It is common to utilize bearings lubricated with seawater that surrounds the hull of vessels, where there is not control of the water flow and the water is not filtered. Therefore, when a vessel is operated in shallow or inland waters, various types of contaminants tend to enter the friction zone, resulting in accelerated wear processes.



Fig.1. Propeller shaft strut bearings [1]

Recent research in the literature deals mostly with the impact of contamination on oil-lubricated slide bearings. Due to the addition of various metallic particles, metal oxides, sulfides, carbon and other chemical compounds, such lubricating oils have a positive influence on the tribological properties of the bearings; the mentioned additions also increase the eco-friendliness of the oils [2]. Research was conducted on surfactant bearing lubricants based on non-organic hybrid nanoparticles with an organic outer shell that could be added to lubricating oils. However, such agents are not stable enough to achieve a sufficient effect on the surfaces of bearings; an acceptable lubrication is a combination of many contributing factors [3]. Problems related to premature wear of the aft stern bearings are reflected in many publications and are related to their lubrication [4], [5] as well as factors influencing the efficiency of this lubrication, such as vibrations [6], [7] or the dynamics of the shaft movement [8], [9].

Throughout the last 100 years, extensive research has been carried out that proved the existence of a relationship between the size and concentration of solid particles in lubricating oils, thickness of an oil film, and wear and temperature of bearings [10]–[12]. Among many factors influencing wear of bearings, special consideration has been given to the relation between the shaft journal hardness and bush hardness [13], influence of the initial shaft roughness and texture of the bearings [14] hydrodynamic journal bearings may suffer serious performance issues due to contamination from moisture, dust, foreign particles and wear debris. This experimental study investigates the effect of surface texturing on the steady-state performance characteristics of highly-loaded journal bearings lubricated with a contaminated lubricant. Special attention is given to the bearings' load capacity and friction and wear at various contamination levels in the lubricant. Rig tests have been performed at selected speeds and loads on plain smooth and surface-textured journal bearings. Variable-size test dust was introduced into the lubrication system (at different rates).

A different kind of research focused on diameter wear, weight loss of the pin, morphology of the worn elements, surface roughness changes, the oil film thickness and friction coefficient for different slip velocities. The parameters were

measured with tribotesters: e.g., ball on disc [15], block on ring [16], cylinder on disc [17]–[19] and pin on disc [20], [21].

The subject of water-lubricated bearings is not very popular in the literature; however, it is still under research. It is unlikely that lubrication-aiding additions could be found in seawater. Instead, typical waters where vessels are operated are quite contaminated, often by contaminants of natural origin, such as sand particles. This is why the propulsion system of vessels, especially propeller shaft bearings, is prone to seizing, damage and extensive wear and tear, which makes replacement of worn parts necessary.

Research of Baltic Sea pollution dealt with the influence of various factors on the concentration and spatial distribution of sediment delivered by rivers [22], concentration and size of solid particles in the aforementioned sediments [23], water salinity, and the temperature and turbidity throughout the seasons [24]. Also, mineral and geochemical diversity of surface sediments [25] and routes for sediment material transport from the rivers of the Baltic Sea and North Sea basin to the deposit basin of the Baltic Sea have been considered [26].

Contamination in the stern bearing of the shaft line of a ship significantly deteriorates the tribological and lubricating properties of friction pairs and may cause serious failures related to the propulsion system of the ship. Based on tests carried out with a tribotester and contaminated water, dependencies were found that could be used to select the optimal operating parameters to minimize the intensive wear of the shaft line slide bearings in a ship. The research activities undertaken by the author [27] took into account a number of different operating parameters, such as loads, sliding velocities and size and concentration of solid particles. They showed that with increasing load and sliding speed, the coefficient of friction and weight loss decrease, while their intensification occurred with an increasing degree of contamination in the water. Other researchers also determined that the above factors increase wear of bearings lubricated with contaminated liquids and pointed to slightly different dependencies: they observed an increase in wear and an increase in surface roughness with increasing sliding velocity, applied load and particle concentration [28] and an increase in the coefficient of friction and the amount of wear with an increase in the applied load and grain size [29].

In order to improve the tribological properties of water-lubricated marine stern bearings, various bearing materials and their textures are increasingly being investigated [30]–[34].

Even though the tests of water-lubricated plain bearings containing solid particles were carried out with the use of tribotesters, their results may constitute important indications for the method of conducting tests on a real object.

TEST METHODS AND WORKING CONDITIONS

To minimize the risk of failure caused by unfavorable operating conditions in the form of lubricating a sliding node

with a liquid containing solid particles, tests were carried out to identify the key parameters affecting the speed of the wear process of cooperating sliding elements. For this purpose, the existing stand for testing water-lubricated plain bearings was adapted and rebuilt in such a way that it was possible to reliably carry out bearing wear tests in water contaminated with solid particles. Figure 2 shows a diagram of the cross-section of the test stand.

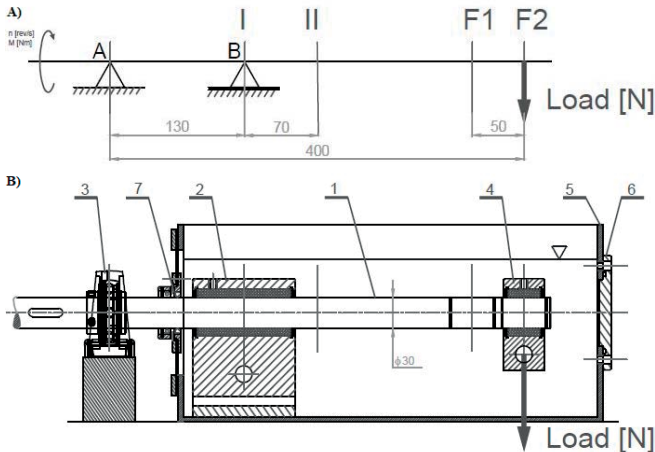


Fig. 2. Test stand description A) diagram of the stand and B) cross-section of the stand: 1 - shaft, 2 - tested bearing in a self-adjusting support, 3 - rolling bearing, 4 - slide bearing through which the load is exerted, 5 - tank filled with water, 6 - cover, and 7 - sealing

A three-phase electric motor was connected to a 30 mm diameter shaft by a torsionally flexible coupling. The shaft (1) was supported on two bearings: a self-aligning roller bearing (3) and a slide bearing located in the self-adjusting support (2), which allows the shaft to freely position in the slide bearing bush during bending. The shaft was partially located in the tank (5) filled with fresh water, which was the medium that lubricated the tested bearing. At its end, the slide bearing was mounted in the housing (4) through which the load was exerted. At the end of the shaft at the bearing mounting point F, a frame was attached and loaded with a concentrated force that simulated a load with a ship propeller. In front of the tank, a rolling bearing was installed, whose task was to ensure

that the seal (7) and a sealed cover (6) are coaxial at the end of the tank. An assembly hole was made that also protected against undesirable leakage of water from the tank. Such an experimental test stand allowed for a controlled application of a bending load on the journal of the tested water-lubricated plain bearing.

The test was carried out on a shaft made of a typical high-alloy steel, namely, an acid-resistant chrome-nickel 1H18N9 used for ship shafts that operated with two types of bushings. The first material used for the research was a fluorinated polymer, namely, polytetrafluoroethylene (PTFE), also known as Teflon, while the second was acrylonitrile-butadiene rubber (NBR), commonly known as rubber. The lubricant was fresh water with a temperature of approximately 30°C. There was a focus on ensuring the same operating parameters: surface pressures in both pairs of bearings B and F, load with a concentrated force of 550 N at the bearing mounting point F, operating time, sliding velocity and the number of start-ups of the stand.

To ensure the same surface pressures while obtaining different values of stresses and bending moments, the length of the tested bearing bush in support B and the position of the supports both B (position I or II) and F (position F1 or F2) were manipulated. The above-mentioned parameters along with the lengths and positions of the bushings during individual measurements are shown in Table 1.

Measurements from A to D were made on solid shafts, two consecutive E and F measurements were made on hollow shafts; since the same position and length of the bushes was used as in the case of the solid shafts, different values of the bending stresses were obtained while maintaining the same surface pressure.

In both series, 6 measurements were carried out for each material under the same conditions, and the positions and lengths of the sliding sleeves were variable. The dose of contaminants supplied to the tank differed with respect to the concentration of solid particles in the water, as presented in Table 1. They ranged from 5 cm³ to 25 cm³, which accounted for from 0.042% to 0.208% of solid particles in water. The concentration of solid particles in the water was changed to determine whether and to what extent the dose

Tab. 1. Measurement table

indication	data			bending		surface pressures		contaminants		
	bush length B	bush length F	position of support B and force F	Bending moment	stresses from the bending moment	in bearing B	in bearing F	particulate dose	average concentration of solid particles	participation in a given volume of water
-	mm	mm	-	Nm	MPa	MPa	MPa	cm ³	ml/l	%
A - G	50	28	II, F1	82.4	32.55	0.641	0.654	15	1.25	0.125
B - H	57	28	II, F2	109.87	43.41	0.643	0.654	20	1.67	0.167
C - I	77	28	I, F1	120.86	47.75	0.640	0.654	5	0.42	0.042
D - J	87	28	I, F2	148.33	58.60	0.648	0.654	5	0.42	0.042
E - K	57	28	II, F2	109.87	73.52	0.643	0.654	10	0.83	0.083
F - L	77	28	I, F1	120.86	80.87	0.640	0.654	25	2.08	0.208

of contaminants in the water that lubricated the sliding node impacted the wear of the friction elements.

Figure 3 shows a photograph of solid particles in the form of sand - a natural material carried by one of the rivers of the Polish Pomerania that originates from the Radunia River. Figure 1 shows the percentage of particles of a certain size added to the lubricant in which the steel-PTFE and steel-NBR tested sliding connections were located. The concentration of solid particles presented in Diagram 1 constituted less than 97% of the contaminants identified in the sand sample. The remaining solid particles from 50-200 μm were very rare and accounted for slightly more than 3%. Particles with a diameter of up to 2 μm (approx. 42%) had the largest share in the sand sample used for the tests. About 23% are particles had a size between 2 and 4 μm . The number of sand particles decreased as their diameter increased.

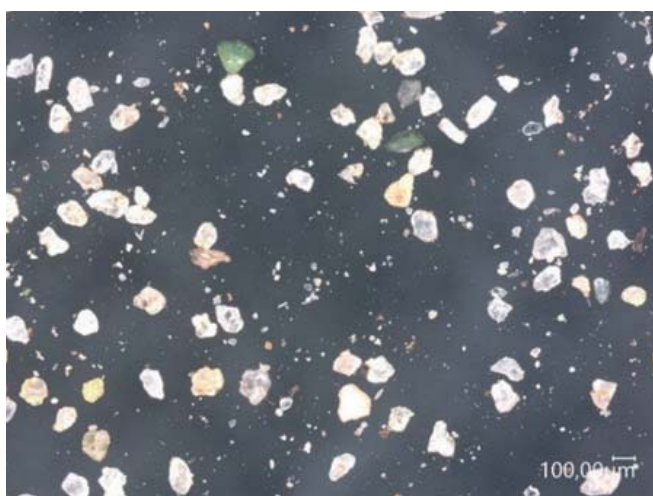


Fig. 3. Sand particles used in the research observed with a Keyence VHX-7000 optical microscope

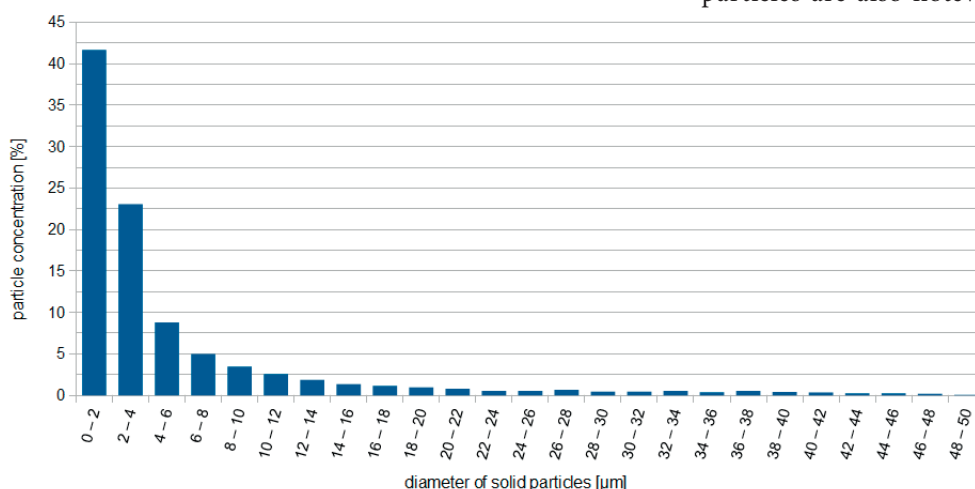


Diagram 1. Concentration of particles from the Radunia River considering their size

Each measurement of the sliding node followed the same procedure. For the first 10 hours, with two engine starts, the bearings were run-in and operated in contamination-free

water. Then, the dose of contaminants indicated in Table 1 was added, and the sliding couple worked for 16 hours when the research stand was started twice. After this time, the water was replaced and supplemented with the same amount of contaminants. This cycle was repeated three times. The total operating time of the bearings during one measurement was 58 hours, after which the bearings were dismantled, and the shaft journals were prepared for further activities related to the study of their geometric structure to identify the impact of contaminants on the wear of the water-lubricated sliding bearings.

RESULTS AND DISCUSSION

The tests were carried out for sliding bushings made of NBR and PTFE operating both in fresh water and in contaminated water containing solid particles. After the experiment, the shaft journals with the bushings were subjected to visual wear assessment. Pictures of the surfaces of the journals are summarized in Table 2. In all cases, grooves are observed along the entire circumference of the journal; however, the condition of the journal surfaces lubricated with an agent containing solid particles indicates their more intensive exploitation.

On the surface of the journals cooperating with the rubber bushings one can also observe the predominant one-sided wear of the journal, namely, from the side where the load was applied due to the deflection of the shaft in the support. On the other hand, in the case of journals cooperating with PTFE bushings, the wear seems to be uniform along the entire length of the journal, indicating a more intense wear pattern on both edges.

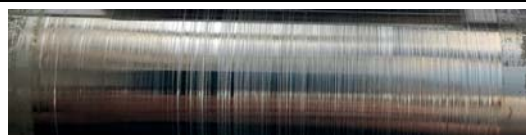
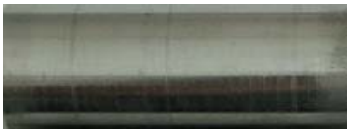
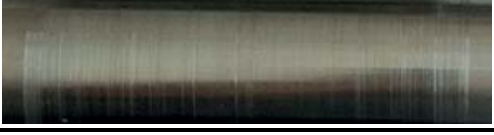
The shaft journals operating in water devoid of solid particles are also noteworthy. While in the case of the

harder material, PTFE, the wear differs slightly, and in the case of the more compliant material, NBR, the bushing material partially melted, transferred to the journal and filled the circumferential grooves due to an increase in the temperature of the lubricating fluid.

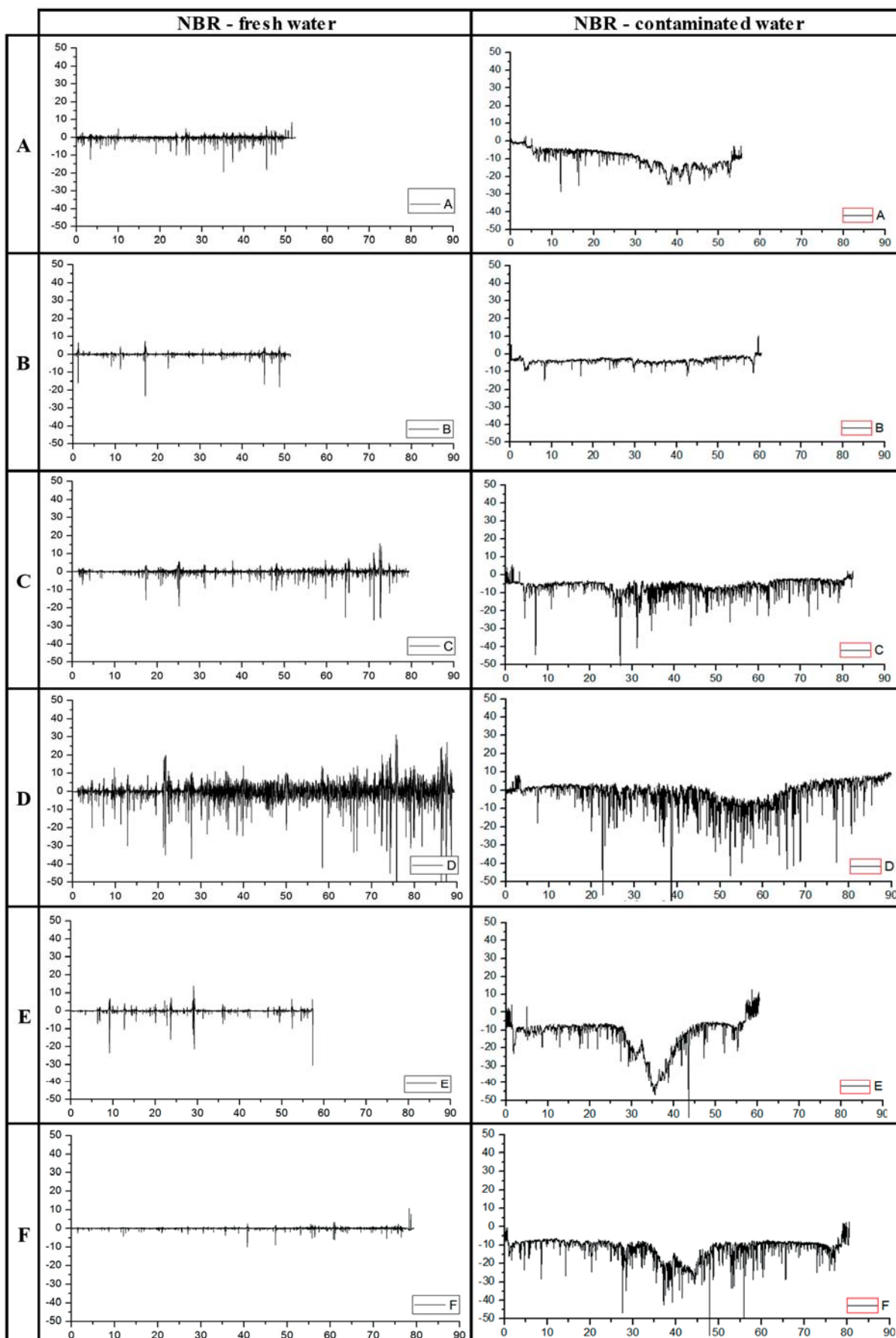
Thorough examinations of the journals were performed on a Jenoptik Hommel Etamic T8000 contact profilometer and a Keyence VHX-7000 optical microscope. The

measured roughness profiles (dependence of the roughness R_a [μm] on the length L [mm] of the specimen) of the journals on the contact surface with the sliding sleeves showed a change in their roughness and material loss on the surfaces of the journals.

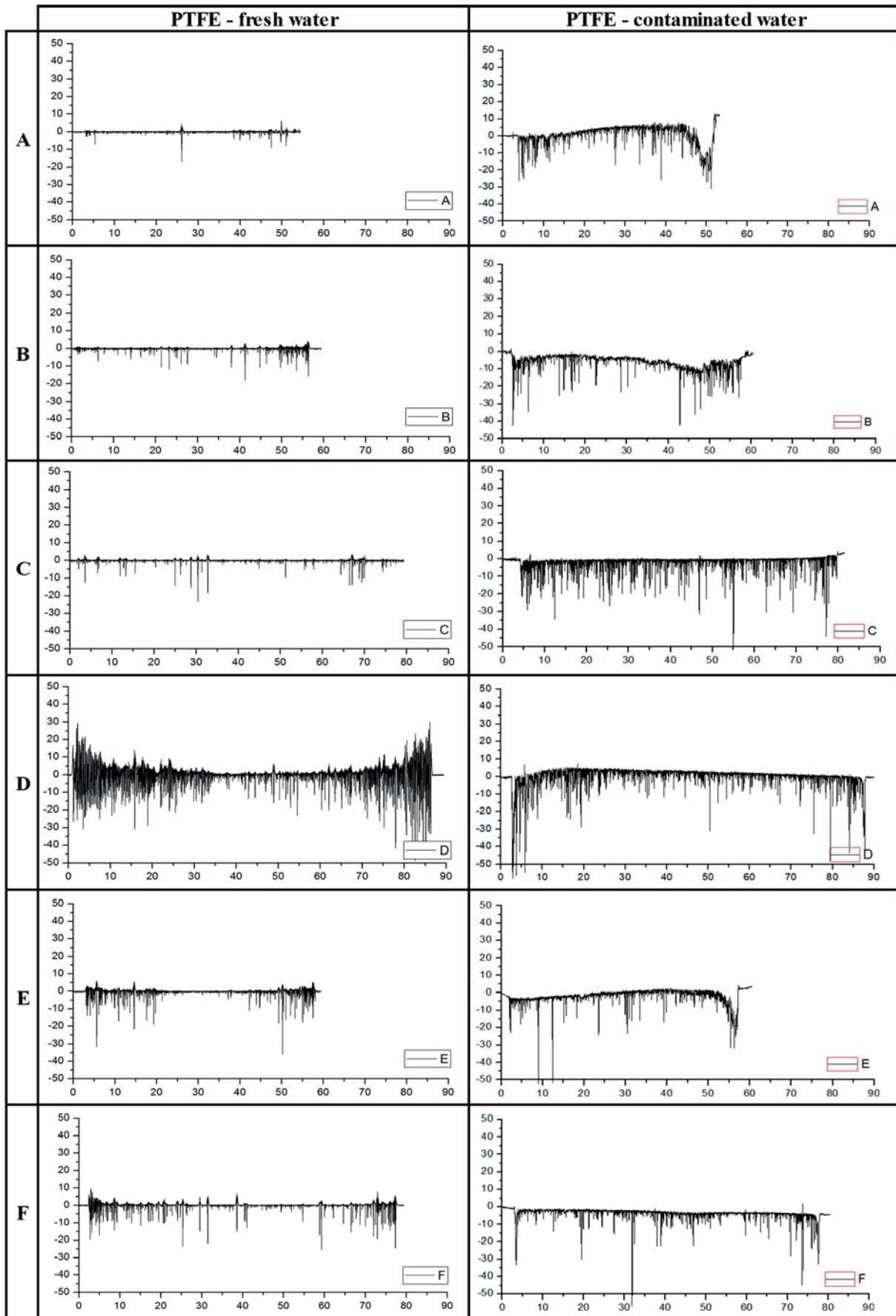
Tab. 2. Photographs of shaft journals cooperating with NBR and PTFE bushings in positions A-F in fresh and contaminated water conditions

		fresh water	contaminated water
NBR	A		
	B		
	C		
	D		
	E		
	F		
PTFE	A		
	B		
	C		
	D		
	E		
	F		

Tab. 3. Roughness profiles of journals cooperating with NBR bushings in positions A-F in fresh and contaminated water conditions obtained with a Hommel Etamic T8000 contact profilometer



Tab. 4. Roughness profiles of journals cooperating with PTFE bushings in positions A-F in fresh and contaminated water conditions obtained with a Hommel Etamic T8000 contact profilometer



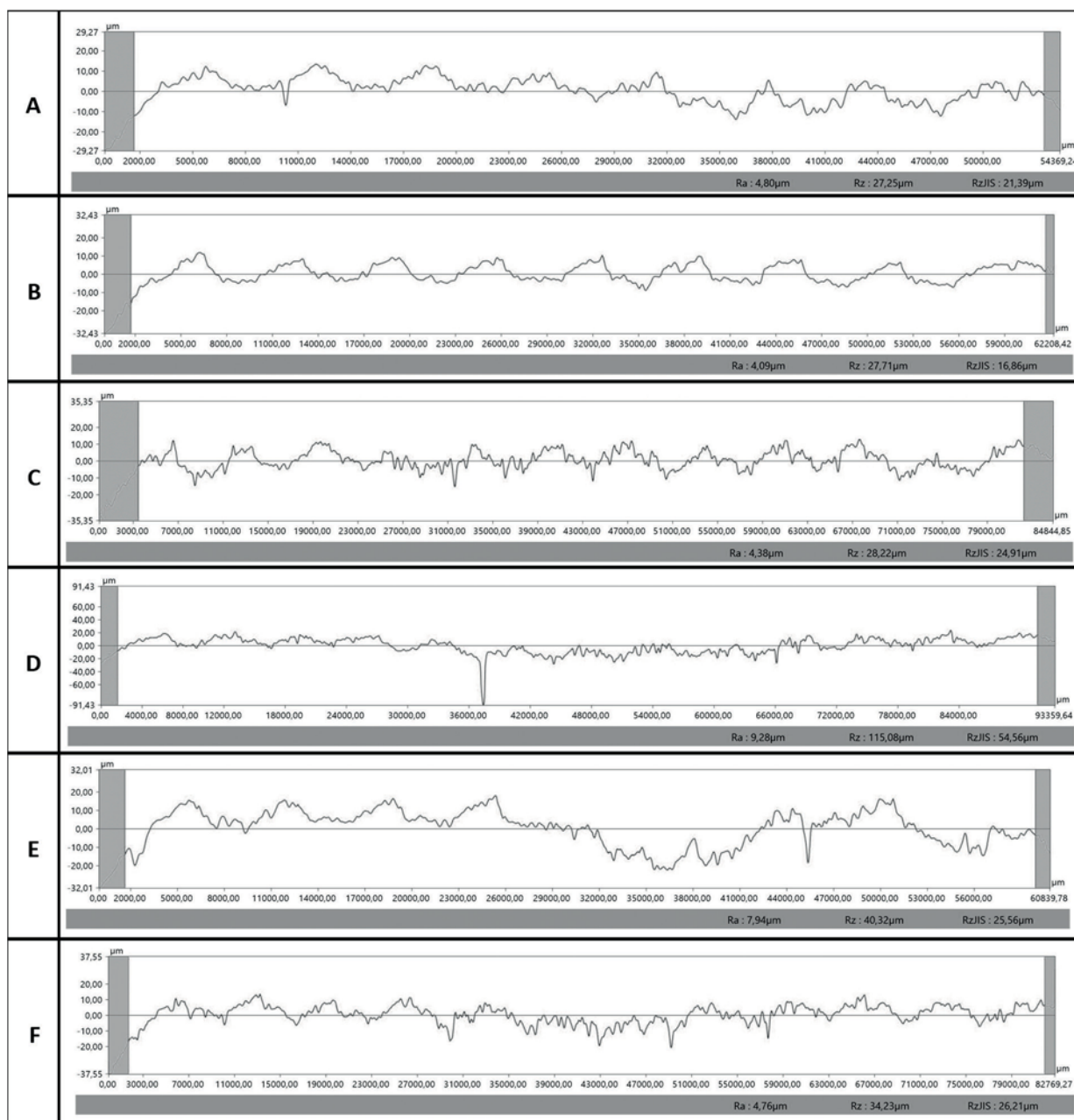
Tables 3 and 4 show the roughness profiles (Ra) of the shaft journals in the position of the self-adjusting support B (samples A-F) after cooperation with the NBR (Table 3) and PTFE (Table 4) sliding sleeves that were lubricated with fresh and contaminated liquids. The measurements were carried out using a contact profilometer.

After cooperation with PTFE, the journals, despite the visible shaft edging, were smoother and their profiles had a much smoother course. On the other hand, the journals that cooperated with the NBR bushings had a more diversified roughness profile and greater material losses were noticeable,

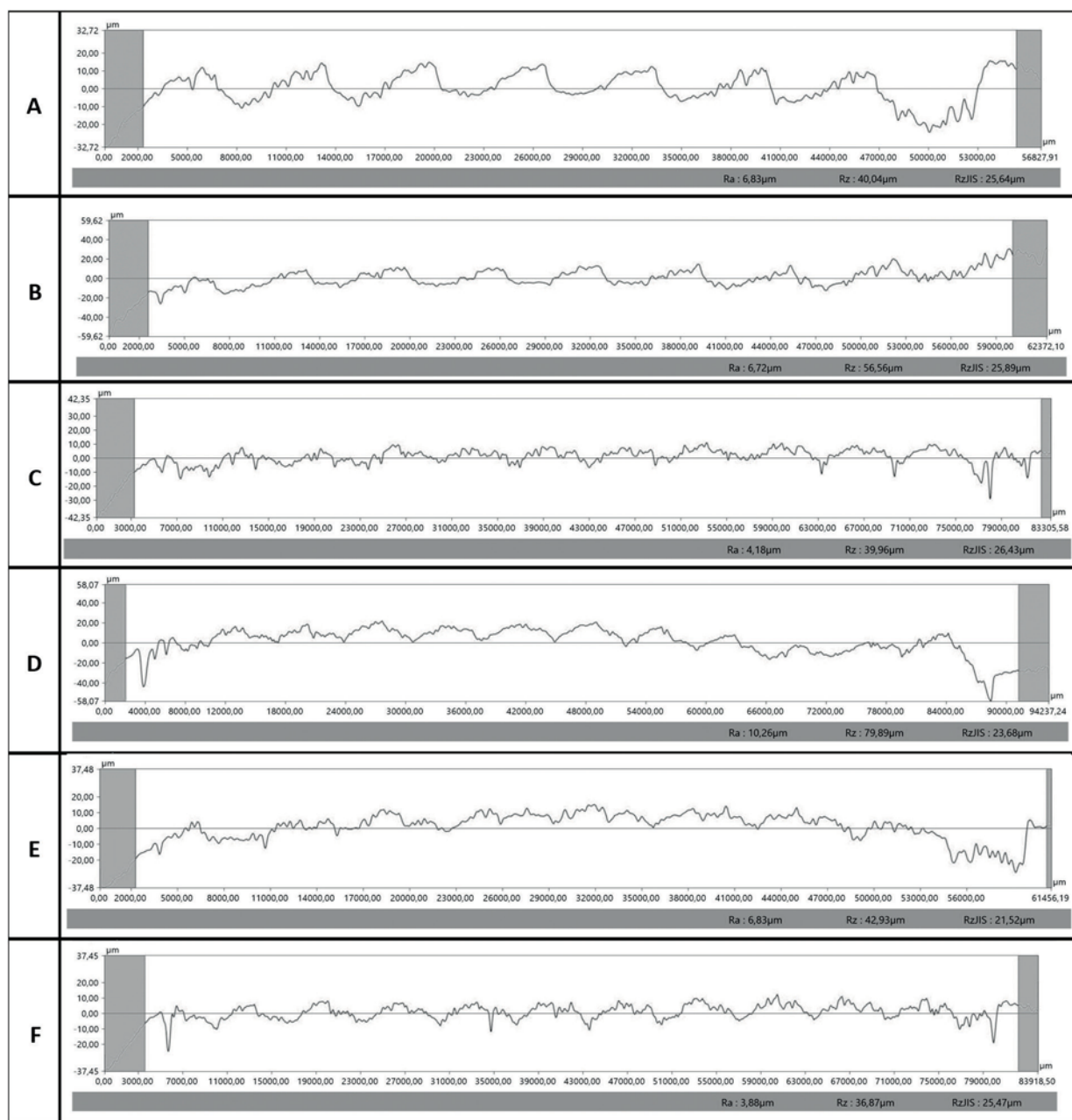
which indicates a more rapid wear process. There also was shaft edge bending, but it was less noticeable than with the PTFE.

Graphs of the roughness profiles made with an optical microscope are presented in Table 5 for the NBR bushings and Table 6 for the PTFE bushings. In this section, the profile of the roughness of the journals working only in contaminated water was limited because the bearings running in water without contamination had a much milder and more regular course.

Tab. 5. Roughness profiles of journals cooperating with NBR bushings in positions A-F in contaminated water conditions obtained with a Keyence VHX-7000 optical microscope



Tab. 6. Roughness profiles of journals cooperating with PTFE bushings in positions A-F in contaminated water conditions obtained with a Keyence VHX-7000 optical microscope



By analyzing the obtained diagrams and amount of contaminants supplied to the system, it was impossible to clearly determine how individual doses of the contaminants affected the wear process. The smallest doses of solid particles were added to the C and D measurements in the amount of 5 cm³, while the largest dose was for the F measurement in the amount of 25 cm³. For the NBR case, it appeared that the journal wear depended on the dose of contaminants, but in the case of PTFE, this did not appear to be the case, as shown by the roughness profiles of journal F in the presented diagrams and the condition of its surface. One thing is clear, namely, the water lubricating the plain bearings containing contaminants in the form of solid particles accelerated the wear process of the steel journal and increased the risk of

failure in the propulsion system of the propeller shaft line in the ship.

One may wonder about the differences in roughness Ra values among the individual samples. This difference is several times higher in the case of measurements using the optical microscope. Moreover, the roughness values of the journals cooperating with the rubber bushings often exceeded the Ra value for the journals mating with the PTFE bushing by ten times, which indicates the creation of a more diversified geometric structure after cooperation and the more intensive wear process of the journals. These differences may result from the time interval between the measurements of the journals with the profilometer and the microscope; also, with such small surfaces, it is impossible to measure the profile at

exactly the same point. An additional difficulty and a huge challenge are also the appropriate arrangement of the sample and setting and leveling the measuring instruments in such a way as to profile it perfectly on the cylindrical surface.

The observations were also made for the NBR and PTFE sliding sleeves. The surface condition after cooperation with a steel journal lubricated with water containing solid particles is shown in Figures 4 and 5 for the NBR and PTFE, respectively.



Fig. 4. The NBR sliding bush (C)



Fig. 5. The PTFE sliding bush (B)

Traces of wear caused by friction are visible on both internal surfaces of the bushings. The circumferential grooves were the result of sand particles getting between the shaft journal and the bush, but deeper grooves were seen in the NBR bush. As for the journals, the rubber bushings had the greatest wear in the middle of the bushing and at the edge of the load application. On the other hand, the wear of the PTFE bushings was evenly distributed over the entire surface of the joint. Inside, there were visible fragmented sand particles embedded in the longitudinal grooves, which could have

caused detachment the upper layer of the sleeve material, as shown in Figure 5.

Due to the observations of the bushings and the geometric structure of the journals, it was concluded that the NBR was more susceptible to deformation; damping vibrations also turned out to be worse than for the three-layer PTFE bushings. Factors that could have influenced such a course of the wear process of the sliding sleeves are the hardness of the material of the sleeves and the geometry of the sleeves. Particulate pollutants, like the sand from the Radunia River, can act as a cutting tool, especially for soft materials. Sand between the bush and the journal „sticks” into the material of the bushing, destroying the inner surface of the bush and the shaft journal at the same time and forming circumferential grooves on its surface. The active surface of both bushings was different due to the different number of grooves arranged longitudinally along the entire perimeter of the bushings. There were 8 NBR bushings and 6 PTFE bushings, which could indicate that the load field (i.e., the actual load) of both bearings operating under the same conditions was different.

SUMMARY

Based on the conducted research and analysis of the results, it can be concluded that both the material and the geometry of the bushing as well as the type of contaminants (the amount and size of the solid particles) are key parameters that influenced the speed of the wear process of the sliding node lubricated with liquid containing solid particles. Even a small dose of contamination can intensify this process, but the higher the concentration of particles in the water was, the greater the bearing wear. Undoubtedly, the material of the bushing, which showed greater wear resistance during operation in the conditions of contaminated water, was PTFE. The rubber bushings experienced more intensive wear. Misalignment of the shaft in the plain bearing bush caused deformation and deflection of the shaft, which led to its edge bending and, consequently, accelerated the wear process of the friction elements.

The results of the tests carried out may have an impact on limiting critical environmental parameters and may also allow one to propose the most optimal design solutions and selection of optimal bushing materials based on the prevailing operating conditions so as to avoid intensive wear of friction elements while also ensuring durability, reliability and trouble-free operation of the sliding node of shaft lines on ships.

ACKNOWLEDGEMENTS

This work was a part of research grant no. 2016/23/B/ST8/03104 entitled “Research on water lubricated sliding couples in conditions of improper lubrication conditions” financed by the Polish National Science Centre.

REFERENCES

1. Author's Archive, 'Propeller shaft strut bearings'.
2. W. Dai, B. Kheireddin, H. Gao, and H. Liang, 'Roles of nanoparticles in oil lubrication', *Tribol. Int.*, vol. 102, pp. 88–98, 2016, doi: 10.1016/j.triboint.2016.05.020.
3. Z. J. Zhang, D. Simionesie, and C. Schaschke, 'Graphite and hybrid nanomaterials as lubricant additives', *Lubricants*, vol. 2, no. 2, pp. 44–65, 2014, doi: 10.3390/lubricants2020044.
4. A. Barszczewska, E. Piątkowska, and W. Litwin, 'Selected Problems of Experimental Testing Marine Stern Tube Bearings', *Polish Marit. Res.*, vol. 26, no. 2, pp. 142–154, 2019, doi: 10.2478/pomr-2019-0034.
5. A. Barszczewska, 'Experimental Research on Insufficient Water Lubrication of Marine Stern Tube Journal Bearing with Elastic Polymer Bush', *Polish Marit. Res.*, vol. 27, no. 4, pp. 91–102, 2020, doi: 10.2478/pomr-2020-0069.
6. N. Vulić, K. Bratić, B. Lalić, and L. Stazić, 'Implementing Simulationx in the Modelling of Marine Shafting Steady State Torsional Vibrations', *Polish Marit. Res.*, vol. 28, no. 2, pp. 63–71, Jun. 2021, doi: 10.2478/pomr-2021-0022.
7. M. Moschopoulos, G. N. Rossopoulos, and C. I. Papadopoulos, 'Journal Bearing Performance Prediction Using Machine Learning and Octave-Band Signal Analysis of Sound and Vibration Measurements', *Polish Marit. Res.*, vol. 28, no. 3, pp. 137–149, 2021, doi: 10.2478/pomr-2021-0041.
8. A. Ursolov, Y. Batrak, and W. Tarelko, 'Application of the Optimization Methods to the Search of Marine Propulsion Shafting Global Equilibrium in Running Condition', *Polish Marit. Res.*, vol. 26, no. 3, pp. 172–180, 2019, doi: 10.2478/pomr-2019-0058.
9. H. Yang, J. Li, and X. Li, 'Calculation of the Dynamic Characteristics of Ship's Aft Stern Tube Bearing Considering Journal Deflection', *Polish Marit. Res.*, vol. 27, no. 1, pp. 107–115, 2020, doi: 10.2478/pomr-2020-0011.
10. J. Duchowski, 'Examination of journal bearing filtration requirements', *Lubr. Eng.*, vol. 09, pp. 1–9, 1998, https://www.researchgate.net/publication/287750536_Examination_of_journal_bearing_filtration_requirements.
11. J. Duchowski, 'Filtration requirements for journal bearings exposed to different contaminant levels', *Lubr. Eng.*, vol. 06, no. July, pp. 34–39, 2002, https://www.researchgate.net/publication/287750720_Filtration_requirements_for_journal_bearings_exposed_to_different_contaminant_levels.
12. D. Hargreaves and S. C. Sharma, 'Effects of solid contaminants on journal bearing performance', *Proc. 2nd World Tribol. Congr.* 3-7 Sept. 2001, pp. 237–240, 2001, https://figshare.com/articles/conference_contribution/Effects_of_solid_contaminants_on_journal_bearing_performance/13463030/1.
13. M. M. Khonsari and E. R. Booser, 'Effect of contamination on the performance of hydrodynamic bearings', *Proc. Inst. Mech. Eng. Part J J. Eng. Tribol.*, vol. 220, no. 5, pp. 419–428, 2006, doi: 10.1243/13506501J00705.
14. A. Dadouche and M. J. Conlon, 'Operational performance of textured journal bearings lubricated with a contaminated fluid', *Tribol. Int.*, vol. 93, pp. 377–389, 2016, 10.1016/j.triboint.2015.09.022.
15. S. M. Park, G. H. Kim, and Y. Z. Lee, 'Investigation of the wear behaviour of polyacetal bushings by the inflow of contaminants', *Wear*, vol. 271, no. 9–10, pp. 2193–2197, 2011, <https://doi.org/10.1016/j.wear.2010.12.033>.
16. L. Peña-Parás et al., 'Effects of substrate surface roughness and nano/micro particle additive size on friction and wear in lubricated sliding', *Tribol. Int.*, vol. 119, no. August 2017, pp. 88–98, 2018, doi: 10.1016/j.triboint.2017.09.009.
17. A. Akchurin, R. Bosman, P. M. Lugt, and M. van Drogen, 'Analysis of Wear Particles Formed in Boundary-Lubricated Sliding Contacts', *Tribol. Lett.*, vol. 63, no. 2, pp. 1–14, 2016, <https://doi.org/10.1007/s11249-016-0701-z>.
18. A. Akchurin, R. Bosman, and P. M. Lugt, 'Generation of wear particles and running-in in mixed lubricated sliding contacts', *Tribol. Int.*, vol. 110, no. February, pp. 201–208, 2017, <https://doi.org/10.1016/j.triboint.2017.02.019>.
19. A. Akchurin, R. Bosman, and P. M. Lugt, 'A Stress-Criterion-Based Model for the Prediction of the Size of Wear Particles in Boundary Lubricated Contacts', *Tribol. Lett.*, vol. 64, no. 3, pp. 1–12, 2016, <https://doi.org/10.1007/s11249-016-0772-x>.
20. G. Pintaude, 'Characteristics of Abrasive Particles and Their Implications on Wear', *New Tribol. Ways*, no. April 2011, 2012, https://www.researchgate.net/profile/Giuseppe-Pintaude/publication/221912389_Characteristics_of_Abrasive_Particles_and_Their_Implications_on_Wear/links/00b49525ef1357bd1d000000/Characteristics-of-Abrasive-Particles-and-Their-Implications-on-Wear.pdf.
21. C. Q. Yuan, Z. Peng, X. C. Zhou, and X. P. Yan, 'The characterization of wear transitions in sliding wear process contaminated with silica and iron powder', *Tribol. Int.*, vol. 38, no. 2, pp. 129–143, 2005, 10.1016/j.triboint.2004.06.007.

22. A. Ya and T. Yu, 'Revealing the influence of various factors on concentration and spatial distribution of suspended matter based on remote sensing data', *Proc. SPIE*, vol. 9638, pp. 1–12, 2015, <https://doi.org/10.1117/12.2193905>.
23. E. Szymczak and D. Burska, 'Distribution of Suspended Sediment in the Gulf of Gdansk off the Vistula River mouth (Baltic Sea, Poland)', *IOP Conf. Ser. Earth Environ. Sci.*, vol. 221, no. 1, p. 012053, Mar. 2019, doi: 10.1088/1755-1315/221/1/012053.
24. M. Damrat, A. Zaborska, and M. Zajaczkowski, 'Sedimentation from suspension and sediment accumulation rate in the River Vistula prodelta, Gulf of Gdańsk (Baltic Sea)', *Oceanology*, vol. 55, no. 4, pp. 937–950, 2013, doi:10.5697/oc.55-4.937.
25. Geological Institute and Geology Institute, 'Lithology and mineral composition of sediments from the bottom of the Gdańsk Basin', vol. 313, no. 2, 1980, https://gq.pgi.gov.pl/article/viewFile/8797/pdf_830 (in Polish).
26. T. Leipe and B. Sea, 'The kaolinite/chlorite clay mineral ratio in surface sediments of the southern Baltic Sea as an indicator for long distance transport of fine-grained material', *Baltica*, vol. 16, pp. 31–36, 2003, https://gamtostyrimai.lt/uploads/publications/docs/211_37972ec38c101346e9b8223cb576dc8b.pdf.
27. Y. Solomonov, Experimental investigation of tribological characteristics of water-lubricated bearings materials on a pin-on-disc test rig, The University of Adelaide, School of Mechanical Engineering, Master of Philosophy Thesis, April 2014, <https://digital.library.adelaide.edu.au/dspace/bitstream/2440/84676/8/02whole.pdf>, <https://hdl.handle.net/2440/84676>.
28. C. L. Dong, C. Q. Yuan, X. Q. Bai, Y. Yang, and X. P. Yan, 'Study on wear behaviours for NBR/stainless steel under sand water-lubricated conditions', *Wear*, vol. 332–333, pp. 1012–1020, 2015, 10.1016/j.wear.2015.01.009.
29. C. Yuan, Z. Guo, W. Tao, C. Dong, and X. Bai, 'Effects of different grain sized sands on wear behaviours of NBR/casting copper alloys', *Wear*, vol. 384–385, pp. 185–191, Aug. 2017, doi: 10.1016/j.wear.2017.02.019.
30. T. Chang, Z. Guo, and C. Yuan, 'Study on influence of Koch snowflake surface texture on tribological performance for marine water-lubricated bearings', *Tribol. Int.*, vol. 129, pp. 29–37, 2019, doi: 10.1016/j.triboint.2018.08.015.
31. Z. Wu, C. Sheng, Z. Guo, F. Li, 'Equivalent Calculate of the Equivalent Radius and the Tribological Performance of the Marine Water-Lubricated Bearing', *Mocaxue Xuebao/Tribology*, vol. 37, no. 5, pp. 656–662, 2017, doi: 10.16078/j.tribology.2017.05.013.
32. Z. Jia, Z. Guo, C. Yuan, 'Effect of Material Hardness on Water Lubrication Performance of Thermoplastic Polyurethane under Sediment Environment', *J. Mater. Eng. Perform.*, vol. 30, no. 10, pp. 7532–7541, 2021, doi: 10.1007/s11665-021-05912-z.
33. X. Liang, Z. Guo, J. Tian, C. Yuan, 'Development of modified polyacrylonitrile fibers for improving tribological performance characteristics of thermoplastic polyurethane material in water-lubricated sliding bearings', *Polym. Adv. Technol.*, vol. 31, no. 12, pp. 3258–3271, 2020, doi: 10.1002/pat.5050.
34. Z. Cui, Z. Guo, X. Xie, C. Yuan, 'The Synergistic Effect Mechanism of PA66 Self-Lubrication Property and Surface Texture on Tribological Performance of HDPE Water-Lubricated Bearing', *Mocaxue Xuebao/Tribology*, vol. 39, no. 4, pp. 407–417, 2019, doi: 10.16078/j.tribology.2018171.

CONTACT WITH THE AUTHOR

Ewa Piątkowska

e-mail: ewapiatk@pg.edu.pl

Gdansk University of Technology,
ul. Gabriela Narutowicza 11/12
80-233 Gdańsk,
POLAND

LETTER TO EDITOR

Krzysztof Wołoszyk

Paweł Michał Bielski

Tomasz Mikulski

Institute of Naval Architecture and Ocean Engineering
Faculty of Mechanical Engineering and Ship Technology
Gdańsk University of Technology
ul. Narutowicza 11/12, 80-233 Gdańsk, Poland

* e-mail for correspondence: krzwolos@pg.edu.pl (K. Wołoszyk)

tel. 58 347 27 39

Prof. Wiesław Tarełko
Editor-in-chief of Polish Maritime Research

Dear Editor,

We regret to inform you that the paper [1] includes misleading information about the photogrammetric measurements. These measurements were carried out using an experimental stand invented, designed and made by A. Tomaszewska, I. Lubowiecka, K. Szepietowska, P.M. Bielski, and C. Szymczak for investigation of deformation of the human abdominal wall in vivo [2].

We acknowledge the use of that stand to obtain the photogrammetric results utilised in the Polish Maritime Research paper [1] and in a subsequent publication [3] which is referred to as „K. Wołoszyk, P. Bielski, Y. Garbatov, T. Mikulski, Photogrammetry image-based approach for imperfect structure modelling and FE analysis, 2020, manuscript in preparation” in the original paper [1].

We apologise for any inconvenience caused.

Yours sincerely,
Krzysztof Wołoszyk
Paweł Michał Bielski
Tomasz Mikulski

References:

[1] K. Wołoszyk, Y. Garbatov, J. Kowalski, L. Samson, Experimental and Numerical Investigations of Ultimate Strength of Imperfect Stiffened Plates of Different Slenderness, *Polish Marit. Res.* 27 (2020) 120–129. doi:10.2478/POMR-2020-0072.

[2] I. Lubowiecka, K. Szepietowska, A. Tomaszewska, P.M. Bielski, M. Chmielewski, M. Lichodziejewska-Niemierko, C. Szymczak, A novel in vivo approach to assess strains of the human abdominal wall under known intraabdominal pressure, (2021). <http://arxiv.org/abs/2107.11313>.

[3] K. Wołoszyk, P.M. Bielski, Y. Garbatov, T. Mikulski, Photogrammetry image-based approach for imperfect structure modelling and FE analysis, *Ocean Eng.* 223 (2021) 108665. doi:10.1016/j.oceaneng.2021.108665.